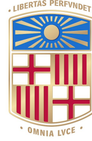

UNIVERSITAT DE BARCELONA

Silicon Nanocrystal Superlattices for Light-Emitting and Photovoltaic Devices

Julià López Vidrier

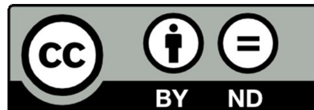

Aquesta tesi doctoral està subjecta a la llicència *Reconeixement- SenseObraDerivada 3.0. Espanya de Creative Commons*.

Esta tesis doctoral está sujeta a la licencia *Reconocimiento - SinObraDerivada 3.0. España de Creative* Commons.

This doctoral thesis is licensed under the *Creative Commons Attribution-NoDerivatives 3.0. Spain License.*

Silicon Nanocrystal Superlattices for Light-Emitting and Photovoltaic Devices

Julià López Vidrier

MEMÒRIA DE TESI DOCTORAL PRESENTADA PER OPTAR AL TÍTOL DE DOCTOR EN FÍSICA PER LA UNIVERSITAT DE BARCELONA

(PROGRAMA DE MENCIÓ INTERNACIONAL)

Directors: Dr. Sergi Hernández Márquez
Prof. Dr. Blas Garrido Fernández

Tutor: Prof. Dr. Blas Garrido Fernández

Facultat de Física, Departament d'Electrònica
Barcelona, Abril de 2015

Programa de Doctorat en Física

Silicon Nanocrystal Superlattices for Light-Emitting and Photovoltaic Devices

Tesi que presenta

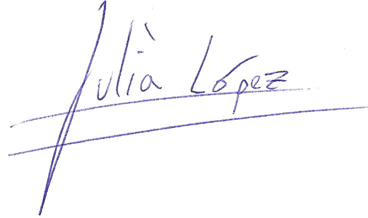

Julià López Vidrier

per optar al títol de Doctor en Física per la Universitat de Barcelona

Directors de Tesi:

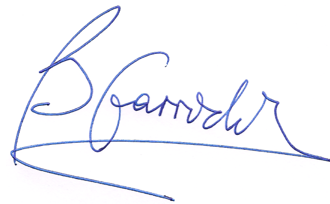

Dr. Sergi Hernández Márquez

Prof. Dr. Blas Garrido Fernández

Departament d'Electrònica, Facultat de Física
Grup de Micro- i Nanotecnologies i Nanoscòpies per Dispositius Electrònics i Fotònics (MIND)
Institut de Nanociència i Nanotecnologia (IN^2UB)

Dedicat a la meva família i als meus amics, que m'han acompanyat en aquest llarg camí.

Abstract

Since the development of electronics, both the scientific community and the industry have focused on the study and usage of silicon, as it presents a good balance between electrical properties and manufacturing costs. Moreover, both the good Si electrical performance (due to proper band gap energy for conduction and excellent crystalline quality) and its abundance in the Earth's crust make Si the optimum candidate for mass production. However, the indirect nature of the Si band gap makes photon-based inter-band transitions low probable according to the dipolar approximation, and thus poor light emission properties are expected from this material. This supposed a great drawback after the onset of optoelectronics and photonics, when light management became the key factor for technological progress. In particular, Si IR emission discarded this material for visible illumination purposes. On the contrary, Si presents the almost ideal properties for single-band gap photovoltaics, although the Si solar cells efficiency soon reached an upper limit that cannot be overcome with the bulk Si configuration.

During the last two decades, nanostructuring silicon was found to improve the Si optical emission properties by relaxing the band-to-band radiative transition selection rules, whose consequences were a higher band gap energy and the discretization of the energetic levels, as well as their dependence on the nanocrystal (NC) size because of the quantum confinement effect that governs these 0-dimensional structures. This way, silicon could become suitable for light-based electronic applications; in particular, it is possible to tune light emission within the visible range, and optimize Si NCs as wide band gap energy absorbers for all-Si tandem solar cells. The potential of Si NCs arise from their size tunability, and therefore their properties can be controlled by achieving NC size confinement. Ordinary techniques such as ion-implantation were not capable to attain controlled-size nanostructures, the diffusion of Si within the embedding matrix inducing large non-confined nanoaggregates. It was the superlattice (SL) approach which gave interesting and reproducible results, which consisted of the deposition of alternated stoichiometric and Si-rich Si-based materials (such as SiO_2 or SiC), the former sublayers acting as barriers for the Si excess diffusion. Among the different existing ultra-thin film (few nm) deposition techniques, plasma-enhanced chemical-vapor deposition was found to allow the control of the mean NC size down to 2 nm values by the precise manipulation of the precursor gas fluxes, and thinner size distributions than in implantation techniques were attained.

The aim of this Thesis Project is the characterization of Si NC superlattices in either SiO_2 or SiC dielectric matrices, aiming at the superlattice parameters optimization towards a proper optoelectronic and photovoltaic performance. With this purpose, superlattice structures alternating Si-rich and stoichiometric SiO_2 / SiC layers were deposited on either Si or fused silica substrates. The precipitation and crystallization of the Si excess within the non-stoichiometric layers was achieved via a high-temperature annealing treatment, which induced phase separation between Si and the embedding matrix. The material preparation processes were carried out in specialist European institutions. In particular, Si NC / SiO_2 superlattices were fabricated at the *Institut für Mikrosystemtechnik* (IMTEK, Albert-Ludwigs Universität, Freiburg, Germany), whereas the Si NC / SiC

superlattices were prepared at the *Istituto per la Microelettronica e i Microsistemi - Consiglio Nazionalle delle Ricerche* (CNR-IMM, Bologna, Italy). Regarding the study of the electrical and electro-optical properties of these material systems, devices containing the NC superlattices were fabricated also with the collaboration of the *Fraunhofer Institut für Solare Energiesysteme* (ISE, Freiburg, Germany). The study of the Si NC-based SL properties was performed from a structural, optical, electrical and electro-optical point of view. For this, different experimental techniques were employed: transmission and scanning electron microscopy (TEM and SEM, respectively), Raman scattering spectroscopy, X-ray diffraction (XRD), photoluminescence spectroscopy (PL), UV-visible absorption spectroscopy (reflectance and transmittance), dark and under illumination electrical characterization, electroluminescence spectroscopy (EL), time-resolved EL measurements, Fourier-Transform photocurrent spectroscopy and light-beam induced current spectroscopy (LBIC).

The first block of the Thesis Project focuses on the physical properties of Si NCs / SiO_2 superlattices. Structural and optical characterization helped determining the structural SL conditions that allowed for an optimum light emission while maintaining the overall superlattice structure. It was found that a SL and size distribution control was achieved for Si-rich layer thicknesses lower than 5 nm. Especially, 3.5-nm NCs exhibited the strongest PL emission and in the reddish part of the visible spectrum. The annealing temperature was found to be a crucial parameter to take into account, being 1150 °C the optimum temperature for the growth of size-controlled highly-crystalline Si NCs. From Raman spectra, a phonon confinement model, which considered the NC size distribution, was employed to assess the crystalline quality of the samples, achieving crystalline fractions around 80−90 %, which is in agreement with an amorphous Si or suboxide NC / SiO_2 interface with a thickness of 1-2 atomic layers. An analysis by TEM combined with electron energy loss spectroscopy in similar samples revealed the stoichiometry of this transition shell, formed by a nitrogen-rich silicon oxide. The PL emission origin was also investigated via Raman and PL measurements under high hydrostatic pressure, being light emission attributed to a competition between radiative excitonic recombination within the NCs and luminescence arising from localized surface states (defects), in agreement with other previously published works.

Embedding the superlattices within a *p-i-n* device structure, the electrical properties of the material could be characterized. Charge transport was proved to be dominated by Poole-Frenkel mechanism, whereas the experiments support impact ionization of accelerated carriers in the SL conduction band as the NC excitation mechanism that yields EL. Despite the low EL emission yield obtained for this material system, the study has allowed determining the ideal structural SL parameters to obtain the optimum emission efficiency (with values of $\sim 10^{-3}$ %). Especially, SiO_2 barrier thicknesses of 2 nm and low Si content (Si excess of ∼12−15 at.%) offer an excellent structural control while yielding a maximum EL emission. Therefore, the overall characterization of Si NCs / SiO_2 SLs was useful to discuss on the material availability for light emission applications.

The second block regards to Si NCs / SiC superlattices as a material candidate for the top part of an all-Si tandem solar cell. Due to the narrow structural parameters variation of Si NC / SiC systems that permit SL maintenance, being one of the main drawbacks the

C atoms diffusion, the NC size control is much more complex. However, the structural and optical characterization of the SLs allowed establishing the variation range of the structural parameters that permitted the SL structure maintenance. It was found that a high Si content was required ($x = 0.85$ in Si_xC_{1-x}), lower values being insufficient for NC formation but larger ones producing continuous Si-rich layer crystallization. As well, C diffusion was only partially avoided for thick SiC barriers (~ 5 nm) and Si-rich layers ($3-4$ nm). In addition, the optimum annealing temperature for the NC formation was found at 1100 °C. Raman scattering, XRD and optical absorption measurements were found to complement TEM observations, their combination being able to predict structural parameters such as layer or total thicknesses, as well as volume fraction of the present material phases (crystalline and amorphous Si, crystalline and amorphous SiC). A crystalline degree between 40 and 60 % was found, the low value being due to a thick substoichiometric transition region surrounding the NC core. This latter region was ascribed to the high Si / SiC interface energy, inducing the creation of two lower-energy interfaces via the transition phase formation.

The electrical characterization carried out on Si NC / SiC multilayers revealed variable range hopping (combined with conduction through extended states) as the dominant charge transport mechanism through this material system. To study the electro-optical properties of the Si NC superlattices, the Si substrate was removed from samples containing the multilayered active material under investigation, achieving a membrane-like *p-i-n* device. It was found that a great absorption takes place within the active material, whose NC-based onset establishes a proof of quantum confinement in these material systems. However, the overall spectral response is orders of magnitude lower, which was attributed to the electrical properties of the NC-based SLs. In particular, the photovoltaic properties were strongly influenced by recombination, which notably hampers the photogenerated carriers extraction towards the electrodes. Although the solar cell efficiency ($\sim 10^{-3}$ %) is still far from commercial purposes, the presented study sheds light to the best material configuration for an optimum wide-band gap absorber for all-Si tandem solar cells.

Acknowledgements

> No one is useless in this world who lightens the burdens of another.
>
> Charles Dickens

Perhaps, writing the following lines constituted the most difficult part of this Thesis Dissertation, since many people have contributed to the achievement of the different results hereby presented. To efficiently manage with this section, the acknowledgements must be divided according to three different ways of support: economic, scientific and emotional.

This work was possible thanks to the European *NASCEnT* (NMP4-SL-2010-245977) and the Spanish *LEOMIS* (TEC2012-38540-C02-01) Projects. I personally acknowledge financial support from the *NASCEnT* and the European *HELIOS* (FP7-ICT-224312) Projects, as well as from the scholarship and later contract I acquired from the University of Barcelona Program towards the Formation of Novel Researchers (APIF from its Catalan acronym).

I could not have succeeded in pulling ahead this Thesis Project without the guidance and wise advices from my Thesis Advisors, Sergi Hernández Márquez and Blas Garrido Fernández. To Sergi I would like to particularly acknowledge his friendship and moral support during the more-than-5 years I have been working in the group, as well as all knowledge he has instilled me regarding semiconductor and material science. I am also very grateful to Blas for all advices received regarding device fundamental physics (which allowed elevating the impact of the obtained results) and his promptness to spend money in all equipment, conferences and other scientific stuff I required along my Thesis. It has been a real pleasure to work under the supervision of both of them.

Also must I mention here my group partners during the 3 years of the *NASCEnT* Project lasted and the time lapsed to date. Thanks to Daniel Hiller, Sebastian Gutsch, Andreas Hartel and Margit Zacharias (members of the IMTEK institute in Freiburg, Germany) for the fabrication of Si NCs / SiO_2 superlattices. Also thanks to Marica Canino, Marco Allegrezza, Michelle Bellettato and Caterina Summonte (members of the CNR−IMM institute in Bologna, Italy) for their counterpart in Si NCs / SiC multilayers fabrication. Special mention to the Fraunhofer ISE partners (Freiburg, Germany), Manuel Schnabel, Philipp Löper, Charlotte Weiss and Stefan Janz, for their help in Si NC-based solar cells during my 3-months stage at ISE, to whom I consider friends. Other project-related partners must not be forgotten: Jan Valenta (from the Charles University in Prague, Czech Republic), Salvo Mirabella and Antonio Terrasi (from the University of Catania, Italy), and Roberto Guerra, Ivan Marri and Stefano Ossicini (from the University of Modena and Reggio Emilia, Italy). All them contributed to the publication of the obtained results.

Working all these years was endurable thanks to the friendship environment within my group, MIND-UB, where I have temporally coincided with very smart and nice people, some of them who I consider my friends. Let me list them: Joan Manel Ramírez

(el *Vedell de la Bisbal*, on tan se'ls en fot quedar bé com mal), Yonder Berencén (el *Jimagua Cubano*, buen tío aunque mandril), Oriol Blázquez (el *Noi del Guinardó*, capaç de detectar gallines en un aeroport internacional), Martí Busquets-Masó (el *Perill de les Comarcals*) and Adrià Huguet (el *Futur Director del Departament*); the prestigious TEM group: Lluís López-Conesa (l'etern número 6, alias *El Sotaneitor*), Josep Manel Rebled (l'*Essència del Despatx*), Alberto Eljarrat (y los −20 °C de Vigo), Gemma Martín (*la del Somriure Perpetu per Tothom...* y la "falda de topos"), Pau Torruella (el *Relaciones Sociales*), Catalina Coll (alias *The Remover*); the gas-issues and synthesis-lab guys: Oriol Monereo (the *Shirt-Over-T-Shirt Knight*), Giovanni Vescio (the *Italian Signorino*), Núria Garcia-Castelló (la *Jazz Woman*), Jordi Samà (el *Samaritano*), Sergio Illera (el *Pseudoempírico*), Beatriz Medina (*La Carnicera*) and Omar Olmedo (*The [too loud] Voice*); Albert Cornet, Francesca Peiró, Paolo Pellegrino, Albert Cirera, Albert Romano, Sònia Estradé, Juan Daniel Prades, Aïda Varea and Atilà Herms, els *Peixos Grossos.* I want to also acknowledge Marta Lluscà, Luis Hernández and Jordi Ibáñez, for fruitful discussions and close collaboration. And other workmates that already left: Sergi Claramunt (el meu primer company de despatx), Alexander Martínez, Sònia Conesa, Marcel Boix, Daniel Navarro-Urríos, Olivier Jambois, Federico Ferrarese-Lupi, Lluís Yedra and Arnau Pou. And, of course, the Electronics Department staff: Roser Marzo, Conchita Panchuelo, Montse Farré, Mari Trini Patús, Josep Maria Herrero, Antonio Cruz and Andrés Romero.

Last, but by no means least, deixo els agraïments que em són més especials. Agraeixo als meus pares el suport que m'han donat durant tots aquest anys, i els anteriors, i molt probablement els futurs. M'han permès estudiar el que vaig voler, i m'han procurat la millor educació i l'afecte més gran possibles, sense posar mai impediments ni queixes i sempre confiant en mi en tot el que he realitzat. A ells vull sumar els meus avis, artífex de bona part de la meva educació des de ben petit, i a qui jo he estimat com uns pares. Estic ben segur que haurien estat molt orgullosos de veure'm doctorar. També al David, mon germà i padrí, que sempre m'ha ajudat en tot el que he necessitat, a la meva cunyada, l'Elisabeth, sempre disposada a acollir-me a casa seva, i la Sílvia, la meva estimada neboda i fillola, a qui desitjo el millor futur possible i una vida molt plena. No menys important ha estat la meva tieta, la Babet, sempre disposada a viatjar i a fer-nos passar una bona estona.

Al grup familiar voldria afegir els meus millors amics, des que vàrem començar l'escola primària, en Jordi Isern i en Roger, amb els quals he anat a classe fins finalitzar l'etapa de l'institut, i amb qui he compartit dels moments més memorables que duré amb mi tota la vida. A ells vull unir la Zaida, l'Helena i la Núria Manresa, tots ells formant el grup de clients habituals del Michael's Tavern (també agrair als seus propietaris, en Miguel i la Maria, per les "morcillitas" i "chupitos d'Orujo d'herbes" gratuït). Tampoc puc oblidar-me d'altres amics de Sant Andreu, l'escola i l'institut, amb qui he compartit molts moments de futbol, videojocs, cerveses i altres aficions (pre ordre alfabètic de nom): Anna Hernando, Àlex Coderch, Àlex Colomer, Dani Pérez, Denís, Guillem, Jordi Coscolla, Laia, Maria Juárez, Marta Perejuan, Muriel, Noelia, Oriol Arronis, Pablo i Sergi Cusidó. També m'agradaria unir en aquest grup d'amistats a tots aquells amb qui he compartit grans moments durant la carrera i també el doctorat: Alba, Alícia,

Alberto Delgado, Bárbara, Carlos Laredo, Carmen, Clara, Cristian, Dani Pacheco, David Frigola, Elena, Elisenda, Gabriel, Gabriele Bellocchi, Gabriele Calabrese, Glòria, Ilaria, Josep Sirvent, Jonatan, Juan, Ione, Manuel, Marc Torres, Maria Martí, Marina, Martina, Noemi, Pau Flores, Raquel, Santi, Sara, Sofia, Toño, Víctor Manuel Freire i Víctor López.

And many other people not listed here, who in some way have helped me walking through this long and harsh path...

Contents

1. Introduction **1**
1.1. Silicon: an Overview 1
1.2. The Role of Silicon in Optoelectronics and Photonics 1
1.3. Nanostructuring Silicon 3
1.4. State-of-the-Art 5
1.4.1. Silicon Nanocrystals in Light-Emitting Devices 5
1.4.2. Silicon Nanocrystals in Photovoltaics 6
1.5. Objectives of the Present Doctoral Thesis 9
1.6. Outline of the Thesis 10

2. Fundamentals of Silicon Nanocrystals **13**
2.1. Quantum Confinement 13
2.2. Silicon Nanocrystals Formation: The Superlattice Approach 17
2.3. Structural and Optical Properties of Silicon Nanocrystals 22
2.3.1. Structural Properties of Silicon Nanocrystals 22
2.3.1.1. The Phonon Confinement Model 25
2.3.1.2. Matrix Stress on Silicon Nanocrystals 27
2.3.2. Optical Properties of Silicon Nanocrystals 28
2.3.2.1. Light Absorption and Emission in Semiconductors 29
2.3.2.2. Luminescence Origin in Silicon Nanocrystals 30
2.3.2.3. Temperature and Pressure Effect on Silicon Nanocrystals 33
2.3.2.4. Recombination Dynamics in Silicon Nanocrystals . 35
2.4. Electrical and Electro-Optical Properties of Si NC Superlattices . . 37
2.4.1. Charge Transport Mechanisms 37
2.4.1.1. Bulk-Limited Mechanisms 38
2.4.1.2. Electrode-Limited Mechanisms 41
2.4.1.3. Transport in Amorphous Superlattices 43
2.4.2. Electro-Optical Properties of Si-NC Superlattices 45
2.4.2.1. Electroluminescence of Si NC Superlattices 45
2.4.2.2. Photoconduction and Photocurrent in Si NC Superlattices 47

3. Experimental Details **51**
3.1. Sample Fabrication 51

3.2. Experimental Techniques 53
3.2.1. Structural Characterization Techniques 53
3.2.1.1. Transmission Electron Microscopy (TEM) 53
Experimental Equipment 55
3.2.1.2. X-Ray Diffraction (XRD) 55
Experimental Equipment 57
3.2.2. Optical Characterization Techniques 57
3.2.2.1. Light-Matter Interaction 57
3.2.2.2. UV-Visible Absorption Spectroscopy 58
Experimental Equipment 61
3.2.2.3. Photoluminescence Spectroscopy (PL) 61
Time-Resolved Photoluminescence (TR-PL) 63
Experimental Equipment 64
3.2.2.4. Raman Scattering Spectroscopy 65
Cross-Section Configuration 68
Experimental Equipment 70
3.2.3. Electrical and Electro-Optical Characterization Techniques . 70
3.2.3.1. Intensity-Voltage Characteristics [$I(V)$] 70
Experimental Equipment 73
3.2.3.2. Electroluminescence Spectroscopy (EL) 73
Time-Resolved Electroluminescence (TR-EL) 75
Experimental Equipment 76
3.2.4. Photovoltaic Characterization Techniques 76
3.2.4.1. Intensity-Voltage Photovoltaic Performance [$I(V)$-PV] 76
Light-Beam Induced Current (LBIC) Spectroscopy . . 79
Experimental Equipment 79
3.2.4.2. Spectral Response (SR) Spectroscopy 79
Experimental Equipment 80

4. Results and Discussion 83
4.1. Material Properties of Si Nanocrystal Superlattices 83
Multilayer versus Superlattice 84
4.1.1. Material Characterization of Si NC / SiO_2 Superlattices . . 85
4.1.1.1. NC Size Study in Si NCs / SiO_2 Superlattices . . . 85
4.1.1.2. Superlattice Maintenance in Si NCs / SiO_2 Systems 93
4.1.1.3. Crystalline Degree Determination of Si NCs in SiO_2 103
4.1.1.4. Phase Imaging and Identification in Si NC Multilayers within Different Dielectric Matrices 116
4.1.1.5. Luminescence Origin Investigation in Si NCs / SiO_2 under High Hydrostatic Pressure 131

4.1.2. Material Characterization of Si NC / SiC Multilayers 140
4.1.2.1. Characterization Drawbacks of Si NCs in SiC . . . 140
4.1.2.2. Initial Approaches on the Structural and Optical Properties 140
4.1.2.3. Superlattice Parameters Optimization 150
4.2. Electrical and Optoelectronic Properties of Si Nanocrystal Superlattices 164
4.2.1. Si Nanocrystal / SiO_2 Superlattices for Light Emission Applications 164
4.2.1.1. On Charge Transport and Electroluminescence . . 164
4.2.1.2. Superlattice Optimization for Light Emission . . . 175
4.2.2. Si Nanocrystal / SiC Superlattices for Photovoltaic Applications 187
4.2.2.1. Electrical Conduction Properties of Si NC / SiC Multilayers 187
4.2.2.2. Si NC / SiC Multilayers as Active Absorber Material for Photovoltaic Applications 204

5. Summary and Conclusions 215
5.1. Si NC / SiO_2 Superlattices 215
5.2. Si NC / SiC Superlattices 217
5.3. Future Approaches for Efficiency Improvement 218

6. Resum en Català 221

A. List of Publications as Part of the Present Doctoral Thesis 225
A.1. Paper Contribution Statement 225
A.2. List of Articles 226

B. Curriculum Vitae 229
B.1. Journal Publications 229
B.2. Book Chapters 231
B.3. Conference Contributions 232
B.4. Participation in Research Projects from Public Calls 237
B.5. Research Stays Abroad 239
B.6. Other Merits 241

Bibliography 247

1. Introduction

> The scientist is not a person who gives the right answers, he's one who asks the right questions.
>
> Claude Lévi-Strauss

1.1. Silicon: an Overview

Among the most important semiconductors, silicon (Si) has become the most vastly employed material, since their abundance (it is the second most abundant chemical element on the Earth's crust, after oxygen) and its simple manipulation convert it into a very cheap candidate for the electronics industry. Moreover, its fundamental structure based on tetragonal covalent bounds makes Si a robust material. When closely inspecting the particular properties of Si, the relatively low band gap energy it exhibits ($E_{\mathrm{g,Si}} = 1.12$ eV), together with the moderately low effective mass for electrons ($m_{\mathrm{e}}^{*} \approx 1.08\ m_0$, being $m_0 = 9.11\times10^{-31}$ kg the free electron rest mass [1]) and the high electron mobility and diffusion coefficient (1450 cm^{-2}V^{-1}s^{-1} and 36 cm^{-2}s^{-1}, respectively, at room temperature [2]), notably favors electrical conductivity. However, the indirect nature of this band gap states a fundamental drawback for band-to-band electronic transitions that involve photon absorption or generation, which are, in quantum mechanics terms, low-probable.

In this Chapter we deal with the usage of Si in the optoelectronics industry, from a historical point of view, and how the advances in semiconductor physics and engineering allowed to improve Si properties by means of nanostructuring. It is within this field that the present Thesis Project is embedded, whose global and particular objectives will be here exposed.

1.2. The Role of Silicon in Optoelectronics and Photonics

Since the introduction of semiconductors, the field of electronics has been largely developed during the second half of the past century. In particular, the integration of transistors and other devices into chips supposed a revolution in the history of computing hardware, which allowed for faster data processing and larger storage capacity. In 1965, G.E. Moore predicted a trend for the evolution of hardware: the number of transistors that could be integrated into a chip would be doubled

every 18 months. This is called the *Moore's law* [3], and has been accomplished to date. However, different physical facts (such as miniaturization size limit, not enough fast interconnections and insufficient heat management) become severe drawbacks for the further development of this technology, which sets a bottleneck for the microelectronics industry. The necessity of a novel strategy to overcome this handicap resulted in varying the means through which information flows: light was then thought to be the future, and different physical and technological approaches needed to be *developed*.

Photonics science studies the photon and the fundamental physics of light, whose application in photonics technology allows for the manipulation and control of light at all stages: emission, absorption, sensing, guiding, signal processing, modulation and switching [4]. The range of application of Photonics extends over almost the whole electromagnetic spectrum, from X-ray (high frequency) to THz (low frequency) radiation manipulation. Of paramount interest for novel Electronics are the photon-electron interaction phenomena (or other general processes involving both particles). This establishes the intersection of Photonics and Electronics, in a combined discipline known as Optoelectronics, whose main goal is the study and development of electronic devices where light develops an important role (light emission, absorption or control). In Fig. 1.1, the typical electromagnetic spectrum involved in optoelectronic applications is displayed, which spans from the NUV to the NIR ranges. All these fields aim at the achievement of *photonic integrated circuits* (PIC), i.e. robust platforms consisting of semiconductor-based optically-active devices where light substitutes the medium-dependent electronic-carrier transport, thus allowing for a greater processing velocity and data storage. Although III-V semiconductors can efficiently perform most of the functions required within a PIC, their expensive cost and difficult integrability with Si electronics and technology result in the need of a new approach.

The concept of Si photonics was born to exploit the optical properties of Si for different applications that span from light emission to light detection [5]. In the case of waveguiding, Si-based materials such as Si-rich SiO_2 or Si_3N_4 are already being used for mid-IR waveguiding, with losses in the order of 2 $dB \cdot cm^{-1}$ [6]. In addition, the doping of these materials with rare earth ions such as Er^{3+}, whose electronic transition is at 1535 nm (the third window of telecommunications), has proved to be useful to efficiently confine, guide and generate NIR light through different optoelectronic components [7, 8]. Regarding visible light emission and absorption, Si-based optical emitters and photoreceptors need to exploit the properties offered by nanostructured Si, aiming at band gap tunability and higher performance efficiency than bulk Si.

Different applications have been recently targeted by Si Photonics research community: light emission and light conversion. In the first case, the use of bulk Si was totally forbidden by its poor emission properties; the use of nanostructured Si enlightened the horizon towards Si-based light emitters in the yellow-red part

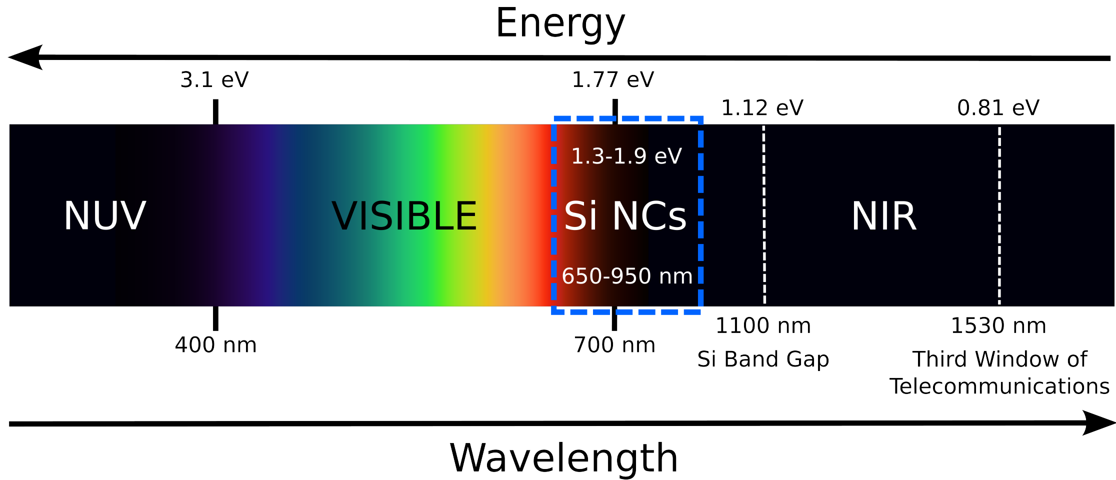

Figure 1.1.: Electromagnetic spectrum corresponding to the main energy (wavelength) range of interest studied by in the field of Optoelectronics. The range within which Si nanocrystals are applied is highlighted.

of the solar spectrum. A different motif led the study of Si nanostructures for photovoltaics, where bulk Si already governs the solar cell market; it was then the increase of efficiency what was pursued. Both topics will be further discussed in this Chapter.

1.3. Nanostructuring Silicon

The poor optical properties yielded by bulk Si have stated the main drawback for its use in optoelectronics and photonics. The indirect band gap that Si presents dramatically decreases the band-to-band transition probability; a change in the wavevector is required, usually provided by the absorption or generation of a lattice phonon. This fact already hinders the existence of photon-involved processes. In addition, the bulk Si band gap energy, 1.12 eV, produces emission in the NIR spectral range, consequently evading visible-light (E in the range $1.77 - 3.1$ eV) and third-window waveguiding ($E \approx 0.8$ eV) applications.

It was in 1988 when Furukawa and Miyasato [9, 10] first reported visible light coming from Si, at room temperature. In particular, they achieved the fabrication of Si nanocrystallites ranging between 2 and 5 nm in size by means of hydrogen plasma sputtering, under the misleading name of *microcrystals*. This work had an additional relevance: they measured optical band gap energies in the visible range, and increasing as the crystallite size was reduced. To explain this effect, they resorted to quantum mechanics formalism (quantum confinement effects, described in Chapter 2, become dominant when the involved spatial dimensions are lower than the Bohr radius, ~ 5 nm). Therefore, they demonstrated for the first time the

achievement of real *Si quantum dots* (Si QDs). Although Furukawa and Miyasato already reported the luminescence yielded by Si QDs in photographs [11], they did not further study the emitted spectra. It was L.T. Canham who, in 1990, published visible photoluminescence spectra from chemically-synthesized mesoporous Si [12]. The particularity of this material was that the variation of the pore width resulted in Si quantum wire arrays whose diameter modification consequently shifted the emission spectrum peak. Two-dimensional (instead of three-dimensional for QDs) quantum confinement could again explain the observations.

These two studies led to an immediate consequence that was not disregarded by the scientific community: nanostructured silicon could not only deliver visible emission but also the latter could be modified by the nanostructure size. This band gap engineering could be therefore developed to introduce Si in optoelectronic technological applications typically governed by direct- (and frequently wide-) band gap materials such as III-V semiconductors, whose superior optical properties have for years counteracted their expensiveness and toxicity during manipulation [13]. As a consequence, the production of Si QDs (in the form of nanocrystals, NCs) attracted the attention of many research groups during the nineties. This was attained by means of different techniques, one of them involving the deposition of thin (oxide) films containing an extra Si concentration above the material's stoichiometry, which was achieved either by Si ion implantation on deposited stoichiometric films (typically amorphous SiO_2 matrix) [14, 15] or directly (chemical vapor deposition, CVD) [16–18]. A post-deposition annealing treatment was then required to initialize the precipitation and crystallization of the Si excess. The control of NC size and crystalline degree could be then addressed by manipulating the material's stoichiometry and annealing conditions [19, 20].

In 1999, a more precise fabrication technique involving amorphous superlattices was adapted by Zacharias *et al.* to attain size-controlled Si NCs [21]. This consisted of the alternated deposition of nanometric amorphous Si/SiO_2 layers, being the latter acting as diffusion barriers for Si atoms, followed by a high-temperature annealing treatment. In 2002, some of these authors reported a modification of this approach, now employing Si-rich SiO_2 instead of amorphous Si as the material containing the Si excess, and studied their luminescent properties [22]. After these works, the multilayer approach was widely employed by many research groups and in different dielectric matrices than silicon oxide, such as silicon carbide (SiC) [23, 24] and silicon nitride (Si_3N_4) [25, 26], all of them observing structural, optical and electrical properties being tailored by the Si QD size, these material structures becoming real candidates for optoelectronic applications.

1.4. State-of-the-Art

1.4.1. Silicon Nanocrystals in Light-Emitting Devices

Light-emitting devices operate by converting an electrical input current flux into light emission, in a physical process driven by the injection of electrons and holes and their localization in the active layer, where they radiatively recombine. This process is called *electroluminescence*, and it is typically achieved by using a *p-i-n* junction (a *p-n* design for homojunctions), with the active layer as the intrinsic region. As it has been already stated, the electrical properties of bulk Si well fit the needs of the electronics industry. However, the increase in the demand of efficient light emitters for optoelectronics has upraised direct- and wide-band gap III-V semiconductors. Besides displaying an emission within the visible range (depending on the particular composition/stoichiometry), and under certain device configuration and operation, these materials allow for electroluminescence external quantum efficiencies even exceeding 50 % [27, 28]. Instead, the NIR and poor (low-probable band-to-band electronic transitions) emission yielded by Si automatically discards this material for illumination purposes.

One of the most crucial objective of illumination technologies is the achievement of white-light emission. So far, broad emission throughout most of the visible spectrum is reached by means of wide band gap emitters (typically blue-light emitters), coated by phosphors acting as down-converters by means of photoluminescence; this way, part of the high-energy photons emitted by the active electroluminescent semiconductor result in lower-energy photons, thus covering the visible range [29, 30]. Another method consists of the combination of several individual-color emission materials (usually in the red-green-blue ranges), using, for instance, rare-earth ions embedded in host materials [31, 32]. In spite of the advances in these illumination approaches, and arisen from the need of a cheap material, as well as its integrability into Si microelectronics processes and technologies, Optoelectronics research was led to the in-depth investigation of nanostructured Si, whose visible and tunable emission (as a consequence of band gap engineering) can be exploited to partially cover the spectrum where the human eye is sensitive (an example of this visible luminescence is shown in Fig. 1.2).

The properties of Si NC-based light emitting devices can be studied by employing metal-insulator-semiconductor (MIS) structures, the insulating layer consisting of embedded nanostructures within different dielectric matrices, (such as organic compounds, SiO_2 or Si_3N_4). The usage of a dielectric material states an obvious drawback for carrier circulation, being high current injection required to activate (excite) the luminescent centers (in our case, the NCs) via different mechanisms that will be studied in Chapter 2 (*Fundamentals of Silicon Nanocrystals*). Because of this the overall power efficiency of NC-based light emitting devices is low, ranging from 5×10^{-3} % for Si NCs in silicon nitride [34] to 0.01 % for NCs in silicon oxide [35]. These results are still far from the results obtained in porous Si (0.37

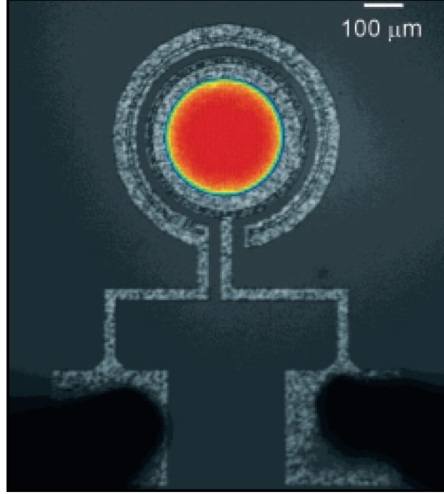

Figure 1.2: Microscopy image of the luminescence yielded by a Si NC-based metal-oxide-semiconductor LED under electrical injection application. From Ref. [33].

%), although the latter material presents a low chemical and mechanical stability as well as low compatibility with Si-based technology [36, 37]. The low emission efficiency reported for Si-rich Si_3N_4 is mainly due to the charge transport mechanism via defects that governs this matrix, in contrast with the tunnel injection typically reported in SiO_2 [38]. In addition, light emission from the latter system is not governed by quantum confinement in Si NCs but from intra-band defects in the silicon nitride matrix, which display a broad visible emission. For this reason, some works have focused in the combination of both matrices in a stack that allows for reddish NC-based (from the oxide region) and whitish defects-related (from the nitride region) emissions [38].

The possibilities offered by Si NC-based light emitters are still a focus of attention for research in optoelectronics and photonics. In particular, the study of the charge transport and electroluminescence excitation mechanisms that take place in such systems have been a matter of investigation during the last years. The understanding of these aspects may then result in the improvement of the composition, device design and the overall performance efficiency of these light emitters.

1.4.2. Silicon Nanocrystals in Photovoltaics

Silicon is the dominant semiconductor in the photovoltaics industry. Aside from its abundance and easy manipulation, the low Si band gap energy allows for absorbing a great part of the IR solar radiation, in contrast to other wide band gap semiconductors, and its high electrical conductivity permits the efficient extraction of the photogenerated carriers. Because of these properties, crystalline Si (c-Si) solar cells have a thermodynamic theoretical efficiency of ∼33 % (the theoretical limit for a 1.34-eV-band gap *p*-*n* single-junction solar cell and under full AM1.5 solar spectrum incidence is 33.7 %, known as the *Shockley-Queisser limit* [39]). This efficiency limit takes into account recombination and thermal losses calculations

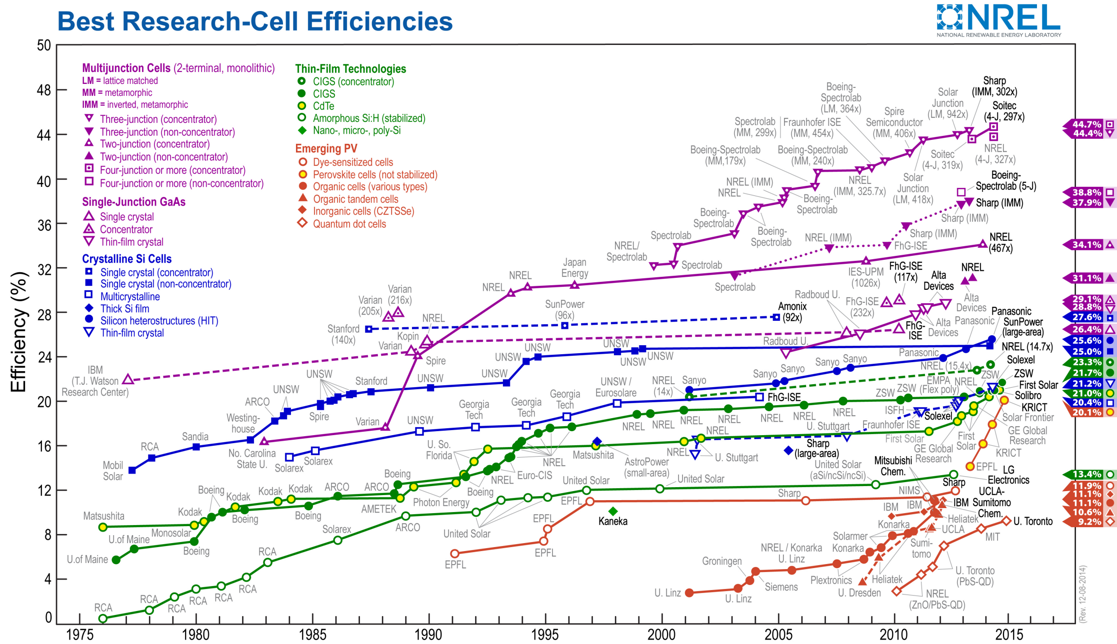

Figure 1.3.: Summary of the best solar cell lab efficiencies for the last 40 years, from the distinct available photovoltaic technologies. From Ref. [43].

amongst other considerations, and makes Si the almost ideal absorber material for single-junction solar cells in terms of overall conversion efficiency [40]. Unfortunately, the efficiency of solar cell modules difficultly reaches 23 % [41]. The frame to which standard c-Si solar cells belong is known as *First Generation Photovoltaics*, whose efficiency is limited by four main sources of losses [42]: (i) non-absorption of lower-energy photons than the semiconductor band gap, (ii) lattice thermalization processes because of high-energy photons absorption, (iii) band-to-band recombination of photogenerated electron-hole pairs, and (iv) junction and contact voltage losses.

Oblivious to most of these problems, the thin-film technology was developed [44], in what was called *Second Generation Photovoltaics*. Within this approach, the use of Si wafers was partially avoided, and the implementation of materials with high absorption coefficient, such as CdTe or CIGS (CuInGaSe), was carried out. The low required thickness of these absorption layers in comparison to c-Si (in the order of μm instead of mm) notably influenced the amount of material that was needed, and allowed for fabricating flexible solar cells. The research cell efficiencies that were reached by thin-film technologies lay in the order of those for single-junction c-Si cells, $\sim$ 20 %. In Fig. 1.3, a summary of the research cell efficiencies from different technologies is displayed, with results recorded for 40 years [43]. A particular case of the usage of thin films that should be mentioned here is rare-

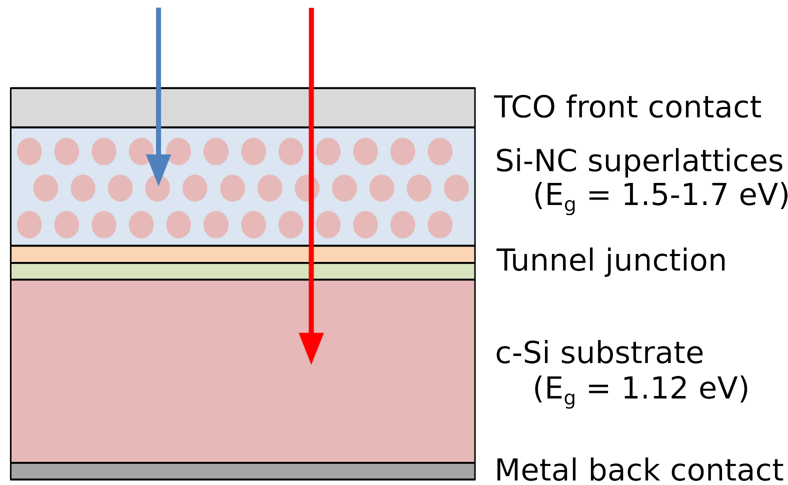

Figure 1.4.: Cross-section scheme of an *all-Si tandem solar cell*, containing a Si NC superlattice stack on top of a c-Si wafer, both absorber materials separated by means of a tunnel junction. A transparent conductive oxide (TCO) is typically used as the front contact, whereas a metal is employed as rear electrode. Blue arrow indicates that high-energy photons are absorbed within the NC-based material, whereas the absorption of low-energy photons (transparent to the latter absorber), takes place at c-Si (indicated by a red arrow).

earth doped transparent conductive oxides, placed on top of conventional cells, aiming at solving the lack of low-energy photons absorption [loss (i) above] by adding rare-earth dopants acting as up-converters, thus generating higher-energy photons that can be absorbed by the solar cell [45, 46]. Aside from the achieved efficiency by this technology, the employed materials are based on scarce elements and the processes involve high vacuum and annealing temperature, so that the overall price was not as low as intended.

It was the concept of *Third Generation Photovoltaics* conceived by M.A. Green [47], which tried to attack the losses problem stated above. In particular, the fundamental employed technology was the multi-band gap engineering, consisting of the use of different band gap materials that allowed for a gradual absorption of different-energy solar photons (being the higher energy ones absorbed on top of the cell structure, see Fig. 1.4). This approach solved losses (i) and (ii) by using low and high band-gap materials, attaining an efficient absorption of low-energy solar photons and avoiding thermalization of high-absorbed ones, respectively. Although the production costs of such approach are high, and despite the need of a tunnel junction to force current to flow through one direction [which generates type-(iv) losses, see above], the achieved efficiency by multi-band gap cells clearly surpasses the rival technologies with research cell efficiencies over 40 % (see Fig. 1.3), being the typical employed materials III-V semiconductors (GaAs, InGaAs, InGaN...) [48].

It is in *Third Generation* solar cells where Si NCs play an important role. The size control shown in these nanostructures allows for tuning their band gap, and therefore accurately selecting the desired band gap to be placed on top of a conventional Si cell. This is the concept of an *all-Si tandem solar cell*, which uses Si-derived materials (both the NCs and their embedding matrix, as well as the wafer) that therefore allow for a full compatibility with Si microelectronics fabrication processes. Using different materials in a tandem stack overcomes the above mentioned *Shockley-Queisser limit* [40]. Specially, the theoretical efficiency limit increases to 42.5 and 47.5 % when 2 and 3 different-band gap materials are employed, respectively [42]. The proper use of Si NCs becomes then promising to overcome the c-Si Photovoltaics efficiency losses. Indeed, during the last 10 years many research groups have focused on NC-based all-Si tandem cells development, leaded by the progresses carried out by Green's group in the University of New South Wales, showing an increase in the absorption of the high-energy part of the solar spectrum [42, 49–51]. However, the efficiency of these devices is still far from conventional c-Si solar cells, mainly due to the lack of efficient cell designs that allow avoiding recombination and extraction losses. Efficient all-Si tandem cells will require a further development on technological aspects in order to be really competitive in the photovoltaics market.

1.5. Objectives of the Present Doctoral Thesis

As already introduced in previous sections, the control of the Si NCs growth is fundamental aiming at the engineering of the physical properties this material system presents. To achieve the proper size confinement, the superlattice becomes a powerful tool to attain size-controlled nanostructures in the growth direction. Therefore, it is the objective of the present Doctoral Thesis **to explore the adequate superlattice structures that present the optimum structural, optical, electrical and electro-optical properties of Si NCs for light emission and photovoltaic applications**, both in silicon oxide and silicon carbide matrix environments. Indeed, this Thesis Project has been performed within the European Project *NASCEnT* (*Si Nanodots for Solar Cell Tandem*), in the frame of the European Community's Seventh Framework Programme (FP7/2007-2013), whose main objective was the procurement of an operative all-Si tandem solar cell, employing Si NC superlattices as high-band gap-energy cell on top of a c-Si bottom cell [52]. As a consequence, all results presented here have contributed to the achievement of *NASCEnT* goals.

This work deals with the characterization of Si NC superlattices by means of different experimental techniques, which will be described in Chapter 3 (*Experimental Details*). These material systems have been fabricated in different European (and material specialist) institutions, for the technological complexity of the involved fabrication processes require particular instrumentation and *know-how*. Indeed,

this Thesis focuses on the use of the performed characterization to determine these superlattices growth parameters that permit their optimum performance as active layers in light-emitting and photovoltaic devices; with this aim, basic device designs have been employed.

Once the global goal of the Thesis Project has been stated, more specific objectives must be listed, which divide the different tasks according to the specific material properties that must be addressed:

- To find out the ideal fabrication conditions that allow for size control of Si NCs embedded in different dielectric matrices (SiO_2 and SiC) and after high annealing temperatures.
- To evaluate the crystalline state of Si NCs and the effect of structural parameters on the superlattice structure maintenance.
- To exploit optical characterization techniques as a non-destructive source of structural information from Si NCs.
- To study the charge transport mechanisms that take place through Si NC / SiO_2 and Si NC / SiC superlattice systems.
- To determine the superlattice structural parameters aiming at optimizing the optical, electrical and electro-optical response of Si NC superlattices.
- To explore the potential of Si NCs as light emitter and/or photovoltaic devices.

1.6. Outline of the Thesis

The present Doctoral Thesis has been built from the results obtained from the Si NC superlattices under study, which have been published during the last four years in several international journals. In order to achieve full comprehension on the present topic, this Thesis has been divided in four Chapters that concatenate each other by following the scientific method on which physics research is grounded: human society needs (state-of-the-art), theory fundamentals, data acquisition by experimental techniques, discussion of results according to established theory and/or generation of new models in agreement with observation. These Chapters are described as follows:

- Chapter 1 (*Introduction*) is devoted to the presentation of the problems and handicaps regarding the optical properties of bulk Si that result in the need of nanostructures. As well, the results reported by some research groups on the use of Si NCs in light emission and photovoltaics fields are addressed.

- Chapter 2 (*Fundamentals of Silicon Nanocrystals*) is written as a self-consistent monograph on the structural, optical, electrical and electro-optical properties of Si NCs. For this, the different fundamental aspects have been contrasted by published works, so that the reader may find in these pages a brief summary that can be in-depth completed by consulting the proposed bibliography. In any case, this Chapter allows understanding the obtained results that will later be discussed.

- Chapter 3 (*Experimental Details*) presents the techniques employed for the achievement of the reported results. However, although a brief presentation of the used measurement set-ups is given, it is the aim of this Section to explain the physical fundamentals of the techniques, according to their structural, optical or electrical nature, and the information they can deliver.

- Chapter 4 (*Results and Discussion*) includes the results on Si NC / SiO_2 and Si NC / SiC superlattice systems obtained during the Thesis Project. Prior to the presentation of the different papers that have been published during the Thesis period, an introduction to the particular issue will be given, where the objectives and achievements of the undergone studies will be discussed.

- Finally, Chapter 5 (*Summary and Conclusions*), summarizes the most relevant achievements in the present Doctoral Thesis, and an overall vision on the accomplished objectives is given. In addition, some remarks about future work on Si NC superlattices are discussed, addressed towards the improvement of the Si NC-based optoelectronic devices performance.

2. Fundamentals of Silicon Nanocrystals

> The good thing about science is that it's true whether or not you believe in it.
>
> Neil deGrasse Tyson

For the last decades, nanostructured materials have attracted great attention to the scientific community as a consequence of the different structural, mechanical, optical and electrical properties they present with respect to bulk. Aiming at studying such properties, novel physical models have been developed, where the classical ones have been partially or totally substituted by quantum approaches, which dominate at the nanoscale. As it has been observed in other nanostructured compounds, silicon nanocrystals display a clear improvement of their optical emission and absorption properties that has awakened general interest for applications typically associated to the semiconductor electronics and photonics industries. The objective of this Chapter is to explore the theoretical background on which state-of-the-art studies on the physical properties of Si NCs lie, which will establish the starting point for the obtained results within this Thesis, based on ordered NC arrangement achieved by means of the superlattice approach.

2.1. Quantum Confinement

A crystal lattice is characterized by its invariance under specific translations. This symmetry can be represented by a periodic potential, V, which allows describing the translation of particles through the structure. These particles then present an associated wavefunction of the form:

$$\Psi(\vec{r}) = e^{\mathrm{i}\vec{k}\cdot\vec{r}}u(\vec{r}) \ , \tag{2.1}$$

where $u(\vec{r})$ is a function containing the same period as the lattice structure, and $\vec{k}$ is called the *wavevector* (whose component for the lattice i^{th}-direction is defined as $k_i = 2\pi r_i^{-1}$), which describes the particle's wavefunction propagation in the reciprocal space (the mathematical representation of the real lattice space) [1]. The functions that can be described by Eq. (2.1) are called *Bloch functions*, and accomplish the following invariability condition under translation within the lattice, T_R:

$$T_R\Psi(\vec{r}) = \Psi(\vec{r}+\vec{R}) = e^{i\vec{k}\cdot\vec{R}}\Psi(\vec{r}) \ , \tag{2.2}$$

which implies that translation only induces a phase modification of the wavefunction, while keeping its main information. This wavefunction invariability after translation through the lattice gives as solutions eigenfunctions with the form of $\exp(i\vec{k}\cdot\vec{r})$. In an infinite lattice, and supposing that carriers (electrons or holes) present a wavefunction of the form in Eq. (2.1), it is possible to calculate their allowed energy states by means of the Schrödinger equation:

$$H(\vec{r})\Psi_n(\vec{r}) = \left[\frac{|\vec{p}|^2}{2m} + W(\vec{r})\right]\Psi_n(\vec{r}) = E_n\Psi_n(\vec{r}) \ , \tag{2.3}$$

being $H(\vec{r})$ the Hamiltonian operator describing the kinetic ($|\vec{p}|^2/2m$) and potential [$W(\vec{r})$] energies that a particle experiments inside the lattice (both appearing in the second term of the equation), $\vec{p}$ and m the linear momentum operator and mass, respectively, of the particle, and E_n the energy of the particle at a given state n. Note that the label n, the band index, accounts for the different solutions of the Schrödinger equation; for a given band n, its dependence with $\vec{k}$ will define the electron dispersion relation in that band, $E_n(\vec{k})$. The energies obtained from solving Eq. (2.3) in the case of a wavefunction propagating through an infinite crystal are:

$$E(\vec{k}) = \frac{\hbar^2}{2m^*}\left({k_x}^2 + {k_y}^2 + {k_z}^2\right) \ , \tag{2.4}$$

where $\hbar$ is the reduced Planck's constant and m^* the effective mass of the carriers (electron or holes). The plot of the energy as a function of the wavevector at different states is called *band diagram*, and describes the allowed energy states of any given material lattice through different crystallographic directions. Fig. 2.1 shows the energy band diagram for the case of bulk Si. The lower energy bands with negative energy values (hole bands) represent bound states within the semiconductor material, and are generally called the *valence band* (VB). The opposite high levels (electron bands) form the *conduction band* (CB), where electrons are allowed to move freely. The shaded region in the figure states for the *band gap energy*, where no electronic states are permitted.

As already mentioned, the carrier wavefunction is extended to the whole semiconductor. In the case that one spatial dimension is finite, the translational symmetry is lost and more restrictive boundary conditions need to be considered. Particularly, for lateral dimensions (L) much larger than the lattice parameter (a), i.e. $L \gg a$, the approach of considering an infinite system is reasonably valid. However, for $L \approx 10a - 100a$, the situation is different, and the finite dimensions must then be taken into account. Let us suppose a quantum well, of thickness t, embedded within a semiconductor material, i.e. an interruption of the material lattice

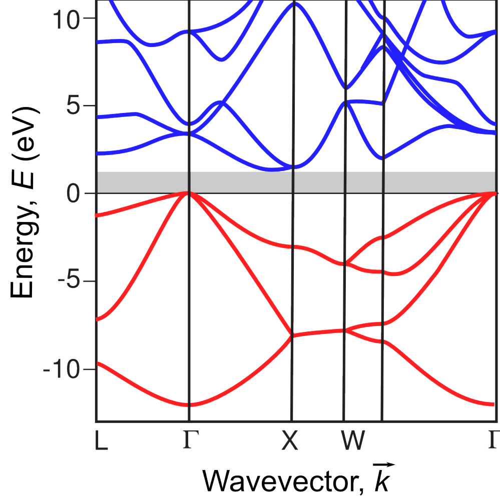

Figure 2.1: Energy band diagram corresponding to bulk silicon. Blue and red lines represent the allowed conduction and valence band states, respectively. Figure adapted from Ref. [53].

where the periodic potential drops to zero. Such a quantum well is depicted in Fig. 2.2(a). With the condition that both the carrier wavefunction and its derivative be continuous at the well boundaries, it is found that, within the (infinite) well, the energies of the allowed states are [1]:

$$E_n(\vec{k}) = \frac{\hbar^2}{2m^*}\left(\frac{n^2\pi^2}{t^2} + {k_y}^2 + {k_z}^2\right) \quad . \tag{2.5}$$

This effect is called *quantum confinement*, and has two immediate consequences: the energetic states become discretized in the confinement direction (x, in this case) and their energy magnitude inversely depends on t^2 [see the scheme in Fig. 2.2(a)]. As a consequence, the electron $E_{\mathrm{e},n}$ and hole $E_{\mathrm{h},n}$ energy bands (in the confinement direction) present an energy shift with respect to the bulk CB minimum and VB maximum, respectively, that can be evaluated as:

$$\begin{aligned} \Delta E_{\mathrm{conf,e}} &= \frac{\hbar^2\pi^2}{2m_{\mathrm{e}}^*}\frac{n^2}{t^2} \\ -\Delta E_{\mathrm{conf,h}} &= -\frac{\hbar^2\pi^2}{2m_{\mathrm{h}}^*}\frac{n^2}{t^2} \end{aligned} \quad . \tag{2.6}$$

These equations take into account the different nature of the CB and VB carriers, namely electrons and holes, respectively, by considering their effective masses, m_{e}^* and m_{h}^* (typically, $m_{\mathrm{e}}^* < m_{\mathrm{h}}^*$). Then, due to quantum confinement, the bulk Si band gap energy ($E_{\mathrm{g,bulk}}$), is modified by $E_{\mathrm{g,bulk}} + \Delta E_{\mathrm{conf,e}} + \Delta E_{\mathrm{conf,h}}$, and increases at thinner quantum wells. Fig. 2.2(b) plots the quantum-confined CB and VB energies for different energy states as a function of the quantum well thickness, as well as the total band gap energy for the fundamental energy level (i.e. $n = 1$).

The case of Si nanocrystals, which can be treated as *quantum dot* (or 0-dimensional) structures (QDs) in the present formalism, the confinement exists in the three

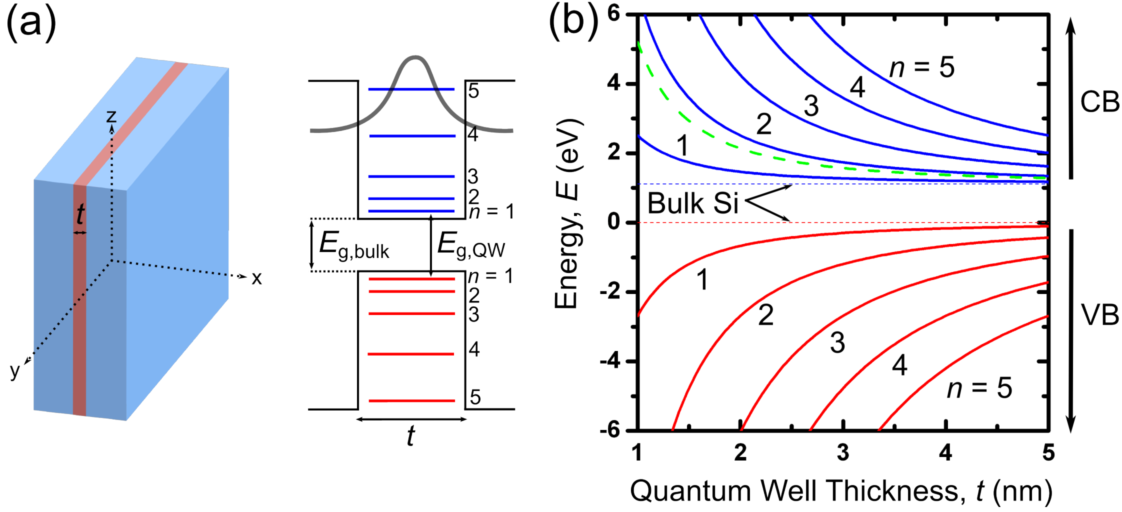

Figure 2.2.: (a) Sketch of a quantum well confined within the x direction. An schematic band diagram shows the higher-energy and discrete energy levels within the well. An example of the concept of wavefunction localization is shown. (b) Evolution of the conduction band minimum (in blue) and valence band maximum (in red) of silicon at different states (i.e. different values of n), as a function of the quantum well thickness (following the quantum confinement theory). The green dashed line indicates the band gap energy (at the fundamental level, i.e. $n = 1$), as the difference between the CB and the VB. Dashed horizontal lines serve as markers for the bulk Si values.

spatial dimensions. The mathematical instruments employed for the QW can be conceptually extrapolated to QDs. In particular, many research groups have coincided in experimentally describing the Si NC band gap energy as a power law of the nanocrystal diameter (d) [54–60]:

$$E_{\mathrm{g,QD}} = E_{\mathrm{g,bulk}} + \frac{A}{d^N} \ , \tag{2.7}$$

which has an analogous form as Eq. (2.6), where N is the power index and A a fitting coefficient. Beyond the fact that the confinement energy in QDs has proved to be higher than in QWs (due to the higher dimensionality confinement) [61], it has been observed that non-negligible deviations of the band gap energy of real NCs exist in comparison to the results from theoretically considering a hard sphere embedded in an infinite barrier potential environment. As a consequence, the phenomenological relation in Eq. (2.7) can display N exponent values notably lower than 2, the one expected from quantum confinement according to Eq. (2.5); such is the case in Ref. [55], where a value of $N = 1.39$ is reported. In particular, the NC-embedding matrix interface is not abrupt, which strongly affects their boundary conditions; the different fabrication methods (not treated in this Thesis) play an important role on NC formation. In addition, the stress exerted by the embedding matrix on the NC also modulates the band gap energy of the

nanostructure. However, different authors have modelled the electronic behavior of Si NCs by *ab-initio* calculations including the diffuse NC edge and stress effects, obtaining very good agreement with experimental results [62–64]. Actually, Eq. (2.7) has interesting consequences, as it predicts the band gap energy tunability of Si NCs by controlling the NC size, so that visible emission is achieved from a naturally IR-emitter such as silicon.

2.2. Silicon Nanocrystals Formation: The Superlattice Approach

When a Si-rich, i.e. non-stoichiometric, silicon-based material (i.e. a Si-based matrix presenting an excess in Si concentration) is submitted to a high-temperature annealing treatment, the exceeding Si undergoes a precipitation process around *nucleation sites*, the regions where a higher Si density is found (randomly distributed after deposition). This is actually a non-equilibrium thermodynamic process that takes place because of the real material inhomogeneity. The continuous application of high temperature induces a progressive crystallization of the precipitated Si, on which the properties of the final nanostructure depend. It is in the scope of this Section to theoretically address the Si NC formation within amorphous dielectric matrices (such as silicon oxide or carbide) according to reported works on this issue [21, 65, 66].

Prior to the in-depth analysis of the NC formation process, it is required to describe the environment structure where nucleation takes place. The first works on Si NCs reported on the properties of the nanostructures freely embedded in Si oxide matrix [67–70]. Researchers soon realised that the material properties were varied at different NC sizes, as the predicted quantum confinement effect is crucially dependent on this parameter (see Section 2.1). The control of the matrix stoichiometry and the employed deposition methodology were then found to modify the NC size, although no true control was achieved. It was in 1999 when Zacharias *et al.* developed a method to attain ordered nanostructures and vertically-constrained (i.e. through the deposition direction) within the Si-rich layer: the *superlattice approach* [21, 22, 71, 72]. It consists of the alternate deposition of stoichiometric and substoichiometric few-nm-thick Si-based dielectric layers. The subsequent annealing process contributes to the precipitation and crystallization of an arranged and controlled distribution of nanostructures. Using this new technique, it is possible to achieve the desired optical, electrical and optoelectronic properties of Si NCs by band gap energy engineering. It is therefore in this finite-thickness media where the NC formation is relevant for the present Thesis, and it will be addressed in the following lines.

We understand by nucleation and crystallization the thermal and kinetic processes by means of which a solid, stable and ordered phase is formed from amorphous or highly-disordered initial phases. We talk about *homogeneous nucleation*

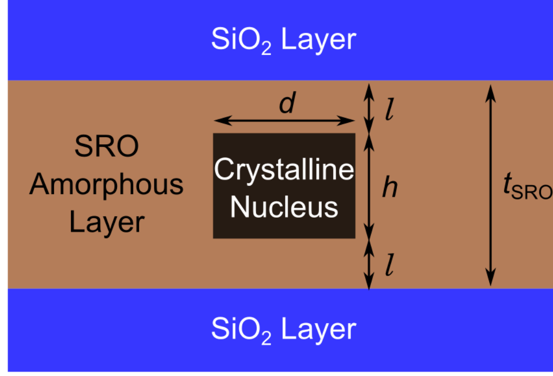

Figure 2.3: Schematic of the nucleation model employed for a cylinder-shaped crystalline nuclei embedded in a SRO matrix, vertically constrained by stoichiometric oxide barriers. Figure adapted from Ref. [66].

when it is originated from the raw amorphous matrix material, without any different compound being required as catalyst (which is called *heterogeneous nucleation*). Within this frame, and according to the minimum energy expense that governs natural laws, the temperature increase gives rise to a spherical nuclei of diameter d. The variation of the Gibbs free energy corresponding to the nucleation process, ΔG, is given by [73, 74]:

$$\Delta G = -\frac{4}{3}\pi \left(\frac{d}{2}\right)^3 \Delta G_\mathrm{v} + 4\pi \left(\frac{d}{2}\right)^2 \sigma \ , \tag{2.8}$$

where the first term accounts for the crystallization energy delivered per unit volume (ΔG_v), whereas the second term refers to the necessary energy for the creation of a new interface of surface tension σ. The critical nuclei diameter, d_c, beyond which nucleation will proceed is given by the maximum ΔG, i.e.:

$$\frac{\mathrm{d}\Delta G}{\mathrm{d}d} = 0 = -\frac{\pi}{2} {d_\mathrm{c}}^2 \Delta G_\mathrm{v} + 2\pi d_\mathrm{c} \sigma \longrightarrow d_\mathrm{c} = \frac{4\sigma}{\Delta G_\mathrm{v}} \ . \tag{2.9}$$

The previous equations describe the classical nucleation theory in an infinite media with slight inhomogeneities that originate precipitation of one of the phases. Let us suppose an example concerning Si-rich silicon oxide (SRO), SiO_x, being x the O/Si ratio indicating the substoichiometry of the material ($x < 2$). In addition, let us consider a finite layer of SiO_x sandwiched between SiO_2 layers that serve as barriers for the excess Si diffusion. According to the model proposed by Zacharias and Streitenberger [66], a crystalline cylindrical-shaped nucleation center (height h, diameter d) is employed for easier calculation purposes, embedded within this amorphous SRO layer of thickness t_SRO; in addition, the cylinder bases are separated a distance $l = (t_\mathrm{SRO} - h)/2$ from the SiO_2 barrier layers. Fig. 2.3 depicts a schematic of such a configuration. Analogously, the Gibbs free energy for the crystalline cylinder can be expressed as:

$$G_\mathrm{crys} = \frac{\pi d^2 h}{4} G_\mathrm{crys,v} + \pi d h \sigma_\mathrm{crys\text{-}SRO} + \frac{\pi d^2}{2} \sigma^\mathrm{eff}_\mathrm{crys\text{-}oxide} \ , \tag{2.10}$$

where the first term corresponds to the free energy of the cylinder volume ($G_{\text{crys,v}}$ is the Gibbs free energy per unit volume), and the second and third ones to the surface energy of the lateral side and both bases of the cylinder, respectively. The surface tensions $\sigma_{\text{crys-SRO}}$ and $\sigma^{\text{eff}}_{\text{crys-oxide}}$ account for the SRO-cylinder and oxide barrier-cylinder interfaces, respectively. The latter surface tension intrinsically considers the separation l between the crystalline cylinder and the oxide barriers:

$$\sigma^{\text{eff}}_{\text{crys-oxide}} = \sigma_{\text{crys-SRO}} + (\sigma_{\text{crys-oxide}} - \sigma_{\text{crys-SRO}}) \cdot e^{-l/l_0} \ , \tag{2.11}$$

indicating an effective surface tension between the SRO-cylinder and SiO_2-cylinder interfaces, modulated by l and a characteristic parameter l_0 interpreted as a bond length in the range of typical interatomic forces for SiO_2 and SRO. In the limit when $l = 0$, one obtains that $\sigma^{\text{eff}}_{\text{crys-oxide}} = \sigma_{\text{crys-oxide}}$ (crystalline cylinder adjacent to oxide barriers), whereas at $l \to \infty$, $\sigma^{\text{eff}}_{\text{crys-oxide}} = \sigma_{\text{crys-SRO}}$ (no oxide barrier in the proximities, only SRO-cylinder interface). The Gibbs free energy of the SRO material surrounding the cylinder must also be calculated:

$$G_{\text{SRO}} = \frac{\pi d^2 h}{4} G_{\text{SRO,v}} + \frac{\pi d^2}{2} \sigma^{\text{eff}}_{\text{SRO-oxide}} \ , \tag{2.12}$$

where the first term corresponds to the free energy of the SRO removed by the cylinder ($G_{\text{SRO,v}}$ is the Gibbs free energy per unit volume), whereas the second term accounts for the cylinder bases. Analogously to Eq. (2.11), the effective surface tension at the SRO-oxide interface can be expressed as:

$$\sigma^{\text{eff}}_{\text{SRO-oxide}} = \sigma_{\text{SRO-oxide}} \cdot e^{-l/l_0} \ . \tag{2.13}$$

Once the Gibbs free energies for both the crystalline cylinder and the amorphous material are presented, the energy of the nucleation process around the cylinder can be calculated in the same way as in Eq. (2.8):

$$\begin{aligned} \Delta G_{\text{nuc}} &= G_{\text{crys}} - G_{\text{SRO}} = \\ &= -\frac{\pi d^2 h}{4} \Delta G_v + \pi d h \sigma_{\text{crys-SRO}} + \frac{\pi d^2}{2} \Delta\sigma_{\text{eff}} \ , \end{aligned} \tag{2.14}$$

which essentially describes the necessary energy to form an interface between the crystalline (cylinder) and amorphous (SRO) materials while being modulated by the presence of the oxide barriers. The new terms appeared in Eq. (2.14) are

$$\Delta G_v = G_{\text{SRO,v}} - G_{\text{crys,v}} \ , \tag{2.15}$$

which must necessarily be > 0 for the thermodynamic process to take place, and

$$\Delta\sigma_{\text{eff}} = \sigma^{\text{eff}}_{\text{crys-oxide}} - \sigma^{\text{eff}}_{\text{SRO-oxide}} \ . \tag{2.16}$$

In order to determine the energetic barrier for nucleation to occur, we require to find the maximum of ΔG_{nuc}, which in turn depends on the geometrical parameters d and h. For analytical calculation purposes, the intrinsic dependence of $\Delta\sigma_{\text{eff}}$ with both variables [as $l = f(d, h)$] will be relaxed by considering a mean value between $l_{\text{min}} = 0$ and $l_{\text{max}} = t_{\text{SRO}}/2$, i.e. $l_{\text{mean}} = (l_{\text{min}} + l_{\text{max}})/2 = t_{\text{SRO}}/4$. With this assumption, the partial derivatives from Eq. (2.14) are immediate, and the critic cylinder diameter and height, d^* and h^* respectively, can be obtained by:

$$\begin{array}{l} \dfrac{\partial \Delta G_{\text{nuc}}}{\partial h} = 0 \longrightarrow d^* = \dfrac{4\sigma_{\text{crys-SRO}}}{\Delta G_v} \\ \dfrac{\partial \Delta G_{\text{nuc}}}{\partial d} = 0 \longrightarrow h^* = \dfrac{4\Delta\sigma_{\text{eff}}}{\Delta G_v} \end{array} . \tag{2.17}$$

Therefore, substituting d^* and h^* into Eq. (2.14), the nucleation barrier energy is:

$$\Delta G^*_{\text{nuc}} = \frac{8\pi\sigma^2_{\text{crys-SRO}}\Delta\sigma_{\text{eff}}}{\Delta G_v^2} , \tag{2.18}$$

where, in the approximation $l \to l_{\text{mean}}$,

$$\begin{aligned} \Delta\sigma_{\text{eff}} &= \sigma_{\text{crys-SRO}} + \\ &+ \left(\sigma_{\text{crys-oxide}} - \sigma_{\text{crys-SRO}} - \sigma_{\text{SRO-oxide}}\right) \cdot e^{-t_{\text{SRO}}/4l_0} . \end{aligned} \tag{2.19}$$

As we are dealing with a thermally-activated process, it is valid to assign this barrier energy to a transition (crystallization) temperature, $k_B T_{\text{crys}} \sim \Delta G^*_{\text{nuc}}$ (being k_B the Boltzmann's constant), beyond which nucleation will occur. Likewise, it is plausible to define, in the limit when $t_{\text{SRO}} \to \infty$ (i.e. the effect of the oxide barriers is neglected), a temperature associated to the crystallization of bulk (since our material is no longer size-confined under this approach), $k_B T_{\text{crys,bulk}} \sim \Delta G^*_{\text{nuc,bulk}}$, where

$$\Delta G^*_{\text{nuc,bulk}} = \frac{8\pi\sigma^3_{\text{crys-SRO}}}{\Delta G_v^2} , \tag{2.20}$$

which is only a modification of Eq. (2.18) under $t_{\text{SRO}} \to \infty$. The relation between both temperatures is then given by:

$$\frac{T_{\text{crys}}}{T_{\text{crys,bulk}}} = \frac{\Delta G^*_{\text{nuc}}}{\Delta G^*_{\text{nuc,bulk}}} \longrightarrow T_{\text{crys}} = T_{\text{crys,bulk}} \cdot \frac{\Delta\sigma_{\text{eff}}}{\sigma_{\text{crys-SRO}}} . \tag{2.21}$$

The crystallization temperature may be further expressed as a function of the most primitive magnitudes by substituting Eq. (2.19) in Eq. (2.21), resulting in:

$$\begin{aligned} T_{\text{crys}} &= T_{\text{crys,bulk}} \times \\ &\times \left(1 + \frac{\sigma_{\text{crys-oxide}} - \sigma_{\text{crys-SRO}} - \sigma_{\text{SRO-oxide}}}{\sigma_{\text{crys-SRO}}} \cdot e^{-t_{\text{SRO}}/4l_0}\right) . \end{aligned} \tag{2.22}$$

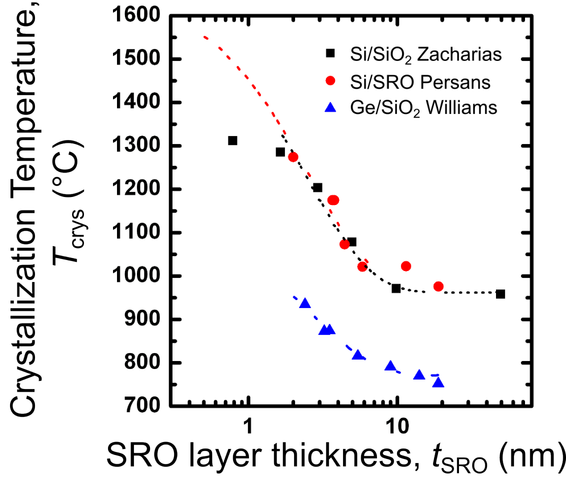

Figure 2.4: Experimentally obtained crystalline temperature, T_{crys}, as a function of the SRO layer thickness, t_{SRO}, for Si NCs embedded in either SiO_2 [66] or SRO matrices [75] and Ge NCs in SiO_2 [76]. Lines refer to the data fit according to the nucleation theory developed by Zacharias and Streitenberger [66].

The presented formalism intended to achieve the crystallization temperature that governs the nucleation process, described by Eq. (2.22). Such a relation has been empirically demonstrated in Si [66, 75] and Ge [76] NCs embedded in either stoichiometric or Si-rich SiO_2 matrix (Fig. 2.4 summarizes the corresponding results), showing an exponential behavior with the Si-rich (or Ge-rich) oxide layer thickness such as:

$$T_{\text{crys}} = T_{\text{crys,bulk}} + (T_{\text{melt}} - T_{\text{crys,bulk}}) \cdot e^{-t_{\text{SRO}}/C} \ , \tag{2.23}$$

where T_{melt} is the temperature of the melting point for the material under study, Si in this case, and C is a characteristic length. Finally, by comparing Eqs. (2.22) and (2.23), one can express the empirically obtained parameters, T_{melt} and C, in terms of the already known material parameters, so:

$$\begin{aligned} T_{\text{melt}} &= T_{\text{crys,bulk}} \cdot \frac{\sigma_{\text{crys-oxide}} - \sigma_{\text{crys-SRO}}}{\sigma_{\text{SRO-oxide}}} \\ C &= 4 l_0 \end{aligned} \quad . \tag{2.24}$$

The crystallization temperature described in Eq. (2.23) presents a clear dependence on the SRO layer thickness. In fact, in the limit of $t_{\text{SRO}} = 0$, $T_{\text{crys}} = T_{\text{melt}}$, recovering the melting point for Si, i.e. 1414 °C, whereas at $t_{\text{SRO}} \to \infty$ (i.e. a bulk SRO layer), $T_{\text{crys}} = T_{\text{crys,bulk}}$, indicating that crystallization takes place at the amorphous-to-crystalline temperature of the bulk material, 973 °C [77]. All cases between both limits establish a relationship between the desired SRO layer thickness (i.e. NC size) and the required post-deposition annealing temperature to achieve highly crystalline Si nanocrystals. Indeed, Fig. 2.4 allows estimating the necessary annealing temperature for the correct growth of Si nanocrystals in silicon oxide matrix, being $T = 1100 - 1200$ °C the optimum for an almost complete crystallization of the Si excess in layers with $t_{\text{SRO}} = 3 - 4$ nm.

The classical nucleation theory has proved to work on spatially constrained amorphous Si-rich SiO_2 layers by oxide barriers, by considering sharp interfaces with well-determined surface tensions. The crystallization process of NCs, however, is never fully completed, always remaining an accumulated non-stoichiometric phase surrounding the crystalline Si inner part (i.e. the core). This conception of the NC structure is called the *core-shell model* [20, 78], and notably varies the optical properties of the nanostructures, being the crystalline core the origin of quantum confinement effects, whereas defect-based properties are dominant in the amorphous shell. In the following section, we will explore in detail the structural and optical properties of such NC structures.

2.3. Structural and Optical Properties of Silicon Nanocrystals

Once the crystallization process of Si NCs has been described, the properties of the resulting nanostructures, embedded in their corresponding environment, must be addressed. In this section, the structural and optical properties of Si NCs, which are closely interrelated, are studied.

2.3.1. Structural Properties of Silicon Nanocrystals

The physical properties of Si NCs strongly depend on the NC morphology and global structure of the NC-matrix system. In particular, the NC size and crystalline degree are of high interest, for the NC mechanical, optical and electrical properties strongly depend on them. On one hand, direct observation of NCs allows for monitoring their size and morphology, requiring high resolution images that can be achieved by electron microscopy techniques (optical microscopy cannot provide enough resolution). On the other hand, the crystalline degree evaluation is usually carried out by Raman scattering, a non-destructive technique with high spectral resolution. The fundamentals of both techniques will be explained in detail in Chapter 3 (*Experimental Details*).

To control the NC size, and consequently their intrinsic properties, the deposition of a stoichiometric Si-based matrix material followed by a controlled dose of Si-implantation was used since powerful optoelectronic applications were ascribed to Si NCs. However, only a rough control of size and distribution of NCs was achieved by the implantation parameters modification [15, 80]. Techniques such as chemical-vapor deposition were developed in order to deposit nanometric-thin layers, the ratio of the employed gases allowing an intrinsic Si excess within the matrix. With this advance, superlattices containing NCs could be fabricated, and the correct multilayers deposition could be examined by techniques such as transmission electron microscopy (TEM). In addition, the possibility of distinguishing different material phases via TEM allowed determining the presence of NCs and

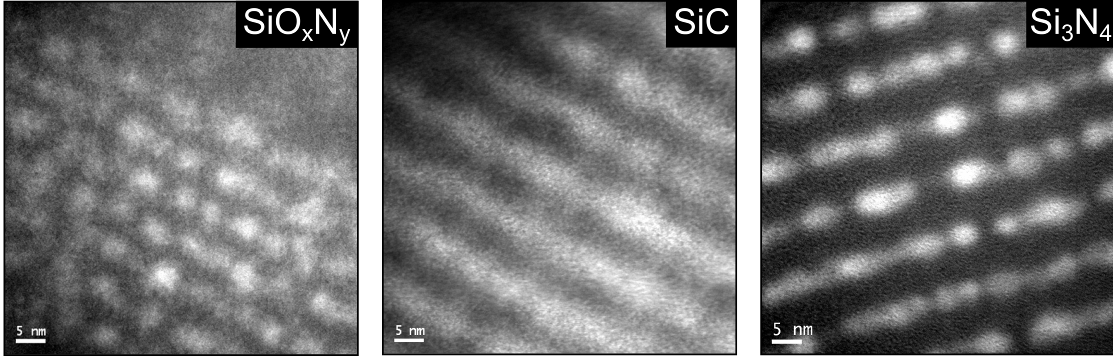

Figure 2.5.: Transmission electron microscopy images filtered around the Si plasmon energy (E_{Si} = 17 eV), corresponding to Si NC superlattices with different matrix materials: silicon oxynitride [79], silicon carbide [24] and silicon nitride [25]. Bright regions account for a higher Si excess, whereas the stoichiometric matrix is presented as a dark background.

analysing their morphology. As an example, Fig. 2.5 shows energy-filtered TEM images corresponding to Si NC superlattices in different matrices, namely silicon oxynitride (SiO_xN_y), silicon carbide (SiC) and silicon nitride (Si_3N_4).

From a structural point of view, SiO_2 and/or SiO_xN_y have proved to be excellent matrices for controlling the NC size [79, 81, 82], even at oxide barrier thicknesses of 1 nm [83]. In contrast, thick barriers and large Si excesses are required in order to avoid Si outdiffusion into SiC, and lateral coalescence is not still controlled under such conditions, inducing almost homogeneous crystallization of the whole Si-rich SiC layers [23, 24, 84]. In the case of silicon nitride, very recent studies have shown controlled growth of NCs using SL structures, although their optical properties have been found not to be affected by quantum confinement [25, 26].

The crystallization process of the Si excess in NC superlattices has raised much interest in the field, because the optical and electronic properties are strongly modulated by the crystalline core environment. Indeed, assuming an incomplete crystallization process, the NC is typically modelled as a crystalline Si core surrounded by an amorphous Si (or substoichiometric) shell that acts as a transition layer between the NC and the embedding matrix (known as the *core-shell model* [78]). Accurate TEM investigations have been carried out to analyse in more detail the chemical and crystalline composition of these SLs by means of electron energy loss spectra (EELS) [85]. From the Si NC/SiO_2 SL system in Fig. 2.6(a), an EELS mapping was performed on a single NC-containing layer, which is displayed in Fig. 2.6(b). The different regions, monitored by filtering the plasmon energies corresponding to the involved materials, allowed clearly distinguishing different phases: the crystalline Si region, with a characteristic plasmon energy of $E_{\mathrm{Si}} = 17$ eV, the oxynitride matrix, $E_{\mathrm{SiO2}} = 23$ eV, and intermediate compositions forming the transition region [see Fig. 2.6(c)]. The work developed in Ref. [85], therefore, not only allowed monitoring the total thickness of the Si-rich and barrier layers,

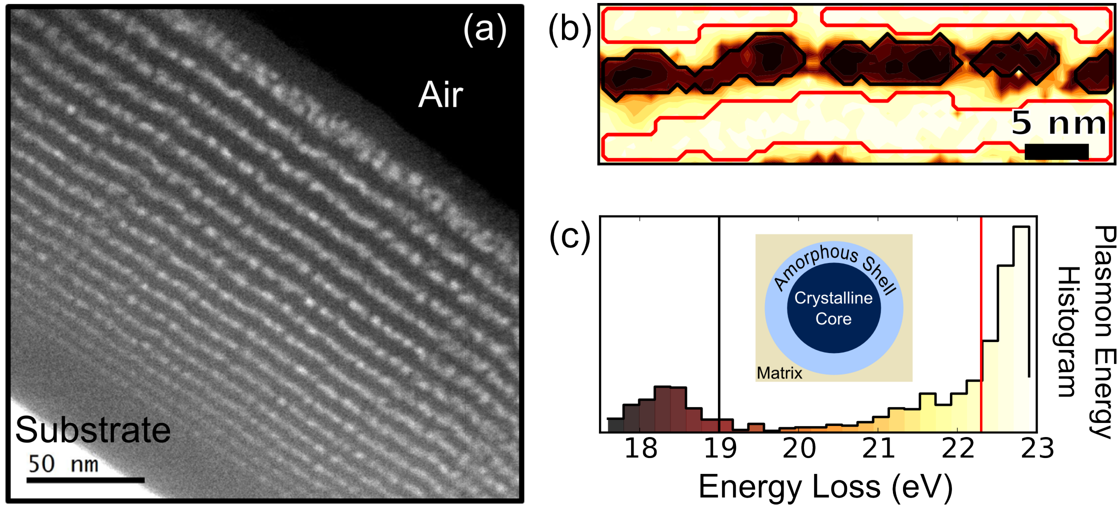

Figure 2.6.: (a) Energy-filtered transmission electron microscopy of a sample containing Si-rich oxynitride layers of varying thickness, spaced by 4-nm SiO_2 barrier layers. The signal was filtered around the Si plasmon energy, E_{Si} = 17 eV (bright in the figure). (b) Plasmon energy map of one of the layers from the sample in (a), obtained from the analysis of the electron energy loss spectra at each image pixel. (c) Histogram corresponding to the plasmon energy map in (b). The inset shows a sketch of a matrix-embedded NC represented according to the core-shell model (a crystalline core surrounded by an amorphous shell). In both (b) and (c) black and red lines indicate the threshold of the crsytalline NC core and the matrix regions, being the middle region corresponding to the substoichiometric amorphous transition shell. Courtesy of A. Eljarrat [85].

but also visualizing the thickness of this transition region, sub-nanometer thick, which is in accordance with studies on similar SLs [86] but thinner than reported for film-embedded NCs [17].

The crystalline state of Si NC-based samples can be more accurately investigated by Raman scattering, provided the different phonon nature in crystalline and amorphous Si. With this technique, it was possible to evaluate the ratio between the crystalline and amorphous Si phases as a function of fabrication parameters such as the Si excess and the annealing temperature. In particular, Raman spectroscopy allowed monitoring the effect of the annealing temperature on the crystallization state of Si nanoclusters [20], useful to determine the crystallization onset, i.e. the temperature beyond which the inner core of the precipitated Si aggregates start presenting an ordered lattice. Fig. 2.7(a) shows the spectra evolution under different annealing temperatures. The effect of the Si excess increase within SiO_x films was studied in the same work, where it was found that larger Si content generally attains a more complete crystallization except at very high annealing temperatures, showing that low excesses result in small NCs that can be fully crystallized at high enough temperatures.

The crystalline degree can be evaluated considering the ratio between the Si crystalline TO-LO mode (optical transversal and longitudinal phonon mode) and

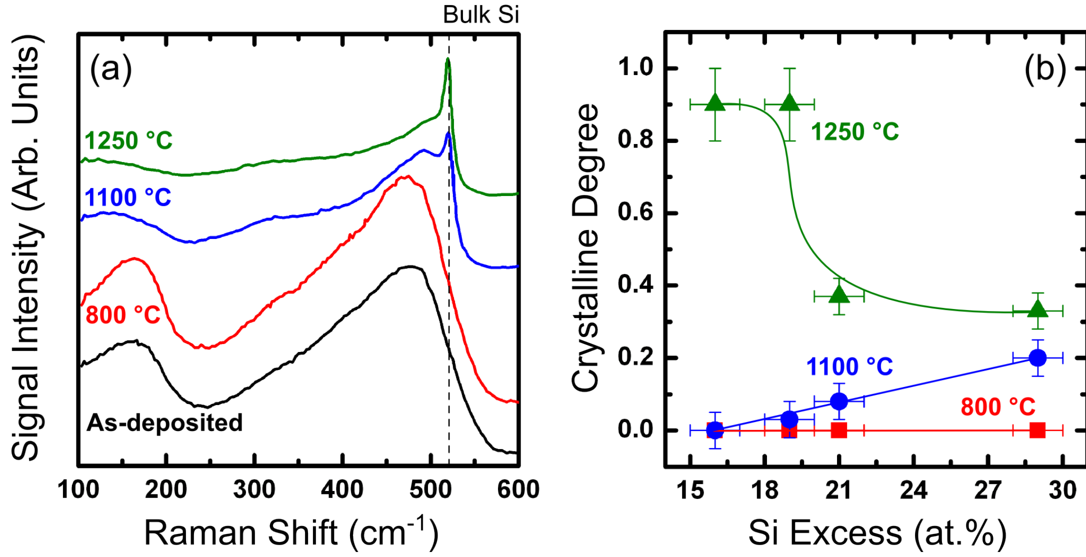

Figure 2.7.: (a) Raman spectra corresponding to SiO_x films with a Si excess of 21 at.%, at different annealing temperatures. The vertical dashed line indicates the Raman peak position for bulk Si. (b) Crystalline degree corresponding to SiO_x films containing different Si excess and annealed at different temperatures. Solid lines indicate the trend followed by the values, as a guide to the eyes. Figure adapted from Ref. [20].

the total NC contribution. Details on the extraction of this value from Raman scattering spectra will be given in Chapter 3 (*Experimental Details*). Fig. 2.7(b) presents the crystalline degrees for Si NC-based samples (in oxide matrix) obtained using this method, under different annealing temperatures and Si excess [20]. Indeed, the crystalline state of NC-based samples could be also evaluated by combining energy-filtered TEM measurements (providing the total NC diameter) and high-resolution TEM (where the crystalline region can be imaged and measured) [85, 87]. However, TEM is a far more destructive and time-consuming technique than Raman scattering.

2.3.1.1. The Phonon Confinement Model

Raman studies of NC-based samples can also provide information about the quantum confinement within the NCs (considered as 0-dimensional QDs). In particular, when the matrix surrounding the Si NCs does not allow the vibrational wavenumbers of the NC material (i.e. the phonon dispersion curves of both materials do not overlap), acoustic and optical phonons cannot propagate through the matrix and thus get confined within the QD, which in turn results in vibrational variations with respect to the bulk material. The *phonon confinement model* explains how the phonon wavefunctions are modulated inside these 0-dimensional structures [88–91].

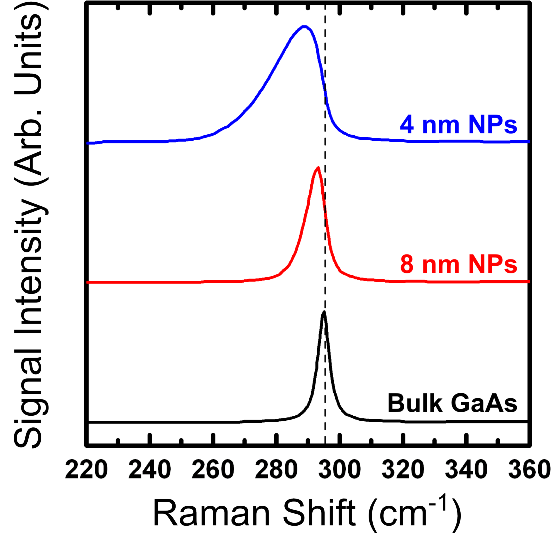

Figure 2.8: Simulated Raman spectra corresponding to the longitudinal optical phonon mode in bulk GaAs as well as in different-size GaAs nanoparticles (NPs). The vertical dashed line indicates the bulk GaAs Raman peak frequency as a guide to the eye. Figure adapted from Ref. [91].

Let us consider a 0-dimensional structure such as a spherical QD, of diameter d_{QD}, through which a phonon presenting an analogous wavefunction as described in Eq. (2.1) is propagated. Owing to the fact that a planar wavefunction cannot exist within the QD because it cannot propagate through this medium, this wavefunction must be modulated by a confinement (or envelope) function presented by the nanostructure geometry, W_{conf}, which decays when approaching to the boundaries of the first Brillouin zone. A Gaussian confinement function can be selected as the envelope function [88], whose validity has been proved in the literature for Si NCs [79, 92]:

$$W_{\mathrm{conf}}(r) = \exp\left(-\frac{\gamma r^2}{d_{\mathrm{QD}}^2}\right) \ , \tag{2.25}$$

where γ is a dimensionless parameter that expresses how rapidly the function decays when approaching the boundary and r is the spacial variable in the real space. Away from the zone center, i.e. near the boundaries, and expressed in the reciprocal (i.e. the frequency) space, the weighing function becomes the Fourier Transform of $W_{\mathrm{conf}}(r)$:

$$C_{\mathrm{conf}}(k) = \int_{-\infty}^{\infty} W_{\mathrm{conf}}(r) e^{-i2\pi kr} \mathrm{d}r = \frac{d_{\mathrm{QD}}}{\sqrt{2\gamma}} e^{-\frac{d_{\mathrm{QD}}^2 k^2}{4\gamma}} \ . \tag{2.26}$$

Once the confinement function has been defined, the Raman intensity lineshape, $I_{\mathrm{Raman}}(\omega)$, can be calculated as a convolution between the bulk phonon (the zone center), expressed by a Lorentzian-shaped function, and the confinement (weighing) function:

$$I_{\mathrm{Raman}}(\omega) = \int \frac{|C_{\mathrm{conf}}(\omega)|^2}{\left[\omega - \omega(\vec{k})\right]^2 + \left(\frac{\Gamma_0}{2}\right)^2} \mathrm{d}\vec{k} \ , \tag{2.27}$$

being $\omega(\vec{k})$ the dispersion curve and Γ_0 the natural (non-confined) width of the zone center phonon in bulk. In Fig. 2.8, the effect of phonon confinement in GaAs nanoparticles (NPs), as modeled for Raman spectroscopy, is displayed, where a Gaussian-like confinement function was employed. As can be seen, smaller NPs present larger asymmetry at lower frequencies (i.e. lower energies), as well as a clear peak shift towards the same direction. Indeed, this model can be generalized to any NC-related material, where the fit of its Raman spectrum using Eq. (2.27) allows determining the size of the NCs. Therefore, Raman spectra provides valuable information about the mean crystalline NC size within a given sample via the exhaustive analysis of the optical TO-LO mode.

Different confinement functions have been employed by different groups, being the Gaussian- [88, 91] and the *sinc*-based functions [89, 90] the most used. Although these different methods result in a slight variation in the Raman spectrum linewidth and peak shift [93], their suitability depends on the nanostructure type that concerns (nanoparticles, nanowires, quantum wells, etc.).

2.3.1.2. Matrix Stress on Silicon Nanocrystals

The effect of the surrounding matrix on the NC is also relevant in terms of stress, provided that it modifies the properties of the nanostructures. It was found that the stress exerted by the matrix on the NCs depended not only on the nature of the former, but also on the substrate on which the Si-excess-containing film (or SL) was deposited [94]. During the NC formation, i.e. when the material is submitted to high temperatures, the overall lattice surrounding the crystallization nuclei is relaxed. However, when cooling down, the temperature difference (ΔT) induces a stress proportional to the expansion coefficients difference between substrate and film (α_{s} and α_{f}, respectively). This stress can be expressed as [95]:

$$\sigma_{\mathrm{str}} = \frac{E}{1-\nu} \left(\alpha_{\mathrm{f}} - \alpha_{\mathrm{s}}\right) \Delta T \ , \tag{2.28}$$

where $E = 1.9 \times 10^{11}$ Pa is the Si Young's (or relaxation) modulus and $\nu = 0.262$ is the Si Poisson ratio. A Si film deposited on Si substrate does not undergo any stress after annealing. Nevertheless, in the particular case of a Si film deposited on fused silica substrate ($\alpha_{\mathrm{f}} = 2.6 \times 10^{-6}$ 1/°C and $\alpha_{\mathrm{s}} = 0.4 \times 10^{-6}$ 1/°C) [96], a cooling of $\Delta T = 1200$ °C induces, according to Eq. (2.28), a stress of $\sigma_{\mathrm{str}} \sim 700$ MPa. Experimentally, Raman spectroscopy is able to unveil such small variations between stressed and relaxed samples, as the Raman peak position has been observed to shift to lower frequencies in the order of several cm^{-1}. As an example,

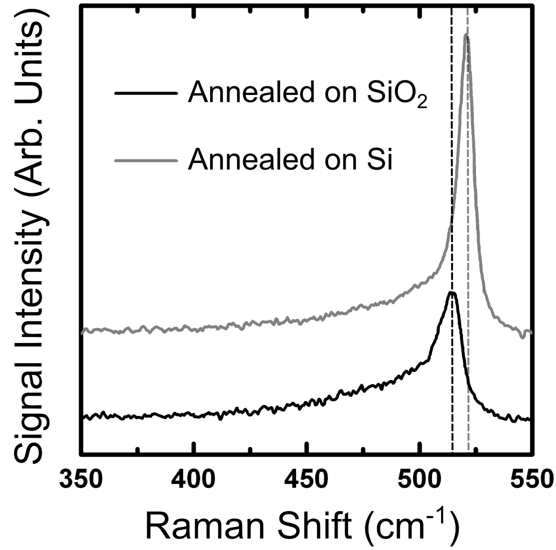

Figure 2.9: Raman spectra corresponding to Si/SiO_2 SLs annealed at 1200 °C, both on Si or fused silica substrate. To highlight the stress effect on the Raman peak position, vertical dashed lines have been employed. Figure adapted from Ref. [94].

Fig. 2.9 displays the Raman spectra corresponding to Si NCs embedded in SiO_2, deposited on either Si or fused silica substrates, where a peak shift to lower energies is clearly observed for the latter substrate case.

Studies of the stress exerted by the oxide matrix on silicon nanocrystals have also been reported as a function of the Si excess [20], i.e. of the NC size. The Raman frequency associated to the TO-LO mode of Si NCs (ω_0) is modified under hydrostatic stress as [97]:

$$\omega = \omega_0 + \Delta\omega = \omega_0 + 4.9[\mathrm{cm}^{-1} \cdot \mathrm{GPa}^{-1}] \times \sigma_{\mathrm{str}} \ . \tag{2.29}$$

Larger NCs, which present a higher thermodynamic stability [64, 98], show an almost negligible Raman frequency shift, whereas when the NC size decreases to 2.5 nm, the exerted stress rapidly increases up to 3.5 GPa, which is translated into a frequency shift of $\Delta\omega = 6.5$ cm^{-1}, as measured in other works [99]. The stress is therefore a relevant fact to take into account in matrix-embedded Si NCs, usually adding to the above mentioned frequency shift resulting from phonon confinement within the nanocrystals, but with no additional broadening.

2.3.2. Optical Properties of Silicon Nanocrystals

The phenomena of light absorption and photoluminescence (PL) taking place in Si NC-based systems have been widely studied in the past [17, 100–104]. Owing to the fact that the latter process is a consequence of the former, it is difficult to treat them separately. In Chapter 3 (*Experimental Details*), we will focus in more detail in the fundamentals of both phenomena. Here, by means of absorption and PL as most employed experimental techniques in this field, we will describe

the origin of general luminescence in these material systems as well as the optical properties of Si NCs under different parameter variations (NC size, temperature, pressure, etc.).

2.3.2.1. Light Absorption and Emission in Semiconductors

One of the main interests of studying the optical properties of semiconductors is the determination of the band gap energy, a particular characteristic of each material. From a point of view concerning band theory, the incidence of photons with higher energy than that of the material band gap (E_g) allows the excitation of an electron bound in the valence band of the material towards the conduction band, leaving a hole in the former. This incident photon has then been *absorbed* by the material, with a probability that quantitatively depends on the density of states corresponding to that energy or, referring to a macroscopic magnitude, to the absorption coefficient (α). After different non-radiative processes, the electron may decay within a short time lapse (mainly via non-radiative processes) to the minimum of the CB; there, different processes can take place (such as non-radiative recombination via defects or Auger electron emission), the most probable one being radiative recombination between the CB electron and the VB hole. Within this last process, one photon will be *emitted* with an energy equal to the band gap one [see the schematic in Fig. 2.10].

After these basic conceptual definitions, it seems immediate to believe that semiconductor characterization techniques monitoring the absorbed and emitted photon energies (such as UV-Visible absorption and PL, respectively) directly result in the precise determination of the band gap energy. Nevertheless, it was early found that the required energy to excite Si NCs was higher than the band gap energy (and it increased with decreasing NC size), because of the non-abrupt density-of-states energy edge, the relaxation to more fundamental levels or the assistance of a third particle (basically phonon-assisted transitions) [1]. As well, the emission process takes place at slightly lower energies than E_g. This difference between the absorption and emission levels is called *Stokes Shift*, $\Delta E_{\mathrm{Stokes}}$, and is related to the absorption ($h\nu_{\mathrm{abs}}$) and emission $h\nu_{\mathrm{emi}}$ energies in the following form:

$$h\nu_{\mathrm{abs}} = h\nu_{\mathrm{emi}} + \Delta E_{\mathrm{Stokes}} \ . \tag{2.30}$$

The Stokes Shift has been studied by many groups and in many semiconductors. In the case of Si NCs in SiO_2, Stokes Shifts of $\sim$ 0.2-0.3 eV were found [105], large enough in order not to neglect this effect. As a consequence, it is difficult to extract the exact value of the band gap energy from these optical techniques; despite this, the trend followed by E_g under different conditions can be precisely analysed.

From a macroscopic point of view, it is possible to quantitatively analyse the luminescence emission efficiency from a given semiconductor in terms of the PL

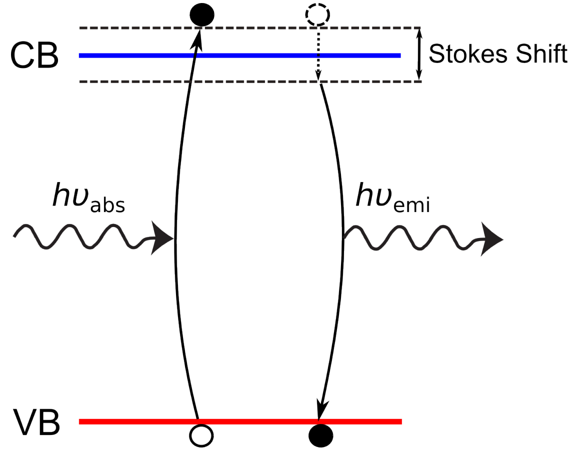

Figure 2.10: Energy bands schematic where the photon absorption and photon emission processes are represented. The dashed arrow indicates non-radiative processes through which the excited electron may decay to the CB minimum. The difference between the absorption and emission levels surrounding the semiconductor band gap (dashed horizontal lines), i.e. the Stokes Shift, is also displayed.

quantum yield, which represents the internal quantum efficiency of the material system, i.e. the ratio between the total number of emitted photons ($N_{\mathrm{ph,emi}}$ and the total number of absorbed ones ($N_{\mathrm{ph,abs}}$):

$$QY[\%] = \frac{N_{\mathrm{ph,emi}}}{N_{\mathrm{ph,abs}}} \times 100 = \frac{W_{\mathrm{emi}}}{(1-R)\cdot e^{-\alpha d}\cdot W_{\mathrm{inc}}} \times 100 \ , \tag{2.31}$$

where d is the total active layer thickness, α is the already mentioned effective absorption coefficient of the material, R the reflectance ($1-R$ is then the non-reflected part of the beam, which penetrates into the material), and W_{emi} and W_{inc} are, respectively, the PL output and excitation input optical power densities.

In the case of Si NC-based systems, where emission is mostly coming from the nanostructures, the quantum yield gives an estimation of the amount of luminescent centers in the sample, i.e. the number of NCs where radiative recombination occurs (highly defective NCs are mainly governed by non-radiative processes). QY values of $\sim 10\%$ have been typically reported for Si NCs [106, 107], being this value raised up to $\sim 60\%$ under favorable specific conditions [108].

2.3.2.2. Luminescence Origin in Silicon Nanocrystals

Since the discovery of the light emission of Si nanostructures [12], optical properties have been of great relevance to study the Si NC band gap energy variation by modifying different parameters. To illustrate this, many research groups have employed the photoluminescence technique aiming at determining a correlation between band gap energy and size [55, 109, 110] (see Fig. 2.11), all of them obtaining experimental relations in the form of Eq. (2.7), thus confirming quantum confinement via experimental obervation. However, the origin of this emission energy shift is not so evident, as many different electronic states exist within the NC-matrix system structure that have to be taken into account.

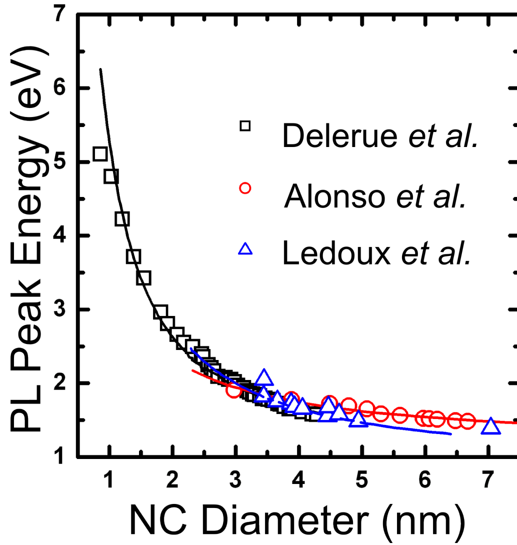

Figure 2.11: Experimental PL peak energies (i.e. PL bandgap energies) as a function of the NC diameter, as obtained from different published studies: Delerue *et al.* [55] (black squares), Alonso *et al.* (red circles) [109], and Ledoux *et al.* (blue triangles) [110]. Solid lines represent fits to the data, according to the phenomenological relation in Eq. (2.7).

Considering the NC morphology, following the core-shell model, the direct ascription of NC luminescence to quantum confinement taking place within the crystalline core [55, 111] has been controversial. The presence of an amorphous/substoichiometric (and non-abrupt) interface between the core and the surrounding matrix induces defects that may give rise to a non-classified luminescence. Apart from intrinsic matrix defects or those produced by the presence of nanostructures (usually generating shallow energy levels within the matrix band gap), defects at the NC surroundings induced by dangling Si bonds [112, 113] present similar energy levels to the nanostructure bands (i.e. deep energy levels within the matrix band gap). This makes the luminescence coming from surface defects almost indistinguishable from that originated by quantum confinement within the NCs [Fig. 2.12(a) summarizes the different electronic states that may give rise to luminescence]. In addition, the fact that this defects-related emission also depends on the NC size increases the analysis difficulty, as both effects are always present in PL studies.

There exists, however, a kind of measurements that allows for discerning between the excitonic recombination within the crystalline core and the recombination of electron-hole pairs at the NC surroundings. This technique is called *magneto-photoluminescence*, and consists of the observation that the quantum confinement energy is modulated under the presence of a strong enough magnetic field (of the order of tens of T), whereas defects remain unaffected. In particular, when such a magnetic field ($\vec{B}$) is applied, the confinement energy defined in Eq. (2.6) is modified by the diamagnetic shift, ΔE_{mag}, as:

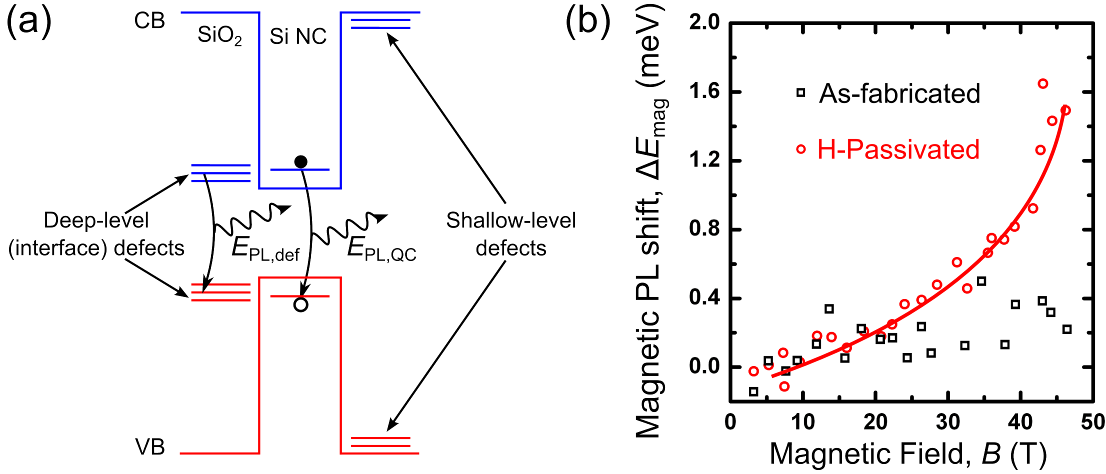

Figure 2.12.: (a) Energy bands schematic showing the nature of different PL origins (quantum confined states, $E_{\mathrm{PL,QC}}$, and interface defect states, $E_{\mathrm{PL,def}}$), as well as matrix shallow energy levels. (b) Experimental magneto-PL results of as-fabricated and H-passivated Si NC/SiO_2 samples, reported in Ref. [114]. The solid red line corresponds to a fit of the magnetic energy shift, ΔE_{mag}, as expressed in Eq. (2.32).

$$\begin{aligned} E_{\mathrm{q},n} &= E_{\mathrm{g,bulk}} + \Delta E_{\mathrm{conf}} + \Delta E_{\mathrm{mag}} = \\ &= E_{\mathrm{g,bulk}} + \frac{\hbar^2\pi^2}{2m_q^*}\frac{n^2}{d^2} + \frac{q^2\langle\rho^2\rangle}{8\mu}B^2 \ , \end{aligned} \tag{2.32}$$

where m_q^* and q indicate the effective carrier mass and carrier charge, respectively, for either electrons or holes, and $\sqrt{\langle\rho^2\rangle}$ is the average extent of the wavefunction (perpendicular to the applied magnetic field). Eq. (2.32) will apply when $\sqrt{\langle\rho^2\rangle}$ is lower than the characteristic magnetic length ($l_{\mathrm{mag}} = \sqrt{\hbar/qB}$) [115, 116], then the wavefunction is delocalized within the magnetic field range and its effect is non-negligible. Therefore, this effect allows establishing a distinction between the highly-localized defect states and the quantum confined states within a 2-to-5-nm NC.

Using the magneto-photoluminescence technique, Godefroo *et al.* were able to observe the difference between the two mentioned components in a Si NC/SiO_2 system [114]. For this, they employed an as-fabricated (deposited and annealed) sample, as well as a hydrogen-passivated one. After applying a magnetic field up to 50 T, they found that no variation in the peak position existed in as-fabricated samples, but passivation of the dangling bonds produced a clear field dependence of the emission energy, as H atoms are bonded to Si free radicals that originate defects. Fig. 2.12 (b) shows the described experimental results. This is indeed a highly relevant result that sheds light to the necessity of passivating the surface dangling bonds to fully observe quantum confinement effects in Si nanostructures.

2.3.2.3. Temperature and Pressure Effect on Silicon Nanocrystals

The study of the optical properties of Si NCs has also been addressed under different operation conditions, which will be of crucial importance aiming at the optimum performance of Si NC-based optoelectronic devices. In particular, the effect of temperature and hydrostatic pressure on the NCs properties has been widely investigated.

In bulk semiconductors such as crystalline Si, the decrease of temperature originates a band gap energy increase resulting from the combination of thermal expansion and electron-phonon interaction. This is indeed a well known behavior that has been phenomenologically described by the *Varshni law* [117]:

$$E_{\mathrm{g}}(T) = E_{\mathrm{g}}(0) - \frac{\alpha_{\mathrm{T}} T^2}{T + \beta_{\mathrm{T}}} \ , \tag{2.33}$$

being $E_{\mathrm{g}}(0)$ the band gap energy at $T = 0$ K, whereas α_{T} and β_{T} are, respectively, the thermal expansion coefficient and a parameter proportional to the Debye temperature, both being characteristic for each material. At high temperatures ($T \gg \beta_{\mathrm{T}}$), this expression becomes linear on T; at very low temperatures ($T \ll \beta_{\mathrm{T}}$), however, the expression is no longer valid (behavior is quadratic, which has no real physical significance). A correction for low temperatures was proposed by Viña *et al.* [118] by considering an average lattice phonon energy, $\hbar\Omega$, and the phonon distribution following the Bose-Einstein statistics formalism:

$$E_{\mathrm{g}}(T) = E_{\mathrm{g}}(0) + \Delta E_{\mathrm{temp}} = E_{\mathrm{g}}(0) - A \cdot \left[\frac{2}{\exp\left(\frac{\hbar\Omega}{k_{\mathrm{B}} T}\right) - 1} + 1 \right] \ , \tag{2.34}$$

where A is a constant describing the electron-phonon interaction strength and k_{B} is the Boltzmann's constant. This expression well agrees with the Si NC band gap energy dependence with temperature (see Fig. 2.13) [119, 120].

The effect of temperature on the Si NC band gap also extends to their quantum yield. As was explained in Section 2.3.2.1, the QY gives an estimation on the amount of NCs that are optically active. Defective (or not well passivated) NCs may present non-radiative paths where recombination takes place that does not contribute to emission; therefore, the most efficient absorption and luminescence will occur in systems where radiative recombination dominates. Temperature has an important role in this sense. Specially, it was found that temperature reduction originates higher emission intensities attributed to more stable radiative recombination centers, whereas higher temperatures are prompt to non-radiative losses [119–121]. However, and as it can be observed in Fig. 2.13, much lower temperatures present a further reduction in emission intensity, i.e. in the QY. This effect is usually attributed to the low exciton migration at temperatures below 50 K

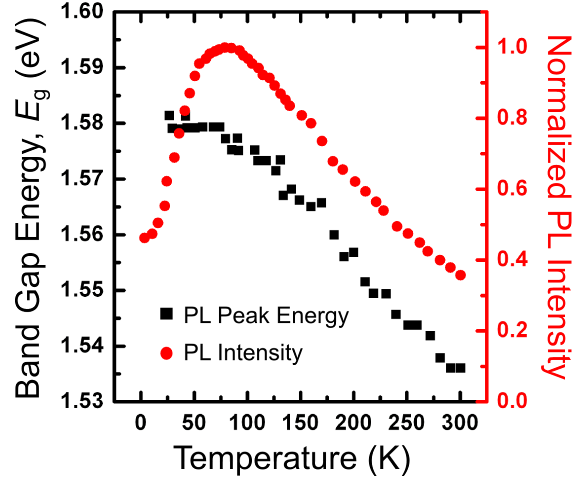

Figure 2.13: Photoluminescence peak energy (black squares) and intensity (red circles) as a function of temperature for a Si NC-based sample containing 3.2-nm nanostructures in SiO_2. Data from Ref. [119].

that favors the large NCs population, thus inducing an overall emission quenching [119].

The Si NC properties under high pressure application (tens of GPa) have also been of relevance, since the quantum confined states within the inner NC core were found to undergo an energy shift depending on the signature of the pressure. In general, the effect of stress in the band structure of solids is expressed in terms of a deformation potential, $a_{\mathrm{n}}(\vec{k})$, which weighs the volume variation under the pressure application, $\mathrm{d}V/V$ [1]. Then, in analogy with the effect of magnetic shift in the quantum confined energy states, as expressed by Eq. (2.32):

$$E_{\mathrm{q},n} = E_{\mathrm{g,bulk}} + \Delta E_{\mathrm{conf}} + \Delta E_{\mathrm{press}} = E_{\mathrm{g,bulk}} + \frac{\hbar^2\pi^2}{2m_q^*}\frac{n^2}{d^2} + a_{\mathrm{n}}\frac{\mathrm{d}V}{V} \ . \tag{2.35}$$

The effect of the different stress nature (i.e. compression or tension) on the band energy diagram of Si NCs is shown in Fig. 2.14(a). According to Eq. (2.35), a tensile stress, $\mathrm{d}V/V > 0$, will result in an increase in the confined levels energy, whereas compression, $\mathrm{d}V/V < 0$, will decrease their energy [122]. From an experimental point of view, the pressure term in Eq. (2.35) can be expressed as a function of the effective pressure modulus of the material system, $\mathrm{d}E/\mathrm{d}P$:

$$\Delta E_{\mathrm{press}} = \frac{\mathrm{d}E}{\mathrm{d}P}P \ . \tag{2.36}$$

Values of the order of $\mathrm{d}E/\mathrm{d}P \sim -10$ to -20 meV·GPa^{-1}, depending on the Si NC core size, have been reported by some authors [123, 124], in good accordance to bulk Si, $\mathrm{d}E_{\mathrm{bulk}}/\mathrm{d}P \sim -10$ meV·GPa^{-1} [125], once quantum confinement effects are considered.

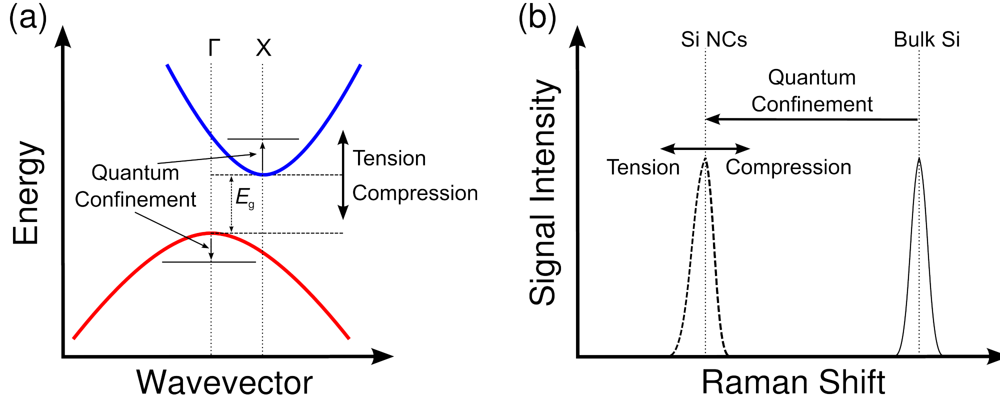

Figure 2.14.: Effect of the pressure exerted by the matrix on Si NCs on (a) the band gap energy and (b) the Raman shift (where the quantum confinement effect is also depicted). The nature of the strain is also considered (tensile or compressive). Figures adapted from Refs. [122] and [83].

This energy shift under different stress conditions is added to the substrate stress effect already discussed in Section 2.3.1.2. Indeed, the matrix stress nature can also be investigated by means of Raman scattering [122, 126], which complements the phonon confinement as a consequence of NC size reduction [see Fig. 2.14(b)]. Therefore, a suitable substrate and matrix materials become extra parameters to take into account for a proper energy band engineering.

In summary, many different parameters exist (either controlled or given by the system) that have to be considered when analysing the quantum confinement in Si NCs by means of band gap measurements. Most of them are related to the environmental conditions under which optical measurements are carried out. Among them, we have here analysed the effect of temperature, pressure and magnetic field, that can be joined in the following expression:

$$\begin{aligned} E_{\mathrm{q},n}(d,T,P,B) &= E_{\mathrm{g,bulk}} + \Delta E_{\mathrm{conf}}(d) + \Delta E_{\mathrm{temp}}(T) + \\ &+ \Delta E_{\mathrm{press}}(P) + \Delta E_{\mathrm{mag}}(B) \ . \end{aligned} \tag{2.37}$$

Other parameters such as the annealing temperature or the excitation source intensity typically involve either the formation of larger aggregates, different NC size populations, the saturation of excited luminescence centers or just a temperature change [120, 126], all four effects affecting the NC size distribution and therefore intrinsically modifying the confinement term in Eq. (2.37).

2.3.2.4. Recombination Dynamics in Silicon Nanocrystals

The study of the recombination dynamics in Si NC-based systems that result in luminescence can provide useful information of their structural properties (size,

crystalline degree, embedding matrix) and the excitation mechanism (be it optical, electrical or by cathodic rays). Despite the complexity of such recombination processes, their study can be carried out by means of a two-level system, where the populations of the ground state (N_1, the total number of NCs, initially non-excited) and excited state (N_2, the number of excited NCs) are considered. In this frame, and considering photons as excitation particles, the population of N_2 through time follows a rate equation of the form [119, 127, 128]:

$$\frac{\mathrm{d}N_2}{\mathrm{d}t} = \sigma_{\mathrm{ph}}\Phi_{\mathrm{ph}}\left(N_1 - N_2\right) - \frac{N_2}{\tau_{\mathrm{decay}}} \ . \tag{2.38}$$

The first term in the right side of Eq. (2.38) accounts for the ground level depopulation in benefit of the excited state, proportional to the injected photon flux, Φ_{ph}, and the NC cross-section for photon absorption, σ_{ph}, i.e. the effective NC surface that can absorb an incident photon; the second term considers the continuous depopulation of the excited level at a rate established by the level lifetime, τ_{decay}, via either radiative (involving photons) or non-radiative (e.g. lattice heating or phonon creation) processes. The solution for the differential equation in Eq. (2.38) takes the form:

$$N_2(t) = \frac{\sigma_{\mathrm{ph}}\Phi_{\mathrm{ph}}N_1}{\sigma_{\mathrm{ph}}\Phi_{\mathrm{ph}} + \frac{1}{\tau_{\mathrm{decay}}}} + C \cdot \exp\left[-\left(\sigma_{\mathrm{ph}}\Phi_{\mathrm{ph}} + \frac{1}{\tau_{\mathrm{decay}}}\right)t\right] \ , \tag{2.39}$$

being C an integration constant that can be obtained by imposing the initial condition that, at $t = 0$, no NCs are excited, i.e. $N_2 = 0$:

$$C = -\frac{\sigma_{\mathrm{ph}}\Phi_{\mathrm{ph}}N_1}{\sigma_{\mathrm{ph}}\Phi_{\mathrm{ph}} + \frac{1}{\tau_{\mathrm{decay}}}} \ . \tag{2.40}$$

Then, the final expression for the time evolution of the excited NCs remains:

$$\begin{aligned} N_2(t) \quad &= \quad \frac{\sigma_{\mathrm{ph}}\Phi_{\mathrm{ph}}N_1}{\sigma_{\mathrm{ph}}\Phi_{\mathrm{ph}} + \frac{1}{\tau_{\mathrm{decay}}}} \times \\ &\times \quad \left(1 - \exp\left[-\left(\sigma_{\mathrm{ph}}\Phi_{\mathrm{ph}} + \frac{1}{\tau_{\mathrm{decay}}}\right)t\right]\right) \ . \end{aligned} \tag{2.41}$$

This expression represents the decay in time of the excited NC population, understood as the total population that can be excited (referred as "1" in the equation) minus its time evolution during the excitation process (the exponential term in the equation). Therefore, we can express the characteristic rise time as:

$$\frac{1}{\tau_{\mathrm{rise}}} = \sigma_{\mathrm{ph}}\Phi_{\mathrm{ph}} + \frac{1}{\tau_{\mathrm{decay}}} \ . \tag{2.42}$$

Finally, considering that the luminescence intensity (in this case PL) is proportional to the decay rate of the excited NCs, i.e. $I_{\mathrm{PL}} \propto N_2/\tau_{\mathrm{decay}}$ [129], then we can deduce from Eq. (2.41) that:

$$I_{\mathrm{PL}}(t) = I_{\mathrm{PL},0}\left(1 - \exp\left[-\left(\sigma_{\mathrm{ph}}\Phi_{\mathrm{ph}} + \frac{1}{\tau_{\mathrm{decay}}}\right)t\right]\right) , \tag{2.43}$$

where

$$I_{\mathrm{PL},0} = \frac{\sigma_{\mathrm{ph}}\Phi_{\mathrm{ph}}N_1}{\sigma_{\mathrm{ph}}\Phi_{\mathrm{ph}}\tau_{\mathrm{decay}} + 1} \tag{2.44}$$

is the maximum PL intensity (maximum excited NC population, reached at $t \to \infty$). It should be taken into account that the formalism hereby described is valid under any excitation mechanism, considering its corresponding cross-section and flux definitions. In particular, in the case of optical excitation, the NC excitation efficiency of Si NCs under a photon flux can be evaluated in terms of their photon absorption cross-section, with values usually around $\sigma_{\mathrm{ph}} \sim 10^{-16} - 10^{-15}$ cm^2 [119, 129].

2.4. Electrical and Electro-Optical Properties of Si NC Superlattices

The transport properties of Si NCs, as well as the resulting luminescence as a consequence of this transport or the current generation after light absorption, are of great importance aiming at the fabrication of electronic devices containing this material. Although the three studies are inter-related, their complexity allows the separation of the distinct transport and electro-optical mechanisms, which will be treated in the following sections.

2.4.1. Charge Transport Mechanisms

The charge transport through Si NC ensembles is far more complex than their optical or structural properties. The main drawback is the embedding matrix, usually consisting of a high band gap energy semiconductor material (treated as an insulator), which sets an important barrier for charge conduction. In addition, charge circulation requires a device structure; the device fabrication is therefore more complex than just sample deposition for material studies. We will focus our study on a vertical metal-insulator-semiconductor (MIS) structure, being the insulator (the material under study, with thickness lower than 100 nm) placed between a *p*-type Si substrate and a metallic electrode. A general sketch of the employed MIS devices is presented in Fig. 2.15. The latter material, the metallic (or highly *n*-doped semiconductor) electrode, introduces energy band offsets with respect to the dielectric matrix, setting another limit for carrier injection within the

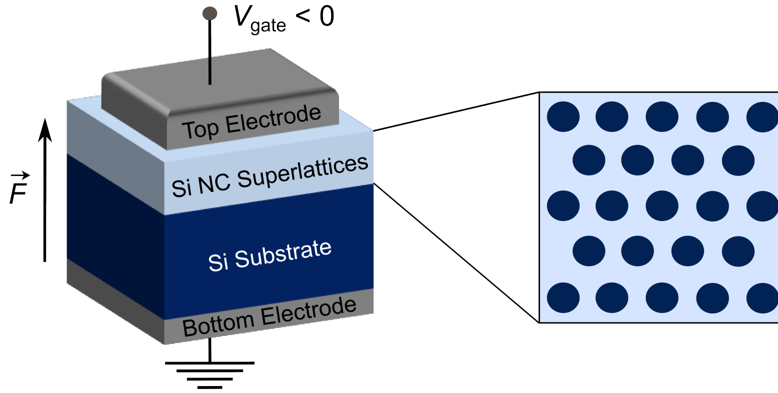

Figure 2.15.: Cross-section scheme of the MIS-based devices employed for the electrical and electro-optical characterization shown in this Thesis. It consists of a Si NC superlattice structure (the insulator) deposited on Si substrate (p-doped), surrounded by metallic (or highly n-type) electrodes. The negative voltage applied at the gate, i.e. the top electrode, induces an electric field ($\vec{F}$) such as the one displayed in the sketch, setting the device in accumulation regime. Figure adapted from [130].

NC-based material under study. At this point, we can already divide the different charge transport mechanisms taking place through NC ensembles as *bulk-limited* or *electrode (injection)-limited*, depending on whether carrier circulation is limited by either the NC-based material properties or the nature of the electrodes. The following lines will be devoted to the in-detail explanation of both transport types.

2.4.1.1. Bulk-Limited Mechanisms

This type of transport generally takes place when the resistance of the electrode-material interface is lower than the material resistance itself (usually achieved when the contact is ohmic); thus, we say that the material under study is limiting the carrier conduction. This requires the existence of allowed states within the material, often provided either by defects in the case of pure dielectrics or quantum-confined states in the case of embedded nanostructures.

Let us now study the general current transport under the application of an external electric field and considering a general conducting material. Under the presence of no magnetic field, the relation between both variables, namely the *current density* ($\vec{J}$) and the *electric field* ($\vec{F}$) is given by the most general *Ohm's law*:

$$J = \sigma F \ . \tag{2.45}$$

This is a constitutive equation where σ is the conductivity, an intrinsic property of every material, which can generally be expressed as:

$$\sigma = q\mu_{\mathrm{n}} n \ , \tag{2.46}$$

being q the elementary charge, $\mu_{\rm n}$ the electron mobility ($\mu_{\rm p}$ for holes) and n the electron concentration (p for holes). When working with high band gap energy semiconductors (also considered as dielectrics), thermal energy is required to increase the carrier mobility through the material trapping centers, as happens to semiconducting materials. We can consequently define bulk-limited conduction mechanisms to be *thermally activated*, which implies a modification in the conductivity following the *Arrhenius law*:

$$\sigma(T) = \sigma_0 e^{-\frac{E_{\rm A}}{k_{\rm B}T}} \ , \tag{2.47}$$

where T is the temperature, $E_{\rm A}$ is the *activation energy* required for conduction to take place, $k_{\rm B}$ is the Boltzmann constant and σ_0 is a pre-exponential factor (interpreted as the system conductivity at an infinite temperature). According to this, even at room temperature (i.e. $k_{\rm B}T \sim 26$ meV) an electron could get out of its localized state originating transport (i.e. electrons reach the conduction band), the probability of this effect increasing with temperature; any dielectric material would therefore present transport under high enough temperature, which obviously states a drawback for their application as conductive devices. In 1938, Frenkel demonstrated that it was possible to skip the temperature inconvenience by applying high electric fields, which gives rise to a strong bending of the energy bands that reduces the effective (barrier) energy for carriers to reach the CB. In such conditions, the conductivity acquires a nonlinear dependence with F [131], and the current density through dielectric materials can be therefore described by the *Poole-Frenkel* (PF) formalism as:

$$J_{\rm PF}(F,T) = \sigma(F,T)F = qN_{\rm t}\mu_n F \exp\left[-\frac{q}{\chi k_{\rm B}T}\left(\phi_{\rm t} - \Delta\phi\right)\right] \ , \tag{2.48}$$

being $N_{\rm t}$ the density of trapping centers (proportional to the carrier concentration), $q\phi_{\rm t}$ the energy that carriers need to overcome to reach the CB, and $\Delta\phi$ is given by:

$$q\Delta\phi(F) = \sqrt{\frac{q^3 F}{\pi\epsilon_0\epsilon_{\rm r}}} \ , \tag{2.49}$$

where ϵ_0 is the dielectric permittivity of vacuum and $\epsilon_{\rm r}$ the relative dielectric permittivity of the material under study. It is interesting to note that the term described in Eq. (2.49) is proportional to the Coulomb interaction potential energy exerted by the trapping center on the trapped carrier (the electric field is inversely proportional to the material thickness, t, the distance that carriers must undergo). In addition, to achieve the maximum generality in the PF expression, the χ parameter was introduced in Eq. (2.48) that takes into account the trapping and detrapping ratio within the localized states that allow transport [132]. Fig. 2.16 presents an energy band diagram where the PF transport process is depicted.

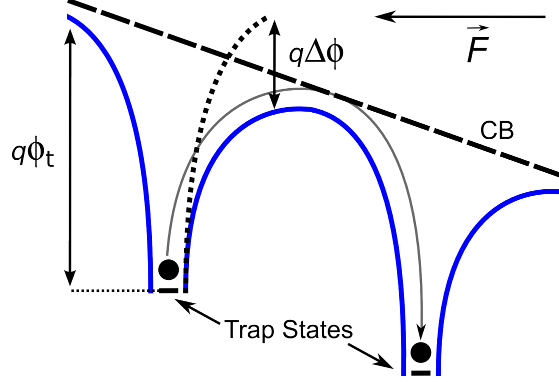

Figure 2.16: Energy band diagram corresponding to a dielectric material presenting trap states, where the Poole-Frenkel conduction mechanism takes place. The polarization under an external electric field, $\vec{F}$, induces a band bending by $q\Delta\phi$, thus reducing the global trap barrier energy, $q\phi_{\mathrm{t}}$. The thermal hopping of carriers (electrons in this example) is represented by a solid grey arrow, whereas dotted lines indicate the unpolarized band. The overall conduction band (CB) is drawn as a dashed-line. Figure adapted from [133].

When the electrode does not limit the carrier injection (the case we are dealing with in this subsection), it is possible that all traps are filled with carriers, mainly because the applied electric field is low enough in order not to allow for a fast detrapping (band bending is insufficient) or detrapping at all (if trapping centers are deep inside the band gap). In this case, carriers are injected at a higher rate than the dielectric detrapping rate. As a consequence, the carrier accumulation near the electrode-dielectric interface (within the dielectric) will generate an electric field that opposes to carrier injection. Under these conditions, transport is *space-charge limited* (SCL) [134, 135]. According to the Mott-Gurney law, considering the multiple collisions underwent by the carriers within the material because of the insulating nature of the latter, the (statistical mean) current density can be expressed as [136]:

$$J_{MG}(F) = \frac{9}{8}\mu_{\mathrm{n}}\epsilon_0\epsilon_{\mathrm{r}}\frac{F^2}{d} \ . \tag{2.50}$$

When also considering the thermal dependence of the SCL mechanism, and given the concentration of injected carriers through the electrode, N_{inj}, and the concentration of traps (i.e. of trapped carriers), N_{t}, the expression for SCL conduction becomes:

$$J_{\mathrm{SCL}}(F,T) = \frac{9}{8}\mu_{\mathrm{n}}\epsilon_0\epsilon_{\mathrm{r}}\frac{N_{\mathrm{inj}}}{N_{\mathrm{t}}}\frac{F^2}{d}\exp\left[-\frac{q\phi_{\mathrm{t}}}{k_{\mathrm{B}}T}\right] \ . \tag{2.51}$$

The SCL mechanism takes place at medium-high applied fields and usually in high-band gap semiconductor and insulators with high defects concentration. When progressively increasing F, trap filling will compete with band bending (which in turn activates detrapping) until reaching the *trap filling limit* (when all traps are filled), beyond which trapping centers will be set free and carrier circulation will again be allowed in a PF frame.

2.4.1.2. Electrode-Limited Mechanisms

When the band offsets between the electrode and the insulating material under study are high enough to state an obstacle for carrier injection, the transport mechanism is said to be electrode-limited. In this case, transport is achieved when high electric fields are applied, which induces a strong band bending. This accelerates the injected carriers, which acquire a high enough kinetic energy (they are also called *hot carriers*), so that they are directly transported through the bands. For this reason, these conduction mechanisms are dominant in defect-free and/or relatively-thick dielectrics.

Given the fact that the electrode-dielectric interface limits the injected current within the material, it is immediate to see that the injection probability will depend on the band offset energy at the interface, $q\phi_{\mathrm{b}}$, as well as on the dielectric material thickness (always implicit in the electric field). Besides, as it has already been stated, the dependence of this probability on the external electric field is strong. Bearing in mind these conditions, there exist two possibilities to overcome the barrier: (i) by hopping or (ii) via tunneling. Whereas the former requires thermal activation, tunneling is independent of temperature.

Let us comment on different transport mechanisms contained within the electrode-limited subgroup. We will first consider the *Schottky* emission mechanism (or *field-enhanced thermionic* mechanism), which presents a strong dependence on temperature. The current density can be expressed as:

$$J_{\mathrm{Schottky}}(F,T) = \frac{4\pi q m^*}{h^3}(k_{\mathrm{B}}T)^2 \exp\left[-\frac{q}{k_{\mathrm{B}}T}\left(\phi_{\mathrm{b}} - \Delta\phi\right)\right] , \qquad (2.52)$$

being m^* the carrier effective mass, h the Planck's constant and $q\Delta\phi$ the apparent energy reduction of the electrode-dielectric barrier caused by the electric field application [2], as described in Eq. (2.49). As a consequence of the barrier height lowering, carrier injection becomes probable by hopping towards the bent conduction band ($F \sim 1$ MV·cm^{-1} is usually sufficient), and therefore transport takes place. A scheme of this process is shown in Fig. 2.17(a).

Another possibility to overcome the injection barrier at higher fields takes into account the quantum probability of carriers for tunneling, i.e. literally crossing the barrier towards the semiconductor (or the dielectric) CB. As no hopping is required, these mechanisms are independent of the temperature. In addition, tunneling is strongly dependent on the thickness to be overcome; therefore, these transport mechanisms will be dominant at thinner insulating layers.

Under the presence of an energy barrier, provided for instance by a QW or a QD, the semiclassical theory predicts that carriers will be confined within the walls [2, 134, 137]. Nevertheless, quantum mechanics allows the possibility for the wave-behaving carrier to tunnel through a finite barrier. Considering a general wavefunction as a solution from the Schrödinger equation [Eq. (2.3)] and the

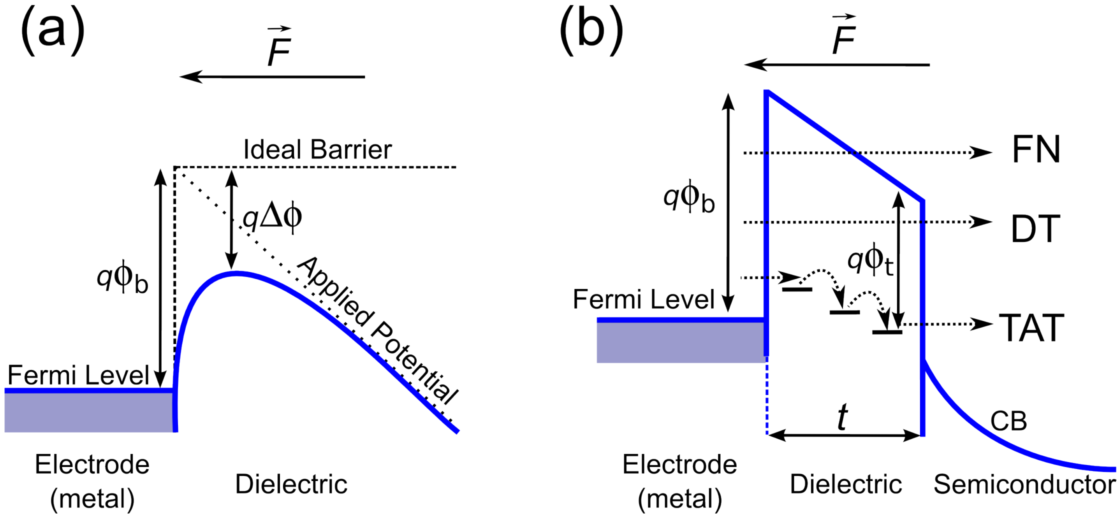

Figure 2.17.: (a) Energy band diagram corresponding to a thermionic (Schottky) transport process, where the application of an external electric field, $\vec{F}$, reduces the effective electrode-dielectric barrier. (b) Energy band schematic summarizing the distinct tunneling transport processes: direct (DT), Fowler-Nordheim (FN) and trap-assisted (TAT). The energy barriers corresponding to the electrode-dielectric interface, ϕ_{b}, and the trap levels, ϕ_{b}, are indicated.

Wentzel-Kramers-Brillouin approximation of a potential W with negligible variation through the dielectric thickness t, one can calculate the ratio between the wavefunctions transmitted through and incident to the barrier, which gives the *tunneling probability* (or *tunnel transparency*), P_{t} (in the unidimensional case):

$$P_{\mathrm{t}}(E) = \exp\left(-\frac{2}{h}\int_{x_1}^{x_2}\sqrt{2m^*[W(x)-E]}dx\right) \ , \tag{2.53}$$

where x_1 and x_2 are the well spacial limits. Taking into account that the barrier shape (i.e. the bands bending level) can vary by modifying the effective well thickness that carriers must overcome, $t = x_2 - x_1$, one can finally find out the current density expression:

$$\begin{aligned} J_{\mathrm{DT}}(F) = & \frac{q^2}{8\pi h\left(\phi_{\mathrm{b}}^{1/2} - (\phi_{\mathrm{b}} - F\cdot t)^{1/2}\right)^2}F^2 \times \\ \times \quad & \exp\left[-\left(\frac{8\pi\sqrt{2m^*q}}{3hF}\left[\phi_{\mathrm{b}}^{3/2} - (\phi_{\mathrm{b}} - F\cdot t)^{3/2}\right]^2\right)\right] \ , \end{aligned} \tag{2.54}$$

which is called *Direct Tunneling* (DT), where the effective barrier presents a trapezoidal shape, i.e. the applied voltage $F \cdot t$ is not sufficient to reduce the effective thickness undergone by most carriers. Under a higher electric field, the bending

of the bands allows for a triangular-shaped barrier, which does reduce the effective thickness, thus increasing the mechanism probability. This is called *Fowler-Nordheim Tunneling* (FN), whose current density can be written as [138, 139]:

$$J_{\mathrm{FN}}(F) = \frac{q^2}{8\pi h \phi_{\mathrm{b}}} F^2 \exp\left[-\frac{8\pi\sqrt{2m^* q}}{3hF} \phi_{\mathrm{b}}^{3/2} \right] . \tag{2.55}$$

Both mechanisms present a quadratic dependence on F (apart from the exponential term), which reveals that they will dominate transport at high fields. In defective materials where electrode-limited mechanisms still dominate, it is possible that a mixed transport exists between tunnel injection and hopping via defect-related traps within the dielectric. This kind of transport is called *Trap-Assisted Tunneling* (TAT), and presents a current density dependence on the electric field such as [140, 141]:

$$J_{\mathrm{TAT}}(F) \propto \exp\left[-\frac{8\pi\sqrt{2qm^*}}{3hF} \phi_{\mathrm{t}}^{3/2} \right] , \tag{2.56}$$

where the $q\phi_{\mathrm{t}}$ is the barrier energy corresponding to the trap levels, the one that carriers must now overcome. All tunneling-based transport mechanisms treated in this section are summarized in Fig. 2.17(b).

2.4.1.3. Transport in Amorphous Superlattices

As already stated in previous sections, superlattices consist of the periodic repetition of QWs based on different materials (i.e. different band gap energies). From a charge transport point of view, such a system is a source of potential barriers that may be overcome via electrode-limited mechanisms or interface-defects and/or localized states that promote bulk-based mechanisms. In the particular case of NC superlattices, the arranged order of the nanostructures allow considering them as a multi-QW structure in the SL deposition direction. It is therefore in this *vertical* direction where interest in carrier transport arises.

In the most general case of a *crystalline superlattice*, as for most III-V semiconductor SL structures [142, 143], where the lattice mismatch is low (i.e. the different involved materials present similar lattice parameters), interfaces within the multi-QW stack are sharp. This implies that the wavefunction from a travelling carrier (electron in the CB or hole in the VB) is strongly confined within the material containing the lowest band gap energy. Considering (i) Bloch-like wavefunctions as described by Eq. (2.1), (ii) the periodicity of the lattice d (i.e. the thickness of two consecutive and different-material wells) and (iii) imposing continuity of the wavefunction and its derivative at the interfaces between two wells and its periodicity over the whole multi-QW stack, it is possible to solve the Schrödinger equation following the Krönig-Penney model [144]:

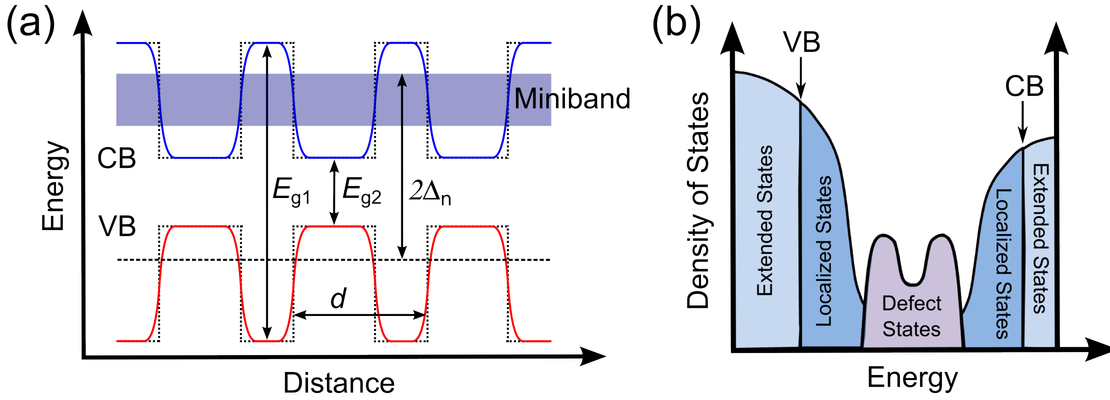

Figure 2.18.: (a) Energy band diagram of a superlattice structure containing two different band gap materials (E_{g1} and E_{g2}). The shaded region represents a miniband of allowed conduction states. Sharp-shaped dotted and curvy solid lines state for crystalline and amorphous superlattices, respectively. (b) Density of states representation for an amorphous superlattice, where the localized and extended states region surrounding the band limits, as well as deep defect levels, are depicted. Figure adapted from Ref. [133].

$$E_n(k) = \Delta_n[1 \mp \cos(kd)] \ . \tag{2.57}$$

The oscillating character of these solutions (i.e. between the "-" −symmetric− and "+" −asymmetric− solutions) defines an energy band (called *miniband*) within the SL diagram, where $2\Delta_n$ is the maximum width of the band as defined from an effective hole-level in the valence band. The miniband can be then understood as an effective conduction band where electrons can be transported through allowed energy states irrespective of the real band gap energies the involved materials present. The concept of miniband is depicted as a shaded region in Fig. 2.18(a).

When working with Si-based compounds (e.g. SiO_2, SiC or Si_3N_4), it is not possible to attain a crystalline SL structure due to their mainly-amorphous nature. These superlattices do not present neither lattice matching nor long-range order. This, in practice, is translated into a non-abrupt band structure [solid lines in Fig. 2.18(a)] that implies a partial loss of wavefunction confinement [145]. The SLs then present a global band energy structure that consists of localized states below, as well as a band of continuum extended states above, the theoretical CB (and analogously for the VB), as shown in Fig. 2.18(b) (in a similar way as minibands are defined in crystalline superlattices). This characteristic reduces the effective height of the present barriers, improving transport through these typically insulating materials. In addition, it has been demonstrated in the past that amorphous superlattices still present quantum confinement effects (even extended states can be localized under the presence of quantum structures such as QWs or QDs) [61, 145, 146].

The charge transport mechanisms in Si NC-based materials have been widely studied in the past, for different growth techniques and under different experimental conditions, which give rise to electrical phenomena spanning from bulk-limited to electrode-limited conduction mechanisms [147, 148]. However, the novelty of arranging these nanostructures in superlattices has induced recent efforts to study these systems, and only few information is available. Si NC superlattices can be treated as amorphous, for the sub-stoichiometric dielectric region that separates the NC core from the embedding dielectric matrix is highly defective, thus presenting highly defective interfaces. This enhances bulk-limited processes in detriment of electrode-limited ones, although the device structure has proved to be crucial. For instance, tunnel-based mechanisms in Si NC/SiO_2 SLs have been reported on structures where poly-Si was selected as n-type electrode (it presents a high band offset with respect to SiO_2) and the first dielectric layer is thicker than the subsequent periods [149, 150]. In contrast, it has been demonstrated on similar SL structures that both the selection of different electrodes (such as transparent conducting oxides) and a different layer thickness engineering originate bulk-limited mechanisms such as Poole-Frenkel, provided that the quantum confinement acting on the extended states create allowed energy levels [130]. Other embedding matrices have been recently investigated such as SiC, where it has been shown that thermally-activated transport through extended states of SiC, rather than through Si NCs, dominates [151, 152]. It is part of the objectives of this Thesis to determine the transport properties of Si NCs embedded in SiO_xN_y and SiC, which will be expanded in Chapter 4 (*Results and Discussion*).

2.4.2. Electro-Optical Properties of Si-NC Superlattices

In Section 2.4.1, the different existing transport mechanisms through dielectric-like materials (bearing in mind amorphous Si NC superlattices) have been reviewed. We have also generalized these conduction mechanisms to all type of carriers, electrons and holes, for both present analogous paths through the energy band diagram, although with different parameter values (for instance, the barrier height, the carrier mobility or the effective mass) that strongly depend on the employed materials (in Si NCs embedded in SiO_2, hole current is much lower than electron current [153]). When electro-optical conversion is considered, however, different mechanisms arise according to the presence of the different carrier species. Here, the electron-to-light (electroluminescence, EL) or light-to-electron (phocurrent and/or photoconductivity) conversion in this kind of materials will be exposed.

2.4.2.1. Electroluminescence of Si NC Superlattices

The origin of luminescence from semiconductor materials under electrical excitation (which is called *electroluminescence*) is well known to be due to band-to-band

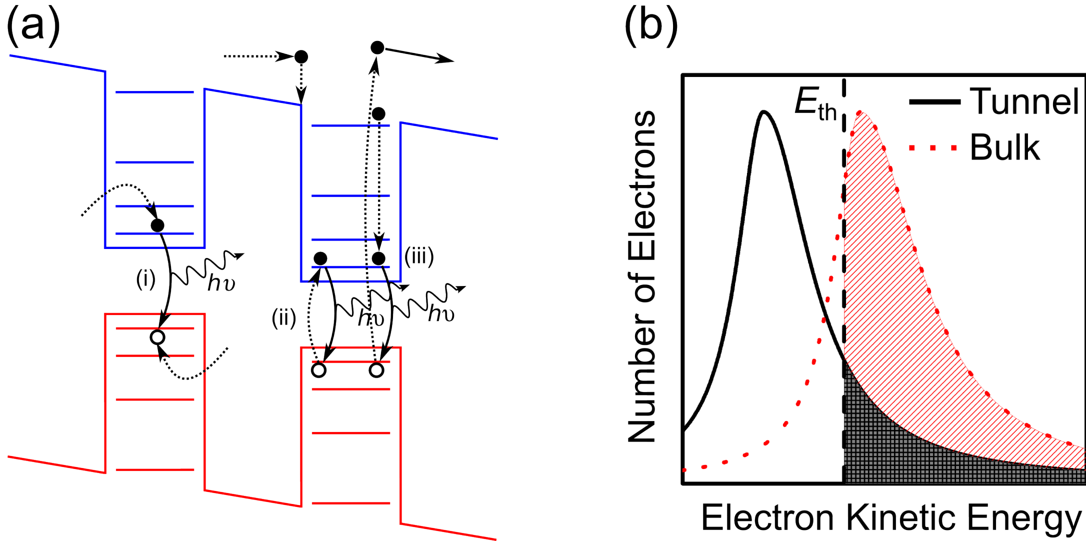

Figure 2.19.: (a) Schematics of the different EL excitation processes in Si NC superlattices described in the text: (i) electron-hole injection, (ii) impact excitation and (iii) impact ionization. (b) Electron energy distribution corresponding to tunnel- and bulk-based transport mechanisms. The vertical dotted line establishes a tentative threshold energy (E_{th}) for impact processes to take place. The shaded regions therefore correspond to the electron populations susceptible to induce these impact processes. Figure adapted from Ref. [130].

recombination between electrons and holes (excitonic recombination), although intra-band gap emission is possible under the presence of lattice defects or impurities/dopants within the semiconductor material. In fact, the luminescence mechanism is analogous to the one obtained from photoluminescence. Therefore, it is the excitation mechanism the one which may vary according to the material conditions.

Focusing on the case of Si NCs embedded in a dielectric matrix, we can distinguish three different EL excitation mechanisms [summarized in Fig. 2.19(a)]: (i) *electron-hole bipolar injection*, (ii) *impact excitation* and (iii) *impact ionization*. On one hand, case (i) is typical in semiconductors, where electrons and holes can be easily injected into the bands, wells or nanostructure energy levels; in the particular case of SiO_2 layers, however, the lower mobility of holes in comparison to electrons (more than 5 orders of magnitude [153]) will cause the electron-hole recombination to more likely take place near the *p*-contact/dielectric interface, where holes are accumulated. On the other hand, cases (ii) and (iii) are based on the energy transfer from one conduction electron to a bound electron (in the VB) occurred after inelastic impact of the former within the semiconductor lattice, the Si NCs in our case. The final state of the excited (initially bound) electron will determine the particular excitation mechanism we are dealing with: whereas impact excitation will upgrade the VB electron towards a localized (confined) energy state

within the NC, impact ionization will promote it to the superlattice CB, i.e. the electron will be set free for conduction. Impact ionization is therefore more prompt to contribute to conduction, given that the empty levels help recapturing new carriers. In addition, a required condition for mechanisms (ii) and (iii) to take place is that the kinetic energy of electrons has to be greater than a threshold energy, E_{th}, equal to or greater than the NC band gap energy (i.e. the first and lower-energy confined level). This, in turn, establishes a relationship between EL efficiency and the transport mechanism, as the number of electrons with higher kinetic energy than E_{th} will depend on the dominant conduction mechanism through a particular system, finding larger hot electron population in tunnel-based [154] rather than in thermally-activated (i.e. bulk-limited) mechanisms [155]. Fig. 2.19(b) displays a tentative schematics of the mentioned electron energy distributions.

Once the excitation process has been studied, the recombination dynamics giving rise to EL can be directed. Under electrical excitation, the same treatment than in Section 2.3.2.4 is still valid. In particular, the resulting EL emission intensity is analogous to Eq. (2.43):

$$I_{\text{EL}}(t) = I_{\text{EL},0}\left(1 - \exp\left[-\left(\sigma_{\text{el}}\Phi_{\text{el}} + \frac{1}{\tau_{\text{decay}}}\right)t\right]\right) \ , \qquad (2.58)$$

being σ_{el} the NC electron cross-section, i.e. the effective section where conduction electrons can impact the NC, and $\Phi_{\text{el}} = J/q$ the injected electron flux. Indeed, from time-resolved EL measurements [which will be extensively introduced in Chapter 3 (*Experimental Details*)], it is therefore possible to evaluate the NC cross-section, which highly depends on the transport mechanism. In this frame, electron impact has shown to give rise to σ_{el} values as large as $\sim 10^{-16} - 10^{-14}$ cm^2 [127, 156], which are very close to the values under optical excitation [119, 129].

2.4.2.2. Photoconduction and Photocurrent in Si NC Superlattices

The study of the electrical response to optical stimulus from Si NCs is particularly interesting for photovoltaic or photodetecting applications. The *photoconductivity* phenomenon takes place when a device is illuminated, both with monochromatic or white light, and under the presence of an external electric field, yielding to the generation of additional carriers, either Δn or Δp:

$$\begin{aligned} n &\xrightarrow{\text{Light}} n + \Delta n \\ p &\xrightarrow{\text{Light}} p + \Delta p \end{aligned} \ . \qquad (2.59)$$

This increment is specially important for minority carriers. In turn, the photogeneration induces an increase in the current density circulating through the device. Indeed, the photogeneration process is analogous to the absorption phenomenon in semiconductor materials, with the extra condition of a band bending due to the

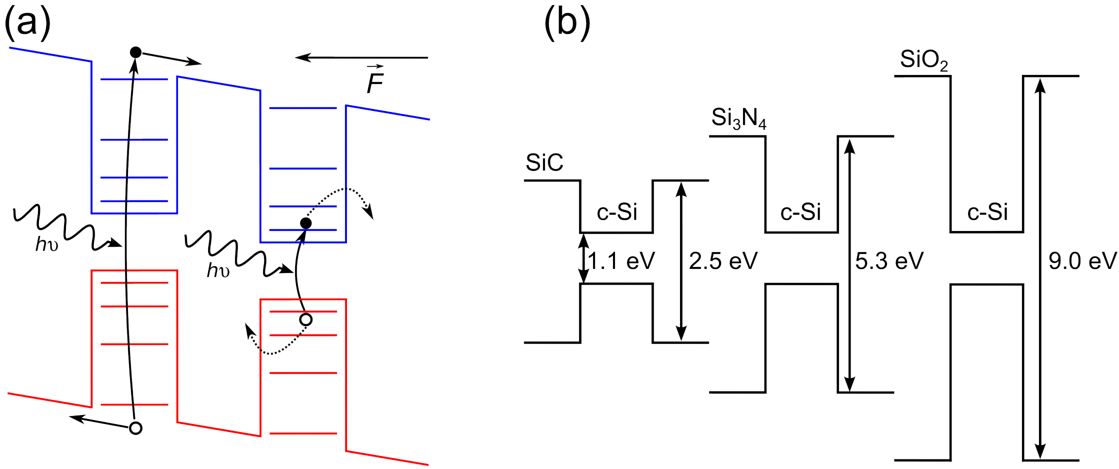

Figure 2.20.: (a) Scheme of the carrier photogeneration mechanism in Si NC superlattices. The probability of generating carriers that can be extracted will directly depend on the applied electric field, i.e. the band bending, as well as the absorbed energy (left incoming photon presents a higher energy than the right one). (b) Band gap energy (written down in the figure) difference between c-Si and different dielectric matrices (silicon carbide, nitride and oxide). Figure adapted from [42].

applied field [see Fig. 2.20(a)]. The generated *photocarrier* concentration can be expressed as (for electrons):

$$\Delta n = G_{\mathrm{n}} \tau_n \ , \tag{2.60}$$

where G_n is the carrier concentration generation per unit time (electrons in this case), indicating the rate of generated electrons per absorbed photon, which will vary according to the material, and τ_n is the carrier lifetime (the carrier decay from previous subsections). This expression is true provided that the generation is constant throughout the active layer (i.e. if there is low absorption). Eq. (2.60) can be analogously applied to hole generation (with parameters Δp, G_p and τ_p). Besides, its dependence on the carriers lifetime points out the inverse relationship character of photogeneration with respect to electroluminescence: larger τ_n implies that carriers will stay longer within the semiconductor and thus avoid recombination until they are extracted through the electrodes.

As we have already stated, a proper extraction of the photogenerated carriers requires the presence of a large enough electric field, to bend the bands and consequently allow carriers to travel towards the contacts before they recombine. However, it is possible that, when a *p-i-n* design (corresponding to a M-I-S structure, respectively) is employed (being the *i*-layer the absorber material), the existent built-in potential induces an internal electric field, large enough to extract carriers. Therefore, in contrast to photoconduction, which takes place when an external electric field is applied, we talk about *photocurrent* when the internal field

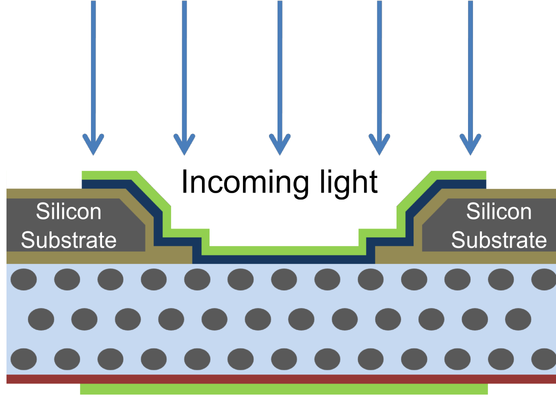

Figure 2.21: Cross-section scheme of a membrane cell device, where the substrate is locally removed to study the electro-optical response and photovoltaic properties of Si NCs alone. Figure adapted from [157].

alone allows for carrier extraction. With all the considerations explained above, the photocurrent density can be defined as [134]:

$$J_{\mathrm{ph}} = qd\left[\frac{G_n\tau_n}{t_n} + \frac{G_p\tau_p}{t_p}\right] , \tag{2.61}$$

where d is the total absorber layer thickness, and t_n and t_p the time that electrons and holes, respectively, need to travel through the whole absorber thickness without being recombined.

The last decade has provided numerous studies of the light-to-electron conversion in group-*IV* NC-based materials (basically Si, Ge and SiGe ensembles). In particular, photoconductivity has been observed in Si and SiGe ensembles embedded in SiO_2 to depend on the NC size [49, 158], proving the quantum confinement effect by these electro-optical measurements. The photocurrent observation is far more difficult in oxide-embedded systems, for its band gap energy becomes a very high barrier for carrier transport than in the case of other dielectric matrix, such as Si_3N_4 or SiC [see Fig. 2.20(b)] [42, 159]. The use of a tandem cell structure, i.e. depositing the NC-based material on top of a Si cell in order to combine both band gap energies absorption, has helped to determine the photovoltaic properties of these materials; however, as most of the obtained current was photogenerated within the Si substrate, the deconvolution of the NC properties from those of the substrate has not been achieved [42]. For this reason, a membrane cell structure was designed (see Fig. 2.21), allowing for the study of the NC-based material alone by locally substracting the substrate [151, 160]. Part of the results of the present Thesis, discussed in Chapter 4 (*Results and Discussion*), describe the electro-optical response and photovoltaic properties of Si NCs embedded in the conductive SiC matrix, using such a membrane cell structure [157].

3. Experimental Details

> Physics is like sex: sure, it may give some practical results, but that's not why we do it.
>
> Richard P. Feynman

This Chapter is devoted to the description of the different experimental techniques employed for measuring the properties exhibited by Si NC superlattices. The first section will focus on the fabrication process of the SL-based material under study. Afterwards, the different characterization techniques will be addressed, and will be classified attending to the kind of characterization they are aimed at: structural, optical, electrical and electro-optical. The fundamental physics that governs each technique will be described, as well as the particular configurations used in each case.

3.1. Sample Fabrication

Although the objective of the present Thesis is the characterization of Si NC-based superlattice systems, it is mandatory to briefly show how these material systems are grown. Due to the complexity of the nanometric layer deposition, the sample preparation was carried out in specialist institutions with whom we have maintained a close collaboration during the last four years. These involved centers are the *Institut für Mikrosystemtechnik* (IMTEK, Albert-Ludwigs Universität, Freiburg, Germany) and the *Istituto per la Microelettronica e i Microsistemi - Consiglio Nazionalle delle Ricerche* (CNR-IMM, Bologna, Italy), which have specialized in the deposition of SiO_2- and SiC- based SLs, respectively.

For a Si-based superlattice structure achievement, the alternated deposition of stoichiometric and non-stoichiometric (Si-rich) Si-based dielectric material layers, of low thickness (few nm), is required. This can be reached using a plasma-enhanced chemical-vapor deposition (PECVD) system (Oxford Instruments *Plasmalab 100*) with a 13.56 MHz driven parallel plate reactor. Ultra-high vacuum conditions were induced inside the chamber, being the sample holder heated at 130 °C or 350 °C for oxide- or carbide-based depositions, respectively. In the case of Si-rich SiO_2 (SiO_x) deposition, a mixture of silane (SiH_4) and nitrous oxide (N_2O) gases were employed as precursors, whereas silane, molecular hydrogen (H_2) and methane (CH_4) were used in the case of Si-rich SiC (Si_xC_{1-x}). The controlled

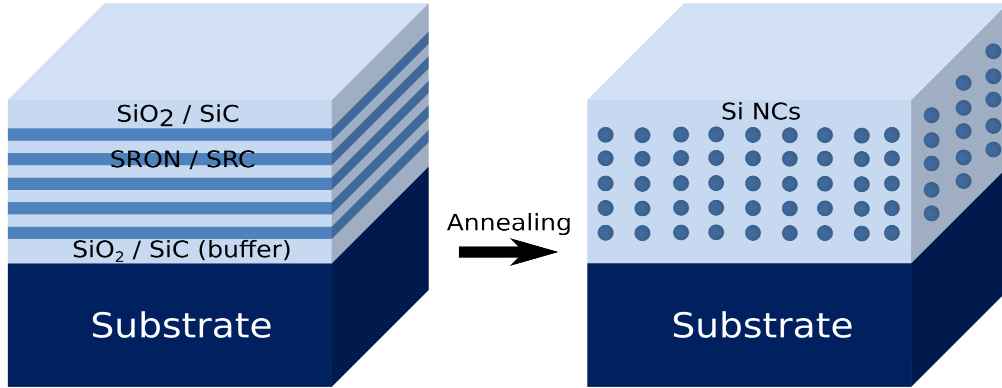

Figure 3.1.: Deposited superlattice structure before (left) and after (right) the high-temperature annealing treatment, when the presence of crystalline nanostructures is achieved.

ratio between the precursor gases concentration allows obtaining the desired Si-rich layer stoichiometry (x) and, therefore, the Si excess. The selected substrates for the SL deposition were piranha-cleaned crystalline (100)-Si and/or fused silica (amorphous SiO_2, quartz glass), depending on the nature of the characterization that had to be carried out.

Once the SL structure is deposited [see the sketch in Fig. 3.1 (left)], a high-temperature annealing treatment is required in order to induce the Si excess precipitation within the Si-rich layers, as well as their crystallization. This is performed inside a conventional quartz tube furnace, in an inert N_2 ambient. The consequent phase separation that takes place within these layers can be expressed as:

$$\mathrm{SiO}_x \longrightarrow \frac{x}{2} \cdot \mathrm{SiO}_2 + \left(1 - \frac{x}{2}\right) \cdot \mathrm{Si} \;, \tag{3.1}$$

for the Si-rich oxide (SRO) matrix case. Indeed, the presence of nitrogen during the precursor gases flow induced an oxynitride (SRON) matrix SiO_xN_y compound. However, the control of this gas flux allowed for a partially controlled stoichiometry of $y = 0.23$, almost constant in all depositions. Finally, for the Si-rich carbide (SRC) matrix we have

$$\mathrm{Si}_x\mathrm{C}_{1-x} \longrightarrow \left(1 - \frac{x}{2}\right) \cdot \mathrm{SiC} + \left(1 + \frac{x}{2}\right) \cdot \mathrm{Si} \;. \tag{3.2}$$

The phase separation quality strongly depends on the annealing temperature and duration. In particular, a typical post-deposition annealing treatment at 1150 °C for 1 h was employed for SRO-based systems, whereas a two-step process of 600 °C (4 h) + 1100 °C (30 min) was required in the case of SRC. Prior to the SL structure deposition, a thicker buffer layer was deposited on top of the substrate in both matrix cases, aiming at avoiding the Si excess diffusion from/towards the

Table 3.1.: Summary of the values corresponding to the different parameters employed for the fabrication of the SL-based samples studied in this Thesis.

Matrix	t_{SRON} / t_{SRC}	t_{SiO2} / t_{SiC}	N	x	T_{ann}
SiO_2	2−5 nm	1−4 nm	20−125	0.64−1.1	900−1250 °C
SiC	2−4 nm	3−5 nm	30	0.6−0.95	600−1100 °C

substrate. The samples also underwent a passivation process by H plasma, in order to get rid of the undesired dangling bonds, which induce defects within the nanostructures and their surrounding matrix. In summary, after the whole fabrication process, stable superlattices and also size-controlled Si NCs are achieved [see Fig. 3.1 (right)]. Further details on these processes are described in Refs. [82, 161]. All structure and process parameters were varied for different sample sets, since different material properties had to be studied: SRON (SRC) layer thickness, t_{SRON} (t_{SRC}), SiO_2 (SiC) barrier thickness, t_{SiO_2} (t_{SiC}), number of SRON/SiO_2 (SRC/SiC) bilayers (N), stoichiometry (x) and annealing temperature (T_{ann}). Tab. 3.1 summarizes the different structure parameters employed for the fabrication of the SL stacks studied in this Thesis.

3.2. Experimental Techniques

The following pages are dedicated to the description of the experimental measurement techniques that have been essential for obtaining the results presented in this Thesis. It has to be stated here that some techniques require special management skills and/or technicians for instrument manipulation and data acquisition. In particular, electron microscopy and X-ray diffraction measurement acquisition were performed by means of the University service and in collaboration with trained specialists, the PhD Candidate's main contribution being the data analysis. However, the rest of the hereby presented techniques were fully operated by the PhD Candidate himself. Finally, it is not the purpose of this Chapter to give a deep insight on the employed experimental set-ups but on the physical background that rules the operation laws of these techniques.

3.2.1. Structural Characterization Techniques

3.2.1.1. Transmission Electron Microscopy (TEM)

The minimum distance that can be resolved by means of the classical optical microscopy is strongly limited by the so-called diffraction limit, which states that an imaging instrument resolution, d, can be expressed as:

$$d = \frac{\lambda}{2n \sin\theta} \approx \frac{\lambda}{2 \cdot \text{NA}} \,, \tag{3.3}$$

where λ is the incident wavelength, n is the diffractive index of the sample, θ the collection angle and NA the system's numerical aperture. So, imaging the nanoscale is not easily achievable via conventional microscopy. Indeed, Eq. (3.3) indicates that the maximum resolution that can be obtained by an optical system is proportional to half the incident wavelength, i.e. a few hundreds of nm. This obviously makes it impossible to image at the nanoscale. In the case of electron microscopy, the wavelength associated to the electron, λ_e, can be obtained from the following relativistic De Broglie equation:

$$\lambda_e = \frac{h}{2m_0 E_e \left[1 + \frac{E_e}{2m_0 c^2}\right]} \; , \tag{3.4}$$

being h the Planck's constant, m_0 the electron's rest mass, E_e the energy associated to the electron and c the speed of light in vacuum. Using Eqs. (3.3) and (3.4) for the typical energies employed in electron microscopy ($\sim 80-300$ keV), the resulting associated wavelength lies in the order of some tens of pm. Therefore, the diffraction limit that conventional microscopy presents is widely overcome. Then, the resolution of electron microscopes is typically not limited by the properties of electrons but by technical issues, basically concerning the quality of the electromagnetic lenses and the correction of aberrations [162]. Consequently, under proper technical and measurement conditions, atomic resolution can be achieved.

Concerning the electron microscopy imaging, it is based in the electron-matter interaction process, which can induce many different effects. A first division can be applied whether the electrons are reflected on the sample or transmitted through it. The first kind of processes belong to the *scanning electron microscopy* (SEM) group, whereas the latter belong to *transmission electron microscopy* (TEM) techniques (a summary of these electron-matter interaction phenomena is sketched in Fig. 3.2). Both groups of processes are governed by interactions within the material that result in a trajectory deviation of the reflected or transmitted electrons (or no interactions if the sample thickness is low enough). This deviation from normal incidence, strongly dependent on the atomic structure and composition of the material, becomes a powerful tool of analysis and imaging.

From an energetic point of view, the electron-matter interaction processes taking place within the material typically involve scattering after electrons elastically or inelastically collide with sample atoms, the latter type of collisions involving an energy loss of the particles. In particular, one of the most employed operation modes in TEM is *electron energy-loss spectroscopy* (EELS), based on the analysis of the lost energy by electrons when inelastically scattered by atoms (electrons bound in internal atomic states) or collective oscillations of the electrons (plasmons) within the sample. Given that different materials (compounds or phases) present a different plasmon energy, it is useful when studying semiconductor materials to energetically filter the transmitted electron beam at the specific plasmon resonance of the material under study, which increases the contrast between the

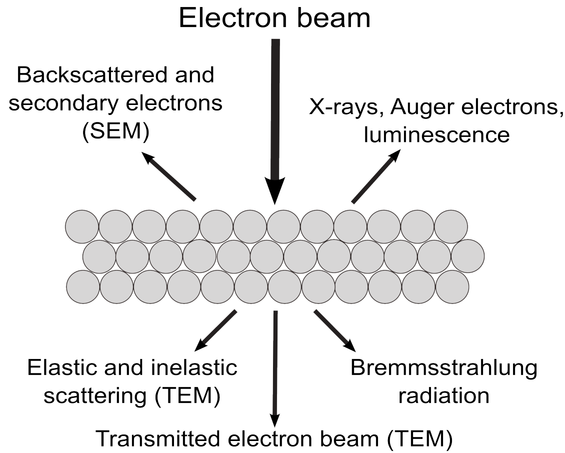

Figure 3.2: Scheme showing the principal phenomena taking place as a result of electron-matter interaction. Those techniques involved in scanning and transmission electron microscopy, SEM and TEM respectively, are written down.

present phases. This technique is known as *energy-filtered transmission electron microscopy* (EFTEM), and it is typically employed in the case of Si NCs embedded in a dielectric matrix, where the contrast between Si and the background (SiO_2 or SiC in our case) is essential to carry out precise NC size statistics.

As discussed, TEM is a very useful technique to image the nanoscale. However, the major limitation of TEM imaging is the need of thin specimens for electron transparency. This requires a thorough sample preparation, which in turn adds to the already time-consuming measurement itself. In addition, this preparation, usually by mechanical procedures, is destructive, as it is the 80−300-kV electron beam incidence on the sample. Therefore, it is convenient to complement this powerful technique with other ones that permit additional structural information of the system under study.

Experimental Equipment Prior to TEM observation, samples were polished up to electron transparency, first mechanically and then by ion milling. This process was monitored by means of an optical interferometer, to ensure the correct sample thickness. The samples prepared in cross-section geometry were observed using a JEOL 2010F instrument, which operates at 200 keV field-emission gun (FEG), equipped with a Gatan Image Filter (with a resolution of 0.8 eV). In order to enhance the Si-to-background contrast, the electron energy-loss spectrum was energetically filtered around the Si plasmon energy ($E_{Si} = 17$ eV).

3.2.1.2. X-Ray Diffraction (XRD)

X-ray diffraction is a structural technique aimed at the analysis of the crystalline properties of materials [163]. For this, it is required that the material under study is crystalline or, at least, presents some crystalline arrangement. This technique is based on the X-ray photons interaction with electrons bound in the lattice planes, being the X-ray wavelength of the order of the atomic radius (~ 0.1 nm),

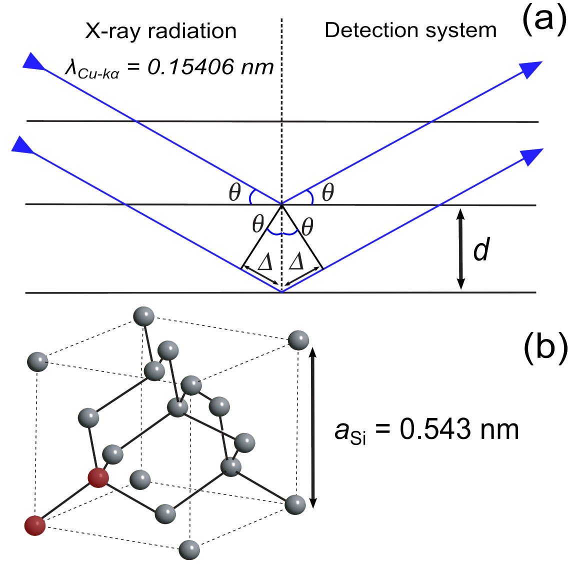

Figure 3.3: (a) Schematic corresponding to the Bragg condition by means of which XRD patterns are obtained. (b) Crystalline silicon unit cell: a face-centered cubic with a diatomic base (highlighted in red).

corresponding to energies of the order of 10 keV; therefore, information about the lattice orientation and atoms position can be obtained.

When X-ray photons are incident on a material lattice, some of them may be elastically scattered by bound electrons, both particles conserving their energy after the process. The photons may be scattered in any direction, but only those whose associated waves are in phase (i.e. the optical path difference be 0 or an integer multiple of their wavelength) will constructively interfere. In a lattice with an *interplanar distance* d (i.e. the separation between lattice planes), the optical path difference between two atoms situated in equivalent positions in consecutive planes is $2\Delta = 2d\sin\theta$. Therefore, these two previously imposed conditions for the X-ray diffraction (equivalently called reflection) observation at an angle 2θ induce the following expression:

$$2d\sin\theta = N\lambda \ , \tag{3.5}$$

where N is the diffraction order and λ is the wavelength corresponding to the X-rays. Eq. (3.5) is called the *Bragg law*, and the angles that accomplish this relation are thus called *Bragg angles*. Fig. 3.3(a) illustrates the Bragg condition. Since in a XRD experiment the detector is placed at the same angle (with respect to the normal to the lattice plane) than the X-rays source, which is varied for an angular scan, the XRD patterns give information about the interplanar distance, characteristic of each material lattice. In particular, silicon presents a *face-centered cubic* unit cell with a diatomic base (diamond-type crystal structure), with a *lattice parameter* (i.e. the cubic side length) $a \approx 0.543$ nm. Fig. 3.3(b) displays the Si unit cell, where the base is highlighted in red. The silicon interplanar distance (for the first diffraction order) can be expressed in terms of the lattice parameter as follows:

$$d = \frac{a}{\sqrt{h^2 + k^2 + l^2}} \ . \tag{3.6}$$

Here, h, k and l are the Miller indexes, which define the equivalent planes the Si cell structure can present. By scanning the lattice at different incident (and thus diffraction) angles, it is then possible to obtain a series of Miller indexes that accomplish Eq. (3.6), which will give information about the lattice orientation and unit cell structure. However, the determined orientation is strongly dependent on the sample position and inclination. If there exists particular interest in studying all possible lattice plains within the material, the reduction of the material to powder allows the random examination of all the possible reflections within the material; this is called the *Debye-Scherrer* method, and it is the one typically employed to study nanoparticle colloidal systems. In the case of matrix-embedded Si NCs, similar conditions than in powder are found, since the NC orientations are randomly distributed within the sample; therefore, the *Debye-Scherrer* method is also applicable.

To further analyse materials containing non-continuous crystalline domains (such as NCs, which are surrounded by amorphous matrix), the Scherrer formalism gives an average approximation for the crystalline grain size $\langle D \rangle$ [164]:

$$\langle D \rangle = \frac{K\lambda}{\beta \cos\theta} \ , \tag{3.7}$$

where K is a shape factor (typically close to unity), β the full-width at half-maximum of the particular reflection and θ the Bragg angle. Then, although the XRD signal of Si NCs is very low, XRD diffraction allows estimating with good approximation the crystalline size of the nanostructures.

Experimental Equipment The XRD measurements were carried out with a *PANalyticalX'Pert PRO MPD Alpha1* powder system. X-ray radiation from Cu K_α line, $\lambda = 0.15406$ nm, was used as the excitation source.

3.2.2. Optical Characterization Techniques

3.2.2.1. Light-Matter Interaction

The incidence of electromagnetic radiation on a given material gives rise to several light-matter interaction processes. Indeed, the radiation interaction with the material atoms depends on the atomic structure the material presents, which is described by its energy band structure, and the polarization state of that incident radiation. Therefore, the probability of the possible interaction processes is related to the incident beam energy and that corresponding to the elementary excitations within the material. As an example to this latter statement, incident electromagnetic radiation in the infrared range will be able to excite (material-dependent)

lattice vibrations, whereas higher-energy radiation (e.g. in the UV range) will induce band-to-band electronic transitions.

Fig. 3.4 depicts the most generic processes taking place when an electromagnetic beam undergoes a change of medium (in our case, from vacuum/air to a certain material medium). At the vacuum/material interface, part of the incident beam will be reflected, whereas the rest will be transmitted. Under particular conditions (which will be treated in the following subsections), the transmitted radiation may be absorbed by the material atoms, a part of it still reaching the backside material/vacuum interface, where internal reflection or transmission might again occur. Experimentally, one can estimate the part of radiation that has been absorbed by measuring the finally transmitted and reflected beams from a solid material, in order to study the material-dependent *optical absorption*.

The radiation absorption of a material leads to a modification of the material's energetic state. This is called *excitation*, and its relaxation (i.e. its return to the original, lower energy, state) originates different physical phenomena that span from the lattice thermalization (i.e. the non-radiative relaxation of the lattice by emitting phonons that increase the material's temperature) to luminescence emission (also called *photoluminescence*). The study of the latter effect is possible by means of optical techniques, since lattice relaxation produces the emission of photons with an energy in the order of the material (semiconductors, in our case) band gap energy, usually in the UV, visible and near-infrared ranges.

Finally, although reflection and absorption are first-order processes, and therefore are the most probable ones, the transmitted electromagnetic radiation may undergo higher order processes such as *scattering* by other elementary excitations of the material lattice (such as phonons or plasmons) [1]. If no energy is expended during the scattering process we can classify it as *elastic*, also called *Rayleigh scattering*; instead, we call it *inelastic* when an energy variation between the incident and the scattered beams exists. Inelastic scattering is called *Raman scattering*, the implied energy difference being measured via optical spectroscopy, from which information of the lattice vibration (closely related to their crystalline state) can be achieved.

Therefore, a basic optical characterization of semiconductor materials can be performed by analyzing these three basic and material-dependent processes: optical absorption in the UV-visible part of the spectrum, the consequent optical emission via photoluminescence and the energy loss resulting after phonon scattering (Raman scattering).

3.2.2.2. UV-Visible Absorption Spectroscopy

From a macroscopic point of view, incident electromagnetic radiation on a given material tends to be transmitted through, reflected on (the top part or internal interfaces) or absorbed within the material. The three processes (transmittance,

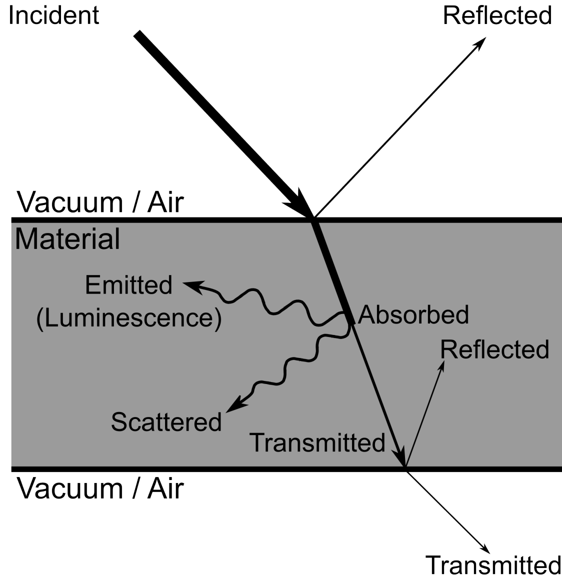

Figure 3.4: Summary of the main light-matter interaction processes undergone by an incident electromagnetic beam from vacuum (or air) to a given material system. Transmission and reflection processes, as well as scattering and resulting radiation emission after absorption within the material, are considered. The arrows thickness was intentionally varied to account for the proportion of the incident radiation that remains (or is lost) at every step. Figure adapted from Ref. [1].

T, reflectance, R, and absorptance, A) are in balance and conserve the incoming energy in the form:

$$T + R + A = 1 \ , \tag{3.8}$$

where *1* states for the total incoming energy (i.e. 100% of the radiation). An example of the spectra corresponding to the three magnitudes in Eq. (3.8) is shown in Fig. 3.5(a), for a sample containing Si NC/SiC superlattices. In order to quantify the absorption response of a given material, we must consider the amount of incoming radiation that is not reflected, i.e. $1 - R$. Then, the transmittance through the material of thickness d presents an exponential decay behavior that is defined by the *Beer-Lambert law*:

$$T = T_0 \cdot \mathrm{e}^{-\alpha d} = (1 - R) \cdot \mathrm{e}^{-\alpha d} \ , \tag{3.9}$$

being T_0 the incident beam intensity at the top part of the material, immediately before transmission through the interface, and α the absorption coefficient, a parameter that is characteristic of each material. From Eq. (3.9) one can thus calculate the absorption coefficient in terms of the measurable magnitudes d, T and R:

$$\alpha = \frac{1}{d} \cdot \ln \left[\frac{T_{\mathrm{subs}} \cdot (1 - R)}{T} \right] \ , \tag{3.10}$$

where T_{subs} is the transmittance of the substrate, usually fused silica (transparent to the visible spectrum). The absorption coefficient is dependent on the incoming radiation energy, and thus it can be spectrally monitored. Apart from quantifying

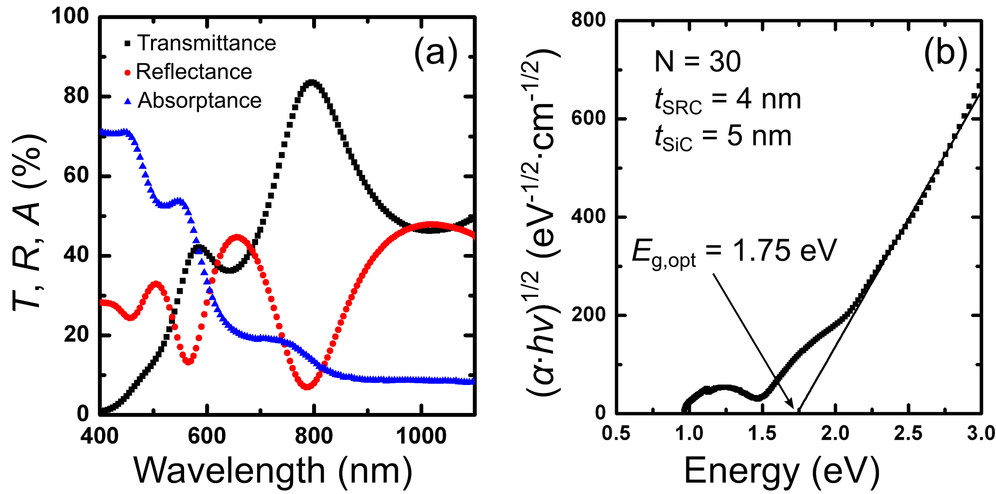

Figure 3.5.: (a) Transmittance (black squares), reflectance (red circles) and absorptance (blue triangles) spectra corresponding to a sample containing Si NC superlattices in SiC, with t_{SRC} and t_{SiC} of 4 and 5 nm, respectively, and a total number of bilayers of $N = 30$. (b) Tauc plot corresponding to the sample in (a). The solid line represents the linear fit at high energies, whose intersection with the energy axis gives $E_{\mathrm{g,opt}}$.

the material absorption as a function of the photon energy, it is possible to estimate the material band gap energy by using the Tauc formalism [165]:

$$\alpha = \frac{B}{h\nu} \cdot (h\nu - E_{\mathrm{g,opt}})^n , \qquad (3.11)$$

where h is the Planck's constant, ν the incident photon frequency, B is the Tauc coefficient, which describes the light absorption efficiency, $E_{\mathrm{g,opt}}$ the *optical band gap energy* and n is an exponent that depends on the band gap nature of the semiconductor material under study. According to the Tauc formalism, the absorption behavior of a direct band gap semiconductor can be modelled by $n = 1/2$ (such as ZnO, GaAs, ...), whereas $n = 2$ is typical for indirect band gap ones (it is the case of Si or Si NCs). $E_{\mathrm{g,opt}}$ can be easily obtained from the so-called Tauc plots, i.e. the $(\alpha h\nu)^{1/n}$ versus $h\nu$, as the intersection of the high-energy region linear fit with the energy ($h\nu$) axis [an example of Tauc plot is displayed in Fig. 3.5(b)].

The concept of optical band gap was further explained in Chapter 2 (*Fundamentals of Silicon Nanocrystals*). Unlike the PL case, where the *emission band gap* is evaluated from the recombination of electron-hole pairs located at the band extremes, photon absorption tends to be effective at larger energies than the band gap. Therefore, the difference between both values, $\Delta E_{\mathrm{Stokes}} = E_{\mathrm{g,opt}} - E_{\mathrm{g}}$, is typically not negligible, and is called *Stokes shift* (Fig. 3.6 shows the difference between both absorption and PL phenomena). It can be thus concluded that the band gap of a given semiconductor can be estimated by means of optical absorp-

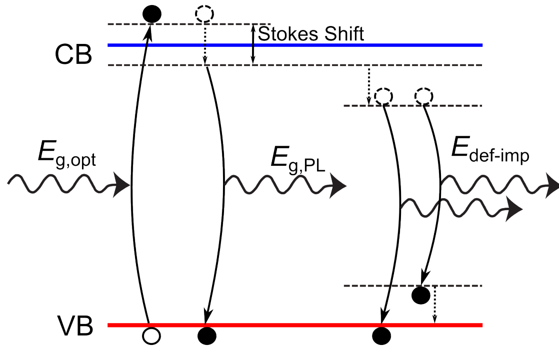

Figure 3.6: Energy band diagram where absorption and photoluminescence (band-to-band and from defects or impurity levels) processes (solid arrows) are depicted. The energy difference between absorption and (band-to-band) PL around the conduction band (CB) minimum is called Stokes Shift. Dotted arrows represent non-radiative transition processes.

tion, but we have to consider little deviations that may exist because of the nature of the technique. In fact, optical absorption is traditionally employed when considering thick enough materials, being PL also influenced by phonon lines and defects emission. In addition, absorption is a particularly useful technique for materials whose low PL signal states a drawback for emission band gap determination, which is the case of SiC.

Experimental Equipment The transmittance spectra from samples deposited on fused silica (transparent to the incoming radiation) was acquired using the integrating sphere of a *Bentham PVE300* photovoltaic spectral response system, illuminating with Xe and quartz lamps coupled to a monochromator. The transmitted light was collected using an InGaAs detector, in the range from 300 to 1700 nm. The spectra were corrected for the fused silica transmittance. Analogously, the reflectance of the samples were collected using the same integrating sphere (in a reflection configuration) and detector.

3.2.2.3. Photoluminescence Spectroscopy (PL)

When a semiconductor is excited with a photon beam, it can (in most cases) spontaneously return to its initial (i.e. lower energy) energy state via a radiative transition, which results in light emission. This phenomenon is called *photoluminescence* (PL). This process is a consequence of optical absorption, and consists of the excitation of valence band-bound electrons by incoming photons of higher energy than the semiconductor band gap (E_g). The excited electrons promote to the material conduction band while leaving a hole in the VB. In addition, if both carriers are not set free within their corresponding bands, i.e. they are bond (usually via Coulombic attractive force), we say that an electron-hole pair (*exciton*) has been formed. Typically via non-radiative processes, such as thermalization, the excited electron relaxes towards the CB minimum (the hole towards the VB maximum); afterwards, the electron-hole pair radiatively recombines, emitting a photon with the band gap energy. These are the so-called *band-to-band* transitions, and require that the exciton (i.e. both the electron and the hole) be spatially lo-

calized (the electron-hole pair must be bound together). The presence of allowed and discrete energy levels within the semiconductor band gap may also originate metastable bands that electrons can populate after non-radiative relaxation from the CB minimum and, consequently, give rise to radiative photon emission. These intra-band gap energy levels are usually introduced by *impurities* and/or *defects* within the semiconductor lattice (see Fig. 3.6). Hence, PL spectra allow obtaining a direct and accurate measurement of the semiconductor band-gap energy, as well as identifying the origin of lattice impurities and defects.

The PL signal intensity yielded by band-to-band transitions (see the example spectrum in Fig. 3.7) is proportional to the number of excited luminescent centers within the semiconductor, and its spectrum lineshape can be modelled by a Maxwell-Boltzmann-type distribution, such as:

$$I_{\mathrm{PL}}(h\nu) \propto (h\nu - E_{\mathrm{g}})^{1/2} \cdot \exp\left[-\frac{h\nu - E_{\mathrm{g}}}{K_{\mathrm{B}}T}\right] , \; h\nu > E_{\mathrm{g}} , \tag{3.12}$$

where h is the Planck's constant, ν the resulting photon frequency ($h\nu$ is therefore the resulting photon energy), E_{g} the semiconductor band gap energy, K_{B} the Boltzmann's constant and T the temperature. Eq. (3.12) has two immediate remarkable points. First, the energy corresponding to the PL-emitted photons must be larger than the material band gap (otherwise $I_{\mathrm{PL}} = 0$), and their difference implies a frequency shift in emission. Second, the dependence with temperature strongly modifies the spectrum width, the equation recovering a Dirac delta shape when $T = 0$ K. Indeed, in a real PL spectrum, band-to-band transitions are not displayed alone, but typically show a lower energy emission band, which results from the convolution of different emission peaks attributed to intra-band impurity- or defects-related energy levels ($E_{\text{def-imp}}$ in Fig. 3.6).

Although most experimental equipments allow for PL spectra acquisition as a function of the originated photon wavelength, it is usually very useful its representation as a function of energy. For this, a direct relation between both magnitudes exist:

$$E = \frac{hc}{q\lambda} \longrightarrow E[\mathrm{eV}] \approx \frac{1240}{\lambda[\mathrm{nm}]} , \tag{3.13}$$

being c the speed of light in vacuum and q the elementary charge. It is a common mistake, however, to finish the spectrum calibration with this operation, as the PL intensity as a function of λ differs when analysing its energy dependence (PL intensity is a distribution):

$$\mathrm{d}I_{\mathrm{PL}}(\lambda) = -\frac{\mathrm{d}E}{\mathrm{d}\lambda} \cdot \mathrm{d}I_{\mathrm{PL}}(E) = \frac{hc}{q\lambda^2} \cdot \mathrm{d}I_{\mathrm{PL}}(E) \approx \frac{1240}{\lambda^2} \cdot \mathrm{d}I_{\mathrm{PL}}(E) . \tag{3.14}$$

The minus sign in the second term of Eq. (3.14) accounts for the decrease in energy step when wavelength increases. The square dependence on the wavelength,

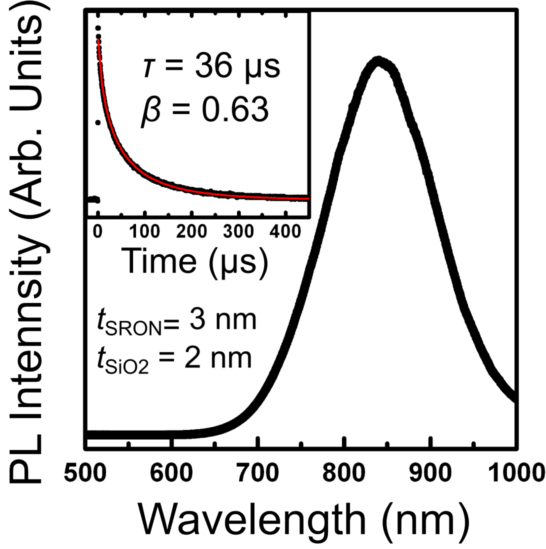

Figure 3.7: PL spectra corresponding to a sample containing Si NC superlattices in SiO_2, with t_{SRON} and t_{SiO2} of 3 and 2 nm, respectively, and a total number of bilayers of $N = 100$. The inset shows a time-resolved PL measurement, at the PL peak position, of the same sample. The solid red line corresponds to the data fit according to the stretched exponential expression in Eq. (3.16), whose τ and β parameters are written down.

resulting from the derivative of Eq. (3.13), implies emission shifts that can be relevant in the case of a detailed numerical study; therefore, it is of crucial importance to carry out the complete PL spectrum conversion.

Time-Resolved Photoluminescence (TR-PL) Photoluminescence spectra can provide information about a semiconductor's intrinsic properties (band gap energy and presence of defects) and/or its extrinsic composition (impurity doping). In addition, the time dependence of PL can be related to the physical origin of the different transitions that take place within the material. In particular, we can divide these transitions into *radiative*, when a photon is emitted, or *non-radiative*, when the exceeding energy is lost by different means, such as the creation of lattice phonons (thermalization). The lifetime of these processes are very characteristic, strongly depending on the material or the nature of the process itself, and can be expressed as:

$$\frac{1}{\tau_{\text{total}}} = \frac{1}{\tau_{\text{rad}}} + \sum_i \frac{1}{\tau_{\text{non-rad,i}}} , \tag{3.15}$$

where τ_{total} is the total measured emission lifetime, whereas τ_{rad} and $\tau_{\text{non-rad,i}}$ are the lifetimes corresponding to the radiative and the different non-radiative processes, respectively. It is necessary to remark here that, being a photon-related technique, PL is only sensitive to radiative transitions taking place within the material. However, different radiative lifetimes can be found for a given material and identical energy, which can be directly related to the level where photons are originated. As an example, most semiconductor materials present both band-to-band recombination and defects-like emission, with a much longer decay time (i.e.

lifetime) of the former. The different decay times are usually superimposed in the time-resolved PL signal, and their evaluation can be usually performed by adjusting a two-exponential function (or a single-exponential, when a given PL signal overwhelms the other emission sources). However, in the case of Si NCs embedded in SiO_2, the determination of the PL emission lifetime is strongly modulated by the NC size distribution (which also induces a broadening in the PL spectrum). For a correct fitting of the time-resolved PL signal in this case, the so-called *stretched exponential* function is employed:

$$I_{\mathrm{PL}}(t) = I_{\mathrm{PL},0} \cdot \exp\left[-\left(\frac{t}{\tau}\right)^{\beta}\right] , \qquad (3.16)$$

with $I_{\mathrm{PL},0}$ a pre-exponential factor, t the time, τ the total radiative lifetime and β the stretching parameter [an example of this kind of fits is shown in the inset in Fig. 3.7]. For an ideal case, $\beta = 1$, and we would recover a single-exponential decay. However, the presence of a broad NC size distribution decreases the β value (typically between 0.5 and 0.9), which modifies the decay. The simultaneous analysis of both parameters, τ and β, provides valuable information of the PL emission originated in NC-based systems.

Experimental Equipment For the sample excitation, a *Kimmon* He-Cd continuous-wave laser (excitation wavelength of $\lambda_{\mathrm{exc}} = 325$ nm, i.e. 3.82 eV) or a *Coherent* Ar^{+} ion one (mainly $\lambda_{\mathrm{exc}} = 488$ nm, i.e. 2.54 eV) were employed, provided the need of a higher excitation energy than the NC-based material (1.4−1.7 eV, depending on the NC size). A system of UV- or visible-designed lenses and mirrors constitute the optical path, guiding the laser beam towards the sample, placed on a sample holder with 3-dimensional positioning. Si substrate-based (instead of fused silica) samples were employed for PL characterization, due to the low (or none) emission Si yields in the visible range and to prevent interference fringes in the spectra. The laser incidence angle on the sample was established at 45°. The total optical power of both lasers on the sample was controlled to lay in the range from 20 to 30 mW.

The PL emission coming from the sample (placed perpendicular to the acquisition system) was collected by a system of two lenses (to collimate the beam and afterwards focalize it on the monochromator entrance). The resulting focalized emission was collected in an *Oriel Cornerstone* monochromator, and the spectrally resolved photons were detected by a *Hamamatsu R928* GaAs photomultiplier tube (PMT). The collected signal was amplified and noise-filtered by a conventional lock-in system and a multimeter. All acquired spectra were corrected by the system response.

In the case of time-resolved PL, the third harmonic frequency of a *Brilliant* Nd^{3+}:YAG 5-ns-pulsed laser was employed as excitation source ($\lambda_{\mathrm{exc}} = 355$ nm,

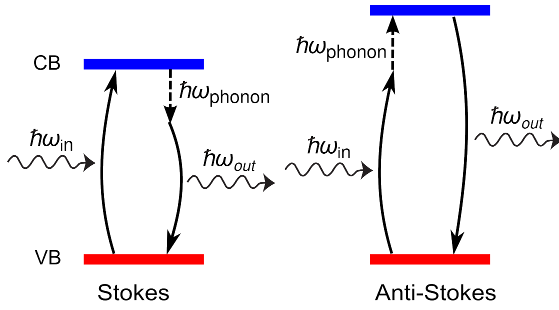

Figure 3.8: Schemes corresponding to the Stokes and anti-Stokes processes that accomplish the energy and momentum conservation in Eq. (3.17).

i.e. 3.49 eV), and the electronic signal from the PMT was monitored by means of an *Agilent Infiniium DSO 8064A* oscilloscope.

3.2.2.4. Raman Scattering Spectroscopy

As described in Section 3.2.2.1, the interaction between photons and matter gives rise to numerous processes in which energy and momentum are conserved. Usually, the incidence of a photon on semiconductor materials induces electron transitions between the bands of continuum states, separated by the band gap, which is called *optical absorption* (see Section 3.2.2.2). Also, the electrons present in the high energy band of states can relax through a recombination process, thus originating a photon; this is, in general terms, known as *luminescence* (see Section 3.2.2.3). However, more complex effects may take place in solids. In particular, when an incoming photon is inelastically scattered by the material lattice, the energy of the resulting photon will be lower or higher than the incident one, because of the creation or annihilation, respectively, of one or more lattice *phonons* (understood as the collective oscillation of the lattice) [166]. This process is called *Raman effect* and, for the first order case (i.e. only one involved phonon), satisfies the energy ($\hbar\omega$) and momentum ($\hbar\vec{k}$) conservation:

$$\begin{aligned} \hbar\omega_{\text{in}} &= \hbar\omega_{\text{out}} \pm \hbar\omega_{\text{phonon}} \\ \hbar\vec{k}_{\text{in}} &= \hbar\vec{k}_{\text{out}} \pm \hbar\vec{k}_{\text{phonon}} \end{aligned} \quad , \tag{3.17}$$

where $\hbar$ is the reduced Planck's constant, ω the angular frequency, $\vec{k}$ the wavevector, and the subscripts "in", "out" and "phonon" state for the input photon, the output photon and the involved phonon, respectively. The particular process when a phonon is created is called *Stokes*, corresponding to "+" sign in Eq. (3.17) ($\hbar\omega_{\text{in}} > \hbar\omega_{\text{out}}$), whereas the opposite process, i.e. when a lattice phonon is absorbed, is named *anti-Stokes*, and corresponds to the "-" sign in Eq. (3.17) ($\hbar\omega_{\text{in}} < \hbar\omega_{\text{out}}$). A scheme of both processes is drawn in Fig. 3.8. The term *Raman shift* is defined as the energy difference between the incident photon and the resulting (scattered) one, being thus equivalent to the phonon energy. Raman scattering spectroscopy is therefore sensitive to the lattice vibrations, whose frequency

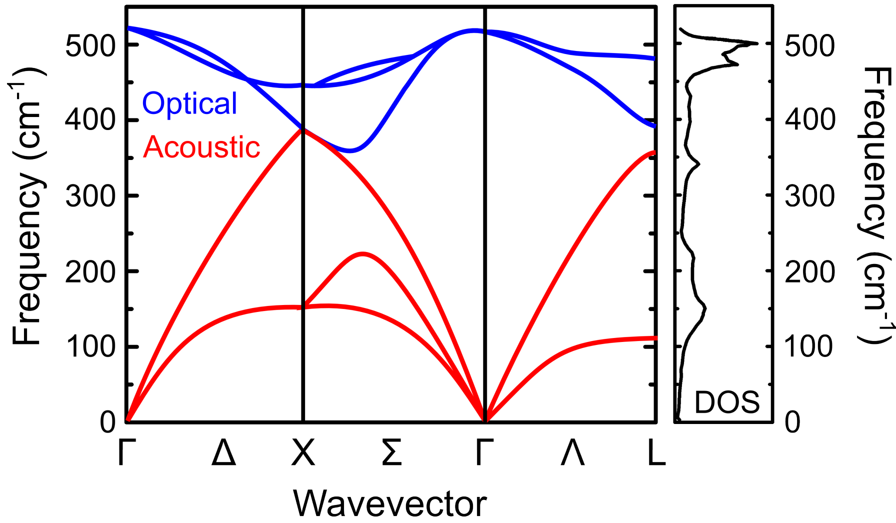

Figure 3.9.: Phonon dispersion curves (frequency as a function of the wavevector) for the case of Si. Acoustic and optical phonon curves are drawn in red and blue, respectively. The right panel displays the normalized density of states (DOS) corresponding to the curves in the left panel. Figure adapted from Ref. [167].

is strongly dependent on the material lattice structure. Moreover, the intensity of the Raman peaks depends on the polarization of the incident and scattered beams, with respect to the sample orientation. In the case of Si NCs embedded in a given matrix, although they may present a well defined lattice structure, their random orientation induces a global signal resulting from these different orientations, and thus the state of polarization of the incident and scattered beams leaves the Raman signal intensity unchanged.

Regarding the origin of the Raman signal, it is closely related to the phonon density of states (DOS) at each phonon frequency. Then, keeping in mind the *phonon dispersion curves* of a given material system, i.e. the lattice phonon energy/frequency as a function of the wavevector $[\omega(\vec{k})]$, it is fundamental to quantify the existing vibration modes, to which Raman scattering spectroscopy is sensitive. Fig. 3.9 shows the phonon dispersion curves and corresponding density of states for the case of Si. A basic division between the phonon modes can be done according to their associated energy: *acoustic* (A) and *optical* (O) modes for low- and high-energy bands, respectively (at $k = 0$, acoustic modes have 0 energy, whereas optical modes present a non-negligible energy). In addition, the modes can be classified as *longitudinal* (L) or *transversal* (T), depending on the vibration propagation and wavevector directions.

Let us come back to the case of Si NCs, whose Raman spectrum can be observed in Fig. 3.10 in comparison to the amorphous fused silica (SiO_2) and crystalline bulk Si. The Raman analysis of this material is not straightforward, as NCs present

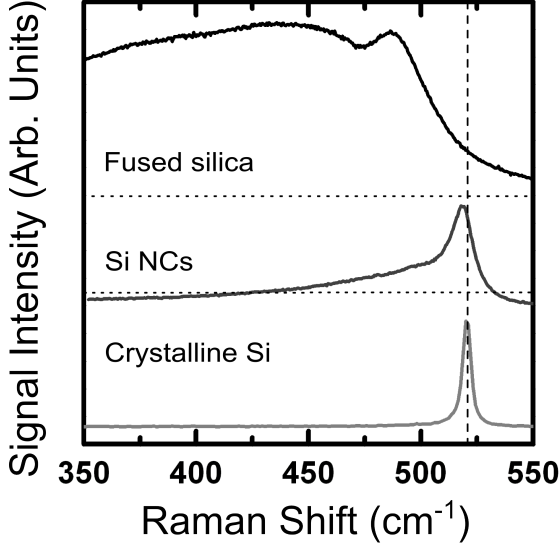

Figure 3.10: Raman spectra from samples containing fused silica, Si NC superlattices and bulk crystalline Si, to show the amorphous-to-crystalline evolution, respectively, of the Raman lineshape. The spectra have been normalized for the sake of comparison. A vertical dashed line has been drawn to indicate the bulk Si Raman shift (521 cm^{-1}).

a crystalline-Si core surrounded by an amorphous-Si shell [20, 78]. This has an important consequence: the crystalline vibration mode (typically attributed to the LO-TO optical mode [20]) is partially masked by different amorphous modes. Actually, the amorphous modes are related to the DOS that can be directly obtained from the phonon dispersion curves (see Fig. 3.9). Another problem exists regarding the crystalline Si contribution, whose signal peak is strongly modified by the NC size [*phonon confinement* occurs; see Chapter 2 (*Fundamentals of Silicon Nanocrystals*) for more details on this issue], the pressure (P) exerted on the nanostructures (either by the matrix or externally applied), and their size dispersion (σ_{d}). With all these considerations, the crystalline Raman signal coming from NCs (I_{c}) can be modelled as [92]:

$$I_{\mathrm{c}} \propto \int_0^{\infty} \left[\int_0^1 \frac{e^{-\frac{(2\pi|\vec{k}|d/a)^2}{2\alpha^2}}}{[\omega - \omega(\vec{k})]^2 - \Gamma^2} |\vec{k}|^2 \mathrm{d}\vec{k} \right] \mathrm{F}(d, \sigma_{\mathrm{d}}) \mathrm{d}d \ , \tag{3.18}$$

being ω the phonon frequency (i.e. the *Raman shift*), a the lattice parameter, Γ the phonon damping parameter, and α a parameter that takes into account the penetration of the confined-phonons wavefunction decay into the surrounding matrix (typically, $\alpha = 3$) [20]. The inner integral defined in Eq. (3.18) is performed over all wavevectors within the first Brillouin zone, whereas the outer integral, being $\mathrm{F}(d, \sigma_{\mathrm{d}})$ a weigh function containing the NC size distribution, takes into account all possible NC diameters. The dispersion curve $\omega(\vec{k})$ is obtained from the Brout sum rule, considering the anisotropic nature of optical phonons in bulk Si and a matrix stress dependence such as [89]:

$$\omega(\vec{k}, P) = \sqrt{[w_0(P)]^2 - \frac{A \cdot |\vec{k}|^2}{|\vec{k}| + 0.53}} , \qquad (3.19)$$

where $A = 1.261 \times 10^5$ cm^{-2} and $w_0(P)$ [cm^{-1}] = 521 + (4.9 cm^{-1} · GPa^{-1}) $\cdot P$ [GPa] [168]. Regarding the mathematical behavior of I_c as a function of its parameters, the phonon confinement (related to the NC mean size) and the matrix stress are phenomena that compete by reducing and increasing, respectively, the Raman shift with respect to bulk Si, whereas the broadening and the lineshape depend on both the mean NC size and the size dispersion (phonon confinement must also be taken into account in broadening). The analysis of this peak can therefore provide information about P and the crystalline size distribution ($d \pm \sigma_d$). Nevertheless, this analysis alone cannot give information about the full nanoclusters size, i.e. taking into account also the amorphous shell. Indeed, it is easy to distinguish the crystalline-Si peak from the amorphous bands, which present a broader and quasi-Gaussian shape (see Fig. 3.10). Then, one can estimate the crystalline fraction (f_c) of the system by considering that the areas of each phase (amorphous and crystalline, A_a and A_c, respectively) are proportional to their volume, following the relation:

$$\frac{V_c}{V_{NC}} \approx f_c = \frac{A_c}{A_c + \gamma A_a} , \qquad (3.20)$$

where (V_c) and (V_{NC}) are the crystalline core and overall NC volumes, respectively, and γ is defined as the ratio between the scattering cross-section presented by amorphous Si and crystalline Si (~ 0.9) [20]. In conclusion, both the fact that it is possible to estimate the total NC size independently of their direct observation (by TEM), as well as the non-destructive nature of the technique, make Raman scattering a very interesting technique to determine the structural characteristics of Si NC superlattices.

Cross-Section Configuration Because of the strong Raman signal that bulk crystalline Si exhibits, a Si-based material such as Si NC SLs cannot be studied on a Si substrate (the bulk signal would mask the low NCs contribution). Instead, the fused silica substrate was selected as the best candidate for this kind of study, presenting amorphous modes at slightly lower frequencies than crystalline-Si. This latter fact is also annoying when estimating the crystalline-to-amorphous ratio within Si NC superlattices. Nevertheless, the fused silica substrate contribution could be minimized when laterally placing the sample under study, in a *cross-section* laser incidence configuration as shown in Fig. 3.11(a).

It can be numerically shown the vast Raman signal improvement, apart from the strong SiO_2 signal reduction, when a cross-section configuration is employed. Let us consider the normal laser incidence on a given SL deposited on fused silica

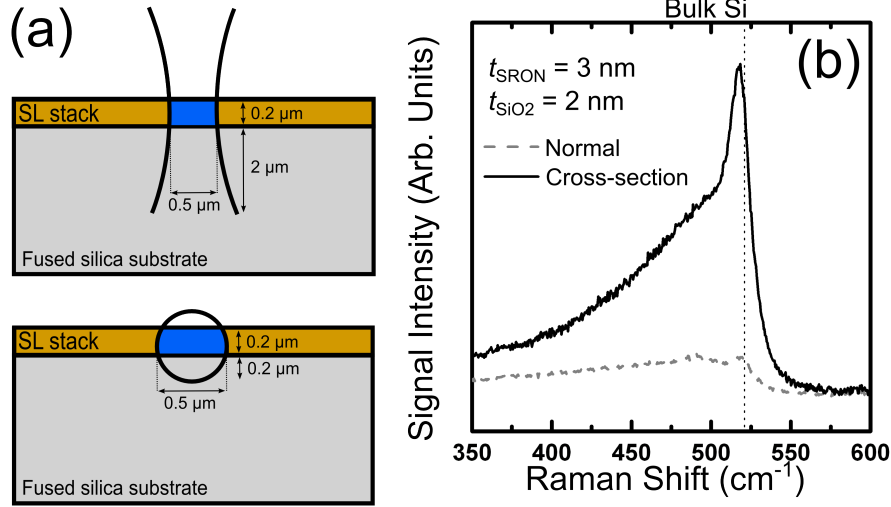

Figure 3.11.: (a) Cross-section schemes corresponding to a typical SL-based sample on fused silica substrate. The top sketch indicates the normal laser incidence and the SL scattered region (in blue), whereas the down figure shows the cross-section laser incidence configuration. (b) Raman spectra corresponding to a sample containing 30 SLs with $t_{\mathrm{SRON}} = 3$ nm and $t_{\mathrm{SiO2}} = 2$ nm, under the different laser incidence configurations shown in (a).

substrate. Let us suppose a cylinder-shaped laser beam with a waist diameter $\phi_{\mathrm{waist}} \sim 0.5$ μm. The laser penetration depth is total in the thin SL stack (l_{SL} 0.2 μm for a usual sample), and around $l_{\mathrm{sub}} \sim 2$ μm into the fused silica substrate (for a visible laser wavelength such as 532 nm). In the cross-section incidence case, the laser beam waist may be controlled to focus on equal areas of the sample, being represented by a rectangular prism of length ϕ_{waist}, thickness $l_{\mathrm{SL}} \approx l_{\mathrm{sub}} = 0.2$ μm, and a penetration depth d similar in both materials (the SL stack and the substrate). With these geometrical considerations, one can estimate the ratio between the substrate and SL-stack scattered volumes, respectively V_{sub} and V_{SL}, as:

$$\begin{aligned} \left|\frac{V_{\mathrm{sub}}}{V_{\mathrm{SL}}}\right|_{\mathrm{normal}} &= \frac{l_{\mathrm{sub}}\pi\left(\frac{\phi_{\mathrm{waist}}}{2}\right)^2}{l_{\mathrm{SL}}\pi\left(\frac{\phi_{\mathrm{waist}}}{2}\right)^2} = \frac{l_{\mathrm{sub}}}{l_{\mathrm{SL}}} \approx \frac{2\mu\mathrm{m}}{0.2\mu\mathrm{m}} \approx 10 \\ \left|\frac{V_{\mathrm{sub}}}{V_{\mathrm{SL}}}\right|_{\mathrm{cross\text{-}section}} &= \frac{l_{\mathrm{sub}}d\phi_{\mathrm{waist}}}{l_{\mathrm{SL}}d\phi_{\mathrm{waist}}} \approx 1 \end{aligned} \quad . \tag{3.21}$$

It is immediate to see that the cross-section configuration strongly reduces the substrate scattered volume with respect to the SL one, which notably favors NC-based Raman scattering signal [a comparison between the Raman spectra obtained from a given SL-based sample by means of both configurations is displayed in Fig. 3.11(b)]. Besides, thicker prepared samples (with a larger number of superlattices) can even decrease the substrate contribution while increasing the scattering volume

of NCs by a factor of 10. It has to be mentioned, however, that the Raman contribution of SiO_2 (when this is the embedding matrix) will always be present within the spectrum analysis, even when the substrate signal is totally avoided.

Experimental Equipment Raman scattering measurements were performed by exciting the samples with the 325-nm (i.e. 3.82 eV) line of a *Kimmon* He-Cd laser or the 532-nm (i.e. 2.33 eV) line (second harmonic) of a Nd:YAG laser, for SiC- and SiO_2-based samples, respectively (attending to the different optical absorption the materials present). The resulting scattering signal, acquired in a backscattering configuration by a 40× NUV or a 100× visible objectives (depending on the excitation wavelength), was collected by means of a *Horiba Jobin-Yvon LabRam* spectrometer, coupled to a high-sensitive charge-coupled device (CCD). A 2400-mm^{-1} diffraction grating was employed for UV-excitation based Raman spectra, whereas a 1800-mm^{-1} one was used for visible excitation, obtaining a maximum spectral resolution of 0.5 cm^{-1}.

In the particular case of Raman measurements under high hydrostatic pressure, the 532-nm line of the Nd:YAG laser was employed, using a 50× long-working distance objective and loading the sample (mechanically polished down to ∼20 μm) into a gasketed membrane-type diamond anvil cell, and collecting the spectra with the *Horiba Jobin-Yvon LabRam* spectrometer via a 1800-mm^{-1} diffraction grating. A 16:3:1 mixture of methanol-ethanol-water was used as pressure transmitting medium. The same conditions were employed for photoluminescence measurements under pressure, although a 300-mm^{-1} diffraction grating was then used.

Si NC-based samples to be investigated by Raman had to be grown on fused silica, to minimize the contribution from the substrate (the bulk crystalline Si Raman frequency is 521 cm^{-1}). In addition, the already mentioned cross-section configuration was employed for thick SL stacks (hundreds of nm), in order to minimize the fused silica substrate Raman signal contribution to the amorphous spectra of NCs. Samples were accurately side-polished for these special configuration measurements.

3.2.3. Electrical and Electro-Optical Characterization Techniques

3.2.3.1. Intensity-Voltage Characteristics [$I(V)$]

To study the electrical properties of any material system, it must be embedded within a device structure that allows for charge injection into and extraction from the material. Typical vertical test devices consist of a metal-insulator-semiconductor (MIS)-like structure, where *metal* stands for the top electric contact, *insulator* is the material under study (in our case, Si NC superlattices exhibit a strong insulating behavior) and the *semiconductor* represents the substrate of known properties (typically Si), above which the insulating material is deposited.

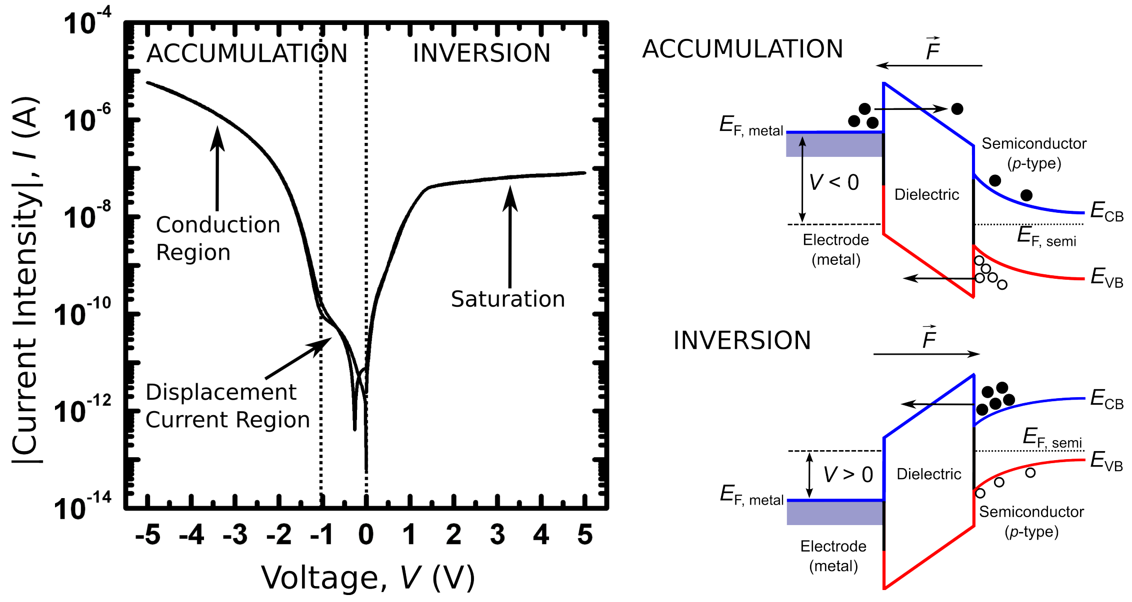

Figure 3.12.: Intensity versus voltage characteristic, under negative and positive applied bias, of a ZnO-based MIS-like device. The employed electrode, insulator and substrate semiconductor are, respectively, indium tin oxide (ITO), 50-nm-thick ZnO and p-type Si. The different regimes are marked by arrows. The band diagrams schemed in the right correspond to the accumulation and inversion regimes for such a MIS device.

It is important the selection of the proper doping design, for the electrical properties will strongly depend on them. In particular, MIS structures typically present a n-i-p structure, where the top metallic contact is n-type, the insulator under study is the intrinsic material and a p-type material (usually B-doped silicon) is used as substrate. When applying a voltage sweep to such an structure, two different behaviors may occur, as observed in the current intensity versus voltage [$I(V)$] characteristic curve and its corresponding band diagrams displayed in Fig. 3.12. First, when a negative voltage ($V < 0$) is applied on top of the metal contact, an electric field is created from the substrate towards the metal. Consequently, electron injection occurs from the metal to the insulator, which tends to accumulate holes (majority carriers within the substrate) at the substrate-insulator interface; this is called the *accumulation regime*, and it implies a fluent current circulation. On the contrary, when a positive voltage ($V > 0$) is applied on top of the metal contact, the inverse electric field is created, and electrons in the substrate (where they are minority carriers) tend to accumulate at the substrate-insulator interface; this is called the *inversion regime*, and leads to a poor conduction [resulting in a current saturation in the $I(V)$ curve].

The typical MIS $I(V)$ curve under accumulation regime displays two different behavior regions; whereas at low voltages a constant current is usually found,

at medium-high voltages intensity presents a particular trend with voltage. The intensity observed in the first stage of the curve is known as *displacement current*, I_{d}, the charging transient current of the capacitor (and therefore not associated to charge movement). From this displacement current, the capacitance of the MIS capacitor can be determined by:

$$C = I_{\mathrm{d}} \left(\frac{\mathrm{d}V}{\mathrm{d}t} \right)^{-1} = \epsilon_0 \epsilon_{\mathrm{r}} \frac{A}{d} \ , \tag{3.22}$$

being $\mathrm{d}V/\mathrm{d}t$ the time variation of the applied voltage (i.e. the measurement voltage step); therefore, the capacitance of the whole system is dependent on the measurement conditions. In addition, C gives information about the geometry and composition of the capacitor as expressed in the second equality of Eq. (3.22), where ϵ_0 and ϵ_{r} are, respectively, the dielectric permittivity of vacuum and the relative permittivity of the dielectric layer, A is the device area and d the dielectric layer thickness.

To study the intrinsic transport properties of the material, the medium-high voltage regime (in accumulation) has to be addressed [a more detailed description of the different involved transport mechanisms in Si NC-based systems was given in Chapter 2 (*Fundamentals of Silicon Nanocrystals*)]. Indeed, the $I(V)$ plots represent the macroscopic electrical behavior of the system; nevertheless, it is more relevant to determine the intrinsic properties of the material, which can be achieved by normalizing the previous magnitudes by the geometrical factors of the device under study, namely, A and d. This way, the *current density* (J) and *electric field* (F) are defined as:

$$\begin{aligned} J &\equiv \frac{I}{A} \\ F &= \frac{V}{d} \end{aligned} \ , \tag{3.23}$$

where the second expression is only applicable as long as the electric field is considered homogeneous along and across the layers. These two expressions allow evaluating the system *conductivity* (σ) at a given point, and consequently the *resistivity* (ρ), which are the intrinsic properties of the material:

$$\begin{aligned} \sigma &= \frac{J}{F} = \frac{d}{A} \left(\frac{\mathrm{d}I}{\mathrm{d}V} \right) = \frac{d}{A} \cdot \frac{1}{R} \\ \rho &= \frac{1}{\sigma} = \frac{A}{d} \cdot R \end{aligned} \ , \tag{3.24}$$

where R is the macroscopic resistance of the device at a given point. It is important to note that the definition by means of a derivative is required to take into account non-linear behaviors, such as diode-like ones, where the resistance (in its

basic definition) varies at each applied voltage. Indeed, the basic definition of the conductivity, i.e. the first equality in Eq. (3.24), is the *generalized Ohm's law*.

The electrical characteristics of a given material system can also be monitored as a function of temperature, T. Usually, the conduction mechanism of a system (especially in semiconductor materials) is strongly dependent on this variable. In particular, if the transport mechanism only takes place after a given temperature (i.e. thermal energy) is applied, we say that this mechanism is *thermally activated*. When plotting the system conductivity as a function of the inverse of temperature, called *Arrhenius plot*, we expect for thermally-activated systems to present an exponential behavior with temperature, following the expression:

$$\sigma(T) = \sigma_0 \exp\left[-\frac{E_\mathrm{A}}{k_\mathrm{B}T}\right], \tag{3.25}$$

being σ_0 a pre-exponential factor (interpreted as the system conductivity at an infinite temperature), k_B the Boltzmann's constant and E_A the *activation energy* for conduction to take place, which will depend on the transport mechanism and the intrinsic properties of the material.

The basic parameters that can be obtained from the basic electrical characterization have been described here. As was discussed in Chapter 2 (*Fundamentals of Silicon Nanocrystals*), the different transport mechanisms present an electric field- and temperature-dependent conductivity that induces a notorious modification of the generalized Ohm's law as expressed in Eq. (3.24). For this reason, from an experimental point of view, it is usually useful to employ, for instance, the so-called Poole-Frenkel or Fowler-Nordheim tunneling representations, i.e. $I \cdot V^{-1}$ vs. $V^{1/2}$ and $I \cdot V^{-2}$ vs. V^{-1}, respectively, whose fits give material parameters such as the dielectric relative permittivity or the metal-dielectric barrier height [see Chapter 2 (*Fundamentals of Silicon Nanocrystals*) for more details on those transport mechanisms]. In addition, the electro-optical characterization may complement the information provided by the electrical measurements.

Experimental Equipment The current versus voltage sweeps were carried out in dark conditions, using a high-resolution ($\sim$ 10 fA) *Agilent B1500* semiconductor device analyzer, placing the devices in a *Cascade Microtech Summit 11000* probe station equipped with a Faraday cage for electrical insulation. The probe station contains a vacuum chuck with a thermal controller, in order to perform temperature-dependent measurements (in the range from room temperature to T = 300 °C).

3.2.3.2. Electroluminescence Spectroscopy (EL)

The emission properties of semiconductor devices that can be derived from electroluminescence (EL) are analogous to what we have already commented in the case

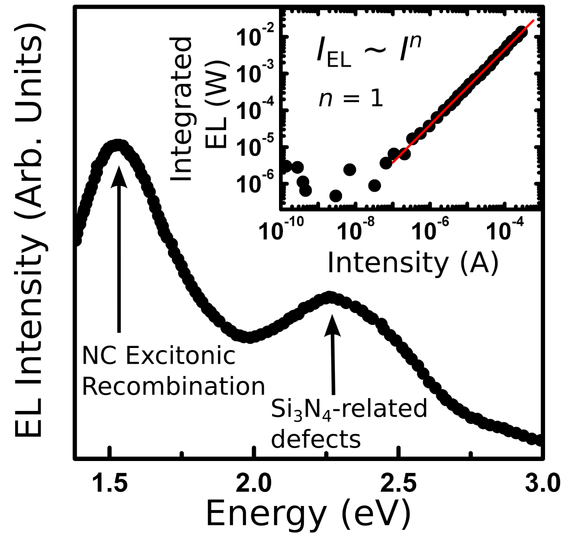

Figure 3.13: Electroluminescence spectrum corresponding to a device containing a Si-rich oxide/Si-rich nitride stack. The lowest energy peak is attributed to Si NCs within the SRO matrix, whereas the highest energy contribution is ascribed to Si_3N_4 matrix-related defects. The inset shows an integrated EL intensity versus current intensity curve corresponding to the same device, the fit exhibiting a power relation such as the one described in Eq. (3.26), with n = 1. Courtesy of Y. Berencén [38].

of PL. Here, the crucial difference is the excitation mechanism, electron- (instead of photon-) related, which has many implications. The first and most important is the excitation source medium: whereas photons can propagate through vacuum, carriers (electrons and holes) require a conductive enough medium. Typically, semiconductors can provide this property, depending on the electrical conductivity they present. However, the EL excitation will also depend on the device design, especially what refers to the contact material deposition, for the whole device band structure should present the optimum *band offsets* (i.e. the energy difference between the metal contact Fermi level and the conduction CB and VB, respectively for electron and hole injection).

As was described in detail in Chapter 2 (*Fundamentals of Silicon Nanocrystals*), different kinds of electrical excitation exist depending on the material nature and device band structure: (i) electron and hole simultaneous injection through opposite contacts, (ii) VB electron excitation by conduction electron impact or (iii) VB electron ionization by conduction electron impact. Whereas process (i) immediately induces the electron-hole recombination and consequent photon emission, the other two processes imply an energy transfer from the carrier (which must have a high kinetic energy) to a VB-bound electron. In (ii) the latter will recombine with the generated hole, whereas the ionization in (iii) involves a third electron (in the CB) that will recombine with the generated hole. All three processes result in photon generation (electroluminescence), mainly with the band gap energy (unless allowed electronic levels are found within the band gap, analogously to PL).

A spectral analysis of EL may then give details about the material composition (defects, doping...). In addition, the EL spectra can show additional information not displayed by PL, such as the nature of some defects only being optically active under electrical excitation [19], which is mainly ascribed to the different cross-

section the VB-bound electrons present to photons or electrons (an example of both types of emission origin is show in Fig. 3.13). Hence, a complete material characterization should include both types of luminescence techniques.

It is also of much interest to study the dependence of the integrated EL intensity I_{EL} (i.e. all the output EL emitted by the device) as a function of the injected electrical current I, which can determine the suitability of any given material to be employed as active material in an efficient *light-emitting device* (LED). In particular, the following relation is usually accomplished:

$$I_{\mathrm{EL}} \propto I^n \; . \tag{3.26}$$

Here, n is an exponent that evaluates the linearity of the relation, tightly related to the photon generation per injected carrier. In the ideal case when $n = 1$, a direct proportionality exists between generated EL emission and injected current at any injection level. In the case when $n < 1$ (sublinear relation), linearity is lost mainly because non-radiative recombination processes are favored at high injection, which limits or saturates luminescence mechanisms at this regime. Finally, the opposite case, $n > 1$ (superlinear relation), corresponds to an enhancement of EL emission at high injection, which might be related to stimulated intensity or favoring the activation of additional EL mechanisms. This discussion on the EL emission as a result from the injected current naturally brings to the device *power efficiency* definition:

$$\eta_{\mathrm{PE}}[\%] = \frac{P_{\mathrm{out,opt}}}{P_{\mathrm{in,el}}} = \frac{P_{\mathrm{EL}}}{I \cdot V} \times 100 \; , \tag{3.27}$$

where $P_{\mathrm{out,opt}}$ and $P_{\mathrm{in,el}}$ are, respectively, the optical output power (i.e. the EL power, P_{EL}) and the input electrical power ($I \cdot V$). The PE value obtained by this expression will give us an idea of the LED overall electrical-to-optical conversion efficiency. In addition, a complementary efficiency definition can be implemented, in terms of the electron conversion to single-wavelength photons. This is called the *external quantum efficiency* (EQE), which is calculated simply by normalizing the power efficiency to the emitted wavelength (λ) under study:

$$\mathrm{EQE}[\%] = \frac{qV\lambda}{hc}\eta_{\mathrm{PE}} \; , \tag{3.28}$$

being q the elementary charge, V the applied voltage, h the Planck's constant and c the speed of light in vacuum. Therefore, EQE will give us information about how many photons of a given energy (e.g. at the maximum peak emission) are created per injected electron.

Time-Resolved Electroluminescence (TR-EL) Analogously to what has been discussed in Section 3.2.2.3, the time-resolved luminescence yielded by LEDs can give us information about the composition of the active layer, for different materials,

phases, defects, etc., present a different and characteristic radiative decay time. This, in turn, can be evaluated from:

$$I_{\mathrm{EL}}(t) = I_{\mathrm{EL},0} \cdot \exp\left[-\left(\frac{t}{\tau}\right)^{\beta}\right] . \tag{3.29}$$

This expression is analogous to Eq. (3.16), with the only difference that we are now dealing with EL emission intensity, I_{EL}. For further references about this technique, the reader is directed to Section 3.2.2.3 and to Chapter 2 (*Fundamentals of Silicon Nanocrystals*).

Experimental Equipment The electrical excitation of the devices was carried out using an *Agilent B1500* semiconductor device analyzer, using the probe system described in Section 3.2.3.1. The light emitted by the devices was collected with a *Seiwa 888 L* microscope, using a near-infrared 20× long working distance objective (with a numerical aperture of NA = 0.4) to also consider the non-visible (NIR) photons that are released. In the case of integrated intensity, a *Hamamatsu R928* GaAs PMT allowed directly collecting the whole-range emission, being the output signal monitored as a function of the applied voltage or intensity with a *HP* multimeter. For the EL spectra acquisition, a constant current intensity was applied, and the emitted light was focalized on a 1/4 m *Oriel* monochromator, coupled to a *Princeton Instruments* LN-cooled CCD.

Time-resolved EL measurements were performed using the pulse generator module of the described *Agilent B1500* instrument, collecting the integrated EL from the device by the PMT and monitoring the resulting signal by an *Agilent Infiniium DSO 8064A* oscilloscope. A 100-kΩ resistor was employed to provide high time resolution.

3.2.4. Photovoltaic Characterization Techniques

3.2.4.1. Intensity-Voltage Photovoltaic Performance [$I(V)$-PV]

The dark electrical characterization of photovoltaic materials is performed in the same way than in LED structures. The difference arises when an experiment under illumination is carried out, required to understand the optical-to-electrical conversion within the active layers of our solar cell devices. When a photon is absorbed within the active layer (usually a semiconductor) of a solar cell, an electron-hole pair is created. It is the objective of the cell design to generate an intrinsic electric field able to extract the photogenerated carriers towards the contacts, and thus to the external circuit. This photocarrier generation and consequent extraction process under no applied external field is called *photovoltaic effect* [169].

At this point, it is convenient to state that, only when a current variation is observed under no external field, we will define it as a photovoltaic process (i.e.

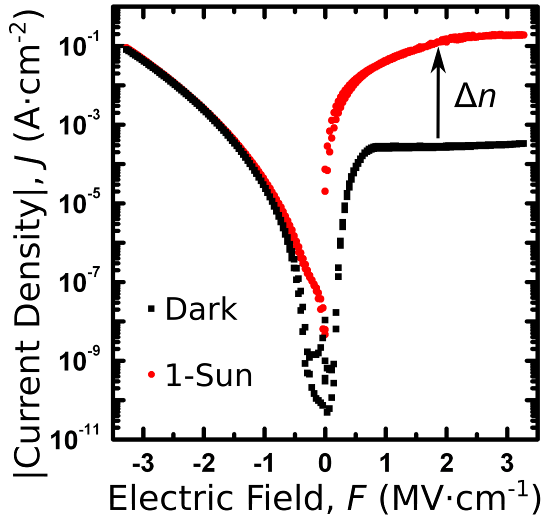

Figure 3.14: Absolute current density versus electric field characteristic of a Si NC-based MIS-like device, in dark (black squares) and under 1-Sun illumination (red circles). The employed electrode, insulator and substrate semiconductor are, respectively, ITO, 5× Si NC/SiO_2 SLs (t_{SRON} = 3.5 nm, t_{SiO2} = 1 nm) and *p*-type Si.

at $V = 0$), named *photocurrent*. On the contrary, the term *photoconductivity* is employed when a variation in current is observed after a given voltage is applied, due to a modification in the carrier concentration, n, by Δn. Fig. 3.14 displays the $J(E)$ characteristic for a Si NC-based MIS-like device, in dark and under 1-Sun illumination, where the mentioned current modification is shown under inversion regime (where $\Delta n \gg n$, i.e. transport is mainly due to minority carriers). On the contrary, the variation is not significant under accumulation, where $\Delta n \sim n$.

Solar cells are designed to work under Sun illumination; the Sun irradiance parameters are then obviously crucial. In particular, the solar irradiance spectrum strongly varies depending on the region on the Earth surface (and also outside it) they are placed to operate. The two most employed spectrum approaches are: (i) AM0, equivalent to the irradiance measured outside the Earth's atmosphere (mainly used in man-made satellites or aero-spacial stuff), and (ii) AM1.5, the solar spectrum measured at sea level (0 m altitude, where the atmospheric gases have absorbed most of UV and larger energy radiation and some IR lines), also taking into account the solar incidence angle contribution on a geographic settlement at a 45° latitude [both solar spectra are displayed in Fig. 3.15(a)]. Just to be mentioned here, AM accounts for *air mass*, a quantification of the amount of gas through which solar radiation must be transmitted (depending on the incidence angle and the altitude within the atmosphere). Whereas the AM0 irradiance power per unit surface is $f = 1361$ W·m^{-2} on top of the atmosphere, known as the *solar constant* [170], this value is rapidly decreased to $\sim$ 1000 W·m^{-2} for the AM1.5 spectrum. Finally, because of the importance of both the spectral irradiance distribution and its total power, it is required for solar simulator equipments to equal both characteristics for a reliable cell performance output.

Graphically, a typical solar cell $I(V)$ characteristic consists of a diode-like curve with a slightly higher slope, due to extra carrier generation, and shifted to $I < 0$

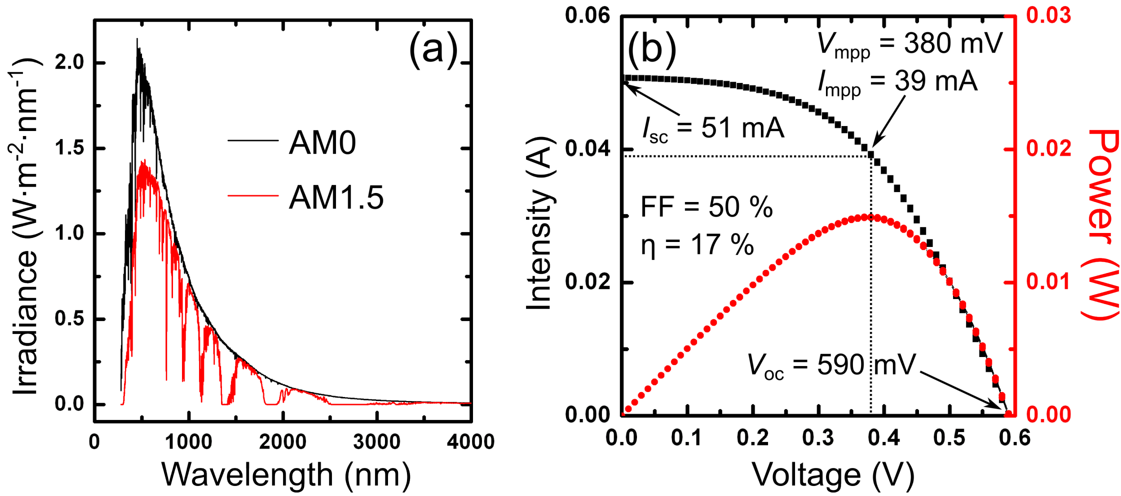

Figure 3.15.: (a) Solar irradiance spectra outside the Earth's atmosphere (AM0) and at sea level (AM1.5). (b) Typical $I(V)$ and $P(V)$ characteristics for a reference crystalline Si solar cell. The solar cell parameters that can be derived from the curves analysis are written down.

when $V = 0$; this intensity is, as previously discussed, the generated photocurrent, also called *short-circuit current* (I_{sc}). This is one of the most important parameters that can be extracted from a solar cell characteristic. Another important cell parameter is the *open-circuit voltage*, V_{oc}, defined as the voltage when $I = 0$, i.e. when there is no intensity circulation through the device. Indeed, V_{oc} is tightly related to the absorber material band gap, although it is also modulated by temperature and the energy band structure (i.e. the design) of the whole device. Plotting the electrical power ($P = I \cdot V$) in the voltage range from 0 V to V_{oc}, a maximum value is found, named the *maximum power point* (MPP). The ratio between the power at the MPP, P_{MPP}, and the ideal cell power (i.e. the product $I_{\mathrm{sc}} \cdot V_{\mathrm{oc}}$) is called the fill factor, FF, and gives an idea of the cell design quality (it graphically measures the sharpness of the curve):

$$\mathrm{FF}[\%] = \frac{P_{\mathrm{MPP}}}{I_{\mathrm{sc}}V_{\mathrm{oc}}} = \frac{I_{\mathrm{MPP}}V_{\mathrm{MPP}}}{I_{\mathrm{sc}}V_{\mathrm{oc}}} \times 100 \; . \tag{3.30}$$

Here, I_{MPP} and V_{MPP} are the intensity and voltage, respectively, at the MPP. The most important parameter a solar cell presents, however, is the solar-to-electrical energy conversion efficiency, which can be calculated as:

$$\eta[\%] = \frac{P_{\mathrm{out,el}}}{P_{\mathrm{in,opt}}} = \frac{P_{\mathrm{MPP}}}{P_{\mathrm{in,opt}}} = \frac{I_{\mathrm{sc}}V_{\mathrm{oc}}\mathrm{FF}}{P_{\mathrm{in,opt}}} \times 100 \; . \tag{3.31}$$

Indeed, η represents the overall cell performance quality, and is a parameter by which the cell operation and commercial availability are directly tested. All de-

scribed parameters can be obtained from an $I(V)$ characteristic such as the one shown in Fig. 3.15(b).

Light-Beam Induced Current (LBIC) Spectroscopy From an engineering point of view, the study of the cell surface is crucial to verify the quality of conversion through the whole exposed area. In fact, fabrication process irregularities may end up in a non-homogeneous absorption of the solar photons within the active material, or leakage currents may be generated that difficult the photogenerated carriers extraction towards the contacts. Light-beam induced current (LBIC) spectroscopy is a technique that allows for scanning the photovoltaic conversion of a given cell surface. It basically consists of white-light illumination on small spatial areas, the generated photocurrent being monitored and displayed in a map, where leakage currents originated by structural imperfections (not observed under conventional optical microscopy) may occur.

Experimental Equipment The dark electrical characterization was performed using a 4-point wiring configuration and a *Keithley* source meter. For the measurements under illumination, the same system was employed, coupled to an *Oriel* solar simulator equipped with a Xe lamp as light source, which simulated an AM1.5 solar spectrum. An irradiance of $\sim$ 1000 W$\cdot$m^{-2} was employed, calibrated with a reference c-Si solar cell. All photovoltaic measurements were performed at room temperature.

To perform LBIC maps on the devices surface, a white light source was employed through an optical fiber, mounted on a *Delta Elektronika* platform to spatially scan the 2 in-plane dimensions (x and y), with a resolution of 100 μm. The generated photocurrent signal was collected by means of a *Keithley* multimeter using a 2-probe system.

3.2.4.2. Spectral Response (SR) Spectroscopy

Apart from the overall cell performance, it is of high interest, from the active material point of view, to determine the spectral conversion efficiency. For this, the external quantum efficiency is defined for solar cells in an opposite way than for LEDs, being now the ratio between the total output electrons and the total input photons. In other terms, the system spectral response (SR) can be related to the EQE following the expression:

$$\mathrm{SR}\left[\frac{A}{W}\right] = \frac{q\lambda[nm]}{hc} \times \mathrm{EQE} \approx \frac{\lambda[nm]}{1240} \times \mathrm{EQE}\ , \tag{3.32}$$

where q is the elementary charge, λ the incident photon wavelength, h the Planck's constant and c the speed of light in vacuum. Indeed, the SR expresses the conversion efficiency as a function of macroscopic (and directly measurable) magnitudes,

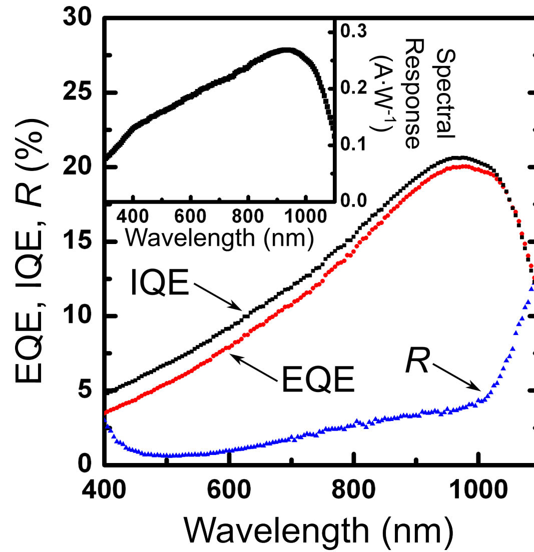

Figure 3.16: EQE (red circles), R (blue triangles) and resulting IQE (black squares) from the same solar cell in Fig. 3.15(b). The inset shows the measured spectral response for the same cell.

and can be interpreted as the ratio between the electrical current intensity output and the incident optical power. The spectral response (photon-energy dependent) can be directly related to the generated potocurrent (I_{ph}) by convolving it with the solar irradiance spectrum in Fig. 3.15(a), $\mathrm{F}(\lambda)$, and integrating over the whole wavelength range [2]:

$$I_{\mathrm{ph}} \propto \int_{\lambda} \mathrm{SR}(\lambda)\mathrm{F}(\lambda)\mathrm{d}\lambda \ , \tag{3.33}$$

where $\mathrm{F}(\lambda)$ serves as weighing function for the SR integration at each λ. The importance of the SR quantification for material characterization lies in the similitude of its onset energy with the band gap-dependent absorption edge. Actually, the ideal spectral response of a semiconductor-based solar cell should abruptly decrease at energies lower than E_{g}.

The spectral response determination is therefore as much important as the overall cell efficiency, for it allows determining the optimum absorber material to be employed for efficiently converting light photons into electrical current within a given spectral range. In addition, from the obtained EQE, the *internal quantum efficiency* [IQE = EQE/(1-R)], i.e. the ratio between the actually absorbed incoming photons and the generated electrical power, can be defined taking into account the lost photons in reflectance (Fig. 3.16 contains the EQE, R and IQE spectra for a crystalline solar cell, as well as its spectral response).

Experimental Equipment To analyse the spectral response of the devices, the SR is measured in the wavelength range from 500 to 1200 nm by means of Fourier-Transform photocurrent spectroscopy, using a supercontinuum white light as ex-

citation source. By simultaneously modulating the different involved frequency components, the Fourier decomposition of the measured photocurrent could be achieved. Further information about this complex technique can be found in Ref. [171].

4. Results and Discussion

> The scientific man does not aim at an immediate result. He does not expect that his advanced ideas will be readily taken up. His work is like that of the planter – for the future. His duty is to lay the foundation for those who are to come, and point the way. He lives and labors and hopes.
>
> Nikola Tesla

In this Chapter, the results obtained during this Thesis Project will be presented and discussed. With this objective, the most relevant published papers on these results will be presented and summarized, as well as unpublished or recently submitted results that are of relevance to the full accomplishment of the Thesis goals, which were already listed in Chapter 1 (*Introduction*). The overall work can be separated by two different blocks (both in SiO_2 or SiC): material and device properties. In the former block, the structural and optical characterization of Si NCs superlattices will be addressed, aiming at optimizing their fabrication parameters. In the latter, the electrical properties of devices containing these Si NC superlattices will be studied, and their performance within light emission and photovoltaic films will be inspected.

4.1. Material Properties of Si Nanocrystal Superlattices

Prior to the utilization of Si NC superlattices for optoelectronic purposes, the investigation was focused on the SL geometrical and annealing parameters that permitted its survival after the whole fabrication process and thus the NC size control. Furthermore, their optical properties are strongly influenced by the SL structure, whose analysis is crucial for optoelectronic applications. The different nature of the SiO_2 and SiC matrices, both studied in this work, induces a separation concerning the structural and optical characterization of NCs embedded in both materials. This, in turn, has resulted in different publications concerning the different matrices.

In general, the SL employed for the following studies present the same structure, which is depicted in Fig. 4.1, valid for both oxide and carbide systems. As has

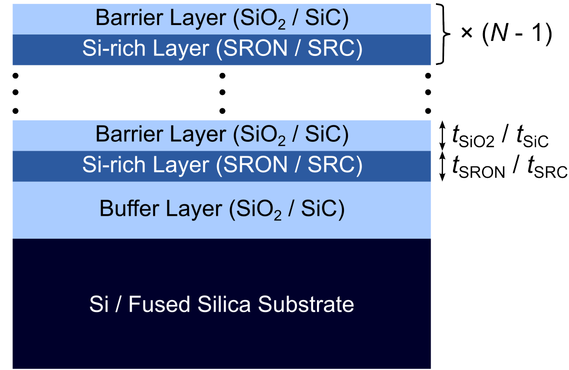

Figure 4.1: General cross-section scheme from the SL samples studied in this Project Thesis. N accounts for the total number of SRON/SiO_2 (SRC/SiC) bilayers, whereas the thicknesses corresponding to the Si-rich and stoichiometric SiO_2 (SiC) are labelled, respectively, as t_{SRON} (t_{SRC}) and t_{SiO2} (t_{SiC}).

already been described in Chapter 3 (*Experimental Details*), the sample design basically consists of $N\times$ Si-rich/stoichiometric matrix bilayers deposited on either Si or fused silica substrates by means of plasma-enhanced chemical-vapor deposition (PECVD). The number N of bilayers, as well as the thicknesses corresponding to the Si-rich wells (either t_{SRON} or t_{SRC}) and stoichiometric barriers (either t_{SiO2} or t_{SiC}) varied according to the required characterization. The usage of Si-rich oxynitride matrix instead of oxide was indeed forced, since the employed gas mixture induced the unavoidable presence of nitrogen [see Chapter 3 (*Experimental Details*)]; nevertheless, the nitrogen excess was controlled, thus allowing for a compound stoichiometry only depending on the Si/O ratio (x in $SiO_xN_{0.23}$). The first layer (*buffer layer*) was intentionally thicker than the N bilayers, consisting of $\sim$ 10–20 nm of SiO_2; as well, a thick oxide layer was deposited on top of the structure to prevent the layers from oxidation after high-temperature application. After the deposition process, the samples were submitted to a high-temperature annealing treatment to precipitate the Si excess in the form of Si NCs. More details on this annealing treatment are found in the previous Chapter (*Experimental Details*).

Multilayer versus Superlattice Before the in-depth exploration and discussion of the results, and in order not to induce confusion to the reader, let us briefly expose the difference between the multilayer (ML) and the superlattice concepts. A *multilayer* system basically consists of multiple layers consecutively deposited, which fits with all material samples studied in this Thesis. A *superlattice* system is based on a multilayer stack whose layers have the appropriated structure to behave as finite-width quantum wells. In other words, SLs are ML systems that exhibit quantum confinement properties (associated with layer thickness and NC size control). These properties have been clearly observed in Si NC / SiO_2 multilayers, but very special conditions are required in the case of Si NC / SiC MLs, as shown in the following sections. For this reason, the term superlattice is indistinctly employed in the former case, whereas the term was carefully used in the SiC-based system.

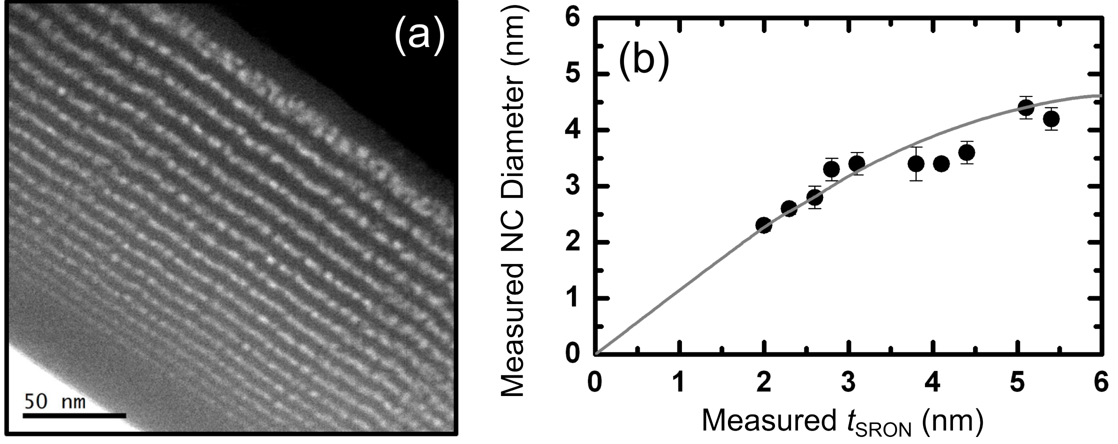

Figure 4.2.: (a) Energy-filtered TEM image corresponding to a SL sample with $t_{SiO2} = 4$ nm and varying t_{SRON}, deposited on Si substrate and annealed at 1150 °C. (b) Measured NC diameter as a function of the measured SRON layer thickness, for the sample imaged in (a).

4.1.1. Material Characterization of Si NC / SiO_2 Superlattices

4.1.1.1. NC Size Study in Si NCs / SiO_2 Superlattices

When working with superlattice structures, the first issue that arises is the thickness limit where the approach is valid. In other words, we need to know to which extent the NC size can be controlled. For this purpose, a special SL sample was fabricated, consisting of 18× $SiO_{1.1}N_{0.23}$ / SiO_2, with fixed $t_{SiO2} = 4$ nm and varying t_{SRON}, annealed at 1150 °C. An EFTEM analysis of the sample was performed, whose result is shown in Fig. 4.2(a). Filtering by the Si plasmon energy, Si domains are thus highlighted as bright spots, the Si nanoclusters, whereas the dark background corresponds to the oxide matrix. One can observe that, as the SRON layer thickness increases, the presence of single 2-dimensional arrays of nanoclusters across the growth direction does no longer occur; vertical size confinement is therefore unaccomplished. Size statistics over more than 50 nanoclusters along each SRON layer was performed, whose results are displayed in Fig. 4.2(b). The nanocluster size is, in general, in good agreement with the measured t_{SRON} up to layer thickness values of 4−5 nm. Beyond this limit, a saturation-like behavior is reached that does not further favor the growth of larger nanostructures. This means that thicker layers than 5 nm no longer constrain the nanocluster growth; a larger number of nucleation centers may then exist and thus different nanocluster populations appear.

The first published results we deal with are presented in Paper I [81], where a first structural and optical characterization on samples consisting of 18× $SiO_{1.1}N_{0.23}$ (t_{SRON}) / SiO_2 (4 nm) deposited on Si substrate and annealed at 1100 °C was carried out. EFTEM images revealed increasing NC size with increasing t_{SRON}, as

well as a low waviness of the deposited layers after the annealing process. Besides, and as it has been mentioned previously, the measured NC size increasingly differed from measured t_{SRON} at thicker SRON layers. In parallel, Raman scattering measurements were analyzed by isolating the c-Si contribution from the overall sample signal, and a phonon confinement model was employed to evaluate the NC size [see also Section 2.3.1.1 in Chapter 2 (*Fundamentals of Silicon Nanocrystals*)]. The diameter found using both structural techniques substantailly differed, being the Raman-related ones between ~ 1 nm lower. This was explained in terms of the *core-shell model* [20, 78], i.e. a crystalline Si core surrounded by an amorphous shell (amorphous Si or substoichiometric oxide) [see Section 2.2 in Chapter 2 (*Fundamentals of Silicon Nanocrystals*)].

An optical analysis of the same samples was performed in terms of the photoluminescence (PL) emission they yielded, resulting from radiative recombination of excitons within the Si NCs. PL spectra showed a clear shift of the emission peak towards shorter wavelengths (higher energies) when the NC size decreased, which is a behavior typically ascribed to quantum confined excitons within the NCs [1, 55]. In addition, the different emission intensity results from the different quantum yield each sample presents, being intermediate NCs the ones exhibiting a better balance between surface-to-volume and crystalline fraction effects. Finally, the peak energies obtained from the PL analysis were compared to other works reported in the literature, the values lying between the ones corresponding to NCs embedded in SiO_2 and Si_3N_4, as expected from an intermediate matrix material (oxynitride).

Available online at www.sciencedirect.com

SciVerse ScienceDirect

Energy Procedia 10 (2011) 43 – 48

Energy Procedia

European Materials Research Society Conference
Symp. Advanced Inorganic Materials and Concepts for Photovoltaics

Structural and optical characterization of size controlled silicon nanocrystals in SiO_2/SiO_xN_y multilayers

J. López-Vidrier[a,*], S. Hernández[a], A.M. Hartel[b], D. Hiller[b], S. Gutsch[b], P. Löper[c], L. López-Conesa[a], S. Estradé[a], F. Peiró[a], M. Zacharias[b], B. Garrido[a]

[a]*MIND, Departament d'Electrònica, Universitat de Barcelona, Martí i Franquès 1, 08028 Barcelona, Spain*
[b]*IMTEK, Faculty of Engineering, Albert-Ludwigs-University Freiburg, Georges-Köhler-Allee 103, 79110 Freiburg, Germany*
[c]*ISE, Fraunhofer Institute for Solar Energy Systems, Heidenhofstr. 2, 79110 Freiburg, Germany*

Abstract

We offer a complete structural and optical study of samples containing silicon nanocrystals (Si-NCs) embedded in SiO_2/SiON multilayers, varying the oxynitride layer thickness from 2.5 to 7 nm. Using energy-filtered transmission electron microscopy we have determined the size distribution of the precipitated Si-nanoaggregates. Raman scattering measurements were used to investigate the Si-NC size and crystalline quality. By combining both techniques, the nanoaggregate crystalline degree has been evaluated, with values around 50% for all the samples. Photoluminescence spectroscopy has shown a blueshift of the emission at smaller NC sizes, presenting the sample with Si-NCs of 3.9 nm the best emission properties.

© 2011 Published by Elsevier Ltd. Selection and/or peer-review under responsibility of Organizers of European Materials Research Society (EMRS) Conference: Symposium on Advanced Inorganic Materials and Concepts for Photovoltaics.

Keywords: Silicon Nanocrystals; Oxynitride; EFTEM; Raman Scattering; Photoluminescence

* Corresponding author. Tel.: +34 93 4039175; fax: +34 93 4021148.
E-mail address: jlopezv@el.ub.es.

1876-6102© 2011 Published by Elsevier Ltd. Selection and/or peer-review under responsibility of Organizers of European Materials Research Society (EMRS) Conference: Symposium on Advanced Inorganic Materials and Concepts for Photovoltaics.
doi:10.1016/j.egypro.2011.10.150

1. Introduction

Silicon solar cells have attracted the attention of science and industry for years for their low fabrication and commercialization costs and their favourable electrical properties. However, silicon is an indirect bandgap semiconductor, with a bandgap energy of 1.12 eV. Its absorption of solar radiation is very poor as the associated energies of most photons coming from sun lay much above the silicon energy gap. Moreover, as a consequence of the indirect bandgap electronic transitions require the intervention of a phonon to couple the momenta and accomplish the conservation law, notably decreasing the transition probability. Because of these extremely poor optical properties of bulk silicon, the efficiency of these photovoltaic devices is far from the desired one [1]. However, by means of the reduction in size of crystalline silicon, a strong localization of the carriers can be reached and the bandgap energy of these nanostructures can be tuned by controlling their size [2]. Therefore, a good determination of the Si-NC size, distribution and optical properties is fundamental in order to reliably characterize the grown samples, thus optimizing the fabrication process. In this paper, a complete structural and optical characterization of Si-NCs embedded in oxynitride matrices is presented, using widely developed techniques such as energy-filtered transmission electron microscopy and Fourier-transform infrared, Raman scattering and photoluminescence spectroscopies.

2. Experimental Details

Silicon rich oxynitride (SRON) films were deposited on (100) Si substrates at 375 °C with a composition of $SiO_{1.1}N_{0.25}$, by means of plasma-enhanced chemical-vapour deposition (PECVD). Samples consist of 20 bilayers of $SiO_2/SiO_{1.1}N_{0.25}$, with different thickness of the latter from one sample to another and keeping the oxide barrier thickness constant at 4 nm for all the samples. After deposition, an annealing of the films at 1100 °C was carried out in a quartz tube furnace for 1 hour in N_2 ambient, in order to precipitate the Si excess. A reference sample containing only a 200 nm thick SRON layer was also prepared under the same conditions, with the aim of checking the unconfined precipitation of Si.

Fourier-transform infrared (FTIR) spectroscopy measurements were performed by means of a BOMEM DA.3 with a spectral resolution of 1 cm^{-1}. A good phase separation between the SiO_2 and SiON matrices has been observed after annealing, as corroborated by the presence of the Si-O-Si asymmetric stretching modes in the two different matrices, at 1065 and 1094 cm^{-1}, respectively [3, 4]. The thickness of the SRON layers, NC size and distribution of the Si nanoaggregates have been measured by means of energy-filtered transmission electron microscopy (EFTEM) using a JEOL 2010 (200 keV FEG) equipped with a Gatan image filter (resolution of 0.8 eV). The silicon contrast was enhanced by energetically filtering the electron energy-loss spectra around the Si plasmon energy (E_{Si} = 17 eV).

Regarding the optical properties, Raman scattering spectra were obtained by exciting the samples using the 325 nm line of a He-Cd laser and analyzed through a LabRam spectrometer, coupled to a high sensitive CCD. The large absorption coefficient of this system at the employed wavelength ($\alpha \approx 10^4$ cm^{-1} [5]) ensures that the probing depth is limited close to the sample surface, allowing the characterization of samples deposited on Si substrates. Nevertheless, some contribution to the Raman spectra from the Si substrate is expected. Photoluminescence (PL) spectra were acquired in the visible range by a combination of a GaAs photomultiplier tube and a CCD, using a standard lock-in technique and exciting the samples also with the 325 nm line.

3. Results and Discussion

3.1. Energy-Filtered Transmission Electron Microscopy

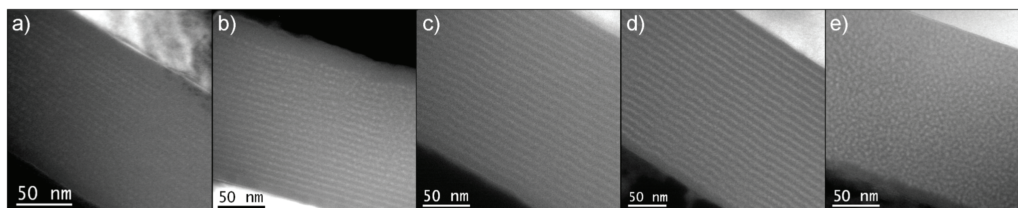

Fig. 1. Cross-section energy-filtered transmission electron microscopy images of the samples with different nominal thickness values of the SiON layers: (a) 2.5 nm, (b) 4.0 nm, (c) 5.5 nm, (d) 7.0 nm and (e) 200 nm bulk SRON.

Energy-filtered transmission electron microscopy measurements were performed for all the samples in order to ensure the correct growth of the Si-NCs within the SRON layers. The obtained images are presented in Fig. 1, and show a excellent quality of the multilayer structure for all the samples. In the images, both SRON and SiO_2 barrier layers can be distinguished as a bright and dark pattern, respectively. A gradual increase of the thickness of the SRON layers can be seen from one sample to another. In addition, the SRON layers present a discontinuity in the brightness, which indicates the presence of Si nanoaggregates, thus corroborating a good precipitation of the Si excess during the annealing process. This observation can easily be checked by observing Fig. 1(e), the sample containing a bulk SRON layer, where the aggregates appear randomly distributed as bright dots. Another feature that can be observed is the waviness present at the interfaces between layers, which cannot be due to the effect of temperature during the annealing process, since as-deposited samples (not shown here) also presented this side effect; the waviness, then, can only be due to the substrate, which propagates the effect to the deposited upper layers.

The high resolution of the employed set-up allowed for a precise measurement of the thickness of the SRON layers as well as the size of Si-NCs, whose values are shown in Tab. 1. The size of NCs was found to follow a Gaussian distribution around a mean value, with an associated dispersion. As can be seen in the table, the nominal thickness of the SRON layers perfectly agrees with the measured size of the precipitated Si-NC for the samples with a nominal thickness of 2.5 and 4.0 nm, while they are slightly larger than the mean size of the NCs for thicknesses larger than 5 nm. Therefore, the size control based on the superlattice for layer thickness is excellent for thicknesses below 5 nm, providing a deviation of the average NC size of only 0.2 nm (with respect to the measured layer thickness), which corresponds to only ± 1 atomic layers in deviation. The rather large dispersion of the size distribution could be an artefact from the cross-section preparation; the images still average over a depth of 30-50 nm, which could result in the observation of apparently larger NCs because of nanocrystals laying behind each other. The size distribution measured this way provides information about the radiative centers delivering energy, and represents an initial point for the discussion of the crystalline quality of the grown nanostructures.

3.2. Raman Scattering

The Raman spectra of the samples are presented in Fig. 2(a). In all the samples we have observed a broad band between 480 and 520 cm^{-1}, whose intensity scales with the SRON layer thickness, and a sharp peak at ≈ 521 cm^{-1}, increasing for thinner SRON layers. The broad structure is related to disorder activated modes, either coming from the SiO_2/SiON matrix or Si, while the sharp peak is attributed to

crystalline Si, as previously reported [6]; their observation indicates that some Si has precipitated in amorphous or crystalline states. Nevertheless, the central frequency and lineshape at high frequencies of the crystalline feature are similar to the ones observed in crystalline bulk Si. Actually, the low thickness of the layers (around 200 nm at most) allows the penetration of light beyond the layers, resulting in a Raman contribution from the Si substrate, whose phonon is superimposed with those originated in the crystalline Si-aggregates (it explains the increasing intensity of the crystalline peak for thinner layers).

Assuming that the substrate contribution corresponds to a lorentzian peak centered at 521 cm^{-1} with a full-width at half-maximum (FWHM) of 4.0 cm^{-1} and deconvoluting it from the SRON layers contribution, we could isolate the information of the latter [see the inset of Fig. 2(a)]. Due to the low volume of the NCs of the thinnest sample (2.5 nm), a low population of phonons are excited (only a few atoms can vibrate), being their Raman efficiency much lower than in larger Si-NCs, and no reliable information of the size for these small NCs can be extracted using this method [7]. Once the Si-substrate contribution is removed, a peak at frequencies slightly lower than 521 cm^{-1} remained visible that comes from the Si-NCs present in the layers, being both its frequency and lineshape strongly dependent on the size of the nanostructures [7]. In Fig. 2(b) we isolated this contribution from the one obtained from disorder modes. It is clearly observed that, on one hand, the crystalline Raman contribution from Si-NCs presents an intensity reduction as the SRON layer thickness is reduced and, on the other, its lineshape also varies with the sample, obtaining a blue shift and a broadening of the peak at lower thicknesses.

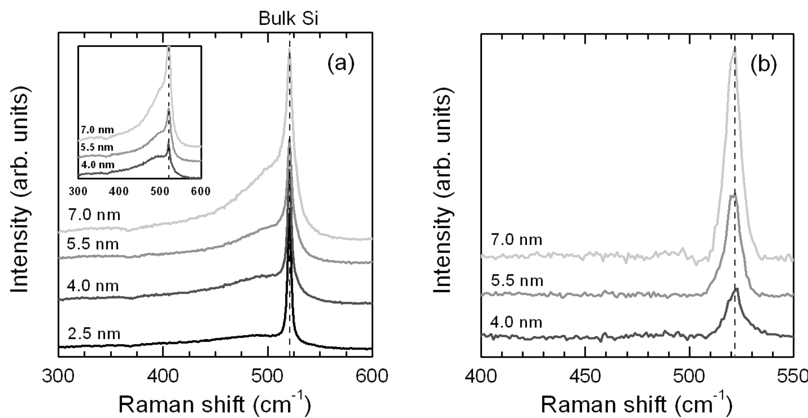

Fig. 2. (a) Raman scattering spectra for the measured samples (the inset shows the spectra after substracting the Si substrate contribution) and (b) the Raman Si-NC peak, once removed the substrate and disorder-modes-related contributions.

We used a previously developed phonon confinement model to analyze the crystalline Raman feature of Si-NCs and to extract their crystalline size (see Ref. [6]). The results obtained by fitting our model to the crystalline Raman peak of the Si-NCs are presented in Tab. 1, showing an increase of the crystalline Si-NC size with the thickness of the SiON layers. We observed that Raman sizes are smaller than the ones obtained by EFTEM measurements. The discrepancy is about 1 nm, which perfectly agrees with previously reported studies using EFTEM and dark-field TEM, where a core-shell model is assumed (a crystalline core surrounded by an amorphous shell) [8]. Our experimental energy resolution in the EFTEM measurements cannot distinguish between amorphous or crystalline silicon states. Consequently, by means of EFTEM we observe the whole Si-nanoparticle while only the crystalline part is evaluated when using the aforementioned confinement model. Considering this kind of structure, it is possible to

estimate the crystalline fraction of the Si-NCs (Γ_c, see Tab. 1), keeping a value around 50% for all of the samples.

Table 1. Nominal and measured thickness of the SRON layers by means of EFTEM, the NC sizes obtained by both EFTEM measurements (expressed as a mean value with an associated dispersion, considering a Gaussian distribution) and from the fitting of the Raman peak (whose errors are associated to data treatment), and their corresponding crystalline fraction.

Nominal thickness (nm)	Thickness measured by EFTEM (nm)	NC size by EFTEM (nm)	Si-NC size by Raman (nm)	Γ_c (%)
2.5	2.5	2.3 ± 0.4	-	-
4.0	4.1	3.9 ± 0.7	3.0 ± 0.3	45 ± 15
5.5	5.0	4.3 ± 0.6	3.3 ± 0.2	45 ± 10
7.0	5.7	4.6 ± 0.6	3.7 ± 0.2	50 ± 10
200 (bulk layer)	184	3.5 ± 0.5	-	-

3.3. Photoluminescence Spectroscopy

In Fig. 3(a) we display the PL spectra of the samples under study, once scaled to their corresponding SRON layer thickness. The spectra show a peak emission in the near-infrared and visible ranges that shifts to longer wavelengths with the Si-NC size, which corroborates the precipitation of Si-NCs [9]. We observe a redshift from approximately 710 to 860 nm for the samples with 2.5 to 7.0 nm SRON layer thickness, respectively [see Fig. 3(b)], as well as a clear dependence of the PL intensity on the thickness of the SRON layer, being maximum for the sample with 4.0 nm SRON layer. The emission of the bulk SRON layer sample is very similar to the one of the thickest sample, suggesting a saturation of the growth process of Si-NCs for the used annealing conditions. The emission from samples with a SRON layer thicker than 4.0 nm presents a FWHM of about ≈ 0.3 eV, associated to both the size dispersion observed by EFTEM and the indirect nature of the recombination process in this system. A rough estimation of the dispersion of the Si-NC sizes can be evaluated by monitoring this parameter. On the contrary, the sample with SRON layers of 2.5 nm presents the largest FWHM and the lowest intensity, probably due to a more pronounced growth of the amorphous phase of NCs instead of the crystalline one.

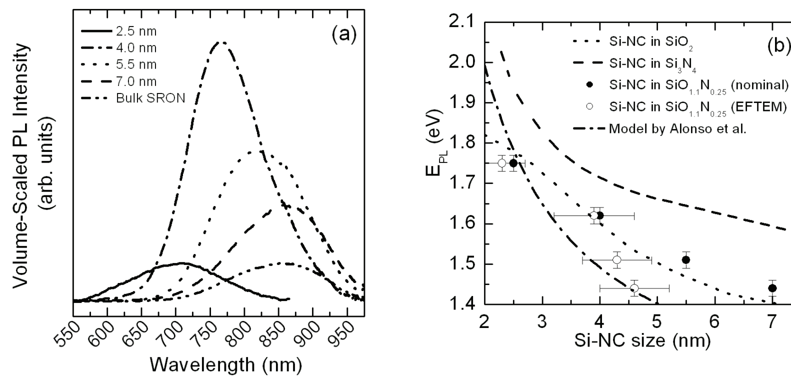

Fig. 3. (a) PL spectra of the studied samples, scaled to the thickness of the SRON layers. (b) Comparison between our PL values, considering the nominal (black points) and the EFTEM (green points) NC sizes, and the ones obtained by other authors, in SiO_2 [10] (blue dashed line) and Si_3N_4 [11] (red dashed line) matrices. Green dot-dashed line represents the calculations by Alonso *et al.* [9].

As can be seen in Fig. 3(b), our PL results from Si-NCs embedded in a SiON matrix lay within the already reported ones for SiO_2 [10] and Si_3N_4 [11] matrices, when the nominal value of the SRON thickness is considered as the Si-NC size. However, a sizeable discrepancy exists when considering the sizes of the nanostructures obtained by EFTEM: lower energies are observed for all Si-NC sizes with respect to previously reported values. Therefore, an overestimation of the Si-NC sizes would be obtained through the previously reported relations [10, 11]. Nevertheless, a reasonable good agreement is found when comparing our results with recently published theoretical calculations of electronic transitions in Si-NCs embedded in SiO_2 [9], establishing a direct relation between the size and the PL emission energy.

4. Conclusions

In summary, we have characterized the structural and optical properties of Si-NCs grown in SiO_2/SiON multilayers deposited by PECVD on Si substrate and annealed at 1100 ºC for different SRON layer thicknesses. The thicknesses of the multilayers and the Si-NC sizes have been determined by EFTEM, in good agreement with their nominal values. Raman scattering was used to evaluate the size and the crystalline fraction of the Si-NCs. The estimated crystalline fraction is found to be in good agreement with previous reports, performed by combining EFTEM and dark-field TEM measurements in PECVD grown samples. PL spectra show a blueshift of the emission up to ~ 1.7 eV (sample with 2.3 nm NC size) with decreasing NC size, being the 4 nm sample the one which shows the highest PL intensity. The comparison of the PL results with recently published theoretical models has allowed us to establish a direct relation between the size and the optical properties of Si-NCs.

Acknowledgements

We acknowledge the financial support from the European Commission under the Seventh Framework (NASCEnT, project number NMP4-SL-2010-245977).

References

[1] Conibeer G, Green M, Cho E-C, König D, Cho Y-H, Fangsuwannarak T et al.. Silicon quantum dot nanostructures for tandem photovoltaic cells. *Thin Solid Films* 2008; **516**: 6748-56.

[2] Canham LT. Silicon quantum wire array fabrication by electrochemical and chemical dissolution of wafers. *Appl. Phys. Lett*. 1990; **57**: 1046-8.

[3] Bensch W, Bergholz W. An FTIR study of SiO_2 for VLSI microelectronics. *Semicond. Sci. Technol.* 1990; **5**: 421-8.

[4] Alayo MI, Pereyra I, Carreño MNP. Thick SiO_xN_y and SiO_2 films obtained by PECVD technique at low temperatures. *Thin Solid Films* 1998; **332**: 40-5.

[5] Mirabella S, Agosta R, Franzò G, Crupi I, Miritello M, Lo Savio R et al.. Light absorption in silicon quantum dots embedded in silica. *J. Appl. Phys.* 2009; **106**: 103505.

[6] Hernández S, Martínez A, Pellegrino P, Lebour Y, Garrido B, Jordana E et al.. Silicon nanocluster crystallization in SiO_x films studied by Raman scattering. *J. Appl. Phys.* 2008; **104**: 044304.

[7] von Behren J, van Buuren T, Zacharias M, Chimowitz EH, Fauchet PM. Quantum confinement in nanoscale silicon: The correlation of size with bandgap and luminescence. *Solid State Commun.* 1998; **105**: 317-22.

[8] Iacona F, Bongiorno C, Spinella C, Boninelli S, Priolo F. Formation and evolution of luminescent Si nanoclusters produced by thermal annealing of SiO_x films. *J. Appl. Phys.* 2004; **95**: 3723-32.

[9] Alonso MI, Marcus IC, Garriga M, Goñi AR, Jedrzejewski J, Balberg I. Evidence of quantum confinement effects on interband optical transitions in Si nanocrystals, *Phys. Rev. B* 2010; **82**: 045302.

[10] Garrido B, López M, Pérez-Rodríguez A, García C, Pellegrino P, Ferré R et al.. Optical and electrical properties of Si-nanocrystals ion beam synthesized in SiO_2. *Nucl. Instr. Meth. Phys. Res. B* 2004; **216**: 213-21.

[11] Park N-M, Choi C-J, Seong T-Y, Park S-J. Quantum Confinement in Amorphous Silicon Quantum Dots Embedded in Silicon Nitride. *Phys. Rev. Lett.* 2001; **86**: 1355-7.

4.1.1.2. Superlattice Maintenance in Si NCs / SiO_2 Systems

The maintenance of the SL structure after several parameters modification and annealing treatment conditions was investigated in Paper II [126], as a logical consequence of the first structural and optical characterization reported above. For the purposes of this study, the variation of the annealing temperature (T_{ann}) and the SiO_2 barrier thickness was addressed, and TEM, Raman and PL techniques were employed to determine the ideal structural and fabrication SL properties for their optimum optical performance. For the sake of clarity to the reader, Tab. 4.1 summarizes the SL parameters corresponding to the samples studied in this Paper. Indeed, this study also confirmed the possibility of correlating the results obtained by different techniques, from an structural and optical point of view, and their complementary usage for the SL properties characterization.

The SL structure was initially investigated by EFTEM imaging under different annealing conditions. We found that the SL was hold even after a high T_{ann} was applied, at temperatures as high as 1250 °C. A closer inspection of the images, however, showed substantial differences between the nanocluster size distribution of different samples: in particular, high-temperature annealing induced larger mean sizes and a broader nanocluster distribution. This is an important result, since it shows that, although the SL structure is still conserved, the Si excess outer-diffusion towards the oxide barriers does not fully restrict the nanocluster confinement within the SRON layers. On analogous samples, a Raman study was carried out that revealed an onset for the precipitated Si excess crystallization beyond 950 °C, in agreement with previous reports in the literature [20]. As well, higher T_{ann} involves a continuously increasing crystalline degree of the samples, with values ranging between 80 and 90 %, the latter establishing an upper limit for crystallization due to the unavoidable amorphous transition shell. We should mention here that Raman measurements were carried out on samples grown on fused silica substrate and employing the cross-section laser incidence configuration [see Section 3.2.2.4 in Chapter 3 (*Experimental Details*)], in order to avoid the Si substrate Raman contribution and minimize that corresponding to silicon oxide, respectively.

Photoluminescence characterization on samples annealed at different temperature exhibited an optimum behavior for intermediate temperatures. The increase of T_{ann} from 1100 to 1150 °C was found to induce a higher PL emission intensity, in agreement with the observation of increasing crystallization state as reported by Raman. This emission intensity remains constant within an interval of 50 °C, dramatically decreasing after $T_{\mathrm{ann}} = 1200$ °C is applied. Regarding the PL peak position, a redshift is observed when increasing T_{ann}, behavior that could be explained in terms of the size distribution observed by TEM, higher temperatures resulting in larger (loosely-confined) NCs. In fact, the lower emission intensity displayed by samples where larger nanostructures dominate the size distribution is believed to be due to a loss of quantum confinement, more evident when thicker

Table 4.1.: Summary of the parameters corresponding to the different samples employed for the study published in Paper II.

Study	t_{SRON}	t_{SiO2}	T_{ann}
Annealing Temperature	2, 3.5 and 5 nm	4 nm	950−1250 °C
Barrier Thickness	4 nm	1, 2 and 4 nm	1150 °C

SRON layers were implied. In addition, the results revealed 1150 °C as the ideal annealing temperature for PECVD-deposited Si NC superlattices, displaying an excellent NC size control as well as a high enough crystalline degree that minimizes the effects of undesired non-radiative recombination on PL emission.

The next step was the study of the barrier thickness reduction limit, for thinner barriers are of great interest towards the achievement of optimum charge transport properties in SL-based optoelectronic devices. Following the same experimental procedure as the one used for the annealing temperature study, EFTEM was employed to image the samples containing different t_{SiO2}. The selected annealing temperature for this study was 1150 °C, for it demonstrated the optimum structure and optical emission. It was observed that the SL structure was conserved when reducing t_{SiO2} from 4 to 1 nm, and that the measured layer thicknesses were in good accordance to the nominal ones. Again, an in-depth analysis of the NC size distribution was carried out, from which similar average NC sizes (as expected from a fixed t_{SRON}) and narrow distributions were determined. This is indicative that even barriers as thin as 1 nm are able to avoid Si out-diffusion from the SRON layers at annealing temperatures as high as 1150 °C. The Raman measurements, however, presented a behavior with not so straightforward conclusions. In this case, we can focus the analysis in two different observations: (i) the different spectra presented identical shape but for (ii) a shift to lower frequencies when reducing the t_{SiO2}. On one hand, effect (i) is indicative that an identical proportion between crystalline and amorphous Si is present in the sample, which well correlates with the similar NC sizes obtained by TEM. On the other hand, (ii) implies a convolution of two different effects: a shift to lower frequencies due to phonon confinement effect and an opposite shift to higher frequencies due to an increasing compressive matrix stress. The former fact affects the same way in all samples, because the NC size does not significantly vary; the latter effect, however, scales with the amount of surrounding SiO_2 matrix when t_{SiO2} increases. Therefore, quantum confinement and stress effects allowed explaining the observed behavior [see Section 2.3.2.3 in Chapter 2 (*Fundamentals of Silicon Nanocrystals*)].

The PL spectra obtained from samples with different SiO_2 layer thickness exhibited a similar lineshape but for a slight (but non-negligible) peak redshift when decreasing t_{SiO2}. In this case, compressive stress arguments were not applicable, as they would suppose a shift towards higher energies [122]. This fact does not necessarily neglect stress effects, which are always present in matrix-embedded NCs;

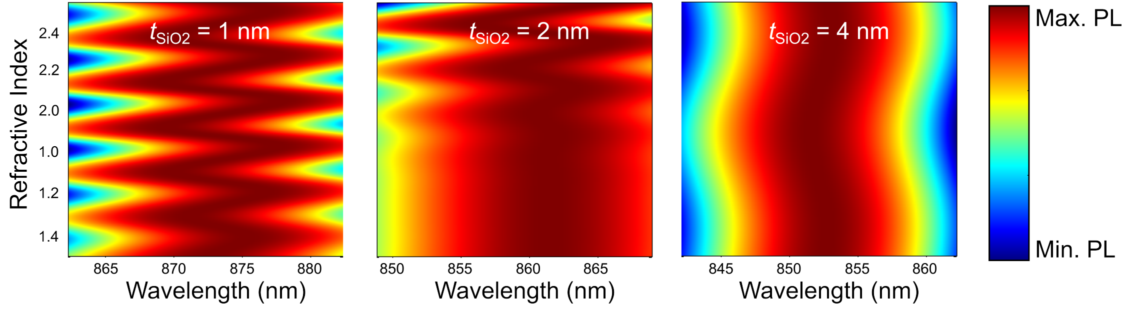

Figure 4.3.: Color maps for the PL emission spectrum evolution under different t_{SiO2} and total refractive index of the layers. The color scale indicates the PL intensity, red corresponding to the highest PL intensity (i.e. the PL peak wavelength). The refractive index was varied considering intermediate values between crystalline Si (~ 3.4) and SiO_2 (~ 1.45), and taking into account their approximate proportion within each sample; as well, the total SL thickness was considered.

instead, it means that another coexisting effect dominates. In order to discard the effect of internal reflections within the SLs (given that the samples contained a different number of bilayers and consequently a different total thickness), we simulated their effect on the PL emission wavelength by taking into account intermediate refractive indices between c-Si and SiO_2, accounting for their proportion in each sample (see Fig. 4.3), and the total SL thickness. Even in the worst case, no overlapping occurred between the different samples, which corroborated that the observed PL shift was real, not just an optical artifact. We finally ascribed the observed variation to a loss of excitonic quantum confinement, not due to a NC size variation (structural observations indicate otherwise) but to the NC proximity in the growth direction that takes place when reducing the oxide barrier thickness.

JOURNAL OF APPLIED PHYSICS **116**, 133505 (2014)

Annealing temperature and barrier thickness effect on the structural and optical properties of silicon nanocrystals/SiO_2 superlattices

J. López-Vidrier,[1,a)] S. Hernández,[1] D. Hiller,[2] S. Gutsch,[2] L. López-Conesa,[1] S. Estradé,[1,3] F. Peiró,[1] M. Zacharias,[2] and B. Garrido[1]

[1]*MIND–IN2UB, Electronics Department, University of Barcelona, Martí i Franquès 1, E–08028 Barcelona, Spain*
[2]*IMTEK, Faculty of Engineering, Albert-Ludwigs-University Freiburg, Georges-Köhler-Allee 103, D-79110 Freiburg, Germany*
[3]*TEM–MAT, CCiT–UB, Scientific and Technological Center - University of Barcelona, Solé i Sabarís 1, E–08028 Barcelona, Spain*

(Received 23 July 2014; accepted 19 September 2014; published online 1 October 2014)

The effect of the annealing temperature and the SiO_2 barrier thickness of silicon nanocrystal (NC)/SiO_2 superlattices (SLs) on their structural and optical properties is investigated. Energy-filtered transmission electron microscopy (TEM) revealed that the SL structure is maintained for annealing temperatures up to 1150 °C, with no variation on the nanostructure morphology for different SiO_2 barrier thicknesses. Nevertheless, annealing temperatures as high as 1250 °C promote diffusion of Si atoms into the SiO_2 barrier layers, which produces larger Si NCs and the loss of the NC size control expected from the SL approach. Complementary Raman scattering measurements corroborated these results for all the SiO_2 and Si-rich oxynitride layer thicknesses. In addition, we observed an increasing crystalline fraction up to 1250 °C, which is related to a decreasing contribution of the suboxide transition layer between Si NCs and the SiO_2 matrix due to the formation of larger NCs. Finally, photoluminescence measurements revealed that the emission of the superlattices exhibits a Gaussian-like lineshape with a maximum intensity after annealing at 1150 °C, indicating a high crystalline degree in good agreement with Raman results. Samples submitted to higher annealing temperatures display a progressive emission broadening, together with an increase in the central emission wavelength. Both effects are related to a progressive broadening of the size distribution with a larger mean size, in agreement with TEM observations. On the other hand, whereas the morphology of the Si NCs is unaffected by the SiO_2 barrier thickness, the emission properties are slightly modified. These observed modifications in the emission lineshape allow monitoring the precipitation process of Si NCs in a direct non-destructive way. All these experimental results evidence that an annealing temperature of 1150 °C and 1-nm SiO_2 barrier can be reached whilst preserving the SL structure, being thus the optimal structural SL parameters for their use in optoelectronics. *© 2014 AIP Publishing LLC*. [http://dx.doi.org/10.1063/1.4896878]

I. INTRODUCTION

Nanostructured silicon has been widely investigated during the last years, as it has proved to offer an enhancement of the optical properties of bulk material.[1] Due to the quantum confinement of the electronic wavefunction inside the Si nanocrystals (Si NCs), they exhibit a higher band gap energy compared to bulk Si ($E_g = 1.12$ eV), which was found to highly depend on the NC size.[2–4] The band gap tunability of these nanostructures has been exploited for optoelectronic applications, such as for developing light-emitting[5,6] or photovoltaic devices,[7–9] as their band gap energy increase is translated into an emission in the visible range and the reduction of high-energy absorbed-photon thermalization losses, respectively. In order to efficiently control the band gap energy of such materials, a control of the NC size becomes essential. For this reason, during the last decade many studies have reported on the structural and optical properties of Si NCs embedded in SiO_2 matrices using the superlattice (SL) approach, by depositing alternated Si-rich Si oxide (SRO) and SiO_2 thin layers (of a few nm).[10] Among the existing techniques for the deposition of thin substoichiometric Si oxide layers, chemical-vapor deposition (CVD) allows for an excellent control of the film thickness and stoichiometry, which means controlling the final Si NC size.[11,12]

Apart from an Å-range layer deposition control, the precipitation and crystallization of the Si excess of the non-stoichiometric layers are required, and this can be achieved by means of a post-deposition annealing treatment. It then becomes a crucial step in the Si NC fabrication process, and it highly depends on the previous deposition. In particular, it can be found that two different annealing temperature regimes affect the properties of NCs in different ways depending on the used deposition method: whereas temperatures around 1050–1100 °C are sufficient for films fabricated by means of physical-vapor deposition (PVD)[13–15] and low-pressure CVD (LPCVD),[12,16] higher annealing temperatures, in the range of 1200–1250 °C, are often reported to induce a good phase separation and crystallization of Si nanoclusters when prepared by plasma-enhanced CVD (PECVD).[12,17–19]

[a)]Electronic mail: jlopezv@el.ub.edu

0021-8979/2014/116(13)/133505/7/$30.00 **116**, 133505-1 © 2014 AIP Publishing LLC

[This article is copyrighted as indicated in the article. Reuse of AIP content is subject to the terms at: http://scitation.aip.org/termsconditions. Downloaded to] IP: 161.116.96.5 On: Wed, 01 Oct 2014 15:59:12

This different optimum temperature range is associated with the unintentional incorporation of N in the films during the PECVD process, which affects the Si diffusion length.[20]

Moreover, the SL approach also allows for controlling the volumetric density of Si NCs by modifying the thickness of the SiO_2 barrier layers (the areal density in each Si-rich layer can be also constrained by the Si excess[21]). Nevertheless, its thickness should be sufficient to prevent the Si diffusion outside the Si-rich layers and, thus, the loss of Si NC size control, especially when the films are submitted to very high temperatures (i.e., when a good stability of the SL structure is required).

In the present work, we study the structural and optical properties of the precipitation and crystalline state of Si NCs formed within Si-rich oxide/SiO_2 superlattices under the influence of the annealing temperature and the effect of the SiO_2 barrier thickness reduction, which are closely related to the SL structure maintenance under these conditions. We use energy-filtered transmission electron microscopy (EFTEM) for directly imaging and monitoring the effect of varying both parameters on the NC size, and we confirm the observation using the Raman scattering technique. Finally, the photoluminescence (PL) technique was employed to monitor the emission of the Si NC/SiO_2 SLs after being submitted to an annealing process at different temperatures in the range of 1100–1250 °C. The PL emission peak parameters (intensity, central wavelength, and broadening) were correlated with the previously mentioned structural techniques.

II. EXPERIMENTAL DETAILS

Samples consisting of bilayers of silicon-rich silicon oxynitride (SRON) and stoichiometric silicon dioxide (SiO_2) were deposited on either wet chemically cleaned (100)-Si or fused silica substrates by PECVD technique. Two different sets of samples were fabricated to determine the influence on the Si NC precipitation of both the annealing temperature and the thickness of the SiO_2 barrier layers. In the study regarding the annealing temperature (T_{ann}), the SiO_2 barrier layer thickness (t_{SiO2}) was held constant at 4 nm, whereas the SRON layer thickness (t_{SRON}) ranged from 2 to 5 nm. On the other hand, for the barrier thickness effect investigation, a 4-nm t_{SRON} was employed, while selecting a $t_{SiO2} = 1$, 2, or 4 nm. Each SL stack is sandwiched between 10-nm SiO_2 layers (buffer and capping layers). In all samples, the SRON stoichiometry was kept constant at $SiO_{1.0}N_{0.23}$, which corresponds to a Si excess of 14.7 at. % within the Si-rich layers. Further details on sample growth are given elsewhere.[20,22] In order to achieve the Si NC formation, the samples were annealed in a quartz tube furnace at temperatures up to 1250 °C for 1 h in high purity N_2 atmosphere.

The structural analyses of the samples were performed by combining EFTEM and Raman techniques, direct and indirect techniques, respectively, from which complementary information could be obtained. Selected SL samples before and after annealing at different temperatures were studied by means of EFTEM for imaging the SLs structure and the Si NC distribution. Samples prepared in cross-section geometry were observed in a JEOL 2010F instrument (operating at 200 keV FEG) equipped with a Gatan Image Filter (with a resolution of 0.8 eV). The Si contrast was enhanced by energetically filtering the electron energy-loss spectra around the Si plasmon energy ($E_{Si} = 17$ eV). The structural characterization was complemented by using Raman scattering measurements performed by exciting the samples with the second harmonic of a Nd:YAG continuum laser (532 nm) through a 100× optical microscope objective, and acquiring the spectra in the back-scattering configuration using a Horiba Jobin-Yvon LabRam spectrometer coupled to a CCD. The selected substrate for the Raman study was fused silica, as a Si substrate Raman signal totally masks the Si NCs contribution. Furthermore, in order to maximize the active layer contribution to the spectra and, therefore, to minimize the SiO_2 signal from the substrate, the excitation was carried out in a cross-section configuration.

The optical emission properties of the samples were investigated by photoluminescence. PL spectra were measured at room temperature using a LN_2-cooled CCD camera attached to a single grating monochromator, exciting the samples with the 325-nm line of a He-Cd laser. In order to avoid over-excitation artifacts,[23] the power density for excitation was reduced to 5 $mW \cdot cm^{-2}$ using tunable polarizers. All spectra were corrected for the spectral response of the setup using a calibrated spectral irradiance standard mounted at sample position.

III. RESULTS AND DISCUSSION

A. Structural analysis of the superlattice system

The structure of the films was imaged by TEM, aiming at the direct observation of the effect of the annealing temperature and SiO_2 barrier thickness on the SRON/SiO_2 SLs. The images were acquired by energy-filtering around the Si plasmon energy ($E_{Si} = 17$ eV), which allowed for highlighting the precipitated Si excess with respect to the SiO_2 matrix background. Fig. 1 shows the EFTEM images corresponding to samples containing 30 SRON/SiO_2 bilayers, with t_{SRON} and t_{SiO2} equal to 4 nm, and annealed at 1150 and 1250 °C, respectively, in a cross-section geometry. For both annealing temperatures, the images evidence the presence of Si NCs in ordered layers, separated by the SiO_2 barrier layers. Nevertheless, for annealing temperatures as high as 1250 °C, the Si NCs have grown considerably (see bright spots in the images), whereas there has been a thickness reduction of the SiO_2 layers. These two facts clearly indicate that the oxide barrier cannot longer limit the Si excess diffusion.

A size statistics was performed using several images taken along the SLs (including over 50 nanostructures) that revealed a log-normal distribution of the Si NCs, as seen in Fig. 1(c).[21] A mean diameter and full-width at half maximum (FWHM) of $L^0_{1150} = 3.3$ nm and $FWHM_{1150} = 1.4$ nm, respectively, were obtained for the sample annealed at 1150 °C, whereas larger values resulted from the sample annealed at 1250 °C (with mean diameter L^0_{1250} and FWHM of 4.3 and 2.4 nm, respectively). Thus, not only the mean NC size was modified by the annealing temperature but also the size dispersion. This increase in both the mean size and the size distribution (i.e., the FWHM) of NCs when the films are

[This article is copyrighted as indicated in the article. Reuse of AIP content is subject to the terms at: http://scitation.aip.org/termsconditions. Downloaded to] IP: 161.116.96.5 On: Wed, 01 Oct 2014 15:59:12

133505-3 López-Vidrier et al. J. Appl. Phys. 116, 133505 (2014)

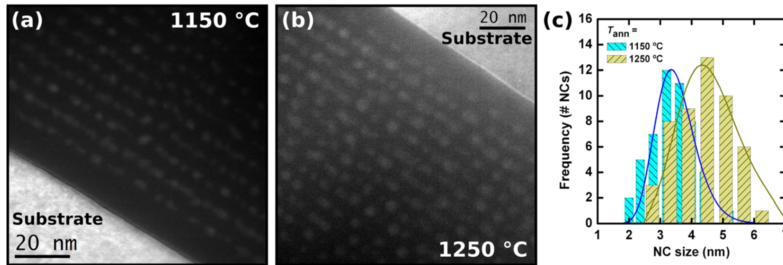

FIG. 1. Cross-section EFTEM images of two samples containing 30× SRON/SiO_2 superlattices, with $t_{SRON} = t_{SiO2} = 4$ nm, annealed at (a) 1150 °C and (b) 1250 °C. (c) NC size distribution obtained for both samples, the solid lines representing their corresponding log-normal fit.

submitted to the highest annealing temperature reflects the lack of size control under these conditions.

Hence, the role of the SiO_2 layers acting as diffusion barriers is strongly affected by the annealing temperature: whereas the formation of NCs at 1150 °C is constrained within the SRON layers, temperatures well above it promote the precipitation of larger nanostructures even outside the Si-rich regions. Actually, at temperatures high enough viscous flow of SiO_2 begins to be relevant,[24] and the SiO_2 no longer avoids the diffusion of Si atoms.

The influence of the SiO_2 barrier thickness on the precipitation of Si NCs was also studied by TEM. For this purpose, three different samples were used with a fixed SRON thickness of $t_{SRON} = 4$ nm and different barrier layer thickness t_{SiO2} with values of 4, 2, and 1 nm, all of them annealed at 1150 °C. The corresponding EFTEM images are reported in Fig. 2. As observed in the figure, the SL system is kept in all samples whereas there is a clear decrease of the barrier thickness, in correlation with the nominal values. A certain waviness effect is observed in all samples, probably due to the large number of deposited bilayers, which in no case affects the undergone analysis. Indeed, a statistical study on the NC sizes revealed a good and similar control size in all the films, with mean values of 3.5, 3.3, and 3.2 nm, and a narrow distribution with a FWHM of 2.8, 1.2, and 2.4 nm, for nominal $t_{SiO2} = 4$, 2, and 1 nm, respectively. Whereas similar mean values are obtained for the three samples, a slightly lower value is obtained for the size broadening corresponding to sample with $t_{SiO2} = 2$ nm. The slightly higher waviness observed for this sample could account for its different size distribution. Despite this small discrepancy, very similar size distributions are obtained in the three samples, irrespective of the SiO_2 barrier thickness, when the samples are annealed at moderate temperatures (i.e., well below 1250 °C).

Additional structural information from a larger number of samples was obtained by means of Raman scattering technique. The Raman spectra of samples annealed at different temperatures (from 950 °C to 1250 °C) are plotted in Fig. 3(a), corresponding to superlattice samples with $t_{SRON} = 4$ nm and $t_{SiO2} = 2$ nm. Similar results were obtained for samples with different SRON thickness (not shown). Essentially, two different features are expected to arise from the precipitated Si: a sharp feature around 518 cm^{-1} and a broad band centered at 470 cm^{-1}, corresponding to the contribution of the optical phonon branch coming from crystalline Si arrangements (redshifted with respect to bulk Si, due to phonon confinement effects[25]) and to the contribution of disorder-activated optical modes from amorphous Si (transversal and longitudinal branches), as reported elsewhere.[25–28] It is clear from Fig. 3(a) that the annealing temperature modifies the local arrangement of Si atoms: films annealed at 950 °C exhibit a broad band in the optical mode region only, related to amorphous Si, whereas the films annealed at 1150 °C show an intense and narrow crystalline feature and a strong intensity reduction of the amorphous band. It is important to note that the appearance of the crystalline feature is an evidence of the precipitation of crystalline domains, whereas the observation of the amorphous band indicates the presence of an amorphous Si phase in the films. For intermediate temperatures ($T_{ann} = 1050$ °C), the Raman spectrum shows both contributions with relative intensities that depend on the annealing temperature (see, for instance, Ref. 29). In addition, these results evidence that the nanocluster crystallization onset can be placed somewhere between 950 and 1050 °C: while annealing temperatures lower than 1050 °C only achieve the formation of amorphous Si clusters, an annealing at 1150 °C induces the formation of crystalline domains that notably surpass their amorphous counterparts. Larger temperatures contribute to minimize the

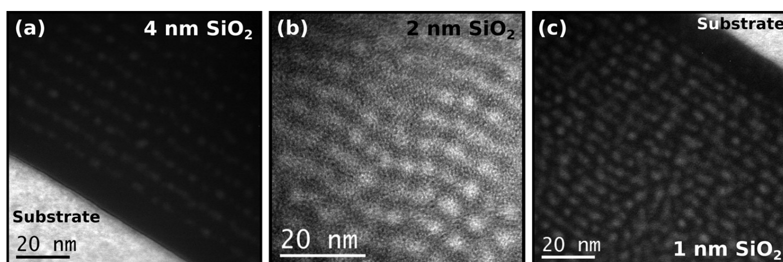

FIG. 2. Cross-section EFTEM images of three 100-bilayer samples annealed at 1150 °C, with a constant $t_{SRON} = 4$ nm, and different barrier thickness: (a) 4 nm, (b) 2 nm, and (c) 1 nm.

[This article is copyrighted as indicated in the article. Reuse of AIP content is subject to the terms at: http://scitation.aip.org/termsconditions. Downloaded to] IP: 161.116.96.5 On: Wed, 01 Oct 2014 15:59:12

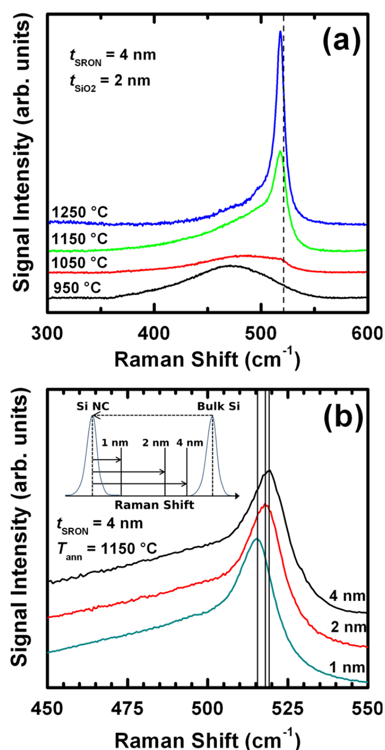

FIG. 3. (a) Raman scattering spectra obtained from samples annealed at different temperatures. The dashed vertical line indicates the bulk Si peak position. (b) Spectra acquired from samples with different SiO_2 barrier thicknesses, and annealed at 1150 °C. The crystalline peak position is highlighted by solid vertical lines. The inset shows the schematics of the crystalline peak shift undergone by the different samples, accounting for two different effects: phonon confinement within the NC (dashed arrow) and compressive stress exerted by the SiO_2 matrix on the NCs (solid arrows).

amorphous component and enhance the crystalline one, in a similar way to what was obtained in the past for bulk SiO_x films.[29] This trend is also observed in the Raman spectrum for the film annealed at 1250 °C, that displays a more intense and narrower crystalline feature, compared to the one at 1150 °C. However, as will be explained below, this implies not a further increase in the actual crystallinity of the NC cores.

A quantitative analysis of the crystalline size and crystalline fraction can be performed by considering the amorphous and crystalline Raman features. In the frequency range between 350 and 550 cm^{-1}, we fitted the experimental data of the samples annealed at 1150 and 1250 °C (samples annealed at 1050 °C exhibit only a weak crystalline feature masked by the amorphous one), following the formalism previously reported in Ref. 25. For this particular study, we selected samples with different SRON layer thicknesses and a constant $t_{SiO2} = 2$ nm. From the lineshape of the crystalline component, we extracted a mean crystalline size of 2.6, 3.1, and 4.0 nm for samples annealed at 1150 °C, for $t_{SRON} = 3$, 4, and 5 nm respectively, which perfectly scale with the SRON thickness. It is worth noticing here that these values correspond to the crystalline region only, without considering the amorphous one from the SiO_x transition shell, and are slightly lower than the ones obtained by EFTEM. When samples are annealed at 1250 °C, larger crystalline sizes are found, with diameters very similar for all samples around 4 nm (3.9, 4.1, and 4.2 nm for $t_{SRON} = 3$, 4, and 5 nm, respectively), which evidences the lack of correlation between the precipitated nanostructures and the thickness of the SRON layers. Hence, the NC size control expected by the SL approach is lost for excessive temperatures.

In addition, the crystalline fraction was also evaluated from the fitted spectra by considering the integrated intensities of the optical amorphous and crystalline contributions. We obtained values around 90% for all annealed samples at 1250 °C, whereas the crystalline fraction of samples annealed at 1150 °C exhibits slightly lower values that scale with t_{SRON} (83, 87, and 89%, for $t_{SRON} = 3$, 4, and 5 nm, respectively). The amorphous and crystalline contributions, in turn, determine the total cluster size, i.e., the NCs consist of a crystalline core surrounded by an amorphous suboxide transition shell.[30] Bearing in mind this consideration, an excellent agreement of total cluster sizes is found between Raman and EFTEM results (for more details, see Ref. 25). In addition, the NC size dependence of the crystallinity reveals the origin of the amorphous contribution to the Raman spectra: the SiO_x shell volume scales with the surface-to-volume ratio, which increases for decreasing NC size. Consequently, the crystallinity appears to be higher for the 1250 °C annealing since the NC size increases due to a breakdown of the integrity of the SiO_2 barrier. In other words, the crystallinity of the NCs measured by Raman is limited to around 90% irrespective of the annealing temperature due to the amorphous contribution of the suboxide transition shell.

As in the TEM study, the influence of the SiO_2 barrier thickness on the precipitation of Si NCs has been also investigated by Raman scattering. Fig. 3(b) shows the Raman spectra corresponding to samples containing a fixed $t_{SRON} = 4$ nm and different t_{SiO2}, all of them annealed at 1150 °C. The Raman spectra of the three samples are very alike, although a shift to lower frequencies appears when decreasing the barrier thickness, with a total variation of 4 cm^{-1} (from 515 to 519 cm^{-1}, for $t_{SiO2} = 1$ to 4 nm, respectively). Actually, and despite this frequency redshift, all the spectra present exactly the same lineshape in the Si optical mode region. This implies that identical Si NCs are precipitated in all samples, with an identical amorphous contribution, but submitted to a different stress field. In the inset of Fig. 3(b), we display a sketch of the frequency position for the three samples with different barrier thicknesses: while phonon confinement produces a shift to lower frequencies with respect to bulk Si, there is a blue-shift induced by a compressive stress. In fact, the higher frequency obtained for the sample with thicker SiO_2 barrier layers indicates that Si NCs are subjected to a stronger compressive stress (of about ≈0.9 GPa), whereas the sample with thinner barrier layers is practically free of stress. This effect is expected from a hydrostatic compressive stress exerted by the SiO_2 matrix on the NCs,[29,31] and is enhanced by a larger amount of surrounding oxide (i.e., at thicker barriers).

[This article is copyrighted as indicated in the article. Reuse of AIP content is subject to the terms at: http://scitation.aip.org/termsconditions. Downloaded to] IP: 161.116.96.5 On: Wed, 01 Oct 2014 15:59:12

In summary, the structural results obtained from EFTEM and Raman scattering techniques provided important information about the growth parameters (T_{ann}, t_{SiO2}, and t_{SRON}) effect on the superlattice structure and, thus, the NC morphology. In particular, an increase in the annealing temperature well above 1150 °C implies the loss of NC size confinement because of outgrowth towards the oxide barriers, which cannot prevent the Si outdiffusion. On the other hand, the characterization carried out on samples with different oxide barrier thicknesses revealed that the SL structure is kept even for thin layers of $t_{SiO2} = 1$ nm,[32] which allows for a higher Si NC density in the films.

B. Photoluminescence properties of Si NC superlattices

The optical emission properties of the fabricated Si NC superlattices were investigated by means of the photoluminescence technique, a non-destructive technique highly sensitive to the structural variations on the radiative processes. Therefore, besides complementing the information derived from the previously studied techniques (EFTEM and Raman), PL allows obtaining the optimum SL structural parameters for minimizing non-radiative recombination paths. As the structural characterization revealed the presence of highly crystalline Si NCs for samples submitted to annealing temperatures of 1150 °C, temperatures in the range from 1100 to 1250 °C have been chosen for the study.

In Fig. 4(a), we show the PL spectra acquired from samples containing $t_{SRON} = 3.5$ nm and a fixed $t_{SiO2} = 4$ nm, annealed at different temperatures. A Gaussian-like emission centered around ≈900 nm is observed for all studied temperatures, attributed to the excitonic radiative recombination within the precipitated Si NCs, with an intensity, central wavelength position, and broadness that depend on the annealing temperature.

Describing the spectra in terms of these three parameters, we observe, in the case of the PL intensity, that it exhibits a non-monotonous variation with the increase of thermal budget with a maximum and an almost constant value around 1100–1175 °C. Moreover, the PL peak position is kept constant around 840 nm up to an annealing temperature of 1150 °C, and it redshifts to 930 nm when the annealing temperature is increased to 1250 °C. Finally, the emission broadening shows a progressive increase with the annealing temperature, with a steep rise for temperatures higher than 1175 °C. It is worth mentioning here that, although T_{ann} lower than 1100 °C are not displayed in the graph, the onset of the PL emission was observed around 1000 °C, with a strong intensity enhancement up to 1100 °C.[20] Identical trends in the PL evolution with the annealing temperature were observed for samples with different t_{SRON} (2 and 5 nm): the emission intensity shows a maximum for temperatures around 1150–1200 °C, whereas PL peak position redshifts and FWHM increases for annealing temperatures above 1150 °C [see Figs. 4(b)–4(d)]. The PL intensity for samples with different SRON thicknesses indicates that there is a maximum emission at medium NC sizes, in agreement with previously reported trends.[33,34]

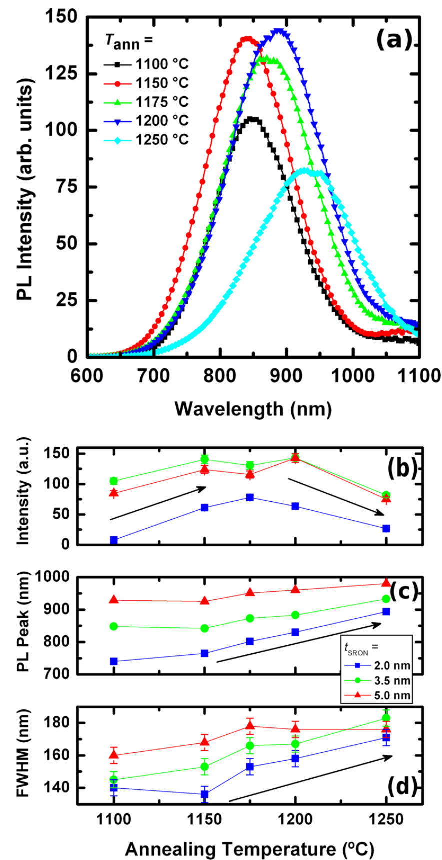

FIG. 4. (a) PL spectra of a 20× SRON/SiO_2 bilayers sample with $t_{SRON} = 3.5$ nm and $t_{SiO2} = 4$ nm, annealed at different temperatures in the range from 1100 to 1250 °C. (b) PL peak intensity, (c) peak position, and (d) FWHM of the emission yielded by 20× SRON/SiO_2 bilayer samples, as a function of their SRON layer thickness and the annealing temperature. Arrows indicate the main trend of the monitored characteristics as a function of the annealing temperature, and are intended to be used as a guide to the eye.

The observed PL emission from Si NCs is, in fact, a consequence of radiative recombination of confined excitons within the Si nanoclusters, which highly depends on their crystalline state.[35] Raman results point out to an almost total crystallization of the Si cluster for an annealing temperature of 1150 °C, where undesired non-radiative recombination processes should be minimized. Therefore, both techniques indicate that high crystallinity is achieved for annealing temperatures around 1150 °C. Nevertheless, samples annealed at much higher temperatures display an intensity decrease and also show a redshift in the PL peak position. Both features indicate a loss of quantum confinement in the nanostructures and, thus, an increase of their size (see, for instance, also Refs. 2 and 3). Hence, at higher T_{ann}, the observed redshift is caused by larger precipitated Si NCs. This is in accordance with the results from EFTEM and Raman studies, where a notably larger mean size was directly observed at higher applied annealing temperatures (see Fig. 1). In addition, the

[This article is copyrighted as indicated in the article. Reuse of AIP content is subject to the terms at: http://scitation.aip.org/termsconditions. Downloaded to] IP: 161.116.96.5 On: Wed, 01 Oct 2014 15:59:12

emission from NCs in all samples broadens for temperatures above 1150 °C [i.e., larger FWHM in Fig. 4(a)], a fact that correlates with the broadening of the size distribution also observed by EFTEM and Raman. This suggests that at temperatures >1150 °C, the Si excess precipitation in the SRON layers is not restricted by the SiO_2 barrier layers, and different NC size populations arise. Therefore, PL results also support the hypothesis of a loss of the vertical size control of the nanoprecipitates within the SL structure when the barrier thickness is reduced. The increase in the FWHM is due to a convolution of different emission lineshapes, provided by the PL emission of different Si NC size distributions. Again, this supports the conclusion that the NC size control is not kept when the annealing treatment is carried out at too high temperatures.

The effect of the reduction of the SiO_2 barrier thickness was also studied. As previously pointed out, the barrier spacing is a fundamental parameter that strongly influences the Si NC volumetric density, without modifying their structure. Fig. 5 displays the obtained spectra for the samples annealed at 1150 °C, shown in Fig. 2, with t_{SiO2} of 4, 2, and 1 nm, while keeping a constant $t_{SRON} = 4$ nm. The measured spectra were normalized in the figure for comparison purposes, although all spectra exhibit similar peak intensities, with a variation below 30%. Observing the PL spectra, all the samples display an emission with a very similar lineshape; however, the central peak position and broadness slightly differ from sample to sample. In particular, the emission lineshape displays similar FWHM of about ≈175, ≈145, and ≈160 nm for $t_{SiO2} = 4$, 2, and 1 nm, respectively, parameter which scales with size distribution (see Sec. III A), with no clear dependence on the barrier thickness. In addition, the peak maximum displays a shift to longer wavelengths (lower energies) when decreasing t_{SiO2}, with peak wavelengths of 852, 861, and 874 nm, for $t_{SiO2} = 4$, 2, and 1 nm, respectively. The origin of this redshift cannot be associated to the size variation from sample to sample, as both TEM and Raman demonstrate almost identical size distributions for all three barrier thicknesses. Therefore, it should be related to the SiO_2 thickness, as the shift perfectly scales with this parameter.

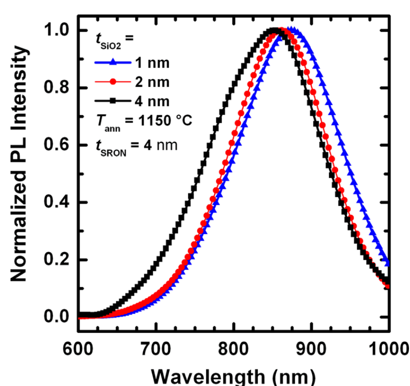

FIG. 5. Normalized PL spectra corresponding to samples containing different SiO_2 barrier thicknesses while keeping constant the SRON layer thickness at 4 nm. The samples under study were annealed at 1150 °C.

Different effects have been considered in order to elucidate the influence of the SiO_2 thickness on the PL peak emission. First of all, the different total thickness and the effective refractive index from sample to sample were considered as the major effect that slightly modulates the PL emission by interference fringes (this, in turn, affects the peak maximum position). For this reason, simulations of the transmittance varying the total thickness and the effective refractive index were performed. We found that there is a strong modulation by these two parameters of the peak maximum, leading to a maximum variation of about ±3 nm, ±5 nm, and ±7 nm for $t_{SiO2} = 4$, 2, and 1 nm, respectively, but with a minimal influence on both integrated intensity and FWHM. Nevertheless, even when accounting for this possible modification, the central peak wavelengths for each sample are well separated, with no overlapping.

Therefore, the explanation for the peak shift at different t_{SiO2} has to depend, necessarily, on other factors. Actually, as commented in the Raman analysis, the SiO_2 matrix stress on the nanostructures originates a Raman shift to higher frequencies. This compressive stress effect should also manifest in the PL spectra, producing an increase of the NC band gap at lower stress,[31] and therefore giving rise to a blueshift (higher energies) of the emission peak at thinner barriers (lower t_{SiO2}), together with an intensity reduction. In fact, the intensity behavior perfectly scales with the compressive stress: larger stress implies lower radiative efficiency.[31] However, the peak maximum shift exhibits the opposite trend, which means that another competing effect is taking place that surpasses the former. Our hypothesis is based again on the quantum confinement loss, whose origin is not related to the NC size (invariant in all samples) but on the inter-NC distance reduction (in the vertical direction). The thickness reduction of the SiO_2 barrier layers propitiates the interaction of Si NCs from adjacent layers, which induces a gradual delocalization of the wavefunction of the carriers, which implies that the quantized energy levels within the nanostructures become closer to the bulk Si conduction and valence bands.[36]

As can be inferred from the discussion thus far, the PL emission is optimum for samples annealed at around 1150 °C, the nanostructures being well crystallized and presenting a controlled size confinement. Besides, it seems that intermediate sizes yield the most intense luminescence. Regarding the most suitable SiO_2 barrier thickness, it was found that the reduction of this parameter induces a strong increase of the PL emission but with a slight loss of quantum confinement of the carriers wavefunction within the nanostructures. In addition, these results support the use of photoluminescence as a direct and non-destructive technique to determine the best structural parameters of Si NC/SiO_2 superlattices.

IV. CONCLUSIONS

In summary, SRON/SiO_2 superlattices were deposited with different SRON and SiO_2 layer thicknesses. To promote

[This article is copyrighted as indicated in the article. Reuse of AIP content is subject to the terms at: http://scitation.aip.org/termsconditions. Downloaded to] IP: 161.116.96.5 On: Wed, 01 Oct 2014 15:59:12

the phase separation and crystallization of the Si excess, the samples were submitted to a post-deposition annealing treatment at different temperatures. The effect on the structural and optical properties of the NC superlattices of both annealing temperature and SiO_2 barrier thickness was studied. EFTEM observations revealed an excellent size control of the nanostructures for an annealing temperature of 1150 °C, whereas temperatures well beyond it induce the formation of larger NCs, indicating that the NC size control is no longer held. An additional analysis by means of Raman scattering confirmed these results and revealed highly crystalline nanostructures when layers are annealed at 1150 °C. These results were confirmed by PL, displaying an optimum emission at $T_{ann} = 1150$ °C, whereas higher T_{ann} implied a loss of quantum confinement due to the growth of different NC size populations. The influence of t_{SiO2} in the structural and optical properties was also studied. The EFTEM images and Raman observations indicated that NCs were correctly confined within the SRON layers while maintaining the SL structure. However, whereas the morphology of the Si NCs is unaffected by the SiO_2 barrier thickness, the emission properties are slightly modified due to a combination of compressive stress (scaling with the SiO_2 thickness) and the interaction between Si NCs from adjacent layers (higher for lower SiO_2 thicknesses), which originates a loss of quantum confinement. Consequently, T_{ann} and t_{SiO2} parameters were optimized and it was found that SRON/SiO_2 superlattices with oxide barriers of 1 nm and submitted to an annealing treatment at 1150 °C provide an excellent control of the size distribution with ideal optical properties for optoelectronic applications.

ACKNOWLEDGMENTS

The research leading to these results has received funding from the European Community's Seventh Framework Programme (FP7/2007-2013) under Grant Agreement No. 245977, under the project title NASCEnT. The present work was supported by the Spanish national projects LEOMIS (TEC2012-38540-C02-01), MAT2010-16407, and the Spanish Consolider Ingenio 2010 program (CSD2009-00013).

[1]A. G. Cullis and L. T. Canham, Nature **353**, 335 (1991).
[2]T. van Buuren, L. N. Dinh, L. L. Chase, W. J. Siekhaus, and L. J. Terminello, Phys. Rev. Lett. **80**, 3803 (1998).
[3]F. Iacona, G. Franzò, and C. Spinella, J. Appl. Phys. **87**, 1295 (2000).
[4]F. Iacona, G. Franzò, V. Vinciguerra, A. Irrera, and F. Priolo, Opt. Mater. **17**, 51 (2001).
[5]N. Lalic and J. Linnros, J. Appl. Phys. **80**, 5971 (1996).
[6]S. Chan and P. M. Fauchet, Appl. Phys. Lett. **75**, 274 (1999).
[7]I. Perez-Wurfl, X. Hao, A. Gentle, D.-H. Kim, G. Conibeer, and M. A. Green, Appl. Phys. Lett. **95**, 153506 (2009).
[8]D. Di, I. Perez-Wurfl, G. Conibeer, and M. A. Green, Sol. Energy Mater. Sol. Cells **94**, 2238 (2010).
[9]G. Conibeer, M. Green, R. Corkish, Y. Cho, E.-C. Cho, C.-W. Jiang, T. Fangsuwannarak, E. Pink, Y. Huang, T. Puzzer, T. Trupke, B. Richards, A. Shalav, and K.-L. Lin, Thin Solid Films **511**, 654 (2006).
[10]M. Zacharias, J. Heitmann, R. Scholz, U. Kahler, M. Schmidt, and J. Bläsing, Appl. Phys. Lett. **80**, 661 (2002).
[11]J. Heitmann, F. Müller, M. Zacharias, and U. Gösele, Adv. Mater **17**, 795 (2005).
[12]Y. Lebour, P. Pellegrino, S. Hernández, A. Martínez, E. Jordana, J.-M. Fedeli, and B. Garrido, Physica E **41**, 990 (2009).
[13]L. X. Yi, J. Heitmann, R. Scholz, and M. Zacharias, Appl. Phys. Lett. **81**, 4248 (2002).
[14]A. R. Wilkinson and R. G. Elliman, J. Appl. Phys. **96**, 4018 (2004).
[15]D. Song, E.-C. Cho, G. Conibeer, Y. Huang, and M. A. Green, Appl. Phys. Lett. **91**, 123510 (2007).
[16]M. Ivanda, H. Gebavi, D. Ristić, K. Furić, S. Musić, M. Ristić, S. Žonja, P. Biljanović, O. Gamulin, M. Balarin, M. Montagna, M. Ferarri, and G. C. Righini, J. Mol. Struct. **834**, 461 (2007).
[17]J. Barreto, J. A. Rodríguez, M. Perálvarez, A. Morales, B. Garrido, and C. Domínguez, Superlattices Microstruct. **43**, 588 (2008).
[18]G. Dalba, N. Daldosso, P. Fornasini, R. Grisenti, L. Pavesi, F. Rocca, G. Franzò, F. Priolo, and F. Iacona, Appl. Phys. Lett. **82**, 889 (2003).
[19]L. Dal Negro, M. Cazzanelli, L. Pavesi, S. Ossicini, D. Pacifici, G. Franzò, F. Priolo, and F. Iacona, Appl. Phys. Lett. **82**, 4636 (2003).
[20]A. M. Hartel, D. Hiller, S. Gutsch, P. Löper, S. Estradé, F. Peiró, B. Garrido, and M. Zacharias, Thin Solid Films **520**, 121 (2011).
[21]S. Hernández, P. Miska, M. Grün, S. Estradé, F. Peiró, B. Garrido, M. Vergnat, and P. Pellegrino, J. Appl. Phys. **114**, 233101 (2013).
[22]J. López-Vidrier, Y. berencén, S. Hernández, O. Blázquez, S. Gutsch, J. Laube, D. Hiller, P. Löper, M. Schnabel, S. Janz, M. Zacharias, and B. Garrido, J. Appl. Phys. **114**, 163701 (2013).
[23]A. M. Hartel, S. Gutsch, D. Hiller, and M. Zacharias, Phys. Rev. B **85**, 165306 (2012).
[24]E. P. EerNisse, Appl. Phys. Lett. **30**, 290 (1977).
[25]S. Hernández, J. López-Vidrier, L. López-Conesa, D. Hiller, S. Gutsch, J. Ibáñez, S. Estradé, F. Peiró, M. Zacharias, and B. Garrido, J. Appl. Phys. **115**, 203504 (2014).
[26]V. Paillard, P. Puech, M. A. Laguna, R. Carles, B. Kohn, and F. Huisken, J. Appl. Phys. **86**, 1921 (1999).
[27]*Group IV Elements, IV-IV and III-V Compounds*, Landolt-Börnstein, New Series, Group III (Springer, Berlin, 1982), Vol. 41, Pt. A1a.
[28]R. Tubino, L. Piseri, and G. Zerbi, J. Chem. Phys. **56**, 1022 (1972).
[29]S. Hernández, A. Martínez, P. Pellegrino, Y. Lebour, B. Garrido, E. Jordana, and J. M. Fedeli, J. Appl. Phys. **104**, 044304 (2008).
[30]F. Iacona, C. Bongiorno, C. Spinella, S. Boninelli, and F. Priolo, J. Appl. Phys. **95**, 3723 (2004).
[31]K. Kůsová, L. Ondič, E. Klimešová, K. Herynková, I. Pelant, S. Daniš, J. Valenta, M. Gallart, M. Ziegler, B. Hönerlage, and P. Gilliot, Appl. Phys. Lett. **101**, 143101 (2012).
[32]S. Gutsch, J. Laube, A. M. Hartel, D. Hiller, N. Zakharov, P. Werner, and M. Zacharias, J. Appl. Phys. **113**, 133703 (2013).
[33]J. Valenta, N. Lalic, and J. Linnros, Opt. Mater. **17**, 45 (2001).
[34]G. Ledoux, J. Gong, F. Huisken, O. Guillois, and C. Reynaud, Appl. Phys. Lett. **80**, 4834 (2002).
[35]D. C. Hannah, J. Yang, P. Podsiadlo, M. K. Y. Chan, A. Demortière, D. J. Gosztola, V. B. Prakapenka, G. C. Schatz, U. Kortshagen, and R. D. Schaller, Nano Lett. **12**, 4200 (2012).
[36]V. A. Belyakov, V. A. Burdov, R. Lockwood, and A. Meldrum, Adv. Opt. Technol. **2008**, 279502.

[This article is copyrighted as indicated in the article. Reuse of AIP content is subject to the terms at: http://scitation.aip.org/termsconditions. Downloaded to] IP: 161.116.96.5 On: Wed, 01 Oct 2014 15:59:12

4.1.1.3. Crystalline Degree Determination of Si NCs in SiO_2

The crystalline degree evaluation of Si NC superlattices was addressed in Paper III [79]. In this case, not only the results on particular samples are of interest, but also the fact that a systematic method to analyze the crystalline fraction out of Raman scattering spectra is established. For this study, samples containing 100× $SiO_{0.93}N_{0.23}(t_{SRON})/SiO_2$(2 nm) superlattices were deposited on fused silica substrate, to get rid of the bulk Si contribution from the substrate to the Raman spectra. The SRON layer thickness was varied from 2 to 5 nm, and samples were annealed at either 950 or 1150 °C, depending on whether amorphous or crystalline structures were needed. The cross-section incidence configuration was employed to increase the Si-to-oxide scattering volume ratio.

A first structural investigation was carried out via EFTEM and XRD experiments. TEM statistics on NC size revealed a good agreement with the SRON layer thickness. Besides, as expected, XRD patterns were fitted by means of Ritveld analyses from which smaller NC sizes were found; the size of the c-Si region is obtained by XRD measurements, sensitive to crystalline domains. The NC sizes obtained from the different characterization techniques are shown in Tab. 4.2. Also from XRD, a decreasing Si lattice parameter from the bulk Si value (a_{Si}=0.5431 nm, a_0 in the paper notation) was determined for smaller NCs, which is translated into a higher pressure exerted by the matrix on the NC, calculated by:

$$P_{XRD} = -3B_0 \frac{\Delta a_0}{a_0} \;, \tag{4.1}$$

where B_0 = 98 GPa is the Si bulk modulus [168], and Δa_0 is the sample lattice parameter variation with respect to bulk Si (a_0). Pressure values ranging from ∼0 to 1 GPa were calculated for decreasing NC size. The strength of the Raman analysis proposed in this paper is the implementation of both the NC size distribution obtained by EFTEM and the matrix stress estimated from XRD in the phonon confinement model, which will allow for a precise crystalline size determination of the NCs.

The next step was the acquisition of Raman spectra from the samples. As usual in Si NC / SiO_2 systems, the spectra exhibited a sharp Si NC-related feature at frequencies around 520 cm^{-1}, corresponding to the TO-LO phonon mode of crystalline Si, as well as a broad-band disorder-activated mode at lower frequencies that is attributed to amorphous phase present in the samples. Also a Raman signal contribution from fused silica appeared that was substracted by acquiring a Raman spectrum on a substrate sample alone. The TO-LO peak position was affected by phonon confinement (shift to lower frequencies at smaller NCs) and the matrix stress (shift to higher frequencies for smaller NCs), as previously commented in Section 4.1.1.2. After isolating the crystalline Raman peak from the amorphous contribution, it is possible to apply a model of confined phonons in hard spheres

Table 4.2.: Summary of the NC sizes obtained, in nanometers, by the different employed experimental techniques. The last column displays the estimated crystalline fraction, f_c.

t_{SRON}	EFTEM	XRD	Raman (c-Si core)	Raman (total NC)	f_c (%)
2	2.4	-	1.9	2.1	78
3	2.8	2.2	2.6	2.8	83
4	3.3	2.6	3.1	3.3	87
5	4.1	3.2	4.0	4.2	89

as the one described in Eq. (2.27) in Chapter 3 (*Experimental Details*), Section 3.2.2.4:

$$I_c \propto \int_0^{\infty} I_{\mathrm{PCM}} \times \mathrm{F}(d, \sigma_{\mathrm{d}}) \mathrm{d}k \ , \tag{4.2}$$

being I_{PCM} the Raman intensity from a given NC size, resulting from the direct application of the phonon confinement model [20, 92]:

$$I_{\mathrm{PCM}} = \int_0^1 \frac{e^{-\frac{(2\pi k d/a)^2}{2\alpha^2}}}{[\omega - \omega(k,P)]^2 - \Gamma^2} k^2 \mathrm{d}k \ , \tag{4.3}$$

and

$$\mathrm{F}(d, \sigma_{\mathrm{d}}) \propto \exp\left[-\frac{(\ln d - \ln \overline{d})^2}{2\sigma^2}\right] \ . \tag{4.4}$$

In the previous equations, ω is the phonon frequency (i.e. the *Raman shift*), a the lattice parameter, Γ the phonon damping parameter (the optimum value of 10.5 cm^{-1} was employed for all samples), α is a parameter that takes into account the penetration of the confined-phonons wavefunction decay into the surrounding matrix [20], and d and $\overline{d}$ are the actual and mean NC diameters, respectively. Eq. (4.4) specifies the selection of a log-normal size distribution, as was proved to best fit the EFTEM data. Please note that the wavevector, $\vec{k}$, is expressed as $\vec{q}$ in the Paper III under discussion. The pressure effects are taken into account in ω by [89, 168]:

$$\omega(k, P) = \sqrt{(521 + 4.9 \cdot P)^2 - \frac{A \cdot k^2}{k + 0.53}} \ , \tag{4.5}$$

where $A = 1.261 \times 10^5$ cm^{-2} and P is the pressure in GPa. After fitting the Raman spectra with this model, slightly lower d values (L in the Paper III notation) than in EFTEM were obtained that correspond to the crystalline NC phase (the inner part, which corresponds to the core in a core-shell model), perfectly scaling with t_{SRON}. In fact, the small variation with respect to the whole cluster size already indicated a high crystalline state of the nanostructures, which was further investigated.

Once the NC size was estimated, the next step in the model was the determination of the crystalline degree of those NCs. For this, the crystalline TO-LO mode had to be separated from the strong amorphous Si Raman contribution. According to the Si phonon dispersion curve displayed in Fig. 3.9 in Section 3.2.2.4, from Chapter 3 (*Experimental Details*), different amorphous Si contributions were considered, mainly due to acoustic and optical modes, whose density of states helped fixing their corresponding Raman shift while leaving their signal intensity as free parameters in the fits. The crystalline fraction, f_c, can be therefore defined from the integrated crystalline and amorphous signal intensities, I_c and I_a, respectively, considering the optical modes:

$$f_c = \frac{I_c}{I_c + \gamma I_a} \ , \tag{4.6}$$

being γ the relative Raman cross-section of c-Si with respect to a-Si. The evaluation of the γ parameter was carried out by considering the absorption coefficients of samples annealed at 900 °C (with dominating amorphous phase) and at 1150 °C (both derived from transmittance and reflectance measurements), α^a and α^c, respectively, and taking into account the laser penetration depth, $l_{laser} \sim 2\ \mu$m (d_{light} in the Paper III notation):

$$\gamma = \frac{\alpha^c \left(1 - e^{-2\alpha^c l_{laser}}\right) I_c}{\alpha^a \left(1 - e^{-2\alpha^a l_{laser}}\right) I_a - \alpha^c \left(1 - e^{-2\alpha^c l_{laser}}\right) I_a} \ . \tag{4.7}$$

The crystalline-to-amorphous Raman cross-section could be generalized as a function of the NC size by considering the approach proposed by Bustarret *et al.* [172]:

$$\gamma(d) = \gamma(\infty) + \left[\gamma(0) - \gamma(\infty) \cdot e^{-\frac{d}{d_{eff}}}\right] \ , \tag{4.8}$$

where d_{eff} is an exponential decay factor. We assumed as boundary conditions that (i) the smallest NCs present an almost amorphous cross-section, i.e. $\gamma(0) = 1$, and (ii) the largest ones might behave as bulk Si, i.e. $\gamma(\infty) = 0.1$ [172]. The application of the γ values determined from Eq. (4.7) into Eq. (4.6) gave crystalline degrees of 78, 83, 87 and 89 % for increasing t_{SRON}, indicating an almost complete Si excess crystallization under the applied annealing conditions ($T_{ann} = 1150$ °C).

Knowing the crystalline fraction and its dependence with the overall NC and c-Si core volumes, $f_c = (d_c/d_{NC})^3$, the total NC diameter was also evaluated (see Tab. 4.2), presenting values in excellent accordance to EFTEM-determined ones. The difference between d_c and d_{NC} is explained by the presence of a suboxide/amorphous Si transition layer between the crystalline NC core and the surrounding matrix, and it was found to present a thickness between one and two atomic layers, a result that confirms the excellent crystallization process achieved by the annealing treatment applied to these samples.

To summarize, this Paper shows how a non-destructive optical technique as Raman scattering can be exploited to obtain precise structural information from

NC-based systems. In particular, the crystalline degree was determined by carefully evaluating the crystalline-to-amorphous Raman scattering cross-section, from which the crystalline degree could be estimated. Finally, it has been demonstrated that the analysis of both the crystalline and amorphous phonon modes in Si NC superlattices allows to attain not only the crystalline core size but also the overall NC one.

JOURNAL OF APPLIED PHYSICS **115**, 203504 (2014)

Determining the crystalline degree of silicon nanoclusters/SiO_2 multilayers by Raman scattering

S. Hernández,[1] J. López-Vidrier,[1] L. López-Conesa,[1] D. Hiller,[2] S. Gutsch,[2] J. Ibáñez,[3] S. Estradé,[1,4] F. Peiró,[1] M. Zacharias,[2] and B. Garrido[1]
[1]*MIND-IN2UB, Departament d'Electrònica, Universitat de Barcelona, Martí i Franquès 1, E-08028, Barcelona, Spain*
[2]*IMTEK, Faculty of Engineering, Albert-Ludwigs-University Freiburg, Georges-Köhler-Allee 103, D-79110, Freiburg, Germany*
[3]*Institute of Earth Sciences Jaume Almera, ICTJA-CSIC, Lluís Solé i Sabarís s/n, E-08028, Barcelona, Spain*
[4]*CCiT, Scientific and Technical Center, Universitat de Barcelona, Lluís Solé i Sabarís 1, E-08028 Barcelona, Spain*

(Received 7 April 2014; accepted 5 May 2014; published online 23 May 2014)

We use Raman scattering to investigate the size distribution, built-in strains and the crystalline degree of Si-nanoclusters (Si-nc) in high-quality Si-rich oxynitride/SiO_2 multilayered samples obtained by plasma enhanced chemical vapor deposition and subsequent annealing at 1150 °C. An initial structural characterization of the samples was performed by means of energy-filtered transmission electron microscopy (EFTEM) and X-ray diffraction (XRD) to obtain information about the cluster size and the presence of significant amounts of crystalline phase. The contributions to the Raman spectra from crystalline and amorphous Si were analyzed by using a phonon confinement model that includes the Si-nc size distribution, the influence of the matrix compressive stress on the clusters, and the presence of amorphous Si domains. Our lineshape analysis confirms the existence of silicon precipitates in crystalline state, in good agreement with XRD results, and provides also information about the presence of a large compressive stress over the Si-nc induced by the SiO_2 matrix. By using the Raman spectra from low temperature annealed samples (i.e., before the crystallization of the Si-nc), the relative scattering cross-section between crystalline and amorphous Si was evaluated as a function of the crystalline Si size. Taking into account this parameter and the integrated intensities for each phase as extracted from the Raman spectra, we were able to evaluate the degree of crystallization of the precipitated Si-nc. Our data suggest that all samples exhibit high crystalline fractions, with values up to 89% for the biggest Si-nc. The Raman study, supported by the EFTEM characterization, indicates that this system undergoes a practically abrupt phase separation, in which the precipitated Si-nanoclusters are formed by a crystalline inner part surrounded by a thin amorphous shell of approximately 1–2 atomic layers. © *2014 AIP Publishing LLC*. [http://dx.doi.org/10.1063/1.4878175]

I. INTRODUCTION

Controlling the size of silicon nanocrystals embedded in silicon oxides and/or silicon nitrides is a fundamental issue for the development of active optoelectronic materials with the desired electronic and optical properties.[1–3] Among the different existing techniques, the "silicon nanocrystal superlattice" approach, i.e., the deposition of alternated silicon-rich oxide (SRO) and stoichiometric silicon dioxide layers (SiO_2) that are subsequently annealed at high temperatures, has been shown to provide excellent control over the size of the precipitated Si nanoclusters (Si-nc).[4–6] During the post-deposition annealing process, a phase separation occurs driven by oxygen outdiffusion from the Si richest regions, that leads to the formation of Si-nc. This phase separation initially results in the precipitation of arbitrary structures that, at later stages of growth, produces the growth of amorphous clusters sphere-like in shape and limited in size by adjacent SiO_2 barriers. The crystallization of those clusters requires a large thermal budget that must be provided by annealing temperatures in excess of 1000 °C.[7] For sufficiently high thermal budgets, only a small region within the Si-nc/matrix interface remains amorphous due to high interfacial stress. The size of the amorphous and crystalline regions, as well as their relative amounts, strongly depends on both the deposition and subsequent annealing processes. Large thermal budgets are typically employed to obtain large, highly crystalline and interfacially relaxed Si-nc[7,8] with reduced non-radiative recombination paths, which are desirable for optoelectronic and photonic applications.

Some approaches have been used in the past for assessing the crystalline degree of the precipitated Si-nc, typically using transmission electron microscopy (TEM) techniques under different configurations.[8–10] Nevertheless, these approaches involve a long and difficult sample preparation that may also influence the structural properties of these systems. As an alternative to electron beam microscopies, non-destructive optical techniques have also been employed to monitor the precipitation process. However, these methods are not able to accurately provide reliable determinations of the crystalline degree of the Si-nc, and provide only rough estimations of it.[11–13] For instance, the intensity of the

 © 2014 AIP Publishing LLC

[This article is copyrighted as indicated in the article. Reuse of AIP content is subject to the terms at: http://scitation.aip.org/termsconditions. Downloaded to] IP: 161.116.96.5 On: Mon, 30 Jun 2014 14:46:08

photoluminescence (PL) emission has been proved to be directly related to the reduction of non-radiative paths (i.e., to lower amounts of defects), showing an emission enhancement for highly crystalline Si-nc.[11,12] Nevertheless, only a relative estimation of the crystallinity from sample to sample can be performed by PL measurements, as the emission strongly depends on the density of luminescent centers and the thickness of the probed region, but with no information from non-radiative recombination processes. Instead, Raman scattering is highly sensitive to both crystalline and amorphous phases of Si-nc. In fact, the amount of each phase in the Raman spectra can be expected to be proportional to the integrated intensities of the corresponding Raman bands. The different scattering cross-section of both phases and its dependence on the Si-nc size, however, make the evaluation of the crystalline degree of the Si-nc complex. Bustarret *et al.* determined the relative scattering cross-section of porous silicon as a function of the porous size,[14] which is useful for the calculation of the crystalline fraction. This approach has been widely employed in the literature for estimating the crystalline fraction in porous silicon and also in silicon nanocrystals (see for instance Refs. 15 and 16, respectively). However, it has recently been shown that this approach is highly inaccurate in the case of Si-nc.[13,17]

In this work, we use Raman scattering to evaluate the crystalline fraction of Si-nc in high-quality samples consisting of silicon-rich oxynitride/silicon dioxide (SRON/SiO_2) multilayers for different nominal SRON layer thickness. The Si-nc were initially characterized by means of energy-filtered transmission electron microscopy (EFTEM) and X-ray diffraction (XRD), revealing the presence of order arrangement of Si-nc with a notable crystalline phase. The Raman spectra for the Si-nc were modeled by considering phonon confinement effects and Gaussian-like functions for the crystalline and amorphous phases, respectively. In addition, using low temperature annealed (LTA) samples containing totally amorphous Si-nc, the relative scattering cross-section between the crystalline and amorphous phases was evaluated and modeled as a function of the crystalline Si domains. The determination of the relative cross sections allowed us to further evaluate the crystalline fraction of the precipitated Si-nc as a function of sizes. Our data and lineshape analysis suggest that all the samples annealed at high temperatures exhibit high crystalline fractions, thus confirming the good crystalline quality of the precipitated Si-nc.

II. EXPERIMENTAL DETAILS

SRON/SiO_2 multilayers have been deposited at 375 °C on fused silica substrates by means of plasma-enhanced chemical-vapor deposition (PECVD). In all samples, the thickness of the SiO_2 layers (t_{SiO2}) was kept constant at 2 nm, whereas the thickness of the SRON layers (t_{SRON}) was varied with nominal values of 2, 3, 4, and 5 nm. The total number of SRON/SiO_2 bilayers for all samples was 100, leading to a total nominal sample thickness of 400, 500, 600, and 700 nm (for SRON layer thicknesses of 2, 3, 4, and 5 nm, respectively). The stoichiometry of the silicon rich layers was $SiO_{0.93}N_{0.23}$, that produces a silicon excess of 17 at. % in the silicon-rich region. The precipitation of the silicon excess in the SRON layers was achieved by a post-deposition annealing process in a quartz tube furnace for 1 h under a N_2 atmosphere. Two identical sets of samples have been annealed at either 900 °C or 1150 °C, to produce amorphous and highly crystalline Si nanoclusters, respectively. Further details on the fabrication process can be found in Ref. 11. The absorption coefficient of low- and high-temperature annealed samples was determined by reflectance and transmittance measurements using the integrating sphere of a Bentham PVE300 photovoltaic spectral response system.

Prior to their study, the high temperature annealed (HTA) samples were cut in two pieces, one for performing TEM and another for XRD and Raman scattering measurements. In the case of TEM, samples were submitted to a mechanical polishing to a thickness below 20 μm followed by ion milling to electron transparency. EFTEM measurements were carried out in those samples using a JEOL 2010F TEM system operating at 200 keV and coupled to a Gatan Imaging Filter (with an energy resolution of 0.8 eV). The Si contrast was enhanced by energetically filtering the TEM image, selecting only the electrons with an energy loss within a window around the Si plasmon energy ($E_{Si} = 17$ eV). The size distribution of the precipitated Si-nanoclusters is, therefore, directly extracted from the analysis of the EFTEM images.

The crystalline ordering of the precipitated Si excess was monitored in the other pieces of the HTA samples by using XRD and Raman scattering techniques. In the case of XRD measurements, grazing-incidence X-ray diffraction (GIXRD) scans were acquired with a Panalytical X'Pert PRO MRD powder diffractometer equipped with a real-time multiple strip PIXcel detector. The measurements were performed with CuK_α radiation ($\lambda = 0.15406$ nm) by using a parallel beam geometry, with a constant angle of incidence of 0.3°. Rietveld full-pattern analyses were performed with the TOPAS 4.2 program (Bruker AXS, 2003–2009) in order to evaluate the lattice parameter and the size of the nanocrystals. For the analyses, the broad XRD band arising from the amorphous SiO_2 matrix was fitted with a split pseudo-Voigt (SPV) function, while a first-order polynomial function was used to fit the background signal.

Raman measurements were carried out using the 532-nm line from the second harmonic of a Nd^{3+}:YAG continuous laser. The Raman spectra were collected by an optical microscope from a Horiba Jobin-Yvon LabRam spectrometer, using an objective of ×100 magnification and analyzed by a highly sensitive CCD camera. The employed configuration provides a spatial resolution <1 μm that allows focusing the laser beam onto the SRON/SiO_2 films, once the samples are positioned under the objective in a cross-section configuration. In this way, an equivalent depth of SRON of about 2 μm is explored, achieving a strong signal enhancement from the Si-precipitates (and, in turn, reducing the relative signal from the fused silica substrate).

III. RESULTS AND DISCUSSION

A. Structural characterization

In Fig. 1, we display the EFTEM images of the HTA samples with different SRON layer thicknesses. As the

[This article is copyrighted as indicated in the article. Reuse of AIP content is subject to the terms at: http://scitation.aip.org/termsconditions. Downloaded to] IP: 161.116.96.5 On: Mon, 30 Jun 2014 14:46:08

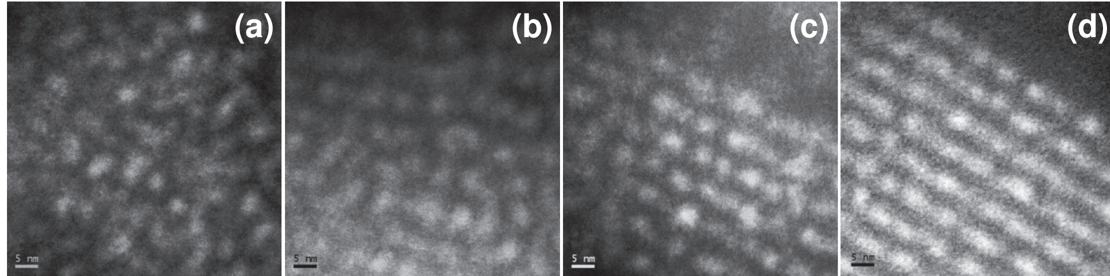

FIG. 1. Cross-section EFTEM images of samples with different nominal SRON thickness: (a) 2 nm, (b) 3 nm, (c) 4 nm, and (d) 5 nm.

transmitted electrons have been energetically filtered around the Si-plasmon, the bright contrast in the images corresponds to Si-precipitates, whereas the dark areas are associated with an environment of SiO_2. The images show two main features that are common for all four annealed samples: the precipitation of Si-nanoclusters and an increasing ordered arrangement of these Si structures at thicker t_{SRON}. It is important to mention here that the Si-nanoclusters are present only in the SRON layers that were intentionally deposited with a silicon excess. Therefore, the thickness of the SRON layers allows for controlling the final size of the aggregates, as previously reported.[18] On the other hand, the dark contrast of about 2 nm in thickness corresponds to the SiO_2 barrier layers, which is indicative that these regions maintain their stoichiometry even after the high temperature annealing[11] and, thus, the multilayered structure is conserved (transmitted electrons through dark areas present an energy loss of ~23 eV, which is typical from pure SiO_2).

Using the data shown in Fig. 1, together with some other images acquired in different regions along the samples, we have been able to determine the size diameter distribution of the Si-clusters for each of them. We have found that the size statistics follows a log-normal distribution with the form:

$$f(L_{0,clu}, \sigma_{clu}) \propto e^{-\left[\frac{(\ln L_{0,clu} - \ln L_{clu})^2}{2\sigma_{clu}^2}\right]}, \quad (1)$$

where L_{clu} and $L_{0,clu}$ correspond to the cluster size and mean cluster size, respectively, whereas σ_{clu} refers to the size dispersion in the log-normal distribution. The HTA sample with $t_{SRON} = 2$ nm shows a mean size of $L_{0,clu} = 2.4$ nm with a dispersion of $\sigma_{clu} = 0.11$. The fact that the Si clusters present a bigger size than the SRON layer thickness clearly indicates that some Si atoms have penetrated inside the SiO_2 barrier layers, making thinner and thicker SiO_2 and SRON layers, respectively, ($t_{SRON} \approx 2.4$ nm and $t_{SiO2} \approx 1.5$ nm). For the rest of the samples, we observed that the cluster size is slightly lower than the nominal thickness of the SRON layers and, thus, the final SiO_2 layer thickness between adjacent Si-nanocluster layers is slightly larger. Overall, the four samples display a narrow size distribution ($\sigma_{clu} \approx 0.1$), with a mean cluster size that scales with the nominal thickness of the SRON layers, displaying values of 2.4, 2.8, 3.3, and 4.1 nm, for $t_{SRON} = 2$, 3, 4, and 5 nm, respectively. In Table I, we have summarized the extracted data from EFTEM measurements.

XRD measurements have also been performed on the same HTA samples. Figure 2 shows a GIXRD scan from the sample with $t_{SRON} = 5$ nm. In addition to the broad and intense background signal arising from the SiO_2 substrate, centered just above 20° in 2θ, weak diffraction peaks corresponding to the (111), (022), and (311) reflections of Si are visible at around 28.6°, 47.5°, and 56.4°, respectively. Similar XRD scans were obtained for the rest of structures with the exception of the sample with $t_{SRON} = 2$ nm, which did not display any clear feature from Si-nc due to the strong contribution from the SiO_2 matrix.

Rietveld analyses allowed us to evaluate the lattice parameter (a_{XRD}) and the X-ray coherence length (L_{XRD}) of the nanocrystals. The inset of Fig. 2 shows the results of the Rietveld fits for the samples with $t_{SRON} = 3$ and 5 nm. Note that, for scaling reasons, the XRD signal from the SiO_2 matrix, fitted with a pseudo-Voigt function, has been subtracted from the spectra. As can be seen in this figure, good

TABLE I. Size distribution of the Si-nanoclusters and their crystalline fraction in HTA samples as determined by either EFTEM, XRD or Raman measurements. The lattice parameter (a_{XRD}) was obtained from Rietveld full-pattern analyses of the XRD scans, from which the effective hydrostatic stress on the Si nanoclusters, P, was further evaluated.

	EFTEM		XRD			Raman		
Nominal SRON thickness (nm) t_{SRON}	Mean cluster size (nm), $L_{0,clu}$	log-Normal σ_{clu}	a_{XRD} (Å)	Crystalline size, L_{XRD} (nm)	P_{XRD} (GPa)	Mean crystalline diameter (nm), $L_{0,cry}$	Log-Normal σ_{cry}	P_{Raman} (GPa)
2	2.4	0.11	…	…	…	1.9	0.11	1.1
3	2.8	0.13	5.416	2.2	1.0	2.6	0.08	0.3
4	3.3	0.09	5.428	2.6	0.2	3.1	0.07	0.09
5	4.1	0.10	5.431	3.2	0.0	4.0	0.06	0

[This article is copyrighted as indicated in the article. Reuse of AIP content is subject to the terms at: http://scitation.aip.org/termsconditions. Downloaded to] IP: 161.116.96.5 On: Mon, 30 Jun 2014 14:46:08

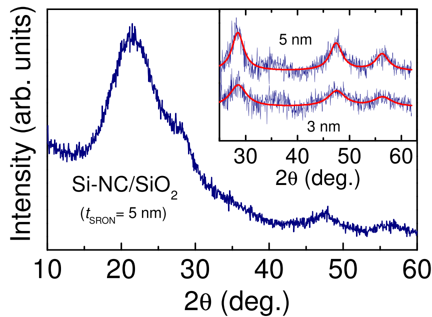

FIG. 2. Grazing-incidence X-ray diffraction scans of the SRON/SiO_2 multilayered sample with $t_{SRON} = 5$ nm. In the inset, the results of the Rietveld fits for the samples with $t_{SRON} = 3$ nm and 5 nm are shown, together with the experimental XRD scans after subtracting the contribution from the SiO_2 substrate.

agreement between the experimental and the calculated scans was found.

In the middle columns of Table I, the nanocrystal size and the lattice parameter (a_{XRD}) obtained from the Rietveld analyses for the samples with $t_{SRON} = 3$, 4, and 5 nm, are shown. In spite of its relatively poor sensitivity in relation to other analytical techniques, the XRD results confirm that the lattice parameter of the Si-nc decreases with t_{SRON}. This observation may be associated to increased matrix-induced compression of the Si-nc when their size is reduced.[9] Using the bulk modulus of Si, $B_0 = 98$ GPa,[19] the effective hydrostatic stress on the Si-nc can be evaluated with the expression $P = -3B_0\Delta a_0/a_0$, where $a_0 = 5.431$ Å (Ref. 19) is the lattice parameter of bulk Si, and $\Delta a_0 = a_{XRD} - a_0$. As can be seen in the table, the XRD results suggest that effective pressures as large as $\sim$1.0 GPa are applied to the Si-nc with $t_{SRON} = 3$ nm.

The Rietveld analysis also allows obtaining a rough estimation of the crystalline size of the Si-nc from the X-ray coherence length (L_{XRD}). We find that L_{XRD} gets reduced with decreasing the nominal SRON thickness, t_{SRON}. The mean sizes thus obtained are slightly lower than the ones determined by EFTEM, which might be related to the fact that the Si-nc contain a sizable proportion of amorphous material.

B. Raman scattering of Si-nc

Raman scattering measurements were also performed using the same set of HTA samples in order to extract further information about the crystalline state and size distribution of the nanoprecipitates. In Fig. 3, we present the Raman spectra in the optical phonon range of Si for multilayered samples with different nominal t_{SRON}. Two main features can be observed in all the spectra: a broad band in the range from 400 to 500 cm^{-1} and one sharp peak at around $\approx$520 cm^{-1}, which are related to Si disorder-activated acoustical and optical modes and to the Si crystalline transversal–longitudinal optical (TO-LO) phonon, respectively.[7] Moreover, some contribution from SiO_2 (either coming from the substrate or from the matrix) is still present in our spectra, even after using a cross-section configuration to acquire them. Despite the fact that the Raman signal of SiO_2 exhibits a low relative intensity in comparison to the signal coming from our Si-nanoclusters, this contribution is still relevant for the sample with the thinnest SRON layers (its Raman spectrum is alike to the one from pure SiO_2, with the addition of weak amorphous and crystalline Si contributions).

The presence of a disorder mode band in all the spectra is an indicator of the amorphous state of some Si aggregates, while the Si TO-LO mode, which is also observed in all the samples, provides a direct evidence of the presence of Si-precipitation in crystalline state (in agreement with XRD analysis). Therefore, these two contributions (amorphous and crystalline) are originated in different arranges of Si atoms within the matrix (i.e., different phases) and can be analyzed independently.

1. Crystalline contribution

First of all, let us consider the Si-related crystalline contribution to the overall Raman signal. One can observe in Fig. 3 that the intensity of the TO-LO mode rapidly increases with the SRON thickness (i.e., with the size of the Si-precipitates), which may be directly associated with an increase of the scattering volume for larger Si-nc. Nevertheless, the position and lineshape of the TO-LO mode is modified from sample to sample, displaying a broadening at lower frequencies and a shift to higher frequencies as the SRON thickness is reduced. Actually, the asymmetric lineshape is a consequence of the confinement of phonons inside the crystalline structures with sizes of about some nanometers, whereas the shift to higher frequencies is an effect caused by a high compressive stress applied to the Si-nc by the SiO_2 matrix (an additional shift to lower frequencies of some cm^{-1} is also produced by phonon confinement effects).[7,13] By analyzing the lineshape and position of the crystalline mode, it is possible to extract information about the crystalline size of Si-nc and the stress field to which they are submitted.

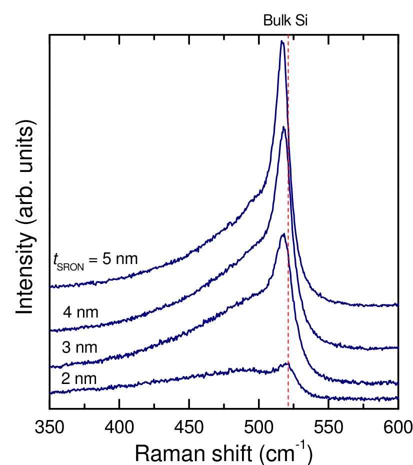

FIG. 3. Raman spectra of samples with different nominal SRON layer thickness of 2, 3, 4, and 5 nm, acquired under cross-section configuration. The vertical dashed line indicates the Raman shift corresponding to bulk crystalline silicon.

[This article is copyrighted as indicated in the article. Reuse of AIP content is subject to the terms at: http://scitation.aip.org/termsconditions. Downloaded to] IP: 161.116.96.5 On: Mon, 30 Jun 2014 14:46:08

The Raman lineshape of the crystalline component of Si-nc under stress can be modeled using the phonon confinement theory modified by Crowe *et al.*,[13] assuming that the Si phonons are confined in hard spheres with a penetration into the surrounding SiO_2 matrix determined by their wavefunction decay [α, that is equal to 3 (Ref. 13)]. In this context, the Raman lineshape can be expressed as[7,13]

$$I(\omega, q, L, \alpha) \propto \int_0^1 \exp[-(2\pi q L/a)^2/(2\alpha^2)] \times [(\omega - \omega(q))^2 + (\Gamma)^2]^{-1} q^2 \mathrm{d}q, \quad (2)$$

where ω is the Raman shift, Γ is the phonon damping, q is the reduced phonon wavevector, and L is the diameter of the crystalline domains. The phonon dispersion $\omega(q)$ is derived from the Brout sum rule to remove any anisotropy of the optical phonons in bulk silicon, modified to include a correction that accounts for the phonon pressure behavior[7,13]

$$\omega(q, P) = \sqrt{\omega_0(P)^2 - \frac{Aq^2}{q + 0.53}}, \quad (3)$$

where A is to $1.261 \times 10^5\,\mathrm{cm}^{-2}$ and $\omega_0(P) = 521 + 4.9P(\mathrm{GPa})\,\mathrm{cm}^{-1}$ takes into account the pressure dependence of the zone-center TO-LO mode.[19] Introducing the possibility of having a log-normal size distribution also for crystalline domains, the total Raman lineshape can be expressed as a convolution of the contributions from the different sizes

$$I(\omega, q, L, L_{0,\mathrm{cry}}, \sigma_{\mathrm{cry}}, \alpha, P) \propto \int_0^\infty I(\omega, q, L, \alpha) \times f(L_{0,\mathrm{cry}}, \sigma_{\mathrm{cry}}) \mathrm{d}q, \quad (4)$$

with L, $L_{0,\mathrm{cry}}$, and σ_{cry} being the size distribution, mean crystalline size, and size dispersion, respectively, in the log-normal distribution of crystalline sizes.

Using this model we have fitted the crystalline part of the Raman spectra (from 490 to 560 cm^{-1}) of all samples by considering as free parameters the mean crystalline size $L_{0,\mathrm{cry}}$, the crystalline size dispersion σ_{cry} and the pressure P, including also a second-order polynomial function as a background to account for possible amorphous contributions. The initial guess of the fits for the effective pressure values applied by the SiO_2 matrix to the Si-nc has been taken from the XRD results. It is worth mentioning that the phonon damping coefficient (Γ) has been maintained constant at 10.5 cm^{-1} for all samples, as it has been found to be the value that better fits all the spectra. Actually, this value is much larger than the one we obtained for bulk silicon under the same experimental conditions, 3.5 cm^{-1}, which indicates reduced phonon lifetimes in the Si-nc.

In Fig. 4, we have plotted the resulting lineshape fits, in comparison to the experimental data. An excellent agreement between calculated and experimental curves is achieved for all samples, as can be observed in the figure. We have estimated the mean crystalline size from the fits, which show that the mean size $L_{0,\mathrm{cry}}$ increases with the SRON thickness: the values thus obtained are $L_{0,\mathrm{cry}} = 1.9$, 2.7, 3.1, and 4.0 nm ($\pm$0.2 nm) for $t_{\mathrm{SRON}} = 2$, 3, 4, and 5 nm, respectively. The log-normal size broadening σ_{cry} displays the opposite behavior, with narrower crystalline distributions for thicker SRON (see Table I). Moreover, the frequency shifts associated to hydrostatic compressive stress suggest reduced pressure values as the Si-nc size is increased (see Table I). The observed evolution with t_{SRON} is in good agreement with the XRD results. Nevertheless, the values obtained with the two techniques are somewhat different, which may be probably attributed to the fact that we have considered, as a first approximation, the properties of bulk Si (phonon pressure coefficient and bulk modulus) to model the compression of the Si-nc embedded in a matrix with much larger compressibility.[4,9,21] Experimental observations of compressive stress in matrix-embedded Si-nc have been reported by some authors by using XRD,[4] Raman scattering,[7,22] and also other experimental techniques such as photoluminescence[20,23] or high-resolution TEM.[24] Typical pressures for Si-nc embedded in SiO_2-based matrices are around some GPa or lower, which is in perfect agreement with the present results. In Table I, we have also summarized the values from crystalline size distribution and the pressures obtained with the Raman analysis.

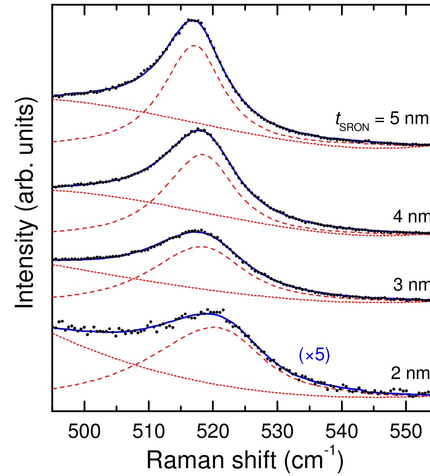

FIG. 4. Experimental Raman spectra of the crystalline part for samples with $t_{\mathrm{SRON}} = 2$, 3, 4, and 5 nm (black dots), compared to the obtained fits using the expression of phonon confined modes described in the text (blue solid-line). The short-dashed lines correspond to a polynomial background, whereas the long-dashed ones refer to the confined crystalline contribution.

Comparing the size values that were determined by EFTEM and Raman measurements, we find a slightly smaller size for the crystalline domains as obtained from the Raman analysis with respect to the total cluster size, with a difference of 0.12–0.14 nm for $t_{\mathrm{SRON}} = 3$, 4, and 5 nm, and slightly larger for $t_{\mathrm{SRON}} = 2$ nm ($\approx$0.5 nm). These data seem to suggest that the Si clusters are almost completely crystallized, exhibiting a thin amorphous layer in the interphase between Si and SiO_2. Nevertheless, a deeper analysis of the Raman data is required in order to properly determine the crystalline degree of the precipitated Si clusters.

[This article is copyrighted as indicated in the article. Reuse of AIP content is subject to the terms at: http://scitation.aip.org/termsconditions. Downloaded to] IP: 161.116.96.5 On: Mon, 30 Jun 2014 14:46:08

2. Degree of crystallinity of the Si-nc

By analyzing the disorder band related to amorphous phases that appears in the range of optical modes (350–500 cm^{-1}, see Fig. 3), further information can be extracted from the Raman spectra. This contribution can be modeled by assuming that each branch of Si optical phonons from the first Brillouin zone contributes to the overall Raman signal due to the relaxation of $k \approx 0$ the selection rule, with a Gaussian-like lineshape.[25] In this way, and using the phonon dispersion curves of bulk Si, the Raman signal in the frequency range where our spectra were acquired (from 350 to 600 cm^{-1}) can be deconvoluted into three Gaussian-like contributions: one from disorder activated longitudinal acoustic modes (DALA) and two from optical modes (the disorder activated TO and LO modes, DATO and DALO, respectively). In Fig. 5, we present the Raman spectrum of a LTA SRON/SiO_2 sample that solely contains amorphous Si. The three contributions obtained for this sample, one acoustic and two optical (also shown in the figure), will be used below to take into account the Raman signal from amorphous Si.

It is worth noticing that the overall Raman intensity arising from amorphous Si aggregates is much larger than the equivalent one from crystalline systems, about one order of magnitude for the sample with $t_{SRON} = 5$ nm. In the inset of Fig. 5 we have depicted the Raman spectra, acquired under the same conditions, of this particular sample before and after HTA. Note that the higher intensity from the amorphous Si-clusters compared to the one from nanocrystalline Si evidences that the scattering cross-section is much larger for amorphous Si. Later, we will evaluate the scattering cross-section of both amorphous and crystalline Si in order to estimate, from the lineshape analysis of all the contributions that appear in the Raman spectra, the degree of crystallinity of Si-nc.

Thus, a deconvolution in the fitting routine of the Raman spectra of the SRON/SiO_2 multilayered samples has been performed by including the three Gaussian-like

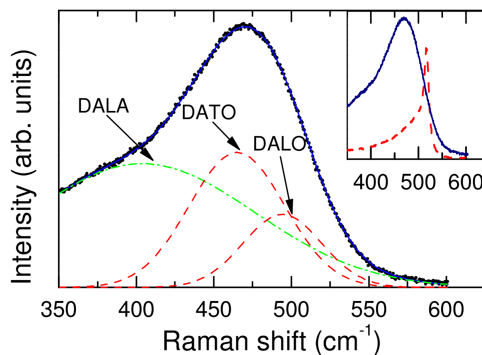

FIG. 5. Raman spectrum from amorphous Si of LTA sample with $t_{SRON} = 5$ nm (black dots), compared to the best fit (blue solid line) once deconvoluted into three different contributions, one acoustic (DATA, green dash-dotted line) and two optical (DATO and DALO, red dashed lines). In the inset, a comparison between the Raman spectra of the same sample before (blue solid line) and after (red dashed line) the annealing treatment at 1150 °C is displayed.

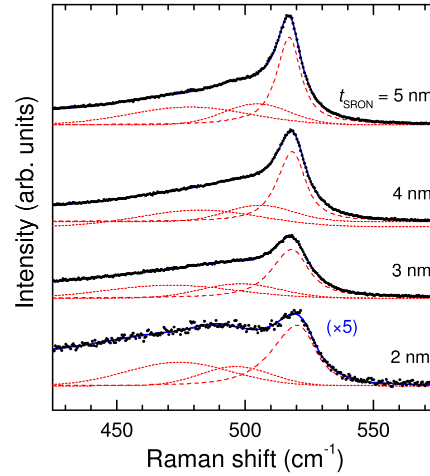

FIG. 6. Experimental Raman spectra in the range of Si optical phonons for samples with $t_{SRON} = 2$, 3, 4, and 5 nm (black dots), together with the best fits (blue full line) obtained by using the lineshape provided by the phonon-confined modes (red dashed line) and including Gaussian functions to account for the optical amorphous contributions (red short-dashed lines), as described in the text.

amorphous contributions and taking into account the previously determined crystalline contribution (see Fig. 6 and Secs. III B and III B I). The intensity factors of the three different amorphous contributions have been left as free parameters in the numerical calculation, whereas their position and their broadening have been taken from the deconvolution of amorphous Si (an interval within 5% of uncertainty was considered in the fitting procedure to account for possible distortions that may affect their lineshapes and positions). A small contribution from the SiO_2 matrix has also been taken into account by including the unpolarized Raman spectrum of SiO_2 with an intensity factor as a free parameter. Although the contribution from the matrix is very small, we found that the best accordance between calculated and experimental curves was achieved when this contribution was taken into account.

From the fits (see Fig. 6), using the data from the crystalline and amorphous contributions, we have evaluated the integrated intensity ratio, I_a^r, between the amorphous modes (i.e., the three disorder optical bands, with overall intensity equal to I_a) and that of the TO-LO band arising from crystalline Si (I_c): $I_a^r = I_a/I_c$. Following this procedure we extracted I_a^r values equal to 1.18, 1.15, 1.16, and 1.16 for $t_{SRON} = 2$, 3, 4, and 5 nm, respectively. These relative intensities can then be used to evaluate the crystalline fraction f_c of the system by using the relation[14]

$$f_c = \frac{1}{1 + \gamma I_a^r}, \tag{5}$$

which considers that the amount of each phase is proportional to its integrated intensity, once corrected for the different scattering cross-section. The factor γ is defined as the relative Raman cross-section of crystalline Si with respect to its amorphous phase and enters in Eq. (5) to include the

[This article is copyrighted as indicated in the article. Reuse of AIP content is subject to the terms at: http://scitation.aip.org/termsconditions. Downloaded to] IP: 161.116.96.5 On: Mon, 30 Jun 2014 14:46:08

different Raman scattering efficiencies of both phases. In the case of bulk Si, it has been reported that the Raman cross-section of crystalline Si is one order of magnitude lower than in each amorphous phase (i.e., $\gamma = 0.1$),[14,26] which is in agreement to what is observed in the inset of Fig. 5 for $t_{SRON} = 5$ nm. This effect is due to the consequence of the scattering process of phonons with $k \neq 0$. In the case of Si-nc, the relative Raman cross-section strongly depends on the crystalline size, as first reported by Bustarret *et al.*[14] According to their work, the effect of crystalline size cannot be neglected to assess the total amount of phase transformed from amorphous to crystalline Si after the annealing process and, in turn, to evaluate the resulting crystalline fraction. For this reason, the relative cross-section γ for each sample was first determined from the Raman spectra of LTA and HTA samples by considering the amount of amorphous phase that is transformed into crystalline one. The integrated intensity of amorphous modes was measured in the same samples before the HTA treatment (i.e., in samples annealed at 900 °C to limit the growth process to only an amorphous state) and afterwards. The intensity of the amorphous contribution has been compared to the integrated intensity of the crystalline modes in the annealed samples, after subtraction of the reminiscent Si-amorphous contributions and correcting for absorption effects. Under these considerations, the relative cross-section γ can be calculated in terms of the expression

$$\gamma = \frac{\alpha^c(1 - e^{-2\alpha^c d_{\mathrm{light}}})}{I_a^{r,a}\alpha^a(1 - e^{-2\alpha^a d_{\mathrm{light}}}) - I_a^{r,c}\alpha^c(1 - e^{-2\alpha^c d_{\mathrm{light}}})}, \quad (6)$$

where the relative scattering volumes are taken into account in terms of the absorption coefficients and the penetration depth imposed by the experimental set-up (d_{light}). In Eq. (6), $I_a^{r,a}$ and $I_a^{r,c}$ are the relative integrated intensities of the amorphous phases with respect to the crystalline ones as respectively obtained in LTA and HTA samples, whereas α^a and α^c are the corresponding absorption coefficients of each kind of samples (see Table II). The superscripts a and c refer to the samples annealed at low temperatures (amorphous Si) and after the HTA treatment (highly crystalline), respectively. In our measurements, it can be assumed that the light penetration d_{light} with the employed Raman configuration was limited to 2 μm, which is mainly determined by the width of the entrance slit of the spectrometer (at 100 μm) that works also as a pin-hole. It is worth mentioning that the absorption coefficients at the probed wavelength (532 nm) were experimentally determined in the studied samples (LTA and HTA ones) by using standard reflectance and transmittance measurements. We found values of the absorption coefficient that are in good agreement with the ones obtained in similar systems (see for instance Ref. 27).

No reliable amorphous signal coming from the LTA sample with $t_{SRON} = 2$ nm was obtained, as the Raman spectrum exhibits a strong background that masks the signal coming from amorphous Si-aggregates. For the rest of the samples, there is an increase of the relative scattering cross-section as the SRON layers get thinner (i.e., for smaller Si-nc), taking values of $\gamma = 0.178$, 0.135, and 0.104 for samples with $t_{SRON} = 3$, 4, and 5 nm, respectively (these results are summarized in Table II).

To obtain information about the dependence of γ on the crystalline size, we have fitted these experimental results to an exponential decay dependence $\gamma(L_{cry}) = \gamma(\infty) + [\gamma(0) - \gamma(\infty)] \times \exp\left[-\frac{L_{cry}}{L_{eff}}\right]$, equivalent to the one proposed by Bustarret *et al.*[14] Imposing that the relative scattering cross-section of very small crystalline domains is equal to that from amorphous aggregates [$\gamma(0) = 1$], and assuming that the one related to very large crystalline domains coincides with bulk Si [$\gamma(\infty) = 0.1$],[14,26] we can restrict the degrees of freedom to only one parameter, that corresponds to the exponential decay factor L_{eff}. In Fig. 7(a), we present the experimental data of γ as a function of the Si-crystalline size, together with the best fit of the exponential decay. An

TABLE II. Absorption coefficient and relative integrated intensities of the amorphous phases (with respect to the crystalline contribution) for amorphous and partially crystalline samples with different SRON thickness (columns 2–3 and 4–5, respectively). The relative scattering cross-section γ (column 6) was calculated from the previous data. The crystalline fraction of each annealed sample (last column) has been evaluated by considering the relative integrated intensity $I_a^{r,c}$ and the corresponding γ values.

t_{SRON} (nm)	α^a (cm^{-1})	α^c (cm^{-1})	$I_a^{r,a}$	$I_a^{r,c}$	γ	f_c (%)
2	6.9×10^2	5.2×10^2	...	1.16	0.235[a]	78
3	2.6×10^3	5.9×10^2	5.00	1.16	0.178	83
4	4.5×10^3	1.2×10^2	4.73	1.15	0.135	87
5	6.1×10^3	1.6×10^2	2.82	1.18	0.104	89

[a]Value extrapolated from the fitted curve. The rest of the γ values were determined from α^c, α^c, $I_a^{r,a}$, and $I_a^{r,c}$.

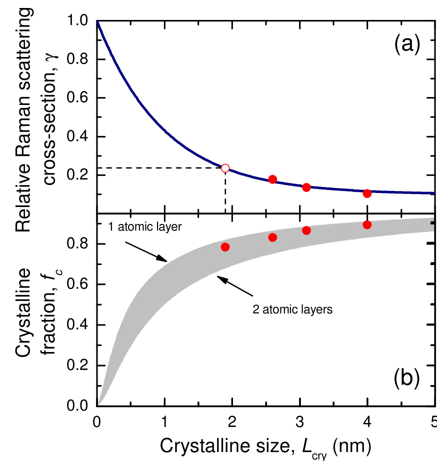

FIG. 7. (a) Relative Raman scattering cross-section γ of crystalline Si with respect to its amorphous phase as a function of the crystalline size. The red points are the experimental data, while the blue solid line corresponds to the function $\gamma(L_{cry}) = 0.1 + 0.9 \times \exp[-L_{cry}]$. The black dashed line indicates γ for the sample with thinner SRON layers ($L_{cry} = 1.9$ nm). (b) Calculated crystalline fraction for the annealed samples, using the I_a^r and γ values from Table II. The shaded region indicates the crystalline fraction of ideally spherical Si-nc with an amorphous shell between 1 (upper limit) and 2 atomic layers (lower limit).

[This article is copyrighted as indicated in the article. Reuse of AIP content is subject to the terms at: http://scitation.aip.org/termsconditions. Downloaded to] IP: 161.116.96.5 On: Mon, 30 Jun 2014 14:46:08

exponential decay factor of $L_{eff} = 1$ nm perfectly reproduces our experimental data. The curve thus obtained allows us to estimate also the relative Raman cross-section for the sample with the smallest Si-crystalline domains [i.e., $\gamma(1.9\text{ nm}) = 0.235$]. This value has been included both in Table II and in the figure (dashed lines).

The determined relative Raman scattering cross-section γ turns out to have values close to that of bulk Si for crystalline sizes larger than $L_{cry} = 4$ nm (see also inset of Fig. 5), while it rapidly increases when the size of the crystalline domains is reduced. This behavior is in contradiction to that previously suggested by Bustarret *et al.* in porous Si,[14] where a decay function with a much longer decay factor of $L_{eff} = 25$ nm was obtained. The latter yields γ values very close to 1 for sizes of some nanometers in diameter (typical of Si-nanocrystals employed in electro-optical studies/applications),[3] overestimating the amorphous contribution in comparison to the crystalline one and, in turn, yielding also underestimated crystalline fractions (see below).[7]

Indeed, the relative Raman scattering cross-section γ already determined can be used to assess the crystalline fraction f_c by using Eq. (5) together with the relative amorphous integrated intensity I_a^r extracted from the Raman spectra of the annealed samples. In Fig. 7(b), we present the crystalline fraction as a function of the crystalline size for the four annealed samples with different SRON layer thickness. We find high crystalline fractions for all samples, which exhibit f_c values of 78%, 83%, 87%, and 89% for samples with $t_{SRON} = 2$, 3, 4, and 5 nm, respectively. Thus, it is concluded that f_c increases with t_{SRON}. Considering that our Si-nc are formed by a crystalline core surrounded by an amorphous shell (core-shell model[10]), the crystalline fraction can provide a direct relation between the crystalline size and the total cluster size, i.e., $f_c = \left(\frac{L_{0,cry}}{L_{0,clu}}\right)^3$. Using these assumptions and the mean crystalline sizes as extracted from the Raman band arising from crystalline Si, we have estimated the total cluster size. The values thus extracted are equal to 2.1, 2.8, 3.3, and 4.2 nm for $t_{SRON} = 2$, 3, 4, and 5 nm, respectively. These values are in excellent accordance to our experimental EFTEM data (see Table I, where L_{clu} values of 2.4, 2.8, 3.3, and 4.1 nm are reported in column 2), which suggests that the employed method provides a reliable evaluation of the crystalline fraction in Si-nc. The sample with the smallest Si-nc shows the largest deviation between both experimental techniques, probably due to the larger uncertainty associated with the small crystalline domains in this sample.

Together with the experimental data from the four samples, we plotted in Fig. 7(b) the crystalline fraction obtained for ideally spherical Si-nc composed by a crystalline core surrounded by an amorphous shell between 1 and 2 Si atomic layers (highlighted in grey).[19] As can be seen in the figure, all our values lie within this region, suggesting that the transition between nanocrystalline silicon and the SiO_2 matrix is practically abrupt. These results are in apparent contradiction with the estimated transition shell thickness reported by Daldosso *et al.*,[28] of about 1 nm. However, their samples consisted of a 200-nm Si-rich oxide, which may not constrain the Si atoms diffusion towards the surrounding SiO_2 matrix, thus forming a thicker amorphous region. Moreover, their theoretical model consisted of a relaxed structure, without considering the influence of the matrix stress exerted on the Si-nc. Actually, the presence of a very thin amorphous shell that surrounds the crystalline core is in perfect agreement with the conclusions of Ref. 9, where the transition shell was found to strongly depend on the Gibbs free energy, which, in turn, is highly influenced by the interfacial stress. Besides, in that work the interfacial stress over the nanoclusters was found to exponentially decrease when the crystalline size was increased, giving rise to a reduction of the thickness of the amorphous transition shell. This result, in agreement with our XRD and Raman results, implies increased crystalline fractions in crystalline Si-nc of increased sizes.

Overall, the results presented in this work confirm the good crystalline quality of Si-nc prepared with the multilayer approach, and also firmly support the non-destructive evaluation by the Raman-scattering technique of the structural properties of Si-nc based materials.

IV. CONCLUSIONS

Multilayers consisting of alternated SRON and stoichiometric silicon oxide layers were deposited on fused silica substrates by means of PECVD, varying the thickness of the SRON layers from 2 to 5 nm. The precipitation and crystallization of the silicon excess from the SRON regions into Si-nc was achieved by a high temperature annealing. EFTEM measurements showed the good structural properties of the resulting nanostructures, with Si-nc sizes proportional to the nominal SRON layer thickness. In turn, XRD measurements confirm the crystalline state of the precipitated Si-nc, suggesting also that these precipitates are subject to a matrix-induced compressive stress. The Raman spectra performed in all the samples were analyzed by considering contributions from crystalline and amorphous phases, using a phonon confinement model and Gaussian-like functions, respectively. By using samples containing amorphous Si-nc, the relative scattering cross-section of amorphous and crystalline phases was evaluated. Finally, the crystalline fraction was determined from the integrated intensities of each phase and considering their relative scattering cross-section. We found crystalline fractions larger than 80% in most samples that scale with the NC size, which is compatible with an amorphous shell thickness between 1 and 2 atomic layers.

ACKNOWLEDGMENTS

The research leading to these results has received funding from the European Community's Seventh Framework Programme (FP7/2007–2013) under Grant Agreement No: 245977, under the project title NASCEnT. The present work was supported by the Spanish national project LEOMIS (TEC2012-38540-C02-01) and MAT2010-16116.

[1] P. Löper, D. Stüwe, M. Künle, M. Bivour, C. Reichel, R. Neubauer, M. Schnabel, M. Hermle, O. Eibl, S. Janz, M. Zacharias, and S. W. Glunz, Adv. Mater. **24**, 3124 (2012).
[2] S. Chan and P. M. Fauchet, Appl. Phys. Lett. **75**, 274 (1999).

[This article is copyrighted as indicated in the article. Reuse of AIP content is subject to the terms at: http://scitation.aip.org/termsconditions. Downloaded to] IP: 161.116.96.5 On: Mon, 30 Jun 2014 14:46:08

[3]J. López-Vidrier, Y. Berencén, S. Hernández, O. Blázquez, S. Gutsch, J. Laube, D. Hiller, P. Löper, M. Schnabel, S. Janz, M. Zacharias, and B. Garrido, J. Appl. Phys. **114**, 163701 (2013).
[4]M. Zacharias, J. Bläsing, P. Veit, L. Tsybeskov, K. Hirschman, and P. M. Fauchet, Appl. Phys. Lett. **74**, 2614 (1999).
[5]J. Heitmann, R. Scholz, M. Schmidt, and M. Zacharias, J. Non-Cryst. Solids **299**, 1075 (2002).
[6]J. Heitmann, F. Müller, M. Zacharias, and U. Gösele, Adv. Mater. **17**, 795 (2005).
[7]S. Hernández, A. Martínez, P. Pellegrino, Y. Lebour, B. Garrido, E. Jordana, and J. M. Fedeli, J. Appl. Phys. **104**, 044304 (2008).
[8]S. Hernández, P. Miska, M. Grün, S. Estradé, F. Peiró, B. Garrido, M. Vergnat, and P. Pellegrino, J. Appl. Phys. **114**, 233101 (2013).
[9]M. Zacharias and P. Streitenberger, Phys. Rev. B **62**, 8391 (2000).
[10]F. Iacona, C. Bongiorno, C. Spinella, S. Boninelli, and F. Priolo, J. Appl. Phys. **95**, 3723 (2004).
[11]A. M. Hartel, D. Hiller, S. Gutsch, P. Löper, S. Estradé, F. Peiró, B. Garrido, and M. Zacharias, Thin Solid Films **520**, 121 (2011).
[12]N. Daldosso, G. Das, S. Larcheri, G. Mariotto, G. Dalba, L. Pavesi, A. Irrera, F. Priolo, F. Iacona, and F. Rocca, J. Appl. Phys. **101**, 113510 (2007).
[13]I. F. Crowe, M. P. Halsall, O. Hulko, A. P. Knights, R. M. Gwilliam, M. Wojdak, and A. J. Kenyon, J. Appl. Phys. **109**, 083534 (2011).
[14]E. Bustarret, M. A. Hachicha, and M. Brunel, Appl. Phys. Lett. **52**, 1675 (1988).
[15]H. Tanino, A. Kuprin, H. Deai, and N. Koshida, Phys. Rev. B **53**, 1937 (1996).
[16]I. Stenger, B. Gallas, L. Siozade, C.-C. Kao, S. Chenot, S. Fisson, G. Vuye, and J. Rivory J. Appl. Phys. **103**, 114303 (2008).
[17]Ch. Ossadnika, S. Vepřeka, and I. Gregora, Thin Solid Films **337**, 148 (1999).
[18]M. Zacharias, J. Heitmann, R. Scholz, U. Kahler, M. Schmidt, and J. Bläsing, Appl. Phys. Lett. **80**, 661 (2002).
[19]S. Adachi, *Properties of Group-IV, III-V and II-VI Semiconductors* (John Wiley & Sons Ltd., 2005).
[20]K. Kůsová, L. Ondič, E. Klimešova, K. Herynková, I. Pelant, S. Daniš, J. Valenta, M. Gallart, M. Ziegler, B. Hönerlage, and P. Gilliot, Appl. Phys. Lett. **101**, 143101 (2012).
[21]R. Guerra, E. Degoli, and S. Ossicini, Phys. Rev. B **80**, 155332 (2009).
[22]T. Arguirov, T. Mchedlidze, M. Kittler, R. Rölver, B. Berghoff, M. Först, and B. Spangenberg, Appl. Phys. Lett. **89**, 053111 (2006).
[23]R. Rölver, S. Bruninghoff, M. Först, B. Spangenberg, and H. Kurz, J. Vac. Sci. Technol. B **23**, 3214 (2005).
[24]H. Hofmeister and P. Ködderitzsch, Nanostruct. Mater. **12**, 203 (1999).
[25]S. Wei and M. Y. Chou, Phys. Rev. B **50**, 2221 (1994).
[26]M. H. Brodsky, M. Cardona, and J. J. Cuomo, Phys. Rev. B **16**, 3556 (1977).
[27]L. Khriachtchev, M. Räsänen, S. Novikov, and L. Pavesi, Appl. Phys. Lett. **85**, 1511 (2004).
[28]N. Daldosso, M. Luppi, S. Ossicini, E. Degoli, R. Magri, G. Dalba, P. Fornasini, R. Grisenti, F. Rocca, L. Pavesi, S. Boninelli, F. Priolo, C. Spinella, and F. Iacona, Phys. Rev. B **68**, 085327 (2003).

[This article is copyrighted as indicated in the article. Reuse of AIP content is subject to the terms at: http://scitation.aip.org/termsconditions. Downloaded to] IP: 161.116.96.5 On: Mon, 30 Jun 2014 14:46:08

4.1.1.4. Phase Imaging and Identification in Si NC Multilayers within Different Dielectric Matrices

Despite the high resolution of TEM images, only the crystalline phase of Si NCs oriented along a high-symmetry crystalline direction can be observed, without having much information regarding phases and/or stoichiometry changes. Consequently, the core-shell morphology of these nanostructures is hardly distinguished, and the combination of different TEM configurations is necessary. In Paper III [79], an analysis method has been proposed to retrieve this structural information from Raman scattering spectra. Paper IV [85] presents a new approach, which takes into account the possibility of treating the EELS spectra at different sample points in order to discern the main plasmon energy contribution at each sample position. This way, phase imaging is achievable, and different electronic properties of the material system under study can be evaluated.

For the present study, Si NC superlattice samples were investigated. In this case, not only the SiO_2 matrix was investigated but also the Si_3N_4 and SiC ones. Given that Si NCs have proved to be very sensitive to high-voltage experiments ($\sim$ 300 kV), the field emission gun was operated at an energy of 80 keV. EELS spectra were acquired at different points of the sample where Si NCs and surrounding matrix were expected, in order to form a spectral mapping of the zone. Afterwards, each spectrum was fitted by Lorentzian-like functions around the plasmon energy peak, the parameter that allowed to distinguish the different compounds present within each sample (the plasmon peak energy values for c-Si and the different matrices under study are summarized in Tab. 4.3). After this analysis, and after selecting the component with major signal contribution within a certain pixel, a plasmon energy map is obtained. Other parameters could be evaluated by means of the reported method, giving information not only of the chemical composition of the Si NCs and their surroundings but also on structural and physical properties (such as involved thicknesses and the electron effective mass).

The described method in the paper was employed to analyse three samples containing Si NCs superlattices in three different matrices: SiO_2, Si_3N_4 and SiC. When focusing on the Si NCs / SiO_2 system, the plasmon maps revealed a plasmon energy difference between the pure dielectric and the surroundings of the nanostructure, which indicates the formation of a nitrogen-rich silicon oxide as expected from the employed precursor gases (note that the deposited Si-rich layers already contained N). The case of Si NCs / SiC multilayers was not so straightforward, since the poorer size confinement resulted in larger nanostrcutures, and the EELS contribution measured in the NCs had much lower impact than it did in the other matrices. Indeed, this fact indicates a strong Si diffusion that strongly affects the multilayer structure, and a generalized coalescence was present. Finally, in the case of Si NCs / Si_3N_4 superlattices, the Si NC size is preserved, although the spectra required further mathematical data filtering than in SiO_2 systems owing to the weaker low-energy peaks characteristic of the nitride matrix.

Table 4.3.: Plasmon energy values corresponding to the different materials studied in this work.

Compound	c-Si	SiO_2	Si_3N_4	SiC
Plasmon Energy (eV)	1.67	22.5	23.7	21.5

In fact, the obtained results in Paper IV [85] regarding the morphology and composition of Si NCs and their surroundings, as well as the superlattice structure maintenance, have been confirmed by other techniques reported in other works (see previous results in this Section 4.1.1 for SiO_2, or Section 4.1.2 for SiC). This reveals that, by means of the reported EELS analysis method, it is possible to obtain direct information regarding the chemical, electronic and structural properties of NC superlattices.

Nanoscale

PAPER

View Article Online
View Journal | View Issue

Cite this: *Nanoscale*, 2014, **6**, 14971

Published on 06 October 2014. Downloaded by Universitat de Barcelona on 02/12/2014 15:14:44.

Retrieving the electronic properties of silicon nanocrystals embedded in a dielectric matrix by low-loss EELS

Alberto Eljarrat,*[a] Lluís López-Conesa,[a] Julian López-Vidrier,[a] Sergi Hernández,[a] Blas Garrido,[a] César Magén,[b,c] Francesca Peiró[a] and Sònia Estradé[a,d]

Received 2nd July 2014,
Accepted 3rd October 2014

DOI: 10.1039/c4nr03691c

www.rsc.org/nanoscale

In this work we apply low-loss electron energy loss spectroscopy (EELS) to probe the structural and electronic properties of single silicon nanocrystals (NCs) embedded in three different dielectric matrices (SiO_2, SiC and Si_3N_4). A monochromated and aberration corrected transmission electron microscope has been operated at 80 kV to avoid sample damage and to reduce the impact of radiative losses. We present a novel approach to disentangle the electronic features corresponding to pure Si-NCs from the surrounding dielectric material contribution through an appropriate computational treatment of hyperspectral datasets. First, the different material phases have been identified by measuring the plasmon energy. Due to the overlapping of Si-NCs and dielectric matrix information, the variable shape and position of mixed plasmonic features increases the difficulty of non-linear fitting methods to identify and separate the components in the EELS signal. We have managed to solve this problem for silicon oxide and nitride systems by applying multivariate analysis methods that can factorize the hyperspectral datacubes in selected regions. By doing so, the EELS spectra are re-expressed as a function of abundance of Si-NC-like and dielectric-like factors. EELS contributions from the embedded nanoparticles as well as their dielectric surroundings are thus studied in a new light, and compared with the dielectric material and crystalline silicon from the substrate. Electronic properties such as band gaps and plasmon shifts can be obtained by a straightforward examination. Finally, we have calculated the complex dielectric functions and the related electron effective mass and density of valence electrons.

1. Introduction

Because of the high availability and low cost of the technological processes involved, silicon-based devices represent the dominant technology for photovoltaic applications both at research and production stages. Theoretically, the efficiency of a bulk silicon solar cell is limited by the fixed band gap energy of this material.[1] In order to overcome this limitation, alternative structures such as tandem solar cells have been proposed.[2,3] In this tandem configuration, the bulk silicon is complemented with one or more solar cells presenting different band gap energies.

A suitable approach is a superlattice (SL) layer that is composed of ordered silicon nanocrystals (Si-NCs) embedded in a dielectric medium.[4] The functionality in this type of nanostructure is related to the Si-NC band gap energy, higher than the one of bulk silicon. The size and spatial distribution of the Si-NCs and the surrounding dielectric medium greatly influence the performance of the final photovoltaic device. Moreover, we know that some of the most important properties of the system are sensitive to subtle changes in the electronic properties of the single Si-NC, such as quantum confinement (QC) of charge carriers, as first discovered in porous Si.[5] Due to the QC effect, this value is inversely proportional to particle size. It is because of this property that control of the NC size and the environment is crucial for the final application of these nanostructures. In practice, this represents a complex problem given that the diameter of the particles should be typically below ~5 nm for the QC effect to be significant.

Beyond these morphological concerns, the experimental techniques that are commonly used for the assessment of performance in these systems – photo- and electro-luminescence,

[a]*MIND-IN2UB, Departament d'Electrònica, Universitat de Barcelona, Martí i Franqués 1, 08028 Barcelona, Spain. E-mail: aeljarrat@el.ub.edu*
[b]*Laboratorio de Microscopías Avanzadas (LMA) – Instituto de Nanociencia de Aragón (INA) and Departamento de Física de la Materia Condensada, Universidad de Zaragoza, 50018 Zaragoza, Spain*
[c]*Fundación ARAID, 50018 Zaragoza, Spain*
[d]*TEM-MAT, Centres Científics i Tecnològics (CCiT), Universitat de Barcelona, Solís i Sabarís 1, Barcelona, Spain*

This journal is © The Royal Society of Chemistry 2014

View Article Online

Published on 06 October 2014. Downloaded by Universitat de Barcelona on 02/12/2014 15:14:44.

charge transport measurements, Raman scattering spectroscopy, to name a few – do not allow us to obtain a direct functional characterization of the individual components. However, different techniques available in transmission electron microscopy (TEM) allow accessing these properties at high spatial resolution. In particular, high resolution (HR-) and energy filtered (EF-) TEM are the most commonly employed techniques. As a combination of structural and chemical characterizations, EFTEM has been intensively used in the evaluation of the Si-NC size after deposition.[3,6,7]

This work aims to characterize Si-NCs embedded in different dielectric materials by means of energy loss spectroscopy (EELS) data obtained from aberration corrected scanning transmission electron microscopy (STEM), using a monochromated sub-eV energy resolution probe. We present here an original methodological approach for EELS data treatment to elucidate the ultimate electronic properties of the Si-NCs. The reasons to propose this strategy stem from the nature of the sample, as will be explained in the following paragraph. The direct result of this approach is the separation of the low-loss EELS contribution of the Si-NCs by multivariate analysis methods. Indirectly, we will be able to obtain properties that are measured or calculated from low-loss EELS. In this sense, plasmon and band gap energies are measured from the shape of certain spectral features; complex dielectric functions and electron effective masses are derived from the spectrum. Three of the most common components in silicon-based photovoltaic devices, silicon dioxide (SiO_2), silicon nitride (Si_3N_4) and silicon carbide (SiC) matrices, will be considered, demonstrating the robustness of the proposed methodology of data analysis.

The analyzed samples are multilayer stacks combining dielectric material and Si-enriched layers where Si-NCs precipitate during the post-deposition annealing treatment.[3,6,8] In this configuration, the Si-NCs are completely surrounded by the dielectric material, and it is unlikely to prepare an electro-transparent TEM specimen that will give a direct and pure Si-NC low-loss EELS measurement in a STEM experiment. In other words, the surrounding material will be present over and/or under the NC in the TEM lamella, so that the incident e^- will go through it and will contribute to the EEL spectra in the NC region. The reason for this limitation is the size of the NCs, below 10 nm in diameter, and the geometry of the embedded particle and matrix system. Moreover, in our TEM experiments it was not possible to obtain a direct measurement of the pure contribution of the Si-NC to the spectra. As in the related literature,[9,10] all the measured spectra present a mixture of nanoparticle and matrix contributions at least. Nevertheless, in this work we show that indirect low-loss EELS calculations revealing the electronic and structural properties of the Si-NCs are feasible by the appropriate use of computational methods. In our case, factorization of the EELS spectrum image (SI) using multivariate analysis (MVA) algorithms, in combination with phase identification and segmentation techniques, enables us to separate the contribution of the Si-NC to the EELS spectra. The selected algorithms, non-negative matrix factorization (NMF),[11] and Bayesian linear unmixing (BLU),[12] have been proven useful for the analysis of other signals present in the EELS spectrum such as surface plasmon resonances[13] or core-loss edges.[14]

The following sections give a detailed description of the studied systems and the experiments performed, as well as a precise account of the computational methods applied to EELS data to disentangle the electronic properties of Si-NCs at the nanoscale.

2. Experiment

The samples considered for the present study, designed as active layers for tandem solar cells, consist of silicon-based multilayer stacks combining stoichiometric- and Si-rich-based dielectric layers. Three dielectric materials were used as a barrier: SiO_2, SiC and Si_3N_4. The respective non-stoichiometric layers were: silicon rich oxynitride, carbide and nitride (SRON, SRC and SRN). The layers were deposited by plasma-enhanced chemical-vapor deposition (PECVD) with thicknesses below 5 nm. After the deposition process, the Si excess is precipitated, and phase separation is induced in order to achieve the Si-NC formation. For this purpose, different accumulative annealing treatments are used, with temperatures ranging from 1100 °C to 1150 °C depending on the compound and, in the SiC sample, a previous annealing step at 600 °C. The final goal is the formation of a silicon quantum dot superlattice, on top of a bulk silicon solar cell (see Fig. 1 for a diagram of the structure). More information regarding the NC superlattice preparation may be found in ref. 8 for the SiO_2 sample, in ref. 3 for the SiC sample and in ref. 6 for the Si_3N_4 sample.

Electro-transparent samples for STEM observation in cross-section geometry were prepared by conventional mechanical polishing and low angle Ar^+ ion milling. In all cases, previous observations were performed in a JEOL J2010 F (S)TEM with a Schottky field emission gun operated at 200 keV. These

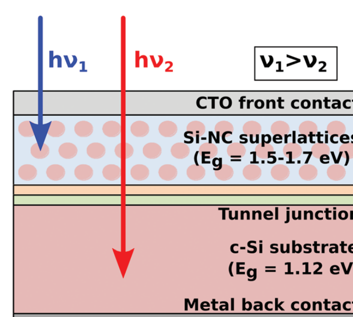

Fig. 1 Tandem solar cell schematic diagram, showing the arrangement of the Si-NC superlattices on the top of the c-Si solar cell. Arrows represent the incoming solar radiation, the high-energy photons (blue arrow) being absorbed by the higher band gap energy material, whereas the low-energy ones (red arrow) are absorbed within the c-Si bottom cell. CTO stands for conductive transparent oxide.

 This journal is © The Royal Society of Chemistry 2014

Published on 06 October 2014. Downloaded by Universitat de Barcelona on 02/12/2014 15:14:44.

measurements evaluated the quality of the fabricated multilayers, routinely measuring abruptness and homogeneity of the layers.[6,8,15] EFTEM experiments confirmed the formation of Si-NCs within alternative layers in the stack, and could give an average crystal size. As expected, crystal sizes were found to be related to the silicon-rich layer thickness, in our cases around or below 5 nm. From these first observations, it was clear that conventional electron microscopy would not suffice for the characterization of Si-NCs and their environment.

Furthermore, some preliminary experiments indicated that higher voltages in STEM mode (*i.e.* 300 keV) and/or larger acquisition times could damage Si-NCs and their environment, modifying or even destroying the studied structures in the process. Given the beam sensitivity of the Si-NCs, low accelerating voltages were used in the experiment. Moreover, as the experiment is usually designed to minimize radiation dosage by maximizing acquisition speed and reducing beam current density, the acquired spectral data may be affected by a low signal to noise ratio (SNR). Nevertheless, since the plasmon signal is the strongest one in the EELS spectrum but for the zero loss peak (ZLP), the acquisition of low-loss EELS at low accelerating voltages and short acquisition times is feasible, in terms of SNR, when probing beam-sensitive materials. A probe-corrected FEI Titan 60-300 (S)TEM operated at 80 kV and equipped with a high-brightness field emission gun (X-FEG), a Wien filter monochromator and a Gatan Tridiem 866 ERS spectrometer was used to obtain the EELS data at high spatial resolution.

Three sets of low-loss EELS-SI and simultaneously acquired high-angle annular dark field (HAADF) images were obtained, from SiO_2, SiC and Si_3N_4 samples, respectively. A collection angle of ~2.5 mrad, a convergence angle of ~26 mrad, and an acquisition time of 0.03 s per spectrum were employed in the acquisition of the EELS data. Pixel sizes between 0.2 and 0.6 nm were selected for the EELS-SIs. The microscope conditions were thus adjusted to acquire HAADF-EELS datasets containing a few Si-NCs and a portion of the barrier layer. Exceptionally, for the silicon carbide sample, bigger datasets were acquired containing more than one period to describe wider scale structural phenomena. Large areas of the specimens in relation to pixel size were covered in this way with no apparent beam damage. According to the full width at half maximum (FWHM) measured from the ZLP of the EELS-SI, energy resolution was kept below 0.2 eV in all experiments.

3. Analytical methodology

The large amount of raw data obtained for each system motivated the development of a simple yet fast and powerful computational treatment based on the prior identification of phase compositions through model based fitting and segmentation of the datasets by mathematical morphology techniques. In this way we analyzed a collection of EELS-SI with hundreds of pixels and 2048 spectral channels each.

A general treatment was applied to all datasets to retrieve information from the spatially localized spectra. The first part of the applied treatment is based on experience gathered through our recent studies on low-loss EELS of semiconducting devices,[16,17] in which the characterization of the plasmon peak revealed structural and compositional information from the examined materials. Following a standard low-loss analysis scheme, all spectra had their energy axis calibrated using the ZLP and a measure of their relative thickness, t/λ, was obtained, from which the absolute thickness of the material can be estimated. This is important because plural scattering contribution to the spectra from thicker specimens can pose a problem to further analyses of the data. Additionally, a Fourier-log algorithm was used to produce single scattering distribution (SSD) spectra that can be compared to the original spectra to assess the impact of plural scattering.

3.1. Identification and segmentation of data regions

The plasmon peak in bulk c-Si has an energy of ~16.7 eV, while the dielectric materials studied in this work have higher energy plasmons, ~22.5 eV for SiO_2, ~23.7 eV for Si_3N_4 and ~21.5 eV for SiC. This difference is large enough to distinguish each material by its characteristic plasmonic signature in the EELS spectra. An example of this, illustrated with EELS spectra from the SiO_2 sample, can be examined in Fig. 2(a) and (b). These spectra contain all the features that we examined in this work: the ZLP around 0 energy loss, the onset of valence transitions at low energies, and the plasmon peaks as the most intense feature in the low-loss region. Plasmon peaks were fitted, using a simple Lorentz model, with 2 fitting regions. These regions were selected according to the position of the low-loss maxima. As the Si-NC plasmon becomes apparent over the "pure dielectric" signal, the fit energy window is modi-

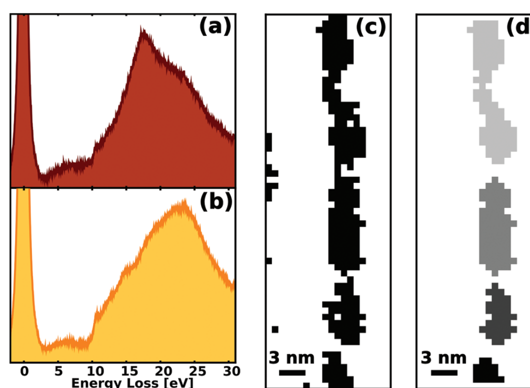

Fig. 2 Panels (a) and (b) show typical EELS spectra from the SiO_2 sample, acquired in the Si-rich and barrier regions, respectively. Panel (c) shows a binary mask resulting from the thresholding of an EELS-SI from SiO_2. In this case, the pixels portrayed in black color have been found to contain spectra with $E_P < 19$ eV. Panel (d) shows the map of individual elements labeled as "dominant Si-NC" regions generated from the previous mask after selecting only connected regions.

This journal is © The Royal Society of Chemistry 2014

Published on 06 October 2014. Downloaded by Universitat de Barcelona on 02/12/2014 15:14:44.

fied to adjust only the area around the Si-NCs plasmon. For each spectrum the fit window is centered on its intensity maximum, which is also a fitting parameter.

From the analysis of a given EELS-SI with this method, a plasmon energy, E_P, map is produced which we then analyze through a histogram thresholding approach. Our aim here is to identify regions of the dataset where spectra and their neighbors show "dominant Si-NC" or "pure dielectric" plasmonic features according to a defined threshold depending on the material. For this plasmon fingerprinting we impose the condition that a certain pixel of the E_P map (associated with a spectrum in the EELS-SI) is labeled as belonging to one of these two classes: the dominant Si-NCs (in fact a mixture of Si-NCs and the surrounding matrix) or the dielectric phase. However, the allocation of each pixel to a specific class (technically, Boolean masks, at this stage) generated by this approach alone may not be useful for various reasons. First, thresholding alone applied to an image may generate a mask including disconnected small spatial features, see Fig. 2(c), like separate regions of only a single or a few pixels without physical meaning. Also, spatial features may appear to be connected and identified as one alone although only joined by a few pixels. Finally, it is desirable to identify big enough yet separate spatial features in the EELS-SI no matter what shape they may have. For this purpose, we developed an application in the framework of the Hyperspy toolbox† that takes advantage of some computer vision tools included in the *n*-dimensional image analysis library of scientific Python (ndimage in SciPy). Operating over the binary identification maps, mathematical morphology operations act as a fast and powerful filter on the mask, allowing us to select the degree of connectivity required from the regions to be labeled. Namely, the E_P map is filtered using binary opening and closing operations, with a structural element that selects only connected regions. Once a filtered mask has been produced, see Fig. 2(d), the labels are assigned in a simple and straightforward step. The result is the possibility to locate a spatial region of the original EELS-SI whose spectra fulfill a certain requirement, then access it regardless of its shape, and operate with it as a separate sub-dataset with the same number of dimensions as the original dataset. Additionally, the size of the identified region is automatically measured as the number of pixels that fulfill the imposed conditions.

After this procedure, a collection of sub-datasets allocated to the class of "dominant Si-NCs" or "pure dielectric" regions was generated. All the results presented in this work were achieved taking those regions as a starting point. For example, by averaging the spectra within them, noise-free spectra can be obtained that reveal the characteristic EELS features from the region. As will be shown in the following sections, using this strategy one can obtain material information or, depending on the case and region, obtain close estimates of the Si-NC or dielectric EELS data.

† hyperspy.org

3.2. MVA factorization

Our analysis continued by focusing on the factorization of the low-loss EELS spectra by MVA within the detached subsets of data of the class "dominant Si-NCs" features. MVA factorization is performed using computational tools that analyze a given matrix of spectral data and decompose it into a number of components. These components constitute additive contributions to a model of the EELS data, and are expressed as the product of the corresponding factors and abundance maps. Factors have the same number of channels as the input EELS spectra and an associated abundance map indicating its spatial distribution, with the same number of pixels as the original EELS-SI. A legitimate guess is that one might be able to retrieve the contribution associated with the Si-NCs by performing a factorization of the whole EELS-SI by using MVA algorithms. It turns out that for most cases this is a difficult task because low-loss EELS is not always optimized as a direct input for MVA. The major reason for this is the fact that, in many cases, the presence of different phases in the examined materials translates into an energy shift of the plasmon peaks, associated with the transition between phases. This peak shift, which is usually an interesting subject of study, increases the number of dimensions for the factorization. As a result, multiple factors appear associated with a single shifting feature, hindering the interpretation of the results. With these limitations in mind, MVA factorization was performed on the aforementioned sub-datasets, which are characterized by the mixture of two competing contributions, the Si-NC plasmon peak over a dielectric-type background peak.

MVA factorization has been traditionally performed in the EELS community using decomposition by principal component analysis (PCA), followed by blind source separation (BSS) by independent component analysis (ICA).[18–22] The application of such an approach to low-loss EELS has an additional difficulty because the mutually independent sources assumption in ICA may not be necessarily fulfilled in the hyperspectral data. In this work we have used two different methods, the non-negative matrix factorization (NMF, included in Hyperspy),[13] and the Bayesian linear unmixing (BLU, presented by the authors as a Matlab code).[12,23] These two algorithms have in common the so-called positivity assumption, *i.e.* sources are supposed to be positive. This constraint fits well to the nature of EELS spectra, as no negative contribution is expected. Conversely, the BLU algorithm applies an extra additivity constraint to the sources, meaning that the sum of all contributions should be equal from pixel to pixel. Additionally, as this algorithm is initialized by a set of factors determined from a geometrical algorithm (N-FINDR in this work), the resulting set of factors is expected to be related to the ability to find pixels which contain the purest spectral contributions as possible (the least mixed pixels).

We added spike removal and Poisson normalization steps to the data prior to the application of any of these MVA algorithms [Keenan04]. In the first step, spikes are detected by

Published on 06 October 2014. Downloaded by Universitat de Barcelona on 02/12/2014 15:14:44.

thresholding the first derivative of the spectral data and removed by spline interpolation. In the second one, the Poissonian nature of the statistical distribution in EELS is taken into account, and data are normalized to approach a Gaussian distribution. With this normalization we expect to improve the suitability of the input data for the BLU algorithm, as a Gaussian statistical distribution is one of the hypothetical requirements for BLU. Both methods are also included in Hyperspy, and a Matlab application was developed in order to use the Poisson-normalized datacubes in conjunction with the BLU program.

3.3. Optoelectronic properties from EELS

Apart from the chemical information contained in the plasmon peak, low-loss EELS from a semiconductor specimen contains information from interband transitions, as well as the band gap of dielectric and semiconductor materials, among others. The methodology exposed so far allows us to obtain information from these in single EEL spectra and average spectra from the identified regions (direct measurements), and MVA factors (indirect measurements). Additionally, a Kramers–Kronig analysis (KKA) was carried out on the spectra to demonstrate the extraction of the complex dielectric function (CDF). A link exists between the EELS and the CDF of a given bulk material based on the semi-classical formula for the single scattering distribution (SSD),[24,25]

$$\mathrm{SSD}(E) = \frac{I_0 t}{\pi a_0 m_0 v^2} \log[1+\beta/\theta_E] \Im[-1/\varepsilon(E)] \tag{1}$$

where I_0 is the elastic scattering (ZLP) intensity, t is the sample thickness, a_0 is the Bohr radius, m_0 is the electron rest mass, v is the electron velocity, β is the collection angle, θ_E is the characteristic angle for inelastic scattering at a given energy loss E, and ε is the energy dependent CDF. Thus the pre-logarithmic factor, which will be called K, depends only on the ZLP intensity and the electron kinetic energy T. The logarithmic factor will be called the angular correction, $\Theta(\beta,E)$.

The first step in KKA is to normalize the SSD, which we obtain from the EELS spectrum of a thin sample to set $\Im[-1/\varepsilon(E)]$. For the normalization step of KKA we have used two main approaches depending on the availability of refractive index values. If this value is available, the sum-rule of the Kramers–Kronig relations allows us to calculate the constant part of the above formula, K,

$$K = \left(1-\frac{1}{n^2}\right)^{-1} \frac{2}{\pi} \int_0^\infty \frac{\mathrm{SSD}}{\Theta(\beta,E)} \frac{\mathrm{d}E}{E} \tag{2}$$

Also, this approach allows measuring the thickness of the sampled region from the expression of K in eqn (1). The refractive indices of all the bulk materials involved in this work are well known, so this approach may be used for the spectra from the dielectric barriers or the crystalline silicon substrate. However, the values to be used for the Si-NCs MVA factors are not clearly known, since n depends on particle size.[26] For this reason, we have developed an alternative approach for the normalization step that rests on the previous estimation of the absolute thickness of the sampled region.[27] In this thickness normalization step, we use the value of t calculated in an adjacent region, of known n,

$$K = \frac{I_0 t}{\pi a_0 m_0 v^2} = \frac{I_0 t}{T 332.5} \left[\frac{\mathrm{nm}}{\mathrm{keV}}\right] \tag{3}$$

Also, for each KKA a measure of the intensity (the sum of channel values) of the ZLP is necessary. In the case of the MVA factors, this value is not directly available because the ZLP has to be cropped off or subtracted before MVA factorization. We measured and stored the t/λ values using the total and ZLP intensities, I_T and I_0, respectively, for each pixel. Using this value we can relate the integral of a given EELS signal, I_S, with the value of the ZLP intensity to which it would theoretically correspond using the following formula,

$$t/\lambda = \log(I_T/I_0) = \log(1+I_S/I_0) \tag{4}$$

Hence, ZLP intensity values that are needed for the normalization step in the KKA of MVA factors can be estimated from the t/λ mean value in a region were the factor is the dominant spectral feature (the highest abundance). The KKA algorithm used, with the two normalization options, is implemented for Hyperspy, and is available to the public through the development version of this toolbox. Also, using this toolbox, every spectrum was prepared for KKA in a similar way: first by subtraction of the modeled ZLP tail and then by an extension of the plasmon tail by interpolation of a power law, with forced-negative exponent, up to the next power of two (4096 channels). Any spurious intensity levels remaining before or inside the ZLP subtraction window (typically set to [0.5,1] eV) were smoothed out using a Hanning taper.

The response of the material to incident electromagnetic radiation is represented by its CDF, which may be compared to other CDFs usually derived from optical measurements. From this result we have also derived electron effective masses for conduction electrons, using an analysis proposed in ref. 28. This analysis is based on the relation between E_P, the electron concentration at this energy, n_{eff}, and the high frequency dielectric constant, ε_∞,[29,30]

$$m^* = \frac{n_{\mathrm{eff}} \hbar^2}{E_P{}^2 \varepsilon_0 \varepsilon_\infty} \tag{5}$$

All these quantities can be measured or derived from the spectral data or the CDF in a straightforward way. For instance, the plasmon energy may be measured from the spectral data using a Drude model based fit. Meanwhile, ε_∞ and n_{eff} are derived from the CDF of the material, also following ref. 28. The electron effective mass derived from this formula is related to the electron mobility and determined by the shape of the conduction band near its bottom. Finally, a measurement of the atomic (molecular) density of electrons involved in the valence plasmon excitation is available if one provides the

This journal is © The Royal Society of Chemistry 2014

View Article Online

Published on 06 October 2014. Downloaded by Universitat de Barcelona on 02/12/2014 15:14:44.

atomic (molecular) density of the studied material. This value was also obtained as a check of coherence for our calculations.

4. Results and discussion

Fig. 3 shows some examples of EELS spectra for the three sets of samples according to the different dielectric matrix (SiO_2, SiC and Si_3N_4 as labeled in the figure). For each matrix, a pair of spectra representative of the classes "Si-NCs" or "pure dielectric" (labeled as a barrier) are drawn. In these plots, the raw spectra are presented as color-filled areas, and the black lines define the averaged spectra of a specific sub-dataset of each class, identified following the segmentation procedure explained above. In the figure, the improvement of the SNR from raw to average spectra is evidenced. But interestingly enough, it is also noticed that the spectra from the class "dominant Si-NC regions" present significant differences depending on the matrix, revealing the impact of the different dielectric backgrounds.

Although this will increase the difficulty in analyzing and interpreting results from the spectra, EELS may be the less problematic STEM technique for extracting information arising solely from the Si-NCs. This was already pointed out in ref. 9, where EELS was shown to be the appropriate technique for a complete and accurate structural characterization of the particles. Other methods were not a reliable source of structural and chemical information regarding the Si-NCs (BFTEM, HAADF, or t/λ imaging). Fig. 4(a)–(c) present some examples of this, and will be thoroughly discussed in the following section. A summary of the obtained parameters (band gap and plasmon energy, and electron effective mass) for the three measured samples can be found at Table 1.

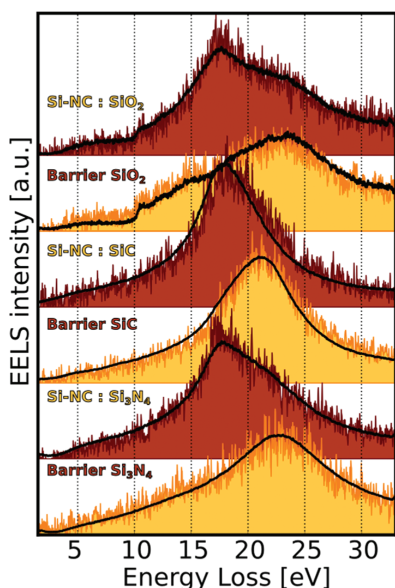

Fig. 3 Raw (color-filled areas) and average (black lines) EELS spectra from the three examined samples. The spectra are averaged or extracted from regions identified as belonging to the class of "dominant Si-NCs" or to the class of "dielectric" using threshold values of the E_P plasmon distribution.

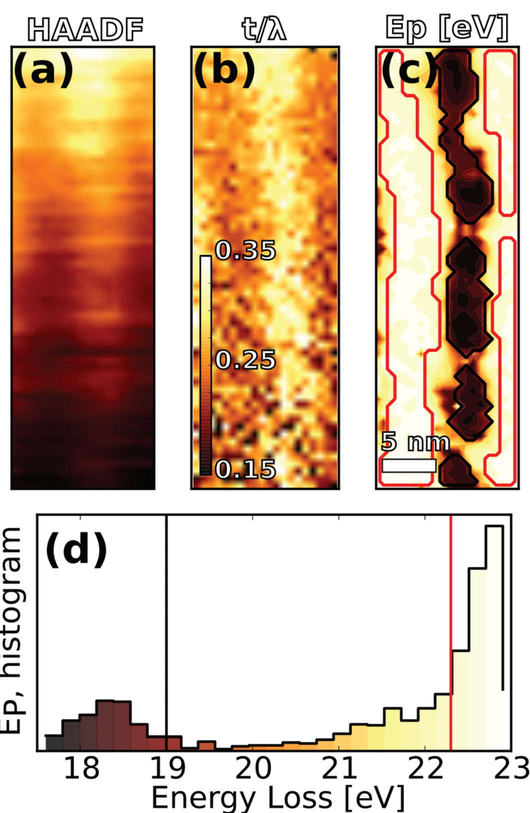

Fig. 4 Panel (a) displays the HAADF intensity while (b) and (c) show the t/λ and E_P, respectively, of the simultaneously acquired EELS-SI from a SiO_2 sample. Panel (d) shows the histogram corresponding to the E_P map in (c). In both the last panels black and red lines indicate the threshold of the "dominant Si-NC" and "pure dielectric" regions. The generating process of the same "dominant Si-NC" regions is illustrated in Fig. 2.

Table 1 Summary of the band gap and plasmon energies and the electron effective masses, obtained for the three different samples in regions of interest. Note that for SiO_2 and Si_3N_4, the values presented from barrier regions are obtained by averaging, while the ones from the matrix and Si-NC regions are obtained by MVA. For SiC, only averaging is used, as explained in the text

Region		E_B/eV	E_P/eV	m^*/m_0
SiO_2	Barrier	9.5	23.7	—
	Matrix	9.5	22.7	0.188
	Si-NC	3.0	17.3	0.129
SiC	Barrier	2.5	21.5	—
	Si-NC	—	17.5	—
Si_3N_4	Barrier	4.0	22.7	—
	Matrix	4.0	22.7	0.160
	Si-NC	3.5	17.8	0.133
c-Si substrate		1.3	16.9	0.1

This journal is © The Royal Society of Chemistry 2014

Published on 06 October 2014. Downloaded by Universitat de Barcelona on 02/12/2014 15:14:44.

4.1. Silicon oxide barriers

Fig. 4 presents some results from one of the HAADF-EELS datasets corresponding to the SiO_2 system. Fig. 4(a) shows the HAADF-STEM intensity image obtained in a region that contains both a silicon enriched SiO_2 layer and the SiO_2 barrier, and Fig. 4(b) and (c) show the t/λ ratio and the E_P maps, respectively, as calculated from the corresponding EELS-SI. The faint contrast through the center of both HAADF and t/λ maps indicates the presence of the Si-rich layer. Also, the t/λ around 0.25 tells us that this is a very thin sample and that the impact of plural scattering to EELS should be low. An alternative to the E_P map is to represent the values of the E_P as a histogram of frequencies as shown in Fig. 4(d). The latter is useful to understand the color code in the map and to assess the E_P distribution. The two significant classes are easily distinguished in the histogram where E_P thresholds of 19 eV and 22.3 eV, indicated by lines in Fig. 4(d) and by region contours in Fig. 4(c), were selected to define the class of "dominant Si-NC" or "pure dielectric" features. Note also that the energy resolution of the experiment, indicated by the ZLP, is below 0.2 eV, the size of one bin in the histogram.

The barriers and the Si-rich region seem to be well defined, with little variation of E_P through consistent areas. While E_P for these areas is below 23 eV, the corresponding plasmon maximum is ~23.7 eV, due to the asymmetric shape of this peak. It is now clear that the examined area contains a full dielectric barrier, which spans along the left side of the image, a total of 4 Si-NC regions, featured at the center, and part of a second barrier, along the right side. The picture also shows that the extent of the dielectric layer and Si-rich layers has remained unchanged, both layers having ~5 nm width. Similarly, the Si-NCs appear to be confined inside the Si-rich layer. Other areas of this SiO_2 multilayer were scanned in the same fashion, showing similar results along the different periods.

Once the regions are defined, average spectra may be obtained from the pixels within. Two of these spectra, from the "dominant Si-NC" region in the center of the image and the "pure dielectric" barrier at the left side, are shown as black lines in the first two panels of Fig. 3. The raw spectra that are shown below the lines as color-filled areas were hand-picked from a single pixel within these two regions. Some features evidence the presence of a contribution from a dielectric-like inelastic scattering to the EELS in the Si-NC region. The major one is the presence of a shoulder at ~24 eV that can be related to the SiO_2 plasmon, present at this energy. Also, a strong peak onset at ~9.5 eV and spanning several more eVs is detected, related with the band gap of SiO_2. This is in accordance with our picture of crystalline silicon particles embedded in a dielectric medium giving an overlapped contribution to EELS, but not a direct confirmation.

However, MVA factorization by the NMF method proved to be useful as an indirect method for this confirmation. Let us use the specific region highlighted at the top of Fig. 4(c) to present the results. Fig. 5(a) shows the three main factors

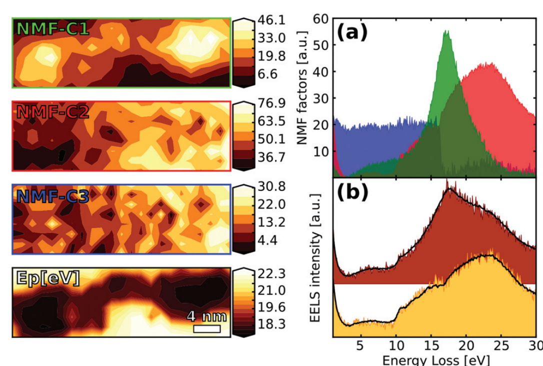

Fig. 5 MVA analysis by NMF of Si-NCs in the oxide sample. In panel (a), the main factors related to the Si-NCs (green), the dielectric barrier (red) and a detector (blue). The three upper left panels show the corresponding abundance of these factors using the same RGB color coding. Meanwhile, a reconstruction of the EELS from the decomposition model *vs.* the raw EELS is shown in panel (b). Finally, a panel with the plasmon energy map for the same area is located in the lower left panel.

extracted from NMF. The contributions to the EELS from both dielectric and Si-NC phases are identified with the first two components. Using a RGB code we assign green color to the C1 component related to the Si-NCs, red color to the component C2 associated with the dielectric contribution, and blue color to C3 that reveals a sudden change in sensibility in the detector at a specific energy.

The number of factors used for NMF was chosen firstly by an examination of the explained variance plot after PCA and secondly by comparison of the decomposition reconstructed signal with the spectra (residuals method). The plot in Fig. 5(b) illustrates this method; the two NMF reconstructed spectra (lines) and two raw spectra from the region show good accord.

The three left panels in Fig. 5 show the abundance maps corresponding to these three factors. Note also that these plots are rotated 90° clockwise with respect to the map in Fig. 4(c), and that a rotated E_P map included at the lower panel at the left hand side can be used as a reference. The spatial distribution of these components evidences two Si-NCs (in accordance with the E_P map) with a variable dielectric background. The last component (blue) presents noise and the intensity step in the middle of the detector (channel number 1024) with a rather random spatial distribution and smaller abundance than the other two. Thus, this last component has a smaller relative weight than the first two.

In summary, the factorization reveals that the EELS contributions corresponding to the Si-NC and the SiO_2 matrix have plasmon maxima of ~17.3 eV and ~22.7 eV. The 1 eV energy shift between the SiO_2 in the barrier (~23.7 eV, plasmon maximum) and around the particle surroundings indicates the probable formation of a nitrogen oxide in the matrix, because of the growth process employing silicon rich oxynitride (SRON).[8] The absence of further plasmon shifting within the barrier indicates a low and homogeneous diffusion of nitrogen from the SRON layers through the dielectric.

This journal is © The Royal Society of Chemistry 2014

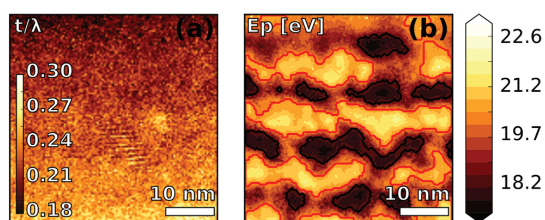

Fig. 6 Panels (a) and (b) display the t/λ and E_P maps, respectively, calculated from the same EELS-SI of the carbide sample. Black and red lines are used, as in Fig. 4(c), as region boundaries.

Published on 06 October 2014. Downloaded by Universitat de Barcelona on 02/12/2014 15:14:44.

4.2. Silicon carbide barriers

For the SiC sample we succeeded in acquiring and analyzing large EELS-SI, with sizes of more than 120 × 120 pixels. The resulting t/λ and E_P maps are shown in Fig. 6. The area covered in this image spans over 3 periods of the multilayer (more than 40 × 40 nm^2), with a pixel-to-pixel resolution smaller than 0.4 nm. Smaller EELS-SI were also acquired and analyzed, as for oxide and nitride samples, but the use of a wider region was justified for studying a larger scale structural phenomenon in the carbide sample using the chemical sensitivity of low-loss EELS. Again, t/λ is used to confirm that the TEM sample is particularly thin in the examined region, around 0.25 times the electron inelastic mean free path, bda. No contrast related with the difference in λ from Si-NC and the dielectric region is found in this image, Fig. 6(a). Nevertheless, some faint fringes can be distinguished at the center of the image, coming from the elastic scattering contrast in the ZLP intensity (equivalent to bright-field imaging), which are indicative of the presence of a crystalline particle. The simultaneously acquired HAADF image (not shown) showed weak contrast in relation to the Z-contrast of the silicon particles in the carbide medium, not useful for the characterization of either particles or barriers.

Fig. 6(b) shows the E_P map with lines at the thresholds of 18.5 eV (red line) and 20.3 eV (black line) with a procedure similar to the one used for the previous sample, to depict the "dominant Si-NC" and "pure dielectric" regions, respectively. These numbers reflect the fact that silicon and silicon carbide plasmons are much closer than in the case of silicon oxide, for which the thresholds were 19 eV and 22.3 eV, respectively. The EELS spectra in the mid-panels of Fig. 3, taken from Si-NC and dielectric regions, also evidence this closeness. From the examination of the maps obtained from this sample, we can tell that the dielectric barriers and silicon rich layers underwent some kind of segregation process. This process is first evidenced by the inhomogeneity of the interfaces between layers. Although the dielectric and silicon rich multilayer structure is preserved, the gradient of E_P values through the map evidences an unintended inter-diffusion of the layers in the growth direction. Also, attending to the energy resolution of the system, below 0.2 eV, the plasmon energies detected in the sample are only spatially consistent (meaning E_P values close to one of the expected values for the two classes) in small areas. In fact, the dielectric barriers do not always show pure silicon carbide energy, indicating that the diffusion from the silicon-rich layer modifies the chemical composition of the barrier layer. Finally, the inhomogeneity of the Si-NCs size is greater than that in the other samples, with some coalescence and out-of-plane growth observed.

MVA factorization of the EELS data was also tested in this dataset, and the separation of a component related to the Si-NCs plasmon was possible. However, it was difficult or impossible to obtain a consistent component associated with the silicon carbide background. We suspect that a continuous change in the position of the silicon carbide plasmon caused by the variability in composition and the faulty separation of phases in the sample might be responsible for this. Thus, no MVA results are shown in this case. Nevertheless, it seems that the EELS low-loss features from this sample are sharp and differentiated when averaging inside the "dominant Si-NC" and "pure dielectric" regions (see Fig. 3). This indicates that the EELS contribution measured in the "dominant Si-NC" region has a much smaller impact in the dielectric phase than in SiO_2 and Si_3N_4 samples, owing probably to the bigger size of the formed Si-NCs. Taking these considerations into account we generated some spatially averaged EELS spectra and examined them in order to identify both band gap and plasmon features. In these spectra a strong signal with an onset at ~2.5 eV is evident, owing to the band gap energy of the SiC. No signal at lower energies could be consistently detected in this case. This indicates that the band gap signal of the Si-NCs, if present, is faint over the delocalized band gap signal of the surrounding SiC. For the plasmon peak, the contrast between regions is clear in both energy and width. The barrier material from the center of the "pure dielectric" regions presents a broad plasmon peak at ~21.5 eV. This peak transforms continuously to lower energies as we examine regions farther away, down to a sharp peak at ~17.5 eV at the center of the "dominant Si-NCs" regions.

4.3. Silicon nitride barriers

As for the previous two samples, the silicon nitride multilayer was probed by HAADF-EELS acquisition and analyzed using a similar methodology. Fig. 7 presents three plasmon energy maps for this sample obtained in different regions of the multilayer stack. Black and red lines show the nature of the EELS plasmon in the enclosed regions, "dominant Si-NC" and "pure dielectric", respectively. To obtain these, the same energy thresholds as in SiO_2, 19 eV and 22.3 eV, have been used since the involved phases (Si-NC and Si_3N_4) show similar plasmon energies. Concerning the morphology, the configuration of barriers and Si-rich layers is preserved, as in the case of SiO_2. However, for the Si_3N_4 the contribution of the dielectric plasmon as a background to the EELS data in "dominant Si-NC" regions is not as evident as in the oxide case. This is because silicon nitride lacks the strong and characteristic low-energy peaks of the silicon oxide EELS features.

 This journal is © The Royal Society of Chemistry 2014

Published on 06 October 2014. Downloaded by Universitat de Barcelona on 02/12/2014 15:14:44.

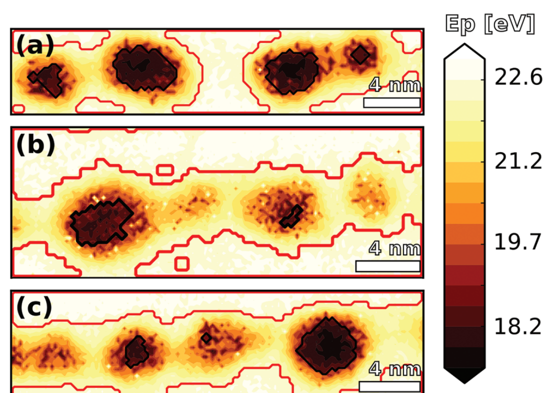

Fig. 7 Panels (a)–(c) feature plasmon energy maps from different EELS-SI acquired in the nitride sample. Black and red lines are used, as in Fig. 4(c) and 6(b), as region boundaries.

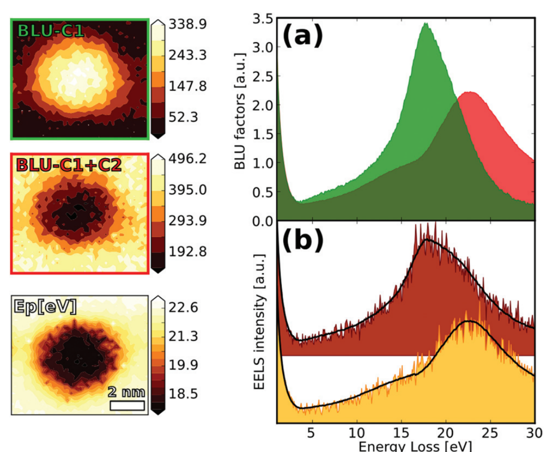

Fig. 8 MVA analysis of Si-NCs in the nitride sample by BLU. Panel (a) shows the estimated main factors related to Si-NCs (green) and a mixture of dielectric and instrument-related components (red). The two upper left panels show the abundance of the factors in panel (a), using the same red-green color coding. Meanwhile, a reconstruction of the EELS from the decomposition model *vs.* the raw EELS is shown in panel (b). Finally, the plasmon energy map for the same area is located in the lower left panel.

Yet, MVA was able to separate the contributions of Si-NC and the dielectric background to the EELS data in the "dominant Si-NC" region. Fig. 8 shows an example of MVA analysis of the particle at the right hand side of Fig. 7(c). In this case we used a BLU algorithm with three components and a wider spatial crop in order to include the dielectric regions on the top and bottom of the particle. The resulting components show an analogous result to the NMF applied to SiO_2. One of these components contained the Si-NC factor with an abundance map localized around the particle, *i.e.* green factor in Fig. 8(a). The other two components contained the same dielectric background plasmon convolved with a small positive or negative intensity step from the detector. When they were added, this contribution canceled out leaving only the background peak, *i.e.* red factor in Fig. 8(a). We also observe a good correspondence between the modeled spectra after decomposition and the raw spectra, depicted in Fig. 8(b). The contribution from the Si-NC particle in Fig. 8 is related to a plasmon energy of ~17.8 eV. The barrier and matrix dielectric plasmon energies determined from averaging and factorization were measured at ~22.7 eV. From this correspondence we expect the dielectric material from the barrier and particle surroundings to have a similar composition, just altered in the nearest vicinity of the Si-NC. In fact, some "pure dielectric" regions are found to exist in the silicon-rich layer, surrounding the Si-NCs, see Fig. 7(a), which supports this assumption.

From the E_P maps presented in Fig. 7 and the BLU abundance maps in Fig. 8, it seems that the particles formed in the silicon nitride matrix are rounder than the ones formed in silicon oxide (and, of course, carbide). We expect the Si-NCs formed in SiO_2 to occupy irregular volumes, as shown in the tomographic study of ref. 9. Conversely, some of the Si-NCs in Si_3N_4 are not completely formed while Si-NCs in SiO_2 appear to have a very homogeneous distribution of sizes. It could be argued that their EELS signal is lower because much smaller Si-NCs are formed in Si_3N_4 in comparison to other systems. Nevertheless, no plasmon shift associated with the smaller size of these particles was found, indicating that these nanoparticles may not be fully crystalline.

Our plasmon energy measurements have to be interpreted in the context of QC theory, in which the plasmon peaks of Si-NCs show higher plasmon energy than that measured in c-Si (~16.9 eV). Nguyen *et al.*[10] propose a phenomenological formula to relate plasmon energy with particle size in a case similar to ours. Following this formula, a plasmon energy of 17.8 eV is related to crystalline Si nanoparticles with diameters around 5.1 nm. In this sense, the obtained values are in excellent agreement with the previous results on plasmon energy shift from QC effects.

A final consideration about the measured Si-NC plasmon energies for all systems is that no consistent shift of this feature related with (apparent) particle size was found. Bearing in mind that the QC effect implies an inverse relation between particle diameter and plasmon energy, this indicates that crystalline particle sizes and environments are similar throughout each sample. The different apparent size occupied by each "dominant Si-NC" region in the E_P map may be identified with the real size of a separate particle. However, our measures indicate that as the Si-NC plasmon energies for these regions are similar, they must contain Si-NCs of similar real size, according to QC. This contradicts in many cases the conclusion that one could, *a priori*, extract from an examination of the apparent sizes of the particles in the raw plasmon energy images.

These considerations do not affect our belief that the separation between particles and surrounding materials, in terms of EELS signal, has been proven feasible. One of the main

This journal is © The Royal Society of Chemistry 2014

Published on 06 October 2014. Downloaded by Universitat de Barcelona on 02/12/2014 15:14:44.

reasons is the smaller delocalization distance for the quantum-confined Si-NC plasmon than for the band gap. Also, the relatively small difference between the dielectric functions of the Si-NCs and surrounding materials, which will be calculated in the following section, diminishes the effects of interface plasmons.[31] We should also mention that for any MVA technique, peak energy shifting and the existence of an intense background signal would affect negatively the final result.[32] In low-loss EELS we easily obtain both effects, the shifting of the plasmons linked to gradients in concentration or strain being a well-known feature in a wide range of samples. To complete the list, ZLP intensity is typically several orders of magnitude above any other feature in low-loss EELS data. This means that MVA techniques are unsuitable to solve problems in which a continuous plasmon shift is a dominant feature or in which the ZLP masks out the desired feature, like in low-lying band gap energies. In our case, the energy stability of the plasmons in selected areas and the correct alignment of the ZLP and energy windows before the MVA have been the key to enable successful NMF and BLU analyses.

To summarize, we have presented three different cases where the analysis of EELS maps is an advantageous technique when compared to other TEM-based approaches, although convolution of the interesting features is an inherent difficulty. In previous studies, a model-based fit containing two Drude plasmons approach proved also reliable.[33] Nevertheless, when applied to these systems it fails to give consistent measurements of neither E_P nor width for all the studied systems. Our present experience indicates that this double plasmon model will only be reliable when the fitted features are well separated in energy and exhibit significant differences in FWHM, *i.e.* a low energy narrow peak *vs.* a high energy wide peak (as in the case of Si-NCs in a SiO_2 matrix). Conversely, when analyzing plasmonic features that are very close in energy and width, this method may not be reliable and may lead to uninterpretable or wrong results (as in Si-NCs in SiC and Si_3N_4 matrices). Other studies that have examined Si-NCs in a silicon nitride matrix using a model-based fit analysis of EELS data found much higher variability of the calculated plasmon energy data for the background.[10] Moreover, an additional disadvantage is that EELS data acquired from thin specimens will be naturally noisy as the inelastic scattering signal is diminished. In spite of all these difficulties, our phase identification and segmentation technique, complemented with factorization by NMF and BLU algorithms, has proved to be capable of extracting valuable information. The following and last section will be devoted to the more complex aspects of the low-loss analysis.

4.4. Optoelectronic properties of the Si-NCs

KKA was used to calculate the CDF from the available spectra, namely, the "pure dielectric" region averaged spectra, the Si-NC and dielectric background spectra from MVA factors, and crystalline silicon (c-Si) single spectra acquired from the substrate (see Fig. 9).

In both silicon oxide and nitride cases, the first step was to perform KKA on the spectra identified as dielectric signals,

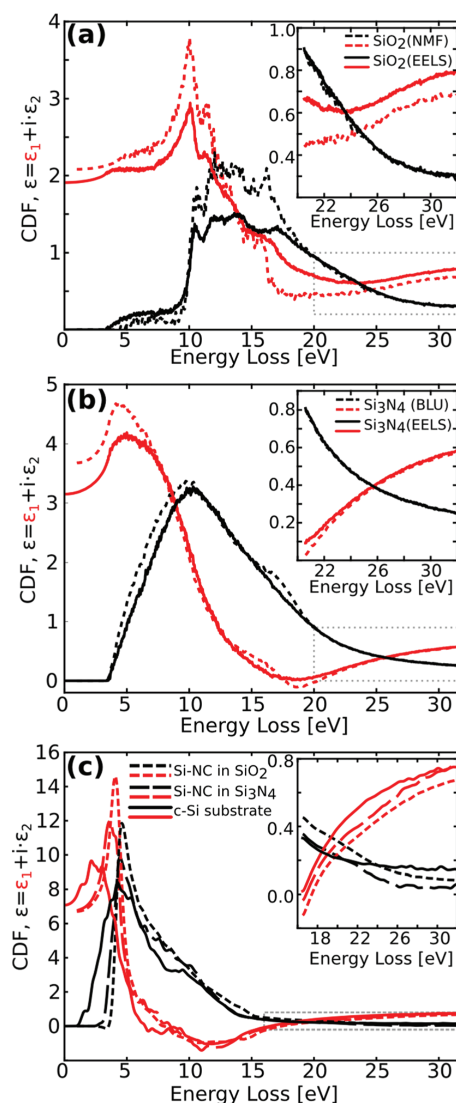

Fig. 9 CDF calculated from the KKA of experimental EELS spectra and MVA factors. In all of them, the real and imaginary parts of the CDF are indicated with red and black colors, respectively. Panels (a) and (b) contain the CDF calculated from silicon oxide and nitride; EELS spectra from the regions (solid lines) or NMF and BLU factors (dashed lines), respectively. Panel (c) contains the Si-NCs CDF calculated from NMF and BLU, from the oxide and nitride samples, respectively, in dashed lines. Also in this panel is the CDF from the EELS spectrum of c-Si substrate, in solid lines. The insets show in detail the higher energy parts of the CDFs, marked using dashed line squares.

using the corresponding refractive index for each material,[34] $n_{SiO_2} = 1.5$ and $n_{Si_3N_4} = 2$. For the MVA factors, the ZLP intensities were calculated from the signal integral and the mean of the calculated t/λ from a selected "pure dielectric" region of the EELS dataset. Both dielectric CDFs, from MVA factors and

View Article Online

Published on 06 October 2014. Downloaded by Universitat de Barcelona on 02/12/2014 15:14:44.

average spectra, showed excellent accordance with one another.

These CDFs are depicted in Fig. 9(a) and (b); note that while the correspondence for silicon nitride is almost perfect, the silicon oxide functions differ in their intensity and plasmon position. This is an expected result, as the EELS average spectrum from the barrier region (SiO_2) differs in plasmon position and width from the EELS contribution from the dielectric surrounding the Si-NC (SRON). Sample thickness values were obtained thanks to the use of the t/λ value for the normalization. Both samples were confirmed to be particularly thin in the examined regions, with $t \sim 48$ nm and $t \sim 18$ nm for the silicon oxide and nitride matrices, respectively. This value is used for the normalization step in the KKA of the MVA factors identified as Si-NC signals. Again, the t/λ mean values for the dominant Si-NC regions linked the signal integral with the ZLP intensity. It was found that this value is typically bigger than that in the dielectric region, indicating a decrease in the electron mean free path, λ, associated with the presence of Si-NC. The Si-NC CDFs were then calculated, see Fig. 9(c), showing good agreement between the results for both particles within the silicon oxide and nitride matrices. For the sake of completeness we also applied KKA to retrieve the CDF from a single spectrum acquired at the c-Si substrate in the silicon nitride system, see Fig. 9(c).

An inherent disadvantage of measuring optoelectronic properties using EELS is the difficulty to recover the information lying at very low energies (*e.g.* band gaps, typically below 5 eV), due to the rather intense tails of the ZLP. However, we have been able to measure band gap energies in our samples and to add this information to our derived CDF, thanks to the good energy resolution in our experiments (*i.e.* ZLP FWHM below 0.2 eV). For the silicon oxide barrier sample, the band gap feature of SiO_2 is observed at ∼10 eV, in good accordance with the literature.[35] This value is also in good accordance with our idea of low and homogeneous nitrogen diffusion from the silicon rich layer (SRON) to the SiO_2 in the barrier.

The band gap in Si_3N_4, measured at ∼4 eV, is lower than the 5 eV value expected from the pure dielectric. Anyhow, this is already in accordance with the measured plasmon energy shift in the barriers from the expected 23.7 eV to the obtained 22.7 eV. We can postulate the formation of a SiN_x ($x < 1$) type matrix, and a general growth mechanism for the Si-NCs from nucleation until a critical size after which coalescence takes over, as in ref. 36, 37 and 10. The authors of those studies attributed the decrease in plasmon energy to an increase of Si–Si bond concentration in the material. Our measurement of both plasmon and band gap energies exhibit a solidary red-shift of ∼1 eV, indicating a consistent energy shift of the whole band structure near the Fermi energy or the addition of new levels.[38–40] Additionally, other studies,[6] on similar samples measured by EFTEM, estimated that 15% of the volume of the dielectric barrier is distributed around the Si-rich layer and around the Si-NC. This measurement is in good accordance with our observations, *e.g.* the "pure dielectric" region in between particles in Fig. 7(a).

The indirect band gap for c-Si is found at energies between 1.2 and 1.4 eV, and it is possible to measure this signal in the EELS spectra from bulk samples.[41] We confirmed the ability of our system to obtain this measurement using c-Si spectra acquired at the substrate of the samples. The CDF from the c-Si substrate is shown in Fig. 9(c) (note the onset of the imaginary part). One may expect to detect a similar indirect band gap signal also in the case of an embedded particle system. In the case of the Si-NCs, we should expect this signal to appear at higher energies, owing to quantum confinement,[26] but below 2–3 eV. However, no such feature was found in any of the Si-NC regions in the SiO_2 and Si_3N_4 systems. It was also impossible to measure any consistent contribution to the spectral intensity levels below ∼3 eV for the Si-NC MVA factors or average spectra from the "dominant Si-NC" regions. We believe that the lack of the silicon indirect band gap signal in these embedded-particle systems should be attributed to the fact that particle dimensions are comparable to the electron delocalization distance, of ∼10 nm for the spectrum at low energy losses.[19,25]

Arguably, this does not exclude the possibility that a contribution from the indirect band gap is present in our low-loss EELS data. On the one hand, this contribution would be among the less intense in the low-loss range, making it difficult to detect above the tail of the ZLP, the band gap signal from the surrounding material, and the noise level. On the other hand, we cannot neglect the possibility that electron energy losses apart from the ones related with the semi-classical interpretation of inelastic scattering may have an impact on the measured EELS spectra (see eqn (1)). García de Abajo treats many of these cases,[24] among them the excitation of Čerenkov radiation and the case of a composite material in which the grain size affects the interface-to-volume loss ratio. Although we are not able to consistently measure such contributions and the use of a low energy beam (80 keV) theoretically reduces the possibility for Čerenkov radiation excitation, we cannot discard the possibility that a mixture of spurious losses could be affecting the measurement of the indirect band gap. Surface losses, whose relative importance increases as sample thickness decreases, were subtracted in the usual way in the KKA algorithm.[25]. The fact that surface loss contribution is relatively more important in the thinner Si_3N_4 sample meant that KKA algorithm required more iterations (10 instead of 5 in the case of the Si-NC CDF) to reach proper convergence. Finally, the shape and energy of the features detected at ∼3–3.5 eV allows us to relate this measurement to the Tauc optical absorption gap, the direct band gap feature of the Si-NC.[26,42,43]

Again, these results are in good correspondence with the QC model for Si-NCs of this size range. Although recent reports have stated that the electronic properties for small Si-NCs could exhibit smaller band gaps than the quantum-confined ones,[44] we believe that these additional features will only be of importance in Si-NCs whose size is around or below the 1 nm range. In this case it would be troublesome to characterize these effects, as the low-loss EELS from particles of such a

This journal is © The Royal Society of Chemistry 2014

View Article Online

Published on 06 October 2014. Downloaded by Universitat de Barcelona on 02/12/2014 15:14:44.

small size will be affected very strongly by delocalized scattering from the surrounding material.

The electron effective mass, m^*, related to carrier mobility can be derived from the CDF.[28] For the Si-NC in silicon oxide and nitride matrices, m^* values of 0.129 m_0 and 0.133 m_0 ($m_0 = 9.11 \times 10^{-31}$ kg) were obtained, respectively. Meanwhile, for the c-Si substrate, a value of 0.1 m_0 was obtained. By supposing an equal atomic density for c-Si and Si-NC of 50.2 nm^{-3}, an atomic density of electrons, n_{eff}, of ~3 electrons was obtained, actually higher for the Si-NCs, up to 3.5, in Si_3N_4. In the case of crystalline silicon, as the *k*-space surfaces of constant energy are ellipsoids, this quantity consists of a combination of the transversal and longitudinal electron effective masses. The generally accepted value of m^* for c-Si is 0.26 m_0, with a valence electron density of 4 electrons per atom.[45] Note that the obtained m^* and n_{eff} values are below the expected. This appears to be a general trend for EELS measurements, as in the work of ref. 28, where the m^* and n_{eff} calculated values for III–V nitride samples were smaller than the theoretically expected ones. However, the good correspondence with other techniques and the possibility to combine the chemical information also present in the spectra justify the use of EELS for the calculation of m^* values. Moreover, our calculation indicates an approximate correspondence of the values for c-Si and the Si-NCs, with an increase of the m^* and n_{eff} in the Si-NCs.

5. Conclusions

Our phase identification and segmentation technique proved that a selective averaging of spectra from regions allocated to a specific "dominant Si-NC" or "pure dielectric" class can enhance the SNR in spectra, thus preserving the features of the EELS spectrum containing valuable information about the probed regions. We showed how MVA can be used to disentangle the individual spectral contributions to the characteristic EELS spectrum of the embedded particle system: the Si-NC and background dielectric signals.

The plasmon energies measured in the SiO_2 barriers are consistent with the literature and indicate mostly pure dielectric barriers that do not suffer from such effects as inhomogeneous silicon or nitrogen diffusion. Conversely, in the case of SiC and Si_3N_4 barrier systems, the significant shifts of the plasmon energy indicate an overall inhomogeneity in composition that can be related to the diffusion of silicon from the Si-rich layer. Moreover, the inhomogeneous shape and distribution of Si-NCs in the SiC sample as compared with the other two indicate that diffusion severely affected the shape of the multilayer structure, with generalized coalescence of the Si-NCs and deformation of the barrier interfaces.

In the SiO_2 case, NMF allowed separating a spurious intensity step in the detector and recovering each contribution as a separate component. This was not possible in the Si_3N_4 case, in which we showed that BLU allowed for the separation of the Si-NC contribution in one component whereas two other components contained the mixed contributions from dielectric plasmon and intensity steps. The different results after applying NMF or BLU highlight the differences between both techniques, *i.e.* the geometrical initialization and additivity constraint of BLU. Both analyses were enabled by the previous use of spike removal and Poisson normalization steps.

A detailed report on the electronic analysis of the EELS data and the derived MVA factors was given. Different KKA normalization steps were employed, using the refractive index or the thickness, depending on the available data. The derived CDFs of the dielectric material in the barriers, the dielectric material surrounding the Si-NCs, and the Si-NCs themselves provided valuable insights into the structural properties of the systems after the growth process. These CDF were compared to the CDF from a c-Si substrate area. Good accordance between the compared CDFs was found, and plasmon and band gap energies (including the quantum confinement effect within the Si-NCs) were taken into account for an optoelectronic characterization of the materials. Finally, electron effective masses and the approximate density of electrons for c-Si and the Si-NCs have been calculated and compared with the expected values.

Acknowledgements

Electron microscopy characterization has been carried out using the TEM facilities of the "Scientific and Technological Centres" (Universitat de Barcelona) and the "Laboratorio de Microscopías Avanzadas" at "Instituto de Nanociencia de Aragón" (Universidad de Zaragoza). The authors acknowledge LMA-INA for offering access to their instruments and expertise. The research leading to these results has received funding from the European Community's Seventh Framework Programme (FP7/2007–2013) under grant agreement no. 245977, under the project title NASCEnT. The present work was supported by the Spanish national projects MAT2010 numbers 16116 and 16407 and CSD-2009-0013 and also by the Catalan government through projects CAM (P2009/ESP-1503) and SGR2014-672.

References

1 F. Meillaud, A. Shah, C. Droz, E. Vallat-Sauvain and C. Miazza, *Sol. Energy Mater. Sol. Cells*, 2006, **90**, 2952–2959.
2 G. Conibeer, M. Green, E.-C. Cho, D. König, Y.-H. Cho, T. Fangsuwannarak, G. Scardera, E. Pink, Y. Huang, T. Puzzer, S. Huang, D. Song, C. Flynn, S. Park, X. Hao and D. Mansfield, *Thin Solid Films*, 2008, **516**, 6748–6756.
3 J. López-Vidrier, S. Hernández, J. Samà, M. Canino, M. Allegrezza, M. Bellettato, R. Shukla, M. Schnabel, P. Löper, L. López-Conesa, S. Estradé, F. Peiró, S. Janz and B. Garrido, *Mater. Sci. Eng., B*, 2013, **178**, 639–644.
4 M. Zacharias, J. Heitmann, R. Scholz, U. Kahler, M. Schmidt and J. Bläsing, *Appl. Phys. Lett.*, 2002, **80**, 661–663.

This journal is © The Royal Society of Chemistry 2014

View Article Online

Published on 06 October 2014. Downloaded by Universitat de Barcelona on 02/12/2014 15:14:44.

5 L. T. Canham, *Appl. Phys. Lett.*, 1990, **57**, 1046–1048.
6 A. Zelenina, S. A. Dyakov, D. Hiller, S. Gutsch, V. Trouillet, M. Bruns, S. Mirabella, P. Löper, L. López-Conesa, J. López-Vidrier, S. Estradé, F. Peiró, B. Garrido, J. Bläsing, A. Krost, D. M. Zhigunov and M. Zacharias, *J. Appl. Phys.*, 2013, **114**, 184311.
7 S. Hernández, J. López-Vidrier, L. López-Conesa, D. Hiller, S. Gutsch, J. Ibáñez, S. Estradé, F. Peiró, M. Zacharias and B. Garrido, *J. Appl. Phys.*, 2014, **115**, 203504.
8 J. López-Vidrier, Y. Berencén, S. Hernández, O. Blázquez, S. Gutsch, J. Laube, D. Hiller, P. Lóper, M. Schnabel, S. Janz, M. Zacharias and B. Garrido, *J. Appl. Phys.*, 2013, **114**, 163701.
9 A. Yurtsever, M. Weyland and D. A. Muller, *Appl. Phys. Lett.*, 2006, **89**, 151920.
10 P. D. Nguyen, D. M. Kepaptsoglou, Q. M. Ramasse and A. Olsen, *Phys. Rev. B: Condens. Matter*, 2012, **85**, 085315.
11 C.-J. Lin, *Neural Comput.*, 2007, **19**, 2756–2779.
12 N. Dobigeon, S. Moussaoui, M. Coulon, J.-Y. Tourneret and A. Hero, *IEEE Trans. Signal Process.*, 2009, **57**, 4355–4368.
13 O. Nicoletti, F. de la Pena, R. K. Leary, D. J. Holland, C. Ducati and P. A. Midgley, *Nature*, 2013, **502**, 80–84.
14 L. Yedra, A. Eljarrat, J. M. Rebled, L. López-Conesa, N. Dix, F. Sánchez, S. Estradé and F. Peiró, *Nanoscale*, 2014, **6**, 6646–6650.
15 C. Summonte, M. Allegrezza, M. Bellettato, F. Liscio, M. Canino, A. Desalvo, J. López-Vidrier, S. Hernández, L. López-Conesa, S. Estradéé, F. Peiró, B. Garrido, P. Lóper, M. Schnabel, S. Janz, R. Guerra and S. Ossicini, *Sol. Mater. Sol. Cells*, 2014, **128**, 138–149.
16 A. Eljarrat, S. Estradé, v. Gačević, S. Fernández-Garrido, E. Calleja, C. Magén and F. Peiró, *Microsc. Microanal.*, 2012, **18**, 1143–1154.
17 A. Eljarrat, L. López-Conesa, C. Magén, v. Gačević, S. Fernā¡ndez-Garrido, E. Calleja, S. Estradé and F. Peiró, *Microsc. Microanal.*, 2013, **19**, 698–705.
18 A. Hyvärinen and E. Oja, *Neural Networks*, 2000, **13**, 411–430.
19 M. Bosman, L. J. Tang, J. D. Ye, S. T. Tan, Y. Zhang and V. J. Keast, *Appl. Phys. Lett.*, 2009, **95**, 101110.
20 F. de la Peña, M.-H. Berger, J.-F. Hochepied, F. Dynys, O. Stephan and M. Walls, *Ultramicroscopy*, 2011, **111**, 169–176.
21 T. Yamazaki, Y. Kotaka and Y. Kataoka, *Ultramicroscopy*, 2011, **111**, 303–308.
22 J. Bioucas-Dias, A. Plaza, N. Dobigeon, M. Parente, Q. Du, P. Gader and J. Chanussot, *IEEE J. Sel. Top. Appl. Earth Obs. Remote Sens.*, 2012, **5**, 354–379.
23 N. Dobigeon and N. Brun, *Ultramicroscopy*, 2012, **120**, 25–34.
24 F. J. García de Abajo, *Rev. Mod. Phys.*, 2010, **82**, 209–275.
25 R. Egerton, *Electron Energy-Loss Spectroscopy in the Electron Microscope*, Springer, US, 3rd edn, 2011.
26 R. Guerra, F. Cigarini and S. Ossicini, *J. Appl. Phys.*, 2013, **113**, 143505.
27 D. T. L. Alexander, P. A. Crozier and J. R. Anderson, *Science*, 2008, **321**, 833–836.
28 M. H. Gass, A. J. Papworth, R. Beanland, T. J. Bullough and P. R. Chalker, *Phys. Rev. B: Condens. Matter*, 2006, **73**, 035312.
29 W. G. Spitzer and H. Y. Fan, *Phys. Rev.*, 1957, **106**, 882–890.
30 H. R. Chandrasekhar and A. K. Ramdas, *Phys. Rev. B: Condens. Matter*, 1980, **21**, 1511–1515.
31 V. J. Keast and M. Bosman, *Mater. Sci. Technol.*, 2008, **24**, 651–659.
32 M. Bosman, M. Watanabe, D. Alexander and V. Keast, *Ultramicroscopy*, 2006, **106**, 1024–1032.
33 A. Eljarrat, L. López-Conesa, J. M. Rebled, Y. Berencén, J. M. Ramírez, B. Garrido, C. Magén, S. Estradé and F. Peiró, *Nanoscale*, 2013, **5**, 9963–9970.
34 E. Palik, *Handbook of optical properties of solids*, Academic, Orlando, 1985.
35 M. Couillard, A. Yurtsever and D. A. Muller, *Phys. Rev. B: Condens. Matter*, 2008, **77**, 085318.
36 F. Delachat, M. Carrada, G. Ferblantier, A. Slaoui, C. Bonafos, S. Schamm and H. Rinnert, *Physica E*, 2009, **41**, 994–997.
37 F. Delachat, M. Carrada, G. Ferblantier, J.-J. Grob and A. Slaoui, *Nanotechnology*, 2009, **20**, 415608.
38 P. E. Batson and J. R. Heath, *Phys. Rev. Lett.*, 1993, **71**, 911–914.
39 Y. W. Wang, J. S. Kim, G. H. Kim and K. S. Kim, *Appl. Phys. Lett.*, 2006, **88**, 143106.
40 V. Gritsenko, H. Wong, J. Xu, R. M. Kwok, I. P. Petrenko, B. A. Zaitsev, Y. N. Morokov and Y. N. Novikov, *J. Appl. Phy.*, 1999, **86**, 3234–3240.
41 L. Gu, V. Srot, W. Sigle, C. Koch, P. van Aken, F. Scholz, S. B. Thapa, C. Kirchner, M. Jetter and M. Rühle, *Phys. Rev. B: Condens. Matter*, 2007, **75**, 195214.
42 J. Tauc, R. Grigorovici and A. Vancu, *Phys. Status Solidi B*, 1966, **15**, 627–637.
43 Z. Zhang, M. He and Q. Li, *Solid State Commun.*, 2009, **149**, 1856–1859.
44 H. Vach, *Nano Lett.*, 2011, **11**, 5477–5481.
45 P. Yu and M. Cardona, *Fundamentals of Semiconductors: Physics and Materials Properties (Graduate Texts in Physics)*, 2010.

This journal is © The Royal Society of Chemistry 2014

4.1.1.5. Luminescence Origin Investigation in Si NCs / SiO_2 under High Hydrostatic Pressure

In Paper V [173], the optical properties of Si NC / SiO_2 superlattices are studied under high hydrostatic pressure. For this study, some of the material samples employed in Paper III were used. In particular, they consisted of 100× $SiO_{0.93}N_{0.23}$ / SiO_2 bilayers, with a constant $t_{SiO2} = 2$ nm while varying the Si NC size ($t_{SRON} =$ 4 or 5 nm). Samples were annealed at 1150 °C to attain an optimum crystallization state, with final NC sizes of 3.2 and 4.1 nm, respectively for $t_{SRON} = 4$ and 5 nm. After properly polishing the samples and loading them to the diamond anvil cell, Raman scattering and photoluminescence measurements were simultaneously performed while increasing the applied pressure from ambient pressure to 5 GPa, and afterwards investigating the downstroke to ambient pressure.

The first characterization of the samples was performed by Raman scattering. The first-order TO-LO phonon mode of crystalline Si (i.e. coming from the NCs) was monitored as a function of the applied pressure, which induced a peak frequency shift to higher frequencies. The peak position was plotted as a function of the pressure, whose fit showed the same phonon pressure coefficient of $\mathrm{d}\omega_{NC}/\mathrm{d}P \sim 8.5$ cm^{-1}/GPa for both samples, larger than the reported value for bulk Si [168]. Since smaller NCs present a smaller lattice parameter than larger ones (as measured by XRD in Paper III [79]), the phonon pressure coefficient should be larger than in bulk Si; however, the observed matrix stress effect on the nanostructures (also evaluated in Paper III [79]) submits them to a large compressive stress, due to the lower compressibility of the oxide matrix. Therefore, the coefficient excess was attributed to a strong pressure amplification due to the embedding matrix.

The optical emission of the samples under high hydrostatic pressure was carried out by means of PL. In general, the PL spectra exhibited an overall shift to lower energies when increasing pressure was applied. Besides, the spectra was progressively split into two contributions: a low-energy one, almost independent from pressure and NC size, and a high-energy one. The latter contribution varied with the NC size (larger NCs displaying lower energy PL emission), indicating quantum confinement effects. On the contrary, the size-independent low-energy peak governed PL emission at high applied pressures, which supports a defects-related origin of this contribution. The pressure coefficients for the high-energy emission [(-27 ± 6) meV/GPa and (-35 ± 8) meV/GPa for 3.2- and 4.1-nm NCs, respectively] were found to be larger (in absolute value) than for bulk Si (-14.1, according to Ref. [174]), which is in accordance with a pressure coefficient amplification as predicted by Raman. Indeed, the experimentally determined pressure coefficient ($\mathrm{d}E_{NC}/\mathrm{d}P$) is proportional to the pressure coefficient of the free-standing NC ($\mathrm{d}E_{free}/\mathrm{d}P$), i.e. without matrix-related stress effect, by:

$$\frac{\mathrm{d}E_{\mathrm{NC}}}{\mathrm{d}P} = \phi_{\mathrm{amp}} \cdot \frac{\mathrm{d}E_{\mathrm{free}}}{\mathrm{d}P} \ , \tag{4.9}$$

where ϕ_{amp}, the pressure coefficient amplification factor, can be estimated as:

$$\phi_{\mathrm{amp}} \sim \frac{\frac{\mathrm{d}\omega_{\mathrm{NC}}}{\mathrm{d}P}}{\frac{\mathrm{d}\omega_{\mathrm{bulk}}}{\mathrm{d}P}} \ , \tag{4.10}$$

being $\mathrm{d}\omega_{\mathrm{NC}}/\mathrm{d}P$ and $\mathrm{d}\omega_{\mathrm{bulk}}/\mathrm{d}P$, respectively, the phonon pressure coefficient obtained from the Raman analysis on the NC multilayer samples and the one tabulated for bulk Si. After applying Eqs. (4.9) and (4.10) on the PL-measured pressure coefficients, the resulting (free-standing) values [(-16 ± 4) and (-21 ± 4) meV/GPa for 3.2- and 4.1-nm NCs, respectively] are close to the bulk Si pressure coefficient. This indicates that the high-energy emission contribution mainly arises from the recombination of confined electronic states in the indirect band gap of Si, the dependence on size again involving quantum confinement.

Actually, the present study reports for the first time Raman scattering measurements under high hydrostatic pressure that help elucidating the origin of photoluminescence in Si NCs embedded in SiO_2. The results, which confirm PL coming from both excitonic radiative recombination within NCs and defects (surface localized states), are in agreement with other investigations as discussed in Section 2.3.2.2 in Chapter 2 (*Fundamentals of Silicon Nanocrystals*). In addition, it has been shown that studies under pressure allow tuning the light emission mechanism in a controlled way.

PHYSICAL REVIEW B **92**, 035432 (2015)

Optical emission from SiO_2-embedded silicon nanocrystals: A high-pressure Raman and photoluminescence study

J. Ibáñez,[1,*] S. Hernández,[2] J. López-Vidrier,[2] D. Hiller,[3] S. Gutsch,[3] M. Zacharias,[3] A. Segura,[4] J. Valenta,[5] and B. Garrido[2]

[1]*Institute of Earth Sciences Jaume Almera, ICTJA-CSIC, Lluís Solé i Sabarís s/n, 08028 Barcelona, Catalonia, Spain*
[2]*MIND-IN$_2$UB, Departament d'Electrònica, Universitat de Barcelona, Martí i Franquès 1, 08028 Barcelona, Catalonia, Spain*
[3]*IMTEK, Faculty of Engineering, Albert-Ludwigs-University Freiburg, Georges-Köhler-Allee 103, D-79110, Freiburg, Germany*
[4]*Departamento de Física Aplicada-ICMUV-MALTA Consolider Team, Universitat de València, 46100 Burjassot, València, Spain*
[5]*Faculty of Mathematics and Physics, Charles University, Ke Karlovu 3, 121 16 Prague 2, Czech Republic*

(Received 24 March 2015; revised manuscript received 30 June 2015; published 27 July 2015)

We investigate the optical properties of high-quality Si nanocrystals (NCs)/SiO_2 multilayers under high hydrostatic pressure with Raman scattering and photoluminescence (PL) measurements. The aim of our study is to shed light on the origin of the optical emission of the Si NCs/SiO_2. The Si NCs were produced by chemical-vapor deposition of Si-rich oxynitride (SRON)/SiO_2 multilayers with 5- and 4-nm SRON layer thicknesses on fused silica substrates and subsequent annealing at 1150 °C, which resulted in the precipitation of Si NCs with an average size of 4.1 and 3.3 nm, respectively. From the pressure dependence of the Raman spectra we extract a phonon pressure coefficient of $8.5 \pm 0.3\ \mathrm{cm^{-1}/GPa}$ in both samples, notably higher than that of bulk Si ($5.1\ \mathrm{cm^{-1}/GPa}$). This result is ascribed to a strong pressure amplification effect due to the larger compressibility of the SiO_2 matrix. In turn, the PL spectra exhibit two markedly different contributions: a higher-energy band that redshifts with pressure, and a lower-energy band which barely depends on pressure and which can be attributed to defect-related emission. The pressure coefficients of the higher-energy contribution are (-27 ± 6) and $(-35 \pm 8)\ \mathrm{meV/GPa}$ for the Si NCs with a size of 4.1 and 3.3 nm, respectively. These values are sizably higher than those of bulk Si ($-14\ \mathrm{meV/GPa}$). When the pressure amplification effect observed by Raman scattering is incorporated into the analysis of the PL spectra, it can be concluded that the pressure behavior of the high-energy PL band is consistent with that of the indirect transition of Si and, therefore, with the quantum-confined model for the emission of the Si NCs.

DOI: 10.1103/PhysRevB.92.035432 PACS number(s): 78.67.Bf, 78.30.Am, 74.62.Fj

I. INTRODUCTION

Silicon nanocrystals (Si NCs) are currently the subject of intense research due to their potential application as efficient all-silicon light emitters and absorbers for optoelectronics and photovoltaics. The interest in nanosized Si was first sparked by the discovery of room-temperature optical emission in porous Si [1,2], and was subsequently boosted by reports of highly efficient photoluminescence (PL) in Si nanostructures [3–6].

In spite of much effort to investigate the optical properties of nanosized Si, the actual origin of its strong PL signal is still under debate [7–10]. While many experimental works point toward strong luminescence due to quantum-confined excitons in Si nanostructures fabricated with different methods [8,11–14], others suggest that the PL emission arises from highly localized surface states [14–17]. Godefroo and co-authors, using PL measurements under high magnetic fields, showed that the optical emission of as-crystallized SiO_x/SiO_2 superlattices may be related to defects, whereas it becomes entirely originated by excitonic quantum confinement (QC) after H passivation [7]. Matrix-induced strain has also been shown to play an important role in the optical emission of matrix-embedded Si NCs relative to free-standing material [9].

High-pressure optical measurements provide a useful benchmark to investigate the fundamental properties of semiconductors and test the validity of theoretical models (for instance, density functional theory) for the calculation of their optical gaps, vibrational frequencies, or dielectric constants. In the particular case of nanosized Si, high-pressure PL studies are expected to provide relevant information about the origin of the optical emission. Cheong and co-authors [18] measured the hydrostatic pressure dependence of the PL signal of Si NCs/SiO_2 fabricated by ion-beam implantation, and found pressure coefficients of the order of $-5\ \mathrm{meV/GPa}$, inconsistent with the QC model. Hannah *et al.* [8] measured the pressure behavior of the PL emission in alkane-terminated colloidal Si NCs. These authors obtained pressure coefficients in close agreement with those of bulk Si ($-14.1\ \mathrm{meV/GPa}$) [19], concluding that the bright emission in their samples mainly arises from the indirect transition in Si. Recently, Goñi *et al.* [10] have used high-pressure experiments to investigate the origin of the visible emission in amorphous Si/SiO_x nanoparticles. Although these authors report PL pressure coefficients that are sizably lower than those of bulk Si, they still conclude that the strong PL signal in their samples is determined by QC, which is supported by the fact that their experimental pressure coefficients seem to be systematically related to nanoparticle sizes and emission energies. Although structural information is crucial to understand the effect of hydrostatic pressure on the optical properties of the Si NCs, among the previous high-pressure studies only Ref. [8] presented structural data as a function of pressure. In that work it was found by means of high-pressure x-ray diffraction that the bulk modulus of their free-standing material is close to that of bulk Si, thus supporting their PL results.

*Corresponding author: jibanez@ictja.csic.es

 ©2015 American Physical Society

In the present work we perform simultaneous Raman and PL measurements under high hydrostatic pressure on two different samples containing high-quality Si NCs/SiO_2 multilayers. The aim of our study is to shed light on the origin of the bright PL of the matrix-embedded Si NCs/SiO_2 system. The Raman spectra show that the phonon pressure coefficients of the Si NCs/SiO_2 are sizably larger than those of bulk Si, indicating that the NCs are subject to a strong pressure amplification effect as a consequence of the larger compressibility of the matrix. In turn, we find that the PL emission of the Si NCs can be separated in two different components: a higher-energy contribution exhibiting a strong redshift with pressure, and a lower-energy one which is much less sensitive to pressure. When the pressure amplification effect observed by Raman scattering is incorporated into the analysis of the pressure-dependent optical emission, it is found that the pressure behavior of the high-energy optical emission is consistent with that of the indirect transition of Si and therefore with the QC model, while the PL signal at lower energies can be attributed to defectlike emission.

II. EXPERIMENT

For this study, controlled-size, high-quality Si NCs were fabricated by depositing 100 silicon-rich oxynitride (SRON)/SiO_2 multilayers (MLs) at 375 °C on fused silica substrates by plasma-enhanced chemical vapor deposition (PECVD). Two different samples, labeled A and B, were studied. The thickness of the SiO_2 layers in both samples was kept constant at 2 nm, while the nominal thickness of the SRON layers was $t_{\mathrm{SRON}} = 5$ nm in sample A and $t_{\mathrm{SRON}} = 4$ nm in sample B, leading to a total sample thickness of 700 and 600 nm, respectively. In order to precipitate the Si excess within the SRON layers, the as-grown samples were annealed for 1 h at 1150 °C in a conventional furnace. In this way, Si NCs of average sizes $L = 4.1$ and 3.3 nm as determined by transmission electron microscopy (see Ref. [20] for details) were precipitated in samples A and B, respectively. Further details of the sample preparation can be found in Ref. [21].

The samples were mechanically polished down to $\approx 20\,\mu$m, and small flakes of around $50 \times 50\,\mu\mathrm{m}^2$ [2] were subsequently detached from the polished material and loaded into a gasketed membrane diamond anvil cell (DAC) [22]. A 16:3:1 mixture of methanol-ethanol-water was employed as pressure transmitting medium, and the applied pressure was evaluated with the ruby fluorescence method [23].

Photoluminescence and Raman spectra were simultaneously acquired, up to ~5 GPa, with a Horiba Jobin-Yvon LabRam spectrometer coupled to a high-sensitive CCD detector. The second harmonic of a continuous-wave Nd:YAG laser ($\lambda = 532$ nm) was employed to excite the samples for both techniques. The excitation radiation was focused with a $\times 50$ long-working distance objective, and the optical emission and Raman-scattering signal were collected in backscattering geometry with the same objective. Two different diffraction gratings were used for each type of measurement: 300 grooves/mm for PL, and 1800 grooves/mm for the Raman measurements.

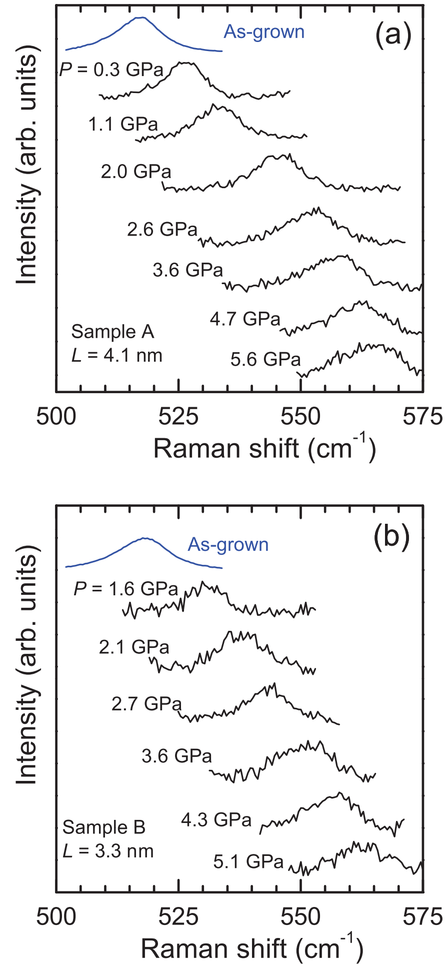

FIG. 1. (Color online) Raman spectra up to ~5 GPa of multilayered Si NCs embedded in a SiO_2 matrix with a NC size $L = 4.1$ nm (sample A, upper panel) and $L = 3.3$ nm (sample B, bottom panel). The top spectra (in blue) correspond to the as-grown samples, before the mechanical polishing for the high-pressure experiments.

III. RESULTS AND DISCUSSION

A. Raman scattering in Si/SiO_2: Pressure behavior

Figures 1(a) and 1(b) show the spectral region corresponding to the first-order optical phonons of crystalline Si as obtained by high-pressure Raman-scattering measurements on samples A and B, respectively. In both figures we have also included Raman spectra corresponding to the as-grown structures outside the DAC, before the mechanical polishing of the substrates. The ambient-pressure Raman spectra of these Si NCs have been discussed in detail elsewhere [20]. In Fig. 1, in order to isolate the Raman signal corresponding to crystalline Si, the contributions from the amorphous phases were carefully subtracted using a second-order polynomial. In this way, a clear Raman feature arising from the first-order

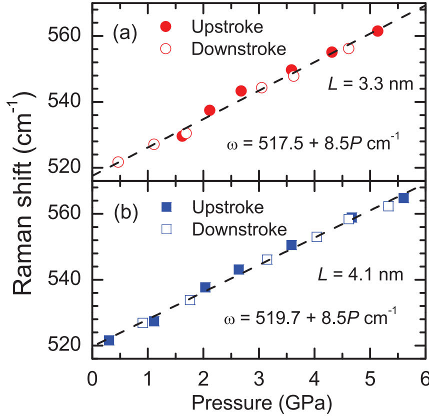

FIG. 2. (Color online) Pressure dependence of the frequency of the first-order optical phonon of Si in the two Si NCs/SiO_2 samples studied in this work. The dashed lines are linear fits to the experimental data.

optical phonons of nanocrystalline Si is clearly visible for both samples at all the explored pressures. The Raman spectra in Figs. 1(a) and 1(b) correspond to the upstroke cycle, up to ~5 GPa. As can be seen in both figures, the Raman peaks exhibit a pronounced shift to higher frequencies with increasing pressure. This trend is completely reversed in the downstroke cycle (not shown). Above ~5 GPa, a sizable intensity reduction of the Raman peaks was observed, accompanied by a decrease of the optical emission (see discussion of the PL data below).

Figure 2 shows the frequency of the first-order optical phonons in the two Si NCs/SiO_2 samples (A and B) as a function of applied pressure. Data obtained in the upstroke and downstroke cycles have been included in the two plots, both of which display a clear linear pressure dependence. From a linear fit to the experimental data, linear pressure coefficients $d\omega_{\mathrm{LO}}^{\mathrm{NC}}/dP$ equal to $8.5 \pm 0.3\,\mathrm{cm}^{-1}/\mathrm{GPa}$ are obtained in both samples. Thus, we conclude that the experimental pressure coefficients in the Si NCs embedded in a SiO_2 matrix are significantly larger than those reported for bulk Si ($d\omega_{\mathrm{LO}}^{\mathrm{bulk}}/dP = 5.1\,\mathrm{cm}^{-1}/\mathrm{GPa}$) [24].

Increased phonon pressure coefficients have also been measured in other Si nanostructures. For instance, increased phonon pressure coefficients of $6.1\,\mathrm{cm}^{-1}/\mathrm{GPa}$ were measured in Si nanowires (NWs) by Khachadorian and co-workers [25]. These authors explained their results in terms of a larger compressibility (lower bulk modulus) of the Si NWs in relation to bulk material as a consequence of an expansion of the lattice parameter. Note that, instead, decreased compressibilities are measured in Si NWs with reduced lattice parameter [26]. The results of Khachadorian *et al.* [25] can be compared to those obtained in porous Si, where a sizable expansion of the lattice parameter [27,28] and increased phonon pressure coefficients ($7.4\,\mathrm{cm}^{-1}/\mathrm{GPa}$, see for instance Ref. [29]) are typically reported.

However, in the case of the Si NCs/SiO_2 MLs studied in the present work, XRD measurements at $P = 0$ reveal that the ambient-pressure lattice parameter of Si is contracted in relation to bulk Si, and decreases with the crystalline size of the NCs [20]. Thus, according to the results of Refs. [25,26], our Si NCs/SiO_2 system should exhibit decreased compressibilities and reduced phonon pressure coefficients. Ambient-pressure Raman-scattering measurements also show that these Si NCs are subject to a sizable degree of compressive strain [20], which can be attributed to a compression effect of the SiO_2 matrix onto the NCs.

The previous considerations (i.e., observation of decreased lattice parameters and matrix-induced compression at $P = 0$) lead us to conclude that the large phonon pressure coefficients measured in our samples originate from a strong matrix-induced pressure amplification effect. Owing to the larger compressibility of the SiO_2 matrix ($\sim 0.027\,\mathrm{GPa}^{-1}$) [30] relative to Si ($\sim 0.01\,\mathrm{GPa}^{-1}$ in bulk samples) [24], the NCs may be subject to an effective pressure which is enhanced in relation to the applied (hydrostatic) pressure. Similar observations have been reported in Ge NCs embedded into SiO_2 [31] and also in thin layers grown on more compressible substrates (see for instance the recent high-pressure Raman scattering study on InGaN/Si(111) epilayers) [32]. In the particular case of the present work, strong Si-O covalent bonding at the NC-matrix interface is necessary in order to have effective transmission of deformations from the matrix to the NCs.

To illustrate the effect of the matrix-induced pressure amplification on the phonon pressure coefficients of the NCs, we first realize that the pressure coefficients, to the first order of the strain and assuming the same compressibility for the NCs and bulk Si, are proportional to the pressure coefficient of the residual (hydrostatic) strain ε in the NCs, which can be written in terms of the elastic properties of the matrix and the NCs [33]:

$$\frac{d\omega_{\mathrm{LO}}^{\mathrm{NC}}}{dP} = \frac{d\omega_{\mathrm{LO}}^{\mathrm{bulk}}}{dP} + \alpha\frac{d\varepsilon}{dP} \approx \frac{d\omega_{\mathrm{LO}}^{\mathrm{bulk}}}{dP} + \frac{\beta b_s}{3}\left(\frac{1}{B_0^m} - \frac{1}{B_0^{\mathrm{Si}}}\right), \quad (1)$$

where b_s is the strain-shift coefficient for the optical phonon modes, B_0^m and B_0^{Si} represent the bulk modulus (i.e., the reciprocal of the compressibility) of the SiO_2 matrix and Si, respectively, and $d\omega_{\mathrm{LO}}^{\mathrm{bulk}}/dP = -b_s/3B_0^{\mathrm{Si}}$ is the pressure coefficient of the optical first-order phonon of bulk Si [33], with $b_s \sim -1470\,\mathrm{cm}^{-1}$ in the case of Si. In Eq. (1), α and β are phenomenological parameters that take into account the particular geometry and partial strain state of the geometrical configuration under study. An upper limit for $d\omega_{\mathrm{LO}}^{\mathrm{NC}}/dP$ can be readily obtained by assuming biaxially strained Si MLs, i.e., $\beta = 1$ in Eq. (1). The value thus obtained, using the bulk modulus values for Si and SiO_2, is $\sim 13\,\mathrm{cm}^{-1}/\mathrm{GPa}$. As expected, this value is much larger than the experimental pressure coefficients measured in our samples. However, a value of β equal to 0.42, compatible with a partial relaxation and redistribution of the strain in the NCs, reproduces the experimental pressure coefficients measured in both samples.

Alternatively, the (hydrostatic) strain in the Si NCs at a given pressure value may be roughly evaluated by using the strain distribution inside a 0D dot embedded in a large matrix as given in Ref. [34], i.e., $\varepsilon = (1/\gamma - 1)\varepsilon_m$, where $\varepsilon_m = a_i(P)/a_m(P) - 1$ is the pressure-dependent lattice mismatch between the inclusion (0D dot) and the matrix, and $(1/\gamma - 1)$

is a constant that depends on the bulk modulus and Poisson ratio of both the matrix and the 0D dot (see Ref. [34] for details). Note that, by taking the pressure derivative of ε_m in terms of the bulk moduli of the NC and the matrix, this model is basically Eq. (1) with $\beta = (1/\gamma - 1)$. Using the appropriate material parameters for Si and SiO_2, we estimate a value of $d\omega_{LO}^{NC}/dP \sim 7.5\,cm^{-1}/GPa$, which is only $\sim 1\,cm^{-1}/GPa$ below the experimental pressure coefficients measured in our samples ($\sim$8.5 cm^{-1}/GPa).

In spite of the large oversimplifications involved in the two previous models, they provide a reasonable approximation to explain the pressure behavior of the first-order optical phonons in the Si NCs/SiO_2 system, thus confirming that matrix-induced compression may be responsible for the increased phonon pressure coefficients measured in our samples.

B. High-pressure optical emission

The pressure amplification effect revealed by the Raman measurements is expected to have an important bearing on the pressure dependence of the PL emission of the Si NCs/SiO_2 MLs. We show in Figs. 3(a) and 3(b) PL spectra as a function of pressure, obtained in the upstroke cycle up to $\sim$5 GPa, for samples A and B, respectively. These spectra were obtained simultaneously to the Raman spectra discussed above by simply shifting the diffraction gratings. In the figure we have also included PL spectra of the as-grown samples, before the mechanical polishing of the SiO_2 substrates. It can be seen that the maximum of the optical emission at ambient pressure of the two as-grown samples is redshifted in relation to the first spectra (i.e., at the lowest hydrostatic pressures) acquired in the DAC experiments. This observation can be attributed to a partial relaxation of the built-in strains in the NCs induced by the mechanical polishing and, more importantly, to dislocations formed during the polishing of the samples, which may be expected to affect more strongly the larger NCs, giving rise to an overall blueshift of the optical emission.

As can be seen in Fig. 3, the PL signal of both samples display a two-band emission that redshifts with pressure. The intensity of the high-energy PL band (peak P1 in Fig. 3) is found to progressively decrease with pressure. At the highest applied pressures, the low-energy portion of the spectra (peak P2) dominates the optical emission in both samples. In the downstroke cycle, the PL signal of both samples was almost totally recovered. This is illustrated in Fig. 4 for the case of sample A. As depicted in this figure, the PL emission of the sample with $L = 4.1$ nm around $\sim$1 GPa is very similar in the upstroke and downstroke cycles. Similar results are found in both samples along the whole pressure range investigated.

The PL peak energy of bands P1 and P2 in both samples was evaluated with a line-shape fit analysis. For this purpose, two Gaussian peaks (as a function of photon energy) were employed, one per each contribution, P1 and P2. In Fig. 4 we show some examples of the line-shape fitting analyses for the particular case of sample A. As can be seen in the figure, good agreement between the calculated and the experimental profiles is found.

Figure 5 shows the PL peak energy E_{Si/SiO_2} for bands P1 and P2 in both samples as a function of hydrostatic pressure. In the case of sample B ($L = 3.3$ nm), given the low PL intensity of peak P1 at the highest hydrostatic pressures, the corresponding curve only includes data below $\sim$3 GPa. As can be seen in the figure, the peak energy and also the pressure behavior of the low-energy PL emission (peak P2) is very similar in samples A and B. A linear fit to the data gives a pressure coefficient of (-10 ± 2) meV/GPa in both structures, thus suggesting that this PL band is independent of size effects.

On the other hand, Fig. 5 clearly shows that the PL peak energy for band P1 is higher in sample B, which is consistent with the larger QC effects expected in this structure in relation to sample A. From a linear fit to the data for peaks P1 in both samples we extract the following pressure coefficients: $dE_{Si/SiO_2}/dP = (-27 \pm 6)$ meV/GPa in sample A, and $dE_{Si/SiO_2}/dP = (-35 \pm 8)$ meV/GPa in sample B. As

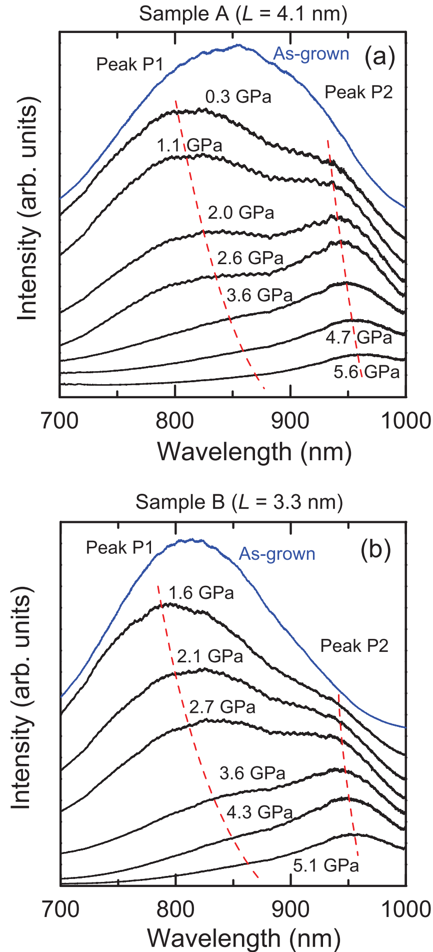

FIG. 3. (Color online) Photoluminescence (PL) spectra of two Si NC/SiO_2 samples with different NC sizes (L). (a) Sample A ($L = 4.1$ nm); (b) the PL spectra of sample B ($L = 3.3$ nm). The spectra on top (in blue) correspond to the as-grown samples before mechanical polishing for the high-pressure experiments.

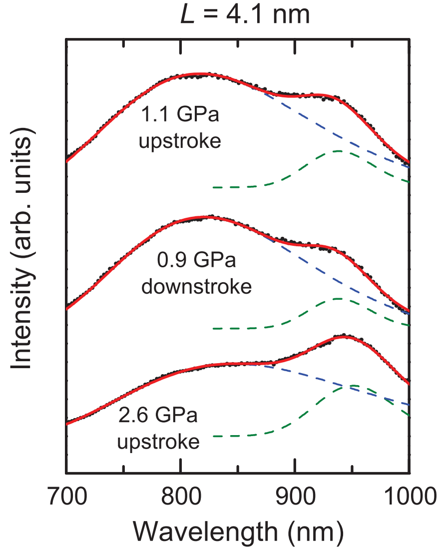

FIG. 4. (Color online) Selected photoluminescence (PL) spectra of sample A ($L = 4.1$ nm) obtained during the upstroke and downstroke cycles. The results of the line-shape fitting analysis of the PL spectra, carried out with two Gaussian functions (as a function of photon energy), are shown.

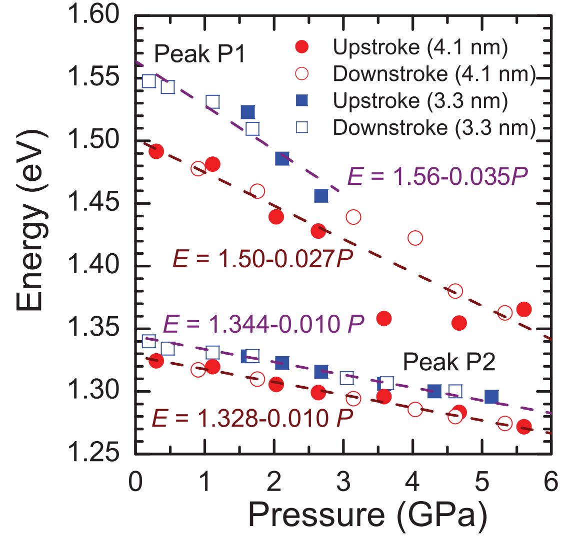

FIG. 5. (Color online) PL peak energies for the high-energy (peak P1) and low-energy (peak P2) optical emission of the two Si NC/SiO_2 samples studied in this work. The dots correspond to sample A (with a NC size $L = 4.1$ nm) and the squares to sample B ($L = 3.3$ nm).

occurred with the Raman-scattering data discussed above, these pressure coefficients are sizably larger (in absolute value) than those measured in bulk Si (−14.1 meV/GPa, see Ref. [19]). Again, we attribute this result to a pressure amplification effect induced by the more compressive matrix.

We would like to note the large error bars in the resulting PL pressure coefficients of peak P1 in both samples, which is a consequence of the observed PL intensity reduction of this band with increasing pressure. Within error bars, the two measured pressure coefficients are quite similar. This result does not alter the main conclusion of the present PL measurements, i.e., the fact that the experimental $dE_{\mathrm{Si/SiO_2}}/dP$ values are much larger (in absolute value) than those of bulk Si.

The matrix-induced pressure amplification on the PL peak energies of bands P1 and also P2, relative to those expected in "free-standing" (i.e., not compressed by the matrix) Si NCs can be roughly estimated by using the following phenomenological (ad hoc) expression:

$$dE_{\mathrm{Si/SiO_2}}/dP = \varphi_{\mathrm{amp}} dE_{\mathrm{free}}/dP \sim \frac{\left(d\omega_{\mathrm{LO}}^{\mathrm{NC}}/dP\right)}{\left(d\omega_{\mathrm{LO}}^{\mathrm{bulk}}/dP\right)}(dE_{\mathrm{free}}/dP), \qquad (2)$$

where E_{free} corresponds to the PL peak energy in free-standing material. In Eq. (2) the amplification factor φ_{amp} is simply evaluated in terms of the amplification of the phonon pressure coefficients in the Si NCs/SiO_2 MLs relative to bulk Si. Taking the experimental $d\omega_{\mathrm{LO}}^{\mathrm{NC}}/dP$ values measured above (8.5 cm^{-1}/GPa in both samples) and that of bulk Si (5.1 cm^{-1}/GPa), we obtain an amplification factor φ_{amp} equal to 1.67. Using this value in Eq. (2) together with the experimental $dE_{\mathrm{Si/SiO_2}}/dP$ values for peaks P1 and P2 in samples A and B, we obtain the corresponding dE_{free}/dP values, which are shown in Table I.

In the case of peak P2, the resulting PL pressure coefficients in free-standing NCs are around −6 meV/GPa in both samples. This value is compatible with radiative emission from localized levels, which suggests that the low-energy emission in these NCs is mainly originated by defects, as for instance highly localized defects at the Si/SiO_2 interface [7]. Such interface states may be close to the band-gap edges of nanocrystalline Si and could partly follow the band-gap dependence of Si with NC size [7]. The fact that the intensity ratio between bands P2 and P1 is found to increase in the polished samples, relative to the as-grown material (see Fig. 3), seems to further support the conclusion that P2 may be related to defects. We would also like to note that the dE_{free}/dP values that we obtain for peak P2 are comparable to those measured in poorly crystalline samples, as for instance those produced by ion-beam implantation in Ref. [18], where pressure coefficients of −4 and − 6 meV/GPa were measured. The similarity between those values and our present results for peak P2 may suggest that the PL emission in the ion-implanted samples [18] is actually originated by radiative defects.

In the case of the high-energy PL emission (peak P1), we find that the resulting pressure coefficients in "free-standing" NCs (see Table I) are not far from those of bulk Si ($dE_g/dP =$ −14.1 meV/GPa). This suggests that peak P1 may be related to the indirect gap of Si. Very similar PL pressure coefficients, ranging from −14.2 to − 21.1 meV/GPa, were reported by

TABLE I. Experimental peak energy (E_{PL}) at $P = 0$ and pressure coefficients ($dE_{Si/SiO_2}/dP$) for the PL peak energy of the high-energy optical emission (peak P1) and low-energy emission (peak P2) measured by high-pressure PL measurements in the two samples studied in this work. The fourth and seventh columns show the corresponding PL pressure coefficients (dE_{free}/dP), which have been recalculated phenomenologically to subtract the pressure amplification effect induced by the SiO_2 matrix. Values for bulk Si, as in Ref. [19], are also given.

	Peak P1			Peak P2		
Sample	$E_{PL}(P = 0)$ (meV)	$dE_{Si/SiO_2}/dP$ (meV/GPa)	dE_{free}/dP (meV/GPa)	$E_{PL}(P = 0)$ (meV)	$dE_{Si/SiO_2}/dP$ (meV/GPa)	dE_{free}/dP (meV/GPa)
A ($L = 4.1$ nm)	1500 ± 10	−27 ± 6	−16 ± 4	1328 ± 2	−10 ± 2	−6 ± 1
B ($L = 3.3$ nm)	1560 ± 10	−35 ± 8	−21 ± 6	1344 ± 2	−10 ± 2	−6 ± 1
Bulk Si [19]	1110 ± 2	–	−14.1 ± 0.6	–	–	–

Hannah *et al.* [8] in colloidal nanoparticles. Thus we can conclude that the high-energy optical emission in the Si NC/SiO_2 system mainly involves confined states associated to the X and Γ electronic states responsible for the indirect transition in bulk Si. In the case of our samples, the pressure behavior of the maximum of peak P1 is strongly affected by an amplification effect induced by the more compressible SiO_2 matrix, which explains the high $dE_{Si/SiO_2}/dP$ values measured in the present work.

Within this picture, the defect states related to peak P2 (see discussion above) may compete with the quantum-confined emission from the Si NCs, giving rise to the observed quenching of peak P1 with increasing pressure (Fig. 3), i.e., when the energy of the quantum-confined states responsible for peak P1 approaches that of the interface defect states. These observations also help us to better understand the effect of the mechanical polishing on the optical emission of the samples at ambient conditions (see Fig. 3). The mechanical polishing may introduce radiative defects (band P2) that compete with the optical emission from the NCs (band P1). Then, the intensity increase of band P2 together with the quenching of part of the high-energy contributions could explain, at least partially, the apparent blueshift of the PL spectra of both samples after the mechanical polishing. As a consequence of the intensity variations of bands P1 and P2, the spectra of the polished samples end up exhibiting two well-resolved PL bands, with an apparent blueshift of the high-energy contribution. As discussed above, the partial relaxation of the built-in strains in the NCs and an additional dislocation-induced quenching of the PL from the largest NCs would also contribute to the observed blueshifts.

Finally, we would like to remark that QC is not expected to strongly affect the $dE_{Si/SiO_2}/dP$ values measured in our Si NCs. The QC energy depends on pressure through volume and effective mass changes. With regard to the former, we follow the discussion of Cheong *et al.* [18] and evaluate the pressure coefficient (in free-standing NCs) of the confinement energy, $E_{conf} \sim E_{PL} - E_g$, where $E_g = 1.11$ eV [19] is the indirect band-gap of Si, with the expression $dE_{conf}/dP = (2/3)E_{conf}/B_0^{Si}$, where a simple cubic-box model for the quantum-confined carriers is assumed. Using the PL peak energies at $P = 0$, we obtain $E_{conf} \sim 380$ meV for sample A and $E_{conf} \sim 440$ meV for sample B. Inserting these values in the expression for dE_{conf}/dP, we obtain values between $2 - 3$ meV/GPa, which are of the order of the experimental errors associated to the high-pressure PL measurements. With regard to changes in E_{conf} due to the pressure dependence of the electron effective mass at the X valleys, there does not seem to be any experimental measurement of the corresponding pressure coefficient. Nevertheless, given that the electron effective mass determines (along with the dielectric constant) the ionization energy of shallow donors, its pressure coefficient is expected to be very small. This can be inferred, for instance, from the very low pressure coefficient of both the shallow donor ionization energy [35] and the dielectric constant [36] of bulk Si. These results, extrapolated to the case of the Si NCs, imply that the pressure behavior of the quantum-confined optical emission is not strongly affected by pressure-induced volume or electron effective-mass changes.

IV. CONCLUSIONS

We have performed Raman-scattering and PL measurements under high hydrostatic pressure on Si NC/SiO_2 MLs grown by PECVD. The aim of the present study is to obtain additional knowledge on the origin of the optical emission of the Si NCs embedded in SiO_2. The Raman-scattering experiments reveal that the phonon pressure coefficients of the Si NCs/SiO_2 (8.5 cm^{-1}/GPa) are sizably larger than those of bulk Si (5.1 cm^{-1}/GPa), which can be attributed to a pressure amplification effect on the NCs as a consequence of the larger compressibility of the SiO_2 matrix in relation to Si. For this purpose, strong covalent Si-O bonding at the NC-matrix interface would be required in order to have effective pressure transmission from the matrix to the less compressible NCs.

The PL spectra acquired as a function of pressure on the Si NCs display two different bands. The high-energy emission is found to strongly redshift with pressure (redshift of 27–35 meV/GPa), while the low-energy band is much less sensitive to pressure (redshift of 10 meV/GPa). By incorporating the pressure amplification effect observed by Raman scattering into the analysis of the PL data, we obtain PL pressure coefficients for the corresponding free-standing (matrix-free) NCs equal to −16 and −21 meV/GPa in the two samples investigated. These values agree well with values measured in colloidal NCs, and are not far from the PL pressure coefficient measured in bulk Si (−14.1 meV/GPa). Thus, we conclude that the pressure dependence of the high-energy optical emission of the Si NCs/SiO_2 is compatible with the indirect transition of Si, while the low-energy PL bands can be attributed to emission from defects.

ACKNOWLEDGMENTS

Work supported by the European Community's Seventh Framework Programme (FP7/2007-2013) under grant agreement No. 245977 (project NASCEnT). Financial support by the Spanish Government through projects LEOMIS (TEC2012-38540-C02-01) and MAT2012-38664-C02-02 is also acknowledged.

[1] L. T. Canham, Appl. Phys. Lett. **57**, 1046 (1990).
[2] V. Lehmann and U. Gösele, Appl. Phys. Lett. **58**, 856 (1991).
[3] S. H. Risbud, L. Liu, and J. F. Shackelford, Appl. Phys. Lett. **63**, 1648 (1993).
[4] T. S. Iwayama, S. Nakao, and K. Saitoh, Appl. Phys. Lett. **65**, 1814 (1994).
[5] Q. Zhang, S. C. Bayliss, and D. A. Hutt, Appl. Phys. Lett. **66**, 1977 (1995).
[6] P. Mutti, G. Ghislotti, S. Bertoni, L. Bonoldi, G. F. Cerofolini, L. Meda, E. Grilli, and M. Guzzi, Appl. Phys. Lett. **66**, 851 (1995).
[7] S. Godefroo, M. Hayne, M. Jivanescu, A. Stesmans, M. Zacharias, O. I. Lebedev, G. Van Tendeloo, and V. V. Moschchalkov, Nat. Nanotechnol. **3**, 174 (2008).
[8] D. C. Hannah, J. Yang, P. Podsiadlo, M. K. Y. Chan, A. Demortière, D. J. Gosztola, V. B. Prakapenka, G. C. Schatz, U. Kortshagen, and R. D. Schaller, Nano Lett. **12**, 4200 (2012).
[9] K. Kůsová, L. Ondič, E. Klimešová, K. Herynková, I. Pelant, S. Daniš, J. Valenta, M. Gallart, M. Ziegler, B. Hönerlage, and P. Gilliot, Appl. Phys. Lett. **101**, 143101 (2012).
[10] A. R. Goñi, L. R. Muniz, J. S. Reparaz, M. I. Alonso, M. Garriga, A. F. Lopeandia, J. Rodriguez-Viejo, J. Arbiol, and R. Rurali, Phys. Rev. B **89**, 045428 (2014).
[11] W. L. Wilson, P. F. Szajowski, and L. E. Brus, Science **262**, 1242 (1993).
[12] D. S. English, L. E. Pell, Z. H. Yu, P. F. Barbara, and B. A. Korgel, Nano Lett. **2**, 681 (2002).
[13] K. Kusova, O. Cibulka, K. Dohnalova, I. Pelant, J. Valenta, A. Fucikova, K. Zidek, J. Lang, J. Englich, P. Matejka, P. Stepanek, and S. Bakardjieva, ACS Nano **4**, 4495 (2010).
[14] M. Sykora, L. Mangolini, R. D. Schaller, U. Kortshagen, D. Jurbergs, and V. I. Klimov, Phys. Rev. Lett. **100**, 067401 (2008).
[15] A. Puzder, A. J. Williamson, J. C. Grossman, and G. Galli, Phys. Rev. Lett. **88**, 097401 (2002).
[16] G. Allan, C. Delerue, and M. Lannoo, Phys. Rev. Lett. **76**, 2961 (1996).
[17] K. Židek, I. Pelant, F. Trojánek, P. Malý, P. Gilliot, B. Hönerlage, J. Oberlé, L. Šiller, R. Little, and B. R. Horrocks, Phys. Rev. B **84**, 085321 (2011).
[18] H. M. Cheong, W. Paul, S. P. Withrow, J. G. Zhu, J. D. Budai, C. W. White, and D. M. Hembree, Appl. Phys. Lett. **68**, 87 (1996).
[19] B. Welber, C. K. Kim, M. Cardona, and S. Rodríguez, Solid State Commun. **17**, 1021 (1975).
[20] S. Hernández, J. López-Vidrier, L. López-Conesa, D. Hiller, S. Gutsch, J. Ibáñez, S. Estradé, F. Peiró, M. Zacharias, and B. Garrido, J. Appl. Phys. **115**, 203504 (2014).
[21] A. M. Hartel, D. Hiller, S. Gutsch, P. Löper, S. Estradé, F. Peiró, B. Garrido, and M. Zacharias, Thin Solid Films **520**, 121 (2011).
[22] R. Le Toullec, J. P. Pinceaux, and P. Loubeyre, High Press. Res. **1**, 77 (1988).
[23] H. K. Mao, P. Bell, J. Shaner, D. Steinberg, J. Appl. Phys. **49**, 3276 (1978).
[24] S. Adachi, *Properties of Group-IV, III-V and II-VI Semiconductors* (John Wiley and Sons, NewYork, 2005), pp. 41–72.
[25] S. Khachadorian, K. Papagelis, H. Scheel1, A. Colli, A. C. Ferrari, and C. Thomsen, Nanotechnology **22**, 195707 (2011).
[26] Y. Wang, J. Zhang, J. Wu, J. L. Coffer, Z. Lin, S. V. Sinogeikin, W. Yang, and Y. Zhao, Nano Lett. **8**, 2891 (2008).
[27] K. Barla, R. Herino, G. Bomchil, J. C. Pfister, and A. Freund, J. Cryst. Growth **68**, 727 (1984).
[28] D. Bellet and G. Dolino, Thin Solid Films **276**, 1 (1996).
[29] D. Papadimitriou, Y. S. Raptis, A. G. Nassiopoulou, and G. Kaltsas, Phys. Status Solidi (a) **165**, 43 (1998).
[30] O. B. Tsiok, V. V. Brazhkin, A. G. Lyapin, and L. G. Khvostantsev, Phys. Rev. Lett. **80**, 999 (1998).
[31] L. Liu, Z. X. Shen, K. L. Teo, A. V. Kolobov, and Y. Maeda, J. Appl. Phys. **93**, 9392 (2003).
[32] R. Oliva, J. Ibáñez, R. Cuscó, A. Dadgar, A. Krost, J. Gandhi, A. Bensaoula, and L. Artús, Appl. Phys. Lett. **104**, 142101 (2014).
[33] J. S. Reparaz, A. Bernardi, A. R. Goñi, P. D. Lacharmoise, M. I. Alonso, M. Garriga, J. Novák, and I. Vávra, Appl. Phys. Lett. **91**, 081914 (2007).
[34] M. Yang, J. C. Sturm, and J. Prevost, Phys. Rev. B **56**, 1973 (1997).
[35] M. G. Holland and W. Paul, Phys. Rev. **128**, 30 (1962).
[36] G. A. Samara, Phys. Rev. B **27**, 3494 (1983).

4.1.2. Material Characterization of Si NC / SiC Multilayers

4.1.2.1. Characterization Drawbacks of Si NCs in SiC

The structural and optical characterization carried out on Si NC / SiO_2 MLs allowed extracting direct information about the optical properties of the system, as well as the reliability of the superlattice approach application. The case of Si NCs embedded in SiC is far different, for the lower NC-matrix system stability during the high-temperature annealing treatments results in the lack of Si excess precipitation and crystallization control, as we will see in this Section. In addition, quantum confinement effect is not straightforwardly reached nor observed in this material system. In particular, *Ab-initio* band structure calculations have recently shown inefficient quantum confinement in Si NCs embedded in SiC as a consequence of the poorly-insulating properties of the matrix, in contrast to wide-band gap materials such as SiO_2 [133]. As well, the highly-energetic NC / SiC interface induced by a distorted transition layer further reduces the effective band gap energy of Si NCs [24, 133].

Regarding the experimental observation of quantum confinement, difficulties arise when inspecting the band gap energy of the materials. Whereas photoluminescence has become a crucial technique to identify structural and optical effects in Si NCs / SiO_2 systems, the weak and broad PL yielded by Si NCs / SiC multilayers was demonstrated to be a consequence of a-Si and SiC intra-band gap defects strongly modulated by interference patterns [175], and no information about the actual NC band gap energy could be obtained. The optical characterization of these systems must then be performed via reflectance and transmittance measurements, which allows for absorption studies [see Fig. 4.4(a), where samples containing different SRC layer thicknesses are studied]. Via the Tauc formalism, described in Section 3.2.2.2 in Chapter 3 (*Experimental Details*), the optical band gap of the overall SL system can be evaluated, as displayed in Fig. 4.4(b), with values around 2.2 - 2.3 eV but presenting no clear trend with t_{SRC}. Actually, the background absorption of SiC and a-Si makes it difficult to attain reliable band gap energy values from this kind of studies. Therefore, efforts must be dedicated to different characterization techniques, and the study must focus on the structural conformation and control of Si NCs.

4.1.2.2. Initial Approaches on the Structural and Optical Properties

The structural and optical characterization of Si NCs embedded in SiC was also performed, the first results being reported in Paper VI [84]. In contrast to SiO_2, SiC is a harsh environment for NC growth control. Therefore, the achievement of NC superlattices is not straightforward, and different batches of samples were fabricated before the optimum structural parameters were achieved. Particularly, in Paper VI, the fabrication of multilayer and single layer samples was addressed. In the ML case, the sublayer thicknesses were fixed at $t_{\mathrm{SiC}} = t_{\mathrm{SRC}} = 3$ nm, whereas

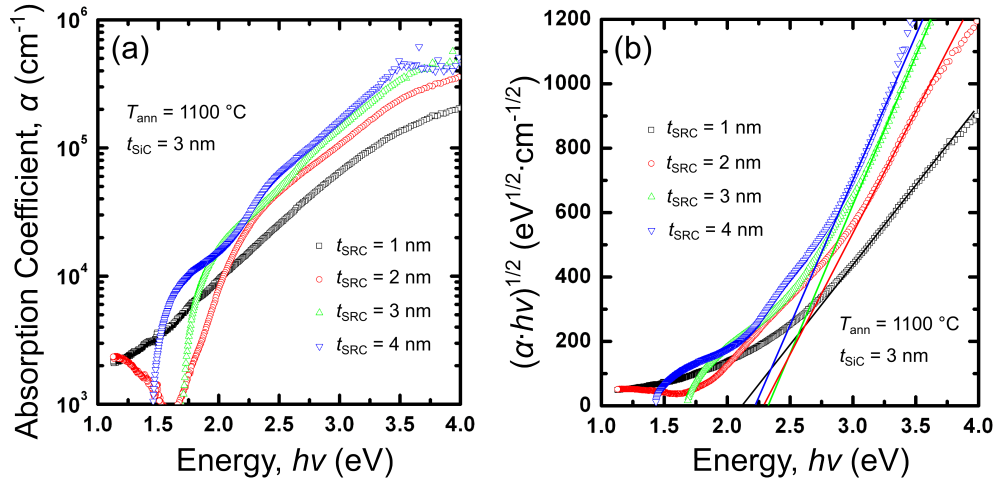

Figure 4.4.: (a) Absorption coefficient (α) versus incident photon energy corresponding to Si NC / SiC multilayers with varying t_{SRC}, t_{SiC} = 3 nm, $x = 0.95$ (in Si_xC_{1-x}) and annealed at 1100 °C. (b) Tauc plots corresponding to the samples in (a), where straight lines represent the data fits at larger energies, whose intersection with the energy axis results in the optical band gap energy of the system.

the SRC sublayer stoichiometry was varied from $x = 0.5$ to 0.75 (in Si_xC_{1-x}), corresponding to a Si excess (within SRC layer) of $[Si]_{exc}$ = 0 to 50 at.%. The annealing treatment consisted of the two-step process at 600 and 1100 °C (for 1 h each) described in Section 3.1 from Chapter 3 (*Experimental Details*).

Energy-filtered TEM images were obtained from the different annealed ML samples, as well as the as-deposited ML sample with higher $[Si]_{exc}$. A strong shrinkage to almost half the initial thickness was observed after the samples were submitted to high temperature, and it was more marked for higher C concentration within the structure (i.e. lower $[Si]_{exc}$). Therefore, this effect was ascribed to C rather than Si diffusion, as the former atom is lighter and more prompt to percolate into adjacent sublayers. Another remarkable feature was the fact that the ML structure, corroborated in as-deposited samples, was not maintained after annealing, the formed Si NCs being randomly distributed along and across the whole sample volume. In fact, as a consequence of the lack of size constrain, the evaluated NC diameter resulted in a size distribution of (6.3 ± 1.7) nm, very far from the confinement reached in SiO_2 (see Section 4.1.1.1). Besides, the NC size was found to decrease, as well as their number (i.e. the volumetric density of NCs), with decreasing $[Si]_{exc}$. As a last feature from the EFTEM images, a layer appeared on top of the structure after annealing, with an intermediate composition between oxide and carbide; this was thought to be due to the top SRC layer oxidation, thus forming an oxycarbide compound (SiC_yO_z).

Raman scattering was employed to analyse the crystalline degree of ML and single layer samples grown on fused silica substrate, in order to avoid the Si sub-

strate Raman signal. Analogous features than in the SiO_2 case were found in the acquired spectra: a crystalline TO-LO peak around 510−520 cm^{-1} from Si NCs and an amorphous broad band at lower frequencies. An additional signal from the oxycarbide layer was expected, which could not be substracted but was taken into account in the discussion of the results. The multilayer samples were compared to bulk layers of identical Si excess conditions, but obviously presenting a larger total Si content due to higher SRC volume fraction. Under the same annealing conditions, the crystalline degree presented by the bulk layers was higher than in ML samples, ascribed to the crystallization of a larger $[Si]_{exc}$ fraction. Optical transmittance and reflectance measurements were also carried out on the same samples, and simulations taking into account the *effective mass approximation* were employed in order to adjust the acquired spectra [176] and thus attain information of the structural parameters: the total active layer thickness and the composition of the different phases present in the layer (c-Si, a-Si, c-SiC, a-SiC).

The crystalline fraction of each sample was evaluated by both techniques, as a ratio of the c-Si to a-Si optical phonon modes signal contribution to Raman spectra according to Eq. (4.6), and considering the volumetric amount of c-Si and a-Si phases obtained from transmittance and reflectance analysis. A great accordance between both techniques was observed at high Si content, where over a 50 % crystallization was achieved. Nevertheless, the results from optical analysis notably drop at lower $[Si]_{exc}$. A discussion on each technique background shed light to the observed difference at low and high Si content regimes. On one hand, the mentioned oxycarbide residual layer could be overestimating the a-Si contribution in the Raman spectra, producing a crystalline degree underestimation at high Si contents. On the other hand, the refractive index (and extinction coefficient) values taken as input parameters when fitting the optical transmittance and reflectance data corresponded to bulk Si instead of nanocrystalline Si (the latter material presenting lower values according to Ref. [177]), which induced an underestimation of the c-Si phase and therefore a lower crystalline degree, effect that was enhanced at low $[Si]_{exc}$. These results helped improving the Raman and reflectance and transmittance spectra analysis, being implemented in the characterization of the following batches of samples that were fabricated.

Finally, a lateral electrical characterization was carried out on annealed Si NC / SiC ML samples, by burying interdigitated TiPdAg contacts into the active layers and depositing an insulating 300-nm-thick SiO_2 layer between the Si substrate and the MLs. The intensity versus voltage curves showed increasing conductivity for lower t_{SRC}, the opposite behavior than expected for an increasing Si volume presence. The ohmic behavior displayed by the curves was attributed to the ohmic characteristics of the contacts. In addition, huge current density values were measured (>2 A·cm^{-1} at 0.5 V in the pure SiC layer), which was ascribed to the presence of a highly defective (and therefore conductive) oxycarbide layer on top of the structure. Electrical measurements were performed as a function of temper-

ature, from which low activation energies (tens of meV) were found; this pointed to a carrier conduction not due to extended band states (for which an energy of about half the band gap would be required), which also led to the conclusion that the oxycarbide layer was strongly influencing charge transport. Later developments on Si NC / SiC multilayers allowed eliminating this residual layer by adding a sacrificial oxide layer on top of the structure, which was chemically removed after the annealing process [161]. As a consequence, the following stages of carbide investigation already used this optimized fabrication process.

Materials Science and Engineering B 178 (2013) 639–644

Contents lists available at SciVerse ScienceDirect

Materials Science and Engineering B

journal homepage: www.elsevier.com/locate/mseb

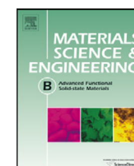

Short communication

Structural, optical and electrical properties of silicon nanocrystals embedded in Si_xC_{1-x}/SiC multilayer systems for photovoltaic applications

J. López-Vidrier [a,*], S. Hernández [a], J. Samà [a], M. Canino [b], M. Allegrezza [b], M. Bellettato [b], R. Shukla [b], M. Schnabel [c], P. Löper [c], L. López-Conesa [a], S. Estradé [a,d], F. Peiró [a], S. Janz [c], B. Garrido [a]

[a] MIND-IN2UB, Electronics Department, University of Barcelona, Martí i Franquès 1, E-08028 Barcelona, Spain
[b] CNR-IMM, Consiglio Nazionale delle Richerche – Istituto per la Microelettronica e Microsistemi, Via Gobetti 101, I-40129 Bologna, Italy
[c] Fraunhofer Institute for Solar Energy Systems ISE, Heidenhofstr. 2, D-79110 Freiburg, Germany
[d] TEM-MAT, CCiT-UB, Scientific and Technological Center – University of Barcelona, Solé i Sabarís 1, E-08028 Barcelona, Spain

ARTICLE INFO

Article history:
Received 5 July 2012
Received in revised form
15 September 2012
Accepted 11 October 2012
Available online 25 October 2012

Keywords:
Silicon-rich silicon carbide
Silicon nanocrystals
Structure shrinkage
Oxycarbide
Crystalline fraction
Electrical measurements

ABSTRACT

In this work we present a structural, optical and electrical characterization of Si_xC_{1-x}/SiC multilayer systems with different silicon content. After the deposition process, an annealing treatment was carried out in order to induce the silicon nanocrystals formation. By means of energy-filtered transmission electron microscopy (EFTEM) we observed the structural morphology of the multilayers and the presence of crystallized silicon nanoprecipitates for samples annealed up to 1100 °C. We discuss the suitability of optical techniques such as Raman scattering and reflectance and transmittance (*R&T*) for the evaluation of the crystalline fraction of our samples at different silicon excess ranges. In addition, the combination of *R&T* measurements with simulation has proved to be a useful instrument to confirm the structural properties observed by EFTEM. Finally, we explore the origin of the extremely high current density revealed by electrical measurements, probably due to the presence of an undesired defective SiC_yO_z ternary compound layer, already supported by the structural and optical results. Nevertheless, the variation of the electrical measurements with the silicon amount indicates a small but significant contribution from the multilayers.

© 2012 Elsevier B.V. All rights reserved.

1. Introduction

For years, silicon solar cells have attracted the attention of the industry due to their low fabrication and commercialization costs, as well as the well investigated electronic properties of Si. Moreover, Si presents almost the optimum band gap energy (1.12 eV) for a single band gap solar cell [1]. However, due to thermalization losses, the photocarriers generated by the highest energy photons of the solar spectrum cannot be efficiently extracted. Tandem solar cells are able to solve this drawback by combining two or more different band gap systems, using the material presenting a larger energy gap on the top of the system [2]. Recent studies have focused on the performance of an all-Si tandem solar cell, consisting of a bulk crystalline Si bottom cell and a top cell containing quantum confined Si nanostructures. Thereby, theoretical conversion efficiencies up to 42.5% can be achieved [3].

Silicon nanocrystals (Si NCs) were demonstrated to be a suitable candidate as top cell material since the quantum confinement of the charge carriers provides a tuneable band gap energy controlled via the Si NC size [4]. The precise control of the NC size is therefore crucial for obtaining desired band gap engineered structures. Many studies have been reported on superlattices of Si NCs in silicon dioxide (SiO_2), which show an excellent control of the multilayer thickness and the resulting NC size [5–7].

Amongst the most employed dielectric matrices as potential barriers, silicon oxides can be found. The excellent growth control of Si NCs embedded in SiO_2 contrasts with the poor electrical conductivity of this material. Instead, the silicon carbide (SiC) matrix, which has not been widely reported in literature [8,9], becomes an interesting candidate for containing the nanostructures, as its better electrical properties allow a more efficient separation of the photogenerated carriers, which is required in a photovoltaic device. In addition, to succeed in the photogenerated carriers separation a high crystalline degree of the NCs is required, in order to reduce non-radiative processes. This way, once generated, the carriers can be extracted before they recombine [10].

In this work, we present a structural, optical and electrical characterization of a system consisting of silicon-rich silicon carbide (SRC) layers properly separated by SiC barrier layers. Song et al. [8] studied the structural and optical properties of SRC/SiC multilayers with different Si content as a function of the annealing

* Corresponding author. Tel.: +34 93 4039175.
E-mail address: jlopezv@el.ub.edu (J. López-Vidrier).

0921-5107/$ – see front matter © 2012 Elsevier B.V. All rights reserved.
http://dx.doi.org/10.1016/j.mseb.2012.10.015

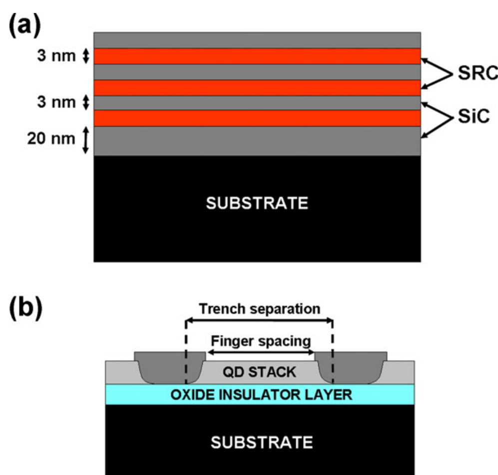

Fig. 1. (a) Cross-section scheme of the material samples grown for this study. (b) Cross-section scheme of the test devices fabricated for lateral electrical characterization, containing a multilayer system as a QD stack. Pictures not to scale (color online).

temperature. The high Si excess they employed leads to a highly dense nanocrystal network that produces their coalescence, thus limiting the quantum confinement of carriers. Instead, our study focuses on the effect of lower Si concentrations on the multilayer properties. We confirm the precipitation and crystallization of the Si nanoaggregates after the whole growth process by means of transmission electron microscopy (TEM) and Raman scattering. Furthermore, we present a comparison between the obtained structural parameters and the optical properties extracted from reflectance and transmittance (*R&T*) spectra. By means of both the Raman and *R&T* techniques, it has been possible to evaluate the crystalline fraction of the NCs. Therefore, we demonstrate the suitability of non-destructive optical techniques to complement the structural characterization methods. Finally, an electrical study is carried out in order to determine the conduction properties of the SRC/SiC structures, to be used in a future photovoltaic application.

2. Experimental details

Alternating superlattices of silicon-rich silicon carbide and silicon carbide barriers (Si_xC_{1-x}/SiC) were deposited on either crystalline Si or fused silica substrates by means of plasma-enhanced chemical-vapor deposition (PECVD). The thickness of both SRC and SiC layers was held constant at 3 nm, and the total number of deposited bilayers was 30 [the cross-section scheme of the structure is displayed in Fig. 1(a)]. A 20 nm buffer layer of SiC was also deposited between the substrate and the multilayers (ML). The SRC layers were deposited using high-frequency PECVD at 13.56 MHz (with a power per surface unit of 4 W cm^{-2}), employing SiH_4, CH_4 and H_2 as gas precursors, and keeping the substrate temperature at 350 °C during deposition. The different compositions were obtained at 0.95 mbar chamber pressure and under 70 sccm (standard cubic centimeters per minute) CH_4 and 10 sccm H_2 flow rates by varying the SiH_4 flow rate between 1.6 and 11.4 sccm. The resulting silicon ratios, checked by Rutherford Back Scattering and X-ray microanalysis (see Ref. [11] for further information on these techniques), were x = 0.5, 0.6, 0.65 and 0.75, where x = [Si]/([Si] + [C]), corresponding to excess Si concentrations of 0, 20, 30 and 50 at%, respectively. Reference samples were also fabricated, presenting no multilayer structure but a single SRC layer (SL).

After the deposition process, and in order to precipitate the Si excess present in the non-stoichiometric layers, the samples underwent accumulative annealing treatments, carried out in a N_2 atmosphere, employing a conventional horizontal furnace. This way, all annealed samples underwent a first process at 600 °C for 2 h. Afterwards, they were further annealed at 900 °C (for 1 h), 1000 °C (for 10 min) and 1100 °C (for 10 min), subsequently. After the annealing process, all samples were treated with plasma hydrogen at 450 °C during 45 min, in order to passivate the dangling bonds. Further details on the samples fabrication are described in Ref. [12].

The correct deposition of the multilayer structures, as well as the presence of Si nanoaggregates after the annealing process, were monitored by means of cross-section energy-filtered TEM (EFTEM) images, using a JEOL 2010F instrument (operating at 200 keV FEG) equipped with a Gatan image filter (0.8 eV resolution). The Si contrast was enhanced by energetically filtering the electron energy-loss spectra around the Si plasmon energy (E_{Si} = 17 eV).

The crystallization degree of the Si nanoprecipitates was studied by Raman scattering. The measurements were performed by exciting the samples with the 325 nm line of a He—Cd laser through a 40× NUV optical microscope objective, and acquiring the spectra in the back-scattering configuration using a Horiba Jobin-Yvon LabRam spectrometer. The reflectance and transmittance (*R&T*) spectra were obtained employing an Avantes UV–vis fiber optics spectrophotometer (210–1100 nm). The treatment of the obtained data was carried out by means of the OPTICAL code (see Ref. [13]), based on a multilayer approach combined with the Bruggeman model (see Ref. [14]) for effective medium approximation (EMA), associated to χ^2 minimization of the computed to experimental data. The electro-optical information of amorphous and microcrystalline Si, required in EMA mixture, was taken from Ref. [15], whereas the *n*–*k* spectra of microcrystalline SiC were deduced from *R&T* measurements taken on a single SiC sample deposited on quartz and annealed at 1100 °C as described above, and fitted using the modified Tauc–Lorentz model proposed by Jellison and Modine [16], further modified to finely account for defect excess absorption.

For the electrical characterization of the samples, simple test devices were fabricated, depositing a multilayer sequence consisting of 30 SRC/SiC bilayers on a Si substrate, with a controlled thermal generated SiO_2 layer (300 nm thick) between them. The multilayer composition was x = 0.65, holding the SiC barrier thickness constant at 3 nm, whereas the SRC layer thicknesses were 2, 3 or 4 nm. A 150 nm SiC single layer was employed for the reference device. After the multilayer deposition, the wafers were submitted to the same type of consecutive annealing as the previous samples, up to 1100 °C. For measuring the lateral electrical properties of the system, the devices were metallized with interdigitated contacts made of a 50 nm Ti/50 nm Pd/200 nm Ag stack. Trenches were etched by reactive ion etching prior to metal deposition to ensure a lateral contact to the multilayers. Fig. 1(b) presents a schematic of the described devices. *J*(*V*) curves under dark conditions and at different temperatures were obtained by means of an Agilent B1500 semiconductor device analyzer.

3. Results and discussion

3.1. Structural characterization

In order to check the deposition process of the SRC/SiC samples, cross-section TEM images were obtained. In Fig. 2, the EFTEM images corresponding to samples containing SRC/SiC multilayers grown on c-Si substrate are presented, with a silicon-to-carbon ratio of x = 0.75 before and after the annealing processes. The smooth interfaces between the SRC (bright) and SiC (dark) layers,

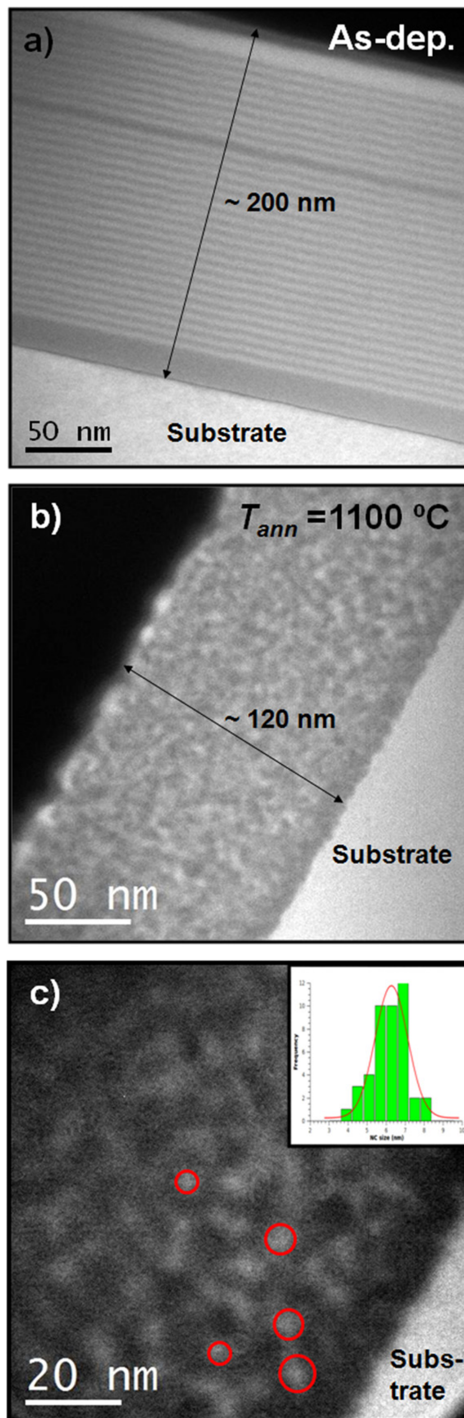

Fig. 2. Cross-section energy-filtered TEM images of the multilayer sample grown on c-Si substrate with $x = 0.75$: (a) as-deposited and (b) post-annealed up to $T_{ann} = 1100\,^{\circ}$C. The scale and the thickness of the active layer are indicated on the images. (c) shows a magnification of (b), where some nanoaggregates have been encircled. The inset in (c) shows a size distribution statistics on the measured Si NCs (color online).

and between the c-Si substrate (bright on the bottom) and the first SiC barrier [see Fig. 2(a)], corroborate the good deposition control of the multilayers and the suitability of the superlattice approach for this material. The SiC buffer layer between the substrate and the multilayers is also observed. It is worth noticing the presence of an uncontrolled oxide layer on the top of the multilayers which, after the annealing process, reacts with the first SRC layer to form an oxycarbide (SiC_yO_z) ternary compound [17]. This uncontrolled layer is undesired for device fabrication, as it introduces additional contacting difficulties.

The effect of the annealing temperature on the fabrication process can be appreciated in Fig. 2(b), where a sample containing the same silicon excess was annealed up to 1100 °C. The first noticeable thing is that the multilayer structure completely disappears, losing control on the spatial distribution of the precipitated Si NCs. A plausible explanation for this effect is that, under the high temperature, the stoichiometric SiC barrier layers are not able to avoid the diffusion of Si atoms in excess, which randomly distribute and precipitate along the whole sample. There is also a notorious shrinkage of the total thickness that was also observed for the different Si contents studied under the same annealing process. Separate experiments (not reported) on SRC single layers have shown that the shrinkage is more marked for higher C concentration in the material, consequently lowering the density of as-deposited material in this case [18].

From Fig. 2(b), one can deduce the presence of roughly spherical bright spots that correspond to Si nanoaggregates, as we are filtering the Si signal. This verifies the precipitation undergone by the Si excess present at the SRC layers once the annealing treatment was applied. The distinguishability of different nanostructures allowed for the performance of a size distribution statistics out of 50 NCs [see Fig. 2(c) and its inset], displaying a Gaussian profile centered around a mean NC diameter of $\mu = (6.3 \pm 0.1)$ nm, the size dispersion being $\sigma = (1.7 \pm 0.3)$ nm. Both the large mean NC diameter and size dispersion account for the effect of an unconfined precipitation at higher temperatures, which is translated into a lack of growth control over the NC size. In contrast, other works on similar materials showed a control on the multilayer structure after the post-deposition annealing process because of extremely large Si contents ($x = 0.85$, 0.9 and 0.96), and thus confined NC sizes around 3–5 nm were obtained [8,9]. Notice that the obtained diameter takes into account both the c-Si core and its surrounding a-Si shell, according to a core–shell NC model [19], as the used EFTEM energy window allowed signal from both crystalline and amorphous Si (with plasmon energies of 17 and 15 eV, respectively) to contribute to the image. The effect of the Si excess on the Si NC precipitation was also explored (results not shown in the figure), yielding increasingly lower NC diameters and density of nanoaggregates as the Si content decreases.

3.2. Optical measurements

In Fig. 3 we present the Raman spectra obtained from both single and multilayer samples containing different Si content and annealed up to 1100 °C, deposited on fused silica substrate. Two main features can be distinguished: a sharp peak centered at 512 cm^{-1} and a broad band around 470 cm^{-1}. Whereas the former signal is attributed to the crystalline Si coming from the Si NCs, the broad band is related to disorder-activated modes in amorphous Si. The vertical dashed line indicates the peak position for the bulk c-Si (520 cm^{-1}), being the difference from the NCs Raman signal due to a combination of quantum confinement effects and the stress provided by the surrounding matrix. It must be mentioned that, although the penetration length of the 325 nm line of the excitation laser (some tens of nm) does not reach the SiO_2 substrate, the undesired ternary compound layer mentioned in the previous section

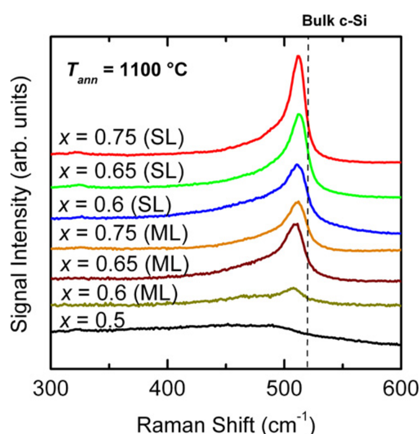

Fig. 3. Raman spectra of different samples grown on quartz substrate. The graph presents a Si excess study of both multilayer (ML) and single layer (SL) samples annealed at 1100 °C. The dashed line indicates the Raman shift corresponding to the bulk crystalline Si (520 cm^{-1}) (color online).

inevitably adds some disorder-related oxide Raman contribution, which may be difficult to distinguish from the a-Si one. It is also apparent in Fig. 3 that there is a strong influence of the silicon content on the vibrational properties of the SRC samples. Moreover, the Raman peak position presents a slight blueshift when increasing the Si content, possibly due to a reduced phonon confinement in larger nanostructures [8,20]. We observed a clear increase of the Raman signal with the silicon-to-carbon ratio, from $x = 0.6$ to $x = 0.75$, that perfectly scales with the silicon excess in the samples. The c-Si Raman signal enhancement observed in the single quantum well layers in comparison to the multilayer samples accounts for the larger Si content they present, due to the greatest SRC total thickness. No Si-related contributions are expected for the stoichiometric SiC sample, although it displays some Raman signal probably from the undesired SiC_yO_z layer on the top.

Further information about optical properties of the samples grown on fused silica substrate could be obtained from the *R&T* measurements. In Fig. 4 the reflectance and transmittance spectra of the annealed multilayer sample with a Si content of $x = 0.65$ is presented. In order to analyze the experimental data, the n–k

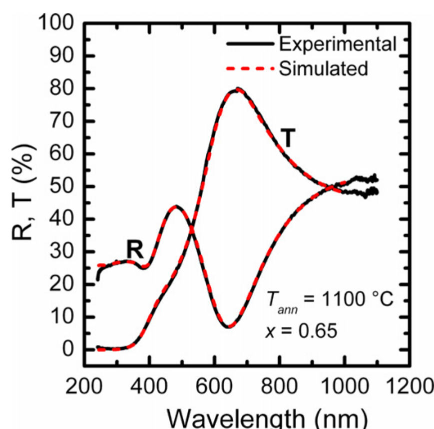

Fig. 4. Reflectance and transmittance spectra of the multilayer sample with a Si content of $x = 0.65$ and annealed at 1100 °C (black). In red, the spectra simulated by means of the modified Tauc–Lorentz model [16] (color online).

Table 1
Total thickness of the samples containing multilayers, as-deposited and annealed up to 1100 °C. The values obtained from energy-filtered TEM images (on Si substrate), optical *R&T* (on fused silica substrate) and only reflectance (on Si substrate) measurements are compared. The nominal thickness of the samples was 200 nm (180 nm for the multilayers plus 20 nm SiC buffer layer).

Sample	EFTEM thickness (nm)	*R&T* thickness (nm)	Reflectance thickness (nm)
$x = 0.75$ – as-dep.	200	197	222
$x = 0.65$ – as-dep.	–	200	227
$x = 0.6$ – as-dep.	–	200	214
$x = 0.75$ – 1100 °C	120	105	127
$x = 0.65$ – 1100 °C	119	107	115
$x = 0.6$ – 1100 °C	122	111	121

spectra of the main phases present in the material (crystalline and amorphous Si and crystalline and amorphous SiC) were introduced in an EMA mixture, and used to fit the *R&T* data, basing on χ^2 minimization. By allowing the variation of both the sample thickness and the volumetric fractions of the involved species, the experimental spectra could be perfectly reproduced (see the red line in the figure) and, therefore, reliable data about the total sample thickness and the concentration of the different materials constituting the samples were obtained (see Ref. [12] for further details on the employed procedure). The obtained composition was then used to simulate the reflectance measured on silicon substrates (as in this case UV–vis transmittance is not available), having thickness as the only free parameter in the simulation. Table 1 presents the total thickness values obtained from the optical spectra of as-deposited multilayer samples and those annealed at 1100 °C, and are compared with the ones obtained from EFTEM images. As can be appreciated, the nominal thickness of each sample completely agrees with that measured on as-deposited samples. After the annealing process, samples undergo severe shrinkage (to almost a 50% of the initial total thickness), as was observed by EFTEM. Table 1 also shows a very good agreement with the thicknesses optically determined on silicon substrates.

3.3. Evaluation of the crystalline fraction of NCs

Based on the results from optical measurements an analysis has been performed in order to evaluate the crystalline fraction of the precipitated NCs. First of all, we calculated the crystalline fraction by considering the volumetric contribution of a-Si and c-Si extracted from the *R&T* fittings using the n–k spectra of the involved materials:

$$f_c = \frac{\bar{V}_{\text{c-Si}}}{\bar{V}_{\text{c-Si}} + \bar{V}_{\text{a-Si}}} \quad (1)$$

where f_c is the crystalline fraction and $\bar{V}_{\text{c-Si}}$ and $\bar{V}_{\text{a-Si}}$ are the relative volume ratios of crystalline and amorphous silicon, respectively.

On the other hand, by applying a phonon confinement model to the Raman spectra (see for more details, for instance, Ref. [20]), we were able to deconvolute the crystalline and the amorphous Si contributions and, thus, evaluate the crystalline fraction also by using this method. Once the two contributions were isolated, their integrated intensity was considered proportional to the amount of each phase within the samples. Under these considerations, it is possible to evaluate the crystalline fraction by using the expression:

$$f_c = \frac{I_c}{I_c + \gamma \cdot I_a} \quad (2)$$

I_c and I_a being the integrated areas under the c-Si and a-Si contributions, respectively, obtained from the spectra deconvolution. The parameter γ represents the scattering cross-section ratio of the NCs, which depends on the involved NC sizes; for a mean

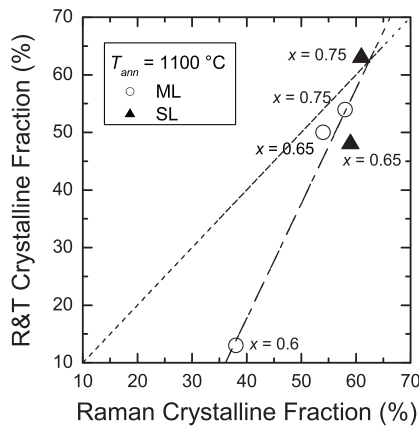

Fig. 5. Comparison between the crystalline fraction values obtained for both multilayers (ML, open circles) and single layers (SL, full triangles) annealed at 1100 °C, with different Si contents, by means of Raman scattering and optical reflectance and transmittance measurements. The dashed line represents the trend followed by the samples whereas the dotted line simulates the complete agreement of both techniques.

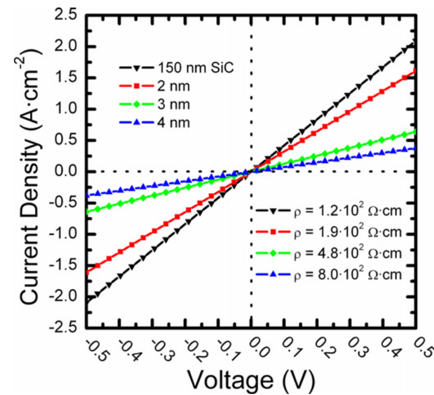

Fig. 6. Room-temperature, dark current density vs. voltage curves showing a SRC nominal layer thickness study on the devices fabricated for electrical measurements. In black, the measurement corresponding to stoichiometric SiC layer. The device structural characteristics were a 50 µm finger spacing and a trench separation of 61 µm. The resistivity obtained for each curve is written within the figure (color online).

diameter size (D) of 6.3 nm, and using the Bustarret's approach $\{\gamma(D) = 0.1 + \exp[-D(\text{Å})/250]\}$ [21], $\gamma = 0.88$.

Fig. 5 presents a comparison between the values obtained by means of optical *R&T* and Raman measurements, where the dotted line represents the complete agreement between the techniques, whereas the dashed line shows the observed trend followed by the samples. As can be seen in the figure, there is a good accordance between the results at high Si content, with crystalline fraction values around or larger than 50%; however, both techniques differ at low Si contents, where the values calculated from *R&T* data notably drop. The behavior at different Si excess ranges can be explained as follows: (i) the Raman spectra could be modulated by the presence of an extra amorphous contribution coming from the oxycarbide layer on top of the structures, which cannot be avoided and adds to the one coming from a-Si; we are then overestimating the amorphous Si contribution and thus underestimating the crystalline fraction. This effect is enhanced at higher Si concentrations, where NCs are larger, and the contribution from the a-Si is minimum in comparison with that of the c-Si core. (ii) When adjusting the *R&T* spectra, we are taking into account the n–k values for microcrystalline Si instead of nanocrystalline Si, the latter presenting lower values, as was reported by Moreno et al. [22]; this way, the volumetric fraction of c-Si is also underestimated. This effect, on the contrary, is more important at low Si excesses, where the nanoaggregates are smaller, and thus the difference between the NC size and bulk is maximum. To summarize, for the study of samples such as the ones presented in this work, optical *R&T* measurements are suitable for the high Si excess range, whereas Raman becomes a more reliable technique at low Si concentrations.

3.4. Electrical characterization

In order to perform lateral electrical measurements, the devices described in previous sections were employed [see Fig. 1(b)]. Notice that the contact fingers are wider than the trenches in which they are deposited, which defines two different intercontact distances: (i) the finger spacing, consisting of the nominal separation between the top of the contacts and (ii) the trench separation, taking into account the real separation between contacts at the maximum depth (resulting from the effect of reactive ion etching before the metallization). The measurements shown in this work were carried out under dark conditions, and employing the same device geometry, a 50 µm finger spacing and a 61 µm trench separation.

In Fig. 6, the obtained current densities at room temperature are plotted as a function of the applied voltage. The area employed for the data treatment was the one comprised between the finger length (0.27 cm) and the multilayer total thickness (after the annealing process) calculated by optical measurements (100, 120, 140 and 100 nm for SRC layer thicknesses of 2, 3, 4 nm and the SiC barrier, respectively). Two interesting features can be observed in the graph: (i) all curves present a clearly linear behavior at both polarization regimes and (ii) the obtained current density values are very high even at the relatively low polarization employed (higher than 2 A cm^{-2} at 0.5 V in the SiC single layer case). The former effect accounts for the Ohmic characteristics of the contacts; the latter, however, indicates that an important part of the current suffers a leakage through the thin SiC_yO_z ternary compound layer on top of the structure (see previous sections), which appears to be extremely defective. This hypothesis, however, is not conclusive due to the fact that a variation of the curves with the SRC layer thickness exists. For this reason, we performed further studies under different temperatures.

In Fig. 7, the conductivity as a function of the inverse temperature is presented, for the different SRC layer thicknesses involved in the characterization. Conductivity values between 10^{-1} and 10^{-2} Ω^{-1} cm^{-1} can be observed, which are clearly higher than the results reported by Song et al. on single layer a-SiC matrices containing Si NCs, around 10^{-6} and 10^{-10} Ω^{-1} cm^{-1} [23]. A clear semiconductor behavior can be interpreted from the increase of conductivity with the temperature. Fitting our experimental data with the Arrhenius law, it can be observed that the experimental data follow a single trend, which points out that the conduction can only be due to one mechanism. The obtained activation energies for the different devices lay between 38 and 76 meV (from the stoichiometric sample to the 4 nm SRC layers, respectively); this low energy required to activate the carrier conduction suggests that the involved mechanism is not extended state conduction within the multilayer, as the activation energy in that case would need to be half of the band gap. Taking into account the semiconductor behavior shown by the measurements and the SRC layer thickness dependence presented by both the current density and activation energy values, it is plausible to conclude that the current is mainly flowing through the top-defective SiC_yO_z layer, although its nature

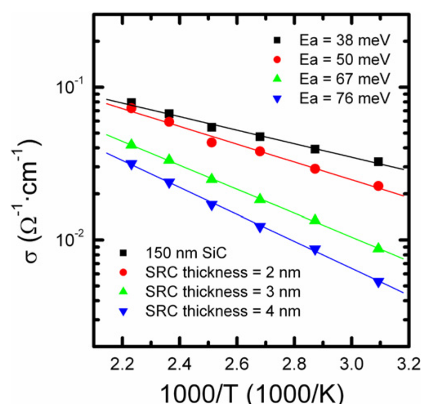

Fig. 7. Conductivity vs. temperature measurements for the devices containing different SRC nominal layer thicknesses. The fits according to the Arrhenius law are presented, and calculated activation energy values are displayed (color online).

is being affected by the characteristics of the layers underneath. Nevertheless, it is not possible to distinguish between the oxycarbide layer contribution and that coming from the multilayer structure; therefore, this capping layer must be removed in order to further understand the electrical properties of Si NCs in our system.

4. Conclusions

We have studied the structural, optical and electrical properties of Si_xC_{1-x}/SiC multilayers with different Si content. Energy-filtered (EF) TEM confirmed the presence of Si NCs after annealing at 1100 °C; however, the lost of the superlattice structure at this point led to lose the control of the NC size. In addition, a severe shrinkage of the total thickness was observed, as corroborated by *R&T* measurements, which was attributed to the Si random diffusion through the whole sample. EFTEM also manifested the presence of an extra SiC_yO_z ternary compound layer on top of the structure. The crystalline fraction of the samples was estimated by means of the Raman scattering and *R&T* techniques, obtaining larger values than 50% at high Si excesses. The study also revealed the suitability of both techniques at different Si contents. Lateral electrical measurements performed on test devices with different SRC layer thickness showed an extremely high current density in comparison with other works in the literature, due to the leakage of the current flow through the defective SiC_yO_z layer. The elimination of this oxycarbide layer in a future work will allow determining the real electrical properties displayed by NCs in these systems, in order to decide on their suitability as the top part of a tandem solar cell.

Acknowledgements

The research leading to these results has received funding from the European Community's Seventh Framework Programme (FP7/2007-2013) under grant agreement no. 245977, under the project title NASCEnT, and the Spanish Consolider Ingenio 2010 program (CSD2009-00013).

References

[1] F. Meillaud, A. Shah, C. Droz, E. Vallat-Sauvain, C. Miazza, Solar Energy Materials and Solar Cells 90 (2006) 2952–2959.
[2] D. Di, I. Perez-Wurfl, G. Conibeer, M.A. Green, Solar Energy Materials and Solar Cells 94 (2010) 2238–2243.
[3] G. Conibeer, M. Green, E.-C. Cho, D. König, Y.-H. Cho, T. Fangsuwannarak, G. Scardera, E. Pink, Y. Huang, T. Puzzer, S. Huang, D. Song, C. Flynn, S. Park, X. Hao, D. Mansfield, Thin Solid Films 516 (2008) 6748–6756.
[4] S. Godefroo, M. Hayne, M. Jivanescu, A. Stesmans, M. Zacharias, O.I. Lebedev, G. van Tendeloo, V.V. Moshchalkov, Nature Nanotechnology 3 (2008) 174–178.
[5] M. Zacharias, J. Bläsing, P. Veit, L. Tsybeskov, K. Hirschman, P.M. Fauchet, Applied Physics Letters 74 (1999) 2614–2616.
[6] M. Zacharias, J. Heitmann, R. Scholz, U. Kahler, M. Schmidt, J. Bläsing, Applied Physics Letters 80 (2002) 661–663.
[7] D. Hiller, S. Goetze, M. Zacharias, Journal of Applied Physics 109 (2011) 054308.
[8] D. Song, E.-C. Cho, G. Conibeer, Y. Huang, C. Flynn, M.A. Green, Journal of Applied Physics 103 (2008) 083544.
[9] D. Song, E.-C. Cho, G. Conibeer, C. Flynn, Y. Huang, M.A. Green, Solar Energy Materials and Solar Cells 92 (2008) 474–481.
[10] M. Avella, A.C. Prieto, J. Jiménez, A. Rodríguez, J. Sangrador, T. Rodríguez, M.I. Ortiz, C. Ballesteros, Materials Science and Engineering B 147 (2008) 200–204.
[11] C. Summonte, R. Rizzoli, M. Bianconi, A. Desalvo, D. Iencinella, F. Giorgis, Journal of Applied Physics 96 (2004) 3987–3997.
[12] C. Summonte, M. Canino, M. Allegrezza, M. Bellettato, A. Desalvo, S. Mirabella, A. Terrasi, Systematic characterization of silicon nanodot absorption for third generation photovoltaics, in: 26th EU-PVSEC, 5–9 September, Hamburg, Germany, 2011.
[13] E. Centurioni, Applied Optics 44 (2005) 7532–7539.
[14] W.R. Tinga, W.A.G. Voss, D.F. Blossey, Journal of Applied Physics 44 (1973) 3897–3902.
[15] G.E. Jellison, M.F. Chisholm, S.M. Gorbatkin, Applied Physics Letters 62 (1993) 3348–3350.
[16] G.E. Jellison, F.A. Modine, Applied Physics Letters 69 (1996) 371–373.
[17] B. Hornetz, H.-J. Michel, J. Halbritter, Journal of Materials Research 9 (1994) 3088–3094.
[18] A. Desalvo, F. Giorgis, C.F. Pirri, E. Tresso, P. Rava, R. Galloni, R. Rizzoli, C. Summonte, Journal of Applied Physics 81 (1997) 7973–7980.
[19] F. Iacona, C. Bongiorno, C. Spinella, S. Boninelli, F. Priolo, Journal of Applied Physics 95 (2011) 3727–3732.
[20] S. Hernández, A. Martínez, P. Pellegrino, Y. Lebour, B. Garrido, E. Jordana, J.M. Fedeli, Journal of Applied Physics 104 (2008) 044304.
[21] E. Bustarret, B. Ranchoux, H. Hamdi, A. Deneuville, S. Huant, P. Depelsenaire, Physica B+C 117 (1983) 950–952.
[22] J.A. Moreno, B. Garrido, P. Pellegrino, C. Garcia, J. Arbiol, J.R. Morante, P. Marie, F. Gourbilleau, R. Rizk, Journal of Applied Physics 98 (2005) 123253.
[23] C. Song, Y. Rui, Q. Wang, J. Xu, W. Li, K. Chen, Y. Zuo, Q. Wang, Journal of Alloys and Compounds 509 (2011) 3963–3966.

4.1.2.3. Superlattice Parameters Optimization

After the structural and optical characterization of the first set of Si NC / SiC samples, numerous structural and fabrication parameters were varied aiming at determining the optimum structure that allowed for the ML maintenance, i.e. the NC size control. For this, different sample batches were fabricated with different structural conditions, which have been summarized in Tab. 4.4. Basically, three sample sets have been employed for this study, which was reported in Paper VII [24]. In particular, Run C1 was devoted to the study of the SRC layer thickness variation, whereas in Run C2 the SRC composition was the key parameter. The results corresponding to both sample batches confirmed the optimum SiC barrier thickness and composition, and these were implemented in Run C6. In the following lines, the different results will be presented and discussed.

First, the structural analysis of the different sample Runs was addressed. EFTEM images corresponding to Run C1 showed an almost continuous crystallization of the Si excess (very large, $x = 0.95$) along the layers, when the layer structure was still preserved after annealing ($t_{SRC} = 3$ and 4 nm). In addition, a careful inspection of NC size showed a very broad size distribution (an larger mean NC size), enhanced at thinner SRC layers. In Run C2, t_{SRC} and t_{SiC} were fixed at 3 nm, and a lower Si excess was employed that ranged between $x = 0.6$ and 0.75. The Si content was found to be insufficient for the SL structure maintenance, and only the sample with highest x presented clearly-formed (and non-constrained size) nanostructures. TEM analysis also revealed an important shrinkage of all samples after the annealing process, being the final total thickness about a factor 0.7 of the as-deposited one. Again, samples with less Si excess (i.e. larger C content) were the ones which exhibited larger shrinkage. Finally, the TEM study revealed that it were a thicker SiC barrier layer and high Si content the crucial parameters to attain a controlled SL structure: with this aim, Run C6 was fabricated, in which the SRC layer thickness was modified ($t_{SiC} = 5$ nm and $x = 0.85$), showing multilayer control (and therefore size confinement) at $t_{SRC} = 3$ and 4 nm.

From the latter batch of samples, and after proving the proper superlattice structure after annealing, Raman and XRD measurements were carried out that evidenced the presence of crystalline Si and crystalline SiC domains within the samples. Indeed, evaluating the fraction of crystallized Si from Raman spectra in an analogous way as described in Section 4.1.1.3, a previous investigation of all analysed samples demonstrated that the Si crystalline degree increases with the Si content, i.e. the SRC layer thickness (and thus the overall Si volume in the sample), but it is barely dependent on the SiC barrier thickness. In particular, crystalline fractions of 41 and 60 % were determined for samples with $t_{SRC} = 3$ and 4 nm in Run C6 ($t_{SiC} = 5$ nm and $x = 0.85$), respectively, which, in turn, evidences the presence of a transition layer between the crystalline Si core and the surrounding SiC matrix. Optical techniques such as reflectance and transmittance spectroscopy

Table 4.4.: Summary of the parameters corresponding to the different samples employed for the study published in Paper VII.

Sample Run	t_{SRC}	t_{SiC}	x in $\mathrm{Si}_x\mathrm{C}_{1-x}$	T_{ann}
Run C1	1, 2, 3 and 4 nm	3 nm	0.95	1100 °C
Run C2	3 nm	3 nm	0.6, 0.65 and 0.75	1100 °C
Run C6	2, 3 and 4 nm	5 nm	0.85	1100 °C

were also employed, whose results corroborated the Si and SiC volumic presence within the samples.

Theoretical calculations were also carried out that retrieved information on the transition layer. Indeed, considering the stiffness of the SiC matrix and the large lattice mismatch between crystalline Si and SiC, a strong difference between the c-Si and SiC surface energies exists. This induces a stress exerted by the SiC matrix on the NCs that can only be relaxed under the presence of an amorphous transition layer, which introduces two new interfaces (c-Si / a-Si and a-Si / SiC) whose global surface energy is energetically favored with respect to the c-Si / SiC case. In addition, it is in these surface energy terms that the observed NC outgrowth towards the SiC barriers can be explained.

In conclusion, Paper VII [24] summarized the main structural results on Si NC / SiC multilayers that were achieved during the present Thesis Project. The ideal fabrication conditions, mainly dependent on a thick SiC barrier ($t_{\mathrm{SRC}} = 5$ nm), a high enough Si content ($x = 0.85$) and an annealing treatment at $T_{\mathrm{ann}} = 1100$ °C, were used for the fabrication of photovoltaic devices that will be described in Section 4.2.2.

Solar Energy Materials & Solar Cells 128 (2014) 138–149

Contents lists available at ScienceDirect

Solar Energy Materials & Solar Cells

journal homepage: www.elsevier.com/locate/solmat

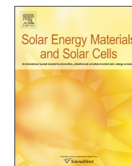

Silicon nanocrystals in carbide matrix

C. Summonte [a,*], M. Allegrezza [a], M. Bellettato [a], F. Liscio [a], M. Canino [a], A. Desalvo [a], J. López-Vidrier [b], S. Hernández [b], L. López-Conesa [b], S. Estradé [b,c], F. Peiró [b], B. Garrido [b], P. Löper [1,d,2], M. Schnabel [1,d], S. Janz [1,d], R. Guerra [e], S. Ossicini [e]

[a] Consiglio Nazionale delle Ricerche – Istituto per la Microelettronica e i Microsistemi (CNR-IMM) – via Gobetti 101, 40129 Bologna, Italy
[b] MIND-IN2UB – Departament d'Electrònica, Universitat de Barcelona – Martí i Franquès 1, 08028 Barcelona, Spain
[c] TEM-MAT, CCiT-UB – Centre Científic i Tecnològic, Universitat de Barcelona – Solé i Sabarís 1, 08028 Barcelona, Spain
[d] Fraunhofer ISE, Heidenhofstr. 2, D-79110 Freiburg, Germany
[e] Centro Interdipartimentale En&Tech and Dipartimento di Scienze e Metodi dell'Ingegneria, Università degli Studi di Modena e Reggio Emilia, via Amendola 2 Pad. Morselli, 42122 Reggio Emilia, Italy

ARTICLE INFO

Article history:
Received 9 December 2013
Received in revised form
30 April 2014
Accepted 4 May 2014
Available online 3 June 2014

Keywords:
Silicon nanocrystals
Third generation photovoltaics
SiC matrix

ABSTRACT

Ordered silicon nanocrystals in silicon carbide are produced by Plasma Enhanced Chemical Vapor Deposition by means of the multilayer approach followed by annealing at 1100 °C. The crystallization is verified by Raman scattering, X-ray diffraction, Transmission Electron Microscopy, and UV–vis spectroscopy. The conditions for the periodic structure to survive the high temperature annealing and for the SiC barrier to confine the Si crystal growth are examined by energy-filtered transmission electron microscopy and X-ray reflection. The final layout appears to be strongly influenced by the structural features of the as-deposited multilayer. Threshold values of Si-rich carbide sublayer thickness and Si-to-C ratio are identified in order to preserve the ordered structure. The crystallized fraction is observed to be correlated with the total silicon volume fraction. The constraints are examined through the use of ab-initio calculations of matrix-embedded silicon nanocrystals, as well as in terms of existing models for nanocrystal formation, in order to establish the role played by the interface energy on nanocrystal outgrowth, residual amorphous fraction, and continuous crystallization. A parameter space of formation of ordered Si nanocrystals is proposed. The diffusivity of carbon in the crystallized material is evaluated, and estimated to be around 10^{-16} cm^2/s at 1100 °C.

© 2014 Elsevier B.V. All rights reserved.

1. Introduction

Silicon nanocrystals (Si NCs) find their application in microelectronics and optics in devices such as discrete-trap storage nodes for fast-switching memories or optical waveguides [1]. The unique property of tuneable band gap [2], achieved through the control of NC diameter, is presently raising interest for application in photovoltaics as top absorber material in all-silicon tandem solar cells [3–6].

Size-controlled Si NCs embedded in a wide band gap matrix, typically SiO_2, can be produced via the multilayer method, that consists in the deposition of alternate Si-rich oxide (SRO)/SiO_2 layers, followed by solid phase crystallization. [2]. The method allows for an independent control of the Si grain size and density.

The efficient confinement associated to the wide band gap of SiO_2 brings about the drawback of poor electrical transport even under high electric field [7], which represents a limitation in electrical devices where efficient carrier transport is required. Efficient carrier transport is expected with a decrease of the band gap of the confining matrix, which has shifted the focus of investigation to a lower band gap material such as silicon carbide [8–15].

With respect to the SiO_2 matrix, the control of Si NC diameter in SiC is not straightforward. In the Si-rich carbide (SRC)/SiC system, the onset of Si crystallization varies between 800 °C and 1100 °C depending on the multilayer layout [9,10,14], with crystallized fraction and NC size increasing for higher temperatures [9,14]. The high thermal budget required to achieve effective crystallization causes the multilayer structure to vanish, and difficulties in confining the Si grain growth have been reported by several authors [9,10,12,14,16]. Considerable Si and C interlayer migration is observed for annealing temperatures higher than 1000 °C [10].

* Corresponding author. Tel.: +39 0516399131; fax: +39 0516399216.
E-mail address: caterina.summonte@cnr.it (C. Summonte).
[1] Tel.: +49 7614588 5021; fax: +49 7614588 9250.
[2] Now with École Polytechnique Fédérale de Lausanne, Photovoltaics and Thin Film Electronics Laboratory, Rue de la Maladière 71b, CH-2002 Neuchâtel, Switzerland.

http://dx.doi.org/10.1016/j.solmat.2014.05.003
0927-0248/© 2014 Elsevier B.V. All rights reserved.

The aim of this paper is to outline the processes occurring in the Si/SiC system, with the intent of identifying the mechanisms that govern the formation of Si NCs in SiC, impact on the final crystal size, and determine the persistence of the residual amorphous fraction. The survival of the multilayer, the bilayer thickness and the nanocrystal size will be determined by energy-filtered transmission electron microscopy (EF-TEM) and X-ray reflectivity (XRR). The crystalline degree will be evaluated by combining Raman scattering, X-ray diffraction (XRD) and UV–vis spectroscopy, and correlated with the multilayer parameters. A theoretical model based on the Density Functional Theory (DFT) will be applied to the Si NC/3C-SiC system, in order to determine the impact of lattice mismatch on nanoparticle structure, for varying nanoparticle sizes. The results will be discussed in terms of existing models for nanocrystal nucleation and growth, and will be put together to delineate a parameter space of formation of Si nanocrystals. The work is intended to contribute to the understanding of the SRC/SiC system and provide a key step forward regarding material engineering and design of devices.

2. Experimentals

SRC/SiC multilayers (=ML) were fabricated by PECVD on quartz and (100) CZ c-Si substrates. All layers were deposited in a plasma of SiH_4, H_2 and CH_4 at 13.56 MHz frequency and 28 mW/cm^2 power density. The SiH_4/CH_4 gas flow ratio was varied in order to achieve the desired silicon rich carbide Si_xC_{1-x} composition. Details on deposition conditions are given in Table 1. The pressure of the gas mixture was adjusted in order to obtain $\pm 5\%$ homogeneity over the (8×8) cm^2 deposition clear area. The multilayers were composed of 30+31 layers, with SiC as the first and the last layer. The first deposited SiC layer was 20 nm thick, intended to prevent epitaxial regrowth driven by the c-Si substrate, as we have observed for lower buffer layer thickness in test samples (unpublished result). Several combinations of SRC composition and SRC and SiC as-deposited thickness (d^0_{SRC} and d^0_{SiC} respectively) were studied. The multilayers are grouped into four sets, labeled with a letter (X or D) followed by a number. The letter indicates the parameter that is kept constant in the SRC, either the Si ratio (X) or the thickness (D). The number stands for the as-deposited SiC thickness d^0_{SiC} expressed in nm. In particular:

Set X3	$x=0.95$	$d^0_{SiC}=3$ nm	$d^0_{SRC}=2,3,4$ nm
Set X9	$x=0.85$	$d^0_{SiC}=9$ nm	$d^0_{SRC}=2,3,4$ nm
Set D3	$d^0_{SRC}=3$ nm	$d^0_{SiC}=3$ nm	$x=0.6, 0.65, 0.75$
Set D5	$d^0_{SRC}=3$ nm	$d^0_{SiC}=5$ nm	$x=0.65, 0.75$

where d^0_{SRC} stands for the as-deposited value of SRC thickness.

Table 1
PECVD deposition conditions of Si_xC_{1-x} layers. Conditions common to all depositions: 13.56 MHz frequency, and 28 mW/cm^2 power density.

Sample set	Layer classification	Si ratio (x)	SiH_4 (sccm)	CH_4 (sccm)	H_2 (sccm)	p (hPa)	$T_{Substrate}$ (°C)
X3	SRC	0.95	20	30	10	0.85	350
	SiC	0.5	1.6	70	0	0.9	350
X9	SRC	0.85	13	13	90	0.7	325
	SiC	0.5	2	70	100	0.9	325
D3	SRC	0.75	11.4	70	10	0.95	350
	SRC	0.65	6.1	70	10	0.95	350
	SRC	0.6	3	70	10	0.95	350
	SiC	0.5	1.6	70	10	0.95	350
D5-1	SRC	0.65	6.1	70	10	0.95	350
	SiC	0.5	1.6	70	10	0.95	350
D5-2	SRC	0.75	11.4	70	10	1	350
	SiC	0.5	2.6	70	10	1	350

Table 2
Multilayer parameters: silicon ratio x, as-deposited SiC and SRC thickness on quartz substrate; SiC, SRC, SiC+SRC bilayer thickness; nanocrystal size obtained by TEM and XRD. $d_{SRC+SiC}$ was determined by TEM, or deduced from total thickness divided by the number of deposited double layers for non-surviving ML structure. d_{SiC} and d_{SRC} were determined as described in Section 2. Note that the statistical error on $d_{SRC+SiC}$ is sometimes lower than the sum of errors on d_{SiC} and d_{SRC}.

Sample	x	**Multilayer structure**					**Nanocrystal size**	
		d^0_{SiC} (nm)	d^0_{SRC} (nm)	d_{SiC} (nm)	d_{SRC} (nm)	$d_{SiC+SRC}$ (nm)	TEM (on C–Si) (nm)	XRD (on quartz) (nm)
X3-1	0.95	3	1	1.8 ± 0.2	0.7 ± 0.5	2.5 ± 1.0[a]	3 ± 2	
X3-2	0.95	3	2	1.8 ± 0.2	1.8 ± 0.2	3.5 ± 1.0[a]	5 ± 2	
X3-3	0.95	3	3	1.8 ± 0.2	2.6 ± 0.2	4.5 ± 0.5	3.5 ± 1.5	
X3-4	0.95	3	4	1.8 ± 0.2	3.5 ± 0.2	5.4 ± 0.5	3.5 ± 2	
X9-2	0.85	6	2	5 ± 1	2 ± 0.5	6.7 ± 0.1[a]		
X9-3	0.85	6	3	5 ± 1	3 ± 0.5	7.6 ± 0.1	4.7 ± 0.3	1.5 ± 1.0
X9-4	0.85	6	4	5 ± 1	4 ± 0.5	9.9 ± 0.5	5 ± 1	4 ± 0.5
D3-1	0.75	3	3	1.7 ± 0.5	2.0 ± 0.5	4.1 ± 0.1[a]	5 ± 1	
D3-2	0.65	3	3	1.7 ± 0.5	2.0 ± 0.5	4.0 ± 0.1[a]		
D3-3	0.6	3	3	1.7 ± 0.5	2.0 ± 0.5	4.1 ± 0.1[a]		
D5-1	0.65	6	3	3 ± 1	2.5 ± 0.5	5.5 ± 0.5[a]	5 ± 1	
D5-2	0.75	6	3	3 ± 0.5	3.5 ± 1.5	6.0 ± 0.2	4 ± 2	

[a] Deduced from total thickness divided by the number of deposited double layers.

140 C. Summonte et al. / Solar Energy Materials & Solar Cells 128 (2014) 138–149

Table 2 summarizes the details of the layers in each sample. The d_{SiC}, d_{SRC}, $d_{SiC+SRC}$ values refer to the thicknesses measured after annealing.

The annealed d_{SiC} and d_{SRC} layer thicknesses were determined as

$$d_{SiC} = F d_{SiC+SRC}; \qquad d_{SRC} = (1-F) d_{SiC+SRC} \tag{1}$$

where the fraction F of SiC in the double layer after annealing is determined as

$$F = \frac{d^0_{SiC} S_{SiC}}{d^0_{SiC} S_{SiC} + d^0_{SRC} S_{SRC}(x)}; \tag{2}$$

the shrinking factor $S_{SRC}(x)$ for SRC, empirically determined on separate test samples, is given by:

$$S_{SRC}(x) = 0.114 + 0.83x. \tag{3}$$

S_{SiC} equals 0.54 for X3 sample set and 0.53 in all other cases.

Table 2 also reports experimental results that will be described below.

On top of X9 and D5 sets an amorphous silicon (a-Si:H) sacrificial layer was deposited in order to prevent the SRC/SiC oxidation during annealing. Such layer was removed by wet etching after annealing. Full details are given in Ref. [17]. Each multilayer was simultaneously deposited on double polished c-Si and on fused silica substrates. The films deposited on silicon substrates are systematically about 10% thicker than on fused silica. This occurrence is attributed to the effect of the different conductivity of substrates on potential distribution in the deposition chamber [18].

Reference single layers were used to calibrate the deposition time and to monitor the SRC composition [19]. The silicon content of test SRC layers was verified by Rutherford backscattering and elastic recoil detection analysis [20].

The precipitation of excess Si in the SRC layers was induced by annealing, using a low-temperature step (600 °C), intended to foster hydrogen evolution, followed by a step at 1100 °C in flowing nitrogen for either 9 or 30 min. In the case of X9 and D5 sample sets, 10% O_2 was introduced in the annealing ambient to induce a controlled oxidation of the top Si sacrificial layer. After annealing the surface was etched in diluted HF (all sets). Samples deposited with the a-Si:H sacrificial layer were also etched in diluted tetramethyl ammonium hydroxide (sets X9 and D5) to remove the residual unoxidized Si [17].

Nanoscale images were taken using a JEOL 2010 FEG TEM operating at 200 keV equipped with a Gatan image filter (0.8 eV resolution). The Si contrast was enhanced by filtering the electron energy around the Si plasmon energy loss (E_{Si} = 17 eV).

Raman measurements were performed by exciting the samples with the 325-nm line of a HeCd laser through a 40 × NUV optical microscope objective, and acquiring the spectra in the backscattering configuration using a Horiba Jobin-Yvon LabRam spectrometer coupled to a CCD. The absorption at this wavelength is higher than 4×10^5 cm^{-1} in all samples (penetration depth lower than 25 nm), which allows us to exclude any contribution from the substrate. The crystalline Si fraction X_c was determined by deconvoluting the Raman signal given by the Si–Si TO–LO vibration mode. A detailed description of the deconvolution procedure is given in Ref. [21].

XRD and XRR were performed using a SmartLab diffractometer (Rigaku), equipped with a rotating anode (*Cu Kα*, λ = 1.54180 Å) followed by a parabolic mirror to collimate the incident beam and Soller slits (divergence 0.114° for XRD and 0.01° for XRR) in front of the detector to collimate the diffracted beam. XRD patterns were collected in an out of plane grazing incidence geometry, where the grazing angle was kept constant and at a small value (0.8°) while the detector moved (2θ scan) in the plane normal to the surface.

Fourier transform infrared spectroscopy (FTIR) measurements were carried out using a Thermo Nicolet 5700 spectrometer. The infrared transmittance of multilayers deposited on c-Si substrates was acquired with 16 cm^{-1} resolution. The absorption spectra were corrected by substrate absorption and baseline subtraction, and normalized to the total thickness.

Reflectance and transmittance (R&T) spectra in the UV–vis–NIR range were acquired using an HP 8452A diode array spectrophotometer and an Avantes fiber optic spectrophotometer. The fitting of the R&T spectra was performed using the computer code Optical [22]. The input data for the simulation are the complex refractive indices of μc-Si, ([23]), a-Si ([24]) and microcrystallized SiC (spectral data separately determined [17]). SiO_2 (spectral data from [25]) was introduced in the simulation of the low density surface layer. The simulations were used to optically determine the crystallized fraction X_c and all thicknesses reported in the paper unless otherwise stated.

3. Results

We start our report from the crystallization of SiC in Si/SiC multilayers. In Fig. 1 the FTIR spectra of the D9 sample set and of a SiC single layer sample are reported. The crystallinity of SiC is evaluated using FTIR by deconvoluting the Si–C stretching mode at about 800 cm^{-1}, and monitoring the Lorentzian (corresponding to crystalline) to Gaussian (corresponding to amorphous) ratio of the components [26]. In the deconvolution, we used a single Gaussian component. A crystallized fraction of 77% and ~63% was obtained for the single layer and the MLs respectively. By integration of the absorption band, the Si–C bond density is determined after thickness normalization and baseline subtraction, using 2.05×10^{19} cm^{-2} as a calibration factor [27]. The Si–C bond density is reported in the inset of Fig. 1. A value of 9.0×10^{22} cm^{-3} is obtained for the SiC reference sample, in good agreement with 1.9×10^{23} cm^{-3} of 3C-SiC. In ML samples the Si–C bond density increases as d^0_{SRC} is reduced, in agreement with the increased SiC volume fraction V_{SiC}. To evaluate the impact of the variation of SiC volume among MLs, the bond density is normalized by V_{SiC} estimated based on ML parameters, see Appendix A for V_{SiC} estimation and more details in [15]. The bond density normalized to V_{SiC} (inset of Fig. 1) saturates close to the bulk value for all ML composition, indicating that the decrease of Si–C bond density with d^0_{SRC} can be fully ascribed to the decreased V_{SiC}. The full width

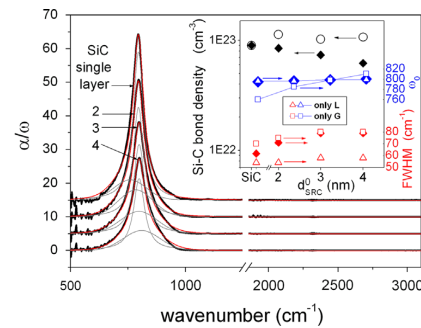

Fig. 1. Infrared absorption spectra of sample set X9. The spectrum of an SiC single layer is also reported. The curves were set off by α/ω = 5, and are labeled with d^0_{SRC}(nm). The Gaussian and Lorentzian components obtained by the deconvolution are also shown. Inset: ◆: Si–C bond density derived from the Si–C stretching vibration absorption; ○: Si–C bond density normalized by the SiC volume fraction; ◆ frequency and ◆ FWHM of the same peak; Δ frequency and Δ FWHM of the Lorentzian component only; □ frequency and □ FWHM of the Gaussian component only.

at half maximum (FWHM) of the same mode, also shown, decreases due to the decreased contribution of the Gaussian component. The FWHM of the Lorentzian component is $56 \pm 2\ cm^{-1}$ for all samples, indicating a grain size of about 7.3 nm if evaluated according to Ref. [28]. We will make use of these conclusions while discussing the optical simulations.

Figs. 2–4 show the cross section energy-filtered (EF) TEM micrographs of X3, X9 and D3 sample sets after annealing. The EF-TEM analyses point out that a strong relationship exists between the survival of the ML structure and x, d_{SRC} and d_{SiC}. It results that, in contrast to the case of SiO_2/SRO multilayers [2,29], the SRC/SiC multilayers do not necessarily maintain the ML structure after high temperature annealing. The situation is summarized in Fig. 5(a). The figure shows the contrast profiles as a function of depth in the EF-TEM micrographs shown in Figs. 2–4, obtained by integrating the signal along the direction parallel to the multilayer. The actual thickness $d_{SiC+SRC}$ of the SiC+SRC bilayers, if present, is reported in the figure. With reference to Figs. 2 and 3, in sample sets X3 and X9 the ML structure is preserved for $d^0_{SRC} \geq 3$ nm and is increasingly defined for increasing d^0_{SRC}. For sample set D3 (Fig. 4) the ML structure is not maintained for any sample. With reference to the annealed thicknesses (Fig. 5(a)), for sample set X3 the ML structure is evident for $d_{SiC+SRC} \geq 4.5 \pm 0.1$ nm. For sample set X9 the ML structure is evident for $d_{SiC+SRC}=9.9 \pm 0.4$ nm, still visible for $d_{SiC+SRC}=7.6 \pm 0.1$ nm, and no longer visible for the last case (sample X9-2).

Figs. 2–4 allow the determination of SiC+SRC thickness variation upon annealing. In fact, as previously noticed, the SiC and SRC materials undergo shrinkage upon annealing, more pronounced in C-rich material, in association with the higher initial hydrogen concentration [20]. The shrinkage is associated to a density increase [14], as a consequence of hydrogen effusion and of the amorphous-to-crystalline phase transition. The annealed MLs are consequently a factor 0.6–0.8 thinner than in the as-deposited state. In Fig. 5(b) the $d_{SiC+SRC}$ obtained from Fig. 5(a), or, for non-

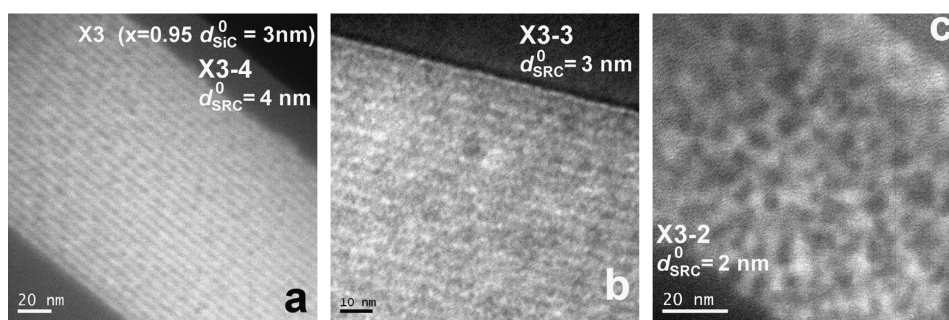

Fig. 2. Cross-section energy-filtered TEM images of sample set X3 (x=0.95, d^0_{SiC}=3 nm): (a) X3-4; (b) X3-3; (c) X3-2.

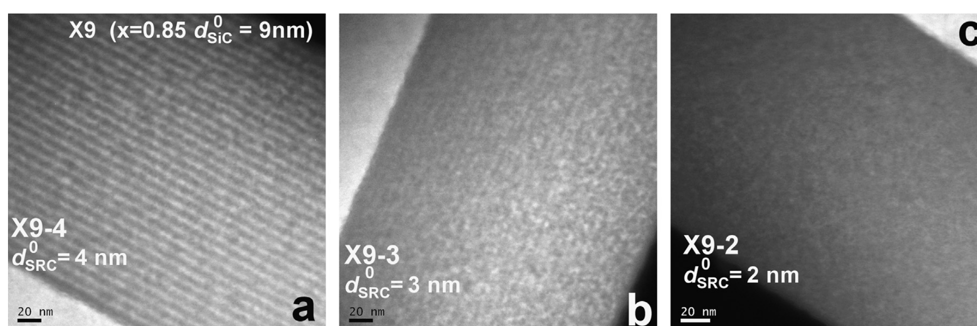

Fig. 3. Cross-section energy-filtered TEM images of sample set X9 (x=0.85 and d^0_{SiC}=9 nm). (a) X9-4; (b) X9-3; (c) X9-2.

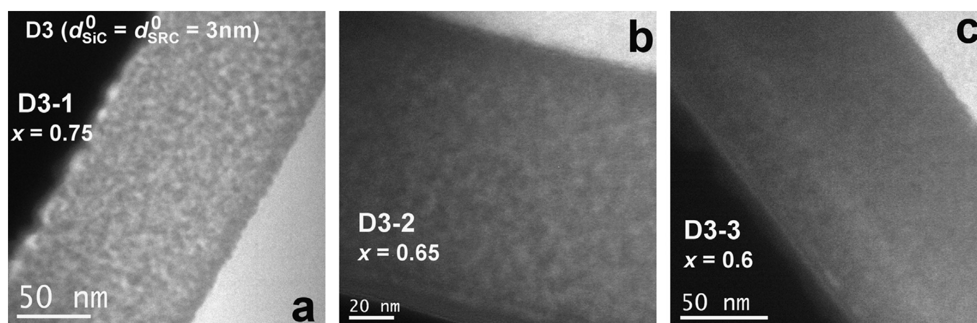

Fig. 4. Cross-section energy-filtered TEM images of sample set D3 ($d^0_{SiC}=d^0_{SRC}$=3 nm); (a) D3-1; (b) D3-2; (c) D3-3.

surviving multilayers, deduced from total thickness divided by the number of double layers, is plotted against $d_{SiC}+d_{SRC}$ obtained as described in Section 2. The figure supports the consistency of data. All thicknesses are reported in Table 2. The meaning of d_{SiC} and d_{SRC} for materials with no evident ML structure may not be immediate. However, keeping track of the expected values allowed us to support our conclusions about the Si NC space of formation.

Figs. 2–4 also give evidence of the material crystallization, that is identified from the highly contrasted spots on the images. A

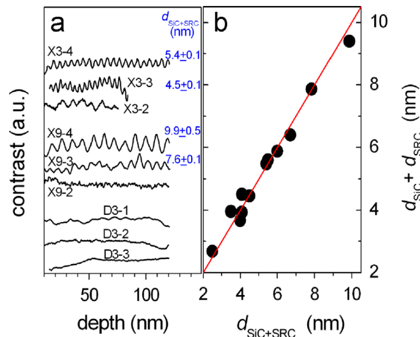

Fig. 5. (a) Gray scale profiles integrated over the dimension parallel to the sample surface of TEM images from Figs. 2, 3 and 4. For surviving ML, the obtained $d_{SiC+SRC}$, is indicated. (b) Sum of SiC and SRC thickness determined as described in Section 2, vs the double layer thickness determined from TEM observations. The line represents equal values.

detailed study of the crystalline aggregates is presented in Fig. 6. Fig. 6(a) shows a high resolution TEM image of sample X9-4 (same as Fig. 3(a)). The inset shows the Fast Fourier Transform (FFT) of the image, reproducing its diffraction pattern. Two rings can be observed, the inner one related to crystalline Si and the outer one to crystalline 3C-SiC. The crystalline Si contribution (inner ring) was used to reproduce the real space image of c-Si, that in Fig. 6 (b) is superimposed in sienna color to the original image (in green). Fig. 6(b) shows evidence of silicon nanocrystal formation, arranged in rows reproducing the initial ML structure, with NC vertical diameter controlled by the ML period with possible coalescence along the SRC plane. Fig. 6(c) reports the EF-TEM of the same sample. The intensity profiles taken across and along the SRC plane are reported in panels (d) and (e). The Si signal does not vanish between individual NCs, either due to Si NC touching each other, or due to isolated Si NCs at different depths being projected onto the same location in a plane image, as a consequence of a detection depth of around 10 nm. Si NC and bilayer sizes obtained by TEM analysis are summarized in Table 2.

More information about the crystallization of Si aggregates is obtained by Raman, XRD and R&T spectroscopy analyses on the multilayers produced on quartz substrates. Fig. 7 shows the Raman spectra from samples of set X9. In the lower frequency region, two main features can be distinguished: a broad band around 470 cm^{-1} and a peak-like contribution centered at 512 cm^{-1}. The former signal is attributed to Si modes activated by the loss of k conservation in the amorphous phase whereas the latter comes from nanocrystalline Si present in the samples [21]. As a reference, the Raman shift of bulk c-Si (520 cm^{-1}) is also indicated. The

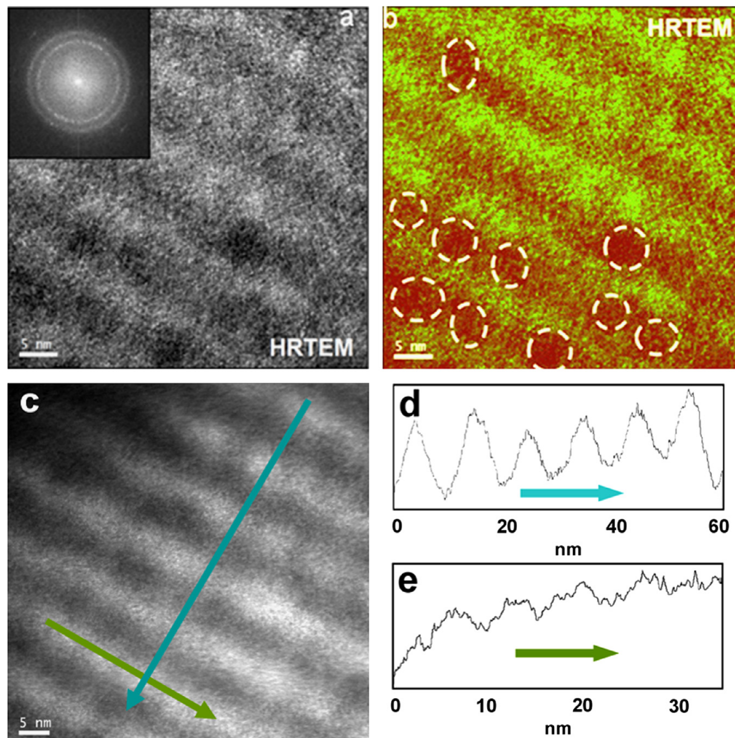

Fig. 6. (a) High resolution TEM image of sample X9-4 after annealing. Inset: Fast Fourier Transform (FFT) of the high resolution image, where the two rings due to Si (inner ring) and 3C-SiC (outer ring) crystalline domains are visible. (b) Image obtained by superimposing the image of panel (a) (in green) to the inverse FFT of the inner polycrystalline ring of the inset (sienna color). The regions in sienna color then correspond to Si nanocrystals. (c) Magnified EF-TEM image of sample X9-4 after annealing. The bright signal is due to the Si plasmon excitation. (d), (e): intensity profiles across the ML (d) and along one SRC plane (e). (For interpretation of the references to color in this figure legend, the reader is referred to the web version of this article.)

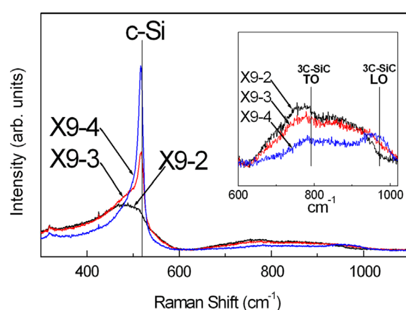

Fig. 7. Raman spectra of sample set X9. The inset shows the region around the TO and LO modes in 3C-SiC.

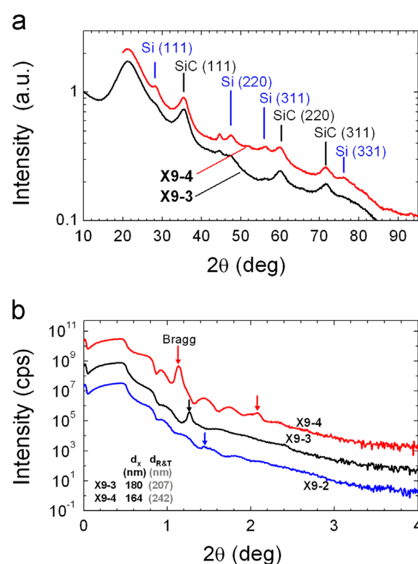

Fig. 8. X-ray diffraction (a) and reflectivity (b) spectra of X9 sample set on quartz substrate. The arrows in panel (b) indicate the position of Bragg's peaks. The corresponding coherent thickness d_X deduced by FWHM is also indicated. The ML thickness detected by R&T on the same substrate is reported in brackets for comparison.

broadening observed in the peak-like contribution, together with its lower frequency with respect to the one in bulk silicon are evidence of the presence of Si-nanoaggregates in crystalline state. This contribution scales with d^0_{SRC}, indicating that the crystalline volume is larger for thicker SRC. At high frequencies (see also the inset of the figure) a broad signal is observed, attributed to the broadening and overlap of the TO and LO modes in polycrystalline 3C-SiC [30] that are located at ~797 and ~972 cm^{-1} in 3C-SiC single crystal [30,31], in agreement with TEM observations of SiC crystalline domains.

X-ray reflectivity (XRR) and X-ray diffraction (XRD) detect direct evidence of superlattices and crystallized phases. The XRD and XRR spectra taken on X9 sample set are reported in Fig. 8.

The diffraction peaks related to 3C-SiC(111), 3C-SiC(220), and 3C-SiC(311) are visible for all samples. Silicon diffraction features are observed for samples X9-3 and X9-4, larger for larger d^0_{SRC} (Fig. 8(a)), indicating Si NC formation, whereas the crystalline volume for X9-2 (evaluated in the range of 2–5% by Raman spectroscopy, and by R&T spectroscopy as described below) is below the detection threshold (spectrum not reported). By applying the Scherrer equation to the FWHM of the diffraction peaks from Si(111), Si(220) and Si(311) planes [32], an average NC diameter equal to (1.5 ± 1.0) nm and (4.0 ± 0.5) nm is deduced for samples X9-3 and X9-4 respectively.

The XRR spectra (Fig. 8(b)) show evidence of Bragg peaks at angle of incidence 1.27° and 1.12° for samples X9-3 and X9-4 respectively, associated to the multilayer structure, [9], whereas for sample X9-2 the Bragg peak is hardly detected, in agreement with TEM results (Figs. 3c and 5).

The periodicity corresponding to $d_{SiC+SRC}$ is deduced from the Bragg peak angular position. A periodicity of 7 and 7.8 nm is obtained for samples X9-3 and X9-4 respectively. The lower value of $d_{SiC+SRC}$ with respect to TEM results (7.6 and 9.9 nm, see Fig. 5) is consistent with the lower thickness obtained on quartz with respect to the c-Si substrate discussed in Section 2.

The FWHM of the Bragg peaks is compatible with coherent domains thinner than the ML thickness (see inset of Fig. 8(b). In fact, a closer inspection of Fig. 3(a), (b), shows an increase of interface roughness due to intermixing of SRC and SiC layers for film regions closer to the sample surface, which therefore do not contribute to the XRR signal. High interface roughness is reported in [12,13].

Table 2 summarizes nominal and measured features of the multilayers: a summary of the ML description, the Si ratio x in SRC, thickness of the as-deposited SiC and SRC layers (d^0_{SRC}, d^0_{SiC}), measured bilayer thickness after annealing ($d_{SiC+SRC}$, d_{SiC} and d_{SRC} measured on the annealed multilayers, and Si NC size obtained by TEM and XRD. The reported values for SiC, SRC and bilayer thickness after annealing for the samples that did not present evidence of a multilayer structure were obtained by dividing the total film thickness by the number of deposited double layers.

A lower grain size is detected by XRD with respect to TEM, which is often observed and typically attributed to the different statistics probed by the two techniques. Further possible reasons include the difference in the $d_{SiC+SRC}$, between deposition on quartz (used for XRD) and c-Si (used for TEM), the validity of the shape factor used in the Scherrer formula (K=0.94, which represents spherical NCs), and the uncertainty in the determination of Si NC size from the TEM image.

To derive a correlation between initial ML parameters and the crystallization mechanism, in Fig. 9 we report the Si NC size for the cases where such determination was possible, normalized to $d_{SiC+SRC}$. The choice for the normalization is based on the consideration that in order for the multilayer to succeed in promoting isolated Si NCs, their size must not exceed d_{SRC} plus ½d_{SiC} above or below the SiC layer, i.e. $d_{SiC+SRC}$. For each point, the figure also reports x and the sample name, underlined if the multilayer structure survived the annealing.

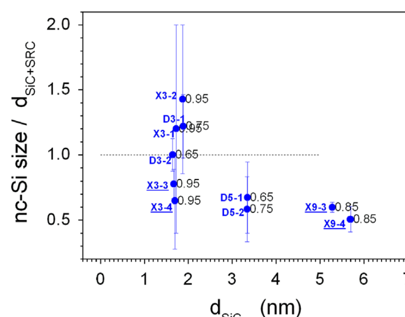

Fig. 9. Si nanodot size normalized by $d_{SiC+SRC}$, as a function of d_{SiC}. The data are labeled with x and with the sample name, underlined if the ML survived the annealing.

The figure shows that for $d_{SiC} < 3$ nm, no control of the Si NC size is achieved. Si NC size larger than $d_{SiC+SRC}$ is observed for samples D3-1, D3-2, X3-1, X3-2, that also show loss of the multilayer structure. With reference to Table 2 it appears that for those cases in which d_{SiC} is too small to prevent ML annihilation ($\leq 1.8 \pm 0.2$ nm), NC outgrowth is favoured by high x and thinner d_{SRC}.

For high x and high d_{SRC}, continuous crystallization is observed by TEM. At the moment, we cannot propose a criterion to distinguish with certainty the case of isolated from interconnected nanocrystals. Contrary to the case of insulators like SiO_2 as dielectric matrix, in the case of the semiconducting SiC matrix a sharp variation of the electrical properties is not observed at the electrical percolation threshold [15]. From geometrical considerations, NC distance between closely packed spherical NCs of radius r in a $2r$ thick layer vanishes for $V_{Si}=0.6$ (all Si NC touching each other), whereas for Si NCs in SiO_2 carrier delocalization was identified already for V_{Si} somewhat above 0.25 [33]. Another possibility to identify continuous crystallization is to detect the presence of resolved c-Si peaks in the UV–vis reflectivity spectrum (R double peak) [34], which are not supposed to exist in nanocrystalline Si, due to the smearing out of the dielectric constant absorption band [35–42]. However, the criterion is rather uncertain for low total silicon volume concentration V_{Si}. In other words, the R double peak gives clear information where present, but cannot be used to discard continuous crystallization if not visible. Among our samples, the R double peak is clearly identified for samples X3-3, X3-4 and X9-4 (result not reported). As a confirmation, a Si signal somewhat continuously distributed along the SRC layers is observed by EF-TEM for those samples, see for instance the EF-TEM images of sample X9-4 in Fig. 6.

The analysis of Raman spectra allows the determination of the crystalline fraction X_c of Si in SRC/SiC multilayered systems. To determine X_c by Raman scattering, we considered the frequency range of the amorphous and crystalline silicon optical modes (450–550 cm^{-1}). By considering that the integrated intensity of each contribution is proportional to the volume amount of each phase (see for instance Ref. [21] for details), we evaluated the crystalline fraction for each sample by deconvoluting the spectra into such components and applying the formula:

$$X_c = I_c/(\gamma I_a + I_c), \quad (4)$$

where I_a and I_c are the integrated intensities of the amorphous and crystalline signals respectively, and γ is the scattering cross section ratio.

The crystalline fraction X_c has also been evaluated by means of R&T spectroscopy. An example of R&T measurement and simulation for sample X9-4 on fused silica is reported in Fig. 10. The parameters used in the simulation of sample X9-4 are reported in the figure caption. A detailed description on how X_c is derived from R&T spectroscopy is reported in Refs. [15,43]. In this analysis, the material is approximated by a mixture of a-Si, nc-Si, and microcrystallized SiC. The dielectric function of the latter was determined on a single layer SiC sample that, based on FTIR results reported above, was assumed to be structurally representative of the SiC actually present within the ML. Due to the lack of a generally agreed spectral function for Si NC [35–42,44,45], the spectral function of continuous microcrystallized silicon [23] was used.

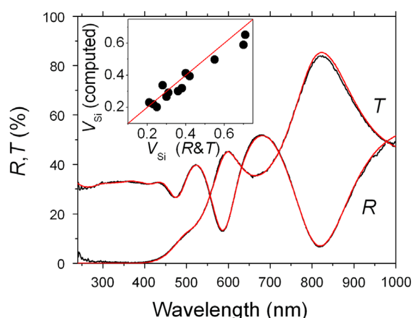

Fig. 10. Reflectance and transmittance on quartz substrate, measured (black) and computed (color), for sample X9-4. Result of the simulation: total thickness 264.6 nm; X_c=57%; V_{Si}=38%. The sample shows a 5 ± 1 nm low density surface layer. Inset: silicon volume fraction determined according to Appendix A, plotted against V_{Si} obtained by R&T simulations.

Qualitatively speaking, the Si/SiC ratio is determined by the fringe contrast at long wavelengths, (700–1000 nm in Fig. 10), which is higher for a higher ratio. The ratio is fairly independent of X_c due to the similarity of optical properties of a-Si and nc-Si in this wavelength range. Once the Si volume content is fixed, X_c is determined by the onset of transmittance (400 nm in Fig. 10), that occurs at shorter wavelenghts for higher X_c. The fitting was accomplished by the Generalized Transfer Matrix method [22]. The material mixtures were treated using the Bruggeman Effective Medium Approximation [46].

The simulation supplies the total film thickness, details on possible surface layers, V_{Si}, X_c, and $d_{SiC+SRC}$ once the number of bilayers is fixed. The separation of $d_{SiC+SRC}$ into $d_{SRC}+d_{SiC}$ can be obtained only upon a hypothesis on V_{Si} in the SRC layer. In fact, qualitatively speaking and within the limitations of the EMA, for a given $d_{SiC+SRC}$ a double layer containing a certain amount of precipitated Si exhibits the same optical response, irrespective of the fact that Si is concentrated within a thin SRC layer with high x, or dispersed within a thicker SRC layer with lower x.

The inset of Fig. 10 shows V_{Si} for all samples obtained according to Appendix A by making use of d_{SiC} and d_{SRC}, plotted against V_{Si} obtained from R&T simulations. The observed agreement supports the consistency of results.

The Si crystallized fraction of MLs is reported in Fig. 11. The figure combines the Raman and R&T results, and reports X_c as a function of the silicon fraction x, d_{SiC} and d_{SRC}, and of the product $V_{Si} \cdot d_{SRC}$, where V_{Si} is the overall silicon volume fraction determined based on the ML parameters (atomic concentrations, d_{SiC} and d_{SRC}, shrinkage, densities, molecular weights) [15,43]. See Appendix A for an explicit derivation. The figure shows very dispersed values for X_c in all panels because all parameters play a role in determining silicon crystallization. However, a trend is observed in panel c, indicating that the most important parameter affecting Si crystallization is d_{SRC}. Higher x is also required, as indicated by the absence of high X_c for low x, but the condition is not sufficient to achieve high X_c. The scattering of X_c data when plotted against d_{SiC} indicate that this may be a secondary condition in determining X_c.

The plot of X_c against $V_{Si} \cdot d_{SRC}$ (Fig. 11(d)) shows a remarkable correlation (correlation coefficient of the linear regression r=0.89). V_{Si} does in fact depend on the three parameters, suggesting that their combination is decisive in determining Si crystallization. As V_{Si} increases for decreasing d_{SiC}, this is in agreement with the idea that a thinner barrier is more transparent to clustering of Si crystallized domains, with nanograins ripening occurring beyond the initial d_{SRC}. V_{Si} increases with x and d_{SRC}, confirming that a mimimum volume is needed to favor the growth of crystallized domains, as a consequence of the fact that small silicon clusters tend to remain amorphous [47,48]. In Fig. 11, the data corresponding to samples for which the ML survival is detected by TEM are circled. Survival of the ML structure is observed for $d_{SRC} \geq 2.5$ nm and $x \geq 0.85$, whereas, down to the 1.6 nm explored in the experiment, d_{SiC} is not decisive for the survival of the ML. However, the existence of a minimum value for the thickness of the barrier layers d_{SiC} can be postulated.

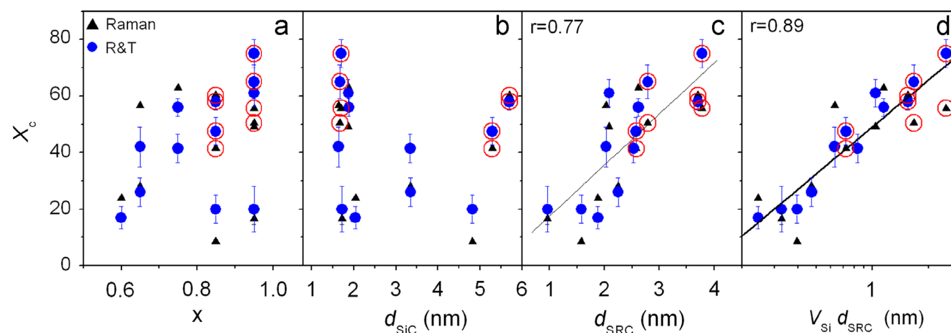

Fig. 11. Silicon crystallized fraction, plotted as a function of composition parameter x, annealed thickness of SiC and of SRC layers, and product $V_{Si} \cdot d_{SRC}$ determined by Raman (▲) and R&T (●) spectroscopy. The lines show the linear regression of data (r=correlation coefficient). The conditions for ML survival are circled.

4. Theoretical results: DFT calculations

The system Si NCs embedded in SiC matrix was also approached theoretically. Whereas it was possible to obtain clear structural, electronic and optical information for Si NCs embedded in SiO_2 or Si_3N_4 matrices [49,50], the situation is quite different for SiC embedded nanocrystals. Starting from a reference 3C-SiC sample (2000 atoms in fcc supercell) and by replacing with Si all the C atoms in a spherical region of given radius, we have generated three different embedded spherical Si NCs consisting of 41, 83, and 147 Si atoms respectively. Using the SIESTA code [51,52] in the framework of the Density Functional Theory (DFT), we have performed a full (atoms+cell) relaxation in order to obtain the ground-state configuration of each system. It is obtained that the relaxed structures show an amorphization of the NC induced by the large difference in the Si/SiC lattice constants. Due to the very large Young's modulus of SiC, the Si NC is burdened of all the compressive stress forming at the Si/SiC interface. Especially for small NCs, such pressure is enough to completely amorphize the NC, while for large NC a crystalline Si-core is possibly maintained.

This is illustrated in Fig. 12(a),(b), where unrelaxed and relaxed structures of Si_{41} NC are reported, when embedded in the fcc SiC matrix (not shown). Fig. 12(c) illustrates the same NC after the relaxation together with all the matrix atoms and cell boundary. From the figure, it is seen that the SiC matrix is subject to a very small stress only at the proximity of the Si–SiC interface, while the Si NC suffers the largest structural rearrangement.

The electronic band structure calculation, not reported, also evidences an important consequence of the NC amorphization, namely the metallic response of the embedded system, similar to the case of Ge NCs embedded in amorphous SiO_2 matrix [53], which possibly supports previous electrical results [20]. The feature is not observed in perfectly crystalline bulk-like structures (i.e. unrelaxed ideal systems) [54]. In addition, simulations suggest that only when a considerable amount (3–4 nm) of SiC material is present around the Si-NC, the latter is well formed and exhibit a clear confinement of the NC states and semiconductor behavior. A more detailed report on these topics is in preparation and will be subject of a separate publication.

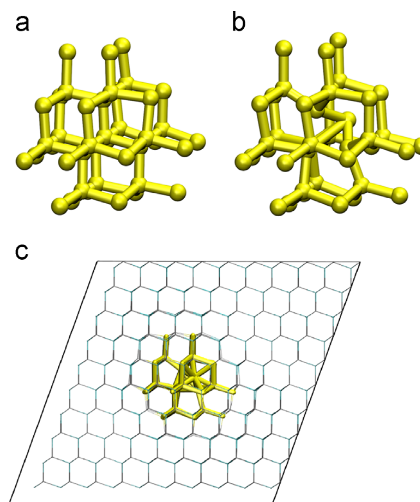

Fig. 12. Unrelaxed (a) and relaxed (b) Si_{41} NC embedded in the fcc SiC matrix (not shown). (c) the same NC after the relaxation together with all the matrix atoms and cell boundary.

5. Discussion

The observations presented in the previous sections point out that the initial structure (including thickness of the SRC and SiC layers) and the composition of the SRC layers strongly influence the state of the superlattice structure after annealing. In particular, we found that the ML structure survives upon annealing only for high d_{SRC} (> 2.5–3 nm, depending on x), and high x (> 0.8), with a presumable lower limit for d_{SiC}. The crystalline fraction is found to correlate with the thickness of the SRC layer and the total Si volume fraction V_{Si}, increasing for higher d_{SRC} and V_{Si}, with V_{Si} increasing with x and the ratio $d_{SRC}/(d_{SiC}+d_{SRC})$ (see the Appendix A). The NC size appears to be confined within the initial thickness only for sufficiently high $d_{SiC+SRC}$, whereas low $d_{SiC+SRC}$ and large x result in an outgrowth of the NCs over the SiC+SRC size and in the disappearance of the ML structure.

Compared to the case of Si NCs in SiO_2, (Si/SiO_2), the Si/SiC system shows pronounced differences. In the case of Si/SiO_2, the ML structure is preserved for barrier thicknesses > 1 nm, and the NC size remains confined within the initial SRO layer [2,29], irrespective of the annealing time [55], while a very weak dependence of the grain size on annealing time was observed for Si nanograins obtained by Si implantation in SiO_2 [56]. On the contrary, the picture outlined throughout this study shows marked analogies with the case of Ge NCs formed in an a-Ge thin layer sandwiched between SiO_2 layers [57]. In this case, the structural evolution upon annealing is observed to proceed through an initial grain nucleation, followed by grain growth

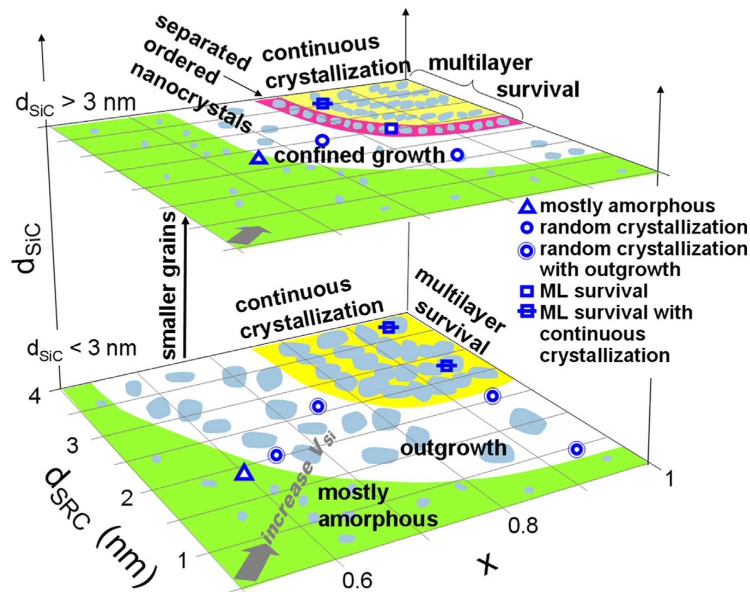

Fig. 13. Space of formation of Si nanodots in SiC multilayers upon 1100 °C annealing. The different regions indicate the conditions for little or no crystallization, random nanodot formation, or multilayer survival. The experimental data are also indicated. Triangle: little or no crystallization. Disks: random nanodot formation, circled if outgrowth is detected. Squares: ML survival. Strikethrough squares: continuous crystallization detected. The gray spots are intended to qualitatively reproduce the Si NC arrangement, and recall the appearance of TEM images.

exceeding the initial Ge layer thickness. A ripening process takes then place. Conversely, for sufficiently thick a-Ge layers, the initial nucleation is followed by homogeneous crystallization of the Ge layer. This occurrence is explained on the basis of thermodynamical considerations of the energy of all involved interfaces. It has been shown that the crystallization of thin layers occurs at remarkably higher temperatures than in the bulk. This is explained by introducing the concept of an effective interface with intermediate energy between a-Si/SiO_2 and the higher c-Si/SiO_2 interface energy. Such an effective interface prevents the crystallization from reaching the SiO_2 [29]. In the case of a-Ge the occurrence is even more important: the high specific interface energy between c-Ge and SiO_2, and its relaxation by structural adaptation of Ge, seem to play an essential role. In fact, it is energetically favoured to preserve two interfaces, that is, with an a-Ge interlayer between c-Ge and SiO_2, rather than to allow the crystallized front to reach SiO_2. This mechanism causes the surrounding Ge atoms to migrate around the growing NC to preserve this amorphous interlayer, also causing deformation of the SiO_2 overlayer. As a consequence, NC outgrowth is observed. In contrast, this mechanism is less effective in the Si/SiO_2 system [57], presumably due to the more moderate energy of the c-Si/SiO_2 interface [58]. The amorphous interlayer will be consequently less energetically favoured.

Going back to the experimental results reported in Section 3, in analogy with the Ge/SiO_2 case we can propose an important role of the c-Si/SiC interface, where the silicon carbide is crystallized as 3C-SiC (Fig. 8). Indeed, the (001)c-Si/(001) (3C-SiC) interface is a quite high energy interface because of the 19% lattice mismatch [59], that, as resulting from the DFT calculations reported in Section 4, has negative impact on the preservation of crystallinity in small silicon nanodots. As a consequence, we may suppose From the figure, it is seen that the mechanism involving migration of Si atoms, a-Si interlayer formation and successive incorporation in the growing NC, with outgrowth over the initial SRC layer.

For large d^0_{SRC} and also sufficiently high x, the high X_c and eventually the continuous crystallization detected in our experiments show marked similarities with the results of the Ge/SiO_2 case [57], and goes in parallel with the survival of a crystalline core for larger Si NC diameter suggested by DFT calculations (Section 4). The residual amorphous component, predicted by DFT calculations and also observed in the literature both in c-Si/SiC [11,12] and c-Ge/SiO_2 systems, [60], is attributed to the reduced system energy that follows the formation of an effective interface layer, which compensates the increase of total surface [29], namely, the c-Si/a-Si and the a-Si/SiC, in place of a single c-Si/SiC high energy interface, in analogy with the Ge/SiO_2 case [57].

Si and C interdiffusion among layers was also detected using StripeSTEM EELS, and mapping the electron energy loss spectra over Si/SiC MLs [12]. Interdiffusion lowers the effective value of x of the SRC layer, and, because the depletion of Si in the SRC layer increases for increased surface/volume ratio, this occurs more effectively for thinner d_{SRC}. The observation qualitatively explains why both x and d_{SRC} have to exceed a certain threshold for the ML structure to be preserved.

The picture can be summarized in a space of formation of NCs based on ML parameters, as reported in Fig. 13, valid for the annealing conditions used in this work. The figure reports the experimental data, with different symbols depending on the structural arrangement, whether with little or no crystallization detected, random NC formation, or periodic ML arrangement. The cases of outgrowth associated to thin SiC are circled. The arrow indicates the direction of increasing V_{Si}. The cases of d_{SiC} thinner or thicker than 3 nm are represented in separate plots, displaced in the vertical direction, the 3 nm demarcation point being suggested by the results reported in Fig. 9.

For low V_{Si}, little or no crystallization is expected, because crystallization can only occur for cluster sizes larger than the critical crystallization radius [29]. For increasing V_{Si}, randomly distributed NCs form, with possible outgrowth depending on d_{SiC}; large V_{Si} results in crystallized Si periodically arranged in multilayers. For $d_{SiC} > 3$ nm, a region for separated NCs exists in between the last two regions (magenta in the figure). As V_{Si} increases further, continuous crystallization is detected.

Finally, we attempt an evaluation of a 'global' diffusion coefficient involved in the process. In analogy with data obtained at higher temperature [61], we suppose that the dominant diffusing mechanism is carbon diffusion along defects and/or grain boundaries. With reference to Fig. 9, we observe that some samples with $d_{SiC}=2$ nm show outgrowth over $d_{SiC}+d_{SRC}$. Specifically, this occurs for samples X3-1 and X3-2 that suffered a 10′ annealing time at 1100 °C. We assume that this reflects a diffusion length of 2 nm. Conversely, a diffusion length shorter than 3.2 nm is observed for samples with a thicker d_{SiC}. In this case, the annealing time was 30′.

The two data allow us to deduce the lower and upper limit for diffusivity in our experiments. A diffusion coefficient around 1×10^{-16} cm^2/s at 1100 °C can be estimated, with possible geometrical corrections that are not considered in this context. The result is in good agreement with extrapolation to 1100 °C of the diffusivity of C in poly-3C-SiC detected in the range 1210 to1300 °C ($D_C=3.4 \times 10^{-14}$, 7×10^{-14}, 2.1×10^{-13} cm^2/s at 1210, 1250, 1300 °C respectively) [62]. The result may be used to predict the behavior of similar systems, as also confirmed by the analogies observed for similar samples [10,12].

We comment that the topic of self diffusivity in 3C-SiC is far from being consolidated. A compilation of results can be found in Ref. [63], where our results settle at the low diffusivity range of the plot. Negligible diffusivity occurs at our temperature for high quality material ([61,64]), so that the specific material quality in terms of grain boundaries and defect density leads to a great variety of results [63]. Low diffusivity was indeed proposed as a criterion to identify a better material quality [63], which positively supports the result obtained in this paper.

6. Summary and conclusions

We studied the silicon nanocrystal formation in Si/SiC multilayers deposited by PECVD. A variety of combinations of SiC and SRC thickness and composition was explored. The samples were studied by FTIR, HR- and EF-TEM, XRD, Raman and R&T spectroscopy. A high crystallization of the SiC matrix is detected by FTIR, associated to Si-C bond density formation close to the bulk value. The Si crystallized fraction is observed to depend on the ML parameters, the most relevant being the total silicon volume fraction. The multilayer structure is observed to survive the high temperature annealing only for sufficiently large SRC sublayer thickness, whereas in other cases the defect and interface driven diffusion results in smearing out of the structure and growth of the Si nanocrystals out of the initial SRC thickness. The experimental outcomes are supported by ab-initio theoretical calculations of Si NCs embedded in a 3C-SiC matrix, that show an amorphization of the NC core, especially at small size, due to the strong matrix-induced stress. From both experimental and theoretical results we conclude that the behavior of the system is dominated by the high Si/SiC interface energy due to the different lattice constants, that favours the survival of a silicon amorphous fraction. The system shows marked similarities with the case of Ge/SiO_2. Self diffusion of C was estimated to be around 10^{-16} cm^2/s, in agreement with low-temperature extrapolation of previous literature results. The data are combined to the definition of a space of formation of silicon nanocrystals in SiC, to provide a guideline for future material development.

Acknowledgments

We are grateful to Prof. D. Nobili for illuminating discussion on diffusion and nucleation processes.

The research leading to these results has received funding from the European Community's FP7 (FP7/2007-2013) under grant agreement no. 245977 under the project title NASCEnT. Authors would like also to acknowledge the Ministerio de Economía y Competitividad (Spanish Consolider Ingenio 2010 program, CSD2009-00013, and LEOMIS Project, TEC2012-38540-C02-01).

Appendix A. Volume fractions

The precipitation of Si in SRC/SiC multilayers represents a particular case of Si precipitation in Si-rich compounds that also include silicon rich oxides, nitrides, oxynitrides. Given the mixture $Si_wC_xO_yN_z$, where $w=1-x-y-z$, here we derive the nominal volume fractions of SiC, SiO_2, and Si_3N_4 and residual Si under the hypothesis of complete phase separation. By defining:

r: Si-to-other element ratio in the formula unit
m: atomic mass of elements
ρ: nominal density of the compound (g/cm^3)
E: concentration of the element other than Si in the formula. For compactness of formulations, in precipitated Si it is assumed that Si represents the 'other element'.

then we have:

	Si	SiC	SiO_2	Si_3N_4
i	0	1	2	3
E	$w=1-x-y-z$	x	y	z
r	0	1	0.5	0.75
m	28	12	16	14
ρ	2.32	3.17	2.62	3.30

The Si excess supposed to precipitate into Si is given by:

$$Si_{exc} = w - x - \frac{y}{2} - \frac{3z}{4} = w - \sum_i r_i E_i = E_0 \quad (A.1)$$

The non-normalized mass M_i of the compound i is given by the mass of silicon, plus the mass of the other atom divided by r_i, times the number of silicon atoms involved in that compound, which in turn is given by $E_i r_i$, thus yielding:

$$M_i = \left(m_0 + \frac{m_i}{r_i}\right) E_i r_i = (m_0 r_i + m_i) E_i \quad (A.2)$$

The volume fraction of the i compound, and of Si by setting $i=0$, is obtained by dividing by ρ_i and normalizing by the sum over the compounds:

$$V_i = \frac{E_i(m_0 r_i + m_i)}{\rho_i} \left(\sum_i \frac{E_i(m_0 r_i + m_i)}{\rho_i} \right)^{-1} \quad (A.3)$$

For a multilayer that alternates a compound barrier layer of thickness d_B, and a well layer of thickness d_W that contains a volume fraction $V_{Si,W}$ of Si precipitates, the overall volume of precipitated Si is given by:

$$V_{Si} = V_{Si,W} \frac{d_W}{d_B + d_W} \quad (A.4)$$

If the multilayer undergoes shrinkage, the shrinked thicknesses must be used for consistency with the use of nominal densities.

References

[1] Z. Yuan, A. Anopchenko, N. Daldosso, R. Guider, D. Navarro-Urrios, A. Pitanti, R. Spano, L. Pavesi, Silicon nanocrystals as an enabling material for silicon photonics, Proc. IEEE 97 (2009) 1250–1268.

[2] M. Zacharias, J. Heitmann, R. Scholz, U. Kahler, M. Schmidt, J. Bläsing, Size-controlled highly luminescent silicon nanocrystals: a SiO/SiO_2 superlattice approach, Appl. Phys. Lett. 80 (2002) 661–663.

[3] G. Conibeer, M. Green, E.C. Cho, D. Konig, Y.H. Cho, T. Fangsuwannarak, G. Scardera, E. Pink, Y.D. Huang, T. Puzzer, S.J. Huang, D.Y. Song, C. Flynn, S. Park, X.J. Hao, D. Mansfield, Silicon quantum dot nanostructures for tandem photovoltaic cells, Thin Solid Films 516 (2008) 6748–6756.

[4] P. Loper, M. Canino, D. Quazzazie, M. Schnabel, M. Allegrezza, C. Summonte, S. W. Glunz, S. Janz, M. Zacharias, Silicon nanocrystals embedded in silicon carbide: investigation of charge carrier transport and recombination, Appl. Phys. Lett. 102 (2013) 033507-1–033507-4.

[5] S. Janz, P. Loper, M. Schnabel, M. Zacharias, D. Hiller, S. Gutsch, A.M. Hartel, C. Summonte, M. Canino, M. Allegrezza, S. Ossicini, R. Guerra, I. Marri, B. Garrido, S. Hernandez, J. López-Vidrier, J. Valenta, T. Kubera, M. Foti, C. Gerardi, The Nascent Project, in: Proceedings of the 26th European Photovoltaic Solar Energy Conference, 2011, Hamburg, pp.22–27.

[6] A.M. Hartel, S. Gutsch, D. Hiller, C. Kübel, N. Zakharov, P. Werner, M. Zacharias, Silicon nanocrystals prepared by plasma enhanced chemical vapor deposition: importance of parasitic oxidation for third generation photovoltaic applications, Appl. Phys. Lett. 101 (2012) 193103-1–193103-4.

[7] S. Gutsch, J. Laube, A.M. Hartel, D. Hiller, N. Zakharov, P. Werner, M. Zacharias, Charge transport in Si nanocrystal/SiO_2 superlattices, J. Appl. Phys. 113 (2013) 133703-1–133703-9.

[8] C.-W. Jiang, M.A. Green, Silicon quantum dot superlattices: modeling of energy bands, densities of states, and mobilities for silicon tandem solar cell applications, J. Appl. Phys. 99 (2006) 114902-1–114902-7.

[9] D.Y. Song, E.-C. Cho, G. Conibeer, Y. Huang, C. Flynn, M.A. Green, Structural characterization of annealed $Si_{1-x}C_x$/SiC multilayers targeting formation of Si nanocrystals in a SiC matrix, J. Appl. Phys. 103 (2008) 083544-1–083544-7.

[10] M. Künle, A. Hartel, S. Janz, Analysis of microstructural transtormations during annealing of a-Si_xC_{1-x}:H/a-SiC:H layer stacks for the preparation of silicon quantum dot superlattices, in: Proceedings of the 23rd European Photovoltaic Solar Energy Conference, 2008, Valencia, pp. 421-425.

[11] M. Künle, T. Kaltenbach, P. Loper, A. Hartel, S. Janz, O. Eibl, K.-G. Nickel, Si-rich a-SiC:H thin films: Structural and optical transformations during thermal annealing, Thin Solid Films 519 (2010) 151–157.

[12] M. Künle, S. Janz, K.G. Nickel, A. Heidt, M. Luysberg, O. Eibl, Annealing of nm-thin $Si_{1-x}C_x$/SiC multilayers, Sol. Energy Mater. Sol. Cells 115 (2013) 11–20.

[13] M. Künle, A. Hartel, P. Löper, S. Janz, O. Eibl, Preparation of Si-quantumdots in SiC: single layer vs multi layer approach, in: Proceedings of the 24th European Photovoltaic Solar Energy Conference, 2009, Hamburg, pp.191-195.

[14] J. López-Vidrier, S. Hernández, J. Samà, M. Canino, M. Allegrezza, M. Bellettato, R. Shukla, M. Schnabel, P. Loper, L. López-Conesa, S. Estradé, F. Peiró, S. Janz, B. Garrido, Structural, optical and electrical properties of silicon nanocrystals embedded in Si_xC_{1-x}/SiC multilayer systems for photovoltaic applications, Mater. Sci. Eng. B 178 (2013) 639–644.

[15] C. Summonte, M. Canino, M. Allegrezza, M. Bellettato, A. Desalvo, R. Shukla, I. P. Jain, I. Crupi, S. Milita, L. Ortolani, L. López-Conesa, S. Estradé, F. Peiró, B. Garrido, Boron doping of silicon rich carbides: electrical properties, Mater. Sci. Eng. B 178 (2013) 551–558.

[16] Z. Wan, R. Patterson, S. Huang, M. Green, G. Conibeer, Ultra-thin silicon nitride barrier implementation for Si nano-crystals embedded in amorphous silicon carbide matrix with hybrid superlattice structure, Europhys. Lett. 95 (2011) 67006-1–67006-5.

[17] M. Canino, C. Summonte, M. Allegrezza, R. Shukla, I.P. Jain, M. Bellettato, A. Desalvo, F. Mancarella, M. Sanmartin, A. Terrasi, P. Loper, M. Schnabel, S. Janz, Identification and tackling of a parasitic surface compound in SiC and Si-rich carbide films, Mater. Sci. Eng. B 178 (2013) 623–629.

[18] G. Bruno, P. Capezzuto and A. Madan, (Eds.), Plasma deposition of amorphous silicon-based materials, 1995, Academic Press; San Diego.

[19] M. Allegrezza, F. Gaspari, M. Canino, M. Bellettato, A. Desalvo, C. Summonte, Tail absorption in the determination of optical constants of silicon rich carbides, Thin Solid Films 556 (2014) 105–111.

[20] Rimpy Shukla, C. Summonte, M. Canino, M. Allegrezza, M. Bellettato, A. Desalvo, D. Nobili, S. Mirabella, N. Sharma, M. Jangir, I.P. Jain, Optical and electrical properties of Si nanocrystals embedded in SiC matrix, Adv. Mat. Lett. 3 (2012) 297–304.

[21] S. Hernández, A. Martínez, P. Pellegrino, Y. Lebour, B. Garrido, E. Jordana, J. M. Fedeli, Silicon nanocluster crystallization in SiO_x films studied by Raman scattering, J. Appl. Phys. 104 (2008) 044304-1–044304-5.

[22] E. Centurioni, Generalized matrix method for calculation of internal light energy flux in mixed coherent and incoherent multilayers, Appl. Opt. 44 (2005) 7532–-7539; see also:⟨http://www.bo.imm.cnr.it/users/centurioni/optical.html⟩.

[23] G.E. Jellison, M.F. Chisholm, S.M. Gorbatkin, Optical functions of chemical vapor deposited thin-film silicon determined by spectroscopic ellipsometry, Appl. Phys. Lett. 62 (1993) 3348–3350.

[24] D.E. Aspnes, A.A. Studna, E. Kjtnsbron, Dielectric properties of heavily doped crystalline and amorphous silicon from 1.5 to 6.0 eV, Phys. Rev. B (1984) 768–779.

[25] E.D. Palik, (Ed), 1985, Handbook of Optical Constants of Solids, Academic Press, Inc.; Orlando, FL.

[26] S. Kerdiles, A. Berthelot, F. Gourbilleau, R. Rizk, Low temperature deposition of nanocrystalline silicon carbide thin films, Appl. Phys. Lett. 76 (2000) 2373–2375.

[27] S.W. King, M. French, J. Bielefeld, W.A. Lanford, Fourier transform infrared spectroscopy investigation of chemical bonding in low-k a-SiC:H thin films, J. Non-Cryst. Sol. 357 (2011) 2970–2983.

[28] M. Dkaki, L. Calcagno, A.M. Makthari, V. Raineri, Infrared spectroscopy and transmission electron microscopy of polycrystalline silicon carbide, Mater. Sci. Semicond. Process. 4 (2001) 201–204.

[29] M. Zacharias, P. Streitenberger, Crystallization of amorphous superlattices in the limit of ultrathin films with oxide interfaces, Phys. Rev. B 62 (2000) 8391–8396.

[30] J. Jeong, G.-S. Chung, S. Nishino, Raman scattering investigation of polycrystalline 3C-SiC film deposited on SiO_2 by using APCVD with hexamethyldisilane, J. Korean Phys. Soc. 52 (2008) 43–47.

[31] A.J. Steckl, J. Devrajan, S. Tlali, H.E. Jackson, C. Tran, S.N. Gorin, L.M. Ivanova, Characterization of 3C-SiC crystals grown by thermal decomposition of methyltrichlorosilane, Appl. Phys. Lett. 69 (1996) 3824–3826.

[32] P. Scherrer, Bestimmung der Grosse und der inneren Struktur von Kolloidteilchen mittels Rontgenstrahlen, Nachr. Ges. Wiss. Gott. Math-Phys. Kl. 2 (1918) 98–100.

[33] I.V. Antonova, M. Gulyaev, E. Savir, J. Jedrzejewski, I. Balberg, Charge storage, photoluminescence, and cluster statistics in ensembles of Si quantum dots, Phys. Rev. B77 (2008) 125318-1–125318-5.

[34] R. Rizzoli, C. Summonte, J. Plà, E. Centurioni, G. Ruani, A. Desalvo, F. Zignani, Ultrathin μc-Si films deposited by PECVD, Thin Solid Films 383 (2001) 7–10.

[35] There is not agreement in the literature on this point. Not resolved peaks are reported in Refs. [36–40]. Not resolved peaks only for the smallest nanocrystals are reported in: Refs. [41], [42].

[36] S. Charvet, R. Madelon, R. Rizk, Structural, ellipsometry and photoluminescence spectroscopy studies of silicon nanograins embedded in a silica matrix, Solid-State Electron. 45 (2001) 1505–1511.

[37] M. Losurdo, M.M. Giangregorio, P. Capezzuto, G. Bruno, M.F. Cerqueira, E. Alves, M. Stepikhova, Dielectric function of nanocrystalline silicon with few nanometers (<3 nm) grain size, Appl. Phys. Lett. 82 (2003) 2993–2995.

[38] D. Amans, S. Callard, A. Gagnaire, J. Joseph, G. Ledoux, F. Huisken, Ellipsometric study of silicon nanocrystal optical constants, J. Appl. Phys. 93 (2003) 4173–4179.

[39] J.A. Moreno, B. Garrido, P. Pellegrino, C. Garcia, J. Arbiol, J.R. Morante, P. Marie, F. Gourbilleau, R. Rizk, Size dependence of refractive index of Si nanoclusters embedded in SiO_2, J. Appl. Phys. 98 (2005) 013523-1–013523-4.

[40] A.-S. Keita, A. En Naciri, F. Delachat, M. Carrada, G. Ferblantier, A. Slaoui, Ellipsometric demonstration of the existence of a strong correlation between size distribution and optical responses of silicon nanoclusters in a nitride matrix, Appl. Phys. Lett. 99 (2011) 131903-1–131903-3.

[41] I. Stenger, B. Gallas, L. Siozade, C.-C. Kao, S. Chenot, S. Fisson, G. Vuye, J. Rivory, Evolution of the optical properties of Si nanoparticles embedded in SiO_2 as function of annealing conditions, J. Appl. Phys. 103 (2008) 114303-1–114303-8.

[42] I. Alonso, I.C. Marcus, M. Garriga, A.R. Goñi, J. Jedrzejewski, I. Balberg, Evidence of quantum confinement effects on interband optical transitions in Si nanocrystals, Phys. Rev. B 82 (2010) 045302-1–045302-8.

[43] C. Summonte, Dielectric function and spectrophotometry: from bulk to nanostructures, in: Jan Valenta, Salvo Mirabella (Eds.), Light Energy Harvesting with Group-IV Nanostructures, Pan Stanford Pub., Kyoto and Catania, 2014.

[44] C. Summonte, E. Centurioni, M. Canino, M. Allegrezza, A. Desalvo, A. Terrasi, S. Mirabella, S. Di Marco, M.A. Di Stefano, M. Miritello, R. Lo Savio, F. Simone, R. Agosta, Optical properties of silicon rich oxides, Phys. Status Solidi C 8 (2011) 996–1001.

[45] A.-S. Keita, A. En Naciri, Size distribution dependence of the dielectric function of Si quantum dots described by a modified Maxwell–Garnett formulation, Phys. Rev. B84 (2011) 125436-1–125436-11.

[46] D.A.G. Bruggeman, Berechnung verschiedener physikalischer Konstanten von heterogenen Substanzen, Ann. Phys. (Leipzig) 5 (1935) 636–664.

[47] F. Gourbilleau, C. Ternon, D. Maestre, O. Palais, C. Dufour, Silicon-rich SiO_2/SiO_2 multilayers: A promising material for the third generation of solar cells, J. Appl. Phys. 106 (2009) 013501-1–013501-7.

[48] H. Rinnert, M. Vergnat, A. Burneau, Evidence of light-emitting amorphous silicon clusters confined in a silicon oxide matrix, J. Appl. Phys. 89 (2001) 237–243.

[49] R. Guerra, I. Marri, R. Magri, L. Martin-Samos, O. Pulci, E. Degoli, S. Ossicini, Silicon nanocrystallites in a SiO_2 matrix: role of disorder and size, Phys. Rev. B 79 (2009) 155320-1–155320-9.

[50] R. Guerra, M. Ippolito, S. Meloni, S. Ossicini, The influence of silicon nanoclusters on the optical properties of a-SiN_X samples: a theoretical study, Appl. Phys. Lett. 100 (2012) 181905-1–181905-4.

[51] P. Ordejón, E. Artacho, J.M. Soler, Self-consistent order-N density-functional calculations for very large systems, Phys. Rev. B 53 (1996) R10441–R10444.

[52] J.M. Soler, E. Artacho, J.D. Gale, A. García, J. Junquera, P. Ordejón, D. Sánchez-Portal, The SIESTA method for *ab initio* order-*N* materials simulations, J. Phys.: Condens. Matter 14 (2002) 2745–2779.

[53] S. Ossicini, M. Amato, R. Guerra, M. Palummo, O. Pulci, Silicon and germanium nanostructures for photovoltaic applications: ab-initio results, Nanoscale Res. Lett. 5 (2010) 1637–1649.

[54] H.-Ch Weissker, J. Furthmüller, F. Bechstedt, Optical properties of Ge and Si nanocrystallites from ab initio calculations. I. Embedded nanocrystallites, Phys. Rev. B 65 (2002) 155327-1–155327-9.
[55] D. Hiller, S. Goetze, M. Zacharias, Rapid thermal annealing of size-controlled Si nanocrystals: dependence of interface defect density on thermal budget, J. Appl. Phys. 109 (054308) (2011) 1–5.
[56] B. Garrido Fernandez, M. López, C. Garcìa, A. Pérez-Rodrìguez, J.R. Morante, C. Bonafos, M. Carrada, A. Claverie, Influence of average size and interface passivation on the spectral emission of Si nanocrystals embedded in SiO_2, J. Appl. Phys. 91 (2002) 798–807.
[57] R. Peibst, T. Dürkop, E. Bugiel, A. Fissel, I. Costina, K.R. Hofmann, Driving mechanisms for the formation of nanocrystals by annealing of ultrathin Ge layers in SiO_2, Phys. Rev. B 79 (2009) 195316-1–195316-13.
[58] Y. Tu, J. Tersoff, Structure and energetics of the Si–SiO_2 interface, Phys. Rev. Lett. 84 (2000) 4393–4396.
[59] A. Severino, 3C-SiC epitaxial growth on large area silicon: thin films, in: Francesco La Via (Ed.) Silicon Carbide Epitaxy, 2012, 145 p., isbn:978-81-308-0500-9.
[60] C.L. Heng, W.W. Tjiu, T.G. Finstad, Charge-storage effects in a metal-insulator-semi-conductor structure containing germanium nano-crystals formed by rapid thermal annealing of an electron-beam evaporated germanium layer, Appl. Phys. A 78 (2004) 1181–1186.
[61] M.H. Hon, R.F. Davis, D.E. Newbury, Self-diffusion of ^{30}Si in polycrystalline β-SiC, J. Mater. Sci. 15 (1980) 2073–2080.
[62] H. Nakashima, T. Sugano, H. Yanai, Epitaxial growth of SiC film on silicon substrate and its crystal structure, Jpn. J. Appl. Phys. 5 (1966) 874–878.
[63] V. Cimalla, Th. Wohner, J. Pezoldt, The diffusion coefficient of silicon in thin SiC layers as a criterion for the quality of the grown layers, Mater. Sci. Forum 338–342 (2000) 321–324.
[64] G. Ferro, Y. Monteil, H. Vincent, F. Cauwet, J. Bouix, P. Durupt, J. Olivier, R. Bisaro, Infrared kinetic study of ultrathin Sic buffer layers grown on Si (100) by reactive chemical vapour deposition, Thin Solid Films 278 (1996) 22–27.

4.2. Electrical and Optoelectronic Properties of Si Nanocrystal Superlattices

The first half of the Thesis Project consisted of the determination of the ideal structural and fabrication conditions that allowed for (i) the superlattice structure maintenance after the annealing process, (ii) NC size confinement, (iii) the highest plausible crystalline degree of NCs and (iv) the optimum optical performance of the SL systems. This was studied in Si NC systems embedded in both SiO_2 and SiC matrices. The following natural step is then the study of the electrical and electro-optical properties of these SL systems, for which a device structure is required. In particular, simple *p-i-n* devices were fabricated that allowed the current flow across the active layer containing the Si NCs (the intrinsic layer), which in turn acts as a light-emitting or absorber material according to the type of study being performed. Of importance is the proper selection of contacts, being a transparent conductive oxide such as ITO employed for the top electrode (in order to allow photons from or towards the active layer), and being the bottom metallized with Al. The scheme of such an structure was presented in Fig. 2.15 [Chapter 2 (*Fundamentals of Silicon Nanocrystals*)].

In particular, since the oxide matrix supposes a high barrier for carrier extraction but allows for an excellent quantum confinement of carriers within QDs, emission properties were studied on this material. On the contrary, a photovoltaic approach was considered for SiC-based systems, given its higher electrical conductivity but poorer confinement constraints, as previously commented on Section 4.1.2. In the following, we therefore explore the electrical and electro-optical properties of Si NCs / SiO_2 and Si NCs / SiC superlattices and their implementation in optoelectronic devices, always bearing in mind the material optimization according to the fundamental physical processes taking place within the material.

4.2.1. Si Nanocrystal / SiO_2 Superlattices for Light Emission Applications

4.2.1.1. On Charge Transport and Electroluminescence

The first electrical and electro-optical results on Si NC / SiO_2 superlattices were reported in Paper VIII [130], where the charge transport and electroluminescence mechanisms were investigated. The employed samples consisted of 5 bilayers with variable t_{SRON}, while keeping constant the barrier thickness ($t_{\mathrm{SiO2}} = 1$ nm, the optimum one for high electrical conductivity [178]) and SRON layer stoichiometry ($SiO_{0.93}N_{0.23}$). The Si excess concentration can be calculated by [179]:

$$[\mathrm{Si}]_{\mathrm{exc}} = \frac{1 - 0.5x - 0.75y}{1 + x + y} \,, \tag{4.11}$$

where x and y correspond, respectively, to the [O]/[Si] and [N]/[Si] ratios. The employed stoichiometry then gives $[\mathrm{Si}]_{\mathrm{exc}} = 17$ at.%. After an annealing treatment

Table 4.5.: Summary of the conduction and electroluminescence threshold voltages ($V_{\mathrm{th,cond}}$ and V_{EL}, respectively), the activation energy (E_{A}) and electroluminescence peak energy (E_{EL}) corresponding to the different devices characterized in Paper VIII.

t_{SRON}	$V_{\mathrm{th,cond}}$	$V_{\mathrm{th,EL}}$	E_{A}	E_{EL}
2.5 nm	4 V	5 V	48 meV	1.51 eV
3.5 nm	5.5 V	7 V	90 meV	1.47 eV
4.5 nm	7 V	9 V	165 meV	1.39 eV

at 1150 °C, ITO and Al contacts were deposited on top and bottom, respectively, of the structure.

The electrical characterization was performed in accumulation regime (i.e. electron injection through the ITO electrode). The first intensity versus voltage characterization of the devices revealed two distinct behaviors at different voltage regimes. On one hand, an almost constant current was observed at low voltages that was attributed to the capacitor structure-related displacement current. On the other hand, device-dependent conduction was found to dominate at medium-high voltages. In addition, the threshold voltage ($V_{\mathrm{th,cond}}$) that separates both regimes increased with the SRON layer thickness (the values are summarized in Tab. 4.5). Indeed, the fact that the conduction regime depends on the SRON layer thickness, i.e. the NC size, made us focus our interest on this region.

To analyse the charge transport mechanism taking place in our superlattices, different bulk- and injection-limited formalisms were employed, as described in Section 2.4.1 in Chapter 2 (*Fundamentals of Silicon Nanocrystals*).The Poole-Frenkel mechanism was found to best fit our data, which was corroborated by the temperature dependence of the electrical measurements. From the latter performance, the activation energy (E_{A}) for conduction to occur was calculated that increased at larger NC sizes (see Tab. 4.5). Again, the dependence of the results with the Si NC structural properties pointed out a system where charge transport takes place through the nanostructures. It has to be mentioned that, although we found evidence of the Poole-Frenkel mechanism to be dominant in our system, the observations did not rule out other coexisting mechanisms such as tunnel-related ones [for further details on these mechanisms, see Section 2.4.1.2 in Chapter 2 (*Fundamentals of Silicon Nanocrystals*)].

The next step was the electro-optical characterization of the devices. The overall (integrated) electroluminescence emitted by the devices under electrical excitation was analysed, showing an EL onset voltage ($V_{\mathrm{th,EL}}$) that also depended on the NC size. Besides, $V_{\mathrm{th,cond}} < V_{\mathrm{th,EL}}$, which indicated that EL emission was closely related to the Poole-Frenkel conduction mechanism. A more detailed spectral inspection of EL emission was carried out under constant current density excitation. The spectra exhibited a Gaussian-like feature typical from photoluminescence observations of the same material systems [126]. This emission was attributed to

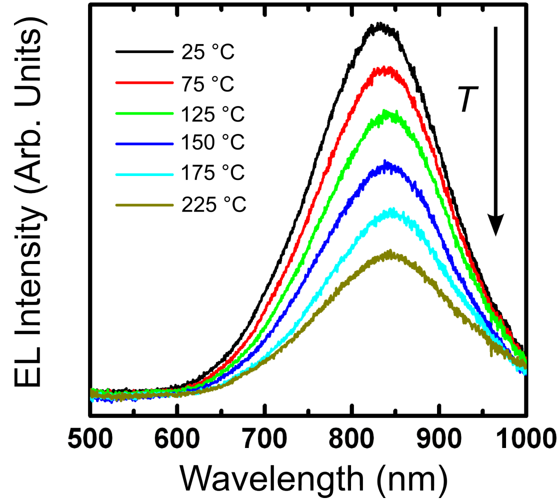

Figure 4.5: Electroluminescence (EL) spectra corresponding to a sample with $t_{\mathrm{SRON}} = 3.5$ nm, $t_{\mathrm{SiO2}} = 1$ nm and $x = 0.93$, acquired at different temperatures ranging between 25 and 225 °C.

radiative recombination of electron-hole pairs formed within the NCs. Indeed, to prove the radiative origin of the emission, a temperature-dependent EL study was performed (EL spectra corresponding to the device with $t_{\mathrm{SRON}} = 3.5$ nm is shown in Fig. 4.5). Although no remarkable peak position modification was observed, the spectra intensity was clearly reduced with temperature, which is expected from the increase of (thermally-associated) non-radiative processes taking place within the lattice [120]. Again focusing on the initial EL characterization, the spectra corresponding to the different devices displayed a peak shift to lower energies (E_{EL}) as the NC size increases, which is a consequence of quantum confinement of excitons within the NCs.

Given the experimental results on charge transport and electroluminescence from the NC-based devices under study and the conduction and EL emission mechanisms determined for this particular system, only the physical interpretation of the EL excitation mechanism was still lacking. For this, the consideration of an amorphous superlattice system is crucial, as no sharp interfaces exist, which is translated into a global SL conduction band. Under this frame, and as reported by Abeles and Tiedje [145], the presence of NCs (quantum dots) may originate quantum confinement (and therefore localization) of the conduction band extended states, which is in agreement with the experimental observation of NC size-dependent activation energy. This corroborated the thermally-activated electron transport through NCs. Regarding the EL excitation mechanism, we believe that some electrons will exist that freely travel through the conduction band (originated from thermal hopping or directly injected from the ITO electrode), which acquire a high kinetic energy. Then, a probability exists that these electrons impact with NCs, thus promoting the generation of an electron-hole pair, whose consequent recombination originates the measured EL. Actually, the low power efficiency of our SL-based devices (in the

order of 10^{-3} %) supports our hypothesis of (low-probable) impact ionization. In addition, our efficiencies are lower than other works on similar structures, where injection-limited transport mechanisms dominate that result in a higher impact probability [149, 150].

JOURNAL OF APPLIED PHYSICS **114**, 163701 (2013)

Charge transport and electroluminescence of silicon nanocrystals/SiO_2 superlattices

J. López-Vidrier,[1,a)] Y. Berencén,[1] S. Hernández,[1] O. Blázquez,[1] S. Gutsch,[2] J. Laube,[2] D. Hiller,[2] P. Löper,[3] M. Schnabel,[3] S. Janz,[3] M. Zacharias,[2] and B. Garrido[1]
[1]*MIND–IN[2]UB, Electronics Department, University of Barcelona, Martí i Franquès 1, E–08028 Barcelona, Spain*
[2]*IMTEK, Faculty of Engineering, Albert-Ludwigs-University Freiburg, Georges-Köhler-Allee 103, 79110 Freiburg, Germany*
[3]*Fraunhofer-Institute for Solar Energy Systems ISE, Heidenhofstr. 2, D-79110 Freiburg, Germany*

(Received 30 July 2013; accepted 8 October 2013; published online 25 October 2013)

Charge transport and electroluminescence mechanisms in Si-rich Si oxynitride/silicon oxide (SRON/SiO_2) superlattices deposited on *p*-type Si substrate are reported. The superlattice structures were deposited by plasma-enhanced chemical-vapor deposition and subsequently annealed at 1150 °C to precipitate and crystallize the Si excess into Si nanocrystals. The dependence of the electrical conduction on the applied voltage and temperature was found to be well described by a Poole-Frenkel transport mechanism over a wide voltage range. On the other hand, the observed dependence of the electroluminescence on the SRON layer thickness is a clear proof of quantum confinement and was attributed to an excitonic radiative recombination taking place in the confined states within the Si quantum dots. A model is proposed based on thermal hopping of electrons between the quantum dots acting as trap states (Poole-Frenkel). A correlation between carrier transport and electroluminescence has been established considering impact ionization of high-kinetic energy electrons on the Si quantum dots. © *2013 AIP Publishing LLC*. [http://dx.doi.org/10.1063/1.4826898]

I. INTRODUCTION

Since the middle of last century, Si has been widely employed in the electronics industry due to its abundance, low-cost extraction, mechanical stability, and good electrical performance. Unfortunately, due to the indirect nature of its band gap, Si optical absorption and emission properties are poor. Nevertheless, it has been found that, by nanostructuring Si, a size-dependent quantization of the allowed electronic states in the band structure occurs, which increases the band gap energy.[1–3] This band gap tunability has been exploited by many research groups to investigate the suitability of Si nanocrystals (NCs) for different optoelectronic applications. In particular, Si nanostructures have been used in light-emitting[4,5] and photovoltaic devices,[6–9] because of the possibility they offer to efficiently emit and absorb photons, respectively, in the visible range.

Up to now, many authors have reported on the carrier transport through systems containing Si NCs embedded in SiO_2,[10–14] as well as the electroluminescence (EL) emission these structures release.[15–18] In most of these studies, Si NCs were fabricated by either Si implantation of SiO_2, chemical-vapor deposition or sputtering of SiO_x thin films, followed by a high temperature annealing process to promote Si phase segregation. These methods allow for precisely monitoring the Si content, but the resulting NC size and shape are barely controlled.[19] In the last decade, an experimental route was proposed to deposit superlattices (SLs) that alternate very thin Si-rich oxide (SRO) layers with stoichiometric SiO_2 barriers by means of plasma-enhanced chemical-vapor deposition (PECVD).[20] After applying an annealing process, the silicon excess in the SRO layers precipitates forming nanoaggregates, leading to a very good control over the NC size that indirectly permits to thoroughly modify the band gap energy according to the final device function. A general approach to the transport properties of Si NC/SiO_2 superlattices was reported by some of the coauthors, according to the variation of different structural parameters, ascribing the origin to trap states mainly originated by dangling bonds.[21] On the other hand, the higher EL efficiency of similar SL systems in comparison with Si NCs embedded in a single layer was also studied by other groups.[22,23] Nevertheless, the correlation between the charge transport properties and the EL mechanism has not yet been studied in-depth for this kind of structures.

In this work, we propose a model for the transport and EL mechanisms through PECVD-deposited SLs consisting of five Si-rich silicon oxynitride (SRON)/SiO_2 bilayers in metal-oxide-semiconductor (MOS)-like devices. The SRON layer thickness was modified in order to determine the NC size effect on the voltage and temperature dependence of the electrical properties, which is described in Sec. III A. A transparent indium tin oxide (ITO) top electrode allowed for observing the luminescence emission coming from the SLs once an electrical excitation was applied. In Sec. III B, we investigate the origin of the observed EL. In Sec. III C, we present a physical interpretation of the correlation between EL and charge transport by means of a quantum-confined impact ionization model. The electron heating within the

[a)]Electronic mail: jlopezv@el.ub.edu

0021-8979/2013/114(16)/163701/7/$30.00 **114**, 163701-1 © 2013 AIP Publishing LLC

superlattice conduction band was considered, which was reported by Antula to be important in amorphous dielectrics where the Poole-Frenkel (PF) conduction mechanism dominates.[24] Therefore, two virtually independent studies, electrical and electro-optical, allow us to describe the combination of both the carrier conduction and the EL excitation mechanisms that takes place within our SL systems.

II. EXPERIMENTAL DETAILS

Alternating SRON and SiO_2 superlattices were deposited on 4-in. wet chemically cleaned (100)-Si *p*-type (B-doped, with a base resistivity of 1–20 $\Omega \cdot$cm) substrates by means of PECVD. Whereas the thickness of the SiO_2 barrier layer was held constant at 1 nm (the optimum achievable thickness for efficient electron conduction),[21] the SRON layer thickness was varied with values of 2.5, 3.5, and 4.5 nm. The total number of deposited bilayers was five, with a total nominal thickness ranging from 17.5 to 27.5 nm. The stoichiometry of the SRON layer was fixed at $SiO_{0.93}N_{0.23}$, which corresponds to a Si excess of 17 at. %, according to $[Si] = (1–0.5x–0.75y)/(1 + x + y)$, x and y being the [O]/[Si] and [N]/[Si] ratios, respectively.[25] Therefore, the total Si excess is 12, 13, and 14 at. %, for increasing layer thickness. The samples underwent an annealing treatment at 1150 °C for 1 h in high purity N_2 atmosphere in order to precipitate and crystallize the Si excess inside the SRON layers. The employed annealing parameters have been shown to be the optimum ones for Si NCs embedded in such superlattice systems.[26] Another annealing step was carried out in a pure molecular hydrogen atmosphere for 1 h at 500 °C to passivate the dangling bonds. A 10 nm oxide layer was deposited on top of the structure before the annealing process, to prevent the oxidation of the layers close to the surface. Afterwards, this oxide layer was etched in precisely controlled, highly diluted HF without overetching into the Si NC layer. Further information about the sample preparation can be found elsewhere.[27] A vertical device structure was achieved by photolithographic patterning of sputtered ITO (70 nm) on top of the SLs and full-area Al sputtering on the rear side of the *p*-type Si substrate. The circular area of the employed devices for the study ranged from 1.6×10^{-3} to 5.2×10^{-3} cm^2. A sketch of the fabricated devices is shown in Fig. 1.

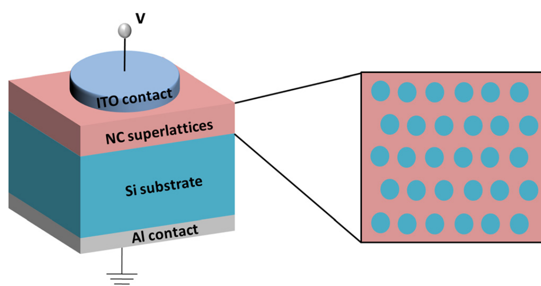

FIG. 1. (Left) Cross-section sketch of the devices with Si NC/SiO_2 superlattices employed for the present study. (Right) Scheme of the 5 Si NC layers distributed along the active superlattice. Lengths are not to scale.

The electrical characterization was performed in dark conditions using an Agilent B1500 semiconductor device analyzer and a Cascade Microtech Summit 11000 probe station with a thermal chuck. The devices were electrically isolated by setting them inside a Faraday cage. The bias limit for the $I(V)$ sweeps was set to 13 V, as larger values induce the device breakdown (13–17 V for samples with 2.5–4.5 nm, respectively). The basic electrical performance was carried out at room temperature. The temperature study of the electrical properties was achieved by increasing the chuck temperature from 25 to 300 °C. Electroluminescence from the devices was collected with a Seiwa 888 L microscope using a long working distance objective. The integrated EL output of the devices was monitored as a function of the applied voltage, acquiring the signal by means of a Hamamatsu GaAs R928 photomultiplier tube. EL spectra were acquired with a Princeton Instruments LN-cooled charge-coupled device via a 1/4 m Oriel monochromator, exciting the devices at a fixed current density of 1×10^{-4} A·cm^{-2}. All spectra were corrected for the optical response of the system.

III. RESULTS AND DISCUSSION

A. Transport properties

Transport properties of Si NCs/SiO_2 superlattices have been studied in the MOS device structures already described (see Fig. 1). After the first $I(V)$ sweeps performed at room temperature (300 K) and in dark conditions, we observed a strong rectifying behavior (not shown) when polarizing in the inversion regime (i.e., $V > 0$ in the configuration shown in Fig. 1), due to a lack of minority carriers in the substrate (electrons). For this reason, our experiments hereafter are focused on the accumulation regime (i.e., $V < 0$), and results will be expressed in absolute values unless otherwise stated. The corresponding $J(V)$ curves are displayed in Fig. 2. The graph shows the progressive and regressive bias sweeps from the devices under study. The first feature one may notice is that the current density increases in samples with thicker SRON layers, i.e., at larger NC sizes, evidencing the effect of the superlattices on the device conduction.

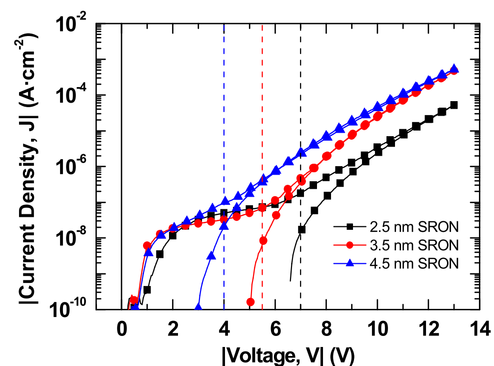

FIG. 2. Current density versus applied voltage corresponding to devices containing different SRON layer thicknesses with 1 nm SiO_2 barriers. Vertical dashed lines indicate the threshold voltage for the change of conduction mechanism.

From Fig. 2, one can also directly observe the different behaviors the curves present at low and high applied voltages, which are attributed to different transport mechanisms. Actually, an almost flat region at low voltages is observed that is associated with the displacement current, I_d, which is related to the charging current of the capacitor structure. This transport region, partly influenced by the device structure, allows us to estimate the device capacitance according to $C = I_d \cdot (dV/dt)^{-1}$, with values around 10 nF. The end of this regime, beyond which the conduction current starts to dominate, establishes a device-dependent threshold voltage ($V_{th,cond}$), whose values are 4, 5.5, and 7 V, increasing for thinner SRON layers (corresponding to electric fields of $\sim$1.5, 2.4, and 4 MV$\cdot$cm^{-1}, respectively). In this regime, we expect the Si NCs to provide allowed states that can take part in the carrier transport. Hence, it is in the scope of this work to focus on the high voltages, the study of which will yield the electro-optical properties of the superlattices.

The obtained $J(V)$ curve behavior was found to be well described by a PF-type conduction mechanism,[28] typically consisting of thermal hopping of carriers through shallow trap states in the superlattice conduction band. Moreover, the assumption of this mechanism is physically consistent if we consider a system where trap states are induced by the Si/SiO_2 interface defects, or even the NCs themselves. The PF formalism presents a dependence of the current intensity on the applied voltage (V) and the temperature (T) of the form

$$I = \frac{q\mu_n N_t A}{d} V \cdot \exp\left(-\frac{q}{k_B T}\left[\phi_t - \sqrt{\frac{qV}{\pi\varepsilon_0\varepsilon_r d}}\right]\right), \qquad (1)$$

q being the elementary charge, μ_n the carrier mobility (electrons), N_t the trap concentration, A the area through which the current flows (i.e., the device area), d the total active layer thickness, k_B the Boltzmann constant, Φ_t the energetic level of the trap taken from the SL conduction band edge, ε_0 the vacuum permittivity, and ε_r the relative effective permittivity of the medium. The results presented in Fig. 2, obtained at room temperature, are in accordance with the voltage dependence stated in Eq. (1). As an example, Fig. 3(a) displays a PF plot ($I \cdot V^{-1}$ vs. $V^{1/2}$) for the device containing 3.5 nm SRON layers. The appearance of a linear region through more than four decades (delimited by vertical dashed lines in the figure) gives proof of the suitability of this model for medium-high gate voltages. Furthermore, the figure shows a fit of the region under study, which is in very good agreement with the PF formalism. The slope of this fit allowed us to estimate the effective ε_r of the superlattice system, obtaining a value of 8.7, that lies between the pure SiO_2 and pure Si values (3.9 and 11.9, respectively).[29] Similar results were obtained for devices with different SRON thicknesses, scaling with this last parameter. However, the permittivity values obtained in this way differ from the experimentally determined values by means of optical techniques, due to the heterogeneity of our samples. In addition, the most general Poole-Frenkel theory also considers the trapping and detrapping rates, which modulate the ε_r value but not the voltage dependence.[30,31] Therefore, the former PF-plot

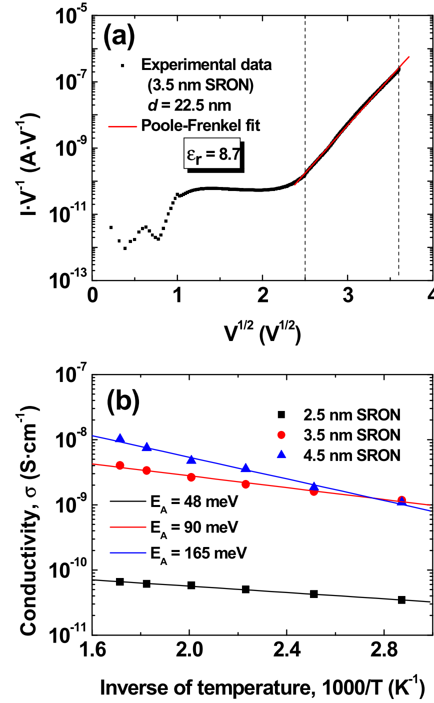

FIG. 3. (a) Poole-Frenkel plot of the device containing 3.5 nm SRON layers. Vertical dashed lines bound the linear region whose linear fit is displayed. The estimated dielectric constant from this particular fit is indicated. (b) Conductivity versus the inverse of temperature for devices containing different SRON layer thicknesses, obtained at a constant applied voltage of 13 V. The corresponding fits according to the Arrhenius law are displayed, and the estimated activation energies are given.

can only provide a rough estimation of the effective dielectric permittivity of the SLs.

The choice of thermally activated conduction assisted by the electric field is, up to now, a plausible hypothesis considering the voltage dependence of the current density that our results present. The PF mechanism was further corroborated by temperature dependent measurements. This time, the dependence in Eq. (1) of the current intensity on the temperature at a fixed applied voltage was exploited. For this, $I(V)$ measurements at different temperatures (ranging from 25 to 300 °C) were carried out. The conductivity values were calculated at 13 V (well within the pure conduction regime) and are displayed in Fig. 3(b) as a function of the inverse temperature (Arrhenius plots). Fits according to Eq. (1) were performed, which are in accordance with the experimental points, providing information about the required activation energy (E_A) for the conduction to occur (closely related to the already defined trap level, Φ_t). Activation energies of $E_A = 48$, 90, and 165 meV were determined for devices containing SRON layer thicknesses of 2.5, 3.5, and 4.5 nm, respectively, in agreement with other works on similar structures.[31]

Therefore, the performed electrical characterization revealed the presence of a bulk-limited conduction at high applied voltages, which could be ascribed to a PF transport

mechanism. This, on the other hand, is not incompatible with the existence of different mechanisms, such as tunnel transport through the SL or space-charge limited conduction due to interface defects. However, the results evidence that the Poole-Frenkel conduction dominates the carrier transport in our devices.

B. Electroluminescence emission

The light emission properties of the devices have been studied by monitoring the spectrally-integrated electroluminescence signal as a function of the injected current density. The curves plotted in Fig. 4(a) show a monotonic increase of the EL with the current density (the applied carrier flux) that demonstrates the direct dependence of the luminescence on the carrier transport. Further information can be obtained from the voltage dependence of the integrated EL, displayed in the figure inset. As can be observed, the trend followed by the curves at different SRON layer thicknesses is analogous to the observed behavior in the $J(V)$ characteristics (see Fig. 2): the thicker the SRON layers (i.e., the larger the NCs), the stronger the emission intensity at a given applied bias. On the other hand, the curves are mainly characterized by a well-defined onset voltage for the EL emission. Regarding the threshold voltage for the EL to occur ($V_{\mathrm{th,EL}}$), the obtained values of 5, 7, and 9 V (for SRON thicknesses of 4.5, 3.5, and 2.5 nm, respectively) are well within the bulk-limited $J(V)$ region, i.e., $V_{\mathrm{th,cond}} < V_{\mathrm{th,EL}}$. This is a clear indicator that EL occurs as a result of the conduction mechanism taking place at high voltages. At low voltages, no EL is observed even though there is a measurable current. This is in agreement with the identification of this current as a charging current, which leaves space charge at the interfaces but does not inject carriers into the bulk where they could recombine.

The integrated EL measurements allow us to determine the onset of light emission, but a spectrally resolved analysis of this luminescence may reveal its physical origin. For this reason, we acquired the EL emission spectra released by our devices in the range from 1.2 to 2.6 eV, electrically exciting them by means of a fixed current density of $\sim 1 \times 10^{-4}$ A·cm^{-2} [indicated in Fig. 4(a) as a vertical dashed line]. The resulting spectra are displayed in Fig. 4(b). As can be observed, the EL emission is clearly dependent on the SRON layer thickness. Whereas a shift of the EL peak towards higher energies is observed when decreasing the NC size (EL peak energies of 1.51, 1.47, and 1.39 eV were obtained for SRON layer thicknesses of 2.5, 3.5, and 4.5 nm, respectively), the emission intensity is maximum at medium NC sizes. In addition, no emission is observed at larger photon energies (shown in the graph), which would be expected from the excitation of oxide-related defects, as has been observed by other authors.[16,32]

The EL emission feature properties can be further interpreted. The size-dependent luminescence intensity has been typically reported from photoluminescence (PL) and EL spectra.[16,33] Furthermore, the observed blueshift at smaller NCs has also been reported in similar material samples by means of PL[1,2,34] and EL.[4,5,18] This is attributed to the quantum confinement of the carriers wavefunction inside 0-dimensional structures, the quantum dots (QDs), where the discretization of the allowed states within the bands takes place, accompanied by an increase of the band gap energy in smaller QDs.[35] Therefore, the observed spectra have their origin in the excitonic recombination of carriers (electrons and holes) confined within the nanostructures, the luminescence being purely NC-related. It should be mentioned that no EL signal was detected under the inversion regime: the low current density is insufficient to excite the luminescent species, due to the strong rectifying behavior this regime presents. In addition, the larger electron mobility in SiO_2 in comparison with holes (by six orders of magnitude)[36] makes the injection of the latter practically unachievable.

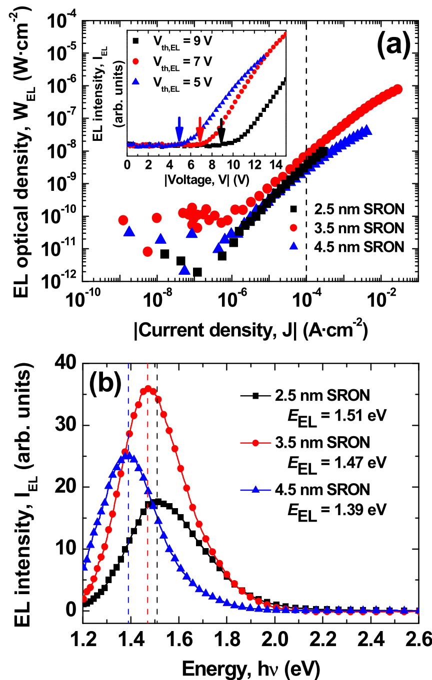

FIG. 4. (a) EL optical density as a function of the injected current density, for the different devices under study. The vertical dashed line indicates the current density employed for the EL spectra acquisition. The inset shows the EL intensity as a function of the applied voltage. The threshold voltages for the EL onset are denoted in the graph, and indicated using arrows. (b) EL spectra for the devices, acquired at a current density injection of 10^4 A·cm^{-2}. Vertical dashed lines refer to the EL peak energy, whose values are shown.

C. Correlation between carrier transport and EL mechanism

So far, we have presented some results that evidence that the Poole-Frenkel transport mechanism dominates the conduction in our SLs. In addition, our experimental observations indicate that there is a clear dependence of the trap-related activation energy and the quantum-confined NC energy levels

163701-5 López-Vidrier *et al.* J. Appl. Phys. **114**, 163701 (2013)

on the NC size using temperature-dependent and EL experiments, which proves the existence of a correlation between the electrical and electroluminescence properties of our system. Therefore, a SL band diagram in presence of an external electric field has been proposed in Fig. 5 to firmly help on the interpretation of the correlation between carrier transport and light emission. In particular, both the amorphous nature of the oxide matrix and the low barrier thickness of SiO_2 have been taken into account, which provides a non-abrupt QD-oxide interface. Additionally, two inter-correlated systems coexist, which cannot be treated independently: (i) the conduction band, with its respective continuum energy states above the SL band gap, and (ii) the QDs, where the allowed energy states are discretized. The experimental data suggest that both systems must be affected by the NC size variation and, in turn, by quantum confinement effects. Considering now the conduction band, their states can be classified in extended (blue region in the Fig. 5) or localized (yellow region), as amorphous materials do not present well-delimited bands. In addition, according to Abeles and Tiedje,[37] the presence of QDs induces a strong localization of the low-energy extended

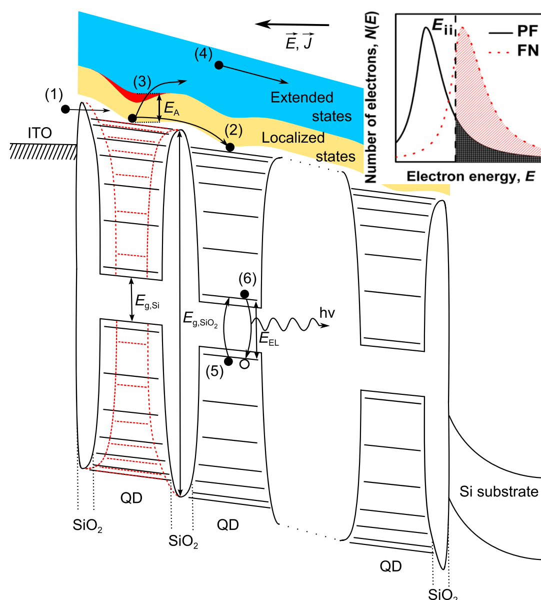

FIG. 5. Schematic energy band diagram of the studied superlattice under the presence of an external electric field, which shows the electron transport process and the EL mechanism, respectively. The changes in the band structure induced by the QD size reduction appear in red. Numbers indicate the different processes that take place: (1) electron injection through the ITO electrode; (2) trap-to-trap electron hopping; (3) thermally-activated electron jump towards the extended conduction band states; (4) high kinetic energy electrons that take part in the impact ionization process; (5) promotion of the bound electrons within the QD valence band states towards their counterpart within the QD conduction band (electron-hole pair generation); and (6) radiative recombination of the electron-hole pair, yielding a photon (EL emission). Energies are not to scale. The inset shows a sketch of electron energy distributions for the Poole-Frenkel (PF, in black) and the Fowler-Nordheim (FN, in red) transport mechanisms. The vertical solid line indicates the impact ionization energy (E_{ii}) of the system. The shaded regions represent the electrons that may contribute to impact ionization.

states (red region in Fig. 5) as a consequence of quantum effects, which is magnified at smaller nanostructures. In the case of QDs, they present a series of allowed energetic states whose energy separation decreases as we approach to the localized states (i.e., the superlattice conduction band edge). The decrease in the NC size increases the discrete energy level of QDs (sketched with red dashed lines in the Fig. 5). This latter effect becomes negligible as we approach the conduction band states, which establishes a reference for the different devices under study.

All the previously commented energy band considerations are involved in the transport and EL processes. The negative gate voltage applied on the ITO electrode is translated into a band bending of the superlattice structure that leads to the tunnel injection of electrons from the electrode to the superlattice [process (1) in Fig. 5]. Although some injected electrons will acquire a high enough kinetic energy to freely move through the SL conduction band, most of them will be easily trapped within the outer confined energy states of the QDs, which are considered as localized traps in our model. The trap-to-trap transport occurs via thermal hopping, assisted by localized states within the SL conduction band [process (2)]. The energy that electrons require to jump from the QD outer confined-energy states towards the extended conduction states is defined as the activation energy [process (3)]. This hypothesis is suggested by the observed trend in the E_A values [see Fig. 3(b)], the smallest QDs inducing the strongest localization of the low energy extended states, i.e., the lowest E_A. Therefore, as a consequence of the carrier injection described by process (1), there is a low number of injected electrons that are traveling through the superlattice extended states [process (4)], without suffering any scattering process. The electric field between contacts will further accelerate these electrons, providing them with a high kinetic energy in comparison with the huge amount of (low-energy) electrons involved in the trap-to-trap conduction through localized states. Hence, this small fraction of highly energetic electrons may impact on the QDs, transferring their energy to the bound electrons within the material.[38,39] This produces the promotion of the latter, from the QD inner states in the valence band towards their counterpart in the QD conduction band [process (5)]. In this process, an electron-hole pair is created, which is followed by radiative recombination between electron and generated hole within the QD fundamental states, yielding a photon (EL emission) with the energy of the QD band gap [process (6)]. This phenomenon is also tunable with the QD size, which is in agreement with the obtained experimental results of E_{EL} [see Fig. 4(b)].

Additionally, to gain more in-depth insight into the physics of these mechanisms, an electron energy distribution of impact ionization by high-energy electrons either in the PF-type mechanism or Fowler-Nordheim (FN) tunneling one has been sketched in the inset of Fig. 5. This figure is considered on the basis that the injected electrons in tunneling-based systems require larger energies to overcome the material potential barriers than the electrons involved in thermally-activated transport through shallow traps.[40,41] Thus, the electron energy distribution associated with the PF-type conduction

mechanism is shifted towards lower energies with respect to the one related to the FN tunneling mechanism. Moreover, DiMaria *et al*. demonstrated that the electron heating process is much more efficient in insulators, such as SiO_2,[42] where the transport is governed by FN conduction, than in defective materials, such as silicon nitride, oxynitride and, consequently, in our superlattices, whose electrical conduction is ruled by PF mechanism. As a result, the total number of electrons that can be heated to energies larger than the threshold for impact ionization to occur (E_{ii}) is greatly reduced in the PF mechanism due to the increased trapping/detrapping rate ascribed to the multiple SRON/SiO_2 interfaces. The trapping and detrapping on localized traps in the band gap control the PF-type conduction (bulk-limited) in these superlattices, and solely very few electrons on the energy distribution tail (see dark shaded area associated to PF in the inset of Fig. 5, corresponding to the most energetic electron population) are allowed to move freely along the extended states. This interpretation is also in accordance with the low EL efficiency observed in our devices [see Fig. 4(a)], in comparison with other works in the literature on Si NC/SiO_2 superlattices,[22,23] and the lack of luminescence under inversion regime, where the effective carrier concentration is strongly reduced.

IV. CONCLUSIONS

In summary, devices containing PECVD-deposited SRON/SiO_2 superlattices were fabricated on *p*-type Si substrate. Before the ITO (front) and Al (back) contact metallization, an annealing treatment at 1150 °C was carried out to precipitate and crystallize the Si excess from the SRON layers as NCs. The independently observed voltage and temperature dependences of the devices' electrical properties revealed a thermally-activated (Poole-Frenkel) carrier transport through the superlattice as the dominant mechanism at high applied voltages. Furthermore, the activation energy for this transport mechanism was found to be strongly dependent on the SRON layer thickness, i.e., on the NC size. To complete the electro-optical study of the devices, an electrical excitation was applied that yielded luminescence. The observed EL threshold is well within the PF conduction regime, which supports the hypothesis that electroluminescence originates as a consequence of the latter. Moreover, the obtained EL peak energies from the spectra for different SRON thicknesses (directly related to the confined electronic states inside the QDs) manifest a quantum confinement effect. A model that considers a trap-to-trap thermal hopping of electrons, the NCs being interpreted as localized trap levels within the SL conduction band, was proposed. In addition, by means of impact ionization, the high-energy electrons injected through the SL may lose their kinetic energy on behalf of the electrons bound within the QD valence band states, thus generating an electron-hole pair. The consequent excitonic recombination releases photons with the QD band gap energy, in excellent agreement with the EL results. Finally, an interpretation on the correlation between electrical and EL mechanisms in these superlattices was established.

ACKNOWLEDGMENTS

The research leading to these results has received funding from the European Community's Seventh Framework Programme (FP7/2007-2013) under Grant Agreement No. 245977, under the project title NASCEnT. The present work was supported by the Spanish national project LEOMIS (TEC2012-38540-C02-01).

[1]T. van Buuren, L. N. Dinh, L. L. Chase, W. J. Siekhaus, and L. J. Terminello, Phys. Rev. Lett. **80**, 3803 (1998).
[2]F. Iacona, G. Franzò, and C. Spinella, J. Appl. Phys. **87**, 1295 (2000).
[3]F. Iacona, G. Franzò, V. Vinciguerra, A. Irrera, and F. Priolo, Opt. Mater. **17**, 51 (2001).
[4]N. Lalic and J. Linnros, J. Appl. Phys. **80**, 5971 (1996).
[5]S. Chan and P. M. Fauchet, Appl. Phys. Lett. **75**, 274 (1999).
[6]I. Perez-Wurfl, X. Hao, A. Gentle, D.-H. Kim, G. Conibeer, and M. A. Green, Appl. Phys. Lett. **95**, 153506 (2009).
[7]D. Di, I. Perez-Wurfl, G. Conibeer, and M. A. Green, Sol. Energy Mater. Sol. Cells **94**, 2238 (2010).
[8]G. Conibeer, M. Green, R. Corkish, Y. Cho, E.-C. Cho, C.-W. Jiang, T. Fangsuwannarak, E. Pink, Y. Huang, T. Trupke, B. Richards, A. Shalav, and K.-L. Lin, Thin Solid Films **511–512**, 654 (2006).
[9]P. Löper, D. Stüwe, M. Künle, M. Bivour, C. Reichel, R. Neubauer, M. Schnabel, M. Hermle, O. Eibl, S. Janz, M. Zacharias, and S. W. Glunz, Adv. Mater. **24**, 3124 (2012).
[10]A. Ron and D. J. DiMaria, Phys. Rev. B **30**, 807 (1984).
[11]I. Balberg, J. Appl. Phys. **110**, 061301 (2011).
[12]J. Carreras, O. Jambois, S. Lombardo, and B. Garrido, Nanotechnology **20**, 155201 (2009).
[13]I. V. Antonova, M. Gulyaev, E. Savir, J. Jedrzejewski, and I. Balberg, Phys. Rev. B **77**, 125318 (2008).
[14]Y. Berencén, J. M. Ramírez, O. Jambois, C. Domínguez, J. A. Rodríguez, and B. Garrido, J. Appl. Phys. **112**, 033114 (2012).
[15]J. Linnros and N. Lalic, Appl. Phys. Lett. **66**, 3048 (1995).
[16]J. Valenta, N. Lalic, and J. Linnros, Opt. Mater. **17**, 45 (2001).
[17]G. Franzò, A. Irrera, E. C. Moreira, M. Miritello, F. Iacona, D. Sanfilippo, G. Di Stefano, P. G. Fallica, and F. Priolo, Appl. Phys. A **74**, 1 (2002).
[18]M. Perálvarez, J. Barreto, J. Carreras, A. Morales, D. Navarro-Urrios, Y. Lebour, C. Domínguez, and B. Garrido, Nanotechnology **20**, 405201 (2009).
[19]A. Yurtsever, M. Weyland, and D. A. Muller, Appl. Phys. Lett. **89**, 151920 (2006).
[20]M. Zacharias, J. Heitmann, R. Scholz, U. Kahler, M. Schmidt, and J. Bläsing, Appl. Phys. Lett. **80**, 661 (2002).
[21]S. Gutsch, J. Laube, A. M. Hartel, D. Hiller, N. Zakharov, P. Werner, and M. Zacharias, J. Appl. Phys. **113**, 133703 (2013).
[22]A. Marconi, A. Anopchenko, M. Wang, G. Pucker, P. Bellutti, and L. Pavesi, Appl. Phys. Lett. **94**, 221110 (2009).
[23]A. Anopchenko, A. Marconi, E. Moser, S. Prezioso, M. Wang, L. Pavesi, G. Pucker, and P. Bellutti, J. Appl. Phys. **106**, 033104 (2009).
[24]J. Antula, J. Appl. Phys. **43**, 4663 (1972).
[25]S. Hernández, P. Pellegrino, A. Martínez, Y. Lebour, B. Garrido, R. Spano, M. Cazzanelli, N. Daldosso, L. Pavesi, E. Jordana, and J. M. Fedeli, J. Appl. Phys. **103**, 064309 (2008).
[26]A. M. Hartel, S. Gutsch, D. Hiller, and M. Zacharias, Phys. Rev. B **85**, 165306 (2012).
[27]A. M. Hartel, D. Hiller, S. Gutsch, P. Löper, S. Estradé, F. Peiró, B. Garrido, and M. Zacharias, Thin Solid Films **520**, 121 (2011).
[28]J. Frenkel, Phys. Rev. **54**, 647 (1938).
[29]S. M. Sze and K. K. Ng, *Physics of Semiconductor Devices*, 3rd ed. (Wiley, New York, 2007).
[30]W. R. Harrell and J. Frey, Thin Solid Films **352**, 195 (1999).
[31]V. Ossiniy, S. Lysgaard, V. I. Kolkovsky, V. Pankratov, and A. Nylandsted Larsen, Nanotechnology **20**, 195201 (2009).
[32]J. Yuan and D. Haneman, J. Appl. Phys. **86**, 2358 (1999).
[33]G. Ledoux, J. Gong, F. Huisken, O. Guillois, and C. Reynaud, Appl. Phys. Lett. **80**, 4834 (2002).
[34]R. Ferre, B. Garrido, P. Pellegrino, M. Perálvarez, C. García, J. A. Moreno, J. Carreras, and J. R. Morante, J. Appl. Phys. **98**, 084319 (2005).
[35]P. Y. Yu and M. Cardona, *Fundamentals of Semiconductors: Physics and Material Properties*, 4th ed. (Springer, Berlin, 2010).

[36]J. F. Verwey, E. A. Amerasekera, and J. Bisschop, Rep. Prog. Phys. **53**, 1297 (1990).
[37]B. Abeles and T. Tiedje, Phys. Rev. Lett. **51**, 2005 (1983).
[38]G. Allan and C. Delerue, Phys. Rev. B **79**, 195324 (2009).
[39]C. Sevik and C. Bulutay, Physica E **38**, 118 (2007).
[40]E. Kameda, T. Matsuda, Y. Emura, and T. Ohzone, Solid State Electron. **42**, 2105 (1998).
[41]H. Tanaka, Appl. Surf. Sci. **147**, 222 (1999).
[42]D. J. DiMaria, T. N. Theis, J. R. Kirtley, F. L. Pesavento, D. W. Dong, and S. D. Brorson, J. Appl. Phys. **57**, 1214 (1985).

4.2.1.2. Superlattice Optimization for Light Emission

Once the charge transport and electroluminescence mechanisms taking place through our NC-based superlattices were understood, the SL conditions that yield the maximum EL emission for efficient NC-based light-emitting devices were investigated. This is the aim of Paper IX [180], where the optimum SRON layer thickness for light emission (t_{SRON} = 3.5 nm, as reported in Paper VIII [130]) was fixed, while varying the oxide barrier thickness and the Si excess within the SRON layers. An annealing temperature of 1150 °C was used, the ideal one for optical emission and superlattice maintenance (as reported in Paper II [126]). An analogous device structure as in Paper VIII [130] was employed. The electrical and electroluminescence properties were correlated to the structural parameters, and the recombination dynamics were also studied. Finally, the luminescence power efficiency was calculated, allowing the determination of the ideal SL conditions for EL emission.

Prior to the electrical and EL characterization, it was necessary to check the quality of the employed superlattices since, although the effect of t_{SRON} has been investigated (see Fig. 4.2) and structural modification due to t_{SiO2} has been reported in Paper II [126], the Si excess variation effect on our samples was not known. With this purpose, Raman scattering measurements were performed. However, since no identical samples grown on fused silica were available, the characterization was done on the same devices by carefully focalizing the laser beam within the thin SL stack, in order to get rid of the Si substrate contribution to the Raman signal. The spectra corresponding to the t_{SiO2} study exhibited no difference, as expected for an excellent size confinement within the SRON layers. On the contrary, the $[Si]_{exc}$ increase induced enhanced crystalline Si- and amorphous Si-related signal intensity. The phonon confinement model described in Paper III [79] was employed to determine the crystalline size of the NCs, found to be ~3.6 nm for all devices. This fact, added to the higher crystalline intensity at higher Si content, implies that larger densities of NCs (i.e. a higher number of NCs), instead of larger NCs, are present within the SRON layers.

The second step consisted of the electrical characterization (in accumulation regime), which revealed a higher conduction at lower t_{SiO2} and higher $[Si]_{exc}$. In addition, it was observed that the displacement current region was reduced in increasingly conductive devices, obtaining a bulk conduction in the whole voltage range for very high silicon contents or really thin barriers. Indeed, the lower inter-NC distance in the vertical direction at thinner oxide barriers and the higher overall Si content at higher Si excess explain the electrical observations. Regarding EL, all devices present a visible-NIR emission attributed to excitonic recombination within the Si NCs. On one hand, no relevant spectra modification was undergone by devices corresponding to different t_{SiO2}, in agreement with an identical NC size, with slight intensity and energy position modifications, as was already anticipated by PL results in Paper II [126]. On the other hand, higher Si excesses exhibited

a shift to lower energies (and an evident EL emission quenching) ascribed to a loss of quantum confinement because of higher amorphous Si phase presence and wavefunction delocalization due to increasing inter-NC proximity.

Time-resolved EL measurements under pulsed-excitation were also carried out, where a SL-dependent EL overshoot was observed that was mainly attributed to trapped charge recombination after switching off the pulse. The important feature for the study was the EL decay, strongly dependent on the SL structural parameters, and which could be fitted by a two-exponential function. This algorithm revealed two decay times: a fast one, dependent on the device, and a slow one, almost constant. The slow decay time, in the order of hundreds of μs, was ascribed to inter-NC cross-talking. The fast decay time, in the order of tens of μs, was found to decrease at higher Si contents, associated to a larger amorphous Si phase that resulted in defects and the presence of other fast non-radiative centers, thus reducing the overall excitonic recombination time. A higher lifetime value was observed at intermediate oxide barrier thicknesses, indicating that different effects may compete. In particular, the high conduction at thinner barriers may originate the higher presence of free carriers that induce lattice heating, whereas the effect of matrix stress is stronger at thicker barriers (as reported in Paper II [126]); the consequence of both effects is the instability of the exciton within the NCs and/or the enhancement of non-radiative processes that contribute to an overall radiative recombination lifetime decrease.

Finally, the power efficiency (PE) of the EL emission delivered by the different devices was evaluated, with maximum values in the order of 10^{-3} %, much lower than in other works reported in the literature [149, 150]. Given that the probability of EL excitation, via impact ionization in our case [130], has a strong dependence on the kinetic energy that electrons present, EL in these systems is more likely when tunnel-related mechanisms dominate charge transport, which is not our case. The deposition of a 20-nm-thick layer on top of the SL structure has proved to accelerate electrons, which allows tuning the transport from bulk- to injection-limited; a consequence is the impact probability enhancement and the efficiency increase, even by several orders of magnitude [181]. Regarding the optimum superlattice conditions for power efficiency, thicker oxide barriers and lower Si contents seem ideal. However, for light emission purposes, a figure of merit (FoM) was created to weigh PE with the spectrally-integrated optical emission (P_{opt}) of the devices:

$$\mathrm{FoM} = \mathrm{PE} \times P_{\mathrm{opt}} \ , \tag{4.12}$$

which is maximized for intermediate oxide barrier thicknesses ($t_{\mathrm{SiO2}} \sim 2$ nm) and low Si excess ($[\mathrm{Si}]_{\mathrm{exc}} \sim 12$ at.%). In fact, this is an important result, revealing that not only a high Si content is unnecessary but also excessively thin barriers, although notably improving conduction, are indeed counterproductive. Therefore, pushing the superlattice fabrication to ultra-thin layers, which sets a huge drawback for mass production, is not required for efficient Si NC-based light emitters.

OPEN ACCESS
IOP Publishing
Nanotechnology
Nanotechnology **26** (2015) 185704 (10pp)
doi:10.1088/0957-4484/26/18/185704

Structural parameters effect on the electrical and electroluminescence properties of silicon nanocrystals/SiO_2 superlattices

J López-Vidrier[1], Y Berencén[1], S Hernández[1], B Mundet[1], S Gutsch[2], J Laube[2], D Hiller[2], P Löper[3,4], M Schnabel[3], S Janz[3], M Zacharias[2] and B Garrido[1]

[1] MIND–IN[2]UB, Electronics Department, University of Barcelona, Martí i Franquès 1, E-08028 Barcelona, Spain
[2] IMTEK, Faculty of Engineering, Albert-Ludwigs-University Freiburg, Georges-Köhler-Allee 103, D-79110 Freiburg, Germany
[3] Fraunhofer-Institute for Solar Energy Systems ISE, Heidenhofstr. 2, D-79110 Freiburg, Germany

E-mail: jlopezv@el.ub.edu

Received 23 December 2014, revised 4 March 2015
Accepted for publication 17 March 2015
Published 15 April 2015

Abstract

The effect of the oxide barrier thickness (t_{SiO2}) reduction and the Si excess ($[Si]_{exc}$) increase on the electrical and electroluminescence (EL) properties of Si-rich oxynitride (SRON)/SiO_2 superlattices (SLs) is investigated. The active layers of the metal–oxide–semiconductor devices were fabricated by alternated deposition of SRON and SiO_2 layers on top of a Si substrate. The precipitation of the Si excess and thus formation of Si nanocrystals (NCs) within the SRON layers was achieved after an annealing treatment at 1150 °C. A structural characterization revealed a high crystalline quality of the SLs for all devices, and the evaluated NC crystalline size is in agreement with a good deposition and annealing control. We found a dramatic conductivity enhancement when the Si content is increased or the SiO_2 barrier thickness is decreased, due to a larger interaction of the carrier wavefunctions from adjacent layers. EL recombination dynamics were studied, revealing radiative recombination decay times of the order of tens of microseconds. Lower lifetimes were found at higher $[Si]_{exc}$, attributed to exciton confinement delocalization, whereas intermediate barrier thicknesses present the slowest decay. The electrical-to-light conversion efficiency increases monotonously at thicker barriers and smaller Si contents. We ascribe these effects mainly to free carriers, which enhance carrier transport through the SLs while strongly quenching light emission. Finally, the combination of the different results led us to conclude that $t_{SiO2} \sim 2$ nm and $[Si]_{exc}$ from 12 to 15 at% are the ideal structure parameters for a balanced electro-optical response of Si NC-based SLs.

Keywords: silicon nanocrystals, superlattices, electroluminescence, barrier thickness, silicon excess

(Some figures may appear in colour only in the online journal)

1. Introduction

Huge efforts have been dedicated to adequately control the size of silicon nanocrystals (Si NCs) at nanometer scale, as it allows for band gap engineering thanks to the quantum confinement effect, which provides an enormous potential for light conversion [1, 2] and light emission [3–5] applications. Sandwiching the nanostructures between the proper Si-based matrix material has been demonstrated to produce the desired

[4] Now with École Polytechnique Fédérale de Lausanne, Photovoltaics and Thin Film Electronics Laboratory, Rue de la Maladière 71b, CH-2002 Neuchâtel, Switzerland.

Content from this work may be used under the terms of the Creative Commons Attribution 3.0 licence. Any further distribution of this work must maintain attribution to the author(s) and the title of the work, journal citation and DOI.

vertical size confinement at dimensions of few nanometers [6]. This can be achieved by means of the superlattice (SL) approach, which consists of the deposition of alternating nanometric silicon-rich and stoichiometric dielectric or semiconductor layers, followed by a high-temperature annealing treatment to induce phase separation within the Si-rich layers and consequent Si excess precipitation and crystallization in the form of Si NCs [6]. In particular, many works have focused on the usage of SiO_2 to contain Si NCs and to be used as thin barriers in SiO_2/Si NC SLs [7], because it efficiently blocks layer intermixing, and its control and manipulation are well achieved in the microelectronics industry.

The structural and optical properties from Si NCs have been extensively studied in the past, as a function of the nanostructure size and the stoichiometry of the Si-rich layers, with the nanostructures embedded either in bulk matrix [8, 9] or in conveniently arranged ensembles (SL structures) [7, 10, 11]. The assessment of the electrical behavior of NCs is more complex, requiring the deposition of metallic contacts to design a metal–oxide–semiconductor (MOS) device, for instance, which allows for a proper charge injection and extraction. Besides, the insulator matrix material usually states a drawback for carrier conduction, especially in the case of silicon oxide, whose barrier height can be hardly overcome by carriers [12]. After the long-term study on the electrical properties of bulk matrix-embedded NCs [13–15], many recent works have focused on the carrier transport taking place through the quasi-dielectric NC SLs. In these systems, lateral transport studies (i.e. along the Si-rich layers) have revealed a strong conduction dependence on the Si content as predicted by percolation theory, Si NC coalescence leading to a tune of transport mechanism from charge migration and Coulomb-like effects to tunneling [16]. Instead, vertical transport (i.e. across the layers) is commonly ascribed to trap-assisted- or tunnel-like mechanisms, depending on the structure parameters and the fabrication technique [17, 18]. The electroluminescence (EL) properties of this material structure have also been investigated and correlated to the vertical transport mechanisms [19, 20]. However, the influence of the different structural parameters involved in the fabrication of NCs (i.e. the Si-rich oxide and SiO_2 layer thicknesses and the Si excess) can be exploited on optimizing the charge transport and EL emission, giving rise to a wide research field still to explore.

In this work, the electro-optical properties of Si-rich Si oxynitride (SRON)/SiO_2 SL-based MOS devices have been investigated by considering the effect of the SiO_2 barrier thickness reduction and Si excess concentration increase. After analyzing the structural properties of the SLs under study by Raman spectroscopy, an electrical characterization was performed that indicates higher conductivities for thinner SiO_2 barrier layers and larger amounts of Si. The EL emission yielded by the devices allowed us to indirectly study the nanostructure morphology by the modification of the structural parameters, which is correlated to the structural investigation, as well as the absolute photon emission. In addition, time-resolved EL measurements allowed studying the carrier recombination dynamics within the SL structures. Finally, the EL emission power efficiency of the SL-based devices allowed determining the ideal SL structural parameters for obtaining a proper balance between carrier conduction and EL.

2. Experimental details

Alternating SRON and SiO_2 SLs were deposited on B-doped (100)-Si substrates (base resistivity of 1–20 Ω cm) via plasma-enhanced chemical-vapor deposition, with a total number of five bilayers. In all samples, the SRON layer thickness, t_{SRON}, was held constant at 3.5 nm, observed in a previous work to be close to the optimum EL performance [20]. The fabricated samples are summarized in table 1. In a first set of samples, labeled as ‘B’ in the table, the SiO_2 barrier thickness (t_{SiO2}) was varied from 1 to 3 nm (leading to a total thickness from 22.5 to 30.5 nm, respectively), whereas the stoichiometry of the Si-rich layers ($SiO_xN_{0.23}$) was fixed at $x = 0.93$, which corresponds to a local Si excess ($[Si]_{exc}$) of 17 at% within the SRON layer. A second set of samples, labeled ‘E’ in the table, was aimed at the study of the Si excess effect on the EL properties. It consisted also of five bilayers with a constant $t_{SiO2} = 1$ nm (the optimum achievable thickness for efficient electron conduction in these SL systems [18]), whereas the stoichiometry of the SiO_x layers ranged between $x = 0.64$ and 1.1, which is translated into $[Si]_{exc}$ from 27 to 12 at%, respectively. A 22.5 nm bulk SRON sample was also deposited for the sake of comparison to the SL structure, with a global Si excess of 17 at%. All samples underwent an annealing treatment at 1150 °C for 1 h in N_2, in order to promote phase separation and achieve the precipitation and crystallization of Si NCs. In addition, the samples were hydrogen passivated in a pure H_2 ambient at 500 °C for 1 h. To analyze the electrical and electro-optical properties of the SLs, MOS-like capacitor devices were fabricated by means of photolithographic patterning of sputtered 70 nm thick ITO layer on top, as well as full-area Al on the bottom (see figure 1). The employed top-electrode circular area was $\sim 2 \times 10^{-3}$ cm^2. Further information on the material deposition and the device processing has been reported in previous works [7, 18, 20].

The structural quality of the Si NC/SiO_2 SLs was monitored by Raman scattering, exciting the devices with the 325 nm line of a He–Cd continuous laser and collecting the resulting Raman spectra (via a 40× near-UV objective) with a Horiba Jobin-Yvon LabRam spectrometer (0.5 cm^{-1} resolution) coupled to a high-sensitive CCD. The laser beam was precisely focalized on the SL structure to get rid of the Si substrate Raman contribution. The electrical characterization was carried out in dark conditions and at room temperature by means of an Agilent B1500 semiconductor device analyzer, placing the devices in a Cascade Microtech Summit 11000

Table 1. Summary of the superlattice characteristics corresponding to the devices fabricated for the present study. Set labeled 'B' states for the barrier thickness study, whereas label 'E' refers to the Si excess (within SRON layer) study. Please note that devices B1.0 and E17 are indeed the same.

Sample ID	t_{SRON} (nm)	t_{SiO2} (nm)	$[Si]_{exc}$ (at%)
B1.0	3.5	1	17
B1.5	3.5	1.5	17
B2.0	3.5	2	17
B2.5	3.5	2.5	17
B3.0	3.5	3	17
E12	3.5	1	12
E15	3.5	1	15
E17	3.5	1	17
E19	3.5	1	19
E27	3.5	1	27
Bulk	22.5	—	17

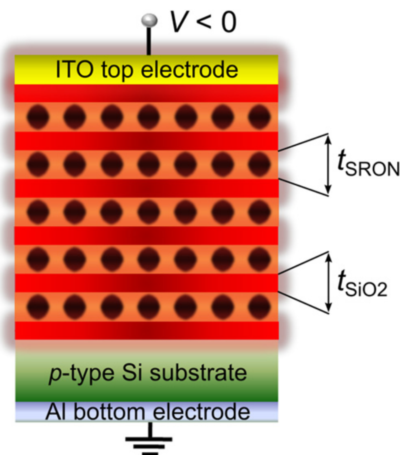

Figure 1. Cross-section sketch of the devices containing the Si NC superlattices employed for the present study. The structure allows for current injection from the ITO top electrode. Lengths are not to scale.

probe station equipped with a Faraday cage for electrical isolation. The EL from the active layers was collected with a Seiwa 888 L microscope using a long working distance 20× objective (NA = 0.4). The integrated EL output of the devices was monitored as a function of the applied voltage or intensity, acquiring the signal by means of a calibrated Hamamatsu GaAs R928 photomultiplier tube (PMT). The spectral distribution of the resulting EL was measured with a Princeton Instruments LN-cooled charge-coupled device via a 1/4 m Oriel monochromator, using an excitation current density of -2.5×10^{-2} A cm^{-2} (in accumulation regime, further details are given in section 3.2). All spectra were corrected for the optical response of the system. Time-resolved EL measurements were performed using the pulse generator module of an Agilent B1500 semiconductor device analyzer, the integrated output EL signal being collected by the PMT and monitored by a high time resolution Agilent Infiniium DSO 8064A oscilloscope.

3. Results and discussion

3.1. Structural investigation of the NC SLs

Prior to the device characterization, the structural quality of the Si NC/SiO_2 SLs was inspected by means of Raman spectroscopy. The resulting Raman spectra acquired for the different sets of devices are displayed in figures 2(a) and (b). The spectra exhibit three main features: (i) a sharp peak around 517 cm^{-1} corresponding to the crystalline Si TO-LO mode, (ii) a broad shoulder growing at lower frequencies than the crystalline peak, coming from the amorphous Si phases present within the SL, and (iii) an overall background ascribed to disorder-activated SiO_2 or acoustic amorphous Si modes [10, 11]. Looking at figure 2(a), which shows the spectra corresponding to devices with different barrier thickness, no obvious variation exists when decreasing t_{SiO2}. On the contrary, when inspecting the Si excess effect in the Raman spectra (figure 2(b)), a clear increase in signal intensity corresponding to both amorphous Si shoulder and crystalline Si peak is observed at higher Si content.

Indeed, the observations from both device sets are tightly related to the structural formation of Si NCs within the SLs, of great importance to understand the electrical and EL properties of the system. From the Raman spectra, it was possible to extract information on the crystallized fraction of Si within the devices. For this, the SiO_2 Raman contribution was substracted. The spectra were then fitted using a phonon confinement model for the crystalline peak and taking into account the shoulder related to the optical phonons contribution from amorphous Si. An average crystalline size of 3.6 nm was obtained for all samples, with a size dispersion of ±0.3 nm. Afterwards, the crystalline fraction (f_c) was retrieved establishing a proportion between the crystalline (I_c) and amorphous (I_a) integrated areas as $f_c = [1-\gamma \cdot (I_a/I_c)]^{-1}$, where γ is the crystalline-to-amorphous Si Raman scattering cross-section, evaluated in a reference sample with the same crystalline size excited at 532 and 325 nm. An exhaustive description of the crystalline size and crystalline fraction estimation method is found in [10]. The final results on f_c are summarized in figure 2(c) for both sets of devices, all displaying a very high crystalline quality. It should be mentioned that, although the Si substrate signal has been carefully avoided, some signal might be still superposing the Si NCs contribution, inducing a systematic overestimation of f_c in all devices; nevertheless, the trends, and therefore the consequent discussion, are reliable. On one hand, and as predicted by the spectra similitude in the barrier thickness device set, the crystalline fraction remains almost constant when increasing t_{SiO2}; therefore, we expect a similar NC structure in all devices. On the other hand, the Si excess increase does induce a reduction of the crystalline fraction. Despite larger Si content implies a higher crystalline signal, and thus a higher

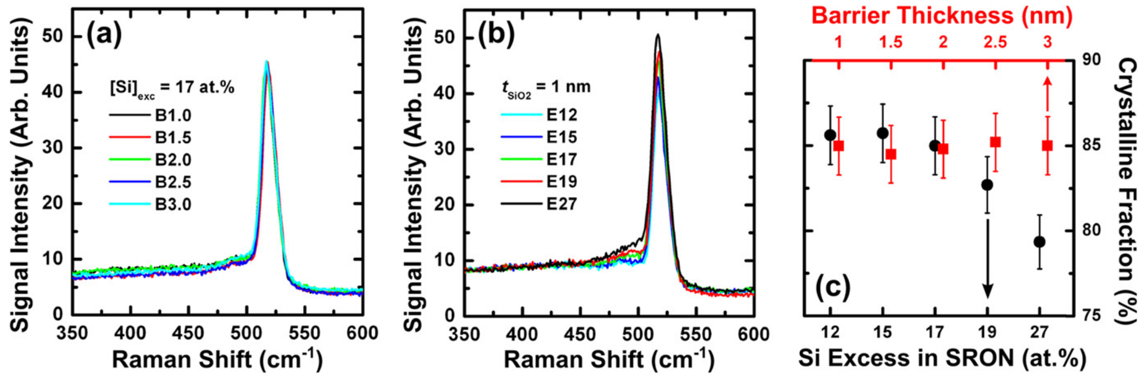

Figure 2. Raman spectra corresponding to the devices of the (a) barrier thickness (constant $[Si]_{exc} = 17$ at%) and (b) Si excess (fixed $t_{SiO2} = 1$ nm) sets. (c) Evaluated crystalline fraction from the spectra displayed in (a) and (b), taking into account the formalism described in [10]. The error bars account for a 2% fitting uncertainty of the Raman spectra.

presence of crystalline Si domains, the amorphous Si counterpart is also enhanced, resulting in an increasing amorphous Si phase within the SL. In addition, the fact that the crystalline signal increases but not the NC crystalline size indicates a larger number of NCs, which is in agreement with reported in-plane TEM images on similar NC-based samples showing higher density of NCs at higher Si contents [9].

3.2. Electrical and EL characterization

To determine the electrical properties of the devices under study, intensity versus voltage sweeps were carried out under accumulation regime ($V < 0$ applied to the gate) at room temperature, employing a constant ramp rate of 50 mV s^{-1}. The results are summarized in figure 3, where the current density (J) versus voltage (V) curves are plotted (both in absolute value), to take into account the device area. The curves corresponding to some devices exhibit two different behaviors; a slowly varying current density is observed at low voltages, whereas it notoriously increases at medium-high voltage range. The former effect, attributed to a capacitor-related displacement current, suggests that charge is being trapped within the material in this regime. Instead, high voltages provide a conduction zone, associated to a Poole–Frenkel (bulk-limited) mechanism through NC allowed energy levels, demonstrated in a previous work on similar structures to be the dominant transport mechanism [20].

To analyze in more detail the effect of the barrier thickness and Si excess variation on the electrical properties of the SL systems, figure 3(a) shows the $J(V)$ curves for different t_{SiO2}, with a constant Si excess in the SRON layers (17 at%), whereas figure 3(b) displays the curves for a different Si-rich layer stoichiometry, being $t_{SiO2} = 1$ nm. The most general feature we can draw from the curves, when decreasing the oxide barrier thickness and increasing the Si excess, is a clear and progressive increase of the current density within the conduction regime, as previously reported [18], indicating a better carrier flux. In addition, the bulk-limited conduction regime starts at lower voltages in increasingly conductive devices, which implies a lower charge trapping within the capacitor structure.

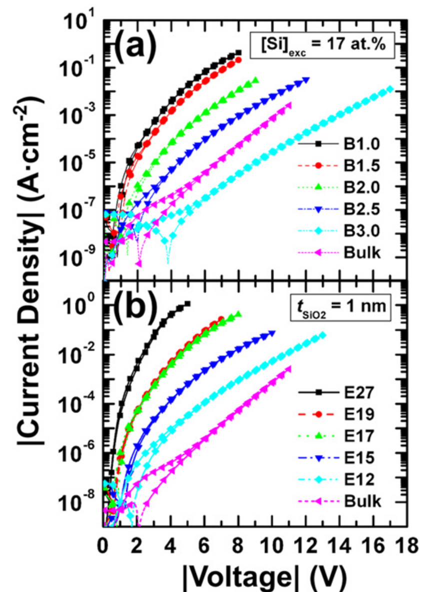

Figure 3. Current density versus applied voltage, both in absolute value, corresponding to devices containing the SL structure under study: (a) different t_{SiO2} at a fixed Si excess of 17 at% and (b) different Si excess at a constant $t_{SiO2} = 1$ nm. The corresponding curve for the bulk SRON layer (global Si excess of 17 at%) is displayed in both graphs.

Regarding the SiO_2 barrier study, when reducing the barrier thickness of the SL stack, the current density gradually increases, which is about several orders of magnitude larger than the single layer sample (device labeled as 'Bulk'). In fact, the progressively lower distance from adjacent Si NCs layers (i.e. t_{SiO2} is reduced) results in an increasing interaction of the carrier wavefunctions that leads to a current increase. It is also remarkable that similar $J(V)$ curves were obtained for

SiO_2 barrier thicknesses of $t_{SiO2} = 1.5$ to 1 nm, which suggests a very similar wavefunctions overlapping from adjacent layers for very short distances. In addition, the charge trapping region decreases when reducing t_{SiO2}, which is directly associated to the decrease of the total thickness of the capacitor-like structure. Finally, and comparing our SL devices with the reference one with a single SiO_x active layer, we observed that the bulk device exhibits a slightly larger conduction than the device containing SLs with $t_{SiO2} = 3$ nm, which is an indication that the inter-NC distance in bulk is lower than 3 nm.

The Si excess effect on the device electrical properties is also relevant. On one hand, the high-field conduction is found to dramatically increase at higher $[Si]_{exc}$, indicating that the presence of larger amounts of precipitated Si notably favors the conductivity of the SL structure. On the other hand, the capacitor displacement current region clearly decreases until disappearing at larger Si excess. Taking into account that no variation exists of the total capacitor dimensions in this set of samples, this observation suggests that the increase of Si content in the SL reduces charge trapping. EL investigation is required in order to determine how this Si excess is affecting the charge transport of the material under study, considering its distribution throughout the SRON layer. In addition, monitoring the time evolution of the EL emission can provide valuable information about the recombination dynamics.

We spectrally analyzed the EL emission from the devices under study. Figure 4 displays the normalized acquired spectra for each structure corresponding to both device sets, the SiO_2 barrier thickness (figure 4(a)) and Si excess (figure 4(b)) dependences. The bulk sample was also analyzed for the sake of comparison to the SL structure results, which presents two well-defined features: a Gaussian-like emission beyond 800 nm and a low-intensity broad band centered around 550 nm. Whereas the former emission is related to the radiative recombination of the excitons formed within the Si quantum dots, the latter is typically attributed to electronic relaxation in oxide-related defects [3, 21]. When observing the spectra provided by the SLs, the absolute EL intensity corresponding to the defects band remains unchanged, while there is an increase of the excitonic recombination emission. In addition, the overall EL emitted by the single layer device is notably lower than its SL counterparts (about two orders of magnitude). The fact that the relative intensity of the recombination emission with respect to the defects-related one is strongly enhanced in the SL structure indicates that the vertical ordered arrangement of NCs (the emitting centers), which modifies transport, strongly affects the EL excitation efficiencies. Therefore, these results evidence the high quality of the fabricated SL structures. It should be noted that almost identical recombination-related peak position is observed for the device containing a bulk SRON layer and the SL-based ones (corresponding to the barrier thickness study and intermediate Si excesses), which is in accordance to the 3.5 nm NC size reported for bulk SRON in [22].

A more in-depth analysis can be performed on the EL emission coming from the SL-based devices, the figure revealing valuable information regarding its dependence on

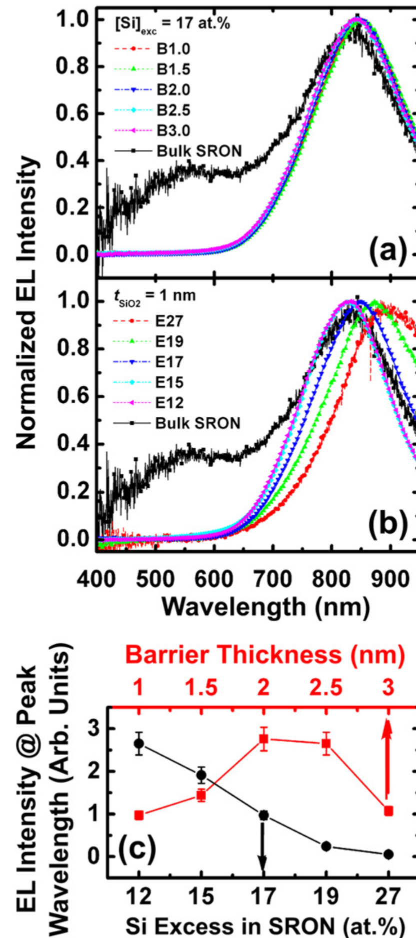

Figure 4. Normalized electroluminescence spectra acquired from the devices containing the SL structure under study: (a) different t_{SiO2} at a fixed Si excess of 17 at% and (b) different Si excess at a constant $t_{SiO2} = 1$ nm. A device containing a reference bulk sample has been employed for the sake of comparison. A constant current density of -2.5×10^{-2} A cm^{-2} was employed to electrically excite the devices. (c) EL intensity at the peak wavelength for the different devices, corresponding to the barrier thickness (red squares) and Si excess (black circles) sets. Error bars account for measurement reproducibility on the same wafer.

the structural parameters under study. Samples with different barrier thickness and constant Si excess exhibit an almost identical emission lineshape centered at ~830 nm (see figure 4(a)), with a small intensity variation from sample to sample. On the other hand, devices with different Si excess concentration display an emission peak that shifts to longer wavelengths (~60 nm between the most opposite stoichiometries), a lineshape broadening and a huge intensity reduction when increasing the Si amount (see figure 4(b)).

Actually, considering that the origin of this emission is tightly related to the quantum confinement of carriers within the nanostructures [23], the structural parameters effect on the

variation of the EL peak position and broadness can be indirectly related to the NC formation and size control. In particular, the invariance of the peak position when reducing the oxide barrier thickness (see figure 4(a)) indicates that the morphology of the nanocluster remains unchanged, which is supported by the almost constant NC crystalline size determined by Raman. In other words, the different barrier thicknesses are acting well avoiding outdiffusion of Si excess into the barrier layer and, therefore, they do not alter the NC size control. Regarding the Si excess increase (see figure 4(b)), the peak redshift and broadening suggests that the quantum confinement within NCs is being progressively lost at larger $[Si]_{exc}$. This latter fact could be associated to the precipitation of larger nanoaggregates and/or a shorter inter-NC distance. Since 1 nm barriers have shown to preserve the vertical SL structure [11], the increase in Si content could induce the in-plane presence of either larger NCs or a higher density of nanostructures [9]. Actually, the Raman analysis described in section 3.1 provides consistence to the hypothesis of a larger number of NCs while preserving the mean NC crystalline size, which induces a shorter inter-NC distance and possibly causes Si coalescence. In fact, Si NC lateral coalescence at high Si content (above the percolation threshold) was reported in [16] in similar SL systems, producing the carrier wavefunction delocalization within the nanostructures and subsequent coupling of the electronic states. Due to the shorter inter-NC distance supported by the structural characterization, this effect might also take place in our devices, resulting in the relaxation of the quantum confinement effect, as observed in the past in III–V semiconductor quantum wells [24–26]. As well, this wavefunction coupling hypothesis is in agreement with the electrical characterization results, larger Si excesses considerably improving the system conductivity as observed in figure 3(b).

The EL peak intensity evolution under the different structural conditions was also monitored, whose results are summarized in figure 4(c). In the figure, a clear decrease of EL intensity is observed at larger Si excesses, whereas for a constant Si excess it exhibits a maximum at intermediate oxide barrier thicknesses ($t_{SiO2} \approx 2$ nm). In the case of higher $[Si]_{exc}$, the larger amorphous Si phase suggested by the structural characterization results in a higher presence of defects and other non-radiative recombination centers that quenches the overall EL intensity. As well, the higher density of Si NCs at higher Si content is translated into a shorter inter-NC distance, which also takes place at thinner oxide barriers, producing the delocalization of the carrier wavefunctions, the consequent radiative recombination diminution and therefore an EL emission decrease. A different mechanism takes place at thicker SiO_2 barriers, probably ascribed to the higher degree of NC isolation (in the SL growth direction), impeding the NC interaction and thus the effective exciton formation within the nanostructures. Further investigation is needed towards the understanding of this latter effect, which, as well as the EL intensity effect on the overall device efficiency, will be discussed in the following sections.

3.3. Carrier recombination dynamics

To complement the information provided by the electrical and EL characterization, the carrier recombination dynamics corresponding to the different SL structures was also investigated by means of time-resolved EL measurements. For this, a square-pulse between 0 and −8 V (with a duty cycle of 25%) was applied to all devices, the resulting integrated EL signal being monitored by a high-sensitive oscilloscope. As an example, figures 5(a)–(c) depict the applied pulse and the resulting current intensity and integrated EL intensity for the sample with $t_{SiO2} = 1$ nm and $[Si]_{exc} = 17$ at% (named B1.0 and E17 in table 1). When the negative voltage is applied, electron injection takes place within the device, as shown by the negative (i.e. under accumulation) current intensity circulating through it. Consequently, EL rapidly increases (in a time scale of some microseconds for all samples) until the stationary emission is reached (labeled as *dc level* in the figure). The EL remains constant for the rest of the voltage pulse until the excitation drops to zero, which produces a sudden emission increase (labeled as *EL overshoot* in the figure). Afterwards, the emission decrease (*EL decay* in the figure) takes place, attaining complete decay at a time that strongly depends on the sample under study. This general behavior was also observed in all devices. In particular, figure 5(d) displays the integrated EL signal dynamics corresponding to the devices with different Si excess. In order to focus the dynamics study on both the overshoot and the EL decay, we normalized all signals to their dc level.

The constant EL emission observed in figure 5(c) within the dc level is in agreement with the constant current injection through the SLs (figure 5(b)), being the electron–hole generation (and thus recombination) rate kept fixed. When the pulsed excitation is switched off, a positive overshoot in current occurs that can be attributed to the extraction of trapped charge towards the opposite electrodes once the electric field disappears, also supported by the fast current intensity overshoot in figure 5(b). This frame can explain the EL overshoot observed at this point, thus ascribed to the created electron–hole pairs by accumulated charge within the device, which almost instantly recombine. In addition, the presence of free carriers in our system may also originate recombination centers that add to the already mentioned discharge carriers. The capacitor-related origin of the overshoot is corroborated by the different signal level in figure 5(d), where the peak intensity notably decreases with the Si excess (it even disappears beyond $[Si]_{exc} = 19$ at%), the SLs becoming increasingly conductive. This, in turn, is in accordance to the lower charge-trapped region found at larger Si contents (see figure 3(b)). The preceding EL decay, on the contrary, is not ascribed to capacitive effects. Evidence of this is given by the fast (almost instantaneous) decay from the current intensity overshoot in figure 5(b) in comparison to the slower decay in EL displayed by the same device in figure 5(c). In addition, the EL decay is different for each device (see figure 5(d)), which reveals a SL structure-dependent characteristic decay time before the emission is totally quenched. To numerically analyze this effect, we fitted

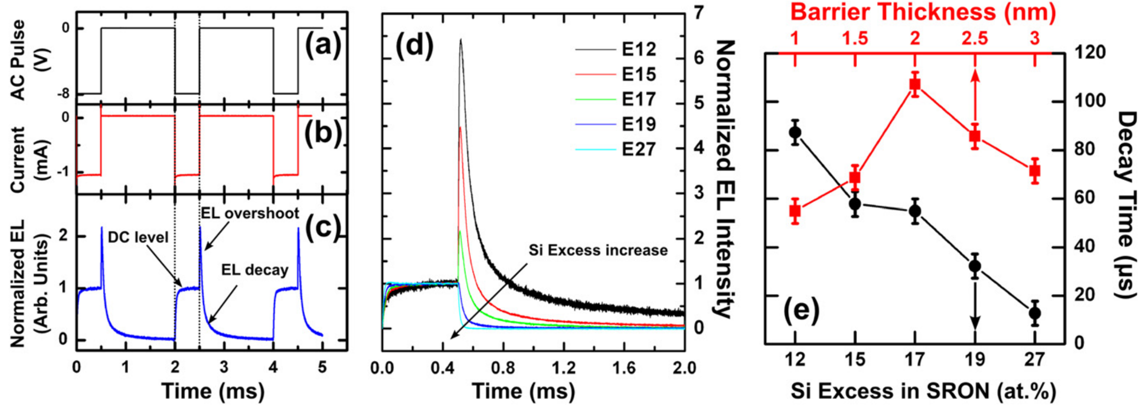

Figure 5. (a) Applied ac voltage pulse on the devices under study. The current (b) and the integrated EL (c) signals from sample E17 (B1.0) (t_{SiO2} = 1 nm and $[Si]_{exc}$ = 17 at%) originated under such ac pulse excitation, are presented as a function of time. The dashed lines indicate the boundaries of a given pulse. The time-resolved EL signal corresponding to the devices containing different Si excess within the SRON layer are displayed in (d). For comparison purposes, all time-resolved EL measurements were normalized to the dc level. Panel (e) shows the fast decay time values obtained from the barrier thickness (red squares) and Si excess (black circles) sets of samples. Error bars take into account the uncertainty in the fitting range selection of the time-resolved EL measurements.

a two-exponential decay function to the obtained decay curves:

$$I_{\rm EL}(t) \propto I_{\rm EL,0} \cdot \left(e^{-t/\tau_f} + e^{-t/\tau_s}\right), \quad (1)$$

where $I_{EL,0}$ is a pre-exponential factor. The fit results show that the EL emission decay obeys two well-differentiated time scales: a fast one (τ_f), in the order of tens of μs (in agreement with many reported works [27–29]), which is typically associated to the excitonic recombination within NCs; and a slow one (τ_s), of several hundreds of μs, which may be ascribed to the emission of larger NCs in the distribution. The origin of the slow lifetime may be related to cross-talk energy transfer between nanostructures, which makes this effect independent from the spectral EL distribution, as proved by the similar lifetime values irrespective of the SL structural conditions. On the contrary, the NC-related fast decay time presents a strong dependence on the SL characteristics (i.e. t_{SiO2} and $[Si]_{exc}$); therefore, it is the latter recombination time which will be studied in the following lines, whose results are plotted in figure 5(e) for both device sets. For the sake of comparing our EL decay time results with typical NC lifetimes reported in the literature [30, 31], we also fitted a stretched exponential function to our experimental curves, resulting in almost identical values than the NC-related fast decay time. This supports the good election of a two-exponential decay to fit our data, and confirms τ_f as the clue value to discuss the recombination properties of our NC-based SLs.

The results from the fast EL decay time analysis are summarized in figure 5(e). As can be seen, a clear decrease in τ_f occurs when the Si amount increases, whereas an optimum decay time is found for intermediate SiO_2 barrier thicknesses. Both behaviors perfectly scale with the EL peak intensity trends mentioned in the previous section (see figure 4(c)), which allows for establishing a direct relation between the excitonic recombination lifetime and the amount of excited emitting centers. In the case of the Si content increase, one could initially ascribe longer EL decay times to a higher crystalline degree of the nanostructures (thus increasing the radiative recombination probability [32]); nevertheless, the lower crystalline fraction at higher Si content determined by Raman (see figure 2(c)) discards this hypothesis, and a τ_f decrease is instead observed in figure 5(e). As previously discussed, higher $[Si]_{exc}$ causes an in-plane larger NC density, which allows associating this exciton lifetime reduction with a loss of quantum confinement of the carriers within the NCs, provided that lower inter-NC distances are found. The consequence is a loss the exciton stability (due to the wave-function delocalization), which strongly reduces τ_f. In addition, the presence of higher $[Si]_{exc}$ induces the presence of larger amorphous Si regions (see section 3.1) that increase the probability of non-radiative recombination, thus reducing the overall (and observed) radiative lifetime and quenching the global EL emission.

The t_{SiO2} variation case must be treated separately, as the peak-like behavior observed for both lifetime and EL intensity necessarily has to combine different effects that compete at the different barrier thickness ranges. For thinner barriers, and bearing in mind that all measurements were performed under the same voltage pulse polarization (i.e. higher current densities circulate through the lower-barrier SLs, see figure 3(a)), free carriers may play an important role in charge time dynamics. This may induce fast processes such as Auger electron emission or other non-radiative processes associated to the heating of the SL by free carriers, reducing the global radiative lifetime of the system. In the opposite case, i.e. for thicker barriers, the higher stress generated by the larger SiO_2 presence surrounding the NCs [11, 33] may give rise to an instability of the confined excitons, thus reducing the recombination time. The optimum conditions when both

effects are minimized, namely, a lower presence of free carriers and low enough matrix stress, are reached at $t_{SiO2} = 2$ nm. Both hypotheses are plausible in the frame where the NC interaction does not cause a loss of exciton confinement within the NCs (the nanostructure morphology is not varied [33]), which is corroborated by identical Raman spectra (see figure 2(a)) and the constant EL peak position in the spectra shown in figure 4(a). Other competing effects may take place regarding the barrier thickness modification that are related to the NC excitation, which requires a further analysis on the correlation between charge injection within the SLs and the luminescence yielded by the structures, as will be treated in the following section.

3.4. Structural parameters effect on the electro-optical conversion

Up to now, the electrical, EL and recombination dynamics properties of the Si NC/SiO_2 SLs have been separately analyzed, as a function of the SL structural parameters variation. To understand the electrical excitation and resulting luminescence coming from these active layers, we quantified the light emission efficiency by measuring the integrated intensity per unit area emitted by the devices. Out of these results, the EL optical power (P_{opt}) was calculated, considering the total amount of light collected by the system microscope in a way as discussed in [34]. Consequently, the emission power efficiency (η_{PE}) from the devices could be determined, defined as the ratio between the optical emission output and the electrical excitation input:

$$\eta_{PE}(\%) = \frac{P_{opt}}{I \times V} \times 100. \quad (2)$$

Prior to an in-depth analysis on the device EL power efficiency, we should describe the transport and EL excitation frame within our SL structures. As it was reported in [20], the electrical and EL experimental observation on these structures suggested a relation between the Poole–Frenkel-type transport and the NC excitation. In particular, it was hypothesized that some electrons traveling through allowed high-energy NC-confined states promote to the effective SL conduction band, where they are accelerated by means of the electric field. If the energy of these electrons is higher than the threshold for impact ionization to occur, then the creation of an electron–hole pair is possible within the NC after direct electron energy transfer. Finally, the consequent electron–hole recombination yields a photon with the nanostructure bandgap energy. To study the device behavior within the regime where these phenomena take place, the power efficiency of the devices must be evaluated at a similar conduction regime (see figure 3). Considering this point we have chosen the maximum η_{PE}, provided that the corresponding current injection and applied voltage satisfied these considerations for all devices. The obtained power efficiencies in this way are summarized in figure 6, with values that span from 10^{-7} to 10^{-3}%, lower than other results in literature on similar samples [17, 19]. In these former works, tunnel injection of carriers dominates charge transport, which results into more efficient impact ionization than in our devices (dominated by bulk-limited transport mechanisms). In this sense, a possible approach to improve EL emission efficiency in our SL-based devices would be the incorporation of a (20- or 30-nm thick) SiO_2 carrier-accelerating layer on top of the SL stack, by means of which injected carriers are accelerated (i.e. they acquire a higher kinetic energy), tunneling becomes dominant and higher emission efficiencies are achieved [34]. However, it is the aim of this work to determine the structural parameters that lead to the optimum SL-based device performance, which will be discussed in the following in terms of the involved physical processes within the SL.

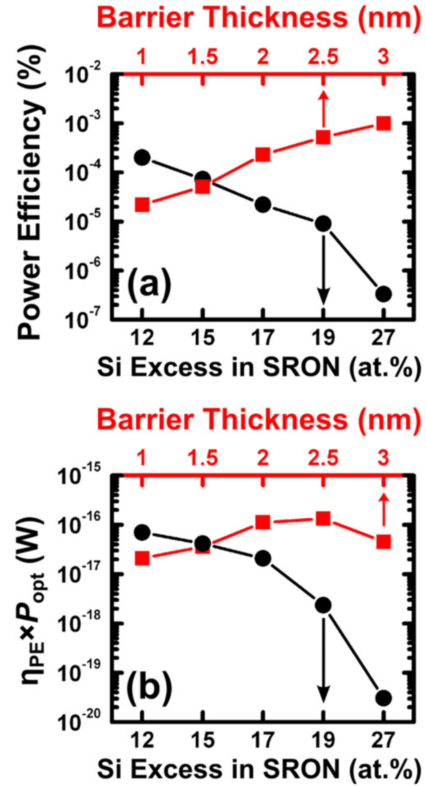

Figure 6. (a) Maximum EL power efficiency, η_{PE}, corresponding to both sample sets: different t_{SiO2} at a fixed Si excess of 17 at% (red squares) and different Si excess at a constant $t_{SiO2} = 1$ nm (black circles). (b) Calculated $\eta_{PE} \times P_{opt}$ under the same conditions, corresponding to the same sample sets in (a).

The graphs shown in figure 6 exhibit a clear decrease in the power efficiency when increasing the Si excess, whereas it increases at thicker oxide barrier layers. The competition between the terms involved in equation (2), i.e. the electrical power input and the EL yielded by the SLs, can be used to explain the different observed behaviors. Regarding the $[Si]_{exc}$ dependence (figure 6(b)), η_{PE} continuously decreases at larger Si content. Mathematically, it can be immediately shown that, as the EL intensity drops and the current density

is enhanced at higher Si excess (see section 3.2), the ratio in equation (2) is translated into a dramatic decrease in power efficiency. As commented in previous sections, at higher Si content we find a higher carrier density, and we as well expect the precipitation of a larger number of nanostructures, which results in the inter-NC distance reduction. On one hand, the consequence of a higher carrier density may give rise to the presence of free carriers that are efficiently extracted without contributing to impact ionization, i.e. not producing EL. On the other hand, inter-NC proximity may give rise to non-radiative paths because of in-plane NC–NC coupling. Both effects contribute to the overall EL emission quenching at higher Si excesses.

The case concerning the SiO_2 barrier thickness variation is simpler. Again, the higher NC–NC coupling (now in the SL growth direction) taking place at thinner barrier layers can explain the observed power efficiency decrease, as non-radiative processes are strengthened. In addition, under the conditions where the maximum η_{PE} was evaluated, thicker barriers require a larger voltage (and thus electric field) that increases the kinetic energy of electrons due to their acceleration within the conduction band, which makes the NCs excitation more probable. These effects result in a more efficient NC excitation at larger t_{SiO2}.

Finally, from the point of view of the SLs potential applications in the optoelectronics field, the power efficiency together with the total emission helped us determining the best structural parameters for the fabrication of efficient light emitters. It was observed that, although thin layers present excellent carrier transport, their electrical-to-light conversion efficiency is limited. In addition, the Si excess increase (involving in-plane morphologic changes in the SLs) dramatically reduces the device efficiency, evidencing higher electrical conduction at the expense of a drastic EL emission drop. In fact, since it is the overall system emission the interesting parameter for optoelectronic applications, a figure of merit can be defined that weights the optical output power yielded by the devices with their conversion efficiency, $\eta_{PE} \times P_{opt}$ (see figure 6(b)). This procedure demonstrates that intermediate barrier thicknesses (2–2.5 nm) and low Si content (12–15 at%) are the optimum SL structural parameters for light emission purposes.

4. Conclusions

We have reported on the electrical and EL properties of devices containing Si NCs/SiO_2 SLs as active material, in terms of the oxide barrier thickness and the Si excess contained in the pre-annealed SRON layers. The crystalline quality of the SLs was retrieved by Raman scattering, from which the crystalline NC size was evaluated for all devices, presenting a constant value of 3.6 nm, with a size dispersion of ±0.3 nm. The electrical conduction was found to strongly improve when reducing t_{SiO2} and increasing $[Si]_{exc}$, attributed, respectively, to lower inter-NC distance and higher in-plane nanostructure density. The lateral inter-NC proximity increase at larger Si contents was found to give rise to a loss of quantum confinement, originating an EL spectra redshift, whereas no morphological variations appeared when employing different t_{SiO2}, as supported by almost identical Raman spectra. The study on the carrier recombination dynamics within the SL-based devices revealed lifetimes of tens of μs associated to typical NC-based structures. The lifetime was found to decrease at higher $[Si]_{exc}$ due to exciton delocalization induced by proximity between nanostructures, whereas a maximum value was observed at intermediate oxide barriers, where a balance between non-radiative processes and the matrix stress is reached. Finally, the EL power efficiency yielded by the devices was calculated, evidencing a clear dependence of the emitted optical power with the impact ionization-based excitation. Again, the EL quenching induced by carrier wavefunction delocalization and non-radiative processes originated by high current densities, might explain the increase in conversion efficiency observed at thicker oxide barriers and lower Si contents. In conclusion, although the overall power efficiencies do not surpass the barrier of 10^{-3}%, we have shown how the SL structural parameters modify the electrical and EL properties of these NC-based devices. Furthermore, we succeeded in determining the optimum parameters for light emission, namely, $t_{SiO2} = 2$–2.5 nm and low $[Si]_{exc}$ 12–15 at%, which will vary depending on the optoelectronic application they are meant to.

Acknowledgments

The research leading to these results has received funding from the European Community's Seventh Framework Programme (FP7/2007-2013) under grant agreement no: 245977, under the project title NASCEnT. The present work was supported by the Spanish national project LEOMIS (TEC2012-38540-C02-01).

References

[1] Conibeer G *et al* 2006 *Thin Solid Films* **511–512** 654–62
[2] Perez-Wurfl I, Hao X, Gentle A, Kim D-H, Conibeer G and Green M A 2009 *Appl. Phys. Lett.* **95** 153506
[3] Valenta J, Lalic N and Linnros J 2001 *Opt. Mater.* **17** 45
[4] Linnros J and Lalic N 1995 *Appl. Phys. Lett.* **66** 3048
[5] Perálvarez M, García C, López M, Garrido B, Barreto J, Domínguez C and Rodríguez J A 2006 *Appl. Phys. Lett.* **89** 051112
[6] Zacharias M, Heitmann J, Scholz R, Kahler U, Schmidt M and Bläsing J 2002 *Appl. Phys. Lett.* **80** 661
[7] Hartel A M, Hiller D, Gutsch S, Löper P, Estradé S, Peiró F, Garrido B and Zacharias M 2011 *Thin Solid Films* **520** 121
[8] Iacona F, Franzò G and Spinella C 2000 *J. Appl. Phys.* **87** 1295
[9] Hernández S, Miska P, Grün M, Estradé S, Peiró F, Garrido B, Vergnat M and Pellegrino P 2013 *J. Appl. Phys.* **114** 233101
[10] Hernández S, López-Vidrier J, López-Conesa L, Hiller D, Gutsch S, Ibáñez J, Estradé S, Peiró F, Zacharias M and Garrido B 2014 *J. Appl. Phys.* **115** 203504
[11] López-Vidrier J, Hernández S, Hiller D, Gutsch S, López-Conesa L, Estradé S, Peiró F, Zacharias M and Garrido B 2014 *J. Appl. Phys.* **116** 133505
[12] Conibeer G *et al* 2008 *Thin Solid Films* **516** 6748

[13] DiMaria D J, Theis T N, Kirtley J R, Pesavento F L, Dong D W and Brorson S D 1985 *J. Appl. Phys.* **57** 1214
[14] Ron A and DiMaria D J 1984 *Phys. Rev.* B **30** 807
[15] Balberg I 2011 *J. Appl. Phys.* **110** 061301
[16] Balberg I, Savir E, Jedrzejewski J, Nassioupoulou A G and Gardelis S 2007 *Phys. Rev.* B **75** 235329
[17] Anopchenko A, Marconi A, Moser E, Prezioso S, Wang M, Pavesi L, Pucker G and Bellutti P 2009 *J. Appl. Phys.* **106** 033104
[18] Gutsch S, Laube J, Hartel A M, Hiller D, Zakharov N, Werner P and Zacharias M 2013 *J. Appl. Phys.* **113** 133703
[19] Marconi A, Anopchenko A, Wang M, Pucker G, Bellutti P and Pavesi L 2009 *Appl. Phys. Lett.* **94** 221110
[20] López-Vidrier J *et al* 2013 *J. Appl. Phys.* **114** 163701
[21] Yuan J and Haneman D 1999 *J. Appl. Phys.* **86** 2358
[22] López-Vidrier J *et al* 2011 *Energy Proc.* **10** 43
[23] Barbagiovanni E G, Lockwood D J, Simpson P J and Goncharova L V 2012 *J. Appl. Phys.* **111** 034307
[24] Suzuki S, Kanisawa K, Janer C, Perraud S, Takashina K, Fujisawa T and Hirayama Y 2007 *Phys. Rev. Lett.* **98** 136802
[25] Ibáñez J, Patanè A, Henini M, Eaves L, Hernández S, Cuscó R, Artús L, Musikhin Y G and Brounkov P N 2003 *Appl. Phys. Lett.* **83** 3069
[26] Solomon G S, Trezza J A, Marshall A F and Harris J S Jr 1996 *Phys. Rev. Lett.* **76** 952
[27] Linnros J, Lalic N, Galeckas A and Grivickas V 1999 *J. Appl. Phys.* **86** 6128
[28] Dovrat M, Goshen Y, Jedrzejewski J, Balberg I and Sa'ar A 2004 *Phys. Rev.* B **69** 155311
[29] Lalic N and Linnros J 1996 *J. Appl. Phys.* **80** 5971
[30] Kenyon A J, Wojdak M, Ahmad I, Loh W H and Oton C J 2008 *Phys. Rev.* B **77** 035318
[31] Pavesi L and Ceschini M 1993 *Phys. Rev.* B **48** 17625
[32] Avella M, Prieto A C, Jiménez J, Rodríguez A, Sangrador J, Rodríguez T, Ortiz M I and Ballesteros C 2008 *Mater. Sci. Eng.* B **147** 200
[33] Kůsová K *et al* 2012 *Appl. Phys. Lett.* **101** 143101
[34] Berencén Y, Wutzler R, Rebohle L, Hiller D, Ramírez J M, Rodríguez J A, Skorupa W and Garrido B 2013 *Appl. Phys. Lett.* **103** 111102

4.2.2. Si Nanocrystal / SiC Superlattices for Photovoltaic Applications

4.2.2.1. Electrical Conduction Properties of Si NC / SiC Multilayers

Analogously to the charge transport investigation carried out in Si NC / SiO_2 superlattices previously presented, an extensive electrical characterization was performed on Si NC / SiC multilayer systems. The results of this study are reported in Paper X [152]. The employed samples depended on whether (i) the presence of NCs or (ii) the multilayer parameters were studied. In particular, for (i) three samples were fabricated: bulk SiC, randomly distributed Si NCs in a single film and Si NCs embedded within a multilayer structure. Apart from the typically employed annealing treatment, different passivation processes were studied to optimize the multilayer electrical conduction. In case (ii), the same samples described in Paper VII [24] were analysed (see Run C6 in Tab. 4.4), plus a bulk SiC reference sample. In addition, the electrical measurements performance was carried out in a lateral configuration: the material was deposited on fused silica substrates and Ti/Pd/Ag interdigitated contacts were buried until the substrate. This way, only current flow through the material under test was expected.

The presence of crystallized Si and SiC was studied by means of XRD and Raman scattering measurements. In particular, all films showed micro-crystalline SiC domains with a mean grain size of (4.2 ± 0.8) nm. In addition, the Raman results performed on samples deposited on fused silica substrate and containing a Si excess revealed crystalline and amorphous contributions from Si NCs, as evidenced, respectively, by a sharp TO-LO mode between 510 and 520 cm^{-1} and a broad disorder-related band at lower frequencies. Further information could be obtained from Raman spectra regarding to the fraction of crystallized Si; for this, the method developed in Paper III [79] was used, which revealed higher values for samples containing a disordered array of NCs (i.e. with no multilayer structure), as predicted by the lower Si volume within the multilayered samples. Besides, Si NC mean crystalline sizes of ~ 3 nm were estimated for NC-containing samples, in good agreement with XRD results and the previously reported work in Paper VII [24].

The charge transport mechanisms dominating Si NC / SiC systems were exhaustively studied. For this, temperature-dependent electrical measurements were performed. Some transport mechanisms were systematically ruled out after a first inspection of the $I(V)$ properties of the samples. For instance, the clear dependence of conduction with temperature automatically discarded tunneling [insensitive to temperature, see Section 2.4.1.2 in Chapter 2 (*Fundamentals of Silicon Nanocrystals*)], whereas the observed Ohmic behavior of the curves eliminates the possibility of conduction through states at grain boundaries or interfaces (with a typical non-linear dependence). The Arrenhius (i.e. conductivity versus inverse of temperature) plots of the different films displayed a non-linear trend, indicating that no single mechanism could explain transport within the Si NC / SiC systems.

Indeed, after considering *variable range hopping* (low-temperature conduction in disordered systems with localized states [182]), these plots could be fitted by:

$$\sigma_{\mathrm{VRH}} = \sigma_{00} \cdot \exp\left[-\left(\frac{T_0}{T}\right)^{\frac{s+1}{s+4}}\right] , \quad (4.13)$$

where σ_{VRH} is the conductivity associated to variable range hopping, T the temperature, σ_{00} and T_0 are fitting parameters and s is an index that depends on the density-of-states and, thus, on the particular transport mechanism under consideration. At different temperature ranges, the curves could be fitted by combining $s = 0$ and $s = 2$ from Eq. (4.13), thus indicating conduction from variable range hopping and through extended band states, which is in agreement with the disordered nature of the material systems under study.

Of interest was also the study of the passivation treatment effect on the conduction properties. For this, samples were treated by either forming gas annealing (FGA) or remote hydrogen plasma treatment (RHPT) at 450 °C. It was found that the conductivity of the films remained almost unchanged after FGA, whereas RHPT improved conduction by one order of magnitude. This could be explained as a function of the passivating particles penetration within the samples: in FGA, the in-diffusion of hydrogen molecules is hindered by the much smaller interstices in SiC than in SiO_2 [183]. On the contrary, atomic hydrogen as employed in RHPT can penetrate through the SiC lattice and reach the Si nanostructures, thus achieving an efficient passivation.

In summary, Paper X [152] exhaustively analyses the transport mechanisms that dominate conduction in SiC systems containing Si NCs. It is indeed the first reported study on these material systems where all the different transport classes have been considered, and where a combination of electrical and structural techniques have been employed to determine the most plausible one. Besides, the effect of different passivation methods has been studied, evidencing the enormous enhancement in conduction that RHPT induces to the system.

PHYSICAL REVIEW B **91**, 195317 (2015)

Charge transport in nanocrystalline SiC with and without embedded Si nanocrystals

M. Schnabel,[1,2,*] M. Canino,[3] S. Kühnhold-Pospischil,[1,4] J. López-Vidrier,[5] T. Klugermann,[1] C. Weiss,[1] L. López-Conesa,[5] M. Zschintzsch-Dias,[6] C. Summonte,[3] P. Löper,[1,†] S. Janz,[1] and P. R. Wilshaw[2]

[1]*Fraunhofer Institute for Solar Energy Systems, Heidenhofstr. 2, 79110 Freiburg, Germany*

[2]*Department of Materials, University of Oxford, Parks Rd, Oxford OX1 3PH, United Kingdom*

[3]*Consiglio Nazionale delle Ricerche-Istituto per la Microelettronica e i Microsistemi, via Gobetti 101, 40129 Bologna, Italy*

[4]*Institute for Physical Chemistry, Albert-Ludwigs-Universität Freiburg, Albertstr. 21, 79104 Freiburg, Germany*

[5]*MIND-IN[2]UB, Electronics Department, University of Barcelona, Martí i Franquès 1, 08028 Barcelona, Spain*

[6]*Institute of Ion Beam Physics and Materials Research, Helmholtz-Zentrum Dresden-Rossendorf e.V., Bautzner Landstraße 400, 01328 Dresden, Germany*

(Received 24 December 2014; published 26 May 2015)

Charge transport in nanocrystalline SiC with and without embedded Si nanocrystals (Si NCs) prepared by annealing of a-$Si_{1-x}C_x$:H precursors is studied using temperature-dependent current-voltage measurements supported by electron spin resonance and mass spectrometry data. Transport is Ohmic in all films at all temperatures and the temperature dependence of conductivity shows that the materials behave as disordered semiconductors, exhibiting extended-state transport at high temperature and variable-range hopping transport at low temperature. Grain-boundary-, surface-, and interface-dominated transport is systematically ruled out. Films are n type, and films with Si NCs exhibit up to 10^3 times higher conductivity (up to 0.1 S cm^{-1}) after exposure to a hydrogen plasma which passivates dangling bonds, particularly on Si NCs. A forming gas anneal does not have such an effect, indicating that atomic rather than molecular hydrogen is required. The conductivity of SiC films without Si NCs is largely unchanged by passivation and the Fermi level is not raised nearly as closely to the conduction band. This is attributed to a type I band offset between Si NCs and SiC that leads to extended-state conduction in films with Si NCs taking place in a Si network. This is confirmed by the dependence of the extended-state mobility on the volume fraction of excess Si. Variable-range hopping is relatively insensitive to the presence of excess Si and is hence considered to take place via shallow defect states throughout the volume of the films. The high conductivities are found to be a consequence of background doping by oxygen and nitrogen.

DOI: 10.1103/PhysRevB.91.195317 PACS number(s): 73.63.Bd, 72.80.Ng, 72.20.Ee

I. INTRODUCTION

Silicon has been the material of choice for electronics for many years; however, optical and optoelectronic applications were long hampered by its indirect band gap. The discovery of luminescence in porous silicon by Canham *et al.* [1,2] sparked a wave of research activity into the optical properties of nanostructured silicon. Silicon nanocrystals (Si NCs) embedded in SiO_2 were synthesized by high-temperature annealing of SiO_2 ion implanted with Si [3,4], as well as by using the multilayer approach pioneered by Zacharias *et al.* [5], and were found to emit visible light due to quantum confinement [6–11] and with high quantum efficiency [11]. For well-separated NCs in SiO_2, electrical transport takes place by tunneling between NCs via dangling bond states [12]; nevertheless, electrical transport is necessarily poor due to the strongly insulating nature of SiO_2, which makes transport between Si NCs difficult even when their density is relatively high [12–14]. Embedding Si NCs in SiC yields a material where the conduction and valence band offsets are much smaller, which leads to a higher density of states in the nanocrystals [15–17] and better carrier transport, even across wider gaps between NCs [16]. Igarashi *et al.* have used neutral beam etching and a ferritin biotemplate to prepare layers of hexagonally ordered Si nanodisks in SiC [18,19] and a comparison of measured current-voltage (IV) curves with simulations revealed that electrical transport may take place via resonant tunneling.

Unfortunately, this sample processing method is rather time-consuming, and in most other works Si NCs embedded in SiC have been prepared in a disordered manner by annealing Si-rich a-$Si_{1-x}C_x$:H films [20–25] or in an ordered manner by annealing a-$Si_{1-x}C_x$:H/a-SiC:H multilayers [26–31]. Annealed films may contain amorphous and nanocrystalline silicon (a-Si nanoclusters, Si NCs), as well as amorphous SiC (a-SiC) and nanocrystalline SiC, which typically crystallizes in the cubic 3C polytype [26,32]. Rui *et al.* prepared p-i-n structures using a-$Si_{0.79}C_{0.21}$:H films annealed at 900°C, and reported transport via Fowler-Nordheim tunneling [33]. However, Summonte *et al.* showed thermally activated transport arising from background doping in both a-$Si_{1-x}C_x$:H bulk layers and multilayer structures annealed at 1100°C [30], in line with what is observed in microcrystalline silicon (μc-Si) [34], as well as in amorphous [35], nanocrystalline [36], and epitaxial *3C*-SiC [37] around room temperature. In Refs. [34] and [37], oxygen is suspected as a background dopant in μc-Si and *3C*-SiC. However, it was demonstrated that a-$Si_{1-x}C_x$:H/a-SiC:H multilayers intentionally doped with oxygen [38,39] and nitrogen [40] exhibit strongly reduced conductivity since oxygen and nitrogen also impede the crystallization of the *3C*-SiC phase on annealing. This was found to be beneficial for photovoltaic applications. Song *et al.* observed space charge-limited current transport in a-$Si_{0.9}C_{0.1}$/a-SiC multilayers annealed at 1100°C [41].

*Corresponding author.

†Present address: École Polytechnique Fédérale de Lausanne, Institute of Microengineering, Photovoltaics and Thin Film Electronics Laboratory, Rue de la Maladière 71b, 2002 Neuchâtel 2, Switzerland.

1098-0121/2015/91(19)/195317(15) 195317-1 ©2015 American Physical Society

The range of proposed conduction mechanisms may stem from variations in sample processing, but it is likewise possible that in some studies premature conclusions were drawn about the conduction mechanism, particularly as few studies show clear trends with processing parameters or structural data. This occurred in studies of the Si NCs in SiO_2 system, where over the years many different conduction mechanisms known from bulk materials were proposed based on how well they fit the electrical data rather than how well they fit the sample nanostructure [13].

In this contribution, temperature-dependent charge transport in the films is studied as a function of the Si NC content and size distribution, annealing ambient, and hydrogenation, and correlated with electron spin resonance (ESR) and secondary ion mass spectroscopy (SIMS) measurements. Based on the systematic exclusion of other conduction mechanisms, conduction in SiC with and without embedded Si NCs is proposed to occur via extended-state transport and variable-range hopping, in analogy to transport in disordered semiconductors [42,43]. Multiple batches of samples from two different laboratories are studied in order to exclude variations in processing and show that the electrical transport model proposed is valid for a wide range of specimens. Details of the sample preparation are given in Sec. II. Section III deals with charge transport in SiC, and changes therein once Si NCs are embedded in the SiC. In Sec. IV, we study the effect of different Si NC arrays in SiC on transport before summarizing our results in Sec. V.

II. EXPERIMENTAL

A. Sample preparation

All samples used in this study were deposited as a-$Si_{1-x}C_x$:H films by plasma-enhanced chemical vapor deposition (PECVD) and thermally annealed to induce crystallization, and are referred to as $Si_{1-x}C_x$ films. Fused silica substrates were used for electrical and Raman measurements and spectrophotometry, and 10 Ωcm p-type FZ-Si substrates were used for grazing-incidence x-ray diffraction (GIXRD), Fourier-transform infrared spectroscopy (FTIR), ESR, and transmission electron microscopy (TEM).

For study in Sec. III, $Si_{0.63}C_{0.37}$ bulk layers (S), $Si_{0.5}C_{0.5}$ bulk layers (C), and superlattices consisting of 6-nm-thick $Si_{0.77}C_{0.23}$ layers sandwiched between 6-nm-thick $Si_{0.5}C_{0.5}$ bulk layers (M) were deposited. Film compositions were measured by use of Rutherford backscattering spectrometry (RBS) at the HZDR Ion Beam Centre using 1.7-MeV He ions and detection under a scattering angle of 170°, and spectra fitted with the SIMNRA code [44]. The PECVD process parameters were 65 W at high frequency (13.56 MHz) with a plasma power density of 100 mW cm^{-2}, 30 Pa of pressure, and a substrate temperature of 270°C. The total as-deposited thickness of all M, S, and C films was 100 nm, and the compositions of the Si-rich layers were selected such that films S and M have comparable average compositions. All films were annealed at 1050°C for 1 h, some in Ar and some in N_2 ambient. After annealing, some of the films underwent a remote hydrogen plasma treatment (RHPT) [45] at 450°C for 15 or 45 min. A recent study showed this to be close to the optimum hydrogenation temperature for Si NCs in SiC [46]. After the treatment samples were cooled to below 400°C under H_2 to avoid hydrogen effusion during cooling. Samples that were not hydrogenated are referred to as "as-prepared" throughout. Sputtered indium tin oxide (ITO) was used to form the contacts, in a van der Pauw configuration [47] for Hall measurements and in a transmission line model (TLM) structure [48] for IV measurements. The latter helps to eliminate parasitic resistances and obtain a precise sheet resistance measurement of the films [48], and also provides a sheet resistance value that is averaged over the entire $25 \times 25\ mm^2$ sample area.

The samples studied in Sec. IV are exactly the same as samples X9-2, -3, and -4 from Ref. [49], and a detailed account of the sample preparation can be found therein. Briefly, they are superlattices of 30 $Si_{0.85}C_{0.15}$ layers sandwiched between 5-nm-thick $Si_{0.5}C_{0.5}$ layers and annealed at 1100°C for 30 min in N_2. Samples X9-2, -3, and -4 have $Si_{0.85}C_{0.15}$ thicknesses of 2, 3, and 4 nm, respectively. A 174-nm-thick bulk $Si_{0.5}C_{0.5}$ film was also prepared which will be referred to as X9-B. All thicknesses for this set of samples are those of the annealed films; as-deposited thicknesses were commensurately greater [49]. Electrical contacts were realized in a TLM structure using a thermally evaporated stack of 50 nm Ti, 50 nm Pd, and 1 μm Ag. Half the samples were kept unhydrogenated while the other half were first exposed to a forming gas anneal (5% H_2 in N_2) for 25 min at 425°C and then a RHPT step at 450°C for 45 min. Before and after each hydrogenation step IV measurements were carried out.

B. Characterization

The structure of films M, S, and C was characterized using GIXRD, FTIR, spectrophotometry, and Raman spectroscopy, as well as ESR measurements. For GIXRD, a Philips X'Pert MRD system with a CuK_α ($\lambda = 0.154$ nm) x-ray source was used and the angle of incidence was set to 0.3°. FTIR spectroscopy was carried out using a Bruker IFS 113v instrument in the range of 400 cm^{-1} to 4000 cm^{-1} with 6 cm^{-1} resolution. To acquire the Raman spectra, a laser scanning confocal microscope with a 355-nm frequency-tripled Nd:YAG laser for excitation and a UV-enhanced silicon charge-coupled device (CCD) detector was used [50]. Spectrophotometry (UV-vis-NIR) of films M, S, and C was carried out using a Varian Cary 500i spectrophotometer with an integrating sphere, and X-band ESR ($\omega = 9.8$ GHz) was performed at room temperature using an EMX instrument and the Super High Q resonator 4122 from Bruker Biospin. The magnetic field was modulated with an amplitude of 3 G, and the magnetic field and spin density were calibrated using DPPH and a 0205 W112 standard from Bruker Biospin, respectively. The ESR signal of each sample was also linearly scaled by the quality factor (Q value), which was determined to be 7700 for the 0205 W112 standard and 1200–2000 for the samples, the latter being significantly lower due to microwave absorption by the Si substrate. Thicknesses of samples X9-2, -3, and -4 were determined from reflection and transmission spectra measured with a HP 8452A diode array spectrophotometer using the computer code OPTICAL, based on the generalized transfer matrix method [51]. Energy-filtered transmission electron microscopy (EFTEM) was carried out using a JEOL 2010 FEG TEM operating at 200 keV and equipped with a Gatan image

filter (0.8 eV resolution). Details on structural measurements on samples X9-2, -3, and -4 can be found in Ref. [49].

Both room-temperature and temperature-dependent IV curves of all samples were acquired in a cryostat under a vacuum of $<5 \times 10^{-4}$ mbar using a HP 4140B picoammeter. IV curves were acquired from -2 V to $+2$ V and each voltage was applied for a sufficiently long time before the current was recorded to allow the current to equilibrate. This means that if the material contains defects that are charged upon application of an electric field, all such defects should be considered to be fully charged during measurement. For temperature-dependent measurements, this hold time was determined at the lowest measurement temperature. Samples were precharacterized by light microscopy, and contact spacings in which the film contained cracks were not measured. For temperature-dependent measurements, the nominal temperature was set with a Eurotherm 902s temperature controller, and the true sample temperature measured using a PT100 thermocouple mounted on the film surface. By measuring the same sample twice and examining the difference in temperature for a given conductivity, a repeatability of ± 3 K was determined for the PT100. The error given for each data point in the temperature-dependent conductivity plots represents the temperature variation during the measurement of the corresponding IV curve.

III. NANOCRYSTALLINE SiC WITH AND WITHOUT Si NCS

A. Nanostructure

Films M, S, and C are expected to consist of nanocrystalline SiC containing ordered, disordered, and no Si NCs, respectively. FTIR and GIXRD measurements (not shown here) confirmed the crystallization of SiC in all films, and Scherrer analysis [52] of the (111) reflections yielded a SiC grain size in the range of 3.5–5.0 nm for all films. Grain sizes derived in this manner have been shown to be in good agreement with grain sizes measured by TEM [53].

Raman spectra of all three films annealed in Ar are shown in Fig. 1. Three measurements were taken at different locations on each sample and are plotted together in the figure. Excellent uniformity across each sample is observed. FTIR and UV-vis-NIR spectra not shown here revealed that, contrary to the findings in Ref. [54], annealing in N_2 instead of Ar makes no difference to the film nanostructure.

Films M and S exhibit clear Si Raman peaks while none are observed for film C, confirming that film C is stoichiometric. After subtraction of a flat background and of the SiC contribution estimated from the SiC volume fraction and the signal of film C, the Raman signals of films M and S are deconvolved into contributions from different phonon modes [57,58]. Nanocrystalline Si (*nc*-Si) exhibits a transverse optical (TO) phonon mode at 500–520 cm^{-1}, while the band centered at 490 cm^{-1} arises from a longitudinal optical (LO) mode in *a*-Si [59,60]. The crystallinity $X_{c,\mathrm{Si}}$ of Si in the films can be calculated from the integrals of these TO and LO peaks (shaded black and red, respectively) and the amorphous-to-crystalline cross section [56] and is given in Table I. These values are a lower limit on the proportion of Si nanoclusters that are crystalline since NCs can also have an amorphous shell which contributes to the *a*-Si peaks even

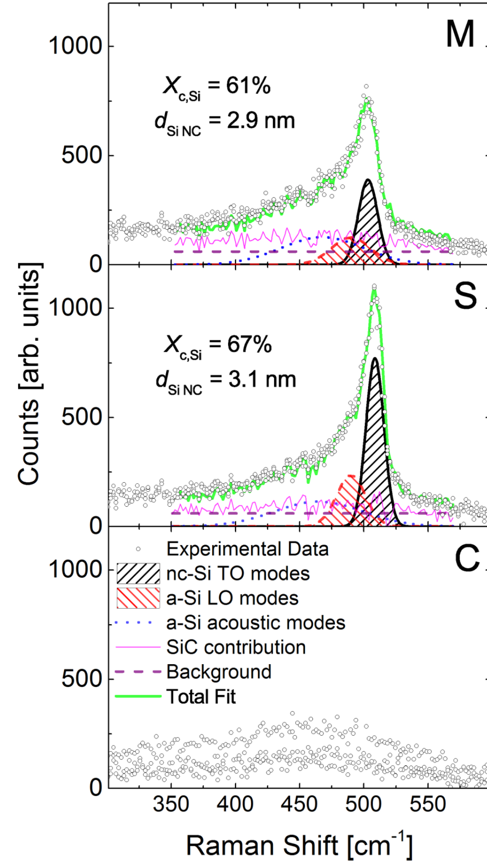

FIG. 1. (Color online) Raman spectra of films M, S, and C. Si NCs are present in films M and S. The NC sizes estimated from the full width at half maximum (FWHM) of the *nc*-Si TO peak [55], as well as the crystallinity of Si calculated from the ratio of *nc*-Si TO band (shaded black) and *a*-Si LO band (shaded red) and the amorphous-to-crystalline cross section according to Ref. [56], are shown in the figure as well as in Table I.

though the cluster itself is crystalline [61]. The majority of the excess Si in films M and S is thus present in the form of nanocrystals.

Assuming complete phase separation of Si and SiC in films M and S [49], the total volume fraction of elemental, or excess, silicon V_{Si} is 0.35–0.40 for both films. This is greater than the

TABLE I. Excess Si volume fraction V_{Si}, Si crystallinity $X_{c,\mathrm{Si}}$, and Si NC size $d_{\mathrm{Si\,NC}}$ in the films. V_{Si} is an upper bound since full demixing is assumed. $X_{c,\mathrm{Si}}$ and $d_{\mathrm{Si\,NC}}$ were determined from the Raman spectra in Fig. 1.

Film	V_{Si}	$X_{c,\mathrm{Si}}$	$d_{\mathrm{Si\,NC}}$ (nm)
M	0.35 (0.69[a])	0.61	≈3
S	0.4	0.67	≈3
C	0	—	—

[a]Refers to the Si-rich sublayers only.

3D percolation threshold for spheres of 0.29 [62]. Provided the multilayer structure of film M survives the anneal, conduction in film M may proceed exclusively via the Si-rich sublayers where $V_{\mathrm{Si}} = 0.69$. This exceeds the relevant 2D percolation threshold of 0.45, obtained by multiplying the percolation threshold for disks in 2D (≈0.676) [63] by the ratio of the volumes of a sphere and the smallest cylinder it fits into (⅔) to account for the nominally spherical shape of Si NCs.

The FWHM of the Si TO mode gives an estimate for the mean Si NC size $d_{\mathrm{Si\ NC}}$ of ≈3 nm for both films [55]. This is in agreement with the GIXRD results of an annealing series of thicker M and S films carried out previously. FTIR and UV-vis-NIR spectra not shown here indicate that the RHPT had no effect on the sample nanostructure: The quantity of hydrogen incorporated is insufficient to produce measurable infrared absorption by Si-H bonds or hydrogen-related band gap broadening. Film parameters are summarized in Table I.

B. Conductivity

The electrical properties of films M, S, and C annealed under Ar are summarized in Fig. 2. The IV curves of all films were Ohmic, as shown for the 45-min-RHPT film C in Fig. 2(b). By plotting the measured resistance as a function of contact spacing [Fig. 2(c)], the sheet resistance of the film can be calculated from the slope of this plot. The Ohmic conductivities of all films are shown in Fig. 2(a).

The conductivities of all as-prepared films are very similar, with values of (2–6) × 10^{-5} S cm^{-1}. However, a RHPT step vastly increases the conductivities of the films containing Si NCs. The conductivity of film S increases by three orders of magnitude, reaching values above 0.01 S cm^{-1} and placing it in the same conductivity range as bulk Si. Tsunoda *et al.* found that pulsed-laser-crystallized Si could be made five orders of magnitude more conductive by treating with an oxygen plasma [64]; this was attributed to a reduction in dangling bond density and the same effect is suspected here. Film M also becomes orders of magnitude more conductive but does not reach the same conductivity as film S, while film C, which contains no Si NCs, exhibits only a slight increase in conductivity. The lower conductivity of the hydrogenated film M as compared to film S is unlikely to be directly related to its nanostructure since $V_{\mathrm{Si}}, X_{c,\mathrm{Si}}$, and $d_{\mathrm{Si\ NC}}$ are similar, and V_{Si} is in fact higher if only the Si-rich sublayers are considered. Rather, the multilayer structure may impede the in-diffusion of hydrogen during the RHPT step which would reduce the associated improvement in conductivity.

C. Role of hydrogenation

Hydrogen can passivate shallow states that act as dopants as well as deep states near midgap that act as traps for free carriers. It can also break open and hydrogenate weak Si-Si bonds [43]. In order to investigate the role of hydrogen in more detail, ESR measurements were performed on as-prepared and 45-min-RHPT films S [Fig. 3(a)] and C [Fig. 3(b)]. Samples

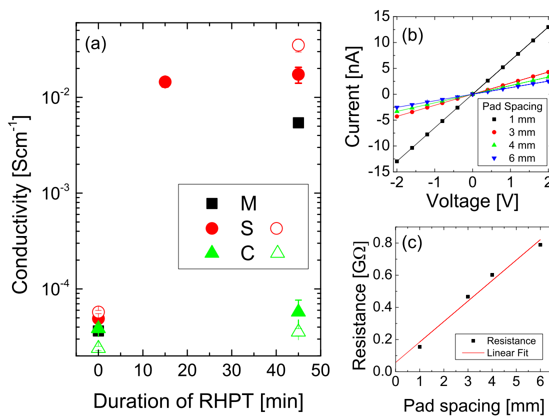

FIG. 2. (Color online) (a) Conductivity of films M, S, and C annealed under Ar as a function of RHPT time. Full and open symbols represent films from two different, nominally identical batches. The IV curves of all samples are Ohmic, as can be seen in (b) where the IV curves of the 45-min-RHPT film C are plotted as an example. This allows the extraction of the resistance, and plotting the resistance as a function of contact (pad) spacing in (c) allows the sheet resistance to be extracted via a linear fit [48].

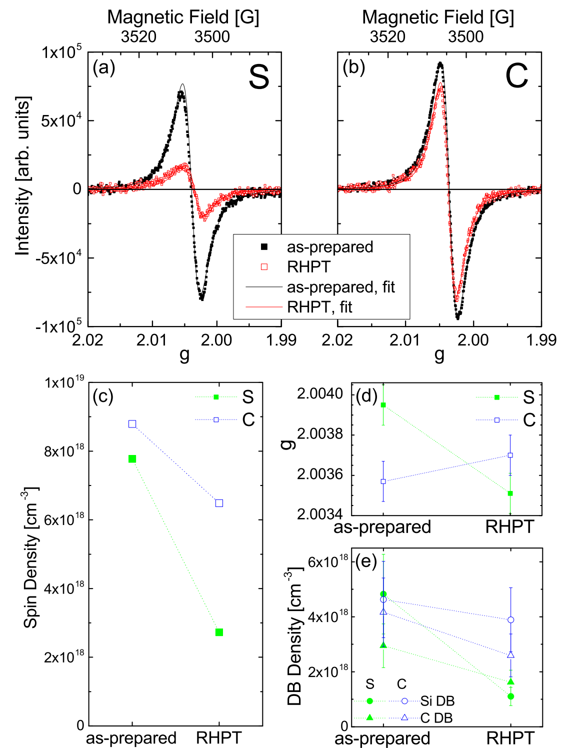

FIG. 3. (Color online) Differential ESR spectra of S (a) and C (b) films before and after 45-min RHPT. The top axis is a magnetic field axis for the as-prepared films [65]. Each spectrum is fitted with a single Lorentzian peak, and excellent fits are obtained. The associated spin density (c) and g factor (d) are shown. Using the model from Ref. [66] the g factor is used to determine the ratio of Si to C dangling bonds, from which the densities of Si and C dangling bonds for each sample are calculated (e). Lines in (c), (d), and (e) are guides to the eye.

from the batch denoted by full symbols in Fig. 2(a) were used. A clear signal is obtained during measurements at room temperature, which must be related to relatively deep states as shallow states are usually ionized at room temperature. Spin densities and g factors are given in Figs. 3(c) and 3(d), respectively. Random errors of the g factor are shown, while the systematic error in spin density quantification is estimated to be $\leq 20\%$. Spin densities of almost 10^{19} cm^{-3} are present in as-prepared films, which is very similar to the dangling bond density in Si NCs synthesized directly by PECVD [67]. A 45-min RHP treatment is successful in reducing their density 3 times for film S but only leads to a reduction by 1.4 times for film C.

The ESR signals are well-fitted by a single Lorentzian peak with a g factor between 2.0035 and 2.0040 and a linewidth between 4.1 and 5.1 G for all films, suggesting that a single trap state is responsible for the signal. However, no single defect with such a g factor was clearly identified in the literature: Si and C vacancies in SiC have $g = 2.000$–2.003 [68], a-Si and a-SiC contain defects with $g = 2.0055$ and $g = 2.003$, respectively [69], PECVD-deposited nanocrystalline SiC exhibits an ESR peak at $g = 2.0065$ that is attributed to neutral Si dangling bonds [70], and a SiC/SiO$_2$ interface state has $g = 2.00478$ [71]. Nevertheless, an ESR peak with $g = 2.004$ [46,72] and a linewidth of 5.6 G [72] has been reported in annealed a-Si$_{1-x}$C$_x$:H films.

Due to the high density of grain boundaries, and the presence of residual a-Si and a-SiC, films S and C are expected to have a high density of dangling bonds (DBs), which ought to lead to separate ESR signals from Si DBs and C DBs. However, an ESR study of sputtered a-Si$_{1\text{-}x}$C$_x$, where x was varied from 0 to 1, showed that instead of separate Si DB and C DB peaks a single symmetrical resonance is observed whose g factor decreases with x, from $g = 2.0057$ for a-Si to $g = 2.0028$ for a-C [73]. A linewidth of 5.1 G was observed for $x = 0.5$ [73]. The authors of that study developed a model to explain the mixing of Si DB and C DB contributions which takes the following form [66]:

$$g(x,r) = \sum_{n=0}^{12} \left[\frac{(1\text{-}x)\overline{g_{Si}}(n) + rx\overline{g_C}(n)}{(1\text{-}x) + rx} C_n^{12} x^n (1\text{-}x)^{12-n} \right], \quad (1)$$

where $g(x,r)$ is the g factor measured experimentally, x is the carbon content, r is the ratio of the probabilities of formation of C DBs and Si DBs (equal to the ratio of the concentration of C DBs to Si DBs for $x = 0.5$), and $\overline{g_i}(n)$ is the calculated g factor for a DB on atom i that is surrounded by n C atoms and (12-n) Si atoms. At any n, $\overline{g_{Si}}(n) > \overline{g_C}(n)$, which means that a decrease in g generally indicates an increase in the proportion of C DBs.

While this model was developed for a-Si$_{1\text{-}x}$C$_x$, it is reasonable to apply it to our results because the trap states are most likely to be present in the residual a-Si and a-SiC domains as well as at grain boundaries which can be considered to be amorphous, because the experimental g factors lie in the range for which Eq. (1) was developed, and because the linewidths we observe are in good agreement with Ref. [73]. With x known for both films r can be determined by fitting Eq. (1) to the measured g factor for each sample [assuming $r \neq r(n)$]. The concentrations $N_{i\text{-DB}}$ of dangling bonds on atom i can then be calculated from the total spin density N_{DB}:

$$N_{\text{Si-DB}} = \frac{(1-x)}{(1-x)+rx} N_{\text{DB}}, \quad (2)$$

$$N_{\text{C-DB}} = \frac{rx}{(1-x)+rx} N_{\text{DB}}. \quad (3)$$

Both quantities are plotted in Fig. 3(e) for films S and C.

$N_{\text{C-DB}}$ is slightly higher for film C than film S, most probably due to the higher carbon content, but decreases by the same ratio upon hydrogenation in both films. $N_{\text{Si-DB}}$ is similar in both as-prepared films, suggesting that film S contains fewer DBs per Si atom than film C, perhaps because Si NCs have fewer DBs than the Si atoms in nanocrystalline SiC. Furthermore, $N_{\text{Si-DB}}$ decreases much more strongly in film S than film C upon hydrogenation. This could be either due to faster hydrogen diffusion in film S, which is plausible as hydrogen diffuses faster in Si than SiC and the nominal V_{Si} exceeds the percolation threshold, or because Si DBs on Si NCs capture a hydrogen atom more readily than those in the SiC. The latter can be explained in terms of fast diffusion within a given Si NC or in terms of a lower energy barrier for the hydrogenation reaction due to the lower stiffness and more open crystal structure of Si as compared to SiC. $N_{\text{Si-DB}}$ in film S after hydrogenation is only 0.3 times that in film C, which is less than the SiC volume fraction in S films (1-V_{Si}). This suggests that all Si DBs in Si NCs or at their surfaces are passivated and that the remaining Si DBs in film S are contained in the SiC matrix.

It is worth noting that this analysis only applies to neutral DBs which contain a single electron (D^0). DBs can capture a hole or an electron, leaving them positively (D$^+$) or negatively (D$^-$) charged, respectively [43]. The charged DBs are not detected by ESR because they have no unpaired electrons, and it is the charged DBs that are more likely to affect the dark conductivity studied here because they affect the free carrier concentration by having captured a carrier and the mobility of free carriers by Coulomb scattering. The question is thus whether the reduction in D^0 that can be measured is associated with an equivalent reduction in D$^+$ and/or D$^-$. When hydrogen reacts with D^0 DBs to form Si-H or C-H bonds the concentration of D^0 is reduced and there is a driving force for detrapping of carriers from charged DBs to reestablish equilibrium among D$^+$, D^0, and D$^-$ [43]. The activation energy for detrapping is E_F-E_D, where E_F is the Fermi level and E_D the defect level. E_D is typically at midgap, while E_F must lie within the band gap which Tauc plots indicate is <2.0 eV for films M, C, and S. The activation energy is therefore <1.0 eV. That for hydrogen diffusion in similar films to ours has been found to be 0.8 eV [74]. It is therefore reasonable to assume that the reequilibration of DB charge states is at least as rapid as the passivation of neutral DBs by hydrogen (which requires, in addition to the 0.8 eV for diffusion, additional energy to drive the hydrogenation reaction), which means a reduction in D^0 is associated with an equivalent reduction in D$^+$ and/ or D$^-$.

ESR therefore shows that remote plasma hydrogenation decreases the dangling bond density, particularly on Si NCs,

and that this is likely to be responsible for the increase in conductivity due to carrier detrapping and/or due to the elimination of scattering centers. However, there is no direct equivalence between the decrease in spin density and the increase in mobile carrier concentration because the density of DBs that actually trap carriers, D^- and D^+, is unknown.

D. Conduction mechanism

Conduction in nanocrystalline SiC films containing Si NCs could be controlled by a range of factors. In this section the following types of transport will be considered: direct tunneling among Si NCs, grain-boundary-controlled transport, surface-controlled transport, transport via bulk defects, transport via extended conduction and valence bands, and transport in disordered semiconductors.

1. Direct tunneling

Direct tunneling of carriers between Si NCs is expected when the NCs are embedded in an insulating matrix that cannot itself conduct a current, and has been observed for Si NCs embedded in SiO_2 [13]. However, in Sec. III B it was observed that the SiC matrix not only conducts a current, but does so just as well with as without NCs before hydrogenation. Furthermore, tunneling between NCs typically leads to an exponential dependence of current on applied voltage [12,13,15,19] while Ohmic behavior is observed here, and would be expected to be independent of temperature, whereas a strong temperature dependence of the conductivity is observed in Fig. 5. There is therefore no evidence for transport via direct tunneling between Si NCs.

2. Grain boundary effects

Since the size of Si and SiC nanocrystals is below 5 nm there is an extremely high concentration of grain boundaries. Grain boundaries contain a higher concentration of defects than the grains themselves, leading to greater charge carrier trapping at grain boundaries than within the grains. It is known from work on polycrystalline semiconductors that this leads to band bending at grain boundaries which impedes transport; such a conduction mechanism has been proposed for polycrystalline Si with a grain size of 25 μm [75] as well as for nanocrystalline SiC with a grain size of 0.1 μm [76,77] and leads to a nonlinear dependence of current on voltage because the applied voltage lowers the transport barriers at grain boundaries [78]. In our samples, Ohmic behavior is observed, which is clearly at odds with this model. The reason is that even though there are many grain boundaries in the films which doubtless contain many defects, the crystals are much smaller than the width of the depletion region associated with carrier trapping at grain boundaries. The trapping of carriers at grain boundary defects does not therefore lead to band bending, but pins the Fermi level E_F across adjacent grains [13]. This makes it impossible to distinguish between trapping by grain boundary defects and bulk defects in these films. It should be pointed out that it is only potential barriers due to band bending that cannot exist in these films. Potential barriers due to differences in electron affinity or band gap are still present. These potential barriers are abrupt steps only 1–2 monolayers wide, even in nanostructures with feature sizes of 1–2 nm [79].

3. Surface and interface effects

Next we consider the role of the film surface and film/substrate interface. To better understand how these affect transport, a separate experiment was conducted where 40- and 80-nm-thick films C were prepared on two different oxidized Si wafers. Annealing, formation of ITO contacts, and IV measurements were performed as for films M, S, and C. Figure 4 shows the sheet conductance of the films as a function of film thickness. Conductance increases with increasing film thickness so transport along the film surface or interface, which would be independent of film thickness, can be ruled out. This applies both to conduction through surface or interface states as well as conduction through a conductive channel induced by band bending at the surface or interface, as observed for *a*-Si in Ref. [80].

Band bending at surfaces and interfaces can also repel charge carriers, restricting the part of the film in which conduction takes place. In extreme cases this leads to a very low carrier concentration in the films and a conduction mechanism where conduction is limited by the space charge in the film. Space-charge-limited current has been observed in silicon nanocrystal films [41,53], albeit due to complete depletion of free carriers by *bulk* defects [53]. Several models exist for space-charge-limited current flow but all have a power-law dependence on voltage or contact spacing or both. Neither effect has been observed here, so this conduction mechanism is discounted.

Nevertheless, the finite abscissa intercept of ≈30 nm in Fig. 4 suggests that ≈30 nm of each film carries no current. This could be due to a different nanostructure in the near-interface or near-surface part of the film or due to surface and interface depletion regions totaling ≈30 nm. This nonconductive proportion of the film is not expected to be higher for the films M, S, and C studied previously as all those samples are more conductive, suggesting they have a higher free carrier concentration leading to reduced depletion regions. This means the conductivities in Fig. 2(a) are correct to within a factor ≤2 and arise from a bulk transport process.

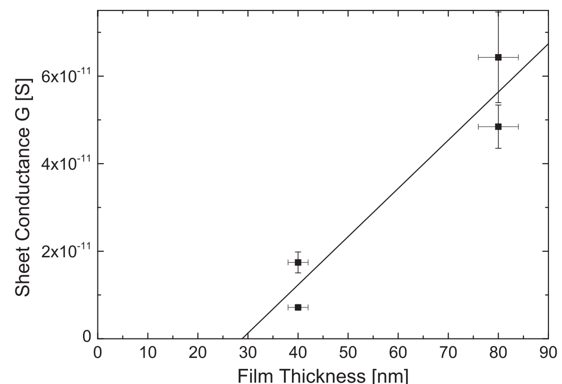

FIG. 4. Sheet conductance of C films as a function of thickness. The line is a linear fit to the data.

4. Bulk conduction mechanism

To gain a better understanding of the bulk transport process(es) responsible for conduction in films M, S, and C, Hall measurements and temperature-dependent IV measurements were carried out. Unfortunately no meaningful Hall voltages were measured. From the limitations of the measurement a lower bound on carrier concentration of $10^{16}\,\mathrm{cm}^{-3}$ and an upper bound on majority carrier mobility of 10 $\mathrm{cm}^2\,\mathrm{V}^{-1}\,\mathrm{s}^{-1}$ can be estimated for hydrogenated S films. A study on nominally undoped nanocrystalline SiC with a grain size of $\leq$100 nm found a mobility μ and free carrier concentration n of 1 $\mathrm{cm}^2\,\mathrm{V}^{-1}\,\mathrm{s}^{-1}$ and 2.5×10^{19} cm^{-3}, respectively [37]. Due to the larger grain size in that material as compared to films M, S, and C it is likely that $\mu < 1$ $\mathrm{cm}^2\,\mathrm{V}^{-1}\,\mathrm{s}^{-1}$ for our films, resulting in $n > 3 \times 10^{17}\,\mathrm{cm}^{-3}$ for hydrogenated S films. Hot probe measurements on hydrogenated S films showed that the films are n type. Films with conductivities $<$0.01 $\mathrm{S\,cm}^{-1}$ did not yield a measurable hot probe signal but there is no evident reason why these films should have a different majority carrier type.

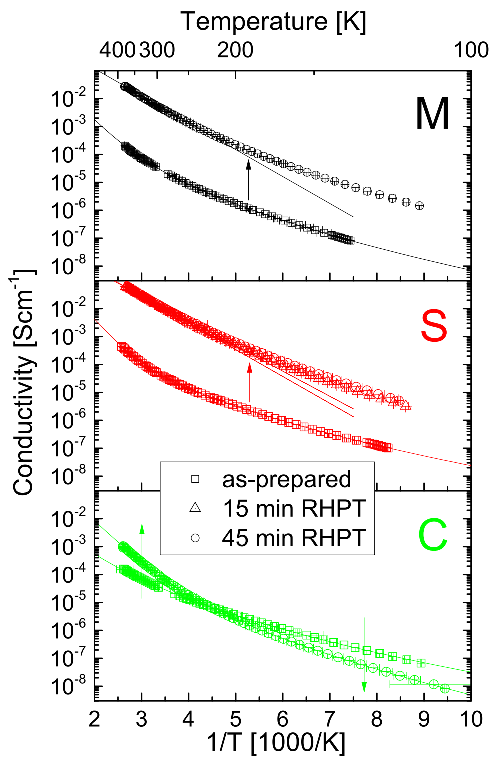

FIG. 5. (Color online) Arrhenius plots of the conductivity of the M, S, and C films denoted by full symbols in Fig. 2(a). Colors denote the different films in analogy to Fig. 2(a) while the different symbols denote the hydrogenation time and arrows indicate the trend with hydrogenation. Error bars are given but most are smaller than the symbols used. Fits of the mechanisms discussed in the text are shown as lines. Except for hydrogenated M and S films, they coincide perfectly with the data. Fit parameters are given in Table II.

Temperature-dependent IV measurements showed that conduction is Ohmic in the temperature range 100–400 K in all films. The Arrhenius plots for the films denoted by full symbols in Fig. 2(a) are given in Fig. 5. The Arrhenius plots of all films have rather similar forms, suggesting that similar conduction mechanisms are active in all films. At the same time, all Arrhenius plots are curved, indicating that transport is not adequately described by a single process with a well-defined activation energy at all temperatures. This is particularly clear from the curves of film C, where hydrogenation has opposite effects on conductivity at high and low temperature.

Thermally activated transport implies the existence of transport barriers that can be overcome by thermal excitation. Thermal activation of carriers from dopant states to the conduction band is improbable because the high-temperature Arrhenius slopes of films with and without Si NCs change in an opposite manner upon hydrogenation, and it is not apparent why hydrogenation should change the position of the dopant level, never mind why the direction of the change should depend on Si NCs. Band bending was already ruled out as a transport barrier, and band offsets between Si NCs and SiC can also be ruled out because the Arrhenius curves of films M and S are not systematically steeper than those of film C, as one would expect in the case of an additional activation energy.

It appears unusual that this should be so since there is necessarily a difference in band gap between Si NCs and SiC which implies band offsets. Two possibilities exist: either transport in films with Si NCs is through a percolating network of Si NCs, or the conduction band offset between Si and SiC is negligible. The resulting band structures are shown in Figs. 6(a) and 6(b), respectively. The literature is divided on this issue [81]—some studies suggest that the band-gap difference between Si NCs and SiC is divided between conduction and valence band offsets in a ratio of roughly 1:2 [33,82,83] while others argue that since the electron affinities of the two phases appear to be very similar (4.05 eV for Si [84], 4.0 eV for *3C*-SiC [85], and 4.1 eV for *a*-SiC [35]), the conduction band offset ought to be very small [86–88]. From a nanostructure viewpoint, transport in a percolating Si

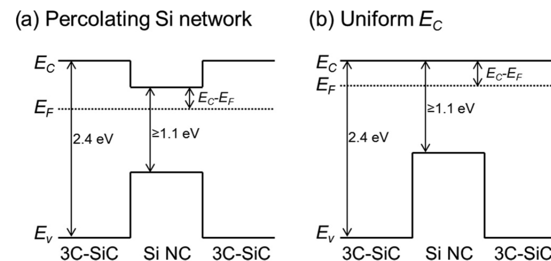

FIG. 6. Band diagram for Si NCs embedded in SiC assuming transport through a Si network (a) or in a conduction band that is uniform throughout the film (b). The structure in (a) is only possible in the case of transport in a Si network because the data do not support thermal activation of carriers from the conduction band of Si to *3C*-SiC. The distribution of Si levels due to the Si NC size distribution, tail states, and deep levels present in amorphous and grain boundary material are omitted for clarity.

network is possible since, as discussed in Sec. III A, V_{Si} of films M and S exceeds the percolation threshold.

In either case, transport occurs in a largely uniform conduction band, which, together with the small grain size, means the films can be legitimately described as disordered semiconductors, albeit with slightly more delocalized states in the nanocrystals than in fully amorphous material. Disordered semiconductors have a finite density of states in much of the band gap [43]. The most general form of electron conductivity $\sigma(T)$ is given by

$$\sigma(T) = q\int_{E_F}^{\infty} n(E,T)\mu(E,T)dE = q\int_{E_F}^{\infty} N(E)\mu(E,T)\exp\left[-\left(\frac{E\text{-}E_F}{kT}\right)\right]dE, \quad (4)$$

where $N(E)$ is the density of states per unit volume and energy, q is the elementary charge, and k is the Boltzmann constant. When $E > E_C$, where E_C is the conduction band edge, this becomes simply

$$\sigma_{\mathrm{ext}}(T) = \sigma_0 \exp\left[-\left(\frac{E_C\text{-}E_F}{kT}\right)\right], \quad (5)$$

where $\sigma_0 = qN(E_c)\mu_{\mathrm{ext}}kT$ because $N(E_C)$ and μ_{ext} are to a first approximation independent of energy and temperature. This is extended-state transport of electrons excited from the Fermi level, at which $N(E)$ and hence $n(E)$ is finite.

For $E < E_C$, hopping transport can occur in localized states. Here $\sigma(T)$ depends on E_F and the form of $N(E)$. If the $N(E)$ available for hopping is narrow compared to kT, or far away from E_F, hopping is also characterized by a well-defined activation energy [42]. If the $N(E)$ available for hopping is at or near E_F and is broad with respect to kT, as we might expect for the band tails of the residual amorphous phase in the films, or the conduction band levels of isolated nanocrystals of different sizes, higher energy states available for hopping do not participate in conduction at low temperature [42]. The conductivity of the sample then becomes a question of the size of the percolating network of low-energy states that can still conduct, for which it was found, given $N(E) \propto (E\text{-}E_F)^s$, that

$$\sigma_{\mathrm{VRH}}(T) = \sigma_{00} \exp\left[-\left(\frac{T_0}{T}\right)^{\frac{s+1}{s+4}}\right], \quad (6)$$

where σ_{00} and T_0 are fitting parameters [89]. Two particular cases are frequently found in the literature: $s = 0$ and $s = 2$. The former corresponds to a uniform $N(E)$ and is known as Mott variable-range hopping (VRH) [42], although it was recently shown by Godet [90,91] that the same behavior $\{\ln[\sigma(T)] \propto T^{-1/4}\}$ is to be expected for $N(E) \propto \exp[(E\text{-}E_F)/E_t]$, where E_t is a fitting parameter, albeit with a different dependence of σ_{00} on T_0. The $s = 2$ case corresponds to hopping in a parabolic $N(E)$ which arises when the Coulomb gap becomes relevant [92], is known as Efros-Shklovskii VRH, and has recently been suggested to describe hopping in an array of nanocrystals in which there is a distribution of conduction band levels due to randomly distributed ionized donors [93].

It is clear from the curved plots in Fig. 5 that Eq. (5) alone cannot describe the data. Equation (6) cannot describe any curve with $s = 2$ but can describe that of the as-prepared film C, and hydrogenated films M and S, with $s = 0$, that is, $\ln[\sigma(T)] \propto T^{-1/4}$. The associated VRH mechanism is plausible for film C but unrealistic for hydrogenated films M and S, which reach conductivities above 0.1 S cm^{-1} (hopping mobilities are typically < 0.01 cm^2 V^{-1} s^{-1} [90,94–96] which would imply $>6 \times 10^{19}$ cm^{-3} hopping electrons, an incredibly high concentration for nominally undoped material). The remaining films are well-fitted by a combination of Eq. (5) for the high-temperature data and Eq. (6) with $s = 0$ for the low-temperature data.

The following is therefore proposed: In as-prepared stoichiometric SiC, transport proceeds by VRH with $s = 0$. This is in agreement with findings on sputtered [97] and irradiated [98] *a*-SiC. Upon hydrogenation, the dangling bond density decreases (as shown in Sec. III C), leading to the detrapping of carriers and an increase in E_F to the point where σ_{ext} is no longer negligible compared to σ_{VRH} and takes over at high temperatures. This also applies to as-prepared films with Si NCs (films M, S), in agreement with the findings of Myong *et al.* for boron-doped nanocrystalline Si-SiC alloys deposited directly by PECVD [99,100]. In Sec. III C as-prepared films M and S did not contain fewer dangling bonds than C so the observation of extended-state conduction in as-prepared M and S films supports the thesis of extended-state transport in a percolating Si NC network at $E_{C,\mathrm{Si}} < E_{C,\mathrm{SiC}}$ [see Fig. 6(a)]. Upon hydrogenation, E_F increases, lowering $E_C\text{-}E_F$ and explaining the decrease in the Arrhenius slope of M and S at high temperatures. Unfortunately, the curvature of the plots of hydrogenated M and S films is too weak to reliably fit a second, low-temperature conduction mechanism so this is not done here, but the presence of a hopping mechanism is reasonable.

It should be noted that it is also possible to fit all curves with two Arrhenius terms, or with a combination of Eq. (5) and Eq. (6) where $s = 2$. However, in both cases $E_C\text{-}E_F$ for film C is then found to increase by 30–70 meV upon hydrogenation, which appears unreasonable. The fits described above [Eq. 6 for the as-prepared film C, Eq. (5) and Eq. (6) for the hydrogenated film C and as-prepared films M and S, and Eq. (5) for hydrogenated films M and S] are shown as lines in Fig. 5 and the fit parameters for both batches of M, S, and C films are listed in Table II.

Hydrogenation leads to a decrease of $E_C\text{-}E_F$ from 0.33–0.38 eV to 0.16–0.19 eV for the films with excess Si, with consistent results obtained across the two batches. The prefactor σ_0 hardly changes upon hydrogenation, indicating that hydrogenation has not had a significant effect on extended-state mobility. The prefactor is in the range 4–26 S cm^{-1} for all but one sample, in good agreement with the theoretical value for *a*-Si:H of 40 S cm^{-1} [43]. By comparing $E_C\text{-}E_F$ for all hydrogenated films, it is seen that $E_C\text{-}E_F$ is lower for the films with Si NCs. It is this difference which causes the over 100 times greater conductivity in these films as σ_0 does not change as strongly. This lends credence to the band structure in Fig. 6(a), where $E_C\text{-}E_F$ is indeed lower for Si NCs than SiC. The fact that the as-prepared samples all exhibited similar conductivity in Fig. 2(a) is not in disagreement with Fig. 6(a) because Fig. 2(a) shows room-temperature conductivities which are dominated by VRH for all as-prepared samples.

TABLE II. Parameters of fits of Eq. (5) and Eq. (6) to the temperature-dependent IV data of M, S, and C films.

Film	RHPT time (min)	Batch[a]	E_C-E_F (eV)[b]	σ_0(S cm^{-1})	T_0 (K)[c]	σ_{00}(S cm^{-1})	$N(E_F)$ (cm^{-3} eV^{-1})[d]
M	0	1	0.35	3.6 ± 0.5	1.4×10^8	$(5.9 \pm 0.5) \times 10^6$	2.6×10^{19}
	45	1	0.19	10 ± 1	—	—	—
S	0	1	0.38	26 ± 3	0.9×10^8	$(6.1 \pm 0.2) \times 10^5$	4.0×10^{19}
		2	0.33	5 ± 0.3	1.3×10^8	$(4.6 \pm 0.1) \times 10^6$	2.8×10^{19}
	15	1	0.19	22 ± 0.5	—	—	—
	45	1	0.18	14 ± 0.6	—	—	—
		2	0.16	14 ± 0.3	—	—	—
C	0	1	—	—	0.7×10^8	$(2 \pm 0.1) \times 10^5$	4.8×10^{19}
		2	—	—	1.4×10^8	$(3 \pm 0.8) \times 10^6$	2.6×10^{19}
	45	1	0.32	9.8 ± 0.6	2.3×10^8	$(3 \pm 0.6) \times 10^8$	1.6×10^{19}
		2	0.27	0.4 ± 0.04	2.3×10^8	$(1.7 \pm 0.3) \times 10^8$	1.5×10^{19}

[a]Batches 1 and 2 were nominally identical and are represented by full and open symbols, respectively, in Fig. 2. Figure 5 shows Arrhenius plots of Batch 1.
[b]The fitting errors are smaller than the last significant digit shown. The actual error is estimated to be ±0.02 eV.
[c]The fitting errors are smaller than the last significant digit shown.
[d]Calculated using Eq. (7) and assuming $\gamma^{-1} = 1$ nm.

In all samples where VRH was found to occur T_0 was in the range (0.7–2.3) $\times 10^8$ K. A positive correlation exists between T_0 and σ_{00} for these samples, which is in agreement with Godet's model of hopping in an exponential $N(E)$ but in disagreement with Mott's model [91]. Therefore Godet's equation

$$N(E_F)\gamma^{-3} = 310/kT_0, \tag{7}$$

where γ^{-1} is the decay length of the electronic wave function typically taken to be 0.3–3 nm [42,43,91], is applied and yields values of $N(E_F)$ given in Table II assuming $\gamma^{-1} = 1$ nm. Equation 7 is valid for hopping between weakly localized states where $10^{-5} \leqslant N(E_F)\gamma^{-3} \leqslant 1$ [42,43,91], which is fulfilled by the data. $N(E_F) = (1.5\text{–}5) \times 10^{19}$ cm^{-3} eV^{-1} for all films. The trends in $N(E_F)$ across films and as a function of hydrogenation are well-correlated with the spin densities measured in Sec. III C. This is unexpected: as the spin density decreases, E_F is raised, and since $N(E)$ typically increases with E, an increase in $N(E_F)$ is expected. The data do not provide a solution to this conundrum but either a nonmonotonically increasing $N(E)$, or a coincidental correlation of $N(E_F)$ with N_{DB}, may be postulated. A direct measurement of $N(E)$ fed into Eq. (4) might provide a more conclusive picture. It is also not clear whether the hopping states are located in a particular phase or at grain boundaries as the grain size is on the order of the hopping distance. However, the similarity in $N(E_F)$ for films with and without Si NCs, and the similarity of room-temperature conductivities of as-prepared films where VRH dominates, indicates that Si NCs are not the main source of hopping sites.

In summary, the data show that conduction is thermally activated, Ohmic at all temperatures, n type, due to a bulk rather than a grain boundary, surface, or interface mechanism, and follows disordered semiconductor behavior. Transport at low temperatures is via hopping, most probably via variable-range hopping in tail states, while extended-state transport takes over at higher temperatures. The transition between the two mechanisms occurs at lower temperatures in films with Si NCs or upon hydrogenation. The Fermi level is <0.4 eV from E_C in all samples where E_C-E_F could be extracted and rises upon hydrogenation. All other fitting parameters are in good agreement with literature values.

E. Background dopant

In the previous section it had been noted that films are n type and that assuming realistic values of mobility, free carrier concentrations in excess of 10^{17} cm^{-3} must be present in the hydrogenated S films. No intentional doping was carried out so the carriers must originate from background doping, which can arise either from point defects that create shallow donor levels or from dopant atoms accidentally incorporated into the films. It is known from growth of SiC [101] and PECVD growth of μc-Si [34] that nitrogen and oxygen, respectively, are easily incorporated. Nitrogen is an excellent n-type dopant with an ionization energy of 50 meV in $3C$-SiC [101] and nanocrystalline SiC with a grain size of ≈0.1 μm [37,76], and given the band diagrams in Fig. 6, electrons donated in the SiC can migrate to Si NCs [102,103]. Oxygen also acts as an n-type dopant in μc-Si [34] and SiC [37,104,105], and oxygen and nitrogen both dope a-Si:H [106].

Hydrogenated S films that had been annealed in argon and nitrogen did not show significantly different conductivities. However, SIMS analysis of both samples and an as-deposited film showed that nitrogen is already incorporated at concentrations of 10^{19}–10^{20} cm^{-3} during deposition. These are essentially unchanged after annealing, except for slight effusion of near-surface nitrogen when annealing under argon.

It was found that the source of nitrogen is residue from the nitrous gases NF_3 and N_2O that are used to etch back SiC parasitically deposited on the PECVD chamber walls at regular intervals before flakes form. Such cleaning processes are unavoidable in PECVD reactors, and it had been found previously that opening and mechanically cleaning the reactor leads to films with even higher nitrogen content (≈10^{21} cm^{-3}). Figure 7 shows the nitrogen content, and conductivity of hydrogenated films S, as a function of the total SiC thickness deposited since the last etchback step. The data points at 1 and 18 μm therein correspond to batches denoted by open and full

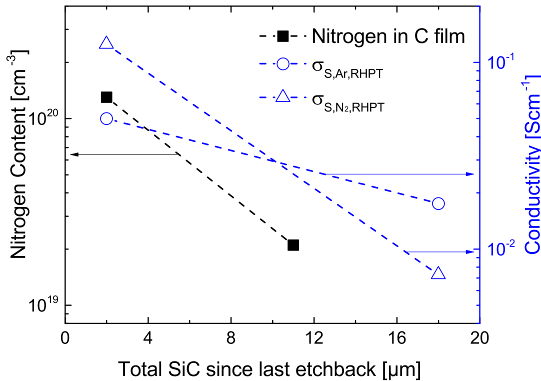

FIG. 7. (Color online) Nitrogen content of a film C and conductivity of hydrogenated films S annealed in Ar or N_2 as a function of the total SiC thickness deposited in the PECVD reactor since the last etchback step (see text). Lines are guides to the eye.

symbols in Fig. 2(a), respectively. The figure indicates that film conductivity is strongly correlated with nitrogen content, which implies that doping due to intrinsic point defects is negligible.

However, as the nitrogen is provided by the etchback process, the other elements present in the process gases—oxygen and fluorine—may also be incorporated into the films. Fluorine is not known to act as an effective dopant in Si [107] or SiC [101] and no evidence that it passivates defects [107] or etches the films during deposition [101] was found. However, oxygen is known to act as a donor, and in one C film deposited directly after etchback was found to be present at similar concentrations as nitrogen.

An estimation of the doping level from SIMS measurements is difficult since it is not known what sites oxygen and nitrogen occupy within the films, but an upper limit can be found by assuming full incorporation of dopants onto sites in crystalline Si or SiC with the lowest ionization energy. Films deposited directly after etchback contain $\approx 10^{20}$ cm^{-3} nitrogen and $\leqslant 10^{21}$ cm^{-3} oxygen according to SIMS. Oxygen has a solubility limit $< 10^{18}$ cm^{-3} in Si [107] and an activation energy of ≈ 0.2 eV in 3C-SiC [105] leading to $\lesssim 10^{18}$ cm^{-3} electrons from oxygen donors. Nitrogen in turn is essentially insoluble in Si [107] but highly soluble and fully activated at room temperature in 3C-SiC [101]. From these considerations an upper limit on doping level of $\approx 10^{20}$ cm^{-3} is given by the nitrogen concentration. This is not an upper limit on free carrier concentration, but an upper limit on the total carrier concentration that is distributed among deep levels, tail states, and the conduction band(s) according to Fermi statistics. It was noted previously that the free carrier concentration in hydrogenated S films had to exceed 10^{17} cm^{-3} if reasonable values of mobility are assumed. Since hydrogenation is unlikely to introduce new dopant atoms, or to move them to different sites in the material, these $\geqslant 10^{17}$ cm^{-3} carriers must have been present in as-prepared films too, albeit distributed differently among deep levels, tail states, and the conduction band(s). Furthermore, it is reasonable to assume that the doping level (not the free carrier concentration) is similar for films with and without Si NCs as background doping occurs during deposition of the amorphous precursors which differ only slightly in plasma chemistry.

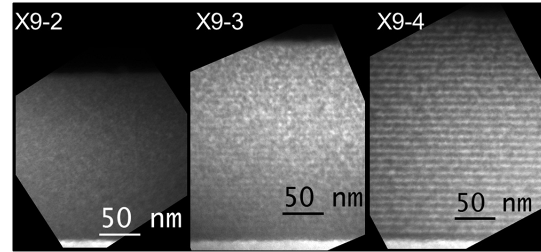

FIG. 8. Energy-filtered transmission electron micrographs of annealed multilayers with $Si_{0.85}C_{0.15}$ thicknesses of 2, 3, and 4 nm. Electrons were filtered around the Si plasmon peak at 17.3 eV so bright contrast represents Si. All images are scaled to the same magnification and show the Si substrate at the bottom (bright contrast) and the film surface at the top (dark).

Nanocrystalline SiC with and without Si NCs thus behaves as an n-type amorphous semiconductor with an estimated doping level of 10^{17} cm^{-3}–10^{20} cm^{-3} from background doping by nitrogen and oxygen.

IV. DIFFERENT Si NC ARRAYS IN NANOCRYSTALLINE SiC

Having examined the role of Si NCs, annealing ambient, background dopants, and hydrogenation on the conductivity of nanocrystalline SiC, this section extends the analysis to different Si NC arrays in SiC. Conductivity and conduction mechanisms are again examined with respect to the sample nanostructure and interpreted with respect to the findings in Sec. III. It will be shown that conduction in the samples studied in Secs. III and IV can be explained with the same conductivity model even though the two batches of samples exhibit different nanostructures and were processed in different laboratories.

A. Nanostructure

Samples X9-2, -3, and -4 are multilayers, and therefore comparable to film M from Sec. III, but with a greater Si excess in the silicon-rich layers ($Si_{0.85}C_{0.15}$) and silicon-rich layer thicknesses of 2, 3, and 4 nm (instead of 6 nm for film M) [49]. EFTEM images of the annealed multilayers are shown in Fig. 8.

It can be seen that the resulting nanostructure varies significantly across samples. In sample X9-2 there is no clear separation of Si and SiC in the sample upon annealing, and no traces of the originally deposited multilayer structure are visible. In sample X9-3 the multilayer structure survives the anneal to some extent, and X9-4 shows a clear multilayer structure. High-resolution TEM (HRTEM) images not shown here confirm that silicon clusters in X9-3 and X9-4 have indeed crystallized, and EFTEM images give mean NC diameters $d_{\mathrm{Si\,NC}}$ of 4.7 and 5.0 nm, respectively. A close inspection of EFTEM images of X9-4 confirms that the Si NCs have not merged into a uniform c-Si sheet, though many Si NCs may be touching [49].

TABLE III. Excess Si volume fraction V_{Si}, Si crystallinity $X_{c,\text{Si}}$, and Si NC size $d_{\text{Si NC}}$ in the films, as well as the derived quantity $V_{c\text{-Si}} = V_{\text{Si}} X_{c,\text{Si}}$ (c-Si volume fraction). V_{Si} is an upper bound since full demixing is assumed. $X_{c,\text{Si}}$ was determined by Raman spectroscopy and $d_{\text{Si NC}}$ was evaluated from EFTEM images.

Film	V_{Si}	$X_{c,\text{Si}}$	$V_{c\text{-Si}}$	$d_{\text{Si NC}}$ (nm)
X9-2	0.23	0.09	0.02	—
X9-3	0.31 (0.82[a])	0.41	0.13 (0.34[a])	4.7 ± 0.3
X9-4	0.36 (0.82[a])	0.60	0.22 (0.49[a])	5.0 ± 1.0
X9-B	0	—	—	—

[a]Refers to the Si-rich sublayers only.

As in Sec. III A, the Si crystallinity $X_{c,\text{Si}}$ was determined by Raman spectroscopy [49] and the excess Si volume fraction V_{Si} calculated from the deposition parameters. Sample details are summarized in Table III, which also lists the volume fraction of nanocrystalline Si, $V_{c\text{-Si}} = V_{\text{Si}} X_{c,\text{Si}}$. $X_{c,\text{Si}}$ varies from 0.09 to 0.6, which means that the excess Si cannot, as for films M and S, be assumed to be present primarily in the form of Si NCs in all films; a-Si nanoclusters are also present. In X9-3 and X9-4, V_{Si} exceeds the 3D percolation threshold for spheres of 0.29 [62], while $V_{c\text{-Si}}$ does not. Since the multilayer structure is preserved to some extent in both films, the formation of a separate percolating network in each Si-rich sublayer is also conceivable. As mentioned in Sec. III A the relevant 2D percolation threshold is 0.45, which is exceeded by V_{Si} in both samples and by $V_{c\text{-Si}}$ in X9-4.

GIXRD and spectrophotometry confirm these trends in Si crystallization, and x-ray reflectivity confirms the survival of the multilayer structure across the entire area of sample X9-4 [49]. Varying the $Si_{0.85}C_{0.15}$ thickness has not lead to a variation in $d_{\text{Si NC}}$, as one might expect, but to a variation in $X_{c,\text{Si}}$. GIXRD and FTIR show that, as with the samples in Sec. III, the SiC matrix has also crystallized, with a Scherrer grain size of 3.4 ± 0.5 nm in X9-2, -3, and -4 and 4.6 ± 0.4 nm in X9-B. The samples are therefore classified as nanocrystalline SiC (X9-B), a disordered Si-SiC alloy (X9-2), isolated and loosely ordered Si nanoclusters embedded in SiC (X9-3), and a superlattice of size-controlled and possibly touching Si NCs (X9-4).

B. Conduction mechanism

All samples exhibited Ohmic behavior between -2 V and +2 V. They were measured independently by three different institutes involved in preparing this article, and measurements agreed to within experimental error. The results are shown in Fig. 9.

The as-prepared samples have conductivities on the order of 10^{-5} S cm^{-1} and samples with thicker $Si_{0.85}C_{0.15}$ layers show higher overall conductivities. Thicker $Si_{0.85}C_{0.15}$ layers are associated with higher V_{Si} and $X_{c,\text{Si}}$ and better nanocluster ordering. X9-4 is about 4 times more conductive than X9-B, which is significantly different to as-prepared films M and S, which are only 20% more conductive than film C. The X9 samples with thicker $Si_{0.85}C_{0.15}$ layers also exhibit lower contact resistances.

The samples were then subjected to a forming gas anneal followed by a remote hydrogen plasma treatment. A forming

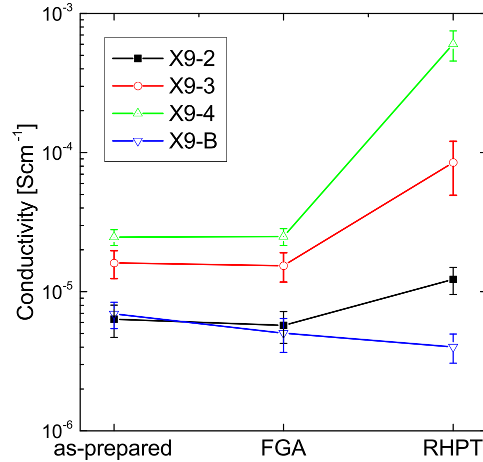

FIG. 9. (Color online) Conductivity of samples X9-2, -3, -4, and -B as a function of postmetallization hydrogen treatment. A forming gas anneal (FGA) has little effect, while a remote hydrogen plasma treatment (RHPT) step significantly increases the conductivity of multilayers. Lines are guides to the eye.

gas anneal (FGA) had no effect on conductivity, whereas RHPT greatly increased the conductivity of X9-2, -3, and -4 and decreased that of X9-B. This shows that merely annealing at 425–450°C or supplying molecular hydrogen is insufficient to passivate defects in the films. Atomic hydrogen, which is provided by the RHP treatment but not by FGA, is required. This agrees with prior studies that found that while molecular hydrogen can passivate Si NCs in SiO_2 [108], it has little effect in nanocrystalline SiC because the $3C$-SiC lattice has much smaller interstices which hinders in-diffusion of H_2 molecules [36]. The conductivity of X9-B decreases slightly, which is reproducible across several batches. This is the opposite of what was observed for film C from Sec. III at room temperature, but since the Arrhenius curves of the as-prepared and RHPT C film intersect around 220 K the most likely explanation is that a slight difference in the properties of X9-B as compared to C has shifted the intersection to above room temperature.

Thus far, we have observed that films X9-2, -3, and -4 are, like films M and S, significantly more conductive after RHPT. However, it has also been shown that the as-prepared samples X9-2, -3, and -4 differ much more significantly in their conductivity than M and S do. Temperature-dependent IV measurements were carried out to determine whether this is due to a fundamentally different conduction mechanism and are shown in Fig. 10.

As in the case of films M and S, Ohmic conduction is observed at all temperatures, the Arrhenius plots are curved, and conductivity increases with hydrogenation at all temperatures. This suggests that the same conduction mechanisms are active. There are, however, significant differences: Whereas for films M and S the high-temperature slope decreased upon hydrogenation, it increases for films X9-2, -3, and -4, as was also observed for film C. Furthermore, the low-temperature slope decreases significantly for all films, which was not

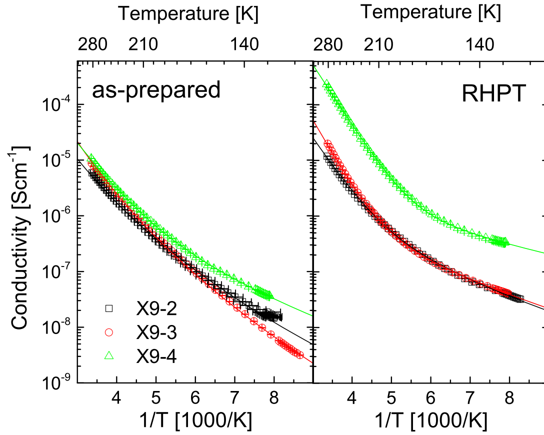

FIG. 10. (Color online) Arrhenius plots of the conductivity of as-prepared (left) and hydrogenated (right) samples X9-2, -3, and -4. Error bars are given but most are smaller than the symbols used. All plots are curved, indicating that a single conduction process with a well-defined activation energy is insufficient to describe the data. Fits of the mechanisms discussed in the text are shown as lines and coincide perfectly with the data. Fit parameters are given in Table IV.

observed for films M, S, or C. In analogy to films M, S, and C the data were successfully fitted by a combination of Eq. (5) and Eq. (6) with $s = 0$ [or Eq. (6) only in the case of the as-prepared X9-2 and -3 samples]. As for M, S, and C, two Arrhenius terms, or a combination of Eq. (5) and Eq. (6) where $s = 2$, also yield good fits to the data but are not applied as they yielded unrealistic fit parameters for M, S, and C. The fits of Eq. (5) and Eq. (6) with $s = 0$ are shown in Fig. 10 and fit parameters given in Table IV.

The increase in the high-temperature slope of the Arrhenius plot of X9-2 and X9-3 is, as for film C, found to be due to σ_{ext} only becoming significant after hydrogenation. X9-4 is the only one of the X9 samples where extended-state transport occurs in the as-prepared film, suggesting that V_{Si} well above the percolation threshold may be a criterion for extended-state transport in as-prepared films. However, this particular result should not be overinterpreted since E_C-E_F of X9-4 increases slightly with hydrogenation, rather than decreasing, which is unreasonable. What is worth highlighting is that E_C-E_F is the same to within experimental error for all the *hydrogenated* X9 multilayers, while σ_0 increases strongly with V_{Si} (or $X_{c,\text{Si}}$). This is in stark contrast to the effect of hydrogenation on films M and S, which increased conductivity by decreasing E_C-E_F, with little effect on σ_0. It appears therefore that the main effect of an RHP treatment is to increase the free carrier concentration and hence raise E_F, whereas the main effect of increasing V_{Si} (or $X_{c,\text{Si}}$) is to increase the extended-state mobility μ_{ext}, hence increasing σ_0. The latter supports the band structure in Fig. 6(a) since μ_{ext} is unlikely to be particularly sensitive to V_{Si} if Fig. 6(b) is correct. The idea of a high-mobility Si network within the band alignment of Fig. 6(b) is not credible because the Si nanoclusters are too small for a Si channel unaffected by scattering centers in the SiC to exist.

Given, then, that extended-state transport occurs in a Si network, the question arises as to whether the entire network of excess Si conducts or whether merely crystalline domains do. Several authors have reported a negligible conduction band offset between Si NCs and *a*-Si [109,110], suggesting that both cases are possible. Several factors make conduction through a network of the entire Si excess more probable: First, of all the samples examined in Secs. III and IV, $V_{c\text{-Si}}$ only exceeds the percolation threshold in the Si-rich sublayers of X9-4, and yet hydrogenated films M and S exhibit very high conductivities through their Si networks. Second, within the X9 batch the activation energy does not depend on $X_{c,\text{Si}}$. If conduction was through $V_{c\text{-Si}}$ only, one would either expect *a*-Si nanoclusters to present a thermally surmountable barrier to transport, in which case the activation energy would be affected, or one would expect them to block current flow completely, in which case it becomes difficult to explain why X9-2, where $V_{c\text{-Si}} = 0.02$, exhibits significantly higher room-temperature conductivity than X9-B after hydrogenation. Extended-state transport therefore appears to proceed through a V_{Si}, not a $V_{c\text{-Si}}$ network.

The X9 data that cannot be described by extended-state transport—that from the as-prepared X9-2 and -3 films, and the low-temperature data of all the other films—is well-fitted by the same Godet VRH mechanism applied in Sec. III D4 (in fact, the correlation between σ_{00} and T_0 is exactly the same), and $N(E_F)$ is again calculated using Eq. (7) and tabulated in Table IV. It can be seen that the decrease in low-temperature slope on hydrogenation (see Fig. 10) is reflected in T_0 and $N(E_F)$; the latter increases by an order of magnitude upon hydrogenation in all X9 films. This is in agreement with hydrogenation raising E_F closer to E_C, where $N(E)$ is increased and σ_{ext} becomes relevant at higher temperatures.

TABLE IV. Parameters of fits of Eq. (5) and Eq. (6) to the data in Fig. 10.

Film	RHPT time (min)	E_C-E_F (eV)[a]	σ_0(S cm^{-1})	$T_0(K)$[b]	σ_{00}(S cm^{-1})	$N(E_F)$ (cm^{-3} eV^{-1})[c]
X9-2	0	—	—	1.2×10^8	$(4 \pm 1) \times 10^5$	0.31×10^{20}
	45	0.21	0.04 ± 0.005	$(2.3 \pm 0.2) \times 10^7$	37 ± 13	$(1.6 \pm 0.2) \times 10^{20}$
X9-3	0	—	—	2.8×10^8	$(2.5 \pm 0.5) \times 10^8$	0.13×10^{20}
	45	0.25	0.28 ± 0.03	1.8×10^7	11 ± 2	2.0×10^{20}
X9-4	0	0.19	0.01 ± 0.001	$(4.1 \pm 0.3) \times 10^7$	$(8 \pm 4) \times 10^2$	$(0.87 \pm 0.06) \times 10^{20}$
	45	0.22	1 ± 0.1	$(4.4 \pm 0.6) \times 10^6$	0.3 ± 0.1	$(8 \pm 1) \times 10^{20}$

[a]The fitting errors are smaller than the last significant digit shown. The actual error is estimated to be ± 0.02 eV.
[b]Where no error is given the fitting error is smaller than the last significant digit shown.
[c]Calculated using Eq. (7) and assuming $\gamma^{-1} = 1$ nm.

Similarly, that $N(E_F)$ for hydrogenated X9-2, -3, and -4 films is up to an order of magnitude larger than for as-prepared films M, S, and C is reasonable since E_C-E_F is lower. It should be noted that the higher E_F may also lead to greater γ^{-1}, decreasing $N(E_F)$ and reducing the discrepancy in $N(E_F)$ between samples from Secs. III and IV.

The values of E_C-E_F extracted for X9 films suggest that these films are also unintentionally doped. To determine whether the background doping in X9 films differs from that in films M, S, and C the nitrogen content of an X9-B film was studied by SIMS. Rather than a homogeneous nitrogen level being present throughout the film there is a high concentration at the surface that decays to zero within 50 nm of the film surface. It is rather unlikely that such a nitrogen profile is produced during deposition; most probably nitrogen diffuses in from the surface during annealing. The effect of nitrogen on the electrical conductivity of these films can thus be examined by annealing the same films under Ar and N_2. New X9-3 films annealed in N_2 and Ar exhibited the same conductivity before and after hydrogenation within experimental error, and a similar experiment with X9-B films showed no significant effect of annealing ambient on conductivity either. Nitrogen doping can therefore be ruled out in these films. On the other hand, it is known from the preparation of microcrystalline silicon films in the same reactor that oxygen is incorporated as a background dopant, and it is reasonable to conclude that oxygen is the dominant dopant in the X9 films studied here as well.

In summary, transport in X9 films is also well-described by amorphous semiconductor models, and plasma hydrogenation increases conductivity at all temperatures by passivating dangling bonds, freeing trapped carriers, and raising E_F such that extended-state transport becomes more dominant. Extended-state mobility increases strongly with V_{Si}, supporting the model of extended-state transport taking place in a Si network. In contrast to M, S, and C, the raised E_F is also reflected in a greater $N(E)$ available for Godet VRH at lower temperatures.

V. CONCLUSION

Electrical transport in nanocrystalline SiC films containing different Si NC arrays prepared in two different laboratories has been studied in depth. All samples exhibit temperature-dependent Ohmic conduction at all temperatures that improves upon treatment in a hydrogen plasma. Molecular hydrogen has no effect but atomic hydrogen successfully passivates dangling bonds. The concentration of dangling bonds in SiC is reduced and dangling bonds in or on Si NCs appear to have been fully eliminated. The room-temperature conductivity of nanocrystalline SiC is only weakly affected, but films with Si NCs become up to 1000 times more conductive and conductivities as high as 0.1 S cm^{-1} can be obtained.

Through a comprehensive review of plausible conduction mechanisms, direct tunneling between Si NCs, transport limited by band bending at grain boundaries, and surface- and interface-dominated conduction have been ruled out. Curved Arrhenius plots show that the bulk mechanism by which electrical transport takes place is extended-state transport at high temperatures and hopping at low temperatures. Trends in E_C-E_F with hydrogenation and with film type indicate that the band structure in Fig 6(a), which shows a finite conduction band offset between Si nanoclusters and SiC, is correct, and that extended-state transport in films with Si nanoclusters proceeds via a network of Si nanoclusters. For multilayer films it may proceed via networks located in the Si-rich sublayers. The extended-state mobility within these networks appears to be controlled primarily by V_{Si} while hydrogenation mainly affects the Fermi level and hence the free carrier concentration. When no excess Si is present, carriers must be activated to the conduction band of SiC, which involves a greater activation energy.

The most plausible hopping mechanism is a variable-range hopping mechanism in tail states as proposed by Godet [90,91]. It was not possible to determine whether the hopping sites are localized in a particular phase or exclusively at grain boundaries as the grain size is on the order of typical hopping length scales, but the relative insensitivity of the hopping parameters to the presence of excess Si suggests that hopping can occur through the entire film volume in all films. The films are *n* type and reasonable assumptions on dopant activation indicate a carrier concentration in the 10^{17} to 10^{20} cm^{-3} range. This is not a free carrier concentration but a carrier concentration that populates deep levels, tail states, and extended states; however, reasonable assumptions on extended-state mobility also indicate $>10^{17}$ cm^{-3} *free* carriers in the most conductive films with Si NCs. This high doping level is related to background doping by oxygen and nitrogen.

The clear and rigorous elucidation of the conduction mechanism for Si NCs in SiC in this study will aid further development of electrical devices based on this material system. In particular, the similarity to amorphous semiconductors which are well-understood, and the relative robustness of the electronic properties with respect to the ordering of Si NCs (in comparison particularly to Si NCs in SiO_2, where transport is strongly dependent on minute differences in Si NC spacing), as well as the high conductivities of up to 0.1 S cm^{-1} that have been attained, are promising for future applications.

ACKNOWLEDGMENTS

The authors thank Michele Bellettato, Manuel Moser, Antonio Leimenstoll, Felix Schätzle, Nicolas König, Harald Steidl, and Benjamin Manrique for help with sample processing; Matthias Breitwieser for Raman measurements; and the accelerator group of the HZDR Ion Beam Center for providing the He ion beam for RBS analysis. The research leading to these results has received funding from the European Community's Seventh Framework Programme (FP7/2007-2013) under Grant No. 245977 under the project title NASCEnT and from the Spanish government under projects Consolider Imagine (CSD2009-2013) and MAT2010-16407.

[1] P. D. J. Calcott, K. J. Nash, L. T. Canham, M. J. Kane, and D. Brumhead, J. Phys.: Condens. Matter **5**, L91 (1993).
[2] L. T. Canham, Appl. Phys. Lett. **57**, 1046 (1990).
[3] B. Garrido, M. Lopez, O. Gonzalez, A. Perez-Rodriguez, J. R. Morante, and C. Bonafos, Appl. Phys. Lett. **77**, 3143 (2000).

[4] L. Pavesi, L. Dal Negro, C. Mazzoleni, G. Franzo, and F. Priolo, Nature **408**, 440 (2000).
[5] M. Zacharias, J. Heitmann, R. Scholz, U. Kahler, M. Schmidt, and J. Bläsing, Appl. Phys. Lett. **80**, 661 (2002).
[6] L. V. Dao, X. Wen, M. T. T. Do, P. Hannaford, E.-C. Cho, Y. H. Cho, and Y. Huang, J. Appl. Phys. **97**, 013501 (2005).
[7] M. Dovrat, Y. Goshen, J. Jedrzejewski, I. Balberg, and A. Sa'ar, Phys. Rev. B **69**, 155311 (2004).
[8] S. Godefroo, M. Hayne, M. Jivanescu, A. Stesmans, M. Zacharias, O. I. Lebedev, G. Van Tendeloo, and V. V. Moshchalkov, Nat Nanotechnol. **3**, 174 (2008).
[9] J. Heitmann, F. Müller, M. Zacharias, and U. Gösele, Adv. Mater. **17**, 795 (2005).
[10] D. Timmerman, I. Izeddin, P. Stallinga, I. N. Yassievich, and T. Gregorkiewicz, Nat. Photon **2**, 105 (2008).
[11] D. Timmerman, J. Valenta, K. Dohnalova, W. D. A. M. de Boer, and T. Gregorkiewicz, Nat. Nano **6**, 710 (2011).
[12] S. Gutsch, J. Laube, A. M. Hartel, D. Hiller, N. Zakharov, P. Werner, and M. Zacharias, J. Appl. Phys. **113**, 133703 (2013).
[13] I. Balberg, J. Appl. Phys. **110**, 061301 (2011).
[14] R. A. Puglisi, C. Vecchio, S. Lombardo, S. Lorenti, and M. C. Camalleri, J. Appl. Phys. **108**, 023701 (2010).
[15] W. Hu, M. Igarashi, M.-Y. Lee, Y. Li, and S. Samukawa, Nanotechnology **24**, 265401 (2013).
[16] C.-W. Jiang and M. A. Green, J. Appl. Phys. **99**, 114902 (2006).
[17] P. Löper, R. Müller, D. Hiller, T. Barthel, E. Malguth, S. Janz, J. C. Goldschmidt, M. Hermle, and M. Zacharias, Phys. Rev. B **84**, 195317 (2011).
[18] M. Igarashi, M. F. Budiman, W. Pan, W. Hu, Y. Tamura, M. E. Syazwan, N. Usami, and S. Samukawa, Nanotechnology **24**, 015301 (2013).
[19] M. Igarashi, W. Hu, M. M. Rahman, N. Usami, and S. Samukawa, Nanoscale Res. Lett. **8**, 228 (2013).
[20] D. K. Basa and F. W. Smith, Thin Solid Films **192**, 121 (1990).
[21] R. Gradmann, P. Loeper, M. Künle, M. Rothfelder, S. Janz, M. Hermle, and S. Glunz, Phys. Status Solidi C **8**, 831 (2011).
[22] M. Künle, S. Janz, O. Eibl, C. Berthold, V. Presser, and K.-G. Nickel, Mater. Sci. Eng. B **159–160**, 355 (2009).
[23] Y. Kurokawa, S. Miyajima, A. Yamada, and M. Konagai, Jpn. J. Appl. Phys. **45**, L1064 (2006).
[24] D. Song, E.-C. Cho, G. Conibeer, Y.-H. Cho, and Y. Huang, J. Vac. Sci. Technol. B **25**, 1327 (2007).
[25] G. Wen, X. Zeng, W. Liao, and C. Cao, Thin Solid Films **552**, 18 (2014).
[26] M. Künle, S. Janz, K. G. Nickel, A. Heidt, M. Luysberg, and O. Eibl, Solar Energ. Mater. Solar Cell. **115**, 11 (2013).
[27] Y. Kurokawa, S. Tomita, S. Miyajima, A. Yamada, and M. Konagai, in *Proceedings of the 22nd European Photovoltaic Solar Energy Conference, Milan, Italy, 2007* (Wirtschaft und Infrastruktur GmbH & Co, Germany, 2007), p. 233.
[28] Y. Kurokawa, S. Tomita, S. Miyajima, A. Yamada, and M. Konagai, in *Proceedings of the 33rd IEEE Photovoltaic Specialists Conference* (IEEE, San Diego, CA, USA, 2008), p. 1.
[29] D. Song, E.-C. Cho, G. Conibeer, Y. Huang, C. Flynn, and M. A. Green, J. Appl. Phys. **103**, 083544 (2008).
[30] C. Summonte *et al.*, Mater. Sci. Eng. B **178**, 551 (2013).
[31] C. Summonte, A. Desalvo, M. Canino, M. Allegrezza, M. Rosa, M. Ferri, E. Centurioni, A. Terrasi, and S. Mirabella, in *Proceedings of the 25th European Photovoltaic Solar Energy Conference and Exhibition, Valencia, Spain, 2010* (Wirtschaft und Infrastruktur GmbH & Co, Germany, 2010), p. 662.
[32] Y. Wang, J. Lin, C. H. A. Huan, Z. C. Feng, and S. J. Chua, Thin Solid Films **384**, 173 (2001).
[33] Y. Rui, S. Li, J. Xu, C. Song, X. Jiang, W. Li, K. Chen, Q. Wang, and Y. Zuo, J. Appl. Phys. **110**, 064322 (2011).
[34] P. Torres *et al.*, Appl. Phys. Lett. **69**, 1373 (1996).
[35] L. Magafas, N. Georgoulas, and A. Thanailakis, Semicond. Sci. Technol. **7**, 1363 (1992).
[36] K. Ding *et al.*, J. Non-Cryst. Solids **358**, 2145 (2012).
[37] M. Eickhoff, H. Moller, J. Stoemenos, S. Zappe, G. Kroetz, and M. Stutzmann, J. Appl. Phys. **95**, 7908 (2004).
[38] Y. Kurokawa, S. Yamada, S. Miyajima, A. Yamada, and M. Konagai, Current Applied Physics **10**, S435 (2010).
[39] S. Yamada, Y. Kurokawa, S. Miyajima, A. Yamada, and M. Konagai, in *Proceedings of the 35th IEEE Photovoltaic Specialists Conference, Honolulu, Hawaii, USA, 2010* (IEEE, Piscataway, 2010), p. 766.
[40] Y. Kurokawa, S. Tomita, S. Miyajima, A. Yamada, and M. Konagai, in *Proceedings of the 24th European Photovoltaic Solar Energy Conference, Hamburg, Germany, 2009* (Wirtschaft und Infrastruktur GmbH & Co, Germany, 2009), p. 398.
[41] D. Song, E.-C. Cho, G. Conibeer, Y. Huang, and M. A. Green, Appl. Phys. Lett. **91**, 123510 (2007).
[42] N. F. Mott and E. A. Davis, *Electronic Processes in Non-Crystalline Materials* (Clarendon Press, Oxford, UK, 1979).
[43] R. A. Street, *Hydrogenated Amorphous Silicon* (Cambridge University Press, Cambridge, UK, 2005).
[44] M. Mayer, AIP Conf. Proc. **475**, 541 (1999).
[45] S. Lindekugel, H. Lautenschlager, T. Ruof, and S. Reber, in *Proceedings of the 23rd European Photovoltaic Solar Energy Conference, Valencia, Spain, 2008* (Wirtschaft und Infrastruktur GmbH & Co, Germany, 2008), p. 2232.
[46] S. Yamada, Y. Kurokawa, S. Miyajima, and M. Konagai, Nanoscale Res. Lett. **9**, 1 (2014).
[47] L. J. van der Pauw, Philips Res. Rep. **13**, 1 (1958).
[48] H. H. Berger, J. Electrochem. Soc. **119**, 507 (1972).
[49] C. Summonte *et al.*, Solar Energ. Mater. Solar Cell. **128**, 138 (2014).
[50] F. D. Heinz, W. Warta, and M. C. Schubert, Energy Procedia **27**, 208 (2012).
[51] E. Centurioni, Appl. Opt. **44**, 7532 (2005).
[52] P. Scherrer, Nachr. Ges. Wiss. Goettingen, Math. Phys. Kl. **1918**, 98 (1918).
[53] H. W. Lau, O. K. Tan, and D. A. Trigg, Appl. Phys. Lett. **89**, 113119 (2006).
[54] G.-r. Chang, F. Ma, D.-y. Ma, and K.-w. Xu, Nanotechnology **21**, 465605 (2010).
[55] C. Ossadnik, S. Veprek, and I. Gregora, Thin Solid Films **337**, 148 (1999).
[56] E. Bustarret, M. A. Hachicha, and M. Brunel, Appl. Phys. Lett. **52**, 1675 (1988).
[57] S. Hernández, J. López-Vidrier, L. López-Conesa, D. Hiller, S. Gutsch, J. Ibáñez, S. Estradé, F. Peiró, M. Zacharias, and B. Garrido, J. Appl. Phys. **115**, 203504 (2014).
[58] R. Tubino, L. Piseri, and G. Zerbi, J. Chem. Phys. **56**, 1022 (1972).

[59] S. Hernández, A. Martínez, P. Pellegrino, Y. Lebour, B. Garrido, E. Jordana, and J. M. Fedeli, J. Appl. Phys. **104**, 044304 (2008).
[60] V. Paillard, P. Puech, M. A. Laguna, R. Carles, B. Kohn, and F. Huisken, J. Appl. Phys. **86**, 1921 (1999).
[61] F. Iacona, C. Bongiorno, C. Spinella, S. Boninelli, and F. Priolo, J. Appl. Phys. **95**, 3723 (2004).
[62] C. D. Lorenz and R. M. Ziff, J. Chem. Phys. **114**, 3659 (2001).
[63] J. A. Quintanilla and R. M. Ziff, Phys. Rev. E **76**, 051115 (2007).
[64] Y. Tsunoda, T. Sameshima, and S. Higashi, Jpn. J. Appl. Phys. 1 **39**, 1656 (2000).
[65] The magnetic field axis for the passivated films differs slightly due to slight differences in the microwave frequency during measurements of the different samples.
[66] N. Ishii, M. Kumeda, and T. Shimizu, Solid State Commun. **41**, 143 (1982).
[67] R. Lechner, A. R. Stegner, R. N. Pereira, R. Dietmueller, M. S. Brandt, A. Ebbers, M. Trocha, H. Wiggers, and M. Stutzmann, J. Appl. Phys. **104**, 053701 (2008).
[68] H. Itoh, A. Kawasuso, T. Ohshima, M. Yoshikawa, I. Nashiyama, S. Tanigawa, S. Misawa, H. Okumura, and S. Yoshida, Phys. Status Solidi A **162**, 173 (1997).
[69] M. H. Brodsky and R. S. Title, Phys. Rev. Lett. **23**, 581 (1969).
[70] O. Chevaleevski, S. Y. Myong, S. Miyajima, M. Konagai, and K. S. Lim, in *Proceedings of the 3rd World Conference on Photovoltaic Energy Conversion, Osaka, Japan, 2003*, Vol. 2 (IEEE, Piscataway, 2003), pp. 1859–1862.
[71] V. V. Afanas´ev, A. Stesmans, M. Bassler, G. Pensl, M. J. Schulz, and C. I. Harris, Appl. Phys. Lett. **68**, 2141 (1996).
[72] K. Ding, U. Aeberhard, W. Beyer, O. Astakhov, F. Köhler, U. Breuer, F. Finger, R. Carius, and U. Rau, Phys. Status Solidi A **209**, 1960 (2012).
[73] T. Shimizu, M. Kumeda, and Y. Kiriyama, Solid State Commun. **37**, 699 (1981).
[74] S. Yamada, Y. Kurokawa, S. Miyajima, and M. Konagai, Nanoscale Res. Lett. **9**, 72 (2014).
[75] C. H. Seager and T. G. Castner, J. Appl. Phys. **49**, 3879 (1978).
[76] W. Hellmich, G. Müller, G. Krötz, G. Derst, and S. Kalbitzer, Appl. Phys. A **61**, 193 (1995).
[77] W. Hellmich, G. Müller, G. Krötz, G. Derst, and S. Kalbitzer, Mater. Sci. Eng. B **29**, 147 (1995).
[78] G. Blatter and F. Greuter, Phys. Rev. B **33**, 3952 (1986).
[79] Y.-M. Niquet and C. Delerue, Phys. Rev. B **84**, 075478 (2011).
[80] I. Solomon, T. Dietl, and D. Kaplan, J. Phys. (France) **39**, 1241 (1978).
[81] C. W. Liu and J. C. Sturm, J. Appl. Phys. **82**, 4558 (1997).
[82] G. Conibeer *et al.*, Thin Solid Films **511–512**, 654 (2006).
[83] J. D. Hwang, Y. K. Fang, K. H. Chen, and D. N. Yaung, IEEE Electron Device Lett. **16**, 193 (1995).
[84] S. M. Sze, *Physics of Semiconductor Devices* (John Wiley & Sons, New York, 1981).
[85] M. J. Bozack, Phys. Status Solidi B **202**, 549 (1997).
[86] M. I. Chaudhry, IEEE Electron Device Lett. **12**, 670 (1991).
[87] L. F. Marsal, I. Martin, J. Pallarès, A. Orpella, and R. Alcubilla, J. Appl. Phys. **94**, 2622 (2003).
[88] J. Pelletier, D. Gervais, and C. Pomot, J. Appl. Phys. **55**, 994 (1984).
[89] M. Pollak, J. Non-Cryst. Solids **11**, 1 (1972).
[90] C. Godet, Philos. Mag. B **81**, 205 (2001).
[91] C. Godet, J. Non-Cryst. Solids **299–302**, 333 (2002).
[92] A. L. Efros and B. I. Shklovskii, J. Phys. C **8**, L49 (1975).
[93] B. Skinner, T. Chen, and B. I. Shklovskii, Phys. Rev. B **85**, 205316 (2012).
[94] D. J. Gibbons and W. E. Spear, J. Phys. Chem. Solids **27**, 1917 (1966).
[95] J. Hirsch, J. Phys. C **12**, 321 (1979).
[96] P. G. Le Comber and W. E. Spear, Phys. Rev. Lett. **25**, 509 (1970).
[97] K. Nair and S. S. Mitra, J. Non-Cryst. Solids **24**, 1 (1977).
[98] L. L. Snead and S. J. Zinkle, Nucl. Instrum. Methods B **191**, 497 (2002).
[99] S. Y. Myong, O. Shevaleevskiy, K. S. Lim, S. Miyajima, and M. Konagai, J. Appl. Phys. **98**, 054311 (2005).
[100] S. Y. Myong, K. S. Lim, and M. Konagai, Appl. Phys. Lett. **88**, 103120 (2006).
[101] G. L. Harris, *Properties of Silicon Carbide* (INSPEC, London, UK, 1995).
[102] D. König and J. Rudd, AIP Adv. **3**, 012109 (2013).
[103] D. König, J. Rudd, S. Shrestha, G. Conibeer, and M. A. Green, in *Proceedings of the 24th European Photovoltaic Solar Energy Conference, Hamburg, Germany, 2009* (Wirtschaft und Infrastruktur GmbH & Co, Germany, 2009), p. 575.
[104] T. Dalibor, H. Trageser, G. Pensl, T. Kimoto, H. Matsunami, D. Nizhner, O. Shigiltchoff, and W. J. Choyke, Mater. Sci. Eng. B **61–62**, 454 (1999).
[105] A. Gali, D. Heringer, P. Deak, Z. Hajnal, T. Frauenheim, R. P. Devaty, and W. J. Choyke, Phys. Rev. B **66**, 125208 (2002).
[106] A. Morimoto, M. Matsumoto, M. Yoshita, M. Kumeda, and T. Shimizu, Appl. Phys. Lett. **59**, 2130 (1991).
[107] P. Pichler, *Intrinsic Point Defects, Impurities, and Their Diffusion in Silicon* (Springer-Verlag, Berlin, 2004).
[108] D. Hiller, M. Jivanescu, A. Stesmans, and M. Zacharias, J. Appl. Phys. **107**, 084309 (2010).
[109] L. Bagolini, A. Mattoni, G. Fugallo, L. Colombo, E. Poliani, S. Sanguinetti, and E. Grilli, Phys. Rev. Lett. **104**, 176803 (2010).
[110] M. T. Lusk, R. T. Collins, Z. Nourbakhsh, and H. Akbarzadeh, Phys. Rev. B **89**, 075433 (2014).

4.2.2.2. Si NC / SiC Multilayers as Active Absorber Material for Photovoltaic Applications

The photovoltaic properties of Si NCs embedded in SiC matrix were investigated in Paper XI [157]. For this, samples containing 30× SRC/SiC bilayers with fixed t_{SiC} = 5 nm and $x = 0.85$ in $\mathrm{Si}_x\mathrm{C}_{1-x}$ (the ideal parameters for multilayer maintenance as reported in Paper VI [24]) were fabricated on Si substrate, with varying SRC layer thickness. In order to eliminate the effect of the bulk Si substrate on the optical, electro-optical and photovoltaic properties of the NC multilayers, the Si substrate was locally removed, thus obtaining a thin membrane structure. To achieve a *p*-*i*-*n* device structure, *p*-type hydrogenated amorphous Si and *n*-type hydrogenated $\mathrm{Si}_{0.95}\mathrm{C}_{0.05}$ layers were deposited at both sides of the SL stack (acting as intrinsic absorber layer), followed by ITO sputtering that served as transparent conductive oxide electrodes. A proper insulation of the surrounding substrate was performed to avoid leakage currents through our vertical structure. This work was carried out by the PhD Candidate during a scientific stage at the Fraunhofer ISE, in Freiburg (Germany).

A basic structural characterization of the membrane structure was carried out via SEM, where cross-section imaging of the membrane structures corroborated the excellent layer deposition control, being the resulting thicknesses well matched with the nominal ones. Additional optical microscopy on the top an bottom parts of the membrane structure revealed a good formation of the membrane cell area with respect to the insulated edges. Finally, LBIC mapping allowed verifying the electro-optical performance of the membrane, being the photocurrent signal mostly coming from the membrane center once illuminated with white light, whereas the non-active cell parts present negligible contribution. All the characterized devices accomplished the mentioned conditions.

The next step was the optical characterization of the membrane cells, for which reflectance and transmittance measurements were employed. From ML samples prior to device fabrication, fittings of their reflectance data were carried out to obtain the structural and optical parameters (total layer thickness, refractive index and extinction coefficient) from the different ML stacks (with $t_{\mathrm{SRC}} = 3$ and 4 nm). This allowed simulating the absorptance of the active ML stack within the membrane structure, obtaining very similar absorption for 3- and 4-nm multilayers, much larger than in the bulk SiC reference sample (i.e. a membrane cell stack containing pure SiC as intrinsic absorber layer). In addition, the generated current density (J_{gen}) was estimated under the hypothesis of complete carrier collection (i.e. IQE = 1), with values in the order of 10^{-3} A·cm^{-2} that increased with the Si content. The spectral response of the membrane cells was quantified using the Fourier-Transform photocurrent spectroscopy [171], scanning at different visible wavelengths to illuminate the active membrane areas, which demonstrated a considerably larger EQE from the 4-nm-SRC ML stack with respect to the 3-nm-SRC one. This, together with the almost constant absorption in both devices, confirmed

that conduction is playing an important role in the membrane cell response. Again, the short-circuit current density (J_{SR}) was estimated from the EQE spectra, now presenting values of 10^{-6} A·cm^{-2}, about three orders of magnitude lower than the generated current density. The collection efficiency, defined as:

$$X_{\mathrm{eff}} = \frac{J_{\mathrm{SR}}}{J_{\mathrm{gen}}} \,, \tag{4.14}$$

was found to increase at thicker SRC layers (i.e. higher Si amount), which is indicates that either the defects density decreases or carrier mobility increases with Si content.

The experimental characterization concluded with a study of the photovoltaic characteristics of the membrane cells, analysed via current density versus voltage curves in dark and under 1-Sun illumination. The obtained ratios between short-circuit current densities well fitted the predictions from SR photocurrent estimation, confirming the accuracy of photocurrent spectroscopy to obtain reliable photovoltaic parameters. Regarding the open circuit voltage (V_{oc}), lower values were found for multilayer-based membranes than for bulk Si solar cells, which suggests that no contribution of the Si substrate exists. Conversion efficiencies in the order of 10^{-3} % were obtained for NC-containing membranes, about 20 times higher than in the case of pure SiC, indicating the efficiency improvement under the presence of Si NCs. Indeed, the low measured V_{oc} and calculated efficiencies support the hypothesis of strong recombination taking place within the ML stack, which impedes the proper photogenerated charge extraction towards the electrodes.

The discussion of the paper is focused on the origin of such recombination sources. Actually, the higher X_{eff} obtained for the sample with thicker SRC layers implies that a higher fraction of carriers are photogenerated in a region where recombination is less probable. The different material regions present in the ML stack are: crystalline and amorphous Si, and crystalline and amorphous SiC. Therefore, since a larger volume fraction of crystallized Si is formed in the sample with 4-nm-SRC multilayers [24], we can deduce that carriers are mainly generated within the Si NCs. This is in agreement with the observed SR (i.e. EQE) onset at 700 nm, and sets the first reported proof of quantum confinement in Si NCs embedded in SiC matrix. Regarding the overall electro-optical conversion of the devices, those containing higher amount of crystalline Si, i.e. thicker SRC layers, will present a lower amount of recombinative regions, which will be also translated into a better photovoltaic performance.

Solar Energy Materials & Solar Cells 144 (2016) 551–558

Contents lists available at ScienceDirect

Solar Energy Materials & Solar Cells

journal homepage: www.elsevier.com/locate/solmat

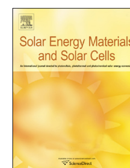

Silicon nanocrystals embedded in silicon carbide as a wide-band gap photovoltaic material

J. López-Vidrier [a,*], P. Löper [b,1], M. Schnabel [b], S. Hernández [a], M. Canino [c], C. Summonte [c], S. Janz [b], B. Garrido [a]

[a] MIND–IN2UB, Electronics Department, University of Barcelona, Martí i Franquès 1, E-08028 Barcelona, Spain
[b] Fraunhofer-Institute for Solar Energy Systems ISE, Heidenhofstr. 2, D-79110 Freiburg, Germany
[c] Consiglio Nazionale delle Ricerche—Istituto per la Microelettronica e i Microsistemi (CNR-IMM), via Gobetti 101, 40129 Bologna, Italy

ARTICLE INFO

Article history:
Received 13 July 2015
Received in revised form
30 September 2015
Accepted 6 October 2015

ABSTRACT

The optical and photovoltaic properties of Si NCs/SiC multilayers (MLs) are investigated using a membrane-based solar cell structure. By removing the Si substrate in the active cell area, the MLs are studied without any bulk Si substrate contribution. The occurrence is confirmed by scanning electron microscopy and light-beam induced current mapping. Optical characterization combined with simulations allows us to determine the absorption within the ML absorber layer, isolated from the other cell stack layers. The results indicate that the absorption at wavelengths longer than 800 nm is only due to the SiC matrix. The measured short-circuit current is significantly lower than that theoretically obtained from absorption within the ML absorber, which is ascribed to losses that limit carrier extraction. The origin of these losses is discussed in terms of the material regions where recombination takes place. Our results indicate that carrier extraction is most efficient from the Si NCs themselves, whereas recombination is strongest in SiC and residual a-Si domains. Together with the observed onset of the external quantum efficiency at 700–800 nm, this fact is an evidence of quantum confinement in Si NCs embedded in SiC on device level.

© 2015 Elsevier B.V. All rights reserved.

1. Introduction

The progress in material technologies together with the ambition for a substantial improvement in solar cell conversion efficiencies has led to the development of the so-called "third generation" concepts aimed at overcoming the Shockley–Queisser efficiency limit of conventional single-junction solar cells [1]. Amongst the proposed solutions, silicon nanocrystals (Si NCs) in a dielectric matrix are attractive for all-silicon tandem cells thanks to their compatibility with silicon processing combined with the possibility of tuning their band gap energy by taking advantage of the size-dependent quantum confinement [2–4]. Si NCs in SiO_2 matrix have been indeed produced using the superlattice approach [5,6], by means of which excellent NC size control and a high degree of crystallinity have been obtained [7,8]. In addition, the charge transport and the electro-optical properties of NCs embedded in such systems have been extensively studied [9–11].

However, it has been recognized that the very high band-gap energy (≈ 9 eV) of silicon oxide sets a serious bottleneck for carrier transport and, therefore, for the achievement of efficient optoelectronic devices [12]. As a consequence, recent research has targeted silicon carbide as the dielectric matrix, which provides a much lower band gap energy (≈ 2.3–2.4 eV for 3C-SiC). Aspects such as improved exciton separation and charge transport; [13–15] control of the NC size [16]; details of the precipitation and crystallization processes of Si NCs and the role of the Si/SiC interface energy on the survival of residual amorphous domains [17]; role of the Si excess in the Si-rich layers [17,18], have been recently addressed and investigated.

However, several points remain open. A crucial open point is the demonstration of quantum confinement in Si NCs when embedded in SiC matrix. Although quantum confinement in Si NCs has been demonstrated for the SiO_2 matrix [5,7], unequivocal evidence for the SiC matrix is still lacking. Band structure calculations have shown that the poorly-insulating properties of the SiC matrix are predicted to lead to inefficient quantum confinement in embedded Si NCs [19]. Moreover, the presence of a distorted transition region at the Si NC/SiC interface [17] further reduces their band gap energy [19]. Experimentally, the difficulties of detecting quantum confinement in Si NCs in SiC derive from the

* Corresponding author. Tel.: +34 93 4039175.
E-mail address: jlopezv@el.ub.edu (J. López-Vidrier).
[1] Now at: École Polytechnique Fédérale de Lausanne, Photovoltaics and Thin Film Electronics Laboratory, Rue de la Maladière 71b, CH-2002 Neuchâtel, Switzerland.

http://dx.doi.org/10.1016/j.solmat.2015.10.006
0927-0248/© 2015 Elsevier B.V. All rights reserved.

weak and broad-band photoluminescence (PL) yielded by SiC [20], which eliminates PL as a straightforward method for determining the band gap energy; and from the background absorption of the SiC matrix and of the unavoidable residual amorphous silicon [17,20], which makes it virtually impossible to study the absorption of the Si NCs independently of their surroundings.

A second crucial point is the transport mechanism in the photovoltaic (PV) device. Thermally-activated transport through the nanostructures has been demonstrated [14,15]. However, the photovoltaic properties remain very poor, which urges on an investigation of the Si NC electrical behavior at the device level. Although the PV properties of Si NC/SiC multilayers (MLs) deposited on Si surfaces were reported by different groups with different architecture [18,21], the most rigorous approach makes use of a membrane-based solar cell structure. This allows us to get rid of the contribution of absorption in the substrate, and to unambiguously attribute the electrical results to the Si NC/SiC material alone [22,23], which is not possible if the design is such that the Si substrate is in electrical contact with the rest of the device. This membrane strategy has also been employed in the field of electrolytes for dye-sensitized solar cells. In a particular study, this structure allowed achieving free-standing arrays of TiO_2 nanotubes, avoiding diffusion of carriers towards the substrate and thus improving the transport properties of the nanostructures [24]; as well, other authors succeeded in the fabrication of electrolytes containing linear polymers instead of cross-linked ones, which notably enhanced the system charge transport properties [25].

In this paper, we make use of the membrane cell structure to isolate the contribution of the Si NCs to the photovoltaic performance of Si NCs within the SiC matrix. Light-beam induced current (LBIC) mapping is used to reveal the real origin of the photocurrent signal. Moreover, we associate the spectral response of the devices to the ML material's optical properties, and show that the procedure is effective to reveal details of photogeneration and carrier collection in Si NC/SiC multilayers. Finally, the analysis demonstrates quantum confinement in Si NCs embedded in SiC at device level, and highlights the role of the overall system and its feasibility as the top junction of a tandem solar cell.

2. Experimental details

2.1. Multilayer preparation and device fabrication

Two series of MLs made up of 30 $Si_{0.85}C_{0.15}$ (Si-rich carbide, or SRC in the following)/SiC bilayers, and pure SiC samples for reference, were deposited by plasma-enhanced chemical-vapor deposition (PECVD) on oxidized (400 nm SiO_2) c-Si (100) substrates, followed by an annealing treatment at 600 °C for 4 h plus 1100 °C for 30 min in an atmosphere of N_2 + 10% O_2. The SRC and SiC layer thicknesses (t_{SRC} and t_{SiC}, respectively) were chosen in order to obtain, after annealing, t_{SRC} equal to 3 nm (sample ML-3) and 4 nm (sample ML-4), and 5 nm for t_{SiC} in both cases. Such conditions produce a NC size equal to (4.7 ± 0.3) nm and (5 ± 1) nm for ML-3 and ML-4 respectively [17]. Further details on ML fabrication and extensive characterization (transmission electron microscopy (TEM), X-ray diffraction, X-ray reflection, reflectance and transmittance (R&T) spectroscopy) on fully similar samples, as well as a discussion for the NC size not being equal to SRC thickness, are reported in Ref. [17]. In that reference, the multilayer structure of samples X9-3 and X9-4 is identical to that of the present samples ML-3 and ML-4, respectively. In the same reference, TEM images showed the maintenance of the ML structure for these material samples, as well as the presence of Si NCs, after the whole fabrication process. The obtained layer thicknesses out of these TEM and R&T analyzes are summarized in Table 1. A crystallized fraction of the Si excess in the SRC sublayer of 41% and 60% was obtained by Raman spectroscopy performed on the X9-3 and X9-4 MLs, respectively [26]. This, together with an overall excess Si volume fraction in the two multilayers of 31% and 36%, as estimated under the assumption of full demixing [17], gives a Si NC volume fraction of 13% and 22%, respectively.

Table 1
Summary of the active layer materials employed as the absorber layer for the membrane cell stack in the present study. The number of bilayers, SiC and SRC sublayer thicknesses evaluated by transmission electron microscopy as described in Ref. [17], ML total thickness obtained from optical simulation, and Si NC volume fraction from the different systems under study are displayed. Thickness values were obtained after annealing. The table also contains the bulk layers consisting of pure SiC ($Si_{0.5}C_{0.5}$), SRC with a composition of $Si_{0.85}C_{0.15}$, and a-Si, as well as the 4 nm multilayer, all them fabricated on fused silica substrates.

Sample	# Bilayers	t_{SiC} (nm)	t_{SRC} (nm)	Total sample thickness (nm)	Si NC volume fraction (%)
Pure SiC	–	265 ± 5	–	265 ± 5	–
ML-3	30	5 ± 1	3.0 ± 0.5	260 ± 5	13
ML-4	30	5 ± 1	4.0 ± 0.5	290 ± 5	22
$Si_{0.85}C_{0.15}$ [a]	–	–	–	174 ± 5	–
SiC [a]	–	–	–	68 ± 5	–
a-Si [a]	–	–	–	143 ± 5	–
X9-4 [a]	30	5 ± 1	4.0 ± 0.5	260 ± 5	22

[a] Deposited on fused silica substrate, for comparison of optical properties.

To study the effect of Si NCs on the photovoltaic properties, membrane-based solar cells were fabricated with Si NC/SiC MLs, or stoichiometric SiC for reference, as absorber material. The SiC reference final thickness was 265 nm. After thermal annealing, all samples for solar cell fabrication underwent a remote hydrogen plasma treatment at 450 °C for 90 min to passivate electronic defects [22]. Table 1 summarizes the structural parameters for the different samples employed as active layers in this study. In addition to the MLs, also bulk layers with the compositions $Si_{0.5}C_{0.5}$, $Si_{0.85}C_{0.15}$, and a-Si, were prepared on fused silica substrates and used to determine the optical properties of the individual films. The a-Si material was obtained from an a-Si:H sample deposited by PECVD at 350 °C and dehydrogenated by annealing at 600 °C for 2 h. The thickness of all layers is reported in Table 1. The table also reports the parameters of the ML with 4 nm SRC on fused silica substrate (sample X9-4 in Ref. [17]), which is used as a reference for optical properties. Note the lower thickness of X9-4 with respect to ML-4 in spite of the same nominal structure, which is attributed to differences in plasma dynamics related to the different thermal and electrical properties of the substrate [17]. The *n*–*k* spectra of all reference layers were extracted from reflectance and transmittance measurements by means of optical modeling as described in [17,20].

Solar cell devices were fabricated by preparing *p*-*i*-*n* membrane-cell structures according to Ref. [22] in the configuration sketched in Fig. 1, with the NC-based material under investigation as the intrinsic (and absorber) active layer. The membrane structure allows the elimination of the c-Si wafer contribution to the PV properties of their structure. The active cell area was defined by locally removing the Si substrate and the SiO_2 insulation layer. To ensure electrical insulation, the regions outside the active cell areas were further covered by a SiO_2 layer. 20 nm thick hydrogenated *n*-type a-$Si_{0.95}C_{0.05}$:H and *p*-type a-Si:H layers were deposited on the rear and front sides of the structure as selective electron and hole contacts, respectively. Finally, 70 nm ITO was sputtered on both sides. After all fabrication steps, and for all measurements performed in this work, devices with an effective membrane area of 1.7×10^{-2} cm^2 were employed. For more detailed information on the device preparation, the reader is directed to Ref. [22].

2.2. Layer and device characterization

The membrane cell structure was inspected by cross-section scanning electron microscopy (SEM), using a Hitachi SU70 instrument with a cold trap, and a conventional optical microscope (using 10 × magnification). As can be observed in Fig. 2(a), which depicts a SEM image for the device incorporating ML-4, the final deposited layer thicknesses are in excellent agreement with the nominal ones. An optical microscope top view of the device is shown in Fig. 2(b), where the different areas can be distinguished as the color is determined by the layer stack in the respective region, labeled according to Fig. 1.

The optical properties of the Si NC/SiC multilayers investigated in this paper were already reported in prior publications [17,27], based on detailed models accounting for all individual sublayers and materials phases (c-Si, a-Si, c-SiC) of the multilayer, previously characterized with dedicated reference samples. Here, we made use of this previously gained knowledge to extract the complex refractive index based on reflectance spectra of the multilayers deposited on oxidized c-Si wafers after thermal annealing prior to device fabrication. Reflectance (R) spectra were recorded with an Avantes UV–visible–NIR fiber-optics spectrophotometer from 250 to 1000 nm (1300 points). The R spectra were simulated using the software OPTICAL [28] which makes use of the generalized transfer matrix method [29] to treat multistack materials, taking into account the complete structure [26] and including a surface and buffer layers, whose properties were kept fixed at previously determined values [20]. The variables in the simulations were the thickness and the optical properties of the multilayer (which was modeled using a single uniform layer), and the thickness of the SiO_2. The absorption was accurately retrieved using numerical inversion associated to the minima and maxima approach [26]. The thicknesses obtained from these simulations for ML-3, ML-4, and pure SiC are reported in Table 1. Light-beam induced current (LBIC) mappings with a spatial resolution of 100 μm were also carried out on the membrane cells to locally verify their electrical response to incident light. For this, a halogen lamp was used as white light source, mounted on a Delta Elektronika scanning platform, and the electrical signal was collected and amplified by an EG&G lock-in system.

The external quantum efficiency (EQE) of the membrane cells was obtained in the wavelength range from 500 to 1200 nm by means of Fourier-Transform photocurrent spectroscopy, exciting the active area [region (1) in Fig. 1] with a commercial pulsed supercontinuum white light source (pulse energy around 100 nJ). By modulating the light with a modulation frequency that varies continuously with wavelength, the Fourier decomposition of the measured photocurrent could be achieved. The measurement system was calibrated with a c-Si reference solar cell with known spectral response, with values ranging between 0.35 and 0.7 A W^{-1} within the 500–1000 nm range. Further details on this technique can be found in Ref. [30].

Finally, the electrical characterization in dark was performed with a four-point wiring configuration using a Keithley 2611A source meter. The same system was also employed to determine the electrical response of the samples under illumination, using a WACOM XB-45TW1 (AAA) solar simulator equipped with a Xe lamp, which simulates an AM1.5G solar spectrum. An irradiance of 1000 W m^{-2} was employed, calibrated with a reference c-Si solar cell. All electrical and photovoltaic measurements were performed at room temperature.

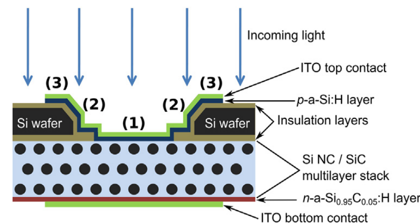

Fig. 1. Cross-section scheme of the substrate-less *p*-*i*-*n* devices containing the Si NC/SiC multilayers as the intrinsic active layer (lengths are not to scale). ITO was employed as top and bottom transparent contact. *n*-type a-$Si_{0.95}C_{0.05}$:H on the bottom and *p*-type a-Si:H layers on top were used as electron and hole contacts, respectively. Numeric labels indicate the regions that might potentially display a different electrical response to incoming light: (1) the *p*-*i*-*n* cell alone, (2) through the *p*-*i*-*n* cell including a thin insulating layer and (3) the substrate.

3. Results

3.1. Characterization of device reliability

Prior to the electro-optical response analysis of the cells, and to complement the structural investigation reported in Section 2.2, a macroscopic inspection by optical microscopy was carried out (under reflection configuration). Fig. 2(b) shows an image of the front side of a membrane cell incorporating ML-4. The different degrees of transparency (i.e. different color) observed are associated to the layers underneath the surface, and the different

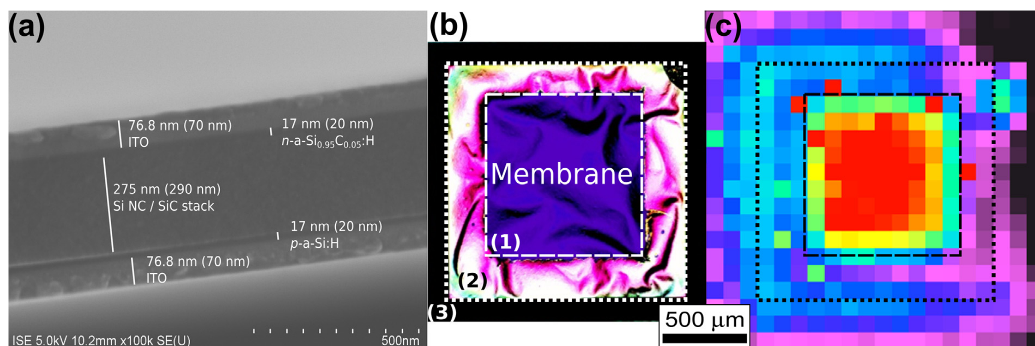

Fig. 2. (a) Cross-section SEM image of a membrane incorporating ML-4. The measured layer thicknesses are specified and compared to their nominal values (in parentheses). (b) Optical microscopy image corresponding to the top view of the same device. Labels correspond to the regions that display a different electrical response to incoming light: (1) the active cell area (surrounded by dashed lines), (2) through a thin insulating layer (dotted lines) and (3) through a thick insulating layer and the remaining substrate. (c) Light-beam induced current map from the same cell as in (b), with a clear photoresponse visible from the active cell area. Dashed and dotted lines frame the equivalent regions in (b) and (c).

regions are labeled according to Fig. 1. Finally, to confirm the proper performance of the device, LBIC investigations were used to map the output photocurrent signal under incident white-light radiation [see Fig. 2(c)]. This map, compared to the conventional microscopy optical image obtained from the same cell, shows that the photocurrent stems from the active cell area [region (1)], and confirms that any contribution from the wafer [region (3)] is effectively suppressed by the insulation layers. Note that the small signal outside the active cell area [region (1)] stems from incident light which is reflected on the slanted sidewalls (see Fig. 1) and then incident on the active cell area. In any case, all the selected devices for the present study were those displaying a similar electro-optical response as in the figure, i.e. mainly coming from the active cell area.

3.2. Optical response

To investigate the optical absorption properties of the Si NC/SiC multilayers under study, R measurements were carried out on the as prepared multilayers prior to membrane fabrication. The R spectra were fitted as described in Section 2.2, and the optical properties (refractive index and extinction coefficient) of the multilayer as a whole (average medium) were obtained. Fig. 3(a) displays the experimental and computed R for ML-3 and ML-4, as well as the pure SiC reference single layer. For all samples, the most evident feature is the rapid oscillating interference pattern

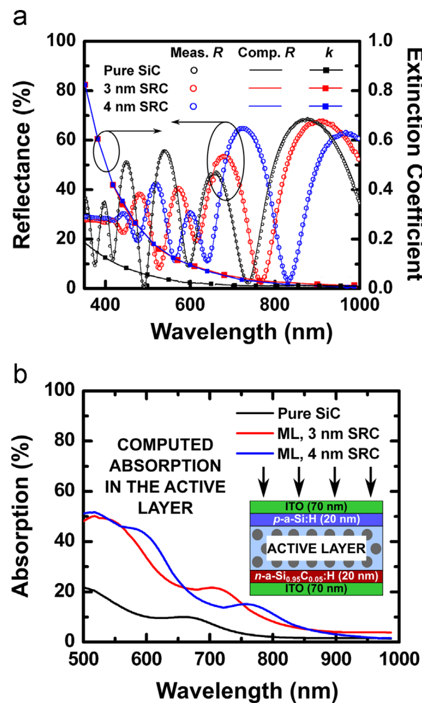

Fig. 3. (a) Left axis: measured (circles) and computed (lines) specular reflectance (R) of ML-3 and ML-4, as well as on a pure SiC sample, on oxidized c-Si substrate, prior to membrane device fabrication. Right axis: extinction coefficient (k) for the three materials, obtained from the simulation. (b) Computed absorptance of the different active layers (ML-3, ML-4 and pure SiC single layer) in (a) when embedded into a membrane cell stack such as the one sketched in Fig. 1. The inset illustrates the structure used in the calculations. The thicknesses of the active layers are those reported in Table 1. The optical properties of each active layer have been obtained by R spectroscopy on the same samples prior to membrane fabrication. The thicknesses and optical properties of the other layers were kept constant in the calculations.

due to the 400-nm SiO_2 layer. This pattern is slowly modulated by the thinner SRC/SiC (or only SiC) layer. For the SRC/SiC samples the interference pattern starts at about 400 nm (3.1 eV), whereas for the SiC material, which is characterized by a higher band gap energy, the onset occurs beyond the blue end of the investigated range. The simulations reproduce all features very accurately. The obtained extinction coefficients (k) of the three materials are reported on the right axis of the same figure. The graph clearly shows that the presence of Si NCs enhances the absorption with respect to bulk SiC. The thickness of the SRC sublayers in the multilayer, however, has little effect.

The next step is the study of the photon absorption from the whole membrane cell stack. For this, optical simulations were performed on the device structure shown in Fig. 1 by means of the OPTICAL code [28]. The film thicknesses listed previously, and refractive index data determined by spectroscopic ellipsometry on separate single layer samples (ITO, a-Si:H, a-$Si_{0.95}C_{0.05}$:H), or derived from R data (Si NC/SiC active layer), were used to simulate absorption within each layer. Fig. 3(b) shows the simulated absorption of ML-3, ML-4 and the SiC layer within the full membrane cell layer stack. The cell structures incorporating ML-3 and ML-4 show similar absorption, yet modulated by the different thickness, as seen from the different interference pattern. Importantly, the absorption of the ML-3 and ML-4 samples is enhanced with respect to the pure SiC active layer. Under the hypothesis of complete charge carrier collection (internal quantum efficiency ≡ 1), the generated current density in the computed range, $J_{gen}^{\Delta\lambda}$, can be estimated by means of

$$J_{gen}^{\Delta\lambda} \propto \int_{\Delta\lambda} A_L(\lambda) \cdot F(\lambda) d\lambda, \quad (1)$$

where $A_L(\lambda)$ is the simulated absorption spectrum of the active layer, $F(\lambda)$ is the AM1.5G solar irradiance spectrum, and, for the sake of comparison, their product is integrated over the same spectral range as for the EQE measurements described below ($\Delta\lambda$=500–1000 nm). The larger k obtained for the ML-based samples reflects in larger values of $J_{gen}^{\Delta\lambda}$ obtained using Eq. (1). The values are summarized in Table 2.

The EQE of the cells under study is presented, in linear scale, in Fig. 4(a). The EQE of ML-4 shows a pronounced increase towards shorter wavelengths, which is much less prominent for ML-3, and even weaker for the SiC sample. To investigate these differences more in detail we plot the EQE in logarithmic representation in Fig. 4(b). The logarithmic plot reveals that the EQE signal exceeds the experimental noise level up to 1200 nm (1.03 eV). This result is surprising, because owing to the small Si NC size and the higher band gap of the SiC matrix, the band gap of the materials are expected to be higher than that of c-Si (1.12 eV). We would like to remind, however, that quantum confinement in Si NCs embedded in SiC has not been proven yet.

Interestingly, even the pure SiC layer, which has a far lower EQE than the Si NC layers, exhibits a clearly detectable signal up to a wavelength of 1200 nm (1.03 eV), the wavelength limit of the employed setup. To elucidate the origin of this near-infrared response, we investigated the optical properties of the corresponding layers more in detail using the reference bulk films specified in Table 1. Fig. 5 depicts the absorption coefficient of the four bulk layers. The $Si_{0.85}C_{0.15}$ layer reported in the figure is not expected to be representative of the same material when inserted in the ML structure. In fact, in the latter case, nanocrystals are formed due to spatial confinement within the surrounding SiC matrix [17], whereas within the bulk SRC film the silicon phase occupies, according to the nominal composition, 82% of the volume and is fully crystallized. Therefore, the microcrystallized silicon phase is continuous, and no confinement effects are expected to occur. In turn, the same layer, when inserted in the

Table 2
Summary of the values obtained after optical, EQE and photovoltaic data treatment. Short circuit current density was estimated from the computed optical absorption data ($J_{gen}^{\Delta\lambda}$), under ideal charge collection hypothesis, from spectral response measurements ($J_{EQE}^{\Delta\lambda}$) and intensity-voltage analysis under 1-Sun illumination (J_{sc}). The open circuit voltage, V_{oc}, was also obtained from the latter measurements. Finally, X_{eff} represents the average or lumped effective collection efficiency.

Sample	$J_{gen}^{\Delta\lambda}$ (A cm^{-2})	$J_{EQE}^{\Delta\lambda}$ (A cm^{-2})	X_{eff} ($=J_{EQE}^{\Delta\lambda}/J_{gen}^{\Delta\lambda}$)	J_{sc} (A cm^{-2})	V_{oc} (mV)
Pure SiC	2.2×10^{-3}	2×10^{-6}	9.0×10^{-4}	2.5×10^{-6}	260
ML-3	6.3×10^{-3}	7×10^{-6}	1.3×10^{-3}	–	–
ML-4	6.5×10^{-3}	6×10^{-5}	1.0×10^{-2}	10^{-4}	180

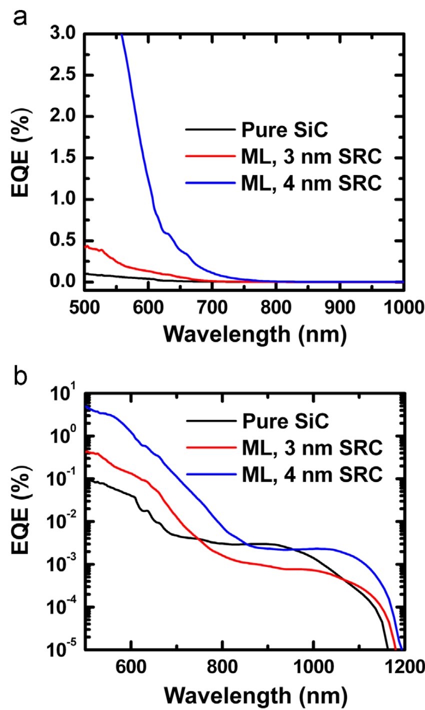

Fig. 4. External quantum efficiency (EQE) in linear (a) and logarithmic (b) representation.

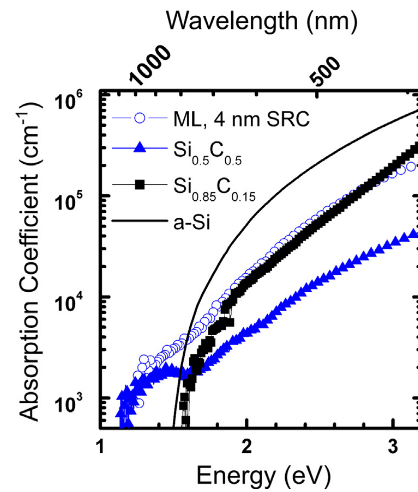

Fig. 5. Absorption coefficient of the 4 nm $Si_{0.85}C_{0.15}$/SiC multilayer (sample X9-4 in Ref. [17]), of the bulk SiC material, the bulk SRC with a composition of $Si_{0.85}C_{0.15}$ and of dehydrogenated a-Si. The total thicknesses corresponding to these samples are summarized in Table 1.

ML, undergoes only partial crystallization, for structural reasons that are described in Ref. [17]. Consequently, a residual Si amorphous fraction survives, which contributes to absorption.

Going back to Fig. 5, the $Si_{0.5}C_{0.5}$ layer clearly shows non-zero absorption down to photon energies as low as 1.24 eV. The same holds for the multilayer structure. In contrast, the absorption onset of the $Si_{0.85}C_{0.15}$ single layer occurs at 1. 6eV, where the blue shift with respect to crystalline silicon (not reported) is related to the presence of carbon in such layer. Approximately the same onset is observed for amorphous silicon, which is supposed to be representative of the residual amorphous Si fraction in the ML. This indicates that the absorption observed for the multilayer in the range 1.24–1.6 eV (wavelengths longer than 800 nm in Figs. 3 and 4) is not to be ascribed to the $Si_{0.85}C_{0.15}$ sublayer, irrespective of its crystallization state, be it either complete as in the bulk $Si_{0.85}C_{0.15}$ layer reported in Fig. 5, or partially amorphous as within the ML [17]. The ML absorption at photon energies of 1.24–1. 6eV can only be ascribed to the SiC sublayer, as it is also seen in the SiC bulk layer reported in Fig. 5. Such absorption is probably related to the presence of a high density of grain boundaries that act as photon scattering centers and/or to the residual SiC amorphous fraction in such layer [17]. In summary, Fig. 5 shows that an onset for absorption can be expected from the *silicon* component in the *ML*, at about 1. 6eV. More important, Fig. 5 does not show any component with an onset at energies similar to the pronounced EQE onset in Fig. 4(a) at 600–700 nm (1.77–2 eV). We therefore ascribe this latter onset to the presence of a different component in the ML that is not present in the single layer materials illustrated in Fig. 5, namely, to a nanocrystalline silicon phase with enlarged band-gap due to quantum confinement.

So far, no direct proof for quantum confinement in Si NCs embedded in SiC has been given. This is actually related to the fact that most research has been concentrating on multilayers, motivated by the growth confinement achieved by the stoichiometric barrier layers. However, Fig. 5 demonstrates that the SiC phase absorbs at photon energies as low as 1.24 eV, thus masking an eventual shift of the absorption of the silicon phase. Fig. 4 demonstrates that EQE measurements, which are based on an electrical signal (more sensitive to the crystalline than to the amorphous Si component due to its better conductivity [31]) given an optical signal (due to the not separable absorption of the Si and SiC components), are able to evidence the presence of a confinement-related component in the absorption spectrum. Indeed, and to the best of our knowledge, Figs. 4 and 5 give the first clear proof of a blue-shifted band gap of Si NCs embedded in SiC.

Fig. 4(a) shows that the EQE is larger when Si NCs are present than when a pure SiC active layer is employed, in accordance with the absorptance spectra displayed in Fig. 3(b). However, a comparison with the absorptance spectra reveals that the difference between ML-3 and ML-4 devices is much more pronounced in the EQE. Considering that the multilayers exhibit similar absorption,

their greatly different spectral response must be attributed to a higher charge carrier collection efficiency, which can be explained by more efficient transport or decreased recombination of photogenerated carriers. Recent results on identical ML systems have shown that charge transport is particularly efficient within a percolative Si network [26]. The larger Si volume fraction contained in ML-4 [17] may therefore be responsible for an improvement in conduction leading to the increased EQE.

Further information can be extracted from the EQE after a more rigorous analysis. In particular, in analogy with Eq. (1), the short-circuit current density derived from EQE, $J_{EQE}^{\Delta\lambda}$, can be expressed as [32]:

$$J_{EQE}^{\Delta\lambda} \propto \int_{\Delta\lambda} EQE(\lambda) \cdot F(\lambda) d\lambda, \quad (2)$$

where $EQE(\lambda)$ is the calculated external quantum efficiency, and the integration is carried out over the same wavelength range as in Eq. (1). Using the formalism in Eq. (2), we can estimate photocurrent values (see Table 2) that indicate a much stronger response from the ML-4 than from the ML-3 device, presenting enhancements with respect to the pure SiC active layer of $J_{EQE,4nm}^{\Delta\lambda}/J_{EQE,SiC}^{\Delta\lambda}=30$ and $J_{EQE,3nm}^{\Delta\lambda}/J_{EQE,SiC}^{\Delta\lambda}=3.5$ times. With the data obtained so far, we can calculate an average effective collection efficiency, defined as the ratio between generated and collected current density, $X_{eff}=J_{EQE}^{\Delta\lambda}/J_{gen}^{\Delta\lambda}$, which is found to increase with the Si content, as can be seen in Table 2. The higher effective collection efficiency for higher Si excess may indicate that either the defect density decreases or carrier mobility increases with Si content.

3.3. Photovoltaic performance

The photovoltaic properties of the membrane cells were also investigated, using devices presenting an electro-optical response coming only from the membrane area, as discussed in Section 3.1. Fig. 6 displays current density versus voltage [$J(V)$] curves on a cell containing ML-4, after different regions were illuminated (see the inset microscopy image in the figure, corresponding to the same device). A very similar $J(V)$ characteristic is obtained in dark and when the membrane surroundings [regions (2) and (3) in the inset image] are illuminated, except for a current increase at positive applied voltages, which is attributed to the additional collection of carriers photogenerated within the selective n- and p- contacts. No short-circuit current is found when illuminating regions (2) and (3), in good agreement with LBIC measurements. Moreover, similar curves are found when either the whole cell or only the membrane [region (1)] are illuminated, with an open circuit voltage (V_{oc}) of approximately 180 mV in both cases. The similarity proves that the measured V_{oc} arises solely from the membrane, and J_{sc} arises primarily from the membrane. Again, illuminating the membrane surroundings along with the membrane yields an increase in photoconductivity attributed to the generation of carriers within the selective n- and p-contacts. The same experiment was performed on all cells discussed in the following so as to ensure that the measured properties arise only from the membrane region in each case.

Given that the photovoltaic performance arises from the membrane only, the effect of the presence of Si NCs within the SiC matrix can be examined by comparing the $J(V)$ curves of a cell with a pure SiC active layer and a cell incorporating ML-4 as the active layer (see Fig. 7). A larger J_{sc} is found for the ML-4 device ($\sim 10^{-4}$ A cm^{-2}) than in pure SiC ($\sim 2.5 \times 10^{-6}$ A cm^{-2}), corresponding to an enhancement of about 40×, which is comparable to the 30× obtained from EQE for a shorter spectral range. Conversely, V_{oc} decreases from 240 to 180 mV. These results are summarized in Table 2. The two orders of magnitude lower short circuit (J_{sc}) with respect to photogenerated ($J_{gen}^{\Delta\lambda}$) current, arises from losses whose origin will be discussed later. It is these losses that restrict V_{oc} to values actually lower than those expected for c-Si [33].

The fill factor (FF) and conversion efficiency (η) were also determined for both devices, with values of FF=28 and 59%, and $\eta=5 \times 10^{-3}$ and 2×10^{-4}%, for ML-4 and bulk SiC, respectively. Both parameters are well comparable to other results reported for Si NC-based solar cells grown on fused silica substrate (i.e. with no bulk Si contribution) [34,35]. The efficiency improvement for the ML-4 with respect to the bulk SiC device ($\eta_{4\ nm}/\eta_{SiC}=25$) indicates that we are able to directly study the effect of the Si NCs on device level, which is a necessary step towards the design of an all-Si tandem solar cell.

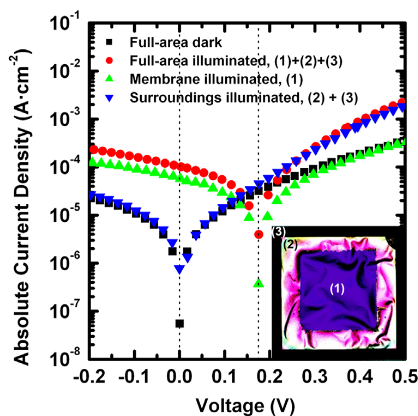

Fig. 6. Current density versus voltage curves from the ML-4 device, obtained under different dark and 1-Sun illumination conditions: "full-area" measurements were performed on the whole membrane cell, whereas "membrane" and "surroundings" labels refer to region (1), and regions (2) and (3), respectively, from the inset microscopy image of the same device. Vertical dotted lines indicate the zero- and open-circuit voltages, and serve as a guide to the eye.

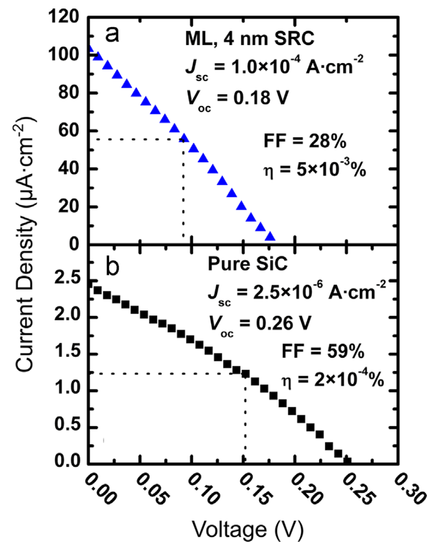

Fig. 7. Current density versus voltage curves under 1-Sun illumination of a membrane cell incorporating (a) ML-4 and (b) pure SiC as the intrinsic absorber layer. The calculated cell parameters are given in the figure.

4. Discussion

The data presented thus far provides the basis for an evaluation of the performance of Si NCs in SiC as wide band gap absorber material. The EQE of the devices [Fig. 4(a)] shows an onset at 600–700 nm (=1.77–2 eV). This occurrence, besides confirming that the contribution of the substrate has been eliminated, gives an indication of quantum confinement in Si NCs within the SiC matrix. Such result is relevant because, contrary to the case of the SiO_2 matrix, the detection of quantum confinement in SiC matrix raises a number of difficulties which have impeded such observation so far (see Section 1).

By comparing Fig. 3(b) with Fig. 4(a), it is apparent that the variation in EQE does not follow a similar variation in absorption, and the ratio between integrated EQE and integrated absorption, previously termed the effective collection efficiency, X_{eff}, varies significantly across the samples, especially between ML-3 and ML-4. This result suggests that in ML-4 there is a higher fraction of carriers that are generated in a region where recombination is less probable. The sample regions where recombination can occur are the Si NCs, the residual a-Si, the microcrystallized SiC matrix, SiC grain boundaries and the residual a-SiC.

ML-3 and ML-4 differ primarily by the Si excess fraction, Si excess crystallinity, and overall Si NC volume fraction (see Section 2). Actually, between ML-3 and ML-4 the SiC fraction decreases, whereas the Si NC volume fraction increases and the volume fraction of the residual a-Si decreases. This leads to the conclusion that carriers generated in Si NCs are the least likely to recombine and thus the most likely to be collected. Conversely, the density of non-radiative recombination centers is expected to be highest in a-Si or SiC domains. This assumption is supported by electrical measurements, which show that transport is dominated by defects in a-Si and microcrystallized SiC, and by extended states in microcrystallized Si [31]. Since collection efficiency is correlated with the Si NC volume fraction, we may postulate that the short-circuit current of cells containing Si NCs is dominated by carriers generated in the Si NCs. Thus, the EQE onset at 700–800 nm can be interpreted as an indication of quantum confinement in the Si NCs, whereas, as shown above, the absorption that takes place at longer wavelengths [Fig. 4(b)] is related to tail or defect absorption located within the related SiC domains. The obtained result (onset of EQE at ~1. 6eV for ML-4, slightly higher but weaker for ML-3) is in remarkable agreement with an excitonic band gap of 1.6 eV predicted for 4 nm nanodot diameter by atomistic calculations for a small-band-gap matrix such as SiC [36]. The onset energy is higher than predicted in Ref. [37] for a 4 nm thick a-Si slab (1.3 eV), which however is expected to show weaker confinement with respect to quantum dots.

The correlation between current collection efficiency and Si NC volume suggests that the current is collected via the NC networks, which are more extensive when there are more Si NCs. The Si NC volume fraction does not reach the percolation threshold of 29% [38] in either sample, so either carriers can travel short distances through a-Si or SiC without recombining, or they are only collected from the small Si NC networks that are directly contacted by the electron and hole contacts. Both are plausible: the reduction of the volume fraction of a-Si and SiC domains can result in shorter recombinative paths that carriers must overcome to travel between NC networks, and similarly, an increased Si NC fraction is likely to lead to the Si NC networks in direct contact with electron and hole contacts. The above uncertainty is actually the reason for not attempting a quantitative evaluation of Si NC band gap value from EQE combined to absorption data.

The $J(V)$ characteristics measured on membrane devices illustrated in this paper confirm the trends in current collection determined from EQE and also show rather low V_{oc} compared to the value expected for a silicon absorber (with or without quantum confinement) [23]. In addition, a low current collection efficiency at $V=0$ V [23] is measured. A lossy junction, as indicated by the non-zero slope at $V=0$ V of the $J(V)$ characteristics (see Fig. 6), is also detected, more evident for higher Si content [see Fig. 7 (a) compared to (b)]. Previous studies on devices including similar material also reported remarkable recombination [22,23]. It has also been shown that the dangling bond density in Si NC/SiC material can be reduced by a hydrogen plasma treatment, and that this is more efficient in Si than in the SiC subdomains [21,26]. Nevertheless, defect concentrations on the order of 10^{17}–10^{18} cm^{-3} are expected for hydrogen-passivated samples [20,21]. This high defect concentration results in a high recombination rate, which is at present the most relevant issue that needs to be addressed in view of the introduction of the proposed material in device applications. Our study indicates that one method to address this is adjusting the Si nanostructure, which increased the effective collection efficiency by an order of magnitude.

5. Conclusions

Optical and photovoltaic characterization has been performed on SRC/SiC multilayers, where a high-temperature annealing treatment induced the precipitation of Si NCs. In order to avoid a Si substrate contribution to the PV performance of the material, a membrane cell structure was used. The cell fabrication was inspected by cross-section SEM analysis of the structures, verifying the good layer thickness correspondence with the nominal values. The optical and electro-optical properties of cells containing 3- and 4-nm SRC MLs and pure SiC as absorber layers were investigated. The combination of optical measurements and simulations allowed isolating the absorption contribution of the absorber layers under study from the rest of the membrane cell stack, as well as assessing the role of each present material phase on photon absorption. From these optical measurements, the generated current ($J_{gen}^{\Delta\lambda}$) was estimated in the range from 500 to 1000 nm and under the hypothesis of complete current collection. Spectral response measurements on the same cells revealed an EQE onset around 700–800 nm, as well as a short circuit current ($J_{SR}^{\Delta\lambda}$) that was three orders of magnitude lower than $J_{gen}^{\Delta\lambda}$, which indicates inefficient photogenerated current extraction. $J(V)$ measurements of the devices confirmed the large J_{sc} drop with respect to $J_{gen}^{\Delta\lambda}$. This indicates that large recombinative losses take place within the membrane cell, which leads to poor overall conversion efficiencies. Finally, since the effective collection efficiency increases with increasing Si NC volume fraction and decreasing SiC volume fraction, current collection from Si NCs is believed to be much more efficient than from a-Si nanoclusters or SiC domains. In this frame, the EQE onset at 700–800 nm for devices with Si NCs may be the first ever indicator of quantum confinement in Si NCs in SiC on device level.

Acknowledgments

The research leading to these results has received funding from the EC Seventh Framework Programme (FP7/2007-2013) under Grant agreement no.: 245977, under the project title NASCEnT. The present work was supported by the Spanish national project LEOMIS (TEC2012-38540-C02-01). The authors acknowledge Michele Bellettato at CNR-IMM for the preparation of the Si NC material, our colleagues at Fraunhofer ISE for their roles in preparing the solar cell devices, and Stefan Fieberg at Fraunhofer IPM

for his help with the Fourier-Transform photocurrent spectroscopy measurements.

References

[1] M.A. Green, Third generation photovoltaics: solar cells for 2020 and beyond, Physica E 14 (2002) 65–70.
[2] P.Y. Yu, M. Cardona, Fundamentals of Semiconductors: Physics and Material Properties, fourth ed., Springer, Berlin, 2010.
[3] F. Priolo, T. Gregorkiewicz, M. Galli, T.F. Krauss, Silicon nanostructures for photonics and photovoltaics, Nat. Nanotechnol. 9 (2014) 19–32.
[4] Nanotechnology and Photovoltaic Devices: Light Energy Harvesting with Group-IV Nanostructures, in: J. Valenta, S. Mirabella (Eds.), first edition,Pan Stanford Pub., Kyoto and Catania, 2015.
[5] M. Zacharias, J. Heitmann, R. Scholz, U. Kahler, M. Schmidt, J. Bläsing, Size-controlled highly luminescent silicon nanocrystals: a SiO/SiO_2 superlattice approach, Appl. Phys. Lett. 80 (2002) 661–663.
[6] J. Heitmann, F. Müller, M. Zacharias, U. Gösele, Silicon nanocrystals: size matters, Adv. Mater. 17 (2005) 795–803.
[7] A.M. Hartel, D. Hiller, S. Gutsch, P. Löper, S. Estradé, F. Peiró, B. Garrido, M. Zacharias, Formation of size-controlled silicon nanocrystals in plasma enhanced chemical vapor deposition grown SiO_xN_y/SiO_2 superlattices, Thin Solid Films 520 (2011) 121–125.
[8] S. Hernández, J. López-Vidrier, L. López-Conesa, D. Hiller, S. Gutsch, J. Ibáñez, S. Estradé, F. Peiró, M. Zacharias, B. Garrido, Determining the crystalline degree of silicon nanoclusters/SiO_2 multilayers by Raman scattering, J. Appl. Phys. 115 (2014) 203504-1–203504-9.
[9] A. Marconi, A. Anopchenko, M. Wang, G. Pucker, P. Bellutti, L. Pavesi, High power efficiency in Si NC/SiO_2 multilayer light emitting devices by bipolar direct tunneling, Appl. Phys. Lett. 94 (2009) 221110-1–221110-3.
[10] S. Gutsch, J. Laube, A.M. Hartel, D. Hiller, N. Zakharov, P. Werner, M. Zacharias, Charge transport in Si nanocrystal/SiO_2 superlattices, J. Appl. Phys. 113 (2013) 133703-1–133703-9.
[11] J. López-Vidrier, Y. Berencén, S. Hernández, O. Blázquez, S. Gutsch, J. Laube, D. Hiller, P. Löper, M. Schnabel, S. Janz, M. Zacharias, B. Garrido, Charge transport and electroluminescence of silicon nanocrystals/SiO_2 superlattices, J. Appl. Phys. 114 (2013) 163701-1–163701-7.
[12] P. Wurfel, Physics of Solar Cells: From Basic Principles to Advanced Concepts, second ed., Wiley, New York, 2009.
[13] P. Löper, R. Müller, D. Hiller, T. Barthel, E. Malguth, S. Janz, J.C. Goldschmidt, M. Hermle, M. Zacharias, Quasi-fermi-level splitting in ideal silicon nanocrystal superlattices, Phys. Rev. B 84 (2011) 195317-1–195317-6.
[14] C. Song, Y. Ruia, Q. Wang, J. Xua, W. Li, K. Chen, Y. Zuo, Q. Wang, Structural and electronic properties of Si nanocrystals embedded in amorphous SiC matrix, J. Alloys Compd. 509 (2011) 3963–3966.
[15] R. Shukla, C. Summonte, M. Canino, M. Allegrezza, M. Bellettato, A. Desalvo, D. Nobili, S. Mirabella, N. Sharma, M. Jangir, I.P. Jain, Optical and electrical properties of Si nanocrystals embedded in SiC matrix, Adv. Mater. Lett. 3 (2012) 297–304.
[16] J. López-Vidrier, S. Hernández, J. Samà, M. Canino, M. Allegrezza, M. Bellettato, R. Shukla, M. Schnabel, P. Löper, L. López-Conesa, S. Estradé, F. Peiró, S. Janz, B. Garrido, Structural, optical and electrical properties of silicon nanocrystals embedded in Si_xC_{1-x}/SiC multilayer systems for photovoltaic applications, Mater. Sci. Eng. B 178 (2013) 639–644.
[17] C. Summonte, M. Allegrezza, M. Bellettato, F. Liscio, M. Canino, A. Desalvo, J. López-Vidrier, S. Hernández, L. López-Conesa, S. Estradé, F. Peiró, B. Garrido, P. Löper, M. Schnabel, S. Janz, R. Guerra, S. Ossicini, Silicon nanocrystals in carbide matrix, Sol. Energy Mater. Sol. Cells 128 (2014) 138–149.
[18] D. Song, E.-C. Cho, G. Conibeer, C. Flynn, Y. Huang, M.A. Green, Structural, electrical and photovoltaic characterization of Si nanocrystals embedded SiC matrix and Si nanocrystals/c-Si heterojunction devices, Sol. Energy Mater. Sol. Cells 92 (2008) 474–481.
[19] R. Guerra, S. Ossicini, Ab initio calculations of the electronic and optical properties of silicon quantum dots embedded in different matrices, in: J. Valenta, S. Mirabella (Eds.), Light Energy Harvesting with Group-IV Nanostructures, Pan Stanford Pub, 2015, pp. 65–98 , Chapter 3.
[20] M. Schnabel, C. Summonte, S.A. Dyakov, M. Canino, L. López-Conesa, P. Löper, S. Janz, P.R. Wilshaw, Absorption and emission of silicon nanocrystals embedded in SiC: eliminating Fabry–Pérot interference, J. Appl. Phys. 117 (2015) 045307-1–045307-13.
[21] S. Yamada, Y. Kurokawa, S. Miyajima, M. Konagai, Silicon quantum dot superlattice solar cell structure including silicon nanocrystals in a photogeneration layer, Nanoscale Res. Lett. 9 (2014) 246-1–246-7.
[22] P. Löper, D. Stüwe, M. Künle, M. Bivour, C. Reichel, R. Neubauer, M. Schnabel, M. Hermle, O. Eibl, S. Janz, M. Zacharias, S.W. Glunz, A membrane device for substrate-free photovoltaic characterization of quantum dot based p-i-n solar cells, Adv. Mater. 24 (2012) 3124–3129.
[23] P. Löper, M. Canino, D. Qazzazie, M. Schnabel, M. Allegrezza, C. Summonte, S. W. Glunz, M. Stefan Janz, Zacharias, Silicon nanocrystals embedded in silicon carbide: investigation of charge carrier transport and recombination, Appl. Phys. Lett. 102 (2013) 033507-1–033507-4.
[24] J. Lin, M. Guo, C.T. Yip, W. Lu, G. Zhang, X. Liu, L. Zhou, X. Chen, H. Huang, High temperature crystallization of free-standing anatase TiO_2 nanotube membranes for high efficiency dye-sensitized solar cells, Adv. Funct. Mater. 23 (2013) 5952–5960.
[25] M. Imperiyka, A. Ahmad, S.A. Hanifah, F. Bella, A UV-prepared linear polymer electrolyte membrane for dye-sensitized solar cells, Physica B 450 (2014) 151–154.
[26] M. Schnabel, M. Canino, S. Künhold, J. López-Vidrier, T. Klugermann, C. Weiss, L. López-Conesa, M. Zschintzsch-Dias, C. Summonte, P. Löper, S. Janz, P. Wilshaw, Charge transport in nanocrystalline SiC with and without embedded Si nanocrystals, Phys. Rev. B. 91 (2015) 195317-1–195317-15.
[27] M. Schnabel, C. Weiss, P. Löper, M. Canino, C. Summonte, P.R. Wilshaw, S. Janz, Nanocrystalline SiC formed by annealing of a-SiC:H on Si substrates: a study of dopant interdiffusion, J. Appl. Phys. 116 (2014) 024315-1–024315-10.
[28] E. Centurioni, Optical 〈https://www.bo.imm.cnr.it/users/centurioni/optical.html〉.
[29] E. Centurioni, Generalized matrix method for calculation of internal light energy flux in mixed coherent and incoherent multilayers, Appl. Opt. 44 (2005) 7532–7539.
[30] C. Petermann, R. Beigang, P. Fischer, Fourier-transform photocurrent spectroscopy using a supercontinuum light source, Appl. Phys. Lett. 100 (2012) 061108-1–061108-3.
[31] C. Summonte, M. Canino, M. Allegrezza, M. Bellettato, A. Desalvo, R. Shukla, I. Crupi, S. Milita, L. Ortolani, L. López-Conesa, S. Estradé, F. Peiró, B. Garrido, Boron doping of silicon rich carbides: electrical properties, Mater. Sci. Eng. B 178 (2012) 551–558.
[32] S.M. Sze, K.K. Ng, Physics of Semiconductor Devices, third ed., Wiley, New York, 2007.
[33] M.A. Green, K. Emery, Solar cell efficiency tables, Prog. Photovolt.: Res. Appl. 1 (1993) 25–29.
[34] I. Perez-Wurfl, L. Ma, D. Lin, X. Hao, M.A. Green, G. Conibeer, Silicon nanocrystals in an oxide matrix for thin film solar cells with 492 mV open circuit voltage, Sol. Energy Mater. Sol. Cells 100 (2012) 65–68.
[35] L. Wu, T. Zhang, Z. Lin, X. Jia, B. Puthen-Veettil, T.C.-J. Yang, H. Xia, G. Conibeer, I. Perez-Wurfl, Silicon nanocrystal photovoltaic device fabricated via photolithography and its current–voltage temperature dependence, Sol. Energy Mater. Sol. Cells 128 (2014) 435–440.
[36] J.-W. Luo, P. Stradins, A. Zunger, Matrix-embedded silicon quantum dots for photovoltaic applications: a theoretical study of critical factors, Energy Environ. Sci. 4 (2011) 2546–2557.
[37] G. Allan, C. Delerue, M. Lannoo, Quantum confinement in amorphous silicon layers, Appl. Phys. Lett. 71 (1997) 1189–1191.
[38] C.D. Lorenz, R.M. Ziff, Precise determination of the critical percolation threshold for the three-dimensional "Swiss cheese" model using a growth algorithm, J. Chem. Phys. 114 (2001) 3659–3661.

5. Summary and Conclusions

Once you have eliminated the impossible, whatever remains, however improbable, must be the truth.

Sherlock Holmes

In the present Doctoral Thesis, the characterization of PECVD-deposited SRON / SiO_2 and SRC / SiC superlattices has been performed. After a proper annealing treatment, the precipitation of size-controlled silicon nanocrystals has been achieved, whose structural, optical and electrical properties have been determined by means of different experimental techniques: TEM, SEM, Raman scattering, XRD, PL, UV-vis optical absorption, $I(V)$ characterization (in dark and under illumination), EL, time-resolved EL, LBIC and Fourier-Transform photocurrent spectroscopy. In addition, light-emitting and photovoltaic devices containing these superlattices have been characterized in order to investigate the viability of size-controlled Si NCs for these optoelectronic applications. Finally, the ideal structural SL parameters for the optimum optoelectronic performance of the analysed devices have been determined, according to the different device functionalities.

The embedding matrix (either silicon oxide or silicon carbide) has been shown to be the most important factor to be taken into account, the Si NC properties strongly depending on the matrix nature. For this reason, we will divide the conclusions in two blocks: Si NC / SiO_2 and Si NC / SiC superlattices. For each block, a list of the most remarkable findings will be given, concerning the different analyses carried out as well as the reported results.

5.1. Si NC / SiO_2 Superlattices

The material characterization of Si NC / SiO_2 superlattices revealed the following facts:

- The silicon oxide matrix has been demonstrated to be an excellent candidate to hold size-controlled Si NCs, correctly acting as vertical size confiner up to 5-nm-thick SRON layers.
- An optimum SRON layer thickness between 3 and 4 nm has been proved to offer excellent size confinement as well as PL emission, whereas the ox-

ide barrier thickness can be reduced down to 1 nm while preserving the SL structure and not implying a great loss of quantum confinement.

- An optimum annealing temperature of 1150 °C has been determined to produce the optimum NC superlattices, from the point of view of both superlattice structure maintenance and crystalline quality.
- Crystalline degree values around 80−90 % have been obtained from an accurate Raman analysis via a phonon confinement model modulated by the NC size distribution, indicating amorphous Si (or suboxide) transition shell (interface between crystalline Si core and oxide matrix) of 1−2 atomic layers.
- The development of a new method to analyze EELS spectra from samples containing Si NCs embedded in different dielectric matrices allowed for retrieving the system structural properties via direct EELS imaging.
- Raman and PL measurements under high hydrostatic pressure were carried out that confirm the luminescence origin in Si NCs from both radiative excitonic recombination and near-edge defects.

Bearing in mind the already exposed considerations, the electrical and electro-optical properties of the superlattices were addressed, whose main results are listed in the following:

- A complete electrical characterization of Si NC SLs-based MIS devices revealed Poole-Frenkel as the dominant charge transport mechanism through Si NC / SiO_2 superlattices.
- Electroluminescence excitation has been hypothesized to be originated from impact ionization of NCs by high-kinetic energy electrons travelling through the overall SL conduction band, resulting in the generation of an electron-hole pair, whose later recombination gives rise to EL emission.
- Since the low probability of having high-energy electrons in a Poole-Frenkel governed system, the obtained EL power efficiencies are low in comparison with other reported values on tunnel-dominated superlattice transport.
- Recombination dynamics is governed by exciton localization, being the reduction of the inter-NC distance (both in the growth or in-plane directions) the origin of instability and thus reduction of the recombination lifetime; in addition, lower crystalline quality of the superlattices also results in the presence of non-radiative centers that decrease the EL decay time and overall yield.
- Although 1-nm-thick barriers and large Si excess present an optimum conduction, intermediate oxide thickness values (∼2 nm) and low Si content (∼12 at.%) present the ideal balance between EL emission and electrical injection.

- The highly insulating behavior of the silicon oxide matrix states a huge drawback for photogenerated charge collection. Consequently, future investigation on Si NC / SiO_2 superlattices must point towards their potential as tunable light emitters.

5.2. Si NC / SiC Superlattices

Regarding the structural and optical characterization of Si NC / SiC superlattices, the following conclusions have been reached:

- In contrast to silicon oxide, the silicon carbide matrix permits Si NC size control and SL maintenance only under a narrow range of structural parameters, the light C atoms being easily diffused throughout the system thus causing structure shrinkage.
- Whereas high Si excesses induce continuous SRC sublayer crystallization and lower ones do not conserve the SL structure, it has been selected $Si_{0.85}C_{0.15}$ as the optimum stoichiometry for controlled NC formation, while partially avoiding Si NC coalescence. In addition, $t_{SRC} \geq 3$ nm and $t_{SRC} = 5$ nm have proved to be necessary for SL structure maintenance.
- Under the optimum conditions, the superlattices present crystalline fractions of ~60 %. The low crystallization of the layers (in comparison with the SiO_2 case) is understood in terms of the large mismatch between crystalline Si and SiC, which induces a high interface energy. This is spontaneously overcome by the creation of two well-separated interfaces, which generates a thick amorphous Si (or substoichiometric SiC) transition layer.
- Light emission studies via PL show an origin related to SiC deep-level defects and internal reflections, which demonstrates the impossibility of determining quantum confinement effects via optical emission; instead, optical absorption has proved to be the adequate technique to extract the optical properties of Si NCs embedded in SiC.
- Reflectance and transmittance measurements can provide information that complements Raman analysis towards the structural and optical characterization of Si NC / SiC superlattices.

The application of the previously studied Si NC / SiC superlattices into a real photovoltaic device led to the following remarks:

- The electrical properties of Si NC / SiC multilayers were exhaustively studied, and variable range hopping (combined with conduction through extended band states) was determined as the dominant charge conduction mechanism taking place within the structure.

- A *p*-*i*-*n* structure was designed to contain Si NC / SiC superlattices as intrinsic absorber layers. A substrate-less (membrane) cell approach was carried out, which allowed the photovoltaic characterization of the NC superlattices alone, while avoiding the Si substrate contribution.

- Even when only a small variation in absorption is observed between devices containing $t_{\mathrm{SRC}} = 3$ or 4 nm, the highest spectral response yielded by the 4-nm-SRC superlattices indicates a most efficient electrical transport in the latter device.

- The low short-circuit current density in comparison with the optically generated current suggests the presence of highly recombinative regions within the Si NC / SiC superlattice stack, also confirmed by the low open circuit voltage as compared to the expected from a standard crystalline Si cell.

- Spectral response measurements indicate an absorption onset near 700 nm, well within the SiC band gap, concluding its NC-related origin. In addition, the spectral response analysis is able to predict the photovoltaic properties of the Si NC superlattices.

- The membrane solar cells containing Si NCs exhibit a conversion efficiency of the order of 10^{-3} %, about 20 times larger than a bulk SiC reference cell, which proves the origin of solar-to-electrical energy conversion mainly coming from the nanostructures.

- The observations indicating the NCs as the absorption centers within the SiC matrix are indeed the first evidence of quantum confinement in Si NCs embedded in SiC matrix.

5.3. Future Approaches for Efficiency Improvement

In summary, the physical characterization of Si NC superlattices in both SiO_2 and SiC matrices allowed determining the ideal structural parameters for an optimum light emission and photovoltaic performance, respectively, the final results being listed in Table 5.1. Nevertheless, the overall efficiencies yielded by these devices are low in comparison with current technology. In order for this material to be competitive in the global energy market, some issues still need to be addressed.

- Since light emission in Si NC / SiO_2 superlattice systems is governed by high kinetic energy carriers, an interesting future approach would be the inclusion of a 20- or 30-nm-thick oxide layer that accelerates carriers and substantially increases the impact ionization probability and, therefore, the overall EL emission efficiency.

Table 5.1.: Summary of the optimum superlattice parameters for light-emission (Si NC / SiO_2) and photovoltaic (Si NC / SiC) applications, as determined from the results achieved during the present Thesis Project.

Matrix	Si-rich Layer Thickness	Barrier Layer Thickness	N	Stoichiometry	T_{ann}
SiO_2	3–4 nm	2–2.5 nm	5	$SiO_{1.1}N_{0.23}$	1150 °C
SiC	4 nm	5 nm	30	$Si_{0.85}C_{0.15}$	1100 °C

- The number of SRON / SiO_2 bilayers has not been accurately investigated. Although current transport is expected to be quenched if the carrier propagating distance of such an insulating material increases, a higher number of luminescent centers will also exist. As a consequence of a larger number of bilayers combined with the previously mentioned accelerating layer, the electroluminescence emission intensity, and thus the light emission efficiency, could be improved.

- Regarding the performance of Si NC / SiC superlattice solar cells, recombination states the most important drawback for photogenerated carrier extraction. The reduction of recombinative regions becomes then crucial to increase the overall cell efficiency. This can be reached, for instance, by attaining a higher crystalline degree of the superlattices, in order to enhance the crystalline Si and crystalline SiC regions.

- The aim of the membrane cell characterization was the study of the NCs photovoltaic response. The next step towards a competitive solar cell device is the implementation of this NC-based SL stack as the top absorber material of an all-tandem Si solar cell which, by means of the proper tunnel junction between both cells, would allow a more efficient absorption of the solar spectrum, and therefore increase the conversion efficiency of commercial crystalline Si solar cells.

- In addition, the study of a top conductive transparent oxide electrode with rare-earth inclusions, not affecting the overall cell structure and then performance, could induce the up-conversion of solar photons of lower energy than the Si band gap, thus leading to an increase of the absorption range of the solar cell.

6. Resum en Català

Des del sorgiment de l'electrònica a mitjan segle XX, el silici ha esdevingut el material més estudiat i empleat en aquest camp. Això és degut a què el Si presenta unes propietats elèctriques i una qualitat cristal·lina excel·lents, a més d'un cost econòmic baix pel que fa a l'obtenció i manipulació del material. Aquesta última propietat deriva de la gran abundància d'aquest element en l'escorça terrestre (és el segon element més abundant després de l'O). Malauradament, la naturalesa indirecta de la banda prohibida del Si comporta una menor probabilitat de les transicions radiatives banda a banda. Les males propietats òptiques del Si van suposar un greu inconvenient per al desenvolupament de l'optoelectrònica i la fotònica, on la manipulació i el control de la llum esdevingueren necessaris. Un exemple d'aquesta afirmació el trobem en l'emissió IR del Si, que el descarta automàticament per aplicacions d'il·luminació visible. D'altra banda, les propietats del Si són gairebé ideals per a aplicacions fotovoltaiques estàndard (on el material absorbent presenta una única banda prohibida), malgrat que l'eficiència d'aquestes cel·les ben aviat va assolir un límit insalvable pel Si massiu.

Durant les dues últimes dècades, la nanoestructuració del Si ha demostrat una millora en les seves propietats òptiques, degut al relaxament de les regles de selecció per les transicions radiatives banda a banda, essent les conseqüències una major energia de banda prohibida i la discretització dels nivells energètics, així com una marcada dependència de dites propietats amb la mida dels nanocristalls de Si (Si NCs) a causa del confinament quàntic que governa dites estructures 0-dimensionals. D'aquesta manera, el Si pot ser utilitzat en aplicacions optoelectròniques. En particular, els Si NCs fan possible sintonitzar l'emissió del silici en la part vermellosa de l'espectre visible. Tanmateix, dites nanoestructures esdevenen candidates com a absorbent d'altes energies dins d'un dispositiu solar de tipus tàndem íntegrament fabricat a partir de Si. Per tant, el potencial dels Si NCs passa pel control de les seves propietats a partir de la manipulació de la seva mida. En aquest aspecte, s'han empleat moltes tècniques per tal de precipitar NCs dins d'una matriu, entre les quals destaca la implantació iònica; no obstant, la lliure difusió de Si impossibilita el control de la mida del nanoagregat. Va ser l'aproximació de superxarxa (SL) la tècnica amb què s'obtingueren resultats interessants i reproduïbles. Aquesta aproximació consisteix en el dipòsit alternat de material estequiomètric i ric en silici (no estequiomètric) basat en Si (com ara SiO_2 o SiC), essent la primera capa la barrera que impedeix la difusió de Si fora de les capes riques en Si. El desenvolupament de les tècniques de dipòsit de capes ultra-primes (pocs nm), com ara el dipòsit de vapor químic, ha permès el control

de la mida mitjana dels NCs fins a 2 nm, així com aconseguir distribucions estretes de mides.

L'objectiu d'aquest Projecte de Tesi és la caracterització de superxarxes de Si NCs dins de matrius dielèctriques de SiO_2 o SiC, per tal d'optimitzar els paràmetres estructurals ideals de les SLs que ofereixen les propietats optoelectròniques i fotovoltaiques més adequades. Amb aquest propòsit, s'han dipositat superxarxes alternant capes riques en Si i estequiomètriques de SiO_2 o SiC sobre substrat de silici o sílice (SiO_2 amorf). A continuació, s'ha dut a terme un recuit a alta temperatura per tal de precipitar i cristal·litzar l'excés de Si en forma de NCs. La preparació del material s'ha realitzat en diverses institucions europees especialitzades: l'*Institut für Mikrosystemtechnik* (IMTEK, Albert-Ludwigs Universität, Freiburg, Alemanya) per l'òxid de silici i l'*Istituto per la Microelettronica e i Microsistemi - Consiglio Nazionalle delle Ricerche* (CNR-IMM, Bologna, Itàlia) per al cas del carbur de silici. De cara a l'estudi de les propietats elèctriques i electro-òptiques del material, dispositius contenint les esmentades SLs varen ser fabricats al *Fraunhofer Institut für Solare Energiesysteme* (ISE, Freiburg, Alemanya). L'estudi de les propietats de les superxarxes de Si NCs, des del punt de vista estructural, òptic, elèctric i electro-òptic, s'ha dut a terme mitjançant les següents tècniques: microscòpia electrònica de transmissió i escombrat (TEM i SEM, respectivament), espectroscòpia de dispersió Raman, difracció de raigs-X (XRD), espectroscòpia de fotoluminescència (PL), espectroscòpia d'absorció UV-visible (reflectància i transmitància), caracterització elèctrica a les fosques i sota il·luminació, espectroscòpia d'electroluminescència (EL), espectroscòpia EL resolta temporalment, espectroscòpia de fotocorrent per Transformada de Fourier i espectroscòpia de corrent induït per feix de llum (LBIC).

El primer bloc del Projecte de Tesi es focalitza en les propietats físiques de superxarxes de Si NCs / SiO_2. La caracterització estructural i òptica han permès determinar les condicions estructurals de la SL que ofereixen la màxima emissió de PL tot mantenint l'estructura de superxarxa. S'ha aconseguit un control d'estructura per capes riques en Si de fins a 5 nm. En particular, els NCs de 3.5 nm exhibeixen l'emissió de PL més intensa i en la part vermella de l'espectre visible. També es va observar que la temperatura de recuit és un paràmetre fonamental per obtenir NCs de mida controlada i alta qualitat cristal·lina, essent 1150 °C la temperatura més adequada per a tal efecte. A partir d'espectres Raman, s'ha utilitzat un model de confinament de fonons (que té en compte la distribució de mides dels NCs) per tal d'avaluar la fracció cristal·lina de les mostres, tot obtenint valors entorn al $80-90$ %, a partir dels quals es dedueix una regió de transició Si / SiO_2 entre 1 i 2 capes atòmiques de gruix. L'origen de l'emissió de PL també s'ha investigat mitjançant mesures de Raman i PL sota alta pressió hidrostàtica, atribuint-se l'emissió resultant a la competència entre la recombinació excitònica radiativa en els NCs i l'emissió d'estats localitzats a la superfície (defectes).

Gràcies a la fabricació d'estructures *p-i-n* on les SLs conformen la capa activa intrínseca, es van poder realitzar mesures elèctriques. S'ha observat que el mecanisme de transport de càrrega dominant és del tipus Poole-Frenkel, mentre que els experiments evidencien que l'excitació dels NCs té lloc per ionització per impacte mitjançant portadors accelerats en la banda de conducció, la seva conseqüent desexcitació originant emissió d'EL. Malgrat la feble emissió obtinguda, l'estudi ha permès determinar els paràmetres ideals per tal d'optimitzar l'eficiència d'EL (aproximadament $\sim 10^{-3}$ %). Especialment, barreres de SiO_2 de 2 nm i excessos de Si no superiors al 15 at.% ofereixen un control estructural ideal acompanyat de la màxima intensitat d'EL aconseguida. En resum, la caracterització completa de superxarxes de Si NCs / SiO_2 ha permès discutir la viabilitat d'aquest material per a aplicacions d'emissió de llum.

En el segon bloc de la Tesi s'han estudiat les propietats de les superxarxes de Si NCs / SiC, com a material candidat per a la part superior d'una cèl·lula solar de tipus tàndem íntegrament fabricada a partir de Si. Degut a què el SiC és una matriu més inestable que el SiO_2, a causa de la major difusió dels àtoms de C, el control de la mida dels NCs és molt més complex. Malgrat tot, la caracterització estructural i òptica de les SLs ha permès establir el rang de variació dels paràmetres estructurals mitjançant els quals és possible mantenir l'estructura de superxarxa i, per tant, confinar la mida dels NCs. S'ha demostrat que continguts de Si en excés massa alts originen la cristal·lització continua de les capes riques en Si, mentre que valors massa baixos no indueixen la precipitació controlada de les nanoestructures, essent $x = 0.85$ (en Si_xC_{1-x}) la composició òptima. Tanmateix, la difusió de C només es pot evitar mitjançant barreres de SiC d'aproximadament 5 nm i capes riques en Si de 3−4 nm, tot mantenint una temperatura de recuit de 1100 °C. Les tècniques de dispersió Raman, XRD i absorció òptica han permès complementar la informació estructural oferta per TEM, i que els paràmetres estructurals de la SL (gruixos de les capes i totals, composició) poden ser determinats combinant dites tècniques. A més, s'ha determinat la fracció cristal·lina del material, entre el 40 i el 60 %; aquests valors tan baixos es deuen a una capa de transició més gruixuda que pel cas del SiO_2. Aquesta regió s'atribueix a l'elevada energia en la interfície Si / SiC, que es tradueix en la formació de dues interfícies de menor energia entremig de les quals existeix l'esmentada regió.

La caracterització elèctrica de les multicapes de Si NCs / SiC ha revelat un mecanisme de transport dominant basat en la conducció a través d'estats extesos dins el sistema. L'estudi de les propietats electro-òptiques de les SLs s'ha dut a terme a partir de la fabricació d'un dispositiu fotovoltaic *p-i-n* sense substrat (dispositiu de membrana). S'ha observat que el dispositiu presenta una gran absorció en la capa activa; en aquest sentit, l'origen d'aquesta absorció, degut als NCs, estableix una prova de confinament quàntic en Si NCs embeguts en una matriu de SiC. Malgrat l'absorció del material, la resposta electro-òptica és ordres de magnitud més feble, la qual cosa s'atribueix a les propietats elèctriques dels NCs.

En particular, les propietats fotovoltaiques del material es veuen reduïdes per la recombinació, que evita l'extracció adequada dels portadors fotogenerats dins el material actiu. Malgrat l'eficiència de conversió dels dispositius fotovoltaics ($\sim 10^{-3}$ %) roman lluny de la comercialització, l'estudi presentat en aquesta Tesi ha permès determinar els paràmetres estructurals ideals d'aquestes superxarxes per tal d'optimitzar la part superior de cel·les solars tipus tàndem íntegrament fabricades a partir de Si.

A. List of Publications as Part of the Present Doctoral Thesis

A.1. Paper Contribution Statement

I hereby declare that the presented articles as part of this Thesis Dissertation contain original results, and that none of these articles have been previously accepted for the award of any other degree or diploma, neither in the University of Barcelona nor in any other collaborating institution. In addition, Tab. A.1 displays the different competencies in which the PhD Candidate has been involved during the preparation of each article.

It should be mentioned here that Papers IV, VII, IX and X (see the next Section A.2) are the ones that accomplish the regulation established by the University of Barcelona regarding article-based Thesis Dissertations. Papers II, III and VIII (published in other high-quality peer-reviewed journals), Papers I, V (Proceedings papers), Paper V (under review in *Physical Review B*) and Paper XI (to be submitted to *Solar Energy Materials and Solar Cells*) are included to concatenate the obtained results along the present Thesis Project.

Table A.1.: Statement of the PhD Candidate contribution to the papers presented as part of the results obtained in this Doctoral Project.

Paper #	I	II	III	IV	V	VI	VII	VIII	IX	X	XI
Sample/Device Design		✓	✓	✓	✓		✓	✓	✓	✓	✓
Experiments	✓	✓	✓		✓	✓	✓	✓	✓	✓	✓
Discussion	✓	✓	✓	✓	✓	✓	✓	✓	✓	✓	✓
Writing	✓	✓	✓	✓		✓	✓	✓	✓	✓	✓
First Author	✓	✓				✓		✓	✓		✓

A.2. List of Articles

In the following, the employed articles as part of the reported results in this Thesis Dissertation are listed, giving information regarding title, authors, journal, volume, initial page, year and the journal impact factor at the time of publication (according to the *Science Citation Index*).

I "Structural and optical characterization of size controlled silicon nanocrystals in SiO_2/SiO_xN_y multilayers", J. López-Vidrier, S. Hernández, A.M. Hartel, D. Hiller, S. Gutsch, P. Löper, L. López-Conesa, S. Estradé, F. Peiró, M. Zacharias and B. Garrido, *Energy Procedia* **10**, 43 (2011). IF: –

II "Annealing temperature and barrier thickness effect on the structural and optical properties of silicon nanocrystals/SiO_2 superlattices", J. López-Vidrier, S. Hernández, D. Hiller, S. Gutsch, L. López-Conesa, S. Estradé, F. Peiró, M. Zacharias and B. Garrido, *Journal of Applied Physics* **116**, 133505 (2014). IF: 2.185

III "Determining the crystalline degree of silicon nanoclusters/SiO_2 multilayers by Raman scattering", S. Hernández, J. López-Vidrier, L. López-Conesa, D. Hiller, S. Gutsch, J. Ibáñez, S. Estradé, F. Peiró, M. Zacharias and B. Garrido, *Journal of Applied Physics* **115**, 43 (2014). IF: 2.185

IV "Retrieving the electronic properties of silicon nanocrystals embedded in a dielectric matrix by low-loss EELS", A. Eljarrat, L. López-Conesa, J. López-Vidrier, S. Hernández, B. Garrido, C. Magén, F. Peiró and S. Estradé, *Nanoscale* **6**, 14971 (2014). IF: 6.739

V "Optical emission from SiO_2-embedded silicon nanocrystals: a high-pressure Raman and photoluminescence study", J. Ibáñez, S. Hernández, J. López-Vidrier, D. Hiller, S. Gutsch, A. Segura, J. Valenta, M. Zacharias and B. Garrido, *Physical Review B* **91**, 035432 (2015). IF: 3.736

VI "Structural, optical and electrical properties of silicon nanocrystals embedded in Si_xC_{1-x}/SiC multilayer systems for photovoltaic applications", J. López-Vidrier, S. Hernández, J. Samà, M. Canino, M. Allegrezza, M. Bellettato, R. Shukla, M. Schnabel, P. Löper, L. López-Conesa, S. Estradé, F. Peiró S. Janz and B. Garrido, *Materials Science and Engineering B* **178**, 639 (2013). IF: 1.846

VII "Silicon nanocrystals in carbide matrix", C. Summonte, M. Allegrezza, M. Bellettato, F. Liscio, M. Canino, A. Desalvo, J. López-Vidrier, S. Hernández, L. López-Conesa, S. Estradé, F. Peiró, B. Garrido, P. Löper, M. Schnabel, S. Janz, R. Guerra and S. Ossicini, *Solar Energy Materials and Solar Cells* **128**, 138 (2014). IF: 5.030

VIII "Charge transport and electroluminescence of silicon nanocrystals/SiO_2 superlattices", J. López-Vidrier, Y. Berencén, S. Hernández, O. Blázquez, S. Gutsch, J. Laube, D. Hiller, P. Löper, M. Schnabel, S. Janz, M. Zacharias and B. Garrido, *Journal of Applied Physics* **114**, 163701 (2013). IF: 2.210

IX "Structural parameters effect on the electrical and electroluminescence properties of silicon nanocrystals/SiO_2 superlattices", J. López-Vidrier, Y. Berencén, S. Hernández, B. Mundet, S. Gutsch, J. Laube, D. Hiller, P. Löper, M. Schnabel, S. Janz, M. Zacharias and B. Garrido, *Nanotechnology* **26**, 185704 (2015). IF: 3.672

X "Charge Transport in Nanocrystalline SiC with and without Embedded Si Nanocrystals", M. Schnabel, M. Canino, S. Künhold, J. López-Vidrier, T. Klugermann, C. Weiss, L. López-Conesa, M. Zschintzsch-Dias, C. Summonte, P. Löper, S. Janz and P. Wilshaw, *Physical Review B* **91**, 195317 (2015). IF: 3.736

XI "Silicon nanocrystals embedded in silicon carbide as a wide-band gap photovoltaic material", J. López-Vidrier, P. Löper, M. Schnabel, S. Hernández, M. Canino, C. Summonte, S. Janz and B. Garrido, *Solar Energy Materials and Solar Cells* **144**, 551 (2016). IF: 5.337.

B. Curriculum Vitae

B.1. Journal Publications

1 "Retrieving the spatial distribution of cavity modes in dielectric resonators by near-field imaging and electrodynamics simulations", A.R. Goñi, F. Güell, L.A. Pérez, J. López-Vidrier, J.O. Ossó, E.A. Coronado and J.R. Morante, *Nanoscale* **4**, 1620 (2011).

2 "Structural and optical characterization of size controlled silicon nanocrystals in SiO_2/SiO_xN_y multilayers", J. López-Vidrier, S. Hernández, A.M. Hartel, D. Hiller, S. Gutsch, P. Löper, L. López-Conesa, S. Estradé, F. Peiró, M. Zacharias and B. Garrido, *Energy Procedia* **10**, 43 (2011).

3 "The NASCENT Project", S. Janz, P. Löper, M. Schnabel, M. Zacharias, D. Hiller, S. Gutsch, A.M. Hartel, C. Summonte, M. Canino, S. Hernández, J. López-Vidrier, B. Garrido, J. Valenta, T. Kubera, M. Foti and C. Geradi, *Proceedings of the 26th European PV Solar Energy Condefernce and Exhibition* (2011).

4 "Structural, optical and electrical properties of silicon nanocrystals embedded in Si_xC_{1-x}/SiC multilayer systems for photovoltaic applications", J. López-Vidrier, S. Hernández, J. Samà, M. Canino, M. Allegrezza, M. Bellettato, R. Shukla, M. Schnabel, P. Löper, L. López-Conesa, S. Estradé, F. Peiró S. Janz and B. Garrido, *Materials Science and Engineering B* **178**, 639 (2013).

5 "Up-conversion effect of Er- and Yb-doped ZnO thin films", M. Lluscà, J. López-Vidrier, A. Antony, S. Hernández, B. Garrido and J. Bertomeu, *Thin Solid Films* **562**, 456 (2014).

6 "Silicon nanocrystals from high-temperature annealing: characterization on device level", P. Löper, M. Canino, J. López-Vidrier, M. Schnabel, F. Schindler, F. Heinz, A. Witzky, M. Bellettato, M. Allegrezza, D. Hiller, A. Hartel, S. Gutsch, S. Hernández, R. Guerra, S. Ossicini, B. Garrido, S. Janz and M. Zacharias, *Physica Satus Solidi A* **210**, 669 (2013).

7 "Charge transport and electroluminescence of silicon nanocrystals/ SiO_2 superlattices", J. López-Vidrier, Y. Berencén, S. Hernández, O. Blázquez, S. Gutsch, J. Laube, D. Hiller, P. Löper, M. Schnabel, S. Janz, M. Zacharias and B. Garrido, *Journal of Applied Physics* **114**, 163701 (2013).

8 "Structural and optical properties of size controlled Si nanocrystals in Si_3N_4 matrix: The nature of photoluminescence peak shift", A. Zelenina, S.A. Dyakov, D. Hiller, S. Gutsch, V. Trouillet, M. Bruins, S. Mirabella, P. Löper, L. López-Conesa, J. López-Vidrier, S. Estradé, F. Peiró, B. Garrido, J. Bläsing, A. Krost, D.M. Zhigunov and M. Zacharias, *Jorunal of Applied Physics* **114**, 184311 (2013).

9 "Investigando las propiedades electro-ópticas de capas delgadas de nitruro de silicio no estequiométrico para aplicaciones fotovoltaicas", O. Blázquez, J. López-Vidrier, S. Hernández, J. Montserrat and B. Garrido, *Ópitca Pura y Aplicada* **46**, 309 (2013).

10 "Abseence of quantum confinement effects in the photoluminescence of Si_3N_4-embedded Si nanocrystals", D. Hiller, A. Zelenina, S. Gutsch, S.A. Dyakov, L. López-Conesa, J. López-Vidrier, S. Estradé, F. Peiró, B. Garrido, J. Valenta, M. Kořinek, F. Trojánek, P. Malý, M. Schnabel, C. Weiss, S. Janz and M. Zacharias, *Journal of Applied Physics* **115**, 204301 (2014).

11 "Electrical and optical characterisation of silicon nanocrystals embedded in SiC", M. Schnabel, P. Löper, M. Canino, S.A. Dyakov, M. Allegrezza, M. Bellettato, J. López-Vidrier, S. Hernández, C. Summonte, B. Garrido, S. Janz and P.R. Wilshaw, *Solid State Phenomena* **205-206**, 480 (2014).

12 "Transport and electroluminescence properties of size-controlled silicon nanocrystals embedded in SiO_2 matrix following the superlattice approach", J. López-Vidrier, Y. Berencén, L. López-Conesa, O. Blázquez, J.M. Ramírez, S. Estradé, F. Peiró, S. Hernández and B. Garrido, *The Electrochemical Society* **61**, 133 (2014).

13 "Electrical and electroluminescence properties of silicon nanocystals/ SiO_2 superlattices", López-Vidrier, Y. Berencén, B. Mundet, S. Hernández, S. Gutsch, D. Hiller, P. Löper, M. Schnabel, S. Janz, M. Zacharias and B. Garrido, *Proceedings of the SPIE Photonics Europe Conference 2014* **1933**, 193331 (2014).

14 "Silicon nanocrystals in carbide matrix", C. Summonte, M. Allegrezza, M. Bellettato, F. Liscio, M. Canino, A. Desalvo, J. López-Vidrier, S. Hernández, L. López-Conesa, S. Estradé, F. Peiró, B. Garrido, P. Löper, M. Schnabel, S. Janz, R. Guerra and S. Ossicini, *Solar Energy Materials and Solar Cells* **128**, 138 (2014).

15 "Determining the crystalline degree of silicon nanoclusters/SiO_2 multilayers by Raman scattering", S. Hernández, J. López-Vidrier, L. López-Conesa, D. Hiller, S. Gutsch, J. Ibáñez, S. Estradé, F. Peiró, M. Zacharias and B. Garrido, *Journal of Applied Physics* **115**, 43 (2014).

16 "Annealing temperature and barrier thickness effect on the structural and optical properties of silicon nanocrystals/SiO_2 superlattices", J. López-Vidrier, S. Hernández, D. Hiller, S. Gutsch, L. López-Conesa, S. Estradé, F. Peiró, M. Zacharias and B. Garrido, *Journal of Applied Physics* **116**, 133505 (2014).

17 "Retrieving the electronic properties of silicon nanocrystals embedded in a dielectric matrix by low-loss EELS", A. Eljarrat, L. López-Conesa, J. López-Vidrier, S. Hernández, B. Garrido, C. Magén, F. Peiró and S. Estradé, *Nanoscale* **6**, 14971 (2014).

18 "Observation of room temperature photoluminescence from asymmetric $CuGaO_2$/ ZnO/ZnMgO multiple quantum well structures", P.M. Aneesh, M.K. Jayaraj, R. Reshmi, R.S. Ajimsha, L.M. Kukreja, A. Antony, F. Rojas, J. Bertomeu, J. López-Vidrier and S. Hernández, *Journal of Nanoscience and Nanotechnology* **15**, 3944 (2015).

19 "Structural parameters effect on the electrical and electroluminescence properties of silicon nanocrystals/SiO_2 superlattices", J. López-Vidrier, Y. Berencén, S. Hernández, B. Mundet, S. Gutsch, J. Laube, D. Hiller, P. Löper, M. Schnabel, S Janz, M. Zacharias and B. Garrido, *Nanotechnology* **26**, 185704 (2015).

20 "Charge Transport in Nanocrystalline SiC with and without Embedded Si Nanocrystals", M. Schnabel, M. Canino, S. Künhold, J. López-Vidrier, T. Klugermann, C. Weiss, L. López-Conesa, M. Zschintzsch-Dias, C. Summonte, P. Löper, S. Janz and P. Wilshaw, *Physical Review B* **91**, 195317 (2015).

21 "Optical emission from SiO_2-embedded silicon nanocrystals: a high-pressure Raman and photoluminescence study", J. Ibáñez, S. Hernández, J. López-Vidrier, D. Hiller, S. Gutsch, A. Segura, J. Valenta, M. Zacharias and B. Garrido, *Physical Review B* **91**, 035432 (2015).

22 "Activation of visible up-conversion luminescence in transparent and conducting ZnO: Er:Yb films by laser annealing", M. Lluscà, J. López-Vidrier, S. Lauzurica, M.I. Sánchez-Aniorte, A. Antony, C. Molpeceres, S. Hernández, B. Garrido and J. Bertomeu, *J. Lumin.* **167**, 101 (2015).

23 "Silicon nanocrystals embedded in silicon carbide as a wide-band gap photovoltaic material", J. López-Vidrier, P. Löper, M. Schnabel, S. Hernández, M. Canino, C. Summonte, S. Janz and B. Garrido, *Solar Energy Materials and Solar Cells* **144**, 551 (2016).

B.2. Book Chapters

1 "*Electrical transport in Si-based nanostructured superlattices*", B. Garrido, S. Hernández, Y. Berencén, J. López-Vidrier, J.M. Ramírez, O. Blázquez and B.

Mundet, in "*Nanotechnology and Photovoltaic Devices: Light Energy Harvesting with Group IV Nanostructures*", edited by J. Valenta and S. Mirabella, Ed. Pan Stanford (2015).

B.3. Conference Contributions

1 "Growth parameters influence on the emission bands of ZnO nanowires", J. López-Vidrier, S. Claramunt, F. Güell, A. Cornet and J.R. Morante, **Poster Presentation**, *Jornada IN^{2}UB*, Barcelona (Spain), 2010.

2 "Growth parameters influence on the emission bands of ZnO nanowires", J. López-Vidrier, S. Claramunt, F. Güell, A. Cornet and J.R. Morante, **Poster Presentation**, *3rd IRUN Symposium on Nanotechnology*, Barcelona (Spain), 2010.

3 "Structural and optical characterization of size controlled silicon nanocrystals in SiO_2/SiO_xN_y multilayers", J. López-Vidrier, S. Hernández, A.M. Hartel, D. Hiller, S. Gutsch, P. Löper, L. López-Conesa, S. Estradé, F. Peiró, M. Zacharias and B. Garrido, **Poster Presentation**, *EMRS (European Materials Research Society) Spring Meeting*, Nice (France), 2011.

4 "(EF)TEM Characterization of photonic nanostructures with applications in tandem solar cells", L. López-Conesa, S. Estradé, A.M. Hartel, M. Zacharias, J. López-Vidrier, S. Hernández, B. Garrido and F. Peiró, **Poster Presentation**, *MSM (Microscopy of Semiconducting Materials)*, Cambridge (United Kingdom), 2011.

5 "Real-space distribution of cavity modes in single ZnO nanowires", F. Güell, A.R. Goñi, J. López-Vidrier, J.O. Ossó, L.A. Pérez, E. Coronado, A. Cornet and J.R. Morante, **Oral Communication**, *CLEO (Conference on Lasers and Electro-Optics) Europe and 12th EQEC (European Quantum Electronics Conference)*, Munich (Germany), 2011.

6 "Correlación teórico-experimental del campo cercano en nanoalambres de ZnO", L.A. Pérez, F. Güell, J. López-Vidrier, J.O. Ossó, A. Cornet, J.R. Morante, A.R. Goñi and E. Coronado, **Oral Communication**, *XVII Congreso Argentino de Fisicoquímica y Química Orgánica*, Córdoba (Argentina), 2011.

7 "Real-space distribution of cavity modes in single ZnO nanowires", A.R. Goñi, F. Güell, J. López-Vidrier, J.O. Ossó, L.A. Pérez, E. Coronado, A. Cornet and J.R. Morante, **Oral Communication**, *PLMCN 11 (11th International Conference on Physics of Light-Matter coupling in Nanostructures)*, Berlin (Germany), 2011.

8 "The NASCENT Project", S. Janz, P. Löper, M. Schnabel, M. Zacharias, D. Hiller, S. Gutsch, A.M. Hartel, C. Summonte, M. Canino, S. Hernández, J.

López-Vidrier, B. Garrido, J. Valenta, T. Kubera, M. Foti, and C. Geradi, **Oral Communication**, *26th EUPVSEC (European PV Solar Energy Condefernce and Exhibition)*, Hamburg (Germany), 2011.

9 "Structural and optical characterization of size controlled silicon nanocrystals for silicon tandem solar cells", J. López-Vidrier, J. Samà, S. Hernández, M. Canino, M. Allegrezza, M. Bellettato, P. Löper, L. López-Conesa, S. Estradé, F. Peiró, C. Summonte and B. Garrido, **Poster Presentation**, *Jornada IN^{2}UB*, Barcelona (Spain), 2011.

10 "Optical properties of SiC_x/SiC multilayers for solar cell applications", J. López-Vidrier, J. Samà, S. Hernández, A.M. Hartel, D. Hiller, S. Gutsch, P. Löper, L. López-Conesa, S. Estradé, F. Peiró, M. Zacharias and B. Garrido, **Poster Presentation**, *Jornada IN^{2}UB*, Barcelona (Spain), 2011.

11 "(EF)TEM Characterization of photonic nanostructures with applications in tandem solar cells", L. López-Conesa, S. Estradé, A.M. Hartel, M. Zacharias, J. López-Vidrier, S. Hernández, B. Garrido and F. Peiró, **Poster Presentation**, *Jornada IN^{2}UB*, Barcelona (Spain), 2011.

12 "Structural, optical and electrical properties of silicon nanocrystals embedded in Si_xC_{1-x}/SiC multilayer systems for photovoltaic applications", J. López-Vidrier, J. Samà, S. Hernández, M. Canino, M. Allegrezza, M. Bellettato, P. Löper, L. López-Conesa, S. Estradé, F. Peiró, C. Summonte and B. Garrido, **Oral Communication**, *EMRS (European Materials Research Society) Spring Meeting*, Strasbourg (France), 2012.

13 "Assessment of the degree of crystallinity of Si-NC/SiO_2 by means of cross-section Raman scattering", J. López-Vidrier, S. Hernández, D. Hiller, A. Hartel, S. Gutsch, M. Schnabel, P. Löper, L. López-Conesa, S. Estradé, F. Peiró, S. Janz, M. Zacharias and B. Garrido, **Poster Presentation**, *EMRS (European Materials Research Society) Spring Meeting*, Strasbourg (France), 2012.

14 "Optical absorption of silicon nanocrystals in silicon carbide matrix", C. Summonte, M. Canino, M. Allegrezza, M. Bellettato, R. Shukla, R. Desalvo, A. Terrasi, S. Mirabella, I. Crupi, S. Janz, P. Löper, M. Schnabel, J. López-Vidrier, L. López-Conesa, S. Hernández, S. Estradé, F. Peiró, B. Garrido and J. Valenta, **Poster Presentation**, *EMRS (European Materials Research Society) Spring Meeting*, Strasbourg (France), 2012.

15 "Silicon quantum dots embedded in SiO_2 for tandem solar cells", J. López-Vidrier, S. Hernández, D. Hiller, A. Hartel, S. Gutsch, M. Schnabel, P. Löper, M. Foti, L. López-Conesa, S. Estradé, F. Peiró, S. Janz, M. Zacharias and B. Garrido, **Oral Communication**, *WoDiM (Workshop in Dielectric Materials)*, Dresden (Germany), 2012.

16 "Near-field imaging and electrodynamics simulations of cavity modes in ZnO nanowire resonators", A.R. Goñi, F. Güell, L.A. Pérez, J. López-Vidrier, J.O. Ossó, E. Coronado and J.R. Morante, **Poster Presentation**, *31st ICPS (International Conference on the Physics of the Semiconductors)*, Zurich (Switzerland), 2012.

17 "Structural and electro-optical properties of silicon-rich silicon oxide superlattices containing silicon nanocrytals for photovoltaic applications", J. López-Vidrier, S. Hernández, O. Blázquez, D. Hiller, S. Gutsch, M. Schnabel, P. Löper, L. López-Conesa, S. Estradé, F. Peiró, S. Janz, M. Zacharias and B. Garrido, **Poster Presentation**, *MRS (Materials Research Society) Fall Meeting*, Boston (United States), 2012.

18 "The NASCENT Project", P. Löper, M. Canino, J. López-Vidrier, M. Schnabel, M. Zacharias, M. Witzky, M. Bellettato, M. Allegrezza, D. Hiller, A. Hartel, S. Gutsch, S. Hernández, J. Valenta, R. Guerra, S. Ossicini, C. Summonte and B. Garrido, **Oral Communication**, *27tt EUPVSEC (European PV Solar Energy Condefernce and Exhibition)*, Frankfurt (Germany), 2012.

19 "Chemical and structural characterization of Si-based electroluminescent and photovoltaic devices through HAADF-EELS", A. Eljarrat, L. López-Conesa, J.M. Ramírez, Y. Berencén, S. Hernández, J. López-Vidrier, S. Estradé, C. Magén, B. Garrido and F. Peiró, **Oral Communication**, *Journées d'EELS*, Aix les Bains (France), 2012.

20 "Si-based electroluminescent and photovoltaic devices: EFTEM-HAADF-EELS characterization", L. López-Conesa, A. Eljarrat, J.M. Ramírez, Y. Berencén, S. Hernández, J. López-Vidrier, S. Estradé, C. Magén, B. Garrido, and F. Peiró, **Oral Communication**, *MSM (Microscopy of Semiconducting Materials)*, Oxford (United Kingdom), 2013.

21 "SiO_x/SiO_2 supperlattices for photovoltaic applications: structural and electro-optical properties", J. López-Vidrier, S. Hernández, O. Blázquez, D. Hiller, S. Gutsch, M. Schnabel, P. Löper, L. López-Conesa, S. Estradé, F. Peiró, S. Janz, M. Zacharias and B. Garrido, **Poster Presentation**, *9th Spanish Conference on Electronic Devices*, Valladolid (Spain), 2013.

22 "Room Temperature Photoluminescence from Symmetric ZnMgO / ZnO / ZnMgO and Asymmetric $CuGaO_2$ / ZnO / ZnMgO Multiple Quantum Well Structures", P.M. Aneesh, M.K. Jayaraj, R. Reshmi, R.S. Ajimsha, L.M. Kukreja, A. Antony, F. Rojas, J. Bertomeu, J. López-Vidrier and S. Hernández, **Poster Presentation**, *Nano India*, Thiruvananthapuram (India), 2013.

23 "Electrical and Optical Characterisation of Silicon Nanocrystals Embedded in SiC", M. Schnabel, P. Löper, M. Canino, S.A. Dyakov, M. Allegrezza, M. Bellettato, J. López-Vidrier, S. Hernández, C. Summonte, B. Garrido, S. Janz and

P.R. Wilshaw, **Oral Communication**, *GADEST (Gettering and Defect Engineering in Semiconductor Technology XV)*, Oxford (United Kingdom), 2013.

24 "Si-based Photonic and photovoltaic devices: a low-loss EELS analysis", L. López-Conesa, A. Eljarrat, J.M. Ramírez, Y. Berencén, S. Hernández, J. López-Vidrier, C. Magén, B. Garrido, S. Estradé, and F. Peiró, **Oral Communication**, *Microscopy at the Frontiers of Science*, Tarragona (Spain), 2013.

25 "Investigating the electro-optical properties of non-stoichiometric silicon nitride thin films for photovoltaic applications", O. Blázquez, J. López-Vidrier, S. Hernández, Y. Berencén and B. Garrido, **Poster Presentation**, *VIII OPTOEL (Reunión española de Optoelectrónica)*, Alcalá de Henares (Spain), 2013.

26 "Determining the crystalline degree of Si-nanocrystals/SiO_2 superlattices"; J. López-Vidrier, S. Hernández, J. Ibáñez, D. Hiller, S. Gutsch, A.M. Hartel, L. López-Conesa, A. Eljarrat, S. Estradé, F. Peiró, M. Zacharias and B. Garrido, **Oral Communication**, *EMRS (European Materials Research Society) Spring Meeting*, Strasbourg (France), 2013.

27 "Structural and Electro-Optical Characterization of Si-Nanocrystals in Carbide and Oxynitride", S. Hernández and J. López-Vidrier, **Oral Communication**, *EMRS (European Materials Research Society) Spring Meeting*, Strasbourg (France), 2013.

28 "Optical properties of silicon nanocrystals under high hydrostatic pressure", S. Hernández, J. López-Vidrier, J. Ibáñez, D. Hiller, S. Gutsch, L. López-Conesa, A. Hartel, S. Estradé, F. Peiró, M. Zacharias and B. Garrido, **Poster Presentation**, *EMRS (European Materials Research Society) Spring Meeting*, Strasbourg (France), 2013.

29 "Space of formation of silicon nanocrystals in silicon carbide", C. Summonte, M. Canino, S. Hernández, J. López-Vidrier, L. López-Conesa, M. Allegrezza, F. Liscio, M. Schnabel, P. Löper, S. Janz, S. Estradé, F. Peiró and B. Garrido, **Poster Presentation**, *EMRS (European Materials Research Society) Spring Meeting*, Strasbourg (France), 2013.

30 "Electro-optical properties of non-stoichiometric silicon nitride films for photovoltaic applications", O. Blázquez, J. López-Vidrier, S. Hernández, J. Montserrat and B. Garrido, **Poster Presentation**, *EMRS (European Materials Research Society) Spring Meeting*, Strasbourg (France), 2013.

31 "Substrate-less photovoltaic devices containing silicon nanocrystals in SiC", J. López-Vidrier, S. Hernández, P. Löper, M. Schnabel, M. Canino, M. Allegrezza, L. López-Conesa, S. Estradé, F. Peiró, S. Janz, C. Summonte and B. Garrido, **Oral Communication**, *SPIE Photonics Europe*, Brussels (Belgium), 2014.

32 "Electrical and electroluminescence properties of silicon nanocrystals/ SiO_2 superlattices", J. López-Vidrier, Y. Berencén, B. Mundet, S. Hernández, S. Gutsch, D. Hiller, P. Löper, M. Schnabel, S. Janz, M. Zacharias and B. Garrido, **Oral Communication**, *SPIE Photonics Europe*, Brussels (Belgium), 2014.

33 "On the origin of the electroluminescence of silicon nanocrystals/ SiO_2 superlattices", J. López-Vidrier, Y. Berencén, S. Hernández, O. Blázquez, S. Gutsch, J. Laube, D. Hiller, P. Löper, M. Schnabel, S. Janz, M. Zacharias and B. Garrido, **Poster Presentation**, *EMRS (European Materials Research Society) Spring Meeting*, Lille (France), 2014.

34 "Membrane cell devices containing silicon nanocrystals in silicon carbide", J. López-Vidrier, P. Löper, M. Schnabel, S. Hernández, M. Canino, L. López-Conesa, S. Estradé, F. Peiró, S. Janz, C. Summonte and B. Garrido, **Oral Communication**, *29th EUPVSEC (European PV Solar Energy Conference and Exhibition)*, Amsterdam (Netherlands), 2014.

35 "Influence of annealing methods on the properties of ZnO:Er:Yb up-converters", M. Lluscà, J. López-Vidrier, I. Sánchez-Aniorte, A. Antony, S. Lauzurica, C. Molpeceres, S. Hernández, B. Garrido and J. Bertomeu, **Poster Presentation**, *EMRS (European Materials Research Society) Spring Meeting*, Lille (France), 2014.

36 "Structural and Electrical Properties of Flexible Ink-jet Printed HfO_2-Based MIM Capacitors after Plasma Treatment", G. Vescio, J. López-Vidrier, O. Casals, S. Hernández, J.D. Prades, B. Garrido and A. Cirera, **Oral Communication**, *EMRS (European Materials Research Society) Spring Meeting*, Lille (France), 2014.

37 "Structural and luminescence properties of silicon-rich oxides and nitrides fabricated by PECVD", J.M. Ramírez, Y. Berencén, J. López-Vidrier, O. Blázquez, S. Hernández, B. Garrido, J. Hurtado, N. Sánchez, T. Ivanova, F. López-Royo and P. Sanchis, **Oral Communication**, *CEN (Conferencia Española de Nanofotónica)*, Santander (Spain), 2014.

38 "Membrane cell devices containing silicon nanocrystals in silicon carbide", J. López-Vidrier, O. Blázquez, S. Hernández, B. Garrido, J. Hurtado, N. Sánchez, T. Ivanova, F. López-Royo, P. Sanchis, **Oral Communication**, *29th EUPVSEC (European PV Solar Energy Conference and Exhibition)*, Amsterdam (Netherlands), 2014.

39 "New strategies in laser processing of TCOs for light management improvement in thin-film silicon solar cells", S. Lauzurica, M. Lluscà, D. Canteli, I. Sánchez-Aniorte, J. López-Vidrier, S. Hernández, C. Molpeceres and J. Bertomeu, **Invited Oral Communication**, *SPIE Optics + Photonics*, San Diego (United States), 2014.

40 "EELS of Si-nanocrystals by hyperspectral segmentation and multivariate factorization", A. Eljarrat, L. López-Conesa, J. López-Vidrier, S. Hernández, S. Estradé, C. Magén, B. Garrido and F. Peiró, **Poster Presentation**, *18th International Microscopy Congress*, Prague (Czech Republic), 2014.

41 "Optoelectronic properties of Si-NCs embedded in a dielectric matrix by low loss EELS", A. Eljarrat, L. López-Conesa, J. López-Vidrier, S. Hernández, S. Estradé, C. Magén, B. Garrido and F. Peiró, **Oral Communication**, *MRS (Materials Research Society) Fall Meeting*, Boston (United States), 2014.

42 "Size-Controlled Silicon Nanocrystal Superlattices for Tandem Solar Cells", B. Garrido, J. López-Vidrier, Y. Berencén, O. Blázquez, J.M. Ramírez and S. Hernández, **Oral Communication**, *Nanospain*, Madrid (Spain), 2014.

43 "Delta-doping approach of SiO_2:Tb:Al by electron beam evaporation", O. Blázquez, J.M. Ramírez, J. López-Vidrier, Y. Berencén, S. Hernández and B. Garrido, **Oral Communication**, *SPIE Microtechnology*, Barcelona (Spain), 2015.

44 "Photoconduction spectroscopy in silicon nanocrystals/SiO_2 superlattices", M. Busquets-Masó, J. López-Vidrier, S. Hernández, O. Blázquez, S. Gutsch, D. Hiller, M. Zacharias and B. Garrido, **Oral Communication**, *EMRS (European Materials Research Society) Spring Meeting*, Lille (France), 2015.

45 "Luminescence of Al^{3+} and Tb^{3+} delta-doped silicon oxide thin films fabricated by electron beam evaporation", O. Blázquez, J.M. Ramírez, J. López-Vidrier, M. Busquets-Masó, L. López-Conesa, S. Hernández, S. Estradé, F. Peiró and B. Garrido, **Oral Communication**, *EMRS (European Materials Research Society) Spring Meeting*, Lille (France), 2015.

46 "Optoelectronic properties of Si-nanocrystals embedded in a dielectric matrix by low-loss EELS", A. Eljarrat, L. López-Conesa, J. López-Vidrier, S. Hernández, S. Estradé, C. Magén, B. Garrido and F. Peiró, **Oral Communication**, *EMRS (European Materials Research Society) Spring Meeting*, Lille (France), 2015.

47 "Structural, vibrational and electronic study of Sb_2S_3 at high pressure", J. Ibáñez, J.A. Sans, O. Gomis, A.L.J. Pereira, C. Popescu, F.J. Manjón, V.P. Cuenca-Gotor, J. López-Vidrier, P. Rodríguez-Hernández, A. Muñoz, J. Pellicer-Porres and A. Segura, **Oral Communication**, *Joint AIRAPT-25 and EHPRG-53 International Conference On High Pressure Science And Technology*, Madrid (Spain), 2015.

B.4. Participation in Research Projects from Public Calls

1 **Title of the project:** PHotonics ELectronics functional Integration on CMOS (HELIOS)

Kind of Program: COOPERATION. ICT. 7th Framework Programme. Information and Communication Technologies
Financing Administration: European Union
Number of the project: FP7-ICT-224312, **Amount:** 222094.00 €, **Duration:** 2008−2012
Number of researchers participating: 21
Main researcher: Prof. Blas Garrido Fernández **Keywords:** Silicon Photonics

2 **Title of the project:** Micro-nanotecnologies i nanoscòpies per dispositius electrònics i fotònics
Kind of Program: Projectes de recerca per potenciar els grups de recerca consolidats
Financing Administration: Agència de Gestió d'Ajuts Universitaris i de Recerca. Generalitat de Catalunya. AGAUR
Number of the project: 2009SGR35, **Amount:** 49920.00 €, **Duration:** 2009−2013
Number of researchers participating: 22
Main researcher: Prof. Albert Cornet Calveras
Keywords: Electron microscopy, polymers, microsystems, photonics, nanotechnology

3 **Title of the project:** Silicon Nanodots for Solar Cell Tandem (NASCEnT)
Kind of Program: COOPERATION. NMP. 7th Framework Programme. Nanosciences, Nanotechnologies, Materials and New Production Technologies
Financing Administration: European Union
Number of the project: NMP4-SL-2010-245977, **Amount:** 275364.00 €, **Duration:** 2010−2013
Number of researchers participating: 7
Main researcher: Prof. Blas Garrido Fernández **Keywords:** Silicon Nanocrystals, Photovoltaics

4 **Title of the project:** Nanopartículas de silicio para la fabricación de células solares tipo tandem
Kind of Program: Energías Convencionales, Alternativas (ENE-CON, ALT) y Fusión Terminuclear (ENE-FTN)
Financing Administration: Spanish Ministry of Science and Innovation
Number of the project: NENE2010-12408-E, **Amount:** 5000.00 €, **Duration:** 2011−2012
Number of researchers participating: 3
Main researcher: Dr. Sergi Hernández Márquez

Keywords: Silicon, renewable energies, solar cells

5 **Title of the project:** Iluminación de estado sólido innovadora e inteligente e interconexiones ópticas a 1.5 micras con fotónica de silicio basada en tecnología CMOS (LEOMIS)
Kind of Program: Tecnologías Electrónicas (MIC) y de Comunicaciones (TEC)
Financing Administration: Spanish Ministry of Economy and Competitiveness
Number of the project: TEC2012-38540-C02-01, **Amount:** 200800.00 €, **Duration:** 2013−2015
Number of researchers participating: 7
Main researcher: Prof. Blas Garrido Fernández
Keywords: Illumination, solid state, rare-earth materials, silicon nanocrystals

6 **Title of the project:** Micro-nanotecnologies i nanoscòpies per dispositius electrònics i fotònics
Kind of Program: Projectes de recerca per potenciar els grups de recerca consolidats
Financing Administration: Agència de Gestió d'Ajuts Universitaris i de Recerca. Generalitat de Catalunya. AGAUR
Number of the project: 2014SGR672, **Amount:** 45000.00 €, **Duration:** since 2014
Number of researchers participating: 27
Main researcher: Prof. Albert Cornet Calveras
Keywords: Electron microscopy, polymers, microsystems, photonics, nanotechnology, graphene, flexible microelectronics

B.5. Research Stays Abroad

Center: Fraunhofer Institute for Solar Energy Systems (ISE)
Place: Freiburg (Germany)
Year: 2013, **Duration:** 3 months (from 1st Sep. to 29th Nov.)
Supervisor: Dr. Stefan Janz
Issue: Characterization of Si NC-based membrane solar cells, and all-Si tandem solar cells, within a *NASCEnT* project collaboration.
Key: Pre-Doctoral stay

Fraunhofer-Institut für Solare Energiesysteme ISE

Institutsleiter
Prof. Dr. Eicke R. Weber

Heidenhofstraße 2
79110 Freiburg

Joana Heizmann
Telefon + 49 (0) 761 4588-5295 | Fax -4588-9295
joana.heizmann@ise.fraunhofer.de
www.ise.fraunhofer.de

Fraunhofer ISE | Heidenhofstraße 2 | 79110 Freiburg

CERTIFICATE OF EMPLOYMENT

With a staff of above 1300, Fraunhofer ISE is the largest solar energy research institute in Europe. The work at the Institute ranges from the investigation of scientific and technological fundamentals for solar energy applications, through the development of production technology and prototypes, to the construction of demonstration systems.

We confirm that Mr. Julià López Vidrier, born on 1986/07/29 in Barcelona Spain, was employed as a visiting scientist during the period from 2013/09/01 to 2013/11/30.

Fraunhofer Institute for Solar Energy Systems ISE
Freiburg, 2013/12/19

Thomas Arnsberg
Head of Human Resources

Joana Heizmann
Human Resources

Fraunhofer-Gesellschaft zur Förderung der angewandten Forschung e.V., München
Vorstand
Prof. Dr.-Ing. habil. Prof. E.h. Dr.-Ing. E.h. mult. Dr. h.c. Reimund Neugebauer, Präsident
Prof. (Univ. Stellenbosch) Dr. rer. pol. Alfred Gossner
Dr. rer. publ. Alexander Kurz

Bankverbindung Deutsche Bank, München
Konto 752193300 **BLZ** 700 700 10
IBAN DE86 7007 0010 0752 1933 00
BIC (SWIFT-Code) DEUTDEMM
USt-IdNr. DE129515865
Steuernummer 143/215/20392

B.6. Other Merits

1 **Merit:** Best Poster Presentation Award
Conference: European Materials Research Society (EMRS), Spring Meeting (2014)
Place: Lille, France
Contribution Title: On the origin of the electroluminescence of silicon nanocrystals / SiO_2 superlattices
Main Author: Julian López-Vidrier
Presented by: Julian López-Vidrier
Symposium: Y – Advanced materials and characterization techniques for solar cells II
Chairs: S. Mirabella, I. Gordon, J. Valenta, R. Turan and H. Atwater

2 **Merit:** Best Oral Presentation Award
Conference: European Materials Research Society (EMRS), Fall Meeting (2015)
Place: Warsaw, Poland
Contribution Title: Optical emission from silicon nanocrystals embedded in SiO_2 under high hydrostatic pressure
Main Author: Sergi Hernández
Presented by: Julian López-Vidrier
Symposium: P – Electronic and optical nature of silicon nanostructures: doping, interface effects and strains
Chairs: D. Hiller, K. Kůsová and D. König

3 **Merit:** Degree of Doctor in Physics (present Thesis Dissertation)
Date: Submitted: April 2015; **Defended**: July 2015
Author: Dr. Julian López-Vidrier
Thesis Advisors: Dr. Sergi Hernández and Prof. Blas Garrido
Examination Board: Dr. Fabrice Gourbilleau (CIMA-LAB – Caen, France), Dr. Rosalía Serna (CSIC – Madrid, Spain) and Juan Daniel Prades (UB – Barcelona, Spain)
Qualification: Excellent *Cum Laude* - International Doctorate Certification

E-MRS 2014 SPRING MEETING

May 26 - 30

EUROPEAN MATERIALS RESEARCH SOCIETY

TO: J. López-Vidrier, Universitat de Barcelona

In recognition of best presentation during EMRS 2014 Symposium Y

Lille, May 2014

Salvo Mirabella	Ivan Gordon	Jan Valenta	Raşit Turan	Harry Atwater
				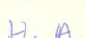

WILEY

Poster Prize

Electronic and Optical Nature of Silicon Nanostructures: Doping, Interface Effects and Strain (Symposium P)

E-MRS Fall Meeting 2015, Warsaw, Poland, September 13-18, 2015

Congratulations!

You won 1 book voucher value of € 150,-

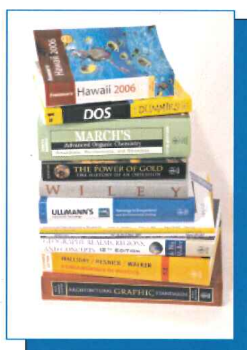

The Prize was won by

Julià López-Vidrier

Weinheim, September 2015

Torben Quasdorf
(4052/3889)
Wiley-VCH Verlag GmbH & Co. KGaA
Weinheim, Germany
www.wiley.com * service@wiley-vch.de

Claiming your prize is easy as 1, 2, 3...

1. Select book(s) at www.wiley.com
2. Find the books you would like up to the value of € 100,-
3. Send the original voucher to Torben Quasdorf with the details of the books you would like us to send you

Universitat de Barcelona

Facultat de Física

Faculty of Physics

CERTIFICATE ATTESTING TO THE SUCCESFUL COMPLETION OF A DOCTORAL DEGREE

I, Atilà Herms Berenguer, Dean of the Faculty of Physics, in accordance with the authority delegated by the Rector on 28 May 2014,

C E R T I F Y: That Julià López Vidrier, born 29 July 1986 in Barcelona (Barcelona), of Spanish nationality, bearer of identity card number 43560542Z, has, on 16 July 2015, successfully completed the studies leading to the award of the official university qualification of

Doctor by the University of Barcelona
The doctoral programme: Physics

and has paid, on 21/07/2015, the fee for the issuance of the certificate.

And to this effect and by request of the interested party, I hereby issue this certificate, which shall hold full validity until the degree certificate is issued.

BARCELONA, 21 July 2015
The Dean

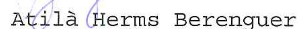

Atilà Herms Berenguer

This document is valid for a period of one year starting on the day it was issued.

Paper ecològic blanquejat sense clor (TCF). Compres UB

Translation

ACADEMIC CERTIFICATE
NID/Passport 43560542
ACADEMIC YEAR 2015-2016

---- UNIVERSITY OF BARCELONA ----

FACULTY OF PHYSICS
DEGREE: DOCTORATE (Royal Decree 1393/2007)
EUROPEAN HIGHER EDUCATION AREA
PROGRAMME: PHYSICS

I, Josep Perelló Palou, Secretary of the Faculty of Physics at the University of Barcelona,

HEREBY CERTIFY: That **JULIÀ LOPEZ VIDRIER,** holder of national identity document / passport number 43560542, was admitted to this degree with the following admission details:

Admission: University Master's Degree in Photonics
University: Universitat Politècnica de Catalunya
Country: Spain

Research period

In order to write the doctoral thesis paper, the doctoral student has enrolled in the research period of the program in the following research line:

Research line
100342 Electronic materials, sensors and micro- and nanosystems

Thesis supervisor
Dr Sergio Hernández Márquez
Department of Electronics
University of Barcelona
Dr Blas Garrido Fernández
Department of Electronics
University of Barcelona

Thesis tutor
Dr Blas Garrido Fernández
Department of Electronics
University of Barcelona

Academic years in which the student has enrolled

2010-2011; 2011-2012; 2012-2013; 2013-2014; 2014-2015

On 30 September 2011, the Monitoring Committee admitted the doctoral thesis paper *Silicon Nanocrystal Superlattices for*

Universitat de Barcelona
Facultat de Física
Secretaria d'Estudiants i Docència

This translation of the original was made by the Language Services of the University of Barcelona

Translation

ACADEMIC CERTIFICATE
NID/Passport 43560542
ACADEMIC YEAR 2015-2016

Light-Emitting and Photovoltaic Devices.

Defence of the doctoral thesis

The student defended the doctoral thesis *Silicon Nanocrystal Superlattices for Light-Emitting and Photovoltaic Devices* on 16 July 2015 and was awarded the grade of Excellent *cum laude*.

The examination board that judged and graded the doctoral thesis was composed of the following members:

CHAIR:
Dr Fabrice Gourbilleau
France (others) CIMA-LAB

MEMBER:
Dr Rosalia Serna Galán
Research centres (SPAIN) Institute of Optics "Daza de Valdés"-(CSIC)

SECRETARY:
Dr Juan Daniel Prades García
Department of Electronics
University of Barcelona

The student paid the fees corresponding to the issue of the certificate on 21 July 2015.

Notes

Qualifications
2014/ On 10 September 2015, the Academic Committee granted the student permission to display the International Doctorate certification on his doctoral degree.

In witness whereof, and by request of the interested party, I hereby issue this certificate.
Barcelona, 30 October 2015
The Secretary

This translation of the original was made by the Language Services of the University of Barcelona

Bibliography

[1] P.Y. Yu and M. Cardona. *Fundamentals of Semiconductors: Physics and Material Properties.* Springer, 4 edition, 2010.

[2] S.M. Sze and K.K. Ng. *Physics of Semiconductor Devices.* Wiley, 3 edition, 2007.

[3] G.E. Moore. Cramming more components onto integrated circuits. *Electronics*, 38(8):1, 2013.

[4] B.E.A. Saleh and M.C. Teich. *Fundamentals of Photonics.* Wiley-VCH, 2 edition, 2010.

[5] L. Pavesi and R. Turan. *Silicon Nanocrystals.* Wiley-VCH, 1 edition, 2010.

[6] Richard Soref. Mid-infrared photonics in silicon and germanium. *Nature Photonics*, 4(August):495–497, 2010.

[7] D. Navarro-Urrios, M. Melchiorri, N. Daldosso, L. Pavesi, C. García, P. Pellegrino, B. Garrido, G. Pucker, F. Gourbilleau, and R. Rizk. Optical losses and gain in silicon-rich silica waveguides containing Er ions. *Journal of Luminescence*, 121(2):249–255, December 2006.

[8] D. Navarro-Urrios, O. Jambois, F. Ferrarese Lupi, P. Pellegrino, B. Garrido, A. Pitanti, N. Prtljaga, N. Daldosso, and L. Pavesi. Si nanoclusters coupled to Er^{3+} ions in a SiO_2 matrix for optical amplifiers. *Optical Materials*, 33(7):1086–1090, May 2011.

[9] S. Furukawa and T. Miyasato. Quantum size effects on the optical band gap of microcrystalline Si:H. *Phys. Rev. B*, 38:5726–5729, Sep 1988.

[10] S. Furukawa and T. Miyasato. Quantum size effects on the optical and electrical properties of microcrystalline Si:H. *Superlattices and Microstructures*, 5(3):317–320, 1989.

[11] S. Furukawa and T. Miyasato. Three-dimensional quantum well effects in ultrafine silicon particles. *Japanese Journal of Applied Physics*, 27(11A):L2207, 1988.

[12] L.T. Canham. Silicon quantum wire array fabrication by electrochemical and chemical dissolution of wafers. *Applied Physics Letters*, 57(10):1046–1048, September 1990.

[13] D.V. Shenai-Khatkhate, R.J. Goyette, R.L. DiCarlo Jr., and G. Dripps. Environment, health and safety issues for sources used in MOVPE growth of compound semiconductors. *Journal of Crystal Growth*, 272:816–821, 2004.

[14] M. López, B. Garrido, C Bonafos, A. Pérez-Rodríguez, and J.R. Morante. Optical and structural characterization of Si nanocrystals ion beam synthesized in SiO_2 : correlation between the surface passivation and the photoluminescence emission. *Solid-State Electronics*, 45:1495–1504, 2001.

[15] T.S. Iwayama, T. Hama, D.E. Hole, and I.W. Boyd. Optical and structural properties of encapsulated Si nanocrystals formed in SiO_2 by ion implantation. *Surface Coatings and Technology*, 159:712–716, 2002.

[16] G. Dalba, N. Daldosso, P. Fornasini, R. Grisenti, L. Pavesi, F. Rocca, G. Franzò, F. Priolo, and F. Iacona. Chemical composition and local structure of plasma enhanced chemical vapor-deposited Si nanodots and their embedding silica matrix. *Applied Physics Letters*, 82(2003):889–891, 2003.

[17] L. Dal Negro, M. Cazzanelli, N. Daldosso, Z. Gaburro, L. Pavesi, F. Priolo, D. Pacifici, G. Franzò, and F. Iacona. Stimulated emission in plasma-enhanced chemical vapour deposited silicon nanocrystals. *Physica E: Low-dimensional Systems and Nanostructures*, 16(3-4):297–308, March 2003.

[18] J. Barreto, J.A. Rodríguez, M. Perálvarez, A. Morales, B. Garrido, and C. Domínguez. Photoluminescence characterization of silicon nanostructures embedded in silicon oxide. *Superlattices and Microstructures*, 43:588–593, 2008.

[19] J. Valenta, N. Lalic, and J. Linnros. Electroluminescence microscopy and spectroscopy of silicon nanocrystals in thin SiO_2 layers. *Optical Materials*, 17:45–50, 2001.

[20] S. Hernández, A. Martínez, P. Pellegrino, Y. Lebour, B. Garrido, E. Jordana, and J.M. Fedeli. Silicon nanocluster crystallization in SiO_x films studied by Raman scattering. *Journal of Applied Physics*, 104(4):044304, 2008.

[21] M. Zacharias, J. Bläsing, P. Veit, L. Tsybeskov, K. Hirschman, and P.M. Fauchet. Thermal crystallization of amorphous Si/SiO_2 superlattices. *Applied Physics Letters*, 74(18):2614–2616, 1999.

[22] M. Zacharias, J. Heitmann, R. Scholz, U. Kahler, M. Schmidt, and J. Bläsing. Size-controlled highly luminescent silicon nanocrystals: A SiO/SiO_2 superlattice approach. *Applied Physics Letters*, 80(4):661, 2002.

[23] D. Song, E.-C. Cho, G. Conibeer, Y. Huang, C. Flynn, and M.A. Green. Structural characterization of annealed $Si_{1-x}C_x/SiC$ multilayers targeting formation of Si nanocrystals in a SiC matrix. *Journal of Applied Physics*, 103(8):083544, 2008.

[24] C. Summonte, M. Allegrezza, M. Bellettato, F. Liscio, M. Canino, A. Desalvo, J. López-Vidrier, S. Hernández, L. López-Conesa, S. Estradé, F. Peiró, B. Garrido, P. Löper, M. Schnabel, S. Janz, R. Guerra, and S. Ossicini. Silicon nanocrystals in carbide matrix. *Solar Energy Materials and Solar Cells*, 128:138–149, September 2014.

[25] A. Zelenina, S.A. Dyakov, D. Hiller, S. Gutsch, V. Trouillet, M. Bruns, S. Mirabella, P. Löper, L. López-Conesa, J. López-Vidrier, S. Estradé, F. Peiró, B. Garrido, J. Bläsing, A. Krost, D.M. Zhigunov, and M. Zacharias. Structural and optical properties of size controlled Si nanocrystals in Si_3N_4 matrix: The nature of photoluminescence peak shift. *Journal of Applied Physics*, 114(18):184311, 2013.

[26] D. Hiller, A. Zelenina, S. Gutsch, S.A. Dyakov, L. López-Conesa, J. López-Vidrier, S. Estradé, F. Peiró, B. Garrido, J. Valenta, M. Kořínek, F. Trojánek, P. Malý, M. Schnabel, C. Weiss, S. Janz, and M. Zacharias. Absence of quantum confinement effects in the photoluminescence of Si_3N_4-embedded Si nanocrystals. *Journal of Applied Physics*, 115(20):204301, May 2014.

[27] E.F. Schubert. *Light-Emitting Diodes*. Cambridge University Press, 2 edition, 2006.

[28] M.R. Krames, M. Ochiai-Holcomb, G.E. Höfler, C. Carter-Coman, E.I. Chen, I.-H. Tan, P. Grillot, N.F. Gardner, H.C. Chui, J.-W. Huang, S.A. Stockman, F.A. Kish, M.G. Craford, T.S. Tan, C.P. Kocot, M. Hueschen, J. Posselt, B. Loh, G. Sasser, and D. Collins. High-power truncated-inverted-pyramid $(Al_xGa_{1-x})_{0.5}In_{0.5}P/GaP$ light-emitting diodes exhibiting $>50\%$ external quantum efficiency. *Applied Physics Letters*, 75(16):2365–2367, 1999.

[29] S. Tanabe, S. Fujita, S. Yoshihara, A. Sakamoto, and S. Yamamoto. YAG glass-ceramic phosphor for white LED (II): Luminescence characteristics. *Proc. of SPIE*, 5941:594112, 2005.

[30] L.Y. Chen, W.-C. Cheng, C.C. Tsai, Y.-C. Huang, Y.-S. Lin, and W.H. Cheng. High-performance glass phosphor for white-light-emitting diodes via reduction of Si-Ce^{3+}:YAG inter-diffusion. *Opt. Mater. Express*, 4(1):121, 2013.

[31] A.J. Steckl, J. Heikenfeld, D.S. Lee, and M. Garter. Multiple color capability from rare earth-doped gallium nitride. *Materials Science and Engineering B: Solid-State Materials for Advanced Technology*, 81:97–101, 2001.

[32] K.P. O'Donnell and V. Dierolf. *Rare-Earth Doped III-Nitrides for Optoelectronic and Spintronic Applications*. Springer, 1 edition, 2010.

[33] G. Franzò, A. Irrera, E.C. Moreira, M. Miritello, F. Iacona, D. Sanfilippo, G. Di Stefano, P.G. Fallica, and F. Priolo. Electroluminescence of silicon nanocrystals in MOS structures. *Appl. Phys. A*, 74:1–5, 2002.

[34] K.S. Cho, N.-M. Park, T.-Y. Kim, K.-H. Kim, G.Y. Sung, and J.H. Shin. High efficiency visible electroluminescence from silicon nanocrystals embedded in silicon nitride using a transparent doping layer. *Applied Physics Letters*, 86(7):071909, 2005.

[35] M. Perálvarez, C. García, M. López, B. Garrido, J. Barreto, C. Domínguez, and J.A. Rodríguez. Field effect luminescence from Si nanocrystals obtained by plasma-enhanced chemical vapor deposition. *Applied Physics Letters*, 89(5):051112, 2006.

[36] A.G. Cullis, L.T. Canham, and P.D.J. Calcott. The structural and luminescence properties of porous silicon. *Journal of Applied Physics*, 82(3):909–965, 1997.

[37] B. Gelloz and N. Koshida. Electroluminescence with high and stable quantum efficiency and low threshold voltage from anodically oxidized thin porous silicon diode. *Journal of Applied Physics*, 88(7):4319–4324, 2000.

[38] Y. Berencén, J.M. Ramírez, O. Jambois, C. Domínguez, J.A. Rodríguez, and B. Garrido. Correlation between charge transport and electroluminescence properties of Si-rich oxide/nitride/oxide-based light emitting capacitors. *Journal of Applied Physics*, 112(3):033114, 2012.

[39] W. Shockley and H.J. Queisser. Detailed Balance Limit of Efficiency of *p-n* Junction Solar Cells. *Journal of Applied Physics*, 32:510–519, 1961.

[40] F. Meillaud, A. Shah, C. Droz, E. Vallat-Sauvain, and C. Miazza. Efficiency limits for single-junction and tandem solar cells. *Solar Energy Materials and Solar Cells*, 90(18-19):2952–2959, November 2006.

[41] M.A. Green, K. Emery, Y. Hishikawa, W. Warta, and E.D. Dunlop. Solar cell efficiency tables (Version 45). *Prog. Photovolt: Res. Appl.*, 23(version 39):1–9, 2015.

[42] G. Conibeer, M. Green, E.-C. Cho, D. König, Y.-H. Cho, T. Fangsuwannarak, G. Scardera, E. Pink, Y. Huang, T. Puzzer, S. Huang, D. Song, C. Flynn, S. Park, X. Hao, and D. Mansfield. Silicon quantum dot nanostructures for tandem photovoltaic cells. *Thin Solid Films*, 516(20):6748–6756, August 2008.

[43] National Center for Photovoltaics (NREL). Basic research-cell efficiencies. `http://www.nrel.gov/ncpv/`.

[44] A. Kitai. *Principles of Solar Cells, LEDs and Diodes*. John Wiley & Sons, 1 edition, 2011.

[45] H.Q. Wang, M. Batentschuk, A. Osvet, L. Pinna, and C.J. Brabec. Rare-earth ion doped up-conversion materials for photovoltaic applications. *Advanced Materials*, 23:2675–2680, 2011.

[46] M. Lluscà, J. López-Vidrier, A. Antony, S. Hernández, B. Garrido, and J. Bertomeu. Up-conversion effect of Er- and Yb-doped ZnO thin films. *Thin Solid Films*, 562:456–461, July 2014.

[47] M.A. Green. Third generation photovoltaics: Solar cells for 2020 and beyond. *Physica E: Low-Dimensional Systems and Nanostructures*, 14:65–70, 2002.

[48] R.R. King, D.C. Law, K.M. Edmondson, C.M. Fetzer, G.S. Kinsey, H. Yoon, R.A. Sherif, and N.H. Karam. 40% efficient metamorphic GaInP/GaInAs/Ge multijunction solar cells. *Applied Physics Letters*, 90(2007):183516, 2007.

[49] E.-C. Cho, S. Park, X. Hao, D. Song, G. Conibeer, S.-C. Park, and M.A. Green. Silicon quantum dot/crystalline silicon solar cells. *Nanotechnology*, 19(24):245201, June 2008.

[50] I. Perez-Wurfl, X. Hao, A. Gentle, D.-H. Kim, G. Conibeer, and M.A. Green. Si nanocrystal *p-i-n* diodes fabricated on quartz substrates for third generation solar cell applications. *Applied Physics Letters*, 95(15):153506, 2009.

[51] D. Di, I. Perez-Wurfl, G. Conibeer, and M.A. Green. Formation and photoluminescence of Si quantum dots in SiO_2/Si_3N_4 hybrid matrix for all-Si tandem solar cells. *Solar Energy Materials and Solar Cells*, 94(12):2238–2243, December 2010.

[52] S. Janz, P. Löper, M. Schnabel, M. Zacharias, D. Hiller, S. Gutsch, A. Hartel, C. Summonte, M. Canino, M. Allegrezza, S. Ossicini, R. Guerra, I. Marri, B. Garrido, S. Hernández, J. López-Vidrier, J. Valenta, T. Kubera, M. Foti, and C. Gerardi. The nascent project. In *Proceedings of the 26th European Photovoltaic Solar Energy Conference and Exhibition*, pages 22–27, September 2011.

[53] M. Rohlfing, P. Krüger, and J. Pollmann. Quasiparticle band-structure calculations for C, Si, Ge, GaAs, and SiC using gaussian-orbital basis sets. *Phys. Rev. B*, 48:17791–17805, Dec 1993.

[54] M.V. Wolkin, J. Jorne, P.M. Fauchet, G. Allan, and C. Delerue. Electronic states and luminescence in porous silicon quantum dots: The role of oxygen. *Phys. Rev. Lett.*, 82:197–200, Jan 1999.

[55] C. Delerue, G. Allan, and M. Lannoo. Theoretical aspects of the luminescence of porous silicon. *Phys. Rev. B*, 48:11024–11036, Oct 1993.

[56] B. Garrido, M. López, O. González, A. Pérez-Rodríguez, J. R. Morante, and C. Bonafos. Correlation between structural and optical properties of Si nanocrystals embedded in SiO_2: The mechanism of visible light emission. *Applied Physics Letters*, 77(20):3143–3145, 2000.

[57] S. Takeoka, M. Fujii, and S. Hayashi. Size-dependent photoluminescence from surface-oxidized si nanocrystals in a weak confinement regime. *Phys. Rev. B*, 62:16820–16825, Dec 2000.

[58] G. Ledoux, J. Gong, F. Huisken, O. Guillois, and C. Reynaud. Photoluminescence of size-separated silicon nanocrystals: Confirmation of quantum confinement. *Applied Physics Letters*, 80(25):4834–4836, 2002.

[59] J. Heitmann, F. Müller, L. Yi, M. Zacharias, D. Kovalev, and F. Eichhorn. Excitons in si nanocrystals: Confinement and migration effects. *Phys. Rev. B*, 69:195309, May 2004.

[60] V.A. Belyakov, V.A. Burdov, R. Lockwood, and A. Meldrum. Silicon Nanocrystals: Fundamental Theory and Implications for Stimulated Emission. *Advances in Optical Technologies*, 2008:1–32, 2008.

[61] M. J. Estes and G. Moddel. Luminescence from amorphous silicon nanostructures. *Phys. Rev. B*, 54:14633–14642, Nov 1996.

[62] M. Luppi and S. Ossicini. *Ab initio* study on oxidized silicon clusters and silicon nanocrystals embedded in SiO_2: Beyond the quantum confinement effect. *Phys. Rev. B*, 71:035340, Jan 2005.

[63] M. Palummo, M. Bruno, O. Pulci, E. Luppi, E. Degoli, S. Ossicini, and R. Del Sole. *Ab-initio* electronic and optical properties of low dimensional systems: From single particle to many-body approaches. *Surface Science*, 601:2696–2701, 2007.

[64] R. Guerra, E. Degoli, and S. Ossicini. Size, oxidation, and strain in small Si/SiO_2 nanocrystals. *Physical Review B*, 80(15):155332, October 2009.

[65] C. Spinella, S. Lombardo, and F. Priolo. Crystal grain nucleation in amorphous silicon. *Journal of Applied Physics*, 84(10):5383–5414, 1998.

[66] M. Zacharias and P. Streitenberger. Crystallization of amorphous superlattices in the limit of ultrathin films with oxide interfaces. *Phys. Rev. B*, 62:8391–8396, Sep 2000.

[67] L. Tsybeskov and P.M. Fauchet. Correlation between photoluminescence and surface species in porous silicon: Low-temperature annealing. *Applied Physics Letters*, 64(15):1983–1985, 1994.

[68] Y. Kanemitsu. Luminescence properties of nanometer-sized si crystallites: Core and surface states. *Phys. Rev. B*, 49:16845–16848, Jun 1994.

[69] Y. Kanemitsu, S. Okamoto, M. Otobe, and S. Oda. Photoluminescence mechanism in surface-oxidized silicon nanocrystals. *Phys. Rev. B*, 55(12):7375–7378, 1997.

[70] M. Zhu, Y. Han, R.B. Wehrspohn, C. Godet, R. Etemadi, and D. Ballutaud. The origin of visible photoluminescence from silicon oxide thin films prepared by dual-plasma chemical vapor deposition. *Journal of Applied Physics*, 83(10):5386, 1998.

[71] J. Heitmann, R. Scholz, M. Schmidt, and M. Zacharias. Size controlled nc-Si synthesis by SiO/SiO_2 superlattices. *Journal of Non-Crystalline Solids*, 299-302:1075–1078, April 2002.

[72] J. Heitmann, F. Müller, M. Zacharias, and U. Gösele. Silicon Nanocrystals: Size Matters. *Advanced Materials*, 17(7):795–803, April 2005.

[73] I.V. Mingarro. Estudio de los mecanismos de nucleación y cristalización en vidrios obtenidos a partir de rocas basálticas canarias. PhD Thesis, 1992.

[74] B.I. Kidyarov. Thermodynamics of crystalline nanonucleus formation from liquid phase. *Journal of Structural Chemistry*, 45(1):S31–S35, 2004.

[75] P.D. Persans, A. Ruppert, and B. Abeles. Crystallization kinetics of amorphous Si/SiO_2 superlattice structures. *Journal of Non-Crystalline Solids*, 102(1-3):130–135, 1988.

[76] G.V.M. Williams, A. Bittar, and H.J. Trodah. Crystallisation and diffusion in progressively annealed a-Ge/a-SiO_x superlattices. *Journal of Applied Physics*, 67:1874, 1990.

[77] M. Zacharias, J. Bläsing, K. Hirschman, L. Tsybeskov, and P.M. Fauchet. Extraordinary crystallization of amorphous Si/SiO_2 superlattices. *Journal of Non-Crystalline Solids*, 266–269, Part 1:640–644, 2000.

[78] F. Iacona, C. Bongiorno, C. Spinella, S. Boninelli, and F. Priolo. Formation and evolution of luminescent Si nanoclusters produced by thermal annealing of SiOx films. *Journal of Applied Physics*, 95(7):3723, 2004.

[79] S. Hernández, J. López-Vidrier, L. López-Conesa, D. Hiller, S. Gutsch, J. Ibáñez, S. Estradé, F. Peiró, M. Zacharias, and B. Garrido. Determining the crystalline degree of silicon nanoclusters/SiO_2 multilayers by Raman scattering. *Journal of Applied Physics*, 115(20):203504, May 2014.

[80] P. Normand, E. Kapetanakis, D. Tsoukalas, G. Kamoulakos, K. Beltsios, J. Van Den Berg, and S. Zhang. MOS memory devices based on silicon nanocrystal arrays fabricated by very low energy ion implantation. *Materials Science and Engineering: C*, 15(1-2):145–147, August 2001.

[81] J. López-Vidrier, S. Hernández, A.M. Hartel, D. Hiller, S. Gutsch, P. Löper, L. López-Conesa, S. Estradé, F. Peiró, M. Zacharias, and B. Garrido. Structural and optical characterization of size controlled silicon nanocrystals in SiO_2/SiO_xN_y multilayers. *Energy Procedia*, 10:43–48, January 2011.

[82] A.M. Hartel, D. Hiller, S. Gutsch, P. Löper, S. Estradé, F. Peiró, B. Garrido, and M. Zacharias. Formation of size-controlled silicon nanocrystals in plasma enhanced chemical vapor deposition grown SiO_xN_y/SiO_2 superlattices. *Thin Solid Films*, 520(1):121–125, October 2011.

[83] J. López-Vidrier, S. Hernández, D. Hiller, S. Gutsch, L. López-Conesa, S. Estradé, F. Peiró, M. Zacharias, and B. Garrido. Annealing temperature and barrier thickness effect on the structural and optical properties of silicon nanocrystals/sio_2 superlattices. *Journal of Applied Physics*, 116(13):133505, 2014.

[84] J. López-Vidrier, S. Hernández, J. Samà, M. Canino, M. Allegrezza, M. Bellettato, R. Shukla, M. Schnabel, P. Löper, L. López-Conesa, S. Estradé, F. Peiró, S. Janz, and B. Garrido. Structural, optical and electrical properties of silicon nanocrystals embedded in Si_xC_{1-x}/SiC multilayer systems for photovoltaic applications. *Materials Science and Engineering: B*, 178(9):639–644, May 2013.

[85] A. Eljarrat, L. López-Conesa, J. López-Vidrier, S. Hernández, B. Garrido, C. Magén, F. Peiró, and S. Estradé. Retrieving the electronic properties of silicon nanocrystals embedded in a dielectric matrix by low-loss EELS. *Nanoscale*, 6:14971–14983, 2014.

[86] D. Hiller, S. Goetze, F. Munnik, M. Jivanescu, J.W. Gerlach, J. Vogt, E. Pippel, N. Zakharov, A. Stesmans, and M. Zacharias. Nitrogen at the Si-nanocrystal/SiO_2 interface and its influence on luminescence and interface defects. *Physical Review B*, 82(19):195401, November 2010.

[87] S. Hernández, P. Miska, M. Grün, S. Estradé, F. Peiró, B. Garrido, M. Vergnat, and P. Pellegrino. Tailoring the surface density of silicon nanocrystals embedded in SiOx single layers. *Journal of Applied Physics*, 114(23):233101, 2013.

[88] H. Richter, Z.P. Wang, and L. Ley. The one phonon raman spectrum in microcrystalline silicon. *Solid State Communications*, 39(5):625–629, 1981.

[89] V. Paillard, P. Puech, M.A. Laguna, R. Carles, B. Kohn, and F. Huisken. Improved one-phonon confinement model for an accurate size determination of silicon nanocrystals. *Journal of Applied Physics*, 86(4):1921–1924, 1999.

[90] G. Faraci, S. Gibilisco, P. Russo, A. Pennisi, and S. La Rosa. Modified Raman confinement model for Si nanocrystals. *Physical Review B*, 73(3):033307, January 2006.

[91] A.K. Arora, M. Rajalakshmi, T.R. Ravindran, and V. Sivasubramanian. Raman spectroscopy of optical phonon confinement in nanostructured materials. *Journal of Raman Spectroscopy*, 38(6):604–617, 2007.

[92] I.F. Crowe, M.P. Halsall, O. Hulko, A.P. Knights, R.M. Gwilliam, M. Wojdak, and A.J. Kenyon. Probing the phonon confinement in ultrasmall silicon nanocrystals reveals a size-dependent surface energy. *Journal of Applied Physics*, 109(8):083534, 2011.

[93] I.H. Campbell and P.M. Fauchet. The effects of microcrystal size and shape on the one phonon raman spectra of crystalline semiconductors. *Solid State Communications*, 58(10):739–741, 1986.

[94] L. Khriachtchev, O. Kilpelä, S. Karirinne, J. Keränen, and T. Lepistö. Substrate-dependent crystallization and enhancement of visible photoluminescence in thermal annealing of Si/SiO_2 superlattices. *Applied Physics Letters*, 78(3):323–325, 2001.

[95] L. Khriachtchev. *Silicon Nanophotonics.* World Scientific Publishing, 4 edition, 2009.

[96] M.J. Madou. *Fundamentals of Microfabrication and Nanotechnology.* CRC Press, 3 edition, 2011.

[97] E. Anastassakis, A. Cantarero, and M. Cardona. Piezo-raman measurements and anharmonic parameters in silicon and diamond. *Phys. Rev. B*, 41:7529–7535, Apr 1990.

[98] T. Bachels and R. Schäfer. Binding energies of neutral silicon clusters. *Chemical Physics Letters*, 324(5-6):365 – 372, 2000.

[99] T. Arguirov, T. Mchedlidze, M. Kittler, R. Rölver, B. Berghoff, M. Först, and B. Spangenberg. Residual stress in si nanocrystals embedded in a SiO_2 matrix. *Applied Physics Letters*, 89(5):053111, 2006.

[100] D. Kovalev, H. Heckler, G. Polisski, and F. Koch. Optical properties of Si nanocrystals. *physica status solidi (b)*, 215(2):871–932, 1999.

[101] T. Shimizu-Iwayama, N. Kurumado, D.E. Hole, and P.D. Townsend. Optical properties of silicon nanoclusters fabricated by ion implantation. *Journal of Applied Physics*, 83(11):6018–6022, 1998.

[102] L. Ding, T.P. Chen, Y. Liu, C.Y. Ng, and S. Fung. Optical properties of silicon nanocrystals embedded in a SiO_2 matrix. *Phys. Rev. B*, 72:125419, Sep 2005.

[103] Dal Negro, L., J.H. Yi, J. Michel, L.C. Kimerling, T.-W.F. Chang, V. Sukhovatkin, and E.H. Sargent. Light emission efficiency and dynamics in silicon-rich silicon nitride films. *Applied Physics Letters*, 88(23):–, 2006.

[104] S. Mirabella, R. Agosta, G. Franzò, I. Crupi, M. Miritello, R. Lo Savio, M.A. Di Stefano, S. Di Marco, F. Simone, and A. Terrasi. Light absorption in silicon quantum dots embedded in silica. *Journal of Applied Physics*, 106(10):103505, 2009.

[105] B. Garrido, M. López, A. Pérez-Rodríguez, C. Garcia, P. Pellegrino, R. Ferré, J. Moreno, J.R. Morante, C. Bonafos, and M. Carrada. Optical and electrical properties of Si-nanocrystals ion beam synthesized in SiO_2. *Nuclear Instruments and Methods in Physics Research Section B: Beam Interactions with Materials and Atoms*, 216:213–221, February 2004.

[106] K. Dohnalová, K. Kůsová, and T. Gregorkiewicz. Silicon quantum dots: surface matters. *J. Phys. Condens. Matter.*, 26(17):173201, 2014.

[107] J. Valenta, M. Greben, S. Gutsch, D. Hiller, and M. Zacharias. Effects of inter-nanocrystal distance on luminescence quantum yield in ensembles of Si nanocrystals. *Applied Physics Letters*, 105(24):243107, 2014.

[108] J.B. Miller, A.R. Van Sickle, R.J. Anthony, D.M. Kroll, U.R. Kortshagen, and E.K. Hobbie. Ensemble brightening and enhanced quantum yield in size-purified silicon nanocrystals. *ACS Nano*, 6(8):7389–7396, 2012. PMID: 22809465.

[109] M.I. Alonso, I.C. Marcus, M. Garriga, A.R. Goñi, J. Jedrzejewski, and I. Balberg. Evidence of quantum confinement effects on interband optical transitions in Si nanocrystals. *Physical Review B*, 82(4):045302, July 2010.

[110] G. Ledoux, O. Guillois, D. Porterat, C. Reynaud, F. Huisken, B. Kohn, and V. Paillard. Photoluminescence properties of silicon nanocrystals as a function of their size. *Phys. Rev. B*, 62:15942–15951, Dec 2000.

[111] B. Delley and E. Steigmeier. Quantum confinement in Si nanocrystals. *Phys. Rev. B*, 47:1397–1400, Jan 1993.

[112] B. Averboukh, R. Huber, K.W. Cheah, Y.R. Shen, G.G. Qin, Z.C. Ma, and W.H. Zong. Luminescence studies of a Si/SiO_2 superlattice. *Journal of Applied Physics*, 92(7):3564–3568, Oct 2002.

[113] A. Puzder, A. Williamson, J. Grossman, and G. Galli. Surface chemistry of silicon nanoclusters. *Phys. Rev. Lett.*, 88:097401, Feb 2002.

[114] S. Godefroo, M. Hayne, M. Jivanescu, A. Stesmans, M. Zacharias, O.I. Lebedev, G. Van Tendeloo, and V.V. Moshchalkov. Classification and control of the origin of photoluminescence from Si nanocrystals. *Nature nanotechnology*, 3(3):174–8, March 2008.

[115] M. Hayne, R. Provoost, M.K. Zundel, Y.M. Manz, K. Eberl, and V.V. Moshchalkov. Electron and hole confinement in stacked self-assembled InP quantum dots. *Phys. Rev. B*, 62(15):324–328, 2000.

[116] M. Hayne, J. Maes, S. Bersier, M. Henini, L. Müller-Kirsch, R. Heitz, D. Bimberg, and V.V. Moshchalkov. Pulsed magnetic fields as a probe of self-assembled semiconductor nanostructures. *Physica B: Condensed Matter*, 346-347:421–427, April 2004.

[117] Y.P. Varshni. Temperature dependence of the energy gap in semiconductors. *Physica*, 34(1):149 – 154, 1967.

[118] L. Viña, S. Logothetidis, and M. Cardona. Temperature dependence of the dielectric function of germanium. *Phys. Rev. B*, 30:1979–1991, Aug 1984.

[119] H. Rinnert, O. Jambois, and M. Vergnat. Photoluminescence properties of size-controlled silicon nanocrystals at low temperatures. *Journal of Applied Physics*, 106(2):023501, 2009.

[120] A.M. Hartel, S. Gutsch, D. Hiller, and M. Zacharias. Fundamental temperature-dependent properties of the Si nanocrystal band gap. *Phys. Rev. B*, 85:165306, Apr 2012.

[121] M. Dovrat, Y. Goshen, J. Jedrzejewski, I. Balberg, and A. Sa'ar. Radiative versus nonradiative decay processes in silicon nanocrystals probed by time-resolved photoluminescence spectroscopy. *Phys. Rev. B*, 69:155311, Apr 2004.

[122] K. Kůsová, L. Ondič, E. Klimešová, K. Herynková, I. Pelant, S. Daniš, J. Valenta, M. Gallart, M. Ziegler, B. Hönerlage, and P. Gilliot. Luminescence of free-standing versus matrix-embedded oxide-passivated silicon nanocrystals: The role of matrix-induced strain. *Applied Physics Letters*, 101(14):143101, 2012.

[123] D.C. Hannah, J. Yang, P. Podsiadlo, M.K.Y. Chan, A. Demortière, D.J. Gosztola, V.B. Prakapenka, G.C. Schatz, U. Kortshagen, and R.D. Schaller. On the origin of photoluminescence in silicon nanocrystals: pressure-dependent structural and optical studies. *Nano letters*, 12(8):4200–5, August 2012.

[124] A.R. Goñi, L.R. Muniz, J.S. Reparaz, M.I. Alonso, M. Garriga, A.F. Lopeandia, J. Rodríguez-Viejo, J. Arbiol, and R. Rurali. Using high pressure to unravel the mechanism of visible emission in amorphous Si/SiO$_x$ nanoparticles. *Physical Review B*, 89(4):045428, January 2014.

[125] W. Paul and G.L. Pearson. Pressure dependence of the resistivity of silicon. *Phys. Rev.*, 98:1755–1757, Jun 1955.

[126] J. López-Vidrier, S. Hernández, D. Hiller, S. Gutsch, L. López-Conesa, S. Estradé, F. Peiró, M. Zacharias, and B. Garrido. Annealing temperature and barrier thickness effect on the structural and optical properties of silicon nanocrystals/SiO$_2$ superlattices. *Journal of Applied Physics*, 116(13):133505, 2014.

[127] L. Pavesi, L. Dal Negro, C. Mazzoleni, G. Franzò, and F. Priolo. Optical gain in silicon nanocrystals. *Nature*, 408(6811):440–4, November 2000.

[128] F. Priolo, G. Franzò, D. Pacifici, V. Vinciguerra, F. Iacona, and A. Irrera. Role of the energy transfer in the optical properties of undoped and Er-doped interacting Si nanocrystals. *Journal of Applied Physics*, 89(1):264–272, 2001.

[129] V. Vinciguerra, G. Franzò, F. Priolo, F. Iacona, and C. Spinella. Quantum confinement and recombination dynamics in silicon nanocrystals embedded in Si/SiO$_2$ superlattices. *Journal of Applied Physics*, 87(11):8165–8173, 2000.

[130] J. López-Vidrier, Y. Berencén, S. Hernández, O. Blázquez, S. Gutsch, J. Laube, D. Hiller, P. Löper, M. Schnabel, S. Janz, M. Zacharias, and B. Garrido. Charge transport and electroluminescence of silicon nanocrystals/SiO$_2$ superlattices. *Journal of Applied Physics*, 114(16):163701, 2013.

[131] J. Frenkel. On pre-breakdown phenomena in insulators and electronic semi-conductors. *Phys. Rev.*, 54:647–648, Oct 1938.

[132] V. Osinniy, S. Lysgaard, V. Kolkovsky, V. Pankratov, and A. Nylandsted Larsen. Vertical charge-carrier transport in Si nanocrystal/SiO$_2$ multilayer structures. *Nanotechnology*, 20(19):195201, May 2009.

[133] J. Valenta and S. Mirabella. *Nanotechnology and Photovoltaic Devices: Light Energy Harvesting with Group IV Nanostructures.* Pan Stanford Publishing, 1 edition, 2014.

[134] K.C. Kao. *Dielectric Phenomena in Solids.* Academic Press, 2004.

[135] S. Takeshita. Modeling of space-charge-limited current injection incorporating an advanced model of the poole-frenkel effect. PhD Thesis, Dec 2008.

[136] P.N. Murgatroyd. Theory of space-charge-limited current enhanced by Frenkel effect. *J. Phys. D: Appl. Phys.*, 3:151–156, Feb 1970.

[137] A.M. Ionescu and H. Riel. Tunnel field-effect transistors as energy-efficient electronic switches. *Nature*, 479(7373):329–37, November 2011.

[138] R.H. Fowler and L. Nordheim. Electron Emission in Intense Electric Fields. *Proc. R. Soc. London, Ser. A*, 119(781):173–181, May 1928.

[139] J.C. Ranuárez, Deen M. J., and Chen C.H. A review of gate tunneling current in MOS devices. *Microelectronics Reliability*, 46:1939–1956, March 2006.

[140] M.P. Houng, Y.H. Wang, and W.J. Chang. Current transport mechanism in trapped oxides: A generalized trap-assisted tunneling model. *Journal of Applied Physics*, 86(3):1488–1491, 1999.

[141] S. Prezioso, A. Anopchenko, Z. Gaburro, L. Pavesi, G. Pucker, L. Vanzetti, and P. Bellutti. Electrical conduction and electroluminescence in nanocrystalline silicon-based light emitting devices. *Journal of Applied Physics*, 104(6):063103, 2008.

[142] N.F. Johnson, H. Ehrenreich, P.M. Hui, and P.M. Young. Electronic and optical properties of III-V and II-VI semiconductor superlattices. *Phys. Rev. B*, 41:3655–3669, Feb 1990.

[143] V. Fiorentini, F. Bernardini, F. Della Sala, A. Di Carlo, and P. Lugli. Effects of macroscopic polarization in III-V nitride multiple quantum wells. *Phys. Rev. B*, 60:8849–8858, Sep 1999.

[144] K. Seeger. *Semiconductor Physics*. Springer, 9 edition, 2004.

[145] B. Abeles and T. Tiedje. Amorphous semiconductor superlattices. *Phys. Rev. Lett.*, 51:2003–2006, Nov 1983.

[146] G. Allan, C. Delerue, and M. Lannoo. Quantum confinement in amorphous silicon layers. *Applied Physics Letters*, 71(9):1189–1191, 1997.

[147] D.J. DiMaria, D.W. Dong, C. Falcony, T.N. Theis, J.R. Kirtley, J.C. Tsang, D.R. Young, F.L. Pesavento, and S.D. Brorson. Charge transport and trapping phenomena in off-stoichiometric silicon dioxide films. *Journal of Applied Physics*, 54(10):5801, 1983.

[148] I. Balberg. Electrical transport mechanisms in three dimensional ensembles of silicon quantum dots. *Journal of Applied Physics*, 110(6):061301, 2011.

[149] A. Marconi, A. Anopchenko, M. Wang, G. Pucker, P. Bellutti, and L. Pavesi. High power efficiency in Si-nc/SiO_2 multilayer light emitting devices by bipolar direct tunneling. *Applied Physics Letters*, 94(22):221110, 2009.

[150] A. Anopchenko, A. Marconi, E. Moser, S. Prezioso, M. Wang, L. Pavesi, G. Pucker, and P. Bellutti. Low-voltage onset of electroluminescence in nanocrystalline-Si/SiO_2 multilayers. *Journal of Applied Physics*, 106(3):033104, 2009.

[151] P. Löper, M. Canino, D. Qazzazie, M. Schnabel, M. Allegrezza, C. Summonte, S.W. Glunz, S. Janz, and M. Zacharias. Silicon nanocrystals embedded in silicon carbide: Investigation of charge carrier transport and recombination. *Applied Physics Letters*, 102(3):033507, 2013.

[152] M. Schnabel, M. Canino, S. Künhold, J. López-Vidrier, T. Klugermann, C. Weiss, L. López-Conesa, M. Zschintzsch-Dias, C. Summonte, P. Löper, S. Janz, and P. Wilshaw. Charge transport in nanocrystalline SiC with and without embedded Si nanocrystals. *Phys. Rev. B*, 91:195317, May 2015.

[153] J.F. Verwey, E.A. Amerasekera, and E.A. Bisschop. The physics of SiO_2 layers. *Rep. Prog. Phys.*, 53:1297–1331, 1990.

[154] D.J. DiMaria, T.N. Theis, J.R. Kirtley, F. L. Pesavento, D.W. Dong, and S.D. Brorson. Electron heating in silicon dioxide and off-stoichiometric silicon dioxide films. *Journal of Applied Physics*, 57(4):1214–1238, 1985.

[155] J. Antula. Hot-electron concept for Poole-Frenkel conduction in amorphous dielectric solids. *Journal of Applied Physics*, 43(11):4663–4668, 1972.

[156] A. Irrera, D. Pacifici, M. Miritello, G. Franzò, F. Priolo, F. Iacona, D. Sanfilippo, G. Di Stefano, and P.G. Fallica. Electroluminescence properties of light emitting devices based on silicon nanocrystals. *Physica E: Low-dimensional Systems and Nanostructures*, 16(3-4):395–399, 2003.

[157] J. López-Vidrier, P. Löper, M. Schnabel, S. Hernández, M. Canino, C. Summonte, S. Janz, and B. Garrido. Silicon nanocrystals embedded in silicon carbide as a wide-band gap photovoltaic material. *Solar Energy Materials and Solar Cells*, 144:551 – 558, 2016.

[158] S. Cosentino, E. Sungur Ozen, R. Raciti, A.M. Mio, G. Nicotra, F. Simone, I. Crupi, R. Turan, A. Terrasi, A. Aydinli, and S. Mirabella. Light harvesting with Ge quantum dots embedded in SiO_2 or Si_3N_4. *Journal of Applied Physics*, 115(4):043103, January 2014.

[159] D. Song, E.-C. Cho, G. Conibeer, C. Flynn, Y. Huang, and M.A. Green. Structural, electrical and photovoltaic characterization of Si nanocrystals embedded SiC matrix and Si nanocrystals/c-Si heterojunction devices. *Solar Energy Materials and Solar Cells*, 92(4):474–481, April 2008.

[160] P. Löper, D. Stüwe, M.S. Künle, M. Bivour, C. Reichel, R. Neubauer, M. Schnabel, M. Hermle, O. Eibl, S. Janz, M. Zacharias, and S.W. Glunz. A Membrane Device for Substrate-Free Photovoltaic Characterization of Quantum Dot Based *P-I-N* Solar Cells. *Advanced Materials*, 24(23):3124–9, June 2012.

[161] M. Canino, C. Summonte, M. Allegrezza, R. Shukla, I.P. Jain, M. Bellettato, A. Desalvo, F. Mancarella, M. Sanmartin, P. Terrasi, P. Löper, M. Schnabel, and S. Janz. Identification and tackling of a parasitic surface compound in SiC and Si-rich carbide films. *Materials Science and Engineering: B*, 178(9):623–629, 2013. Advanced materials and characterization techniques for solar cells.

[162] D.B. Williams and C.B. Carter. *Transmission Electron Microscopy. Part 1: Basics*. Springer, 2 edition, 2009.

[163] N.W. Ashcroft and N.D. Mermin. *Solid State Physics*. Brooks/Cole, 1 edition, 1976.

[164] P. Scherrer. Bestimmung der Grösse und der inneren Struktur von Kolloid-teilchen mittels Röntgenstrahlen. *Nachr. Ges. Wiss. Gött. Math-Phys.*, 2:98–100, 1918.

[165] J. Tauc. Optical properties and electronic structure of amorphous Ge and Si. *Materials Research Bulletin*, 3:37–46, September 1968.

[166] C. Kittel. *Introduction to Solid State Physics*. Wiley, 8 edition, 2004.

[167] S. Wei and M.Y. Chou. Phonon dispersions of silicon and germanium from first-principles calculations. *Phys. Rev. B*, 50:2221–2226, Jul 1994.

[168] S. Adachi. *Properties of Group-IV, III-V and II-VI Semiconductors*. John Wiley & Sons Ltd., 1 edition, 2005.

[169] P. Wurfel. *Physics of Solar Cells: From Basic Principles to Advanced Concepts*. Wiley, 2 edition, 2009.

[170] H. Karttunen, P. Kröger, H. Oja, M. Poutanen, and K.J. Donner. *Fundamental Astronomy*. Springer Verlag, 4 edition, 2003.

[171] C. Petermann, R. Beigang, and P. Fischer. Fourier-transform photocurrent spectroscopy using a supercontinuum light source. *Applied Physics Letters*, 100(6):061108, 2012.

[172] E. Bustarret, M.A. Hachicha, and M. Brunel. Experimental determination of the nanocrystalline volume fraction in silicon thin films from Raman spectroscopy. *Applied Physics Letters*, 52(20):1675–1677, 1988.

[173] J. Ibáñez, S. Hernández, J. López-Vidrier, D. Hiller, S. Gutsch, M. Zacharias, A. Segura, J. Valenta, and B. Garrido. Optical emission from sio_2-embedded silicon nanocrystals: A high-pressure raman and photoluminescence study. *Phys. Rev. B*, 92:035432, Jul 2015.

[174] B. Welber, C.K. Kim, M. Cardona, and S. Rodriguez. Dependence of the indirect energy gap of silicon on hydrostatic pressure. *Solid State Communications*, 17(8):1021 – 1024, 1975.

[175] M. Schnabel, C. Summonte, S.A. Dyakov, M. Canino, L. López-Conesa, P. Löper, S. Janz, and P.R. Wilshaw. Absorption and emission of silicon nanocrystals embedded in SiC: Eliminating Fabry-Pérot interference. *Journal of Applied Physics*, 117(4):045307, 2015.

[176] E. Centurioni. Generalized matrix method for calculation of internal light energy flux in mixed coherent and incoherent multilayers. *Appl. Opt.*, 44(35):7532–7539, Dec 2005.

[177] J.A. Moreno, B. Garrido, P. Pellegrino, C. Garcia, J. Arbiol, J.R. Morante, P. Marie, F. Gourbilleau, and R. Rizk. Size dependence of refractive index of Si nanoclusters embedded in SiO_2. *Journal of Applied Physics*, 98(1):013523, 2005.

[178] S. Gutsch, J. Laube, A.M. Hartel, D. Hiller, N. Zakharov, P. Werner, and M. Zacharias. Charge transport in Si nanocrystal/SiO_2 superlattices. *Journal of Applied Physics*, 113(13):133703, 2013.

[179] S. Hernández, P. Pellegrino, A. Martínez, Y. Lebour, B. Garrido, R. Spano, M. Cazzanelli, N. Daldosso, L. Pavesi, E. Jordana, and J.M. Fedeli. Linear and nonlinear optical properties of Si nanocrystals in SiO_2 deposited by plasma-enhanced chemical-vapor deposition. *Journal of Applied Physics*, 103(6):064309, 2008.

[180] J. López-Vidrier, Y. Berencén, S. Hernández, B. Mundet, S. Gutsch, J. Laube, D. Hiller, P. Löper, M. Schnabel, S. Janz, M. Zacharias, and B. Garrido. Structural parameters effect on the electrical and electroluminescence properties of silicon nanocrystals/SiO_2 superlattices. *Nanotechnology*, 26(18):185704, 2015.

[181] Y. Berencén, R. Wutzler, L. Rebohle, D. Hiller, J.M. Ramírez, J.A. Rodríguez, W. Skorupa, and B. Garrido. Intense green-yellow electroluminescence from Tb^+-implanted silicon-rich silicon nitride/oxide light emitting devices. *Applied Physics Letters*, 103(11):111102, 2013.

[182] N.F. Mott. Conduction in non-crystalline materials. *Philosophical Magazine*, 19:835–852, 1969.

[183] K. Ding, U. Aeberhard, O. Astakhov, U. Breuer, M. Beigmohamadi, S. Suckow, B. Berghoff, W. Beyer, F. Finger, R. Carius, and U. Rau. Defect passivation by hydrogen reincorporation for silicon quantum dots in SiC/SiO_x hetero-superlattice. *Journal of Non-Crystalline Solids*, 358(17):2145–2149, 2012.